Methods, Microstructure and Mudrocks:
Towards an Improved Understanding of Deep-water Mudrocks

Shereef Adebayo Bankole

Submitted for the degree of Doctor of Philosophy

Heriot-Watt University

Institute of Petroleum Engineering
Energy, Geoscience, Infrastructure and Society

July 2018

ABSTRACT

Microstructure controls the petrophysical properties of mudrocks. Knowledge about mudrock microstructure in general is maturing and there is an on-going research field aimed at developing accurate, reliable and fast methods to characterise them.

The focus of this research is on mudrocks from the deep-water setting, which are deposited by three principal processes operating in the deep-water: downslope turbidity currents (turbidites), along-slope bottom currents (contourites) and vertical fall-out from surface suspension (hemipelagites). Distinguishing between these respective deposits is challenging but very important in understanding the deep-water environment in terms of their petroleum systems and reservoir characteristics. Hence, the present research entails methodology development and documenting the microstructure of the three principal sedimentary facies in the deep-water.

Scanning electron microscopy is a common technique for studying mudrock microstructure. An efficient and effective method for analysing grain size of mudrocks was developed, which gives closely comparable results to laser diffraction granulometry. A fast and reliable approach for characterising detailed mudrock microstructure using automated large-area, high-resolution scanning electron microscopy and image processing is also presented. The method is automated, free of human subjectivity and provides robust information on mudrock microstructure. Interestingly, the developed method gives comparable results with a synchrotron x-ray diffraction technique.

Furthermore, the research presents exciting new insights on microstructure of deep-water fine grained sediments. A microfabric model is presented for the deep-water fine grained sediments. Turbidites have pronounced preferred bedding parallel fabric, produced by turbulence and high sedimentation rate, with little or no bioturbation effect. Contourites possess mixed fabric (random - semi random and parallel to the bedding). The mixed fabric is suggested to be developed by weak turbulence (bottom currents) and distortion of the fabric by bioturbation. Hemipelagites are characterised by random and oblique preferred microfabrics, which are produced by absence of current and pervasive bioturbation. The oblique preferred microfabric is suggested to be a product of extensive burrowing, in which grains are aligned along the length of the burrows. Additional important findings are that, depositional processes and sedimentation rate as well as burial depth are the most important controlling factors of microstructure development within the deep-water sediments.

Mudrocks are prevalent is all sedimentary environments. The need for a cleaner source of energy for the 21st century has revolutionized interest in mudrocks, as they are recognised as potential unconventional reservoirs. They are also important in terms of carbon storage, as repositories for nuclear waste and as records of environmental change. The contributions presented on mudrock microstructure in this research are relevant to studying the generality of mudrocks without recourse to their environment and not just restricted to deep-water mudrocks.

ACKNOWLEDGEMENTS

First and foremost, my sincere appreciation is due to Almight Allah (SWT), the lord of the worlds for His countless blessings bestowed on me, for granting me respite till this moment and for seeing me through till the end of the Ph.D programme. All praise is due to Allah Who by His blessings, good things are accomplished.

This research benefitted from the Oversea Scholarship Scheme by the Petroleum Technology Development Fund (PTDF) Nigeria. The management of PTDF are appreciated for the sponsorship. Many thanks to the International Ocean Discovery Programme (IODP) for providing access to the core samples and special thanks to Dr Walter Hale and Alex Wülbers for their support during the core sampling at the IODP repository, University of Bremen, Germany. The staff scientist of expedition 355; Dr Denise Kulhanek and the co-chiefs; Prof. Peter Clift and Prof. Dhananjai Pandey as well as the IODP curator at the Kochi Core Centre, Japan; Dr. Lallan Gupta are well appreciated for providing access to the core samples from expedition 355.

I am very grateful to my Ph.D supervisors; Prof. Dorrik Stow and Dr Jim Buckman for their all-time support, encouragement, patience and guidance. Their relentless efforts and words of encouragement were pivotal to the success of this research. I also appreciate Dr Helen Lever who was the source of my coming to Heriot-Watt University. Her guidance at the beginning of the Ph.D programme is acknowledged. I am always surprised with amazing attribute of Prof. Dorrik. He is such a gentle, down to the earth and a great intellect. I have learnt a great deal of research from him as well as from Jim.

Alastair Reid is appreciated for his kind gesture and most importantly for giving me access to the PVT laboratory to perform some analyses. I equally thank Sean McMenamy, Hugh Barras and Vicky Goodfellow for the access to some of their facilities at the former School of Life Sciences and for their guidance with respect to freeze drying technique. Indeed Vicky is really a good fellow! Tianshen Huang and Dr. Zeyun Jiang are both appreciated for their guidance regarding digital rock physics. Stephen Mitchell of the Department of Biological Science University of Edinburgh is also acknowledge for his guide through critical point drying technique. Manuel Ojeda is remembered for introducing me to low pressure nitrogen gas adsorption. The kindness and good gesture of Dr Mark Curtis of the University of Oklahoma, USA is also praised, especially for milling some of my samples. I cannot forget the support

received from Sally Hamilton at the Rock Mechanic Laboratory, the Enhanced Oil Recovery Group led by Prof. Mehran Soharbi, Dr Lorraine Boak and Dr Helen Lewis. These are good people that have rendered help in the course of my research through one way or the other. Special thanks to the procurement team, IT guys and the staff office at the Institute for making life easy during the programme. Colleagues and friends at Heriot-Watt University: Usman Taura, David Egya, Mustapha Lamorde, Eltazy Khalid, Zayyad Abdul-Baki, Kabeer Akande (Edinburgh University), Abdulati Araibi. Phil Green, Zeinab Smillie, Rachel Brackenridge and others that made my stay at Heriot-Watt University memorable are acknowledged.

This research benefited from Adrian Todd Golden Key Student Fund for sample preparation and in this regard Prof. Patrick Corbett and other members of the award committee are thanked for their initiative. I am grateful to Dr Andreas Busch for providing access to his micrometric gas adsorption facility and for providing the computer work station attached to the SEM facility, which reduced the run time for the pore network simulations and machine learning segmentation performed in this research. Prof. Andrew Aplin of Durham University, David Dewhurst of the Commonwealth Scientific and Industrial Research Organisation (CSIRO) Australia, Prof. Juergen Schieber of the Indiana University, USA, Dr. Maartje Houben, Utrecht University and Dr. Naohisa Nishida of the Tokyo Gakugei Univeristy are gratefully acknowledged for the useful discussions I had with them when I took the bull by the horns to study mudrock microstructure.

Contributions and advice received from Prof. Rudy Wenk and Dr Wenk Voltoloni both from the University of California, Berkeley, USA are well appreciated with respect synchrotron powder diffraction technique. A very big thank goes to Dr. Carlotta Giacobbe, Dr. Jonathan Wright and the people at the Sample Environment at the European Synchrotron Radiation Facility (ESRF), Grenoble, France for making our experience during the beam shifts memorable and for the good quality data acquired. The management of the ESRF are also thanked for their magnanimity in funding my trip to Grenoble to perform the synchrotron X-ray powder diffraction experiment at their facility.

Many thanks to my wife, Faoziyah and children: Aishah, Abdurrahman and Mardiyah for their patience, perseverance, and passion for the past three and half years. The support received from you is greatly acknowledged as it is critical to the success witnessed today. Many thanks to my siblings: Ummu Abdur-rahman, Ummu Fathiah, Dhkirillah and Samsudeen for their support, prayers and care through thick and thin. And my sincere appreciation goes to my parents: Mr

Ashola Solihu Bankole and Mrs Salamat Bankole, for their parental care, kindness, prayers and guidance right from my childhood. And now the time has come for those that have been addressing me as Dr., the doctorate degree has now been accomplished. And lastly, I say I Alihamdulillahi Rabbil Alamin.

DECLARATION STATEMENT

ACADEMIC REGISTRY
Research Thesis Submission

Name*:*	SHEREEF ADEBAYO BANKOLE		
School:	INSTITUTE OF PETROLEUM ENGINEERING		
Version: *(i.e. First, Resubmission, Final)*	FINAL	Degree Sought:	Ph.D Petroleum Geoscience

Declaration

In accordance with the appropriate regulations I hereby submit my thesis and I declare that:

1) the thesis embodies the results of my own work and has been composed by myself
2) where appropriate, I have made acknowledgement of the work of others and have made reference to work carried out in collaboration with other persons
3) the thesis is the correct version of the thesis for submission and is the same version as any electronic versions submitted*.
4) my thesis for the award referred to, deposited in the Heriot-Watt University Library, should be made available for loan or photocopying and be available via the Institutional Repository, subject to such conditions as the Librarian may require
5) I understand that as a student of the University I am required to abide by the Regulations of the University and to conform to its discipline.
6) I confirm that the thesis has been verified against plagiarism via an approved plagiarism detection application e.g. Turnitin.

* *Please note that it is the responsibility of the candidate to ensure that the correct version of the thesis is submitted.*

Signature of Candidate*:*		Date:	

Submission

Submitted By *(name in capitals):*	SHEREEF ADEBAYO BANKOLE
Signature of Individual Submitting:	
Date Submitted:	

For Completion in the Student Service Centre (SSC)

Received in the SSC by *(name in capitals):*			
Method of Submission *(Handed in to SSC; posted through internal/external mail):*			
E-thesis Submitted (mandatory for final theses)			
Signature:		Date:	

CHAPTER 1 – INTRODUCTION

1 Introduction

Muds and mudrocks are a hugely important part of the global sedimentary record. Their microstructure has always been especially challenging to study, in part because of their very small grain size. This thesis, therefore, is firstly concerned with developing new methods and an efficient workflow for the study of mudrock microstructure. Secondly, it focuses on deep-water mudrocks, in particular, and on elucidating the microstructural characteristics of fine-grained turbidites, contourites and hemipelagites. An important challenge, in this respect, is to ascertain whether these characteristics can be applied as a new and reliable means of distinguishing between the deposits of these three different processes.

This introductory chapter gives an overview of what the research entails. It provides the background to the study, the rationale on which it is based and its ultimate importance. It outlines the aims and objectives, the overall research questions and the specific hypotheses to be tested.

1.1 Background of the study

Fine-grained sediments and sedimentary rocks are the most abundant group of sedimentary rock in the Earth's crust (Stow, 1981; Potter, Maynard and Depetris, 2005; Schieber, 2015). They constitute an essential element of petroleum systems by serving as source rocks and seals, as well as reservoirs for shale gas and shale oil. There has been a lack of in-depth study of mudrocks in the past, partly due to their fine grain-size, which is difficult to examine by conventional methods (methods applied to sandstones and carbonates). Conventional optical microscopy, for example, yields limited information about their mineralogy, composition and porosity. In part, the lack of in-depth research with respect to fine-grained sediments can be attributed not only to grain-size but also to their inherent heterogeneity (Aplin and Macquaker, 2011).

Fine-grained sedimentary rocks require laboratory-based analyses, as there are many very small-scale features that cannot be extracted from cores and outcrops in terms of visual inspection alone. Most of the techniques used for textural characterization involve disaggregation of the sediments with dispersant, which may alter the original nature of particles produced through clay flocculation. Thus, textural characterization of fine-grained sediments can yield inappropriate information on the hydrodynamic process involved during their

deposition. Reconstruction of fine-grained sediments depositional microstructures is fraught with a high degree of uncertainty due to post-depositional changes and biogenic activities (Stow and Piper, 1984b). Due to their extremely small grain-size (< 63 μm), understanding the micro to nano-scale features of fine-grained sedimentary rocks requires high resolution microscopy such as transmission electron microscopy (TEM) and scanning electron microscopy (SEM). Analysis of micron to submicron features of fine-grained sediments including pores, grain to grain relationship (grain fabric), and grain orientation among others, are essential for complete microstructural microstructural characterization.

Many previous works on fine-grained sediments have concentrated on organic rich mudrocks commonly known as black shale. This is not unexpected, given their economic importance with respect to hydrocarbon exploration and production. However, organic rich mudrocks constitutes a very small percentage of the total amount of fine-grained sediments in the geological record (Schieber, 2003), hence, efforts which are concentrated on organic rich fine-grained sediments only accounts for a fraction of mudrocks. Owing to the abundance of mudrocks in the geological records, a good reconstruction of the Earth history requires putting fine-grained sedimentary rocks into consideration, as this will engender better interpretation of the sedimentological record. Recent awareness of the importance of fine-grained sediments with respect to shale gas development (Bowker, 2007; Loucks *et al.*, 2009; Abouelresh and Slatt, 2011; Slatt, 2011) and recognition of mudrocks as a potential repository for long term storage of radionuclide materials from nuclear plants (Houben *et al.*, 2014; Hemes *et al.*, 2015) have initiated greater interest in studying fine-grained sedimentary rocks in detail.

Much research has been carried out on mudrock depositional processes (e.g Schieber, Southard and Thaisen, 2007; Abouelresh and Slatt, 2011; Schieber, 2011; Hints *et al.*, 2014; Schieber, 2014), controls of microfabric (e.g Moon and Hurst, 1984; Aplin *et al.*, 2006; Day-Stirrat *et al.*, 2010; Day-Stirrat, 2014), porosity and permeability (e.g Dewhurst, Yang and Aplin, 1999; Yang and Aplin, 2007; Loucks *et al.*, 2009; Curtis *et al.*, 2010; Yang and Aplin, 2010; Chalmers, Ross and Bustin, 2012; Curtis *et al.*, 2012a; Casey *et al.*, 2013; Houben, Desbois and Urai, 2013; Houben *et al.*, 2014; Hemes *et al.*, 2015; Zhang *et al.*, 2015), as well as compaction and diagenesis (e.g Matenaar, 2002; Aplin, Matenaar and van der Pluijm, 2003; Lash and Blood, 2004; Nygard *et al.*, 2004; Aplin *et al.*, 2006; Mondol *et al.*, 2007). In recent years there has been a paradigm shift in understanding the detailed features of mudrocks from a nanometre to micrometre scale (e.g Loucks *et al.*, 2009; Wirth, 2009; Curtis *et al.*, 2012b;

Silin and Kneafsey, 2012; Camp, Diaz and Wawak, 2013; Clarkson *et al.*, 2013; Keller *et al.*, 2013); however, studies targeted on microstructure of specific depositional setting or process are rare. In this research, focus is centered upon the microstructure of mudrocks within the deep-water setting. Limited efforts in the past have focused on clay particle orientation (clay fabric) of deep-water fine-grained rocks. However, clay orientation is a subset of microstructure and those efforts contain inconclusive, controversial and debatable conclusions (Ochoa, Wolak and Gardner, 2013; Kase *et al.*, 2016; Nishida, 2016).

Microstructure is an important feature in sediments that can be studied in detail from small samples. This feature is partly controlled by depositional style and is also affected by diagenesis. It is a recognised fact that microstructural characteristics of a rock are a strong determinant of their porosity and permeability (Davies *et al.*, 1991; Hildenbrand and Urai, 2003; Loucks *et al.*, 2009; Klaver *et al.*, 2012; Hemes *et al.*, 2013). Studying the variation in porosity of mudrocks within the deep-water setting is aimed at putting into sharp focus the understanding of migration of fluids in rocks from this depositional setting. This information can help provide significant insight to the expulsion of hydrocarbon from the source rock.

Porosity and permeability which are the most important physical parameters that constrain fluid movement within the reservoir, are closely linked with the microstructural characteristics of the rock. Numerical simulation of fluid flow of stored carbon requires porosity and permeability values as key modelling inputs. Hence, research involving microstructural study of rock is relevant to contemporary issues such as development of unconventional reservoirs, understanding the sealing capacity of cap rock, carbon sequestration and transportation of radioactive waste materials within their repository.

In the deep-water setting, there are three principal mechanisms by which sediments can be deposited (Figure 1.1): vertical settling from suspension (hemipelagite and pelagite), bottom currents (contourite) and turbidity currents (turbidites). Many deep-water successions occur as a complex association of these different facies, and may be challenging to interpret. Efforts have been made in the past to propose models and put forward criteria for the recognition of hemipelagites (e.g Stow and Tabrez, 1998), contourites (e.g Stow, 1979; Gonthier, Faugères and Stow, 1984; Stow *et al.*, 1998; Stow *et al.*, 2002b; Stow and Faugères, 2008) and fine turbidites (e.g Stow, 1979; Stow and Piper, 1984a; Dean, Leinen and Stow, 1985; Stow and Omoniyi, 2018). Aside from the numerous conflicting models in the literature (Rebesco *et al.*, 2014; Nishida, 2016), differentiating among deep-water sediments is challenging

(Shanmugam, 2000; Ochoa, Wolak and Gardner, 2013) especially in core where features are hard to observe (Nishida, 2016). Despite the numerous published papers on microstructural characteristics of mudrocks, such studies on deep-water fine-grained sediments microstructure are rare and with an exception of few studies that present conflicting and controversial results (Bennett, Bryant and Keller, 1981; O'Brien, 1987; Shephard and Rutledge, 1991; Reynolds and Gorsline, 1992; Kawamura and Ogawa, 2004; Ochoa, Wolak and Gardner, 2013). Recent advances in electron microscopy have greatly contributed to the understanding of composition and microfabric of fine-grained sediments at both a micro-scale and the nano-scale (Camp, Diaz and Wawak, 2013).

Most studies on microstructure of deep-water were carried out when scanning electron microscope techniques were less advanced (e.g O'Brien, Nakazawa and Tokuhashi, 1980; Bennett, Bryant and Keller, 1981; Shephard and Rutledge, 1991). The early methods for preparation of samples for scanning electron microscopy generally used inadequate drying techniques and presented broken surfaces for examination. These often incurred sample (and fabric) shrinkage and suffered from substantial surface roughness, both of which have a significant negative effect on observed microstructural characteristics. Sample preparation for microstructural studies is paramount in order to preserve the original fabric at deposition (Schieber, 2015). Currently, the best method for preparing samples for microstructural studies is through the use of argon or gallium ion milling as this preserves the original fabric and it is associated with limited surface roughness (Erdman and Drenzek, 2013; Schieber, 2015). Several more recent studies aimed at differentiating the muddy sediments within the deep-water setting adopted the broken surface sample preparation technique and hence the results from such studies are believed to be inconclusive and controversial (e.g Ochoa, Wolak and Gardner, 2013; Kase *et al.*, 2016; Nishida, 2016).

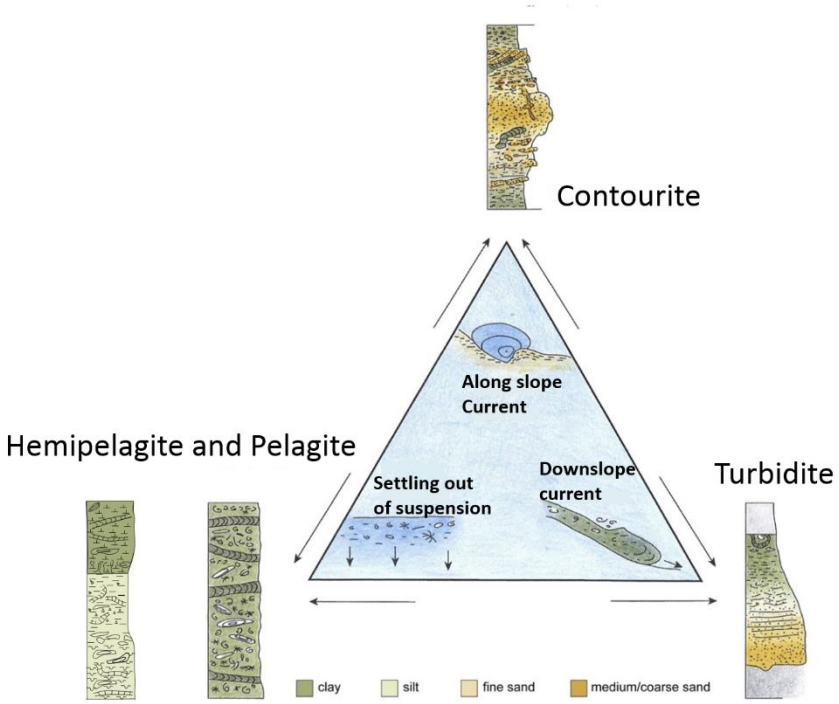

Figure 1.1. Ternary diagram showing the three main sedimentary deposits within the deep sea and their depositional facies model (Modified after, Rebesco *et al.*, 2014)

1.2 Statement of problems

In the present day, exploiting hydrocarbon production from unconventional reservoirs remains an on-going discussion in both the oil industry and global scientific community. In the United State of America, unconventional reservoirs have been recognised since the 1970s, with significant production from 2005 (Wang and Krupnick, 2013). The recognition of untapped unconventional resources in countries such as Canada, Poland, Argentina and others currently benefits from the experiences of the United States of America (Graham, Rupp and Schenk, 2015).

Unconventional hydrocarbon occurs in shale and tight sandstone, both of which are characterized by exceedingly small-scale pores (micrometre to nanometre scale) and low permeability. The importance of mudrocks is manifold as they do not only serve as unconventional reservoirs but also as source rocks and seals in petroleum systems. They hold an important history of the processes occurring at the earth's surface, and of the paleoclimate and paleoenvironment (Schieber and Zimmerle, 1998). They have been recognised as a potential repository for nuclear waste disposal and as a safe place to store unwanted carbon dioxide (carbon sequestration). Because of the foregoing importance, much effort on mudrock

research is concentrated on understanding their microstructural characteristics. This is a key property that controls pore connectivity and permeability in rocks. Despite this growing interest, the knowledge of mudrock microstructure is still sparse (Camp, Diaz and Wawak, 2013) and there are on-going efforts to address the implication of microstructure on geomechanical properties of mudrocks as well as on fluid migration within them.

As an emerging field, microstructural studies are replete with several issues. One such issue that is unresolved to date, is upscaling observed features from the smallest scale of observation to the largest scale. A good starting point to address the upscaling problem is to completely quantify features at the nanometre to micrometre scale. The scanning electron microscopy imaging technique forms a direct method of visualizing micron to submicron features. The technique has revealed that mudrocks are not homogeneous as preconceived in the past but highly heterogeneous (Macquaker and Howell, 1999; Macquaker and Jones, 2002). However, most SEM images are restricted to few hundred to thousand square micrometres, which are not likely to be fully representative of any given mudrock at the centimetre scale.

Recently large high-resolution SEM images of mudrocks have been acquired to accentuate wider features than obtained in the past (Lemmens and Richards, 2013; Bankole *et al.*, 2016) as a methodology for solving issues related with representativeness of sample but more work is still required. There is desirability to match features e.g. porosity from imaging techniques with results from experimental methods (Houben *et al.*, 2016). Intuitively, scale of observation in modelling physical parameters of rocks varies from the nanometre scale, to micrometre scale, to borehole scale and to seismic scale (Figure 1.2). As it stands there is no unique technique that reconciles all the different scales of observation. The upscaling problem is likely to be due to resolution differences in the equipment or techniques used and the heterogeneity that is naturally present in mudrocks. Even at a nanoscale to micrometre scale heterogeneity in mudrocks is prominent (Bernard *et al.*, 2010; Silin and Kneafsey, 2012; Reed, Loucks and Ruppel, 2014). In addition, variation in sedimentary structures at a centimetre scale such as lamination and bioturbation are not unusual in mudrocks. The heterogeneity in mudrocks at different scales is partly due to the fact that there exist compositional variation in the amount of quartz, feldspar, organic matter, carbonate, clay minerals, pyrite and other minerals that have been identified in them (Macquaker and Jones, 2002; Loucks *et al.*, 2009; Bernard *et al.*, 2012).

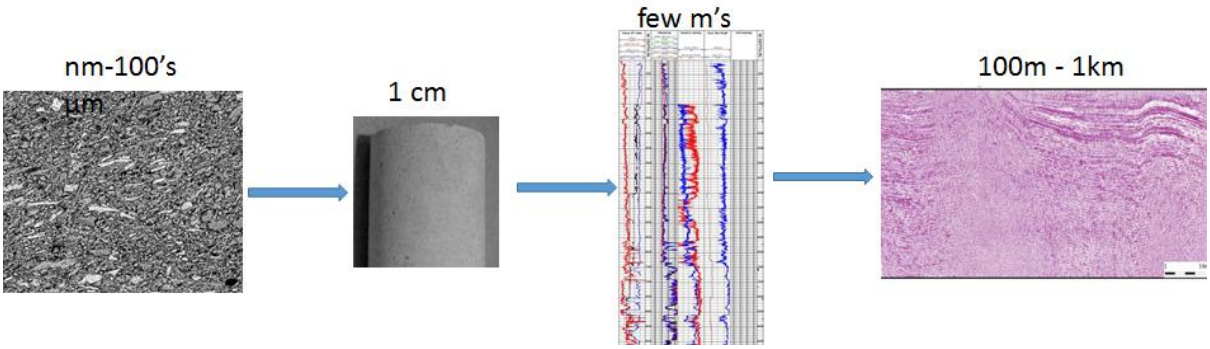

Figure 1.2. The cartoon above presents different scales at which petrophysical observation can be made starting from SEM image of small area to experiment on core sample to well log and seismic section.

Mudrocks contain fine-grained particles (≤ 63 µm) and most of the standard techniques for studying the coarser particles are not appropriate for studying them. Techniques to study the microstructure of mudrocks is now evolving but there is generally a lack of standardization. For example, studying pore size and distribution within fine-grained sediment is achieved through direct visualisation (imaging by SEM and TEM) or through indirect means (nuclear magnetic resonance (NMR), neutron scattering, mercury intrusion porosimetry (MIP), helium porosimetry and gas adsorption among others). There is a wide range in resolution among all the techniques (Figure 1.3) and this makes their results difficult to compare and compounds the methodological problems.

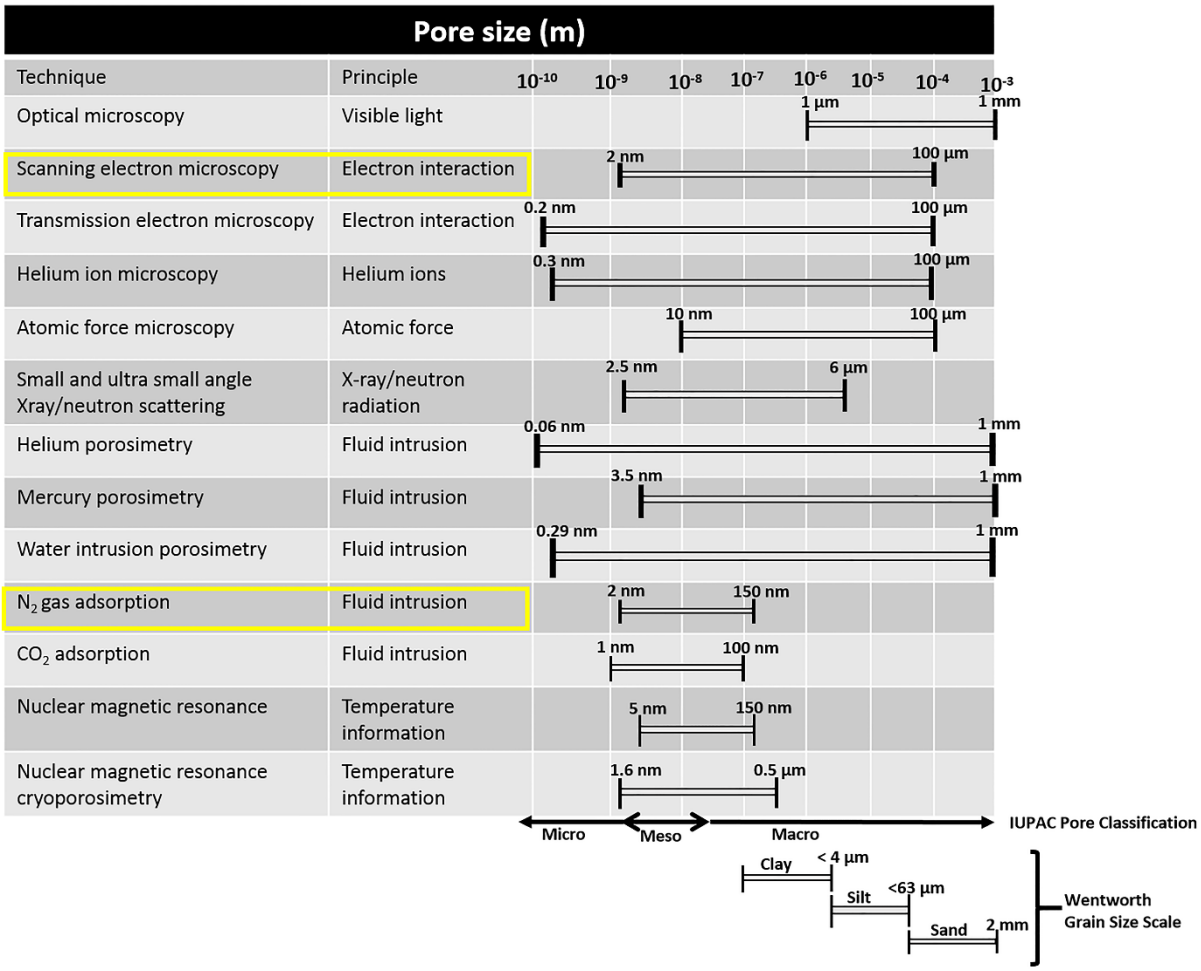

Figure 1.3. Direct and indirect methods of measuring pores sizes and their resolution. The techniques used in this study are highlighted with rectangular boxes.

Mudrock microstructure, being a new field of study, is fraught with methodological problems and standardisation of existing techniques. Hence, the current research aims to advance our understanding of mudrock microstructure by developing new techniques for analysing mudrock microstructure, especially through automated scanning electron microscopy. It also aims to advance our knowledge of deep-water sediments and processes by focusing on the three principal deep-water facies – turbidites, contourites and hemipelagites.

1.3 Aims and objectives

The overall aims of this research is twofold: (1) to develop a new methodology and efficient workflow applicable to mudrock microstructure studies; and (2) to compare the microstructural characteristics of sediments deposited through turbidity currents (turbidites), along slope bottom currents (contourites) and those that settle out of suspension through hemipelagic

sedimentation (hemipelagites). The research questions that are attached to addressing the overall aims of the thesis include:

(1) What is the most efficient and effective method of studying mudrock microstructure?
(2) Does grain-size have any effect on microstructure of fine-grained sediments?
(3) Is there any relationship between microstructure and depositional process within the deep-water setting?
(4) Does mineralogical composition have any effects on microstructure?
(5) Is there any quantifiable effect of depth and physical compaction on microstructural development especially at depths less than 1000 m?

The key objectives associated with these aims and basic questions are highlighted as follows:

(1) To carefully review relevant literature on mudrock microstructure and more importantly those that are aimed at linking microstructure to depositional processes.
(2) To review extensively the methodology in use and the best practice in studying microstructural characteristics of fine grained sediments and sedimentary rocks.
(3) To design a workflow for analyzing microstructure of fine-grained sedimentary rocks.
(4) To investigate the effect of grain-size, sedimentation rate and mineralogy on microstructure of fine-grained sediments.
(5) To attempt to distinguish among turbidites, hemipelagite and contourites based on their microstructure.
(6) To elucidate the impact of burial (depth not more than 1000 m) and mechanical compaction on microstructural changes.

1.4 Research hypothesis

To effectively achieve the research aim and objectives mentioned above, statistical analyses are incorporated and a series of null hypotheses are set out which are to be tested against specific objectives of the research. The null hypotheses are:

(1) Variation in grain-size has no significant effect on microstructure of fine-grained sediments.
(2) Mineralogical composition does not affect mudrock microstructure.
(3) Variation in sedimentation rate does not cause modification of mudrock microstructure.
(4) There is no significant difference in microstructure among the various fine-grained sediment facies in the deep-water setting.

(5) Burial depth and physical compaction have no significant effect on mudrock microstructure at burial depths of less than 1000 m.

1.5 Significance of the research

Microstructural study of fine-grained sedimentary rocks has been intensified by the need to understand the physical properties of mudrocks owing to shale gas development around the world. Microstructure is so important because it is a key feature that controls pore properties such as pore size, pore connectivity and rock permeability. Significant hydrocarbon has been recognized in deep-water settings (Shanmugam, 2000; Stow and Johansson, 2000) in the past, especially within the conventional reservoir. Knowledge about the microstructural characteristics of the mud-rich parts in the deep-water is a requirement to understand their potential with respect to unconventional exploration, carbon sequestration, fluid transport and their sealing capacity.

Mudrock microstructure has empirical effects on fluid migration, capillary pressure and trapping of fluid in rocks (storage capability). The importance of having a full grasp about microstructure of mudrocks has geomechanical implication in terms of pressure build up and is intrinsically applicable to pore pressure and well bore stability in both conventional and unconventional reservoirs. Understanding the pore morphology and structure is the first input required in pore scale modelling and ultimately in numerical simulation of multiphase fluid transport, carbon storage and movement of contaminants in porous media (Busch *et al.*, 2008; Rhodes, Bijeljic and Blunt, 2008; Bustin and Bustin, 2012; Hemes *et al.*, 2015).

Measuring permeability in mudrocks is difficult to achieve using conventional methods. Hence, understanding the pore structure in fine-grained sedimentary rocks is useful in predicting permeability. Modelling permeability effectively is significant to monitoring reservoir production rate and well performance.

1.6 Scope of the research

The scope of the research is restricted to investigating the microstructural characteristics of fine-grained sediments in the deep-water setting and within burial depths of less than 1000 m. Samples were therefore collected from three Expeditions (Expeditions; 317, 339 and 355) of the International Ocean Discovery Program. Expedition 317 took place in the Canterbury Basin in New Zealand. Samples from this Expedition were used only for preliminary testing of some of the methods that are presented in Chapter 4.

Although, the samples from Expedition 317 are rich in hemipelagites (Expedition 317 Scientists, 2010), which is one of the sedimentary deposit in the deep-water setting, the collection of the samples predates the present research and hence the samples have dried-out under room conditions. It is suspected, therefore, that the samples may have undergone physical changes at the microscopic level, hence the usage of the samples was limited to methodology development in chapter 4. Expedition 339 in the Gulf of Cadiz is noted for contourites and is considered as a natural repository for contourites (Hernández-Molina *et al.*, 2013; Stow *et al.*, 2013). This expedition also targeted a series of hemipelagic deposits off the SW margin of the Iberian Peninsula. In the case of Expedition 355, which was drilled in the Indus Fan, the sediments are dominantly turbidites with minor hemipelagites. Therefore, Expedition 339 and 355 contain sediments well suited to address the research objectives.

1.7 Thesis structure

The thesis contains 8 chapters, broadly organised into introduction, literature review, methods and method development, principal results and discussion. A summary of what each chapter entails is as follows:

- Chapter 1: This chapter provides the general background and scope of the research, and a detailed account of the aims, objectives, and research questions. It also sets out a series of null hypotheses to be tested.
- Chapter 2: This chapter reviews the key literature and concepts about mudrocks, their microstructure, terminologies, microstructural development and common methodology for studying mudrock microstructure, as well as the major challenges associated with mudrock study. The section also gives an overview of the key concepts about deep-water depositional processes and their products. Previous work on microstructure of deep-water mudrocks and the various conflicting results are highlighted.

- Chapter 3: This chapter gives an in-depth description of the materials and methodology adopted in the thesis. Data set used for this research are core samples retrieved during some Expeditions of the International Ocean Discovery Program (IODP). Overview on the specific expeditions where the data comes from were highlighted. Different methodology adopted starting from core handling and sample preparation as well as laboratory experiment are explained.
- Chapter 4: This chapter presents a developed method for determining grain size analysis based on image analysis via scanning electron microscopy. Scanning electron microscopy is a standard method for studying mudrock microstructure while grain size is a key factor that controls several physical properties of the rock. The aim was to develop an efficient and effective method for characterising grain size so that grain size as well as microstructure can be analysed simultaneously without the need for further equipment. The grain size results through the developed method are compared with those obtained using laser diffraction granulometry.
- Chapter 5: This chapter presents a method for the automated analysis of mudrock microstructure. The acquisition of the SEM images is unique and image processing involved supervised machine learning segmentation. The chapter describes various measurements on mudrock microstructures such as microfabric, mineralogy, porosity and pore size distribution, which were derived through automated processes. It focuses on hemipelagic sediments from IODP Expedition 339.
- Chapter 6: Chapter 6 presents the full results on microstructure of contourites, hemipelagites and contourites, with an attempt to differentiate among them based on microstructural characteristics.
- Chapter 7: This chapter provides the main discussion of the thesis. It briefly reviews the new methodology developed and explained in Chapters 4 and 5. It then discusses the microstructural characteristics of deep-water mudrocks, and considers what these contribute to our understanding of depositional processes. The key differences in microstructure between the different facies are elucidated.
- Chapter 8: The thesis concludes with a brief summary of key findings and conclusions, suggested recognition criteria for the different deep-water facies as well as outlining suggestions of future research on microstructure of deep-water sediments.

CHAPTER 2 – LITERATURE REVIEW

2 Review of literature

In this chapter, issues associated with mudrock terminologies and their proliferation are presented. The chapter also reviews the many classification schemes that are found in the literature, reflecting the varied debates on appropriate classification of mudrocks. Previous works on microstructure from the earliest point of view to current efforts are mentioned. Highlights on microstructure of deep-water sediments are also discussed. A brief description is provided of deep-water deposits - turbidites, contourites and hemipelagites - and their respective facies.

2.1 Problem associated with mudrock terminology

In the field of geoscience the most widely accepted terminology to describe fine-grained sediments and sedimentary rock in general is mudrock (Javadpour, 2009). The definition is based on textural property i.e. sediments with mean grain-size less than 63 μm.

Sediments or sedimentary rocks within this group must contain a minimum of 50% silt to clay size particles (Ingram, 1953; Folk, 1980; Stow, 1981). The consolidated and massive (non-fissile) mudrock is referred to as claystone, mudstone, or siltstone, whereas the unconsolidated sediment, which has not undergone significant compaction and diagenesis, are known as clay, mud or silt. Fissile fine-grained sedimentary rocks that are characterised by bed-parallel, closely-spaced partings are referred to as shale.

The ambiguous and unstandardized terminologies in mudrocks studies prompts confusion such that multiple terminologies are attributed to the same feature (Aplin, Fleet and Macquaker, 1999; Milliken, 2014; Lazar *et al.*, 2015). An example of the common and unresolved disagreement that might persist for generations to come among sedimentologists lies in the description of ‘shale’. One definition of shale is based on mineralogical composition – i.e it must contain a minimum of 35% of clay or mica (Krynine, 1948; Davies *et al.*, 1991). Other definitions are based on lamination (Lundegard and Samuels, 1980) and fissility (Grainger, 1984). To professionals in the oil industry shale is synonymous to mudrocks as it is used as a general name for fine-grained sediments or sedimentary rock (Potter, Maynard and Pryor, 1980; Passey *et al.*, 2010). Also, it is not unusual to attach stratigraphic importance to shale, by using it in naming successions of strata perceived to have predominantly fine-grained

sediments for example the Bakken Shale, the Barnett Shale and the Woodford Shale (Schieber, 1999; Curtis *et al.*, 2012b; Gamero Diaz, Lewis and Miller, 2013).

In order to have uniformity and reduce confusion that might ensue from proliferation of terms, Ingram (1953) proposed the term mudrocks as a name to encompass all fine-grained sediments and sedimentary rock whose dominant grain-size is less than 63 μm. The term was welcomed and supported by a number of authors (Lundegard and Samuels, 1980; Stow, 1981). There is an on-going debate on the appropriateness of mudrocks as a general name for all types of fine-grained sedimentary rock. The antagonists believe the term is ambiguous being a combination of two words; mud and rock. In their own view, mud and rock are perceived to mean two contrasting physical states; mud is unconsolidated fine-grained sediment and rock means consolidated or a hard substance. It was argued that biogenically derived fine-grained components - siliceous and calcareous muds- are not reflected in this term. In view of the latter, description to incorporate biogenic and calcareous composition was provided e.g siliceous mudrocks and calcareous mudrocks (Dean, Leinen and Stow, 1985; Milliken, 2014). Despite the modification in description, a group of authors still find mudrocks unacceptable and suggest mudstone as a suitable term which is consistent with the classification of other group of sedimentary rocks e.g sandstone and limestone (Aplin, Fleet and Macquaker, 1999; Macquaker and Adams, 2003; Aplin and Macquaker, 2011; Milliken, 2014; Lazar *et al.*, 2015).

However, this view (mudstone) is not accepted here, as the word also suffers from similar reason for abandoning the term mudrock, so that in this thesis the term mudrock is chosen as a preferred term to connote the generality of fine-grained sediments and sedimentary rocks, whether they are unconsolidated, semi-consolidated or consolidated, and without reference to their organic or inorganic carbonate content.

Despite the rigour involved in studying mudrock, a study one might like to abandon along the way, the effort is especially worthwhile as mudrocks are one of the principal sediment types in the Earth's crust (Schieber and Zimmerle, 1998; Potter, Maynard and Depetris, 2005; Schieber, 2015) and a history of the Earth without recourse to studying fine-grained sediments would be very incomplete. The depositional processes, fabric and microstructure of fine-grained sedimentary rocks can be linked to their physical properties, especially porosity and permeability, which are important in relation to fluid flow, nuclear waste disposal and carbon sequestration. Mudrock studies can give an insight to the paleoclimatic and oceanographic

history of the Earth in geologic time as well as to the carbon cycle within the Earth (Lazar *et al.*, 2015).

2.2 Classification

Fine-grained rock classification has witnessed a proliferation of terminologies over the last few decades and more terms are being added either by slightly modifying previous used terms (e.g. Dean, Leinen and Stow, 1985; Milliken, 2014) or by incorporating details such as grain-size, bedding and composition (Lazar *et al.*, 2015). The proliferation of terminologies without reaching a consensus is unhelpful. Correlating similar works in terms of stratigraphy, depositional processes and interpretation are stymied. The classification of mudrocks is generally based on some distinguishable criteria such as texture, colour, mineral composition, fissility, lamination, chemical composition and degree of metamorphism (Picard, 1971). A good classification should provide easily identifiable features in the field, although a later laboratory analysis might be required to confirm the mineralogical composition. Albeit, because mudrocks are deficient in large scale structures in the field, it is a herculean task to differentiate them at outcrop scale. The underlying principle in the classification of sediments is to group together materials that have similar features and then give each group a name. Each of the criteria used in classifying mudrocks is presented hereinafter.

2.2.1 Classification based on texture and structure

Texture in sediments and sedimentary rocks is a description of the shape, size, orientation and fabrics of the grains, clasts or crystals. Textural classification is the simplest method for quick classification of mudrocks especially in the field, but no universal agreement exists with respect to the boundary limits for the different classes. The underlying principle in using texture as a criterion for classification is to group together materials with similar textural properties and then adopting a name for the group (Blatt, Middleton and Murray, 1980). Textural analysis is unique and can give information relating to provenance, transport mechanisms and hydrodynamic regime by which sediments were deposited. Structure on the other hand relates to the geometry and features larger than the grains. It is manifested by groups of grains that occur in association. Mudrocks are commonly seen as structureless, massive and homogeneous materials, except where they display lamination and fissility.

2.2.1.1 Textural classification

In textural classification of mudrocks, the main feature commonly in use is grain-size. Grain-size is the average diameter of the grains. The grain shape, orientation and grain fabrics are left out due to the difficulty associated with characterising them.

Wentworth (1922) presented a simple and straightforward classification of mudrocks with fewer number of classes than earlier classification schemes (Udden, 1914)- see Table 2.1. His boundaries for siliciclastic grain-size were widely adopted by sedimentologists and are still in use today. Sedimentary rock with particle sizes below 63 μm are divided into silt and clay. Silts are fine-grained sediments with grain-size ranging from 63 μm to 4 μm. Wentworth objected to the classification of mudrocks as shale with respect to grain-size as shale contextually implies structural features (i.e. fissility) rather than grain-size.

Clay or silt implies the sediments contain clay or silt size particles respectively and the composition is more than 80% of the overall constituent. Prefixes such as sandy and silty are added to clay when the composition is less than 80% and likewise silt is preceded by sandy and clayey in a similar fashion.

Table 2.1. Grain size scale adopted in this thesis in comparison with Udden (1914) and as well as the scheme adopted in this thesis.

Grain size		Udden (1914)	Wentworth (1922)	This thesis
Phi scale	Microns			
4	63	Coarse silt	Silt	Coarse silt
5	31	Medium silt		Medium silt
6	16	Fine silt		Fine silt
7	8	Very fine silt		Very fine silt
8	4	Coarse clay	Clay	Coarse clay
9	2	Medium clay		Medium clay
10	1	Fine clay		Fine clay
11	0.5			Very Fine clay
<11	>0.25			

Picard (1971) presents a textural classification of fine-grained rock. The classification is quick and useful in field operations and was a modified version of the original Wentworth's classification. Siliciclastic sediments with grain-size particles between 63 µm and 4 µm are described as silt and must contain at least 75% of the overall constituents. Where case the silt content is less than 75% but more than 50%, prefixes such as sandy or clayey are prescribed (Figure 2.1). Mudrocks with clay size particles (less than 4 µm size particle) of more than 50% qualifies to be within the clay class. Where the clay size particles are less than 75% of the overall composition but more than 50%, clay is modified by sandy or silty depending on which of the two dominates. This means that clay with higher sand particles compared with silt is sandy clay and clay in which the silt content is more than the sand content is silty clay.

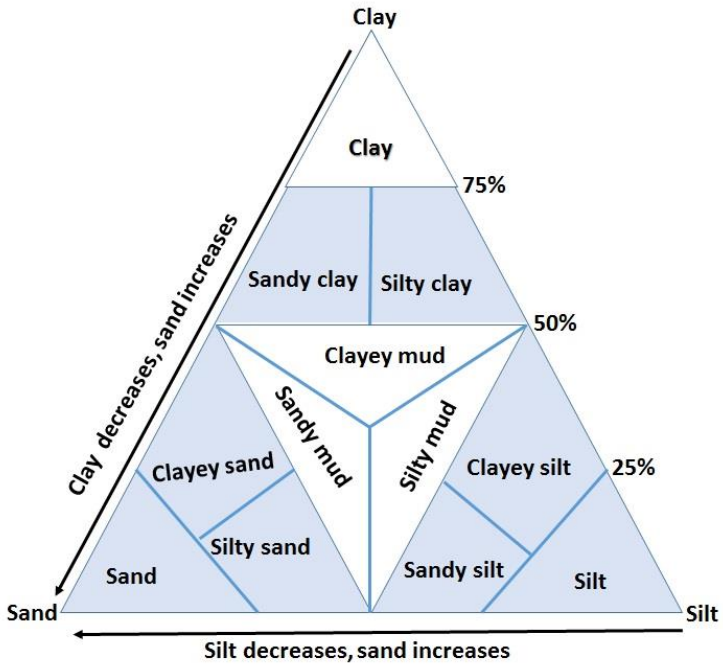

Figure 2.1 Ternary plot of fine-grained sediments (Picard, 1971).

Lundegard and Samuels (1980) classified fine-grained rocks based on two primary sedimentary features that they believe are linked to the genesis of the sediments. Their classification employs grain-size (silt content) and lamination. Lamination was distinguished into three types; fabric lamination, biolamination and grain lamination. They asserted that lamination is a primary sedimentary structure and has both genetic and paleoenvironmental implication. The maximum grain-size for mudrock was set at 62 µm. According to their classification, when silt content is greater than 67%, the rock is siltstone. Depending on lamination, siltstone could be

described as laminated siltstone when it contains laminations or non-laminated siltstone (Table 2.2). Mudrocks with less than 67% silt size particles and greater than 10% laminae were referred to as shale. In case the lamination is less than 10% and with silt size particles less than 67%, the rock was classified as either claystone or mudstone (Table 2.2).

Mudrocks classification by Stow (1981) was based on multiple parameters such as grain-size, fissility and lithification. He suggests that classification based on chemical composition, colour and other genetic terms should only be adopted as descriptive terms. Unconsolitated fine-grained sediments are classified as silt, mud and clay while the lithified equivalents were described as siltstone, mudstone and claystone respectively (Table 2.2). In each class, the grain-size is expected to be greater than 66% of the overall composition e.g. siltstone must contain 66% silt size particle (63 μm – 4 μm). Modifiers such as sandy, clayey or silty are suggested as prefixes in case the dominant grain-size fall short of 66% and provided the modifier is up to 10% (Table 2.2).

2.2.1.2 Structural classification

Fissility is the regular or repetitive splitting of rocks. It is believed to be a function of the mineral composition, temperature, weathering and water content (Ingram, 1953; Lundegard and Samuels, 1980; Weaver, 1980; Milliken, 2014). Fissility in mudrocks is associated with parallelism of micaceous clay materials which is a consequence of gravity settling or flocculation (Ingram, 1953).

According to Ingram (1953), the splitting characteristics of mudrocks could be represented on a ternary plot with massive, flaky fissile and flaggy fissile representing each corner of a triangle. Ingram believed that the scale of splitting repeatedly is a function of the cementing materials. He stated that the cementing materials is a requisite on which classification can be based upon. Massive was used to describe mudrocks in which the platy clay minerals show a random orientation. Flaggy describes mudrocks with large scale thickness of fissility i.e the repetitive splitting of the layers occurs in slab such that the length and width of the mudrocks are wider than the thickness. Flaky on the other hand was used to describe mudrocks with repetitive irregular thin flakes of platy clay minerals with parallel orientation. Flaky fissile mudrocks are cemented by weak cementing materials and the sediments are only held in slices. Ingram opined that moderate weathering enhances fissility and a massive siltstone at depth can appear with high degree of fissility close to the surface. He correlated fissility types with colour such that flaggy mudrocks were reportedly black or grey black. Flaky shales were advocated

to be grey or grey black, while mudstones were suggested to be white, grey, yellow etc. He stated that cementing materials other than organic materials create a massive structure and this imparts random fabric on mudrocks.

Table 2.2 Mudrock classification based on texture and quartz content.

Reference	Silt/Clay %	Fissility	Quartz content	Lamination	Nomenclature
Lundegard and Samuel (1980)	> 67% Silt	_	_	< 10% or > 10%	Siltstone or laminated siltstone
	< 67% silt	_	_	< 10% or > 10%	Shale or mudstone
Spear (1980)		Non/ fissile	> 40%	_	Massive/flaggy siltstone
		Non/ fissile	30-40%	_	Very coarse mudstone/shale
		Non/ fissile	20-30 %	_	Coarse mudstone/shale
		Non/ fissile	10-20%	_	Fine mudstone/shale
		Non/ fissile	< 10%	_	Very fine mudstone/shale
Stow (1981)	> 66% silt	Non/ fissile	_	_	Siltstone/silt-shale
	Silt & clay mixture	Non/ fissile	_	_	Mudstone/mud-shale
	> 66% clay	Non/ fissile	_	_	Claystone/clay-shale

2.2.2 Classification based on composition

Mudrocks essentially consist of physically broken siliciclastic materials, chemically derived constituents and biogenically synthesized components. The physically derived materials are the product of weathering and are transported to the basin; such allochthonous materials are likely to include quartz, transformed feldspars (clay minerals), orthoclase, plagioclase and heavy minerals. The most abundant constituent is likely to be the most resistant component and this depends on the effectiveness of abrasion during transport. In a basin, there are chemical (authigenic) and biogenic derived constituents that are known as autochthonous. Most of the chemically derived components are produced due to chemical transformation resulting from diagenesis and compaction especially in calcareous rich sediments. For example, limestone can be transformed into dolomite in the presence of magnesium or siderite if iron is able to replace the calcium. The biogenic components are shelly materials derived from the remains of

organisms (Schnurrenberger, Russell and Kelts, 2003) such as siliceous materials (e.g. diatom, radiolarian, sponge etc.) or calcareous materials (foraminifera, nannofossil, coccolith etc.).

In the deep-water setting the material composition is unique owing to detrital contribution from the continent and carbonate compositions that are derived *in situ*. Hence there is need for a classification to consider the constituents present in the deep-water setting. The fine-grained sediments here mainly consist of three distinctive components that can be related to their genetic classification (Dean, Leinen and Stow, 1985). The components are siliceous biogenic, calcareous biogenic and non-biogenic components (terrigenous sediments that are silt to clay size particles). Dean, Leinen and Stow (1985) suggest that each content could be placed on a ternary plot as end members. Their classification is based on core samples recovered during Deep Ocean Drilling programme of Leg 75 and 89 (Figure 2.2). The description of mud as combination of silt and clay is found inexplicit with respect to the origin of the sediments. Based on their classification scheme, any constituent that makes up more than 50% of the sediments takes the principal name. A constituent that is between 25% and 50% of the overall component is used as a major modifier. Minor modifier percentage was set at 10 % to 25% while less than 10% constituent does not have any effect on the naming of the rock except if the constituent is genetically significant. For fine-grained sediments containing non-biogenic components that is more than 50%, the main name of the rock could be silt or clay depending on which of the two dominates. In case the biogenic components dominate, and the percentage is more than 50% (siliceous biogenic or calcareous biogenic), the name of the sediment is ooze and is preceded by a modifier to reflect abundant biogenic constituent e.g radiolarian ooze, foraminifera ooze, diatom ooze (siliceous ooze), nannofossil ooze etc. Ooze implies microscopic remains of organisms e.g. diatom, radiolarian and foraminifera among others (Schnurrenberger, Russell and Kelts, 2003). The naming of the rock commences with the least abundant to the abundant constituent. Therefore, a fine-grained sediment with 50% radiolarian, 26% clay, and 19% nannofossil would be referred to as nannofossil clayey radiolarian ooze. While a fine-grained sediment with 60% foraminifera, 15% nannofossil and 25% silt would be described as nannofossil silty foraminifera ooze.

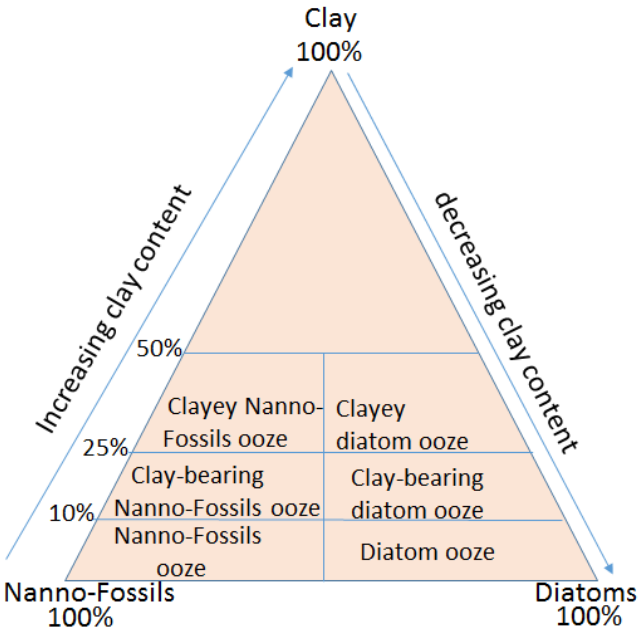

Figure 2.2 Biogenic and non-biogenic classification of mudrocks (after, Dean, Leinen and Stow, 1985).

Revamping the classification of Dean, Leinen and Stow (1985), Milliken (2014) took a step further to produce a tripartite classification on a ternary diagram. The classification is based on composition and has an undertone of relating mudrocks to their original source. The vertices of the ternary diagram are represented by tarl, sarl and carl (Figure 2.3). Tarl is a representation of terrigeneous-argillaceous sediments. Sarl implies siliceous-argillaceous and carl intimates fine-grained sediments that are calcareous. Both carl and sarl are biogenically derived and they are otherwise known as intrabasinal sediments (autochthonous). The classification is based on theoretical assumptions and requires further testing and validation using a variety of mudrocks (Milliken, 2016). Tarl is chosen for fine-grained sediments whose grain assemblages are more than 75% terrigenous sediments (mainly clay, quartz and feldspars). In case the terrigenous composition is less than 75% but more than 50% the rock is referred to as argillaceous rock. Sediments and rocks with less than 50% terrigenous components are described as sarl if the biosiliceous components prevail over biogenically derived calcareous sediments. Whereas carl depicts preponderance of the calcareous component compared to biosiliceous sediments. Mudrocks with less than 10% terrigenous component are not captured in Milliken's classification.

Milliken (2014) compositional classification is much more interpretative and difficult without laboratory analyses such as X-ray diffraction and scanning electron microscopy (Energy dispersive X-ray analysis and QEMSCAN (Quantitative Evaluation of Minerals by Scanning Electron Microscopy) to determine the mineral assemblages. The classification did not survive a long time before it was strongly criticised. It was seen as an affront to replace earlier classifications based on composition and textural characteristics. Comments by Camp *et al.* (2016) are in part valid such that a general classification of mudrocks is better to be descriptive and all-inclusive to observation made in the field as well as description of samples from cores whereas Milliken's classification scheme is far from being all inclusive. However, the classification could still be valid for detailed and compositional classification after required analyses have been performed.

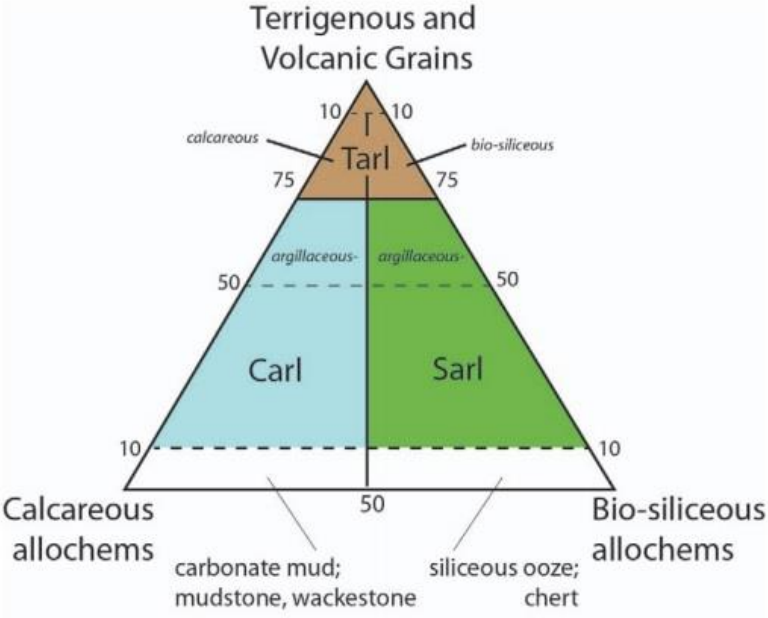

Figure 2.3 Compositional classification of mudrocks (After, Milliken, 2014).

Tarl implies detrital materials (terrigeneous argillaceous, Carl (carbonaceous-argillaceous) and Sarl (siliceous argillaceous). Note that argillaceous is also synonymous to fine-grained sediments.

Spear (1980) felt classification of mudrocks without due consideration to mineral composition (laboratory analysis) is incomplete. His classification relies on the percentage of quartz and fissility. He recognised lamination or fissility as an essential criterion required in order to classify fine-grained rocks. According to Spear, fissility means the repeated splitting of rock at a regular interval. His classification was in line with Elliot and Strauss (1967) and confirmed the upper limit of 40% quartz content set by the latter for clay. In Spear's classification, fissile fine-grained sediments with quartz content greater than 40% are described as flaggy siltstone (Table 2.2). The non-fissile equivalent with more than 40% quartz is described as massive siltstone. Mudrocks with quartz content ranging from 30% to 40% is named very coarse shale provided it is fissile while the non-fissile equivalent is described as very coarse mudstone. Fine-grained rock with 20% to 30% quartz is named coarse shale when the rock is fissile while the non-fissile equivalent with the same quartz content is termed coarse mudstone. In situation, whereby the quartz content of a fissile fine-grained rock falls between 10% and 20%, Spear described the rock as fine shale and in case the rock is non-fissile the rock is described as fine mudstone. Fine-grained rock with less than 10% quartz content and fissile in nature is described as very fine shale while the non-fissile equivalent is described as very fine mudstone (Table 2.2).

In Weaver (1980), classification of fine-grained sediments is based on a set of different criteria with intent to make the classification interpretative and relating sediments to their origin. To bring about simplicity and a genetic classification of fine-grained rock. The classification scheme relies on grain-size and mineralogical composition (phyllosilicate content). He contended that fissility should be limited to field usage. Hence shale as rock should only be applied to field description. His findings showed that shallow buried claystone might occur as fissile due to weathering, low temperature and dewatering at or close to the surface but at greater depth, the same rock exists as non-fissile siltstone. It is on this ground that he concluded that shale as a rock does not exist at the subsurface but rather as a potential shale.

In Weaver's nomenclature, he suggests physil and physilic as prefixes for describing mudrocks with greater than 50% and less than 50% phyllosilicate respectively (Table 2.3). He disproved the belief that phyllosilicate is the same thing as clay minerals. This belief was challenged by his findings in which he found that in shallow buried areas, phyllosillicate have the same percentage as clay minerals but as the burial depth increases, there is disparity in clay minerals and phyllosilicate content.

Weaver's classification contains physil clay, physil silt and physil silty clay which are loose and uncemented fine-grained materials containing more than 50% of phyllosilicate minerals. Physilic clay, physilic silt and physilic silty clay contain less than 50% phyllosilicate minerals. The consolidated mudrocks with greater than 50% phyllosilicate are physil claystone, physil siltstone and physil silty claystone etc. The lithified equivalent of fine-grained rock with less than 50% phyllosilicate are physilic claystone, physilic siltstone and physilic silty claystone. Weaver attributes his classification to the genesis of the rock. Physil siltstone and physil claystones are suggested to have been derived from the marine environment and have undergone lengthy diagenetic transformation. On the other hand, physilic siltstone and claystones are linked to fluvial to deltaic environment and have been moderately compacted.

2.2.3 Classification based on metamorphism

Flawn (1953) classified fine-grained rock based on the degree of metamorphism. The criteria for his classification are the reconstitution of clay minerals and grain-size, parting (fissility) and induration. The upper limit of clay size particles was set at 10 µm contrary to 4 µm (Wentworth, 1922; Picard, 1971; Stow, 1981; Grainger, 1984). He stated that 10 µm of grain-size is the least size of micaceous grain that is detectable with a petrographic microscope at x80 magnification. Based on his classification, fine-grained rock with grain-size less than 10 µm without reconstitution of the clay and micaceous minerals (i.e without parting) are described as clay. Indurated mudrocks whose grain-size is less than 10 µm and associated with partings (micaceous minerals) are described as shale. When the reconstituted minerals are less than 50% but still micaceous the rock is termed clay-slate but when the rock shows no partings, it is referred to as argillite. Where the reconstituted minerals are more than 50%; meta-argillite was used to describe the non-parting type while the one with partings was referred to as slate.

Table 2.3 Classification of fine-grained sediment base on metamorphism.

(After Flawn, 1953)				
Reconstitution	Grain size (μm)	Parting	No Parting	Foliated
Unreconstituted	< 10	Claystone	Shale	_
< 50%	10-50	Argillite	Clay-slate	_
> 50%	10-50	Meta-argillite	Slate	_
Completely	10-50	_	_	Phyllite
	10-500	_	_	Schist
	> 500	_	_	Gneiss
(After, Weaver 1980)				
Silt/clay %	Unindurated		Indurated	
	> 50% Physils	< 50% Physils	> 50% Physils	< 50% Physils
> 50% silt (63-4 μm)	Physil silt	Physilic silt	Physil siltstone	Physilic siltstone
> 50% clay (63-4 μm)	Physil clay	Physilic clay	Physil claystone	Physilic claystone

2.2.4 Definition of terminologies for this study

Due to the controversies associated with mudrock terminology, it is essential to define some of the terminologies used in this thesis to inform the reader about the contextual meanings of the terms.

In this thesis, non-ambiguous terminology is adopted in which the term mudrock is used for unconsolidated, semi-lithified and indurated sediment in which more than 50% of its grain-size less than 63 μm. The group of rocks that fall into this category are silt, siltstone, clay, claystone, mud, mudstone, shale, marl and marlstone.

The classification scheme of mudrocks based on grain size adopted in this thesis is similar to that presented by Udden (1914). Further subdivision in which the principal name is modified in order of increasing abundance is similar to the classification systems of Shepard (1954) and Stow (2005).

The principal name used is the one that comprises greater than 50% of the constituents and, for mixed composition mudrocks, the modifier preceding the principal name refers to the second

most abundant component, which comprises more than 10% of the overall components. Terms in which the principal name is modified are, for example, silty clay, clayey silt, sandy clay and sandy silt.

Mudrock(s): fine-grained sediments and sedimentary rocks that consists of more than 50% silt and clay size particles, irrespective of their organic or mineral composition.

Argillaceous: fine-grained sediments in which clay size particles dominate or a sedimentary rock containing essentially clay particles e.g shale, clay and claystone

Marl/marlstone: admixture of carbonate and fine-grained siliciclastic material in which the carbonate content is significant (30-70%), which can also be described as clayey calcareous sedimentary rock (Dean, Leinen and Stow, 1985). Marl is the unconsolidated type while the indurated rock with similar composition is known as marlstone.

Clay/claystone: fine-grained siliciclastic rock that is dominated by a particle size of less than 4 μm, provided the particle size is more than 50% of the overall components. The unconsolidated rock is clay while the indurated equivalent is referred to as claystone.

Silt/siltstone: fine-grained sediments or sedimentary rocks in which more than 50% of its grain-size is between 63 μm and 4 μm. Silt refers to the unconsolidated type while the consolidated type is siltstone.

Mud/mudstone: a fine-grained siliciclastic sediments or sedimentary rocks lacking fissility that is made up of a mixture of silt and clay size particles such that neither of the two is up to 75% of the total.

Shale: semi-consolidated to consolidated mudrocks that are characterised by parting/fissility.

Lamination: thin layering in rocks that is of sub-centimetre scale and is produced as an original depositional structure.

Fissility: a descriptive term for the splitting of rock at regular intervals along planes of weakness, which are parallel to stratification.

2.3 Microstructure

Improvement in drilling technology coupled with success in exploration of shale gas in the United States of America, has increased the interest in studying microstructural characteristics of mudrocks. Previously mudrocks were seen to be of little economic value, except for organic shales which serve as source rocks for hydrocarbon. To understand fluid transportation and its storage within mudrocks, the starting point should be the nanometre to micrometre microstructure. Upscaling of these observations from the small scale can then be linked to borehole scale, through well logs, and subsequently correlating the latter to seismic data (Ambrose, 2011). However, characterising mudrocks from the nano-scale to a seismically resolved feature is problematic, due to the widely disparate scales.

Microstructure of mudrocks is historically based on pedantic notions that were later supported by experimental observation. Popular descriptive terms based on this conjectural hypothesis are honeycomb, cardhouse, bookhouse and domain microstructure among others (Sergeyev *et al.*, 1980). The pioneering efforts on microstructural studies are restricted to description of clay particle orientation.

Microstructure for shale gas explorationists has been described as studying mudrocks particle size and the composition of shale. However, presently the study is advancing and entails the summation of all observations made on mudrocks at a nanometre to micrometre scale, which includes the relationship among grains (microfabric), grain orientation and alignment, pore shape and morphology, porosity and its connectivity, mineralogical composition and other small micron to submicron features that are present in them (e.g. microfractures and microbioturbation).

In the past, microstructural studies were usually restricted to studying grain and mineral arrangement at a microscopic scale (microfabric). The advent of sophisticated microscopes (field emission scanning electron microscope and transmission electron microscope) has revolutionalised microstructural research, as it allows observation of small scale features down to the nanometre scale. Despite the progress made and the current renewed interest in microstructure of mudrocks, knowledge on microstructural characteristics of mudrocks is still limited (Camp, Diaz and Wawak, 2013).

Common high-resolution techniques usually employed in studying microstructure include but are not limited to transmitted light microscopy (Egenhoff and Fishman, 2013; Plint, 2014), scanning electron microscopy (Curtis *et al.*, 2010; Curtis *et al.*, 2012b; Erdman and Drenzek, 2013), transmission electron microscopy (Curry *et al.*, 2007; Wirth, 2009; Janssen *et al.*, 2012), mercury injection porosimetry, helium porosimetry (Kuila *et al.*, 2012), x-ray micro computed tomography (Houben, Desbois and Urai, 2013; Boruah and Ganapathi, 2015; Hemes *et al.*, 2015) neutron scattering (Clarkson *et al.*, 2012; Clarkson *et al.*, 2013; Gu *et al.*, 2016), nuclear magnetic resonance (Sondergeld *et al.*, 2010; Josh *et al.*, 2012; Mehana and El-monier, 2016) and gas adsorption techniques (Kuila and Prasad, 2013; Lin *et al.*, 2015; Houben *et al.*, 2016). The aim of using these techniques is to capture the nanoscale and microscale features with high-resolution equipment.

2.3.1 Macrofabric and microfabric

Mudrock fabric can be described as the geometrical arrangement or orientation, spatial distribution and interactions or interrelationships existing among closely packed particles of fine-grained sedimentary rocks (Bennett, Bryant and Keller, 1981; Altschaeffl and Thevanayagam, 1991). The geometrical arrangements of the particles are commonly observed as particle orientation; therefore fabric in this context is synonymous with orientation of particles (O'Brien, Brett and Taylor, 1994). Mudrock fabrics can be distinguished into macrofabric and microfabric. Macrofabrics are large scale preferential orientation of fine-grained particles at a centimetre to millimetre scale. Such macrofabrics are manifested as fissility, lamination and micro-depositional features. These features are best studied using X-radiography (O'Brien and Slatt, 1990), optical microscopy (Egenhoff and Fishman, 2013; Plint, 2014) and X-ray computed tomography (CT) imaging (Diaz and Walls, 2012). Microscale study of fabric otherwise known as microfabric requires higher resolution and commonly utilised equipment include optical microscope, electron microscope and other high-resolution techniques.

Microfabric of mudrock is a building block and a subset of microstructure. Hence, microstructure is defined as an interplay between fabric, gravitational forces, electrochemical mechanism and the surrounding fluid (Bennett, O'Brien and Hulbert, 1991). The importance of fabric is enormous as it has considerable impact on specific aspects of rock properties, such as porosity, permeability and stress-related behaviour of the rock. These physical properties are important in order to understand salient phenomena such as primary migration of

hydrocarbon from the source rock (O'Brien, Slatt and Senftle, 1994), suitability of shale for radioactive storage and also providing quantifiable data for enhanced numerical modelling of both single and multi-phase fluid flow (Hemes *et al.*, 2015).

The study of microfabric in mudrocks predates the era of scanning electron microscopy and transmission electron microscopy. The story of microstructure will be incomplete without reference to the excellent works of pioneers in the field.

Microfabric studies of mudrocks is a study that cuts across an array of disciplines, including: soil mechanics, civil engineering, chemistry, geotechnical engineering, sedimentology and other fields. The earliest advances in microfabric studies were initiated by non-geologists (Moon, 1972) led by the field of soil mechanics.

The classical works of Terzaghi (1925) and Casagrande (1932) who described honeycomb structure in mudrocks and its subsequent modification due to mechanical compaction (Figure 2.4), laid the foundation for microstructural studies. Models from both authors described clay particles aggregation in terms of single units known as honeycomb structure. The honeycomb structure describes random association of clay aggregates typified by an edge to edge pattern. One of the famous frontier studies of microfabric is that of Lambe (1958) who distinguished freshwater mudrocks from marine mudrocks based on particle arrangement. He noticed that clay platelets from mudrocks deposited in the marine environment are randomly arranged with reasonable amount of void space, whereas clay particles from freshwater mudrocks are orderly arranged and have lesser voids. He described the lack of orientation of the particles as cardhouse structure, a term attributed to Goldshmidt (Sergeyev *et al.*, 1980), and which is still a popular term in the literature (e.g Lash and Blood, 2004; Blume *et al.*, 2016; Kasprzhitskii *et al.*, 2016; Yu, Chow and Wang, 2016). The cardhouse structure is synonymous to the honeycomb structure in which the aggregates of clay particles can both contain heterogeneous particles arranged in edge to edge and edge to face patterns (Figure 2.4). A further explanation of the cardhouse and arrangement of mud particles was offered by Van Olpen (1963) through an electrolytic approach. He stated that settling mud can aggregate in three ways which may be through edge to edge contact (E-E), edge to face contact (E-F) and face to face contact (F-F). The first two contacts are the products of random orientation while a face to face arrangement is manifestation of distinct (preferred) orientation of clay particle present in mudrocks (see Figure 2.5).

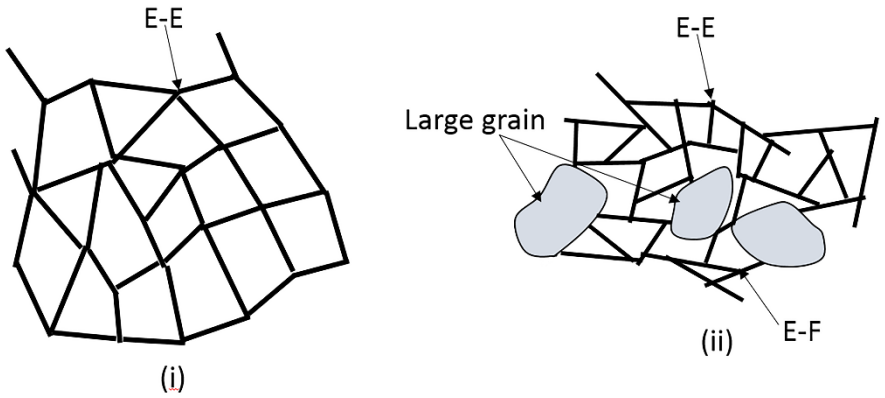

Figure 2.4 Cartoon of early model of clay particles aggregation (i) honeycomb (ii) cardhouse (modified after, Bennett, O'Brien and Hulbert, 1991).

The honeycomb and cardhouse structures are typical of freshly deposited clay particles with insignificant burial. The structures have high volume of voids and contain single plate aggregate. Note the E-E (edge to edge) and E-F (edge to face) contacts.

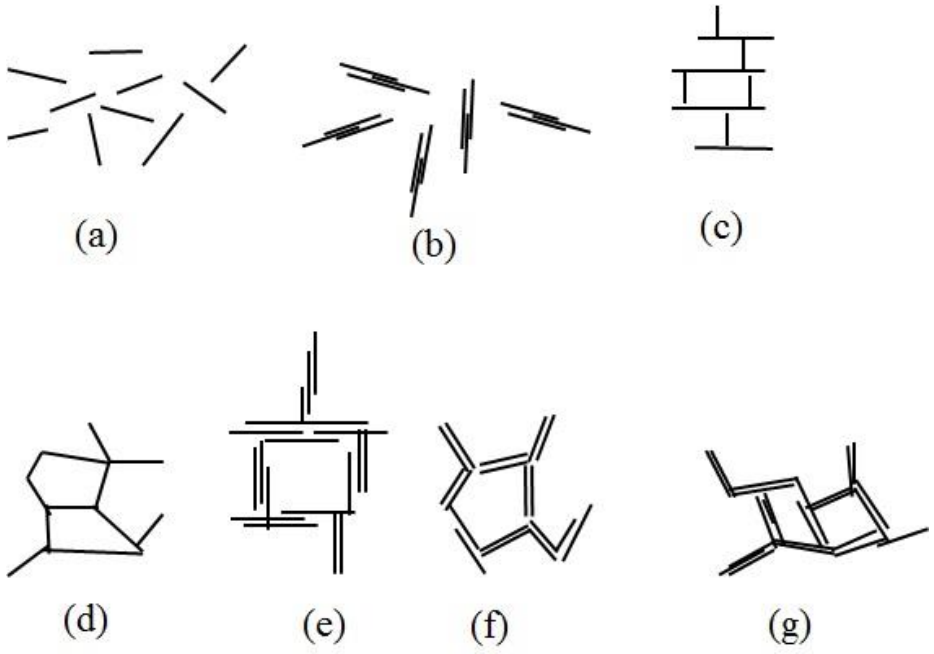

Figure 2.5 Mode of particle aggregation in freshly deposited fine-grained sediments (after, Van Olphen, 1963).
(a) dispersed/deflocculated (b) aggregated but deflocculated (c) flocculated with edge-face relationship (d) flocculated and aggregated with edge to edge relationship (e) Flocculated and aggregated with edge to edge association (f) flocculated and aggregated with edge to edge relationship (g) flocculated and aggregated with edge to edge and edge to face relationship.

The arrangement of fine-grained particles into edge to edge (E-E), edge to face (E-F) and face to face (F-F) are important determinants of other physical properties such as pores and pore network and resultant microfabric. Fine-grained sediments with particle arrangement into edge to face are likely characterised with higher porosity compared with those arranged in face to face domain (Davies *et al.*, 1991). At similar burial depth conditions the latter is likely to have a preferred oriented fabric while the former is likely to have more random orientation. Aggregates of fine-grained particles with considerable edge to edge and face to face is likely to facilitate pore connectivity which is vital to fluid flow due to the possibility of both lateral and vertical connectivity (Figure 2.6). Simple configurations like this are likely to be rare in the subsurface because overburden pressure will bring about changes to the original arrangement of grains with increase in burial depth. For example, larger grains are like to collapse into the matrix.

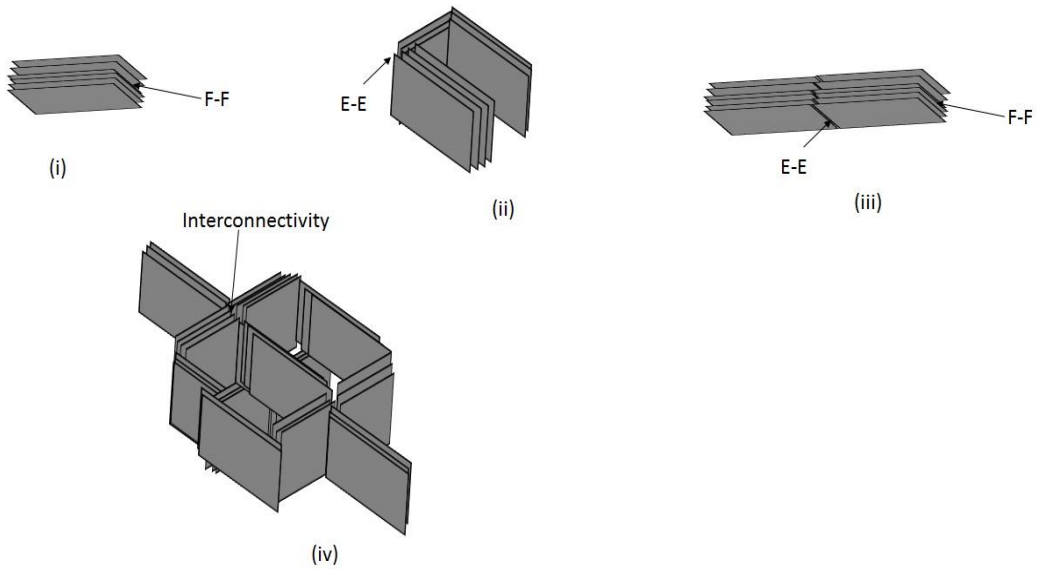

Figure 2.6 Cartoon showing arrangement of clay particles (i) face to face domain (ii) edge to edge arrangement (iii) combined edge to edge and face to face pattern (iv) series of edge to edge and face to face domain pattern.

2.3.1.1 Factors controlling development of microfabric

Development of microstructure in fine-grained rock is dependent, at least in part, on the processes that in operation in a depositional setting. Numerous mechanisms or models have been proposed to explain how microstructure in mudrocks develops. Of all these models, it is hard to give priority to any one over the other, as there is the possibility that the development of mudrock fabric involves an interplay among several factors (Day-Stirrat, 2014). Pioneering models were generally simple; however, the advanced technology and improved sample preparation (broad ion beam milling -BIB- and focussed ion beam microscopy -FIB) call for better understanding of mudrock microstructure and a more robust model to explain the factors that are responsible for its development.

Early microstructural studies of mudrocks, suggested that the presence of platy minerals was the main factor responsible for mineral orientation in mudrocks (Hurst, 1987). However, the presence of platy minerals alone does not indicate the processes involved in having a mudrock with a preferred orientation, massive or random orientation. Several studies have enunciated the importance of mechanical stress on mudrock anisotropy (e.g Sintubin, 1994; Matenaar, 2002; Aplin, Matenaar and van der Pluijm, 2003; Lash and Blood, 2004; Aplin *et al.*, 2006). Smectite to illite transformation has also been suggested as a critical factor that could be responsible for microfabric development (Ho, Peacor and van Der Pluijm, 1999; Charpentier *et al.*, 2003; Aplin *et al.*, 2006). The transformation process of smectite to illite is caused by

high temperature and pressure effect on clay minerals. The authors that hold this view concentrated their studies on burial depth to create the temperatures at which smectite transforms to illite. Their findings showed to an extent that there is a correlation between smectite transformation to illite and clay mineral orientation. A brief discussion of some of the controversies and conflicting conclusions from past researches are outlined below.

In 1967, Odom published a paper aimed at investigating the structural properties of argillaceous rocks and their relationship to clay fabric. The paper alluded to the fact that well defined orientation of clay (fabric) increases as the organic matter content increases and with increase in fissility of the rock. Odom concludes that argillaceous rocks with high content of carbonate minerals are likely to produce random orientation. The studies find no relationship between fine-grained sedimentary rock fabric and factors such as geologic age, burial and clay content. However, Odom reported that high level of montmorillonite in some mudrocks imparts random orientation. He concluded that preferred orientation in mudrocks is independent of compaction, but suggests that mudrock fabric could be associated with physicochemical conditions of the environment of deposition.

The study of shale by O'Brien (1970) using scanning electron microscopy (SEM) in studying microfabrics of mudrocks suggests that there is a correlation between orientation of clay minerals and fissility. Shale with the highest degree of fissility has the highest level of preferred orientation and it was acknowledged that well oriented fabric in shale is ostensibly dependent on the pattern of deposition of clay. Well oriented fabric is attributed to originally dispersed clay particles or deflocculated particles of clay while random orientation is suggested as due to flocculation during deposition.

A number of authors believe that orientation in mudrock (fabric) is dependent on the environment of deposition (Odom, 1967; Moon, 1972; Moon and Hurst, 1984). In order to explain the mechanism behind dispersion and flocculation of fine-grained particles, Moon and Hurst's (1984) position on microfabric is that fine-grained sediments deposited within an anoxic setting become dispersed (Figure 2.7). The model suggests that the presence of organic compounds in anoxic environments causes deflocculation of earlier formed flocs (random clay aggregation) by acting as a peptising agent. Peptisation by organic matter is proposed as the force that triggers dispersion of fine-grained particles in an anoxic environment. Subsequently overburden pressure on such particles would accentuate a well oriented mudrock fabric. However, in an oxic setting, the condition does not favour preservation of organic matter, and

the model assumes an absence of organic compounds in such an environment and therefore random orientation of clay particles is produced as a resultant effect of flocculated particles that are undispersed.

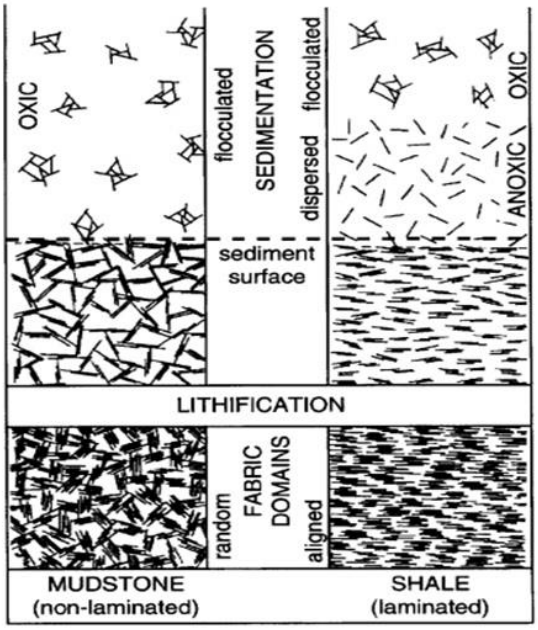

Figure 2.7 Diagram of proposed model of fine-grained sediments in relation to oxygen content of the bottom water (after, Moon and Hurst, 1984).
Note the flocculation in oxic condition and segregation of the particles in the anoxic water conditions.

In furtherance to this position, later work was aimed at establishing the relationship between environment of deposition and fabric in mudrock and the significance of fabric on geotechnical properties (Hurst, 1987). The study was conducted on natural samples and in a simulated conditions. The outcome of the study conforms with Moon and Hurst (1984) and therefore concludes that organic-rich fine-grained sediments display preferred orientation, while organic-poor fine-grained sediments exhibit randomly oriented fabric.

Apart from generation of preferred orientation through physical or chemical means, a biological factor has also been considered. There is discrepancy in the rate at which organisms thrive in oxygenated environments (aerobic) and low or oxygen depleted environments (anaerobic). A prominent geological imprint that differentiates the two dissimilar environments is biogenic activities and this is marked by bioturbation. In an oxic environment there is a lot of biogenic activities and the environment is prone to destruction of the original fabric of the rock, but in contrast, in an anoxic environment there is less biogenic activity and hence the original fabric would be preserved. In this regard, O'Brien (1987) documents three types of

fabrics (macrofabric and microfabric) of shale based on biogenic activities using x-radiography and scanning electron microscopy.

(1). Highly bioturbated sediments showed homogeneous grey tone and randomised particles similar to flocculated clay particles in mudstone, but differs with the absence of the cardhouse domain which characterises the latter.

(2). Mildly bioturbated sediments are reported to have indistinct fabric with relics of primary laminations and both sub parallel and parallel microfabric.

(3). Non-bioturbated sediments, with low abundance and low diversity of fossils, produced well laminated fabric under x-ray radiography and well-preserved orientation of original fabric.

Charpentier et al. (2003) studied the relationship between fabric and mineral diagenesis. They noted that at great depth, despite the huge effective stress involved, anisotropic alignment of mudrock minerals was not observed until there is transformation of smectite mineral to illite. They suggest that the preferred alignment of minerals in fine-grained rock can be attributed to diagenetic transformation of smectite to illite, which is a function of burial depth and thermal gradient. Preferred orientation of clay minerals as a product of smectite to illite transformation has been supported by a number of authors (e.g Ho, Peacor and van Der Pluijm, 1999; Aplin *et al.*, 2006; Wenk *et al.*, 2008a) and their works are focused on stratigraphic depth at which smectite transforms to illite. Smectite to illite transformation is dependent on temperature and it has been documented by earlier research that this occurs between a temperature of 100^0C and 120^0C (Berger, Velde and Aigouy, 1999; Aplin *et al.*, 2006). However, preferred orientation in mudrock has been reported at shallow depth specifically from outcrop samples (Lash and Blood, 2004), which are situated below the required temperature at which transformation of smectite to illite occurs. Hence, it is inconclusive to relate preferred orientation of mudrock particles to transformation of smectite to illite. This is particularly true in sediments where such minerals are not present.

Nygard et al. (2004) simulated field conditions in the laboratory by subjecting outcrop samples from two different locations within the UK to mechanical compaction. They stated that production of fabric by mechanical compaction in mudrock is a function of the state of cementation of the rock prior to overburden pressure. They mentioned that if the constituents are uncemented mud, mechanical compaction will facilitate alignment of the mineral constituents, but in cases where the materials are cemented prior to mechanical compaction,

the cementing material is said to constitute a barrier and will hinder development of preferred orientation. The Nygard et al. (2004) position is similar to a previous report by Moon and Hurst (1984) who suggest that flocculated mud produces a random orientation while dispersed mud generates preferred orientation, and that these fabrics are maintained during compaction.

Among other factors that have been reported as being responsible for imparting preferred orientation on mudrock are consolidation due to overpressure and reaction of the mineral constituents to the pressure (Day-Stirrat, 2014). The effect of these factors can vary according to the burial condition such as temperature and depth. Day-Stirrat (2014) presumes that transformation of a mudrock from non-preferred orientation to that with well oriented fabric is dependent on the temperature condition at burial depth coupled with mechanical consolidation and reaction of the mineral constituents. He states that silt to clay ratio is an important parameter that has a strong influence on mudrock fabric. Abundance of silt is likely to prevent well oriented fabric development through reducing the effectiveness of overburden pressure. Hence, mudrock with high silt content might retain its original random fabric while clay dominated mudrock will induce an anisotropy in the arrangement of the particles as burial progresses. At shallow depth, the effect of silt content will likely be insignificant in controlling mudrock fabric due to the fact that the overburden pressure at such condition is minimal unless the basin evolved rapidly (i.e. rapid sedimentation). The assumption that silt content affects microfabric of mudrock is similar to how concretions effect mudrock macrofabric (Figure 2.8) as outlined by Lash and Blood (2004).

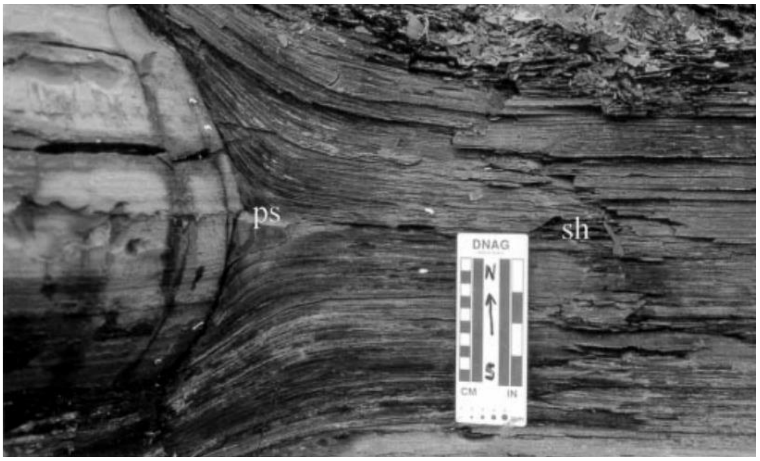

Figure 2.8 Picture of concretion within a shale lithology which highlight difference in fissility between pressure shadow (ps) and the adjacent shale (sh) (Lash and Blood, 2004). Note that the pressure shadow (ps) in the diagram are not fissile while the adjacent shale shows strong fissility.

Research carried out by Wilkinson and Fenton (2015) suggests that preferred orientation in mudrocks could be attributed to a number of factors including sedimentary processes, grain shape, bioturbation, depth of burial, tectonic events, weathering and age of the rock. They suggest that at the time of deposition, sedimentation process could be responsible for the arrangement of mud particles but subsequently, post depositional effects modify and contribute largely to the final arrangement of the particles. The authors mentioned that the degree of preferred orientation in fine-grained sedimentary rock is inversely proportional to the silt content of mudrocks which is in tandem with the position of Day-Stirrat (2014).

The study of mudrock microstructure took a different approach in recent times compared to the earlier studies which were focused on grain to grain relationship, orientation of grains/mineral and pores. Current research efforts on microstructural characterisation of mudrock are concentrated on the understanding of the pores, pore morphology, pore networks, pore connectivity and permeability in order to determine mudrocks sealing capacity, and carbon storage potential (e.g Houben, Desbois and Urai, 2013; Hemes *et al.*, 2015) and fluid movement mechanisms (Loucks *et al.*, 2009; Curtis *et al.*, 2012b; Kuila *et al.*, 2012; Sondergeld, Curtis and Rai, 2012). Mineralogical components of mudrocks have been identified as a controlling factor of porosity, so that most microstructural studies incorporate X-ray diffraction (XRD), X-ray fluorescence (XRF) and energy dispersive X-ray analysis (EDX) among others to determine the mineral composition of the rock.

2.3.2 Pores and porosity

Pores and porosity are the first parameters to consider in addressing issues related to fluid movement within porous media. Fluids, for example hydrocarbon (oil and gas) and water, reside within pore spaces. Pores are defined as the voids or portion of rock that is devoid of grains. In mudrocks, pores are small and range from a nanometre to micrometre scale. These pores are described as interparticle and intraparticle, with respect to the location of the pores with respect to the matrix (Loucks *et al.*, 2012). Pores can also be described as open or closed depending on whether there exists a connection between them and other adjacent pores. Open pores have connection with adjacent pores and in most cases, they are likely to be interparticle (pores between rock grains), owing to the likelihood of being connected, compared with intraparticle (pores within rock grains). Therefore, open pores are the most important with respect to fluid flow. The closed pores are disconnected from neighbouring pores and they can be described as isolated pores. Pores have non-uniform and irregular structures and therefore a variety of descriptive shapes have been used in describing them e.g. bubble-like and sheet-like (Gu *et al.*, 2015), elongated (Desbois, Urai and Kukla, 2009), sponge-like (Milliken *et al.*, 2013) and slit-like (Curtis *et al.*, 2012a). A cartoon of a porous material is illustrated in Figure 2.9.

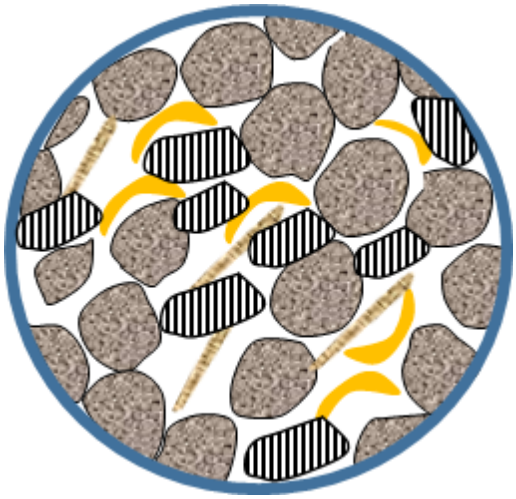

Figure 2.9 Cartoon showing pores and mineral grains in a rock. The white background represents the pores in the rock. As depicted in the figure above, the varying shapes and shades represent different mineral grains that can be present in rocks e.g. quartz (rounded), feldspar (diagonal striped pentagon) microfossil (yellow crescent), mica (elongated). The storage and movement of fluids (gas, oil and water) is a function of connectivity of the pores. A well-connected pore network would allow easy movement of pores while tight and unconnected pore network would impede movement of fluid.

There is lack of agreement on classification of pores in mudrocks and there is an increase in publication on terminologies of pores in mudrocks. This adds a layer of confusion when reading texts in which different classification schemes are used, as this does not allow easy comparison among publications. Most classifications of pores in mudrocks are based on two criteria; diameter of the pores and location in which the pores are found. It is not uncommon seeing authors referring to pores of the same size range with a different name (Rouquerol *et al.*, 1994; Loucks *et al.*, 2012) as presented in Table 2.4. Rouquerol *et al.* (1994) present a classification agreed upon by the International Union of Pure and Applied Chemistry (IUPAC). In their classification, pores are differentiated into three groups, based on pore size; micropore (less than 2 nm), mesopore (2-50 nm) and macropore (greater than 50 nm). The IUPAC classification is known to have a wide acceptance among mudrock researchers (Bustin *et al.*, 2008; Chalmers, Ross and Bustin, 2012; Hemes *et al.*, 2015; Houben *et al.*, 2016)

Table 2.4 Comparison two schemes of pores classifications based on diameter.

(Loucks *et al.*, 2012)	**IUPAC classification (Rouquerol *et al.*, 1994)**
256 – 4 mm macropore	> 50 nm macropore
< 4 mm – 62.5 µm mesopore	
<6.25 µm – 1 µm micropore	
< 1 µm – 1 nm nanopore	
	2 – 50 nm mesopore
< 1nm Picopore	< 2 nm micropore

Considering the material composition in which pores are located, several names have been applied to similar pores (e.g Milliken and Reed 2010, Schieber, 2010, Desbois 2009, Curtis, 2010). For example pore constrained by organic matter have been described as organophilic pore (Curtis *et al.*, 2010), organic pore (Kang *et al.*, 2011), organic matter pores (Loucks *et al.*, 2012) and organic matter-hosted pore (Milliken *et al.*, 2013). A list of terminologies as used by several authors with respect to the material surrounding a pore is presented in Table 2.5.

Table 2.5 Terminologies used for description of matrix related pores with respect to their location (Modified after, Loucks *et al.*, 2012).

Description	Terminology	Reference
Pore within organic matter	Organophilic pore	(Curtis *et al.*, 2010; Gu *et al.*, 2015)
	Organic matter pore	(Loucks *et al.*, 2009; Wang *et al.*, 2009)
	Organic pore	(Ambrose, 2011)
	Organic matter-hosted pore	(Milliken *et al.*, 2013)
Pore between grains	Interparticle pore	(Loucks *et al.*, 2009; Slatt and O'Brien, 2011; Loucks *et al.*, 2012; Wang *et al.*, 2014)
	Dissolution pores	(Loucks *et al.*, 2010; Milner, McLin and Petriello, 2010; Schieber, 2010)
	Intergranular pore	(Wang *et al.*, 2009; Chalmers, Ross and Bustin, 2012)
	Phyllosilicate	(Curtis *et al.*, 2010; Curtis *et al.*, 2012b)
	Type III- large connected pores	(Desbois, Urai and Kukla, 2009)
Pore within grains	Intraparticle pores	(Slatt and O'Brien, 2011; Loucks *et al.*, 2012; Wang *et al.*, 2014)
	Phyllosilicate	(Curtis *et al.*, 2010; Curtis *et al.*, 2012b)
	Phyllosilicate framework	(Milner, McLin and Petriello, 2010; Schieber, 2010)
	Type I- elongated (unconnected) Type II – crescent shape (unconnected)	(Desbois, Urai and Kukla, 2009)

For simplicity, pore classification as used in this thesis is akin to that of Loucks *et al.* (2012) for matrix related pore such as interparticle, intraparticle and organic matter pores. However, when considering the diameter of the pore the IUPAC classification is subscribed to. Apart from matrix related pores natural fractures exist in mudrocks and these are unrelated to

individual grains and they range from sub-micrometre to a few micrometres in width. The different pore types related to fracture and matrix as used in this thesis are presented in Table 2.6.

Table 2.6 Different pore types that are associated with mudrocks as used in this thesis (Modified after, Loucks *et al.*, 2012).

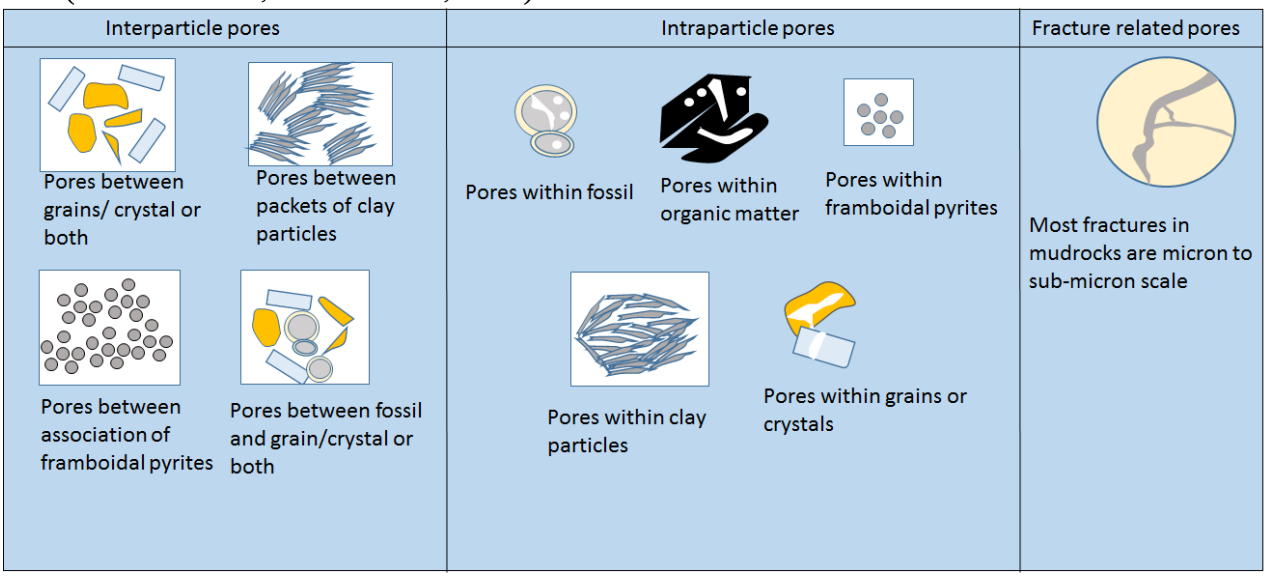

Porosity is defined as the measure of the ratio of pore volume (volume of pore spaces) to bulk volume (total volume) of the rock. It is expressed as a fraction or percentage and it is dimensionless. Mathematical expression for determining porosity is presented in equation 2.1. Porosity is an essential petrophysical property of rock, which has a strong control on movement and storage of fluid in rock. It is one of the three parameters that are of concern to petrophysicists. The other two are permeability and hydrocarbon occurrence which are in one way or the other dependent on porosity.

$$\emptyset = \frac{V_v}{V_b} = \frac{V_b - V_g}{V_b} \quad \text{..... Equation 2.1}$$

Where ø is porosity, V_V is the volume of voids (pore volume), Vb is the bulk volume and Vg is the volume of grains

Permeability is defined as the ease with which fluid moves within the rock and this strongly relies on capillary pressure and buoyancy. While capillary pressure impedes and enhance trapping of hydrocarbon, buoyancy enhances fluid movement within the pore space. In order for fluid to flow within the reservoir rock, buoyancy pressure must overcome capillary force.

Capillary force is dependent on the pore throat and the tighter the pore throat, the higher the capillary force and vice versa. The equation for calculating the buoyant pressure and the capillary pressure are:

$$\boldsymbol{P_b = (\rho_w - \rho_o) g h}$$ ..... Equation 2.2

Where

P_b is the buoyancy pressure,

ρ_w is the density of water

ρ_o is the density of oil

g is acceleration due to gravity

h is the height above free water level

$$\boldsymbol{P_c = \frac{2\sigma cos\theta}{r}}$$ ..... Equation 2.3

Where

P_c is the capillary pressure

σ is the interfacial surface tension

θ is the contact angle between water and the grain

r is the radius of the pore throat.

Understanding pore structures and their connectivity is the first parameter required to estimate fluid flow in reservoir rocks as it constitutes a requirement for quality assessment of reservoir and its predictive models (Bloch, 1994). Porosity be a useful indicator for determining subsidence history of seafloor, which can then be used to estimate marine tectonic and eustatic changes (Kominz, Patterson and Odette, 2011 and references therein).

Pores in mudrocks are commonly within three orders of magnitude (nanometre to few micrometre). Microfractures can be up to few micrometres. Most pores have diameters that are less than 100 nm. Due to the variation in the pore sizes in mudrocks, there are many techniques utilised in determining the pore size and porosity of unconventional reservoirs. These different techniques have disparity in their resolutions. There is no unique technique that can capture the wide-range of pore sizes in mudrocks. Hence, in most cases a combination of techniques is used so that they can serve as complementary to each other. Basically, the methods commonly used can be divided into direct methods and indirect methods. The direct methods provide opportunity to visually inspect pore structures and their connectivity. The technique involves imaging samples in both 2D (SEM and TEM) and 3D (MicroCT and FIB-SEM). The highest resolutions recorded so far from direct techniques are 5 nm and 2 nm for FIB-SEM and TEM respectively (Bustin *et al.*, 2008; Anovitz and Cole, 2015). The indirect methods are laboratory techniques that are used for determining pore size and porosity aside from direct imaging. These include NMR, neutron scattering, water immersion, helium porosimetry, mercury porosimetry and gas adsorption. The choice of a method for characterizing porosity and pore size distribution is constrained by factors such as clay content, thermal maturity and range of the pore sizes (Saidian *et al.*, 2014).

2.4 Deep-water fine-grained sediments

The ocean can be subdivided into shallow and deep-water on the basis of the water depth and slope morphology (Mulder, Hüneke and Van Loon, 2011). In the field of geoscience, deep-water is synonymous to deep-sea and it can be described as a water environment in which the water depth is beyond 200 m (Figure 2.10 Shanmugam, 2006; Shanmugam, 2012a). This region mostly exceeds the continental shelf and is restricted to the continental slope, continental rise and deep ocean floor. The general term of associating deep-water with water depth is not unanimously accepted by geoscientists as different science communities have defined deep-water in diverse ways. To sedimentologists deep-water is defined as a water environment that is below the storm wave base (Pickering and Hiscott, 2015). Accepting this definition connotes that there might be variation in depth of deep-water setting one region to the other because storm wave base varies around the globe (Shanmugam, 2012a). To marine geologists and oceanographers, deep-water is defined according to water depth and it is anything beyond 100 m -200 m water depth (Stow *et al.*, 2012).

The usage of deep-water adopted in this thesis is that of the marine geologist and oceanographers, and this is consistent with terminology used by the International Ocean Discovery Program (IODP) as the samples used for this study were retrieved during IODP expeditions by the expedition scientists.

An important group of deep-water sediments are clastic sediments transported through sediment gravity flow along the slope down to the basin floor. The deposits arising from such a process are referred to as submarine fans when describing modern and unconsolidated sediments. In contrast, turbidite systems is coined from the ancient equivalent when dealing with outcrops and subsurface samples (Mutti and Normark, 1987; Stelting, Bouma and Stone, 2000).

According to Stow and Piper (1984b), deep-water fine-grained sediments are consolidated or unconsolidated, biogenic or clastic materials whose grain-size is within the clay and silt range. They are deposited beneath the storm wave base, generally deeper than the shelf in the open ocean and in the deeper parts of lakes. There are a number of processes by which sediments are deposited within the deep-water including downslope gravity-driven turbidity currents, alongslope ocean-driven bottom currents, and vertical settling of pelagic and hemipelagic material through the water column. These three processes give rise to three end-member deposits turbidites, contourites and hemipelagites (or pelagites). They exist as complex associations and represent deposition through a continuum process (Reynolds and Gorsline, 1991). There is, therefore, variation in facies within each of the groups (Stow and Piper, 1984a).

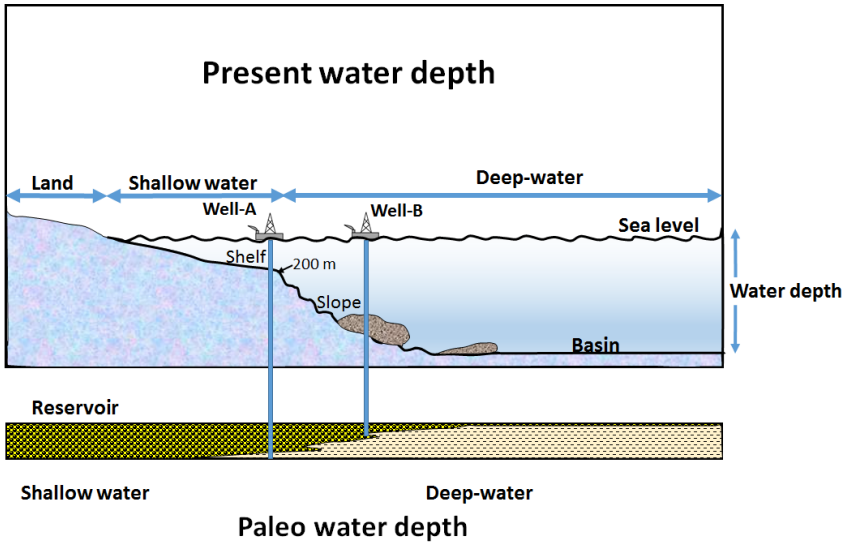

Figure 2.10. Cartoon showing the starting point of deep-sea (> 200 m water depth) below the shelf break (Shanmugam, 2000).
Processes such as slides, grain flow, slumps, turbidity currents and bottom currents occur below the continental shelf break.

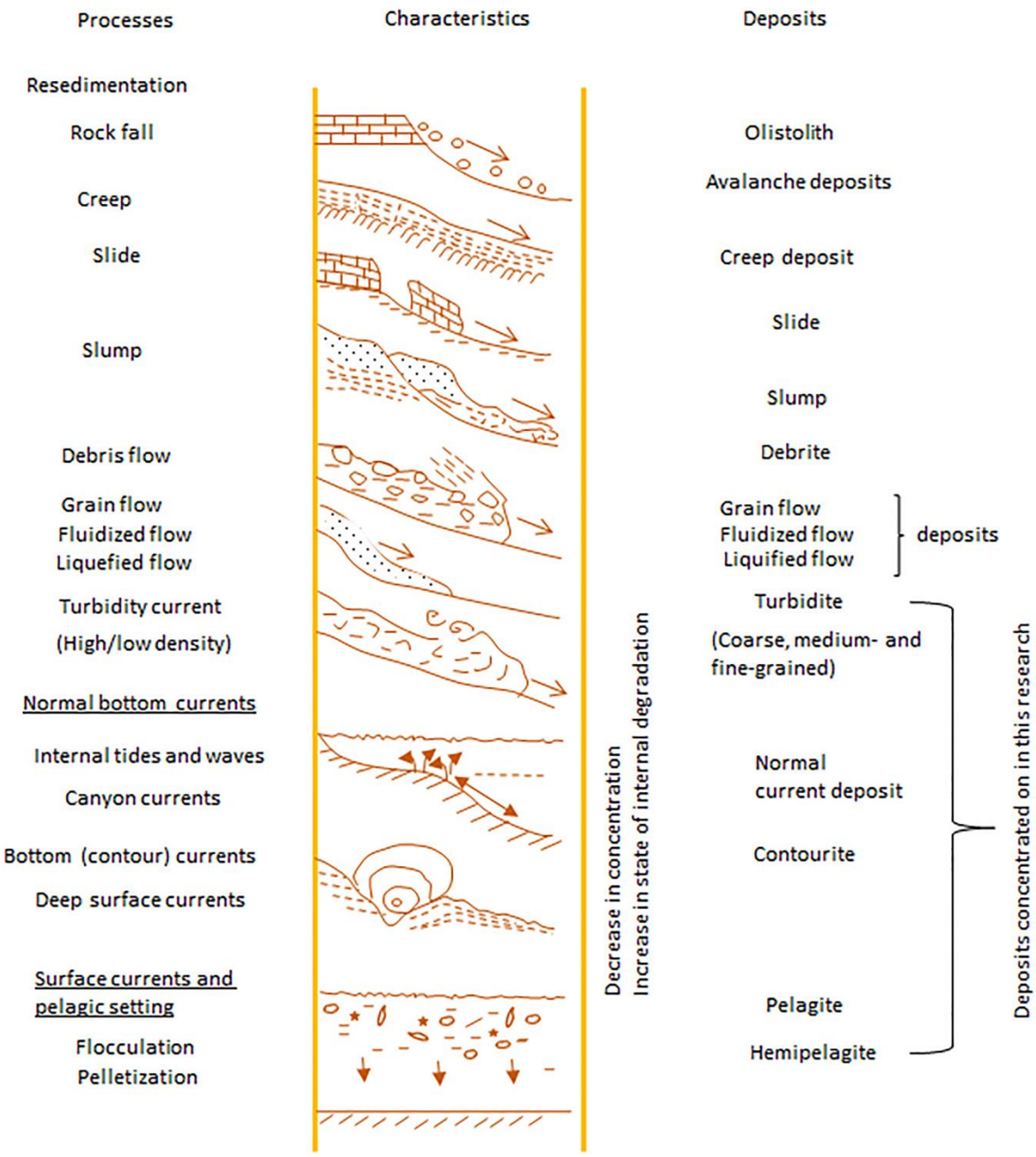

Figure 2.11. Schematic diagram of the transport mechanisms, depositional processes and deposits within the deep-water setting (Stow, 1985a).

There are variations in transport mechanisms, sedimentation rate and some sedimentary structures among the deep-water facies (turbidites, contourites and hemipelagites) and these are likely to impart different microfabric and subsequently affect the petrophysical characteristics of the rocks. A list of the differences is highlighted in Table 2.7.

Table 2.7. Major difference in deep-water facies in terms of depositional processes, transport medium and sedimentary structures among others

Features	Turbidites	Contourite	Hemipelagites
Depositional process	Turbidity current	Bottom current	Vertical settling
Initiating force	Gravity acting on high density mixture of water and sediments Tectonics/earthquake	Thermohaline current Internal tides Vertical eddies Wind	Inertia of river plumes, turbid layer plumes Internal tides and waves Slow moving water currents Glacial meltwater diffusion
Velocity of transporting medium	20 cm/s to 20 m/s	<0.3 cm/s to 20 cm/s	<0.3 cm/s
Sedimentation rate	Generally rapid but varied (from < 10 cm/ky to 200 cm/ky)	Moderate to high (10-100cm/ky)	Generally slow but diverse (<1 cm/ky to 20 cm/ky).
Grading	Positive grading	Bigradational	No grading
Bioturbation	lacks bioturbation	Moderately bioturbated	Thoroughly bioturbated
Sedimentary structures	Parallel to ripple/wavy laminations,	Indistinct to discontinuous lamination	No sedimentary structure

2.4.1 Turbidites

Turbidites constitute the most abundant and widely studied clastic sediments within the deep-water setting (Mutti *et al.*, 1999). The interest in turbidites has a long-standing relationship with economic importance, especially since the recognition of high-quality hydrocarbon reservoirs within them. Also of profound significance is the shaping of the ocean floor by turbidite systems which has a gross effect on oceanographic studies, reconstruction of

paleoenvironment and paleoclimate of the ancient ocean sediments (García *et al.*, 2015). In the literature there are discreet definitions of turbidites but to keep it simple the definition by Mutti *et al.* (1999) seems devoid of ambiguity and all-encompassing as to what most field geologists and marine geologists commonly accept as a turbidite. The definition describes turbidites as a sequence of graded coarse-grained (sandstones) and fine-grained (mudrocks) sedimentary deposits transported down the slope of the ocean by turbidity currents. The turbidity current is the mechanism of transportation by which turbidites are deposited and as the current becomes depletive it has two separate meanings (Normark and Piper, 1991). One of the meanings is by regarding turbidity current as a movement of fluid under the influence of gravity in which sediment dispersal is maintained at a turbulent state throughout the flow period. The second evolved definition is acknowledging a turbidity current as a movement of sediments and fluid by turbulence. Other processes, such as grain flow, debris flow and other flow mechanisms, might also be involved at some stages of turbidity current evolution.

The origin of turbidity currents has been attributed to storm surge, hyperpycnal flow, sediment failure and over steepening, seismic triggers, river discharge and debris flow among others (Normark and Piper, 1991; Stelting, Bouma and Stone, 2000; Plink-Björklund and Steel, 2004). It has also been on record that tectonic activity, sea level fluctuations, sediment supply and climate have significant effects on turbidity currents (Bouma, 2000a; Piper and Normark, 2009). Regardless of the process involved in the initiation of the turbulence, turbidity currents can be a short lived (surge type) or long lived (steady type) and each of them can be categorised into high density and low density flows (Stow and Johansson, 2000). Despite more than seven decades of awareness and studying turbidites, the turbidite paradigm is still frequently debated and a common controversy is associated with differentiating turbidites from other mass transport deposits (Shanmugam, 2006; Shanmugam, 2012a).

Kuenen in 1957 proposed the term turbidites for sediments deposited from turbidity current but prior to that moment, publication from Migliorini in 1943 on submarine density currents and other publications by Kuenen and co-authors in the 1950's set the stage for the turbidite paradigm (Mutti *et al.*, 1999). The Bouma sequence forms the foremost structural scheme of turbidite successions in which the sequence is divided into five successions; A, B, C, D and E (Figure 2.12). Each of the beds represents a change in the condition of the transport mechanisms. At the initial stage of turbulence the sediments are held in suspension and the propelling force is the suspended sediments coupled with gravity and increased sediment

density and this is known as autosuspension (Miall, 2015). Subsequently, coarse grained sediments settle out of the turbulent current and this contains structureless and massive but graded coarse sand with or without pebbles (Bouma division A). Subsequent waning in the energy of the transporting medium results in deposition of parallel laminated sand (B division), ripple sands (C division), and silt with ripple structures (D division). The final division in the ideal Bouma sequence consists of mud (E division).

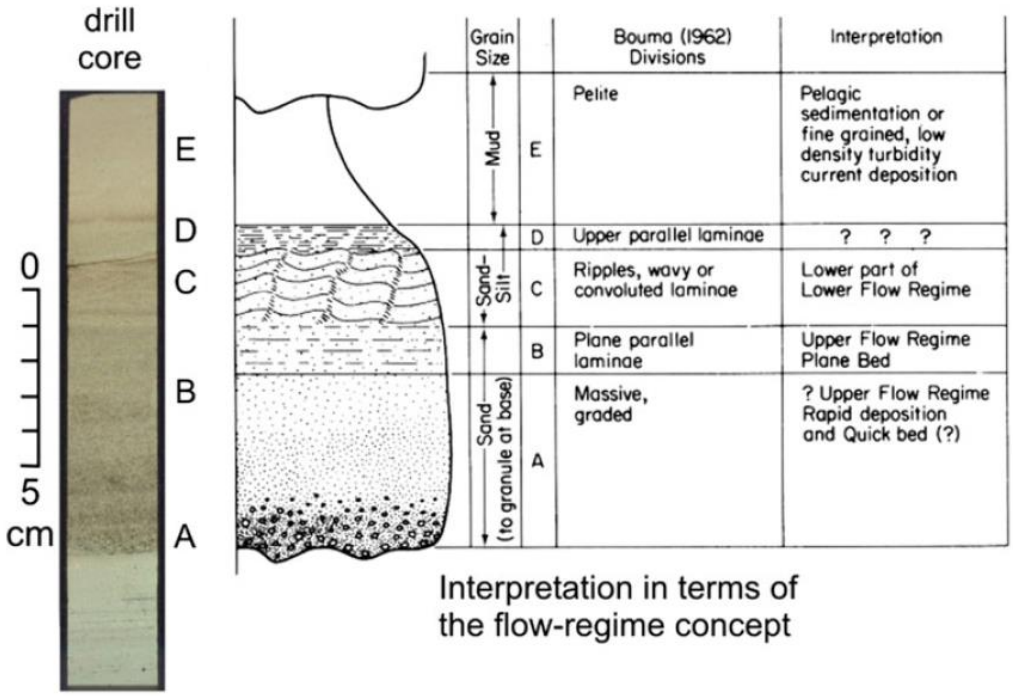

Figure 2.12. A diagram showing the ideal Bouma sequence (from, Miall, 2015)
Division A is deposited at the upper flow regime and not really associated with turbulence. B to D divisions are deposited by turbidity current. The planar structure in B results from traction along the sea floor. C and D are successive beds deposited as the power of turbulence dwindles and E is deposited through pelagic settling.

In this research, the focus is on the microstructural characteristics of fine-grained deep-sea sediments of which fine-grained turbidites is a member. There exists a variation in facies distribution, geomorphological features and architectural stacking pattern of the beds between fine-grained turbidites and the coarse grained counterpart (Stelting, Bouma and Stone, 2000). Fine-grained or muddy turbidites are dominated by materials or sediments that are of grain-size diameter of less than 63 μm; essentially, the clay to silt particles are more than 50% of the overall composition of the rock. Fine-grained turbidites are equivalent to D and E subdivision

of an ideal Bouma sequence and they show normal grading silt to mud (Piper and Deptuck, 1997). They have been further subdivided into mud-rich turbidites (which contain silty clay or clayey silt), silty turbidites when the silt content is more than 70% (Stow and Piper, 1984a; Strachan *et al.*, 2016), biogenic and disorganised turbidites (Stow, 1985b). The four facies models according to Stow (1985b) are presented below (Figure 2.13). Muddy turbidites are believed to be restricted to the distal end of the marine setting because their fine grain composition allows them to be transported a long distance from the source (Strachan *et al.*, 2016), hence, they are characterised by lower velocity settling in comparison with sand-rich turbidites.

Recognition of fine-grained turbidites can be very challenging because of their small grain-size and the poor quality of outcrops in ancient sedimentary records due to their susceptibility to weathering. In hand specimens, it might take the experience of an expert in marine sedimentology to identify a muddy turbidite due to the fact that such sample size is often devoid of very obvious structural or sedimentary feature that could aid in their recognition. There exist several models for fine-grained turbidites (Stow, 1979; Jones, McCave and Weaver, 1992; Piper and Deptuck, 1997; Bouma, 2000b; Mutti *et al.*, 2009). Fine-grained turbidites are typically mud-rich with low sand to mud ratio. They are found within the passive margin and transported through efficient flow mechanisms far from the source (Bouma, 2000a). Stow and Shanmugam (1980) proposed a sequence of nine subdivisions for mud turbidites. The subdivisions consist of alternating silt and mud laminae through a graded bed (T_0-T_8). These subdivisions are: at the base a cross bedded/parallel laminated/ fading ripple silt lamina (T_0), mud lamina +/- convolute lamination (T_1), very low amplitude climbing ripple (T_2), thin regular silt/mud laminae (T_3), thin indistinct laminae (T_4), thin wispy or convolute laminae (T_5), graded mud (T_6), ungraded mud (T_7) and bioturbated mud (T_8). The separation of silt and mud laminae is due to a process of shear sorting or hydraulic sorting as sediment settles through the benthic boundary layer (Stow and Bowen, 1980).

Other models exist, for example Jones, McCave and Weaver (1992) propose a different model in terms of sedimentary structure for very thick-bedded muddy turbidites. Relying on positive grading e.g. sharp base silt that grades up into mud or silty mud that shows a fining upward sequence (Piper and Deptuck, 1997) is not wholly satisfactory for recognition of fine-grained turbidites. Sediment deposits having similar characteristics have been described from a different process e.g. hyperpycnites during the episode of waning current (Mulder *et al.*, 2003),

generated in a different depositional setting other than the deep-water can show a normal grading (Mutti *et al.*, 2009).

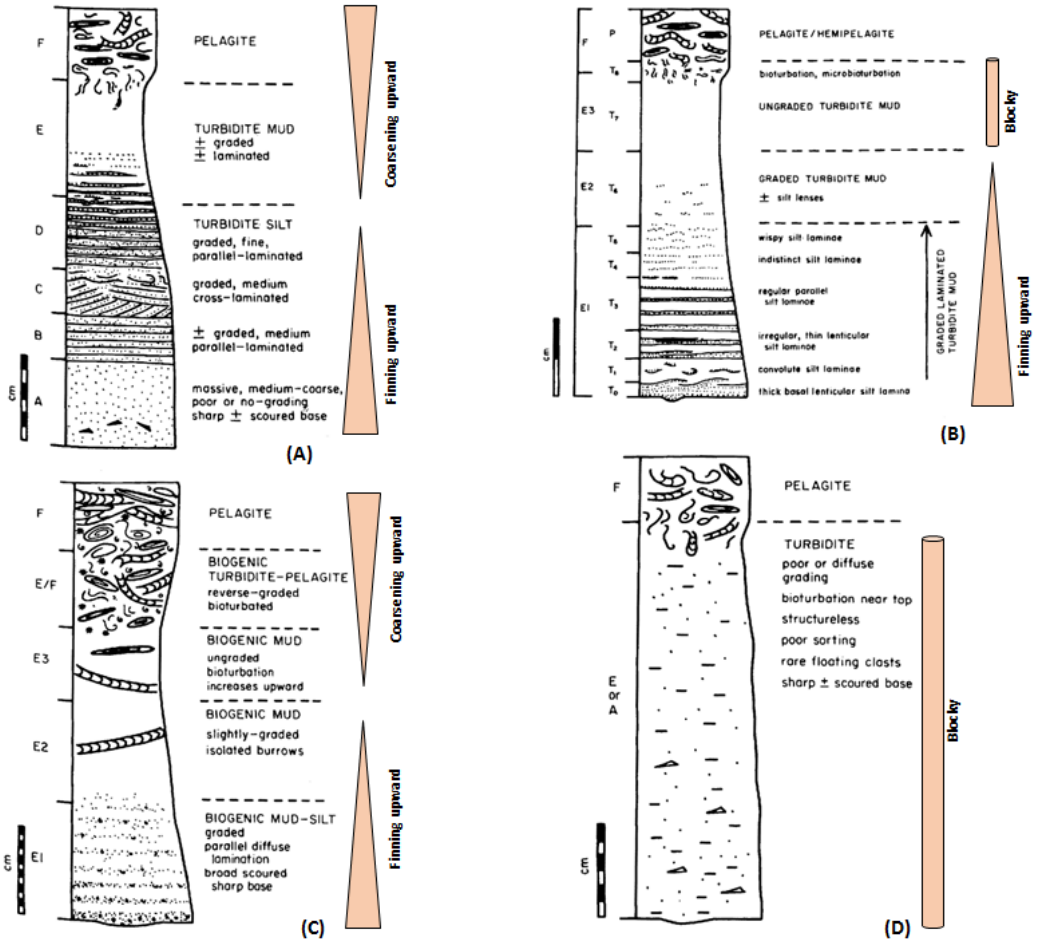

Figure 2.13 Facies model of fine-grained turbidites and their subdivisions (A) silt turbidites (B) mud turbidites (C) biogenic turbidites (D) disorganised turbidites (Modified after, Stow and Piper, 1984a; Stow, 1985b).

2.4.2 Contourites

Contourite is used to describe sediments mainly deposited, or reworked, by bottom currents that generally flow in an alongslope direction (Stow *et al.*, 1998; Hernández-Molina *et al.*, 2011; Brackenridge *et al.*, 2013; Rebesco *et al.*, 2014). In other words, the currents that generated such deposits run parallel to slope contours. They are difficult to identify, especially in the ancient record (Stow *et al.*, 1998). The process by which bottom currents can be generated has been linked to thermohaline geostrophic currents, major wind-driven surface

currents, internal tides and waves, benthic storms, interfaces between water masses and tsunamis, among others (Stow and Piper, 1984a; Shanmugam, 2012b; Rebesco *et al.*, 2014).

Contourites have perhaps lacked investigation from researchers in part due to the relative difficulty in their identification, and in part due to the perception of the oil and gas industry that they have low economic value in terms of hydrocarbon reservoir (Viana *et al.*, 2007). However, in recent times there has been a renewed interest focused on contourite deposits as they are now seen to be significant to exploration of deep-water oil and gas. Their importance is varied: they influence the slope stability, sandy contourites are potential hydrocarbon plays, and muddy contourites are good candidates for trapping hydrocarbon within the reservoir, or serving as a potential source rock for oil and gas (Duarte and Viana, 2007; Viana *et al.*, 2007; Rebesco, 2014; Rebesco *et al.*, 2014). Equally significant is the fact that they contain an expanded and sensitive record of the past environmental and climate change.

The main criteria used in recognising contourite deposits includes: association of both positive and negative grading, i.e. bi-gradational beds (Gonthier, Faugères and Stow, 1984), textural and compositional features that depict association of both *in situ* and derived sediments, and the presence of bioturbation throughout that has kept with the pace of deposition (Stow and Piper, 1984a). A cursory look at contourite deposits particularly in cores might show no discernible features, but rather a homogeneous deposit. However, structures such as faint lamination, cross bedding, subtle variation in grain-size from sand to silt to mud and biogenic structures have been reported in the literature as common features inherent in contourites but only observable with painstaking inspection (Stow and Piper, 1984a). However, there is still a lack of unambiguous and generally accepted diagnostic criteria for recognising contourites (Rebesco *et al.*, 2014). Recognition of contourites from the deep-water is further made difficult by the process continuum between sediments deposited by turbidity current, bottom currents and pelagic settling (Mulder, Razin and Faugeres, 2009).

Contourite facies have been classified based on grain-size into rare gravel rich contourites, and common sandy, silty and muddy contourites. The composition is commonly mixed terrigenous-biogenic, but purely calcareous and volcaniclastic contourites also exist. In this research, the interest is focused on fine-grained contourites, otherwise known as muddy contourites. Muddy contourites are rich in both clay and silt grain-size particles, and have poor sorting and are usually made up of compositional mixture of terrigenous or volcaniclastic and biogenic components (Stow *et al.*, 1998). The process by which contourites are generated are currently

witnessing a hot debate among deep-water sedimentation researchers, but there is a common understanding that most contourites are produced by thermohaline geostrophic currents (Shanmugam, 2017).

The samples of contourites for this research are from one of the world's renowned contourite repositories from the Gulf of Cadiz. Contourite deposits in this area result from deposition and reworking by the strong bottom current produced by the Mediterranean Outflow Water (Stow *et al.*, 2013). Thermohaline induced currents cause dense water masses to sink to the bottom of the ocean (Figure 2.14). The dense water masses then move along the slope due to gravitational and Coriolis forces. As the dense water masses (bottom current) move, they erode large amounts of sediments along the continental slope and the large deposits resulting from this process are called contourite drifts (Brackenridge *et al.*, 2013; Stow *et al.*, 2013).

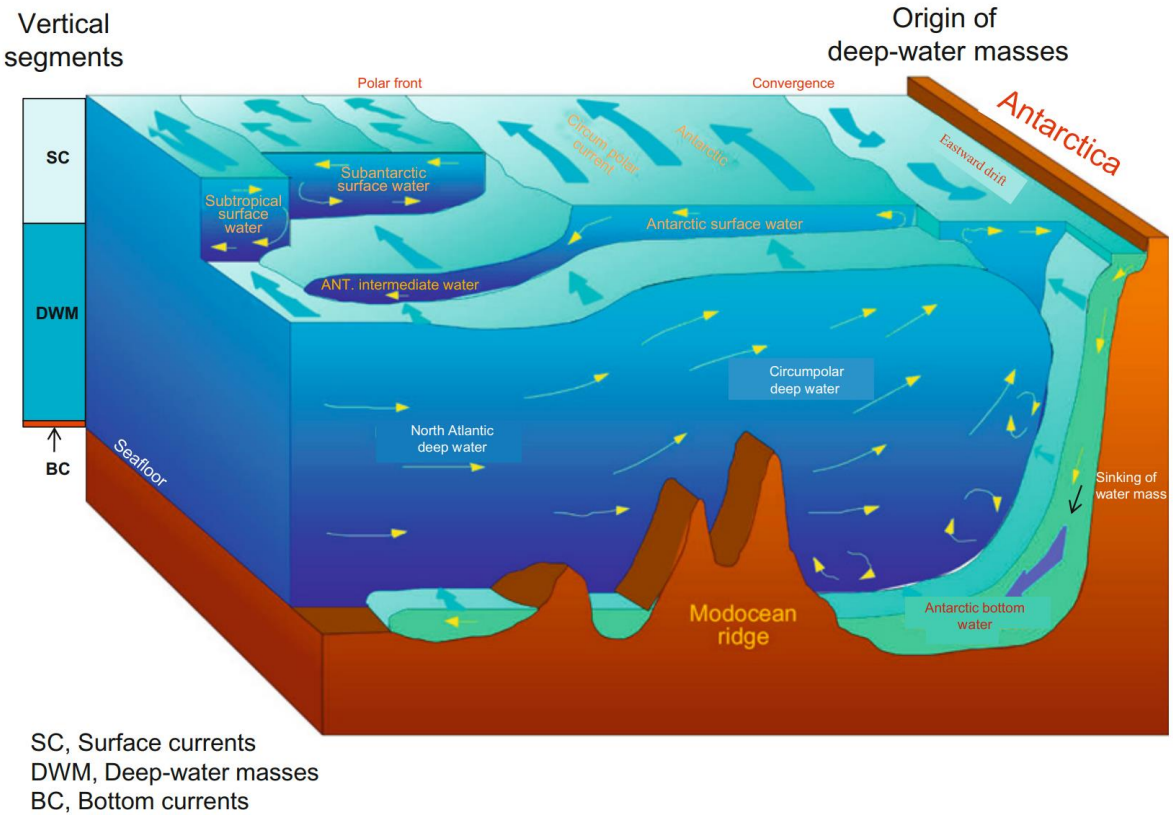

Figure 2.14. Cartoon of water masses of the Southern Ocean showing the three component of water bodies; surface currents, intermediate currents and bottom currents (Shanmugam, 2012b). Note that the bottom current here is generated due to thermohaline (disparity in temperature and salinity) resulting from the freezing of the water mass at the shelf and subsequent resistant to movement by surface currents. The water then sinks due to increase in density and traces the bottom of the slope.

Stow *et al.* (1998) propose a significant model which highlights some criteria useful for not only recognising fine-grained contourites but differentiating contourite deposits from fine-grained turbidites and hemipelagites/pelagites. The authors state that muddy contourites are commonly homogeneous, bioturbated and show a variable and irregular distribution of coarser silt, either dispersed or in lenses and discontinuous laminae (Figure 2.15).

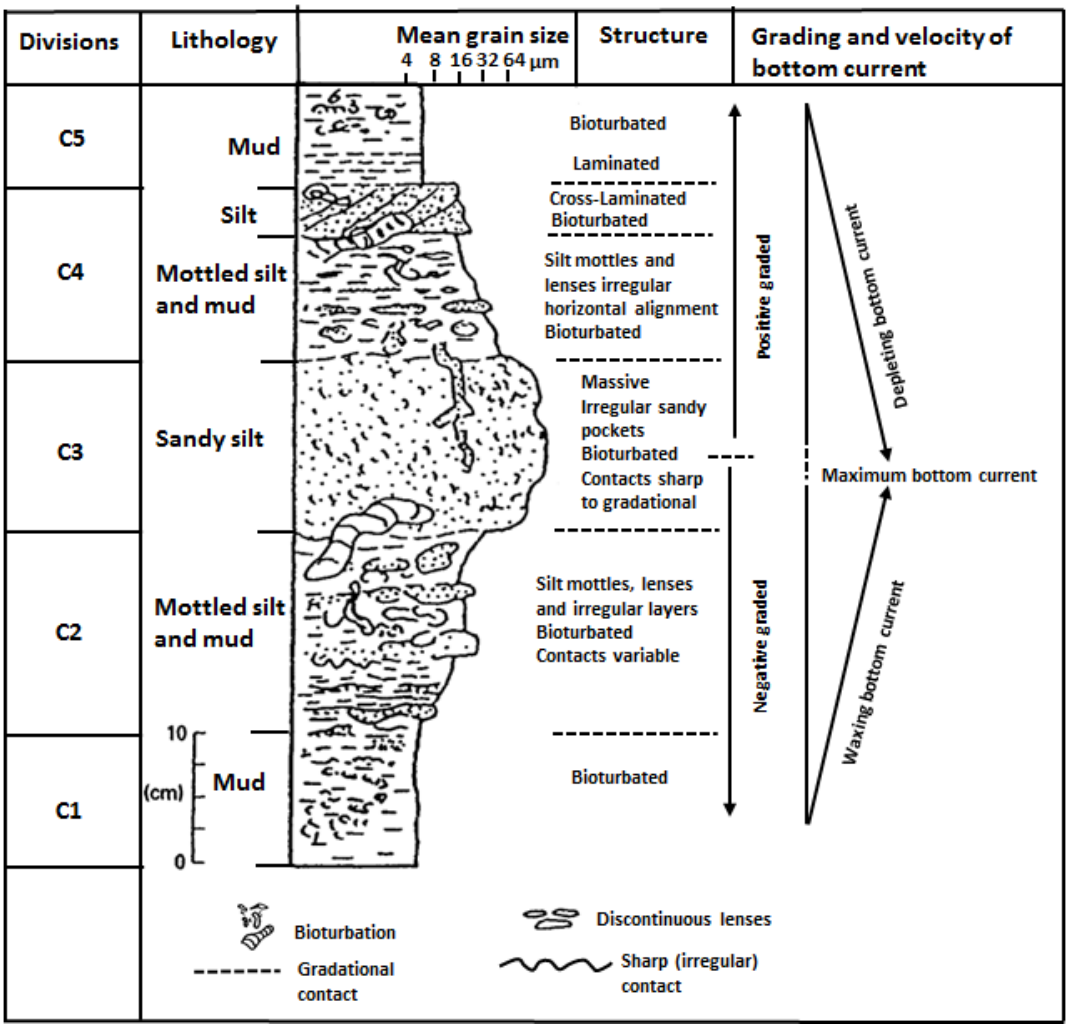

Figure 2.15. Conceptual model for contourite facies with bigradational grading; initial negative grading and subsequent positive grading (Modified after, Stow *et al.*, 1998).

2.4.3 Hemipelagites and Pelagites

Hemipelagites/pelagites are the third group of common sediments within the deep-sea setting. Sediments belonging to this group are fine-grained, structureless and thoroughly bioturbated. Hemipelagites consist of an admixture of biogenic and terrigenous materials in which both terrigenous and biogenic components are more than 10%. The silt-size fraction of the terrigenous constituent is more than 40% (Stow and Piper, 1984a; Stow and Tabrez, 1998). In the case of pelagites, the terrigenous fraction is dominantly clay-sized, as in deep-ocean 'red clays', but mostly they are dominated by pelagic biogenic material. Both hemipelagites and pelagites are deposited through a complex interaction between vertical settling and very slow lateral advection (Stow, Huc and Bertrand, 2001) in the absence of strong turbidity or bottom currents. There exists an ambiguous and non-unique set of criteria for differentiating

hemipelagites from muddy contourites and fine-grained turbidites (Dall'Olio, Felletti and Muttoni, 2013). In most cases, hemipelagites and pelagites are deposited during a transformation of flow processes from turbidity current to bottom current and hemipelagic sedimentation which results in a complex association of sedimentary facies (Figure 2.16).

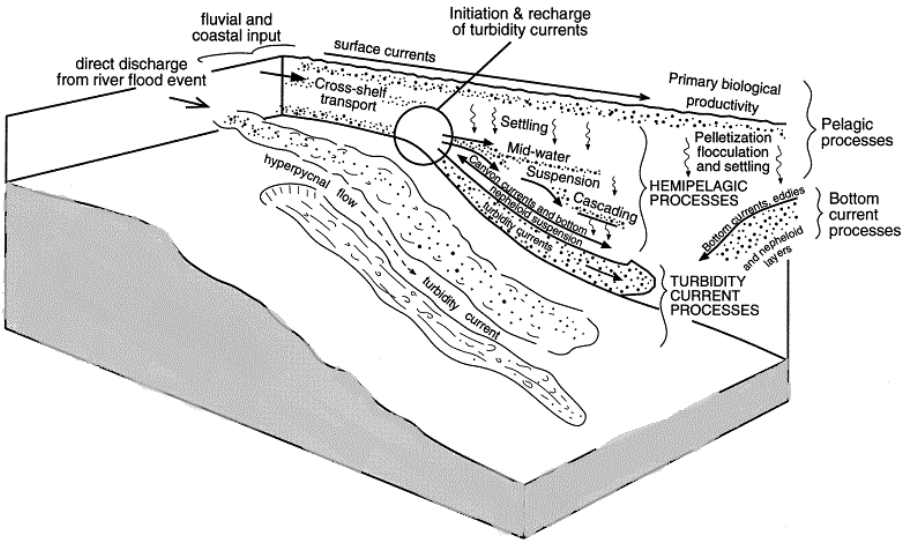

Figure 2.16 Schematic diagram showing the important depositional process responsible for deposition of sediment within the deep water setting (Stow, 1985b). Note the complex interplay of processes operating beyond the shelf break; ranging from turbidity currents to bottom current and hemipelagic or pelagic sedimentation. Hemipelagic is an intermediate depositional mechanism between turbidity flow and pelagic settling.

Pelagic sediments have been subdivided into pelagic ooze, muddy pelagic ooze and pelagic clay in which the biogenic content is more than 75%, biogenic content is between 25 and 75% but terrigenous clay more than silt and biogenic content less than 25% with clay more than 60% respectively (Stow and Piper, 1984b).

According to Stow and Tabrez (1998), criteria for identifying hemipelagites include: very homogeneous sediment with a low sedimentation rate, the absence of any current-induced structures or grading, a biogenic fraction dominated by pelagic material, a very fine-grained silt/clay terrigenous fraction, and a high degree of bioturbation. Hemipelagites deposited within an anoxic setting generally lack bioturbation and may preserve a greater proportion of organic matter. Hemipelagites typically exhibit an indistinct colour and/or compositional bedding that is regular and cyclic.

Hemipelagites are most commonly deposited along the continental margin (both shelf and slope). They are ubiquitous in most oceans of the world and are present in both ancient and modern sedimentation. Most hemipelagic sediments are thoroughly bioturbated, a resultant effect of slow rate of sediment deposition (Stow and Piper, 1984b); however, in areas of rapid deposition of hemipelagites (Stow and Tabrez, 1998), the oxygen content of the hemipelagites will be low and anaerobic and therefore the sediments are less disturbed or less homogenised by biogenic activities. Such hemipelagic sedimentation ensuing from rapid sedimentation can be a good candidate for preservation of organic matter and thus a good source rock for hydrocarbon reservoir provided other criteria are met.

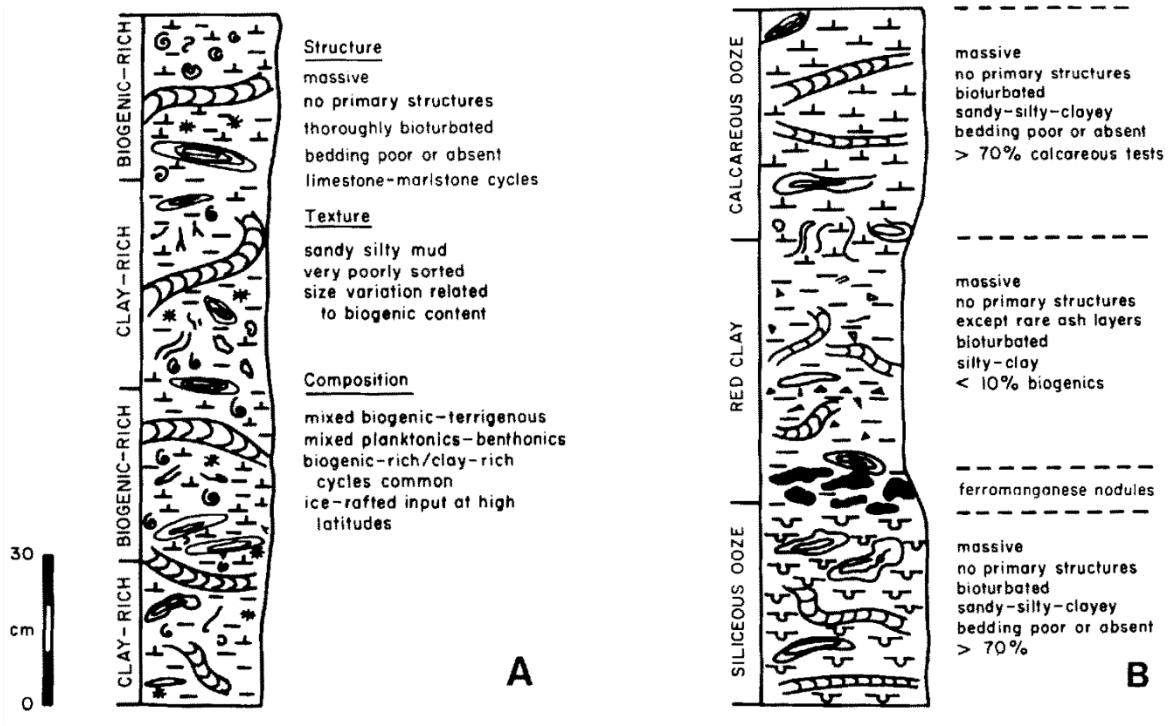

Figure 2.17 Diagram showing proposed facies model for (a) Pelagite and (B) Hemipelagite (After, Stow, 1985b)

CHAPTER 3 – MATERIALS AND METHODS

3 Materials and methods

The success of any research is dependent on the selection of relevant materials and the method of collection of the data (methodology). Here in this chapter, the materials and methodology chosen, which match the set objectives of the research, are presented. Core samples used for this research were collected from expeditions 317, 339 and 355 that were carried out by the International Ocean Discovery Program (IODP). The sample collection from the three expeditions were informed by the fact that sediment retrieved during expedition 317 and 339 are dominantly contourites and hemipelagites, whereas those from expedition 355 are dominated by turbidites.

In this chapter, a brief description of the Expeditions is made. This is followed by an outline of methods used for grain-size analysis, and then by sample preparation via different drying techniques for microstructural study. The different laboratory analyses performed, include: laser diffraction granulometry, imaging with scanning electron microscopy (SEM), energy dispersive x-ray analysis (EDX), low-pressure nitrogen gas adsorption, x-ray diffraction analysis, and synchrotron powder diffraction.

Because methodology is a significant part of this thesis, the chapter reviews in some detail the operational techniques, theories and challenges associated with each of the methods. The further development of these methodologies into an efficient and effective workflow for grain-size analysis and microstructural study, respectively, are then presented in Chapters 4 and 5.

3.1 Materials

3.1.1 Expedition 317

Expedition 317 is one of the IODP projects which took place between 4th of November 2009 and 3rd of January 2010. The expedition was aimed at understanding the consequence of global sea-level and local tectonic activities on preservation of sedimentary sequence within the continental margin. It was an opportunity to core sediments from continental shelf (shallow-water) down to continental slope (deep-water). The expedition is situated at the eastern margin of South Island in the Canterbury Basin in New Zealand. Four sites were drilled within the continental margin of the Canterbury Basin and they were tagged 1351, 1352, 1353 and 1354 (Figure 3.1 and Figure 3.2). Three of the sites (1351, 1352, and 1353) are located within the

shelf of the continent and only site 1352 is situated within the slope (Expedition 317 Scientists, 2010; Fulthorpe, Hoyanagi and Blum, 2011).

The sedimentary sequence targeted ranges from Oligocene (Marshall Paraconformity) to Holocene (Fulthorpe *et al.,* 2009) but most of the sediments recovered at the end of the expedition are restricted to Miocene to Recent sediments (Fulthorpe, Hoyanagi and Blum, 2011). Sediments belonging to Oligocene to Eocene age were only recovered in site 1352. On a broad note, sediments recovered during the expedition have been subdivided into three units (I, II and III). The subdivision is based on lithological facies variation such that in site 1351 (outer shelf), 1353 (inner shelf) and 1354 (mid shelf) only units I and II are present. Unit I facies are heterolithic containing mixed terrigenous sediments and calcareous sediments (Expedition 317 Scientists, 2011). The boundary between unit I and II is gradational. Unit II is homogeneous, and it contains muddy terrigenous sediments in the shelf (sites; 1351, 1353 and 1354) but in site 1352 that is located within the continental slope, unit II contains marlstone to sandy marl. A third unit (unit III) restricted to continental slope site is hemipelagic to pelagic sediments made up of foraminifera-bearing nannofossil limestone of Oligocene to Eocene age. This unit has been recognized as the equivalent of the Amuri Limestone. Further details on the sedimentary units recovered from each of the sites can be found in proceedings related to Expedition 317 of the International Ocean Discovery Program (Fulthorpe *et al.*, 2009; Expedition 317 Scientists, 2010; Expedition 317 Scientists, 2011; Fulthorpe, Hoyanagi and Blum, 2011). The initial target of the expedition was to get to the bottom of the Marshal Paraconformity which was believed to have resulted from thermohaline current circulation (Fulthorpe *et al.,* 2009) and such thermohaline induced current would have produced contourites. However, at the completion of the expedition, the sediments recovered possess ambiguous characteristics that are untypical of contourites (Expedition 317 Scientists, 2011).

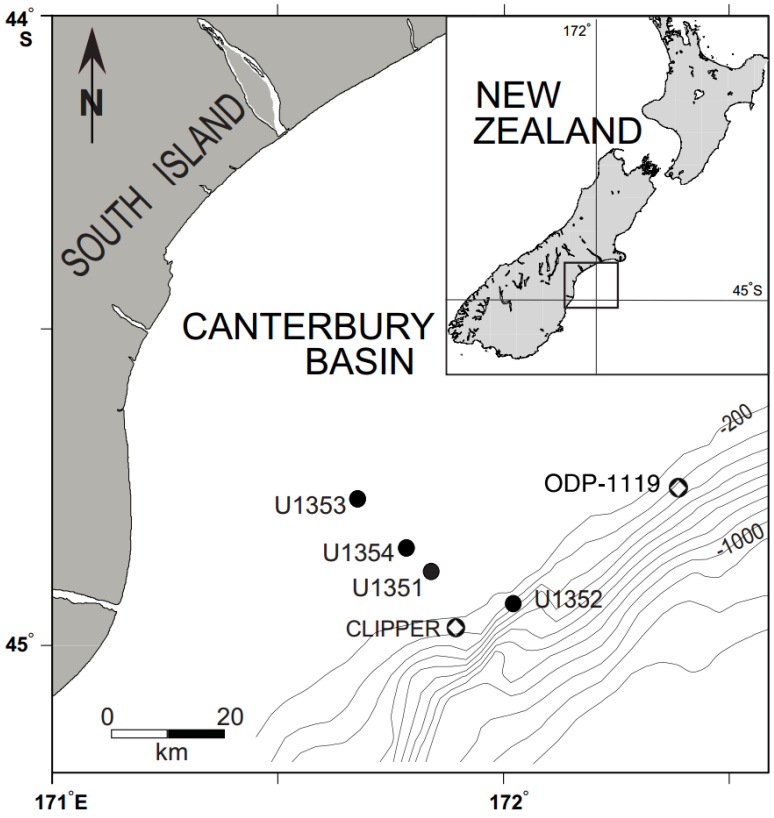

Figure 3.1 map showing location of Expedition 317 sites (Hoyanagi *et al.*, 2014)

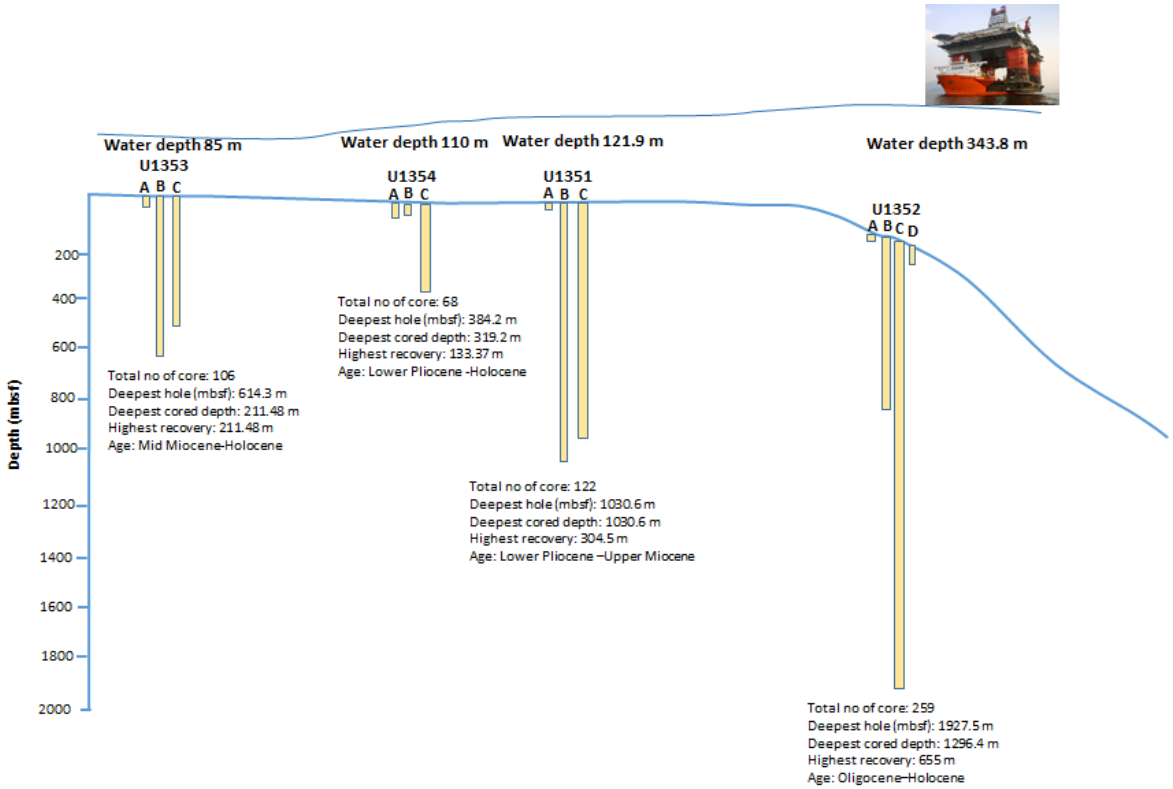

Figure 3.2. Information on the sites and holes drilled during Expedition 317.
The deepest hole is at site 1352 (1927.5 m) and it is the only site located on the continental slope, other sites are within the continental shelf.

3.1.1.1 Geological setting

The Canterbury Basin in New Zealand is situated at the landward edge of the eastern margin of South Island which is part of the continental margin and has experienced rifting during the late Cretaceous (Expedition 317 Scientists, 2010).

The South Island, New Zealand includes; the Campbell Plateau, Chattam Rise and Bounty Trough (Figure 3.3). In the present day, the basin underlies the continental plain and the offshore province. The basin is extensive and covers an area of about 50,000 km^2 with a shelf width of approximately 100km (Uruski, 2012). The basin is bounded by volcanic centres; the Bank Peninsula (5.8 -12 Ma) to the northeast and the Otago Peninsula (9.6-12.9 Ma) to the southwest (Lu, Fulthorpe and Mann, 2003). The Canterbury Basin remained a passive margin after the Late Cretaceous. There was convergence between the Australian and Pacific plates and this resulted in development of the Alpine Fault which is close to the Canterbury Basin. However, despite proximity of Alpine Fault to the basin, the basin is presently stable (Lu,

Fulthorpe and Mann, 2003) and mainly characterised by subsidence (Browne and Field, 1988; Vandeginste and John, 2013). Primarily, three stratigraphic groups of marine sediments are documented in the basin as part of post-rift sedimentation; Onekakara, Kekenodon and Otakou Groups (Figure 3.4). The post-rift sedimentary sequence is associated with transgressive and regressive tectonic cycles (Expedition 317 Scientists, 2010) in which the Onekakara, Kekenodon and Otakou Groups were deposited during the transgressive, highstand and regressive cycles respectively (Lu, Fulthorpe and Mann, 2003; Vandeginste and John, 2013). The sediments after the post-rift transgressive phase are first order (~80 Ma) and deposition end in the Eocene period (Fulthorpe, Hoyanagi and Blum, 2011). These are the Onekakara group which are terminated during the Eocene when flooding was at its peak (maximum flooding).

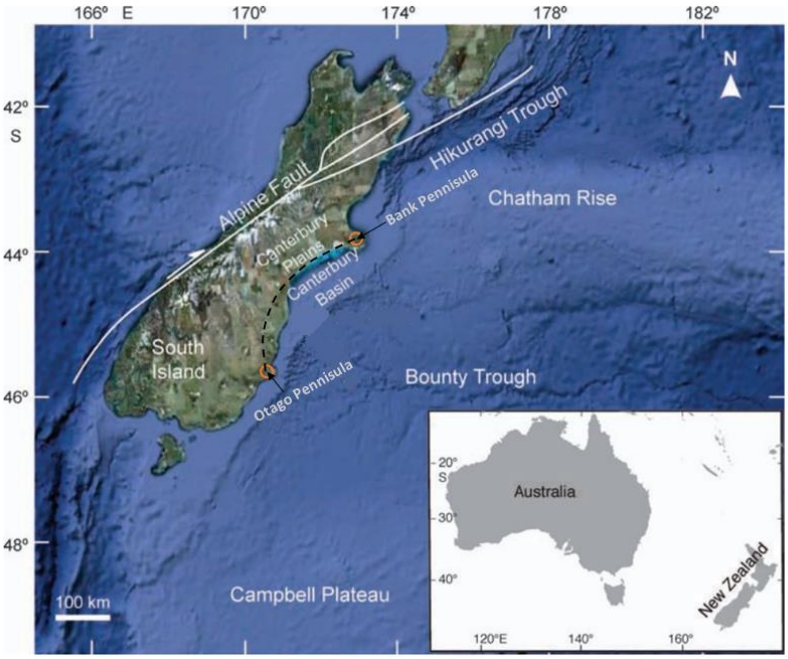

Figure 3.3. Map of South Island, New Zealand showing location of Canterbury Basin bounded by Bank Pennisula to the northeast and Otago Pennisula to the southwest (modified after, Vandeginste and John, 2013).

The Onekakara Group is recognised as having a ramp like geometry onlapping on older basement rocks in seismic section (Fulthorpe *et al.*, 1996; Expedition 317 Scientists, 2010). The group is made up of alluvial sandstone, siltstone and mudstone (Vandeginste and John, 2013). In the early Oligocene period there was starvation in the supply of terrigenous sediments to the basin and this led to deposition of pelagic to hemipelagic bioclastic limestone units of the Amuri Formation. The Amuri Formation which is early Oligocene in age (~ 33 Ma) is

separated from the overlying units by a prominent unconformity (Marshal Paraconformity) which then passes to the mid Oligocene to Late Oligocene cross-bedded glauconitic sand (Concord Formation) and calcarenite limestone (Weka Formation). Both Concord Formation and Weka Formation belong to the Kekenodon Group (Expedition 317 Scientists, 2010).

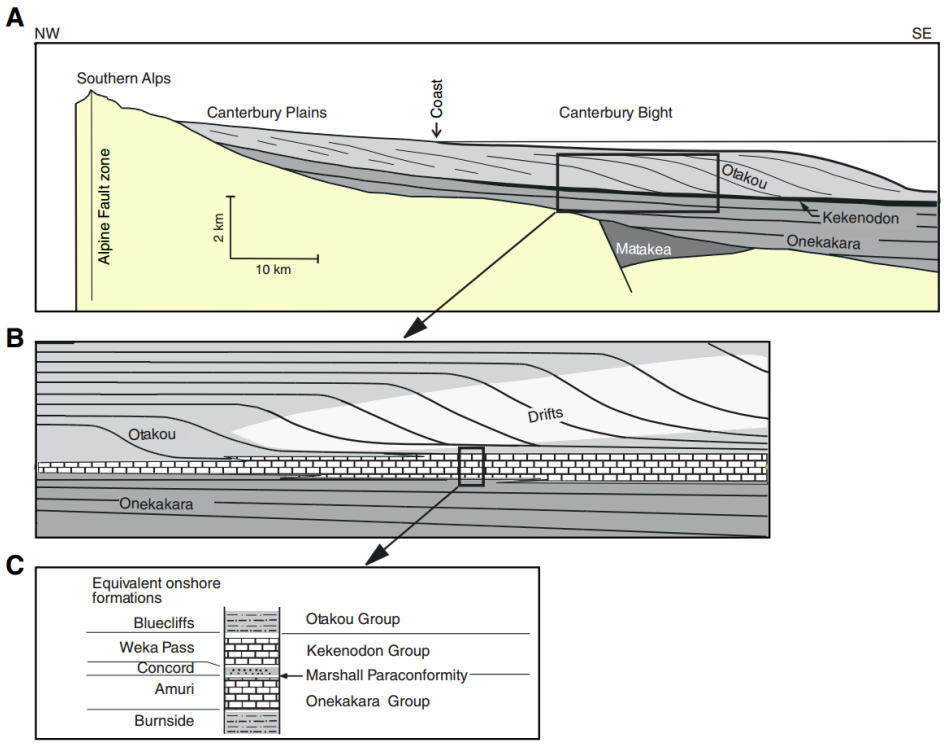

Figure 3.4 Diagram showing the stratigraphy of Canterbury basin at varying scales; (A) Large scale post-rift stratigraphy (B) Seismic scale stratigraphy with successive clinoforms prograding over older clinoforms (C) Outcrop scale stratigraphy showing Marshal Paraconformity (Fulthorpe *et al.*, 2009).

3.1.2 Expedition 339

Expedition 339 took place between November 2011 and January 2012. The objectives of the expedition include: understanding the influence of Mediterranean Outflow Water through the Gibraltar Gateway on global ocean circulation and climate: documenting the influence of tectonic activities on Gibraltar Gateway; and elucidating the effect of MOW-driven bottom currents on contourite sedimentation within the continental margin (Expedition 339 Scientists, 2013). At the end of the Expedition more than 5.5 km of cores were retrieved and a total of seven sites (1385-1391) were drilled (Figure 3.5 and Figure 3.6); five sites within the Gulf of Cadiz and two sites within the Iberian margin. Six of the sites were focused on contourite depositional system (1386-1391), and one site (1385), situated at the southwest of Portugal,

sampled Quaternary (1.4 Ma) hemipelagic deposits. The Gulf of Cadiz is a classic world recognized laboratory for contourite deposits (Hernández-Molina *et al.*, 2013; Stow *et al.*, 2013). It is characterized by a series of flowing water masses and the slope is devoid of major canyons that would prevent progress of along slope currents (Bahr *et al.*, 2014 and references therein). The Expedition gives an opportunity to test the contourite paradigm (Expedition 339 Scientists, 2012; Rebesco *et al.*, 2014).

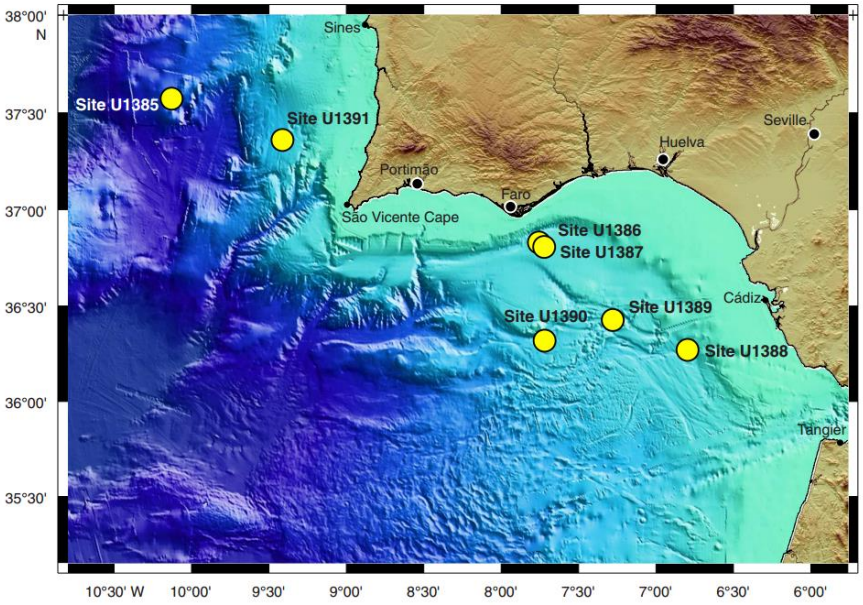

Figure 3.5. Location map of Western Iberian Margin showing drilled sites during Expedition 339 (Hernández-Molina *et al.*, 2016).

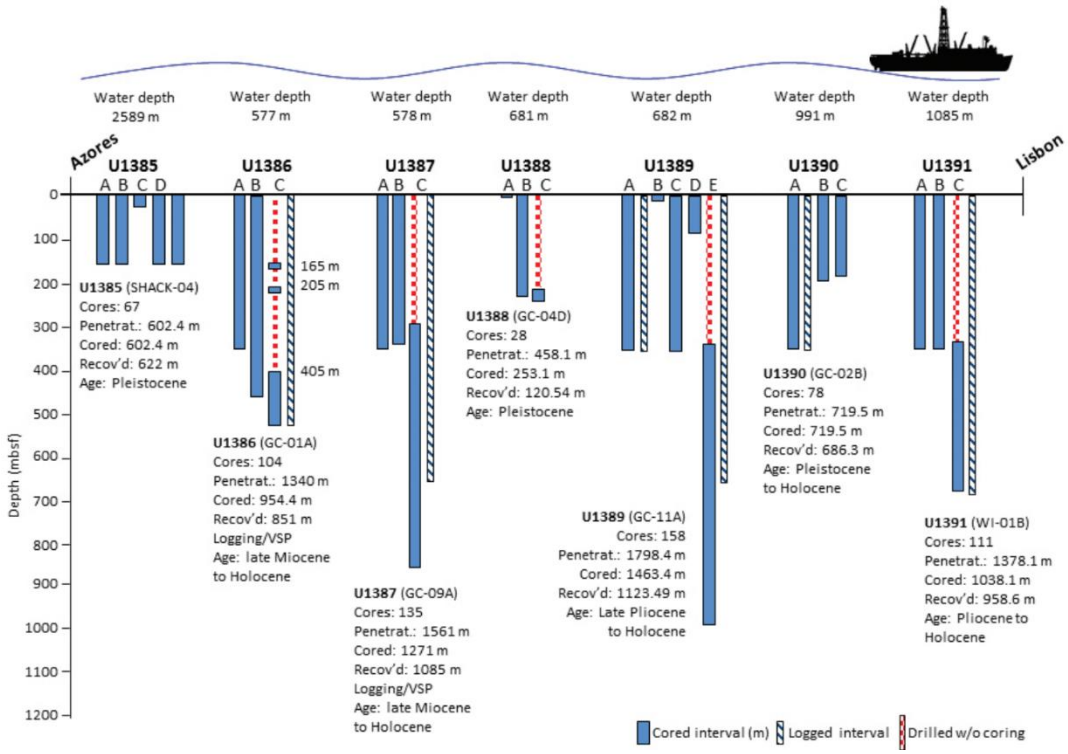

Figure 3.6. Information on site drilled during Expedition 339 (Adapted from, Hernández-Molina *et al.*, 2013).

3.1.2.1 Geological Setting

The Gulf of Cadiz is within the diffuse boundary that marks the separation of the Eurasia Plate from the Africa Plate (Pinheiro *et al.*, 1996; Hernández-Molina *et al.*, 2013). It has a complex tectonic history and it is bounded to the west by the Azores-Gibraltar fault zone and to the east by the Gibraltar arc (Figure 3.7).

The formation of the Iberian plates are marked by two events; south Iberian continental margin formed as a result of continental break up between North America and Africa during the Jurassic and the western Iberia continental margin formed during the Cretaceous time when Iberia separated from North America (Zitellini *et al.*, 2009). The Iberian plate separated as part of the African Plate during the Late Cretaceous to Eocene but at present the plate is part of the Eurasia plate as a result of its later movement during the Oligocene period (Srivastava *et al.*, 1990). The Iberian plate had acted independently during the middle Cretaceous until it merged with the African plate in the Late Cretaceous (Maldonado, Somoza and Pallares, 1999).

The Gulf of Cadiz is situated at the present day at the point of convergence between the Eurasia (Iberia) Plate and Africa Plate which trend northwest to southeast (Expedition 339 Scientists, 2012; Expedition 339 Scientists, 2013) and the convergence rate is about 4 mm per year (Argus *et al.*, 1989; Maldonado, Somoza and Pallares, 1999; Llave *et al.*, 2011). The tectonic history of the Gulf of Cadiz is complex as shown in Figure 3.7 and it is associated with different phases of rifting, convergence and strike slip motions (Maldonado, Somoza and Pallares, 1999). The complexity of the tectonic history has a great consequence on the physiographic setting of the area. Evolution of the Gulf of Cadiz has been linked to three successive phases: (1) development of passive margin during the late Mesozoic due to rifting and seafloor spreading; (2) compressive phase during Eocene to Miocene and development of foredeep and its associated Betic-Rif orogeny during the Miocene period (Stow *et al.*, 2002a); and (3) a phase of relative tectonically stability during Pliocene to Recent. The onset of contourite deposition and drift development occurred at around 4.5 My in the Early Pliocene. The major phase of drift growth has been from about 2.5 My to the present.

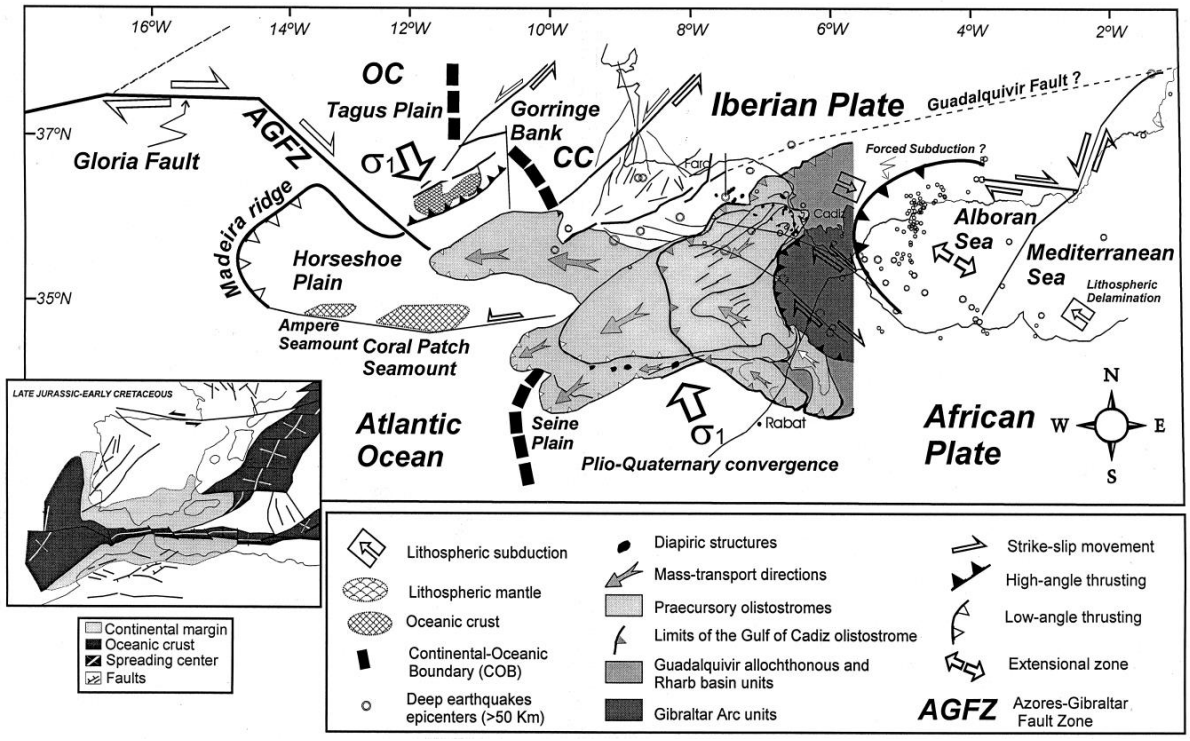

Figure 3.7 Tectonostratigraphic framework of the Gulf of Cadiz and its associated complex structures. The inset map at the bottom left shows paleotectonic structures during the Jurassic to the Cretaceous (After, Maldonado, Somoza and Pallares, 1999).

In the Miocene the Gulf of Cadiz was associated with compression coupled with extensional collapse of the Beltic orogeny front and emplacement of unstable allochotonous units (Olistostrome of the Gulf of Cadiz) which resulted in subsidence and strong halokiness along its margin (Maldonado, Somoza and Pallares, 1999; Llave *et al.*, 2011). Between the Pliocene to Quaternary, glacio-eusatic sea level changes resulted in erosion, sedimentary progradation and production of canyons which partly masked the paleotectonic structures in the Gulf of Cadiz (Llave *et al.*, 2011). Although the Gulf of Cadiz is stable at present (Maldonado, Somoza and Pallares, 1999; Brackenridge *et al.*, 2013), neotectonics characterized by diapiric activity, mud volcanism and fault reactivation have had a great control on the seafloor morphology and the contourite depositional system in the region (Llave *et al.*, 2011).

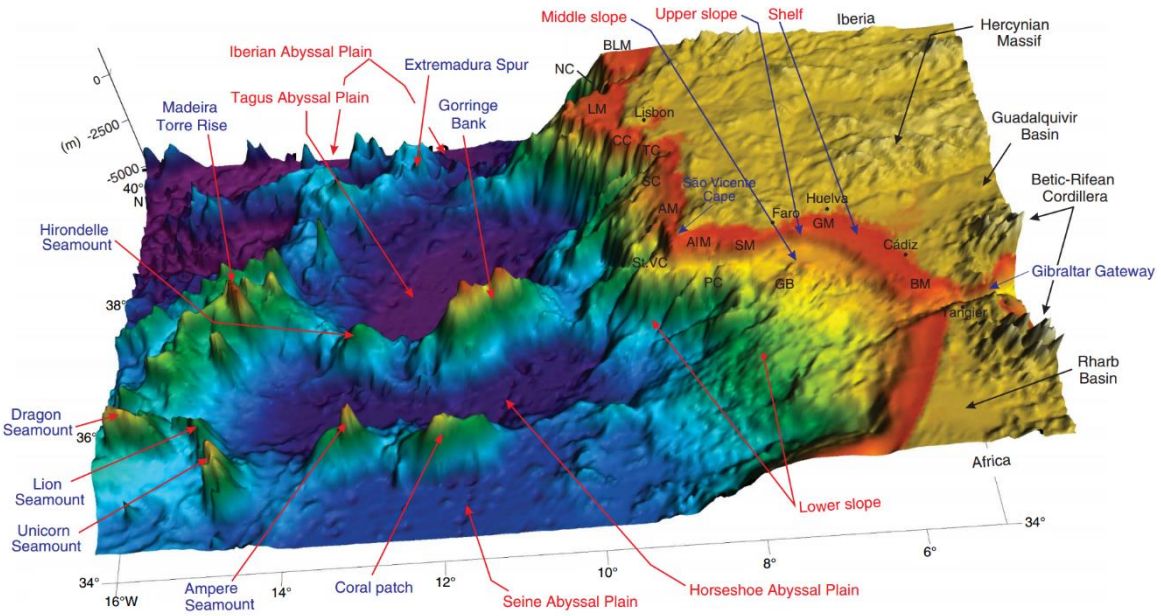

Figure 3.8 Three dimension regional physiographic map of the Gulf of Cadiz. AlM: Algarve margin; BM: Betic domain Margin; BLM: Beira littoral margin, CC: Cascais Canyon; GB: Guadalquivir Bank; GM: Guadalquivir Margin, LM: Lisbon margin; NC: Nazaré Canyon; PC: Portimao Canyon; SC: Setúbal Canyon; SM: Sudiberic Margin; St. VC; São Vicente Canyon: TC: Tagus Canyon; (Adapted from, Expedition 339 Scientists, 2012).

3.1.2.2 Oceanographic setting

The present oceanographic setting of the Gulf of Cadiz is controlled by interaction between the Atlantic Ocean and Mediterranean Outflow Water (Stow *et al.*, 2002a; Bahr *et al.*, 2014; Hernández-Molina *et al.*, 2016). The Mediterranean water is warm and saline and it is made up of two water masses; Levantine Intermediate water (LIW) water and Western Mediterranean

Deep water (WMDW), although the LIW constitutes 90% of its composition (Bryden and Stommel, 1984; Bahr *et al.*, 2014). The isolated nature of the Mediterranean Outflow coupled with the dry climate in the region facilitates the temperature increase and its high salinity (Baringer and Price, 1999). The Atlantic Inflow Water is colder and less saline and as the Mediterranean Water Outflows through the Gibraltar Gateway, it underlies the colder, turbulent and less saline Atlantic Inflow Water. This process produces a strong bottom current that flows along the slope through thermohaline circulation (Baringer and Price, 1999; Hernández-Molina *et al.*, 2013).

The Mediterranean Outflow exits the Gibraltar Gateway in a northwest direction due to Coriolis force (Llave *et al.*, 2007) at a speed of about 2.8 m/s and 0.7 m/s at the Gibraltar Strait and Cape Sao Vicente respectively (Bahr *et al.*, 2014 and reference therein). The influx of the exiting Mediterranean Outflow has a strong effect on the temperature and salinity of the North Atlantic Central Water (Hernández-Molina *et al.*, 2006). As the Mediterranean Outflow exits the Gibraltar Gateway, it flows down the continental slope due to its density but later neutralize toward the westward direction and becomes buoyant (Baringer and Price, 1999). During the exit it also experiences a drop in salinity and temperature as it interacts with the Atlantic Inflow Water and then splits into two main water cores; Mediterranean Upper Core and Mediterranean Lower Core (Figure 3.9). The Mediterranean Upper Core flows at the base of the slope between 500 m to 800 m while the Mediterranean Lower Core flows between 750 m and 1200 m (Llave *et al.*, 2007). The differential pathways of Mediterranean Outflow have been attributed to some ridges adjacent to the Gibraltar opening due to neotectonics and density current driven forces (Brackenridge *et al.*, 2013; Hernández-Molina *et al.*, 2016). The Mediterranean Lower Core according to its flow paths subdivides into three branches (Figure 3.9); (Intermediate, Principal and Southern branches). The interplay between the Mediterranean Outflow moving along slope, Atlantic Inflow water and sedimentation resulted in the widely known contourite depositional system extending from the Portuguese margin up to the continental slope of the Irish margin (Llave *et al.*, 2011).

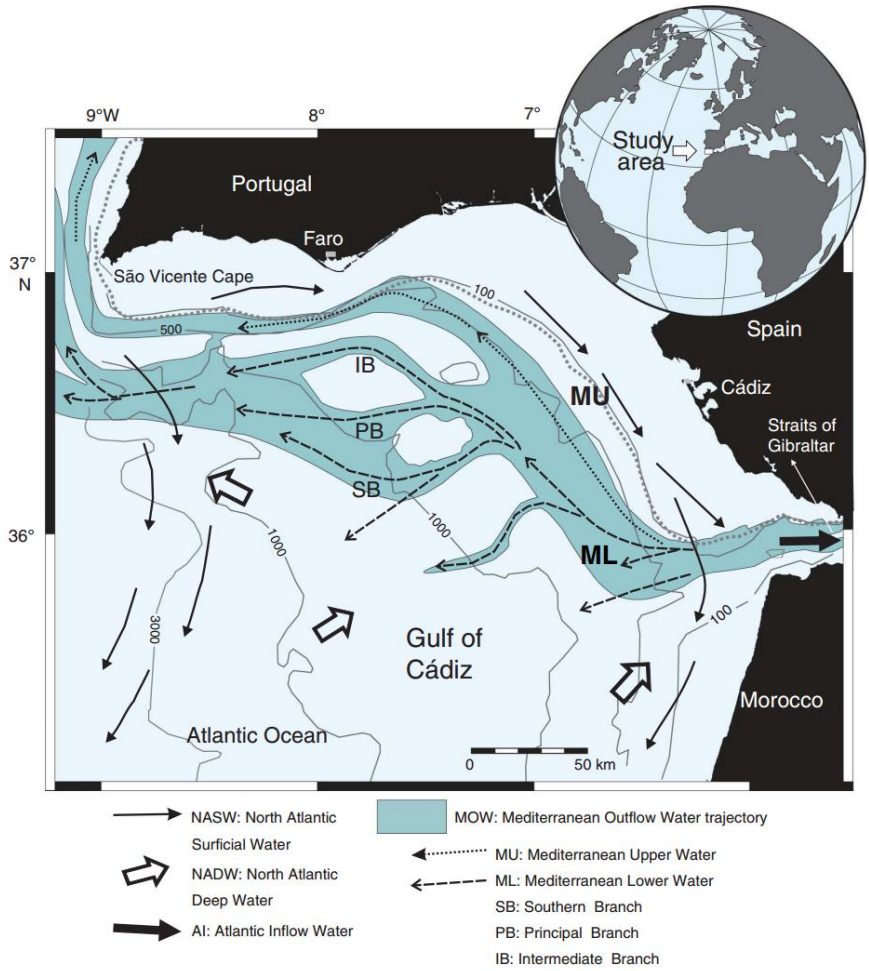

Figure 3.9 Oceanographic map showing water circulation in the Gulf of Cadiz (Expedition 339 Scientists, 2012).

3.1.3 Expedition 355

Expedition 355 was carried out in the Laxmi Basin within the Indian continental margin impinging on the Arabian Sea. The expedition took place between 31st March 2015 and 31st May 2015 and it is partly aimed at understanding the interplay between mountain building, weathering, erosion and climatic changes at a multiple time scale (Pandey *et al.*, 2015). The expedition is also aimed at explaining the break up between the Indian continental margin and the Seychelles and its relationship to the plume-related volcanism of the Deccan Plateau. At the end of the expedition two sites, 1456 and 1457 were drilled. The recovered sediments were Holocene up to early Miocene. Drilling in both sites 1456 and 1457 reached about 1109.4 m and 1108.6 m below the seafloor respectively. Sediments recovered during the expedition are dominated by turbidites and hemipelagites; site 1457 is richer in fine-grained turbidites in comparison with site 1456. Thus, because this research in centrally focused on fine-grained

turbidites and hemipelagic sediments, core samples were retrieved from intervals of interest from site 1457.

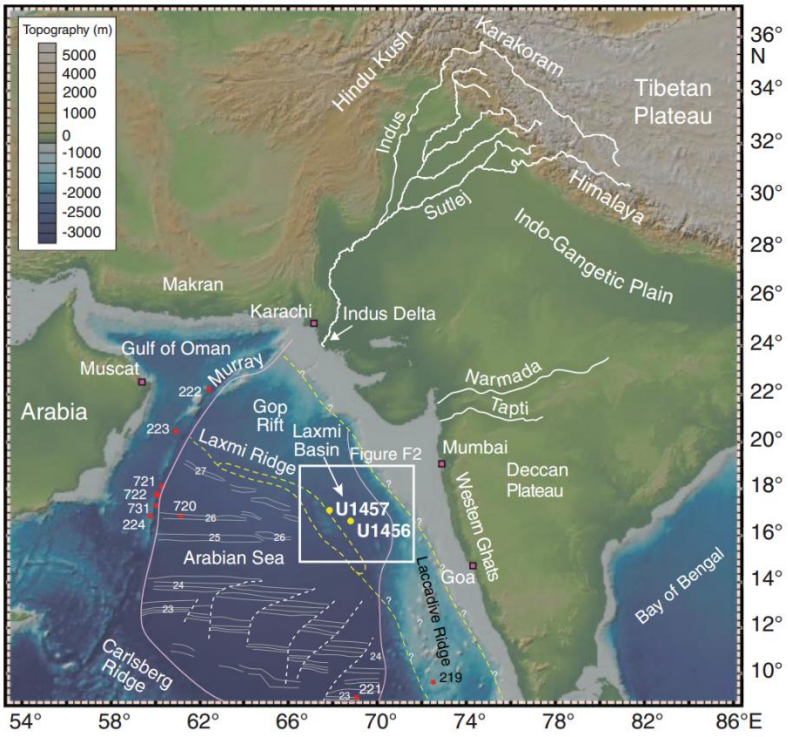

Figure 3.10. Bathymetric map showing the physiographic features around the Laxmi Basin and site locations for Expedition 355 (Pandey *et al.*, 2015). Yellow circles: location of sites; White lines: major river tributaries; pink lines; marks the extent of the Indus fan; red stars: early scientific drilled sites sampling Indus fan; yellow dash lines: speculated boundary between oceanic and continental margins; grey lines; magnetic anomalies.

3.1.3.1 Geological Setting of the Laxmi Basin

The present day western continental margin in India is linked to rifting, drifting and break up between India, Madagascar and the Schelleyes between the mid to late Cretaceous (Malod *et al.*, 1997; Miles, Munschy and Ségoufin, 1998; Krishna, Rao and Sar, 2006). The prominent features in the continental margin include; Laxmi Ridge and Laccadive Ridge which are within the Indus Fan sediments (Figure 3.10). Between the two ridges is located the Laxmi Basin which has been of much geological interest (Bhattacharya *et al.*, 1994; Chaubey *et al.*, 2002a). The Laxmi Basin was earlier known as the Eastern Basin (Naini and Talwani, 1982; Malod *et al.*, 1997) and it is located at the centre of western India margin and the ridges (Krishna, Rao and Sar, 2006). The combined expression of both Laxmi Ridge and the Laxmi Basin is sometimes known as Gop Rift (Corfield *et al.*, 2010). The basin occupies an area of about 2.4

X 10^5 km^2 (Krishna, Rao and Sar, 2006) and is bounded to the south by Laccadive Ridge, to the west by the Laxmi Ridge and to the north by the Indian continental shelf (Bhattacharya *et al.*, 1994). The affinity of the Laxmi Basin to either oceanic crust or continental crust is still an enigma (Pandey *et al.*, 2015), although some authors have attributed the basin to a rifted continental block (e.g Naini and Talwani, 1982; Miles, Munschy and Ségoufin, 1998; Chaubey *et al.*, 2002b; Krishna, Rao and Sar, 2006; Minshull *et al.*, 2008), for some authors the basin is part of an oceanic crust (e.g Bhattacharya *et al.*, 1994; Talwani and Reif, 1998; Subrahmanyam and Chand, 2006; Corfield *et al.*, 2010).

In the entire Arabian sea, the collision of the Eurasian and Indian Plate is accompanied by large amounts of sediment deposition (Indus Fan) by the Indus River (Kolla and Coumes, 1987; Clift, 2002). The Indus Fan is the second largest deep-water fan in the world. The Indus Fan covers an area of ca. $1.1x10^6$ km and it is the most extensive physiographic feature in the Arabian Sea. The area around the Indus River is mountainous, and falls within the temperate and subtropic climates and therefore associated with low rain fall (35 cm/year) (Kolla and Coumes, 1987). The major source of the sediments discharged by the Indus River to the Arabian Sea are from the Himalaya mountains (Clift *et al.*, 2002). The fan predates the Miocene period (Kolla and Coumes, 1987; Clift *et al.*, 2001). In the Laxmi Basin, the Indus Fan overlies the basement and is the primary target of Expedition 355 (Pandey *et al.*, 2015). The Indus Fan is differentiated into an upper, middle and lower fan. The boundaries between the subdivisions are not distinct and marked by gradational boundaries which are associated with episodes of sedimentation and migration of channels (Kolla and Coumes, 1987). The upper and middle fan are characterised by channel avulsion but which are derived from a single principal channel known as the Indus Trough (Prins *et al.*, 2000). Sediments from the Indus Fan primarily consists of mass transport deposits, pelagic and hemipelagic sediments, and turbidites (Pandey *et al.*, 2015). .

3.2 Methodology

3.2.1 Grain-size analysis

Grain-size is an important physical parameter as it affects the petrophysical properties of rocks. The size of common measured grains of sediments can range from submicrometre to centimetre scale. Grain-size can give a clue to source of sediments (Blott *et al.*, 2004) and also affect the chemical and physical properties of rock (Eshel *et al.*, 2004).There is an interplay among grain-size, grain shape, specific surface area, porosity, permeability and microstructure. Grain-size

is a three-dimensional property and to accurately quantify it measurement in three dimensions is recommended. However, due to the rarity of three-dimensional techniques for determining grain-sizes most measurement of particle size analysis is limited to estimating grain-size from two dimensional feature (diameter) as a representation of the true size of the particle. Such measurement involve making some assumptions e.g. assuming equivalent spheres (Sahagian and Proussevitch, 1998) and therefore taking the equivalent diameter of the spheres.

All traditional techniques employed in particle size distribution are flawed, which means there is no method that is perfect. Most of the techniques for grain-size measurement only give an estimation of the grain-size distribution, partly because of irregularity in particle shape (Eshel *et al.*, 2004). There are a variety of techniques by which grain-size analysis is performed. Each of the techniques has its own advantages and disadvantages coupled with resolution limit. In this research two techniques were adopted; laser diffraction and automated imaging techniques. The techniques were used to validate the results achieved from each other. However, it is noteworthy that the results from the two techniques usually differ because image analysis produces grain-size results based on number weighted distribution, whereas laser diffraction results is based on volume weighted distribution.

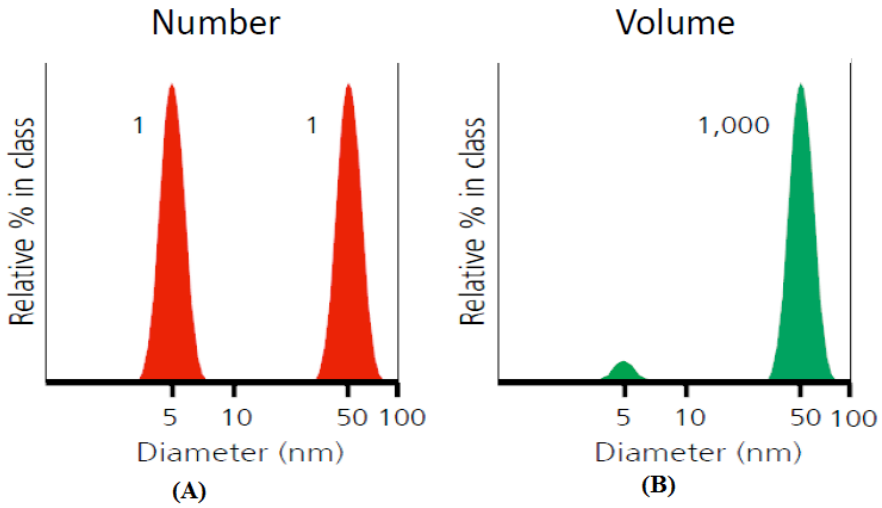

Figure 3.11. Illustration showing grain-size distribution results for two different techniques; (A) Image analysis (B) laser diffraction (From, Malverns Instruments Limited, 2012). The sample for the distributions above contains equal number of 5 nm and 50 nm grains.

3.2.1.1 Disaggregation of samples

In performing grain-size analysis of unconsolidated sediments, the first step is to ensure that individual grains are dispersed through homogenisation for each grain to be accounted for. A standard disaggregation method is by applying a dispersing liquid (dispersant). The dispersant weakens the cementing material (attraction) among the grains therefore reducing the surface energy.

Textural analysis of mudrocks such as grain-size requires disaggregating the grains in order to obtain consistent results is susceptible to generating artificially fine particles (Lewis and McConchie, 1994). In this research, owing to the semi-consolidated nature of the samples, satisfactory dispersion was achieved following a two-step procedure of chemical and mechanical disaggregation. Disaggregation was achieved by soaking small representation portions of the sample in a 0.5g/l solution of sodium hexametaphosphate (Calgon) for at least 24 hours. The dispersion was then completed by further treating the soaked sample with an ultrasonic device with a long thin tip probe in a plastic tube. The plastic tube containing the sample was two-third filled with Calgon solution and the probe was adjusted to about 1 cm above the base of the plastic tube to prevent breakage of the plastic tube during sonication. Duration for complete disaggregation ranges between 10 to 15 minutes. Sodium hexametaphosphate acts as a dispersant and prevents the sample from flocculation after the ultrasonic treatment. The degree of dispersion was confirmed by mounting the dispersed particles on a slide and observing under a scanning electron microscope (Figure 3.13).

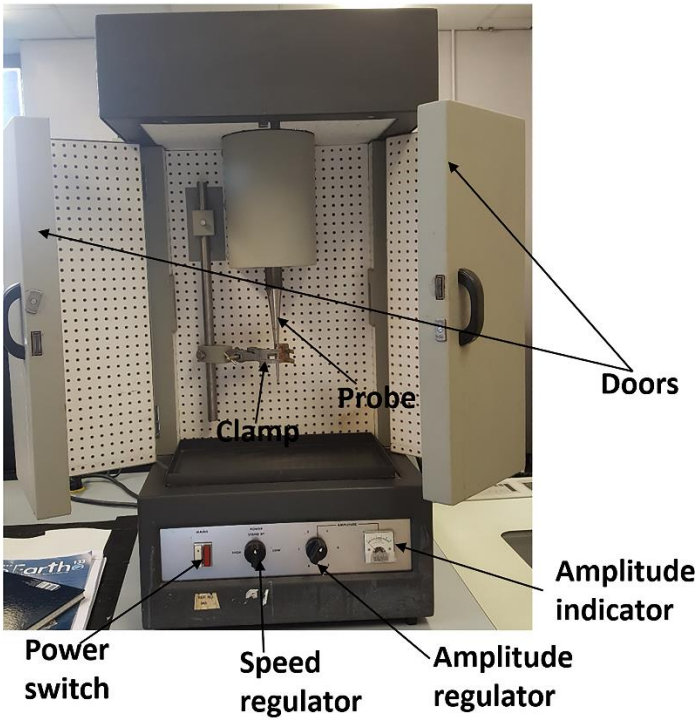

Figure 3.12. Picture of ultrasonic disaggregator with its components used for dispersion of samples.

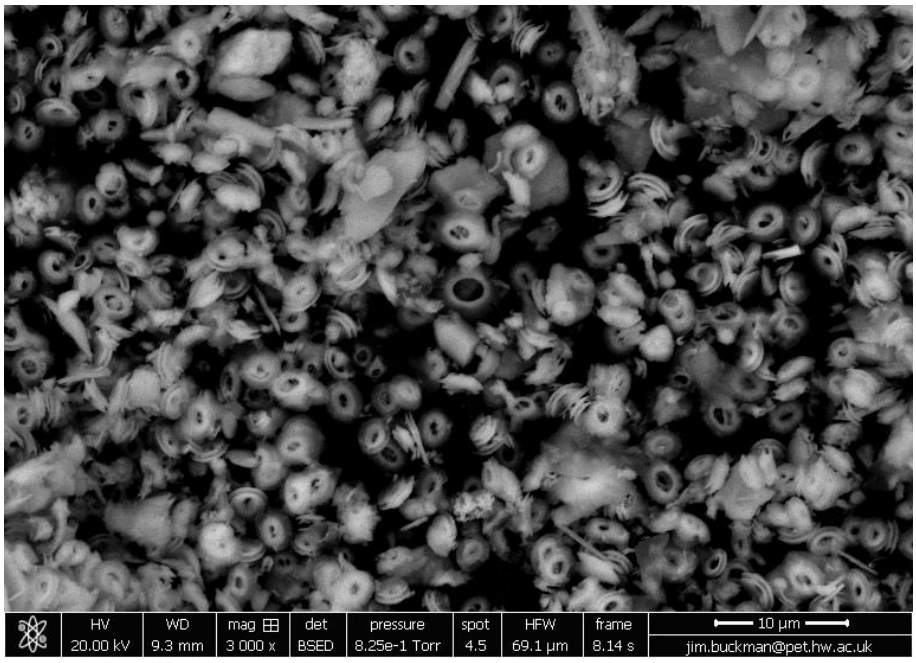

Figure 3.13. Backscattered SEM image of dispersed sample showing coccoliths of clay size particles with few silty materials. The figure showed that the sample is well disaggregated. Individual coccoliths can be seen separated from one another and well preserved without being broken up.

3.2.1.2 Laser diffraction

The laser diffraction technique involves the interaction between grains and light. The particles scatters light at an angle (diffraction) as it interacts with the beam of light passing through it. The amount of light scattered is a function of grain-size such that smaller grain-sizes cause greater amount of light scattering than larger grain-sizes. A parallel monochromatic light is passed through suspended particles and the scattered light in the process is focussed on the detector by a pair of lenses. The result of the distribution using the laser diffraction method is based on weighted volume distribution, such that volume contribution by each individual grain is accounted for. The advantage of laser over most other techniques used for grain-size analysis are: (1) short time of analysis, (2) small sample size and (3) reproducibility of results (Eshel *et al.*, 2004).

Based on the laser diffraction technique several commercially available laser diffraction granulometers have been manufactured e.g. Coulter, Fritsch, Horiba, Leeds and Northrup, Malvern and Retsch.

A typical laser diffraction system contains three components (Figure 3.14 and Figure 3.15); (1) optical bench, (2) sample dispersion units (sample cell) and (3) instrument software. The sample dispersion unit ensures a dispersed sample is delivered to the optical bench where measurements are made. In a wet dispersion unit, liquid (deionised water) is used and the sample is recirculated to maintain homogenisation as the measurement of grains proceeds. The instrument software controls the entire process and it also analyses the data acquired producing grain-size distribution curves and a result table of the different grains that fall within specified diameters.

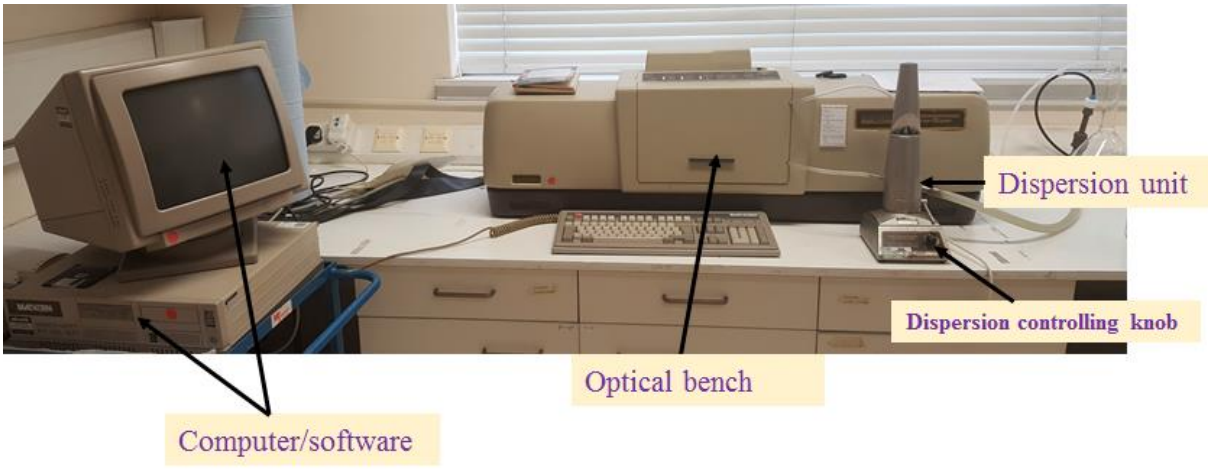

Figure 3.14. Malvern Mastersizer 2000 laser diffraction granulometer

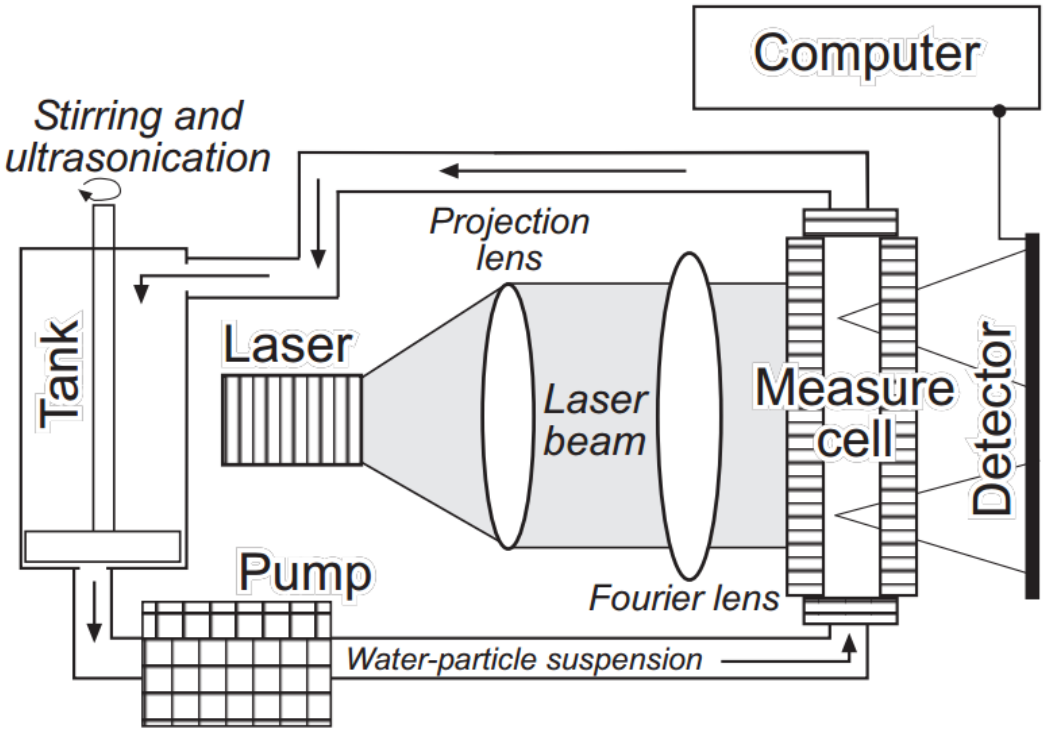

Figure 3.15 Schematic diagram showing the components of a laser diffraction granulometer (Storti and Balsamo, 2010).

In this research a Malvern Mastersizer 2000 laser diffraction granulometer was used. The instrument is capable of measuring particle sizes between 100 nm and 600 µm and it is equipped with three Fourier lenses. Due to the fact that the samples analysed for this current study are mudrocks in which the largest grain-size is not more than silt size (< 63 µm) the smallest Fourier lens which has a resolution of between 100 nm and 80 µm was sufficient except for few samples that contained fine sand and in such cases, a second lens which can measure a grain-size range of between 500 nm and 180 µm was used and the results from both lens were combined.

The samples were ultrasonically dispersed and a small portion introduced to the sample cell which contains degassed water to avoid gas bubbles with particle size below 500 µm (Loizeau *et al.*, 1994). The intensity of light adsorbed to the sample which is dependent on the amount of sample introduced to the dispersion unit and this is measured as obscuration. Grain-size distribution is calculated based on Fraunhofer theory or Mie theory. There is a limit to the usefulness of the Fraunhofer theory as the grain-size approaches the wavelength of the beam

used or perhaps less than multiple of ten of the wavelength of the monochromatic light (Loizeau *et al.*, 1994; Eshel *et al.*, 2004). Here, Mie theory was used because it is preferred (Eshel *et al.*, 2004) and this requires knowledge of the refractive indices of water and the sample. The Mie theory is based on a number of assumptions; (1) The mineral composition of the particles are homogeneous (2) the particles are spherical (3) the intensity of light scattering by a particles in the suspended fluid is detected before other particles re-scatter the light (4) the refractive indices of the sample and dispersing liquid is known (Storti and Balsamo, 2010).

In a laser diffraction measurement, samples pass through the optical bench, which is illuminated by laser beam. The intensity of the returned light scattered by the particle components of the sample is measured by detectors at varying angles. Angular variation in the intensity of scattered light is measured as the light beam passes through the sample. The intensity of light scattered is translated into the particle sizes, using the Mie theory of light scattering. The angle of diffraction is inversely proportional to the particle size (Figure 3.16) and the intensity at varying angle is measured for a number of particles. The particle size is transformed into volume equivalent sphere diameter. Further details on operational techniques of laser diffraction granulometer are in the literature (Loizeau *et al.*, 1994; Beuselinck *et al.*, 1998; Blott *et al.*, 2004; Eshel *et al.*, 2004; Sperazza, Moore and Hendrix, 2004; Storti and Balsamo, 2010; Malverns Instruments Limited, 2012).

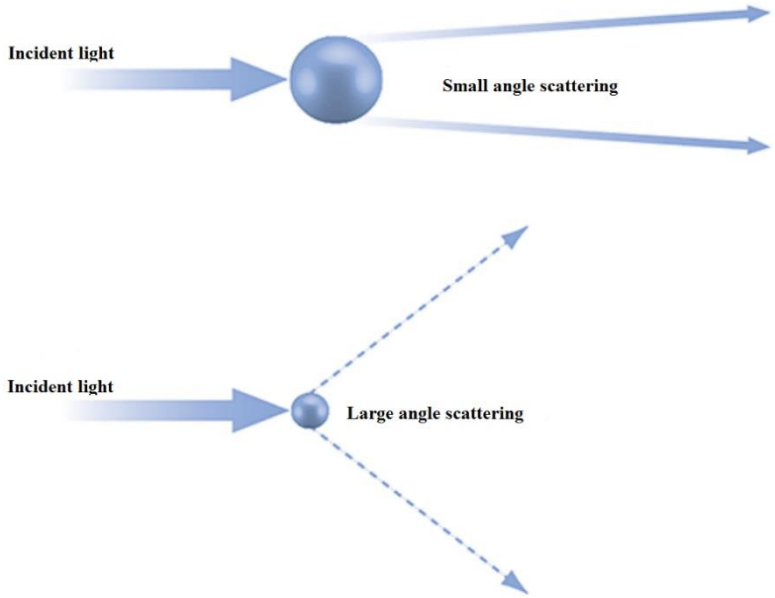

Figure 3.16. Schematic representation of scattered light from large and small particle sizes (From, Malverns Instruments Limited, 2012).

3.2.1.3 Imaging

Imaging is employed for particle size determination as a direct method. Data from imaging method might require validation by other techniques e.g. laser diffraction, pipette and hydrometer methods. It is the only known technique for particle size analysis that gives the shape of the particle. It can serve as a check to detect whether samples are properly dispersed and devoid of agglomeration or damage through breakage. Imaging can be carried out statically or dynamically. In dynamic imaging, particles can flow through a cell during measurement while in static imaging, dispersed particles on a slide or polished thin-section are imaged directly using an optical microscope or scanning electron microscope.

Here, polished thin-sections were imaged using the scanning electron microscope at high-resolution. The polished thin-section is required to be well polished in order to enhance contrast among the individual grains and more importantly reduce background noise or else the image analysis will give unreliable results. Grain-size analysis based on imaging technique provides weighted number distribution and this is in disparity to all other techniques that are converted to weighted diameter or volume distributions. Hence comparing results from image analysis with other techniques will give disparate results. Despite this challenge, grain-size analysis

through the imaging technique is useful when number of grains and shape of the grains in the sample are required.

Here, grain-size analysis was carried out on large-scale high-resolution images. Acquisition of the high-resolution large-scale images follows automatic imaging and stitching as described in (Buckman, 2014; Bankole *et al.*, 2016). Particle sizes and grain orientation were determined using 'Fiji' Software, an adaption of 'ImageJ' (Schindelin *et al.*, 2012). Its usage in particle analysis has mostly been restricted to coarse grain-size particles (Keulen *et al.*, 2007; Cuven, Francus and Lamoureux, 2010) with limited uses for analysing fine-grained particles (Camp and Wawak, 2013). In this study, with the image resolution used, particles as small as 150 nm were measured. 'Fiji' can return numerical data on a range of particle characteristics such as diameter, circularity and aspect ratio among others. The software is useful for analysing fine-grained sediments.

Usage of Fiji software requires no prior knowledge about programming language and it is user friendly. The software has a high precision with good reproducibility of results while minimising human bias. The diameter of thousands of grains was determined within a short duration of time and the results were analysed in Microsoft 'Excel'. The management of the data involves using macro codes in Excel to determine the sand, silt and clay size particles. In addition to particle sizes (diameter) some of the information returned by Fiji are circularity, aspect ratio and grain orientation degree among others which provides useful information concerning the shape and form of the grains. Data on grain orientation were plotted using GeOrient (Holcombe, 2011).

The diameter of particles was determined based on Feret diameter. To analyse particles, the first step is to segment the grains through segmentation and thresholding. The pores within the grains were rendered to the background (white) while the grains were rendered to the foreground (black). In this study the default threshold was found to be satisfactory. Segmentation of images is usually associated with noise, therefore median filter at 4 radius pixels to reduce the noise effect was applied.

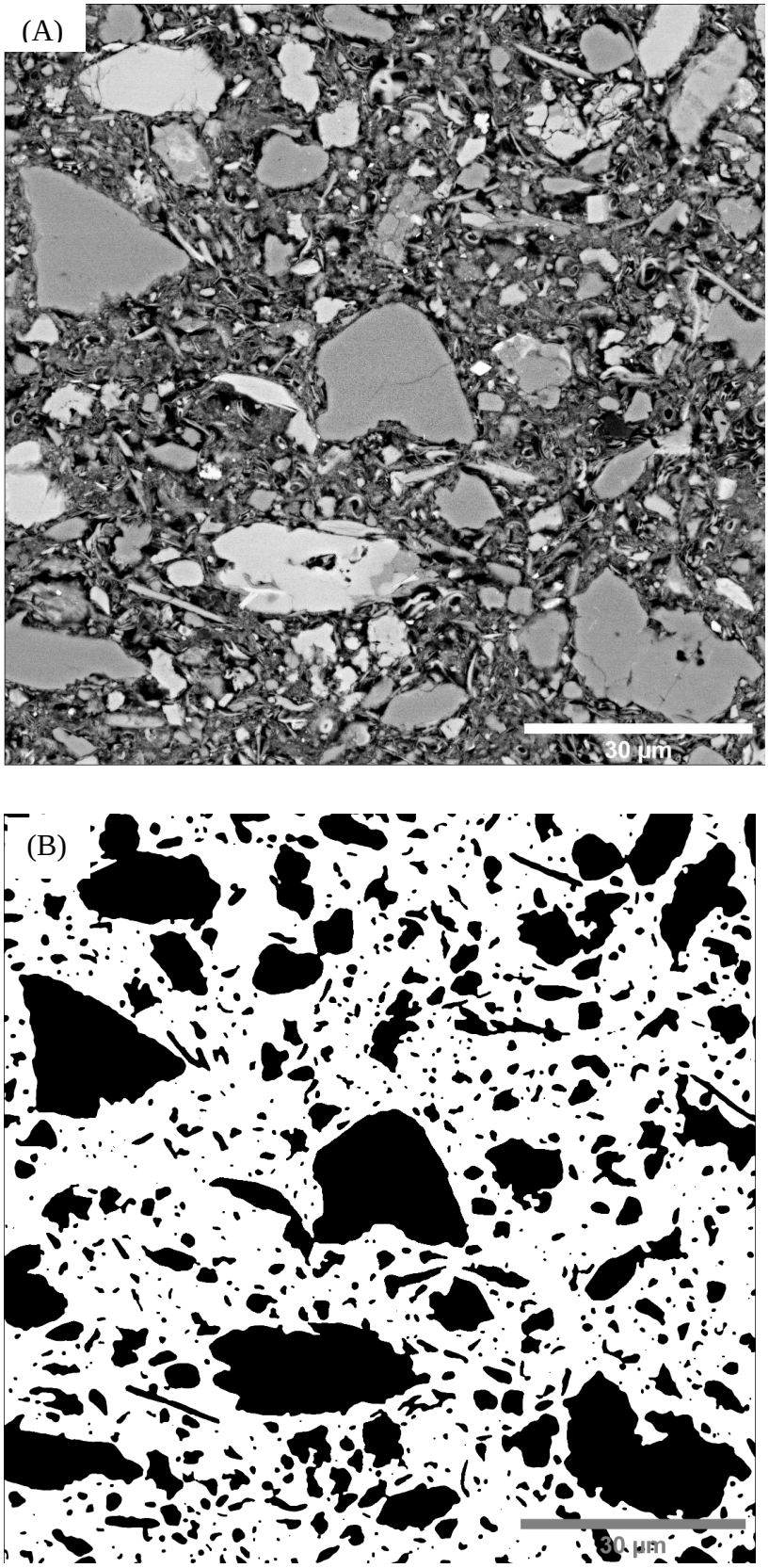

Figure 3.17. Diagram showing segmented image. (A) Raw SEM image showing grains (grey to light grey) and pores (black). (B) Segmented and binarised SEM image. Grains are black while other features have been rendered to the background (white). Sample ID: 339-1389A-6H1-28-30

3.2.2 Sample Preparation and drying.

Microstructural study of fine-grained rocks requires some pre-treatment and sample preparation, which may vary with respect to the method of study. For example, optical microscopy will require preparation of thin-section slides about 25 to 30 µm thick. Transmission electron microscopy requires preparation of an ultra-thin slice of approximately 90 nm thickness. Scanning electron microscopy requires peeling or fracturing of sample to get a fresh broken surface (e.g O'Brien and Slatt, 1990), well-polished thin-sections (Milliken *et al.*, 2007), broad ion beam milling (e.g. Klaver *et al.*, 2012; Houben, Desbois and Urai, 2013) or focused ion beam milling (Wirth, 2009; Curtis *et al.*, 2012b). Procedures on how to obtain freshly broken surfaces for electron microscopy are presented by O'Brien and Slatt (1990). However, research has advanced and the best practice to study microstructural characteristics is by producing a surface with minimum surface roughness through ablating the sample either by broad ion beam or focused ion beam.

Usage of a conventional scanning electron microscope as employed in this study demands drying of the samples. Environmental scanning electron microscopy is suitable for imaging wet and oily sample (Reichelt, 2007; Echlin, 2009), but due to the fact that microstructure is best imaged on a smooth and flat surface (polished surface or ion milled surface) drying of the sample is unavoidable.

Drying of mudrocks for microstructural studies is associated with some problems and this aspect is crucial in obtaining reliable results as well as preserving the original microstructure. The challenge associated with drying is removal of water without altering the microstructure because water has a high surface tension (Echlin, 2009; Schieber, 2015) therefore, a special drying procedure is required.

Most samples of unconsolidated clays have some amount of moisture content (water) and exposure to atmospheric condition results in gradual evaporation of the moisture content. The surface tension between water and air is high and this leads to shrinkage of the sample and simultaneous distortion of the original microstructure (Reynolds and Gorsline, 1992; Matenaar, 2002; Schieber, 2015). The distortion sometimes is accompanied by hairline cracks (Soe *et al.*, 2009). Thus, air drying of samples is associated with the challenge of maintaining integrity and preserving primary microstructure.

Previous works have examined the effect of different drying techniques such as oven drying, air drying, room temperature drying, freeze drying and critical point drying on the preservation of original microstructure (Reynolds and Gorsline, 1992; Houben, 2013). Oven drying produces minimal microfabric distortion when compared to air drying technique (Matenaar, 2002). In an air dried sample there is the possibility of water still being retained within the lamina especially in a stratified shale (Dewhurst, Jones and Raven, 2002). Two widely used drying techniques for microstructural study, which are believed to be associated with the least distortion are: freeze drying and critical point drying (Wierzchos *et al.*, 1992). There have been concerns that formation of ice crystals during the freeze drying process are likely to alter the original microstructure (Reynolds and Gorsline, 1992) especially in larger samples. Getting comparable results on microfabic of clay rich sediments dried using critical point drying and freeze drying methods remains inconclusive and controversial.

A number of authors have modified the standard freeze drying method by using organic chemical compounds as transitional liquids e.g. Freon and Peldri II (Delage and Lefebvre, 1984; Wierzchos *et al.*, 1992; Matenaar, 2002) and also cutting the samples into thin slices (Shi *et al.*, 1999). Despite these modifications in the freeze drying method, critical point drying is acknowledged as the best drying technique for preserving primary microstructure (Schieber, 2015). It has the advantage of preserving internal structure of bulky samples which might be difficult with the freeze-drying method. For this research drying techniques such as freeze drying, oven drying, and critical point drying and low viscosity resin impregnation were performed. Part of the reasons for performing different drying tests on the samples are: (1) mudrock samples utilised for this research are semi-consolidated and different from materials used by previous workers; and (2) to examine the suitability of the drying techniques for semi-consolidated mudrocks. A brief description of the drying techniques are presented here.

3.2.2.1 Room temperature drying

Samples retrieved from Expedition 317 were sampled in 20 cc cylindrical sampling plastic tubes, wrapped in thick nylon and were dried slowly at room temperature. The samples have undergone gradual drying and believe to have been protected from humidity effects because they were in sealed thick nylon bags. The initial research interest for collecting the samples was not related to microstructure. However, the samples provide an avenue to compare gradually dried samples at room temperature with other drying techniques. An example of a

backscattered SEM image of a polished thin section that has been dried slowly at room temperature is shown in Figure 3.18.

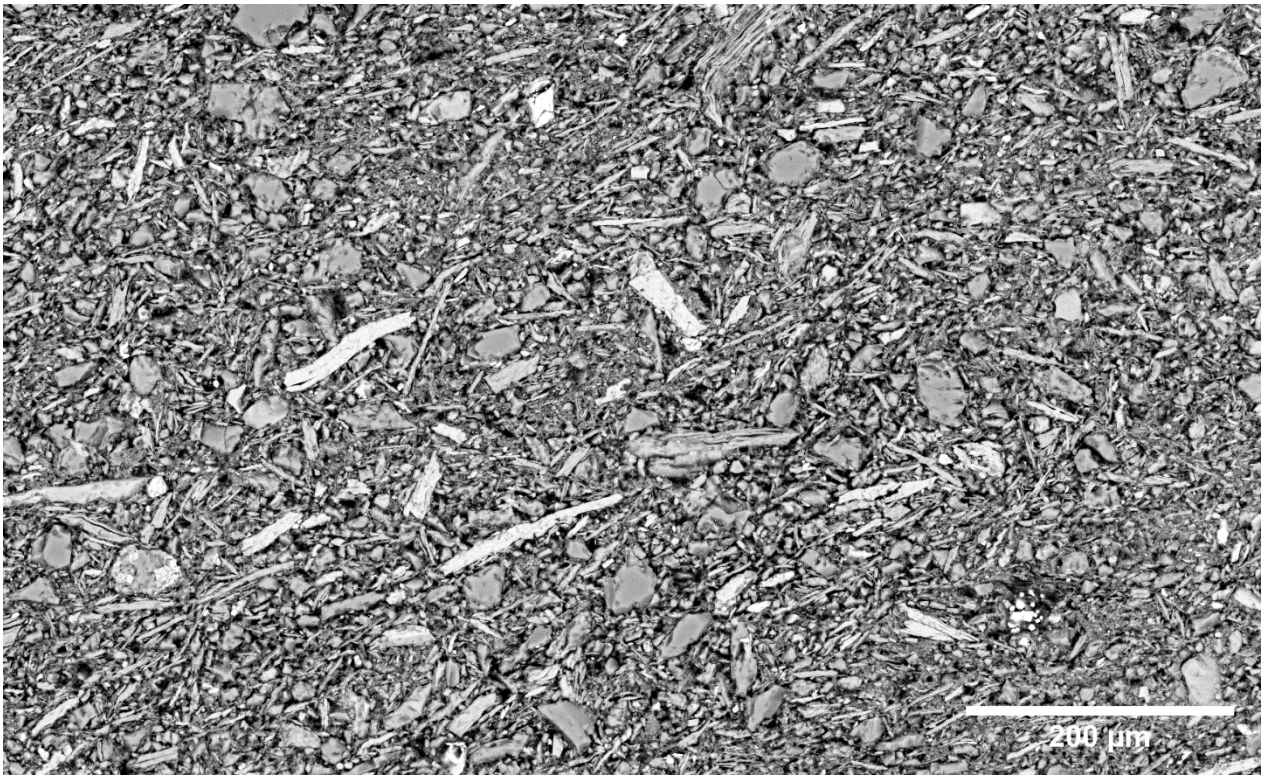

Figure 3.18. Backscattered SEM image of a polished thin-section for a sample dried at room temperature. The grain to grain contacts as well as the orientations of the grains can be observed. Sample ID: 317-1352-137R1-116-118

3.2.2.2 Freeze drying

Freeze drying is a common drying technique used to get rid of water from sample without causing major damage to the original microstructure. Because of the high surface tension of water, the process involves freezing of sample in a normal standard freezer at 0^{o}C or rapidly freezing the sample (at about -196^{o}C) by plunging it into liquid nitrogen. The sample is kept in the liquid nitrogen to ensure that the pore water turns to ice crystals and by placing the sample inside a freeze dryer, the ice crystals are removed through sublimation without going through the liquid phase.

Rapid freezing of samples have been applied to many samples by earlier researchers in order to preserve the delicate and microscopic structures (Dewhurst, Jones and Raven, 2002). Other low temperature liquids that have been used in the past to accelerate ice growth of the pore fluid are Freon, admixture of liquid nitrogen and Pedri II (Delage and Lefebvre, 1984;

Wierzchos *et al.*, 1992; Dewhurst, Aplin and Sarda, 1999; Dewhurst, Jones and Raven, 2002). Both Pedri II and Freon are fluorocarbon substances and due to their depleting effect on the ozone layer they are no more available for usage.

Here, subsamples of approximately 1 cm thickness, 1 cm width and 2.5 cm length were plunged into liquid nitrogen and kept in the liquid for about 15 to 20 mins. Before submerging the sample into a liquid nitrogen containing jar, the subsamples were wrapped in cling film in order to circumvent the effect of bubbling of liquid nitrogen on the microstructure. The frozen samples were later transferred into a standard freeze dryer operating at a temperature of -80^{0}C and 0.1 mbar for 4-5 days to gradually remove the frozen pore water through sublimation. In the freeze-dried samples, there were several micro-cracks observed when viewed by scanning electron microscope (Figure 3.19).

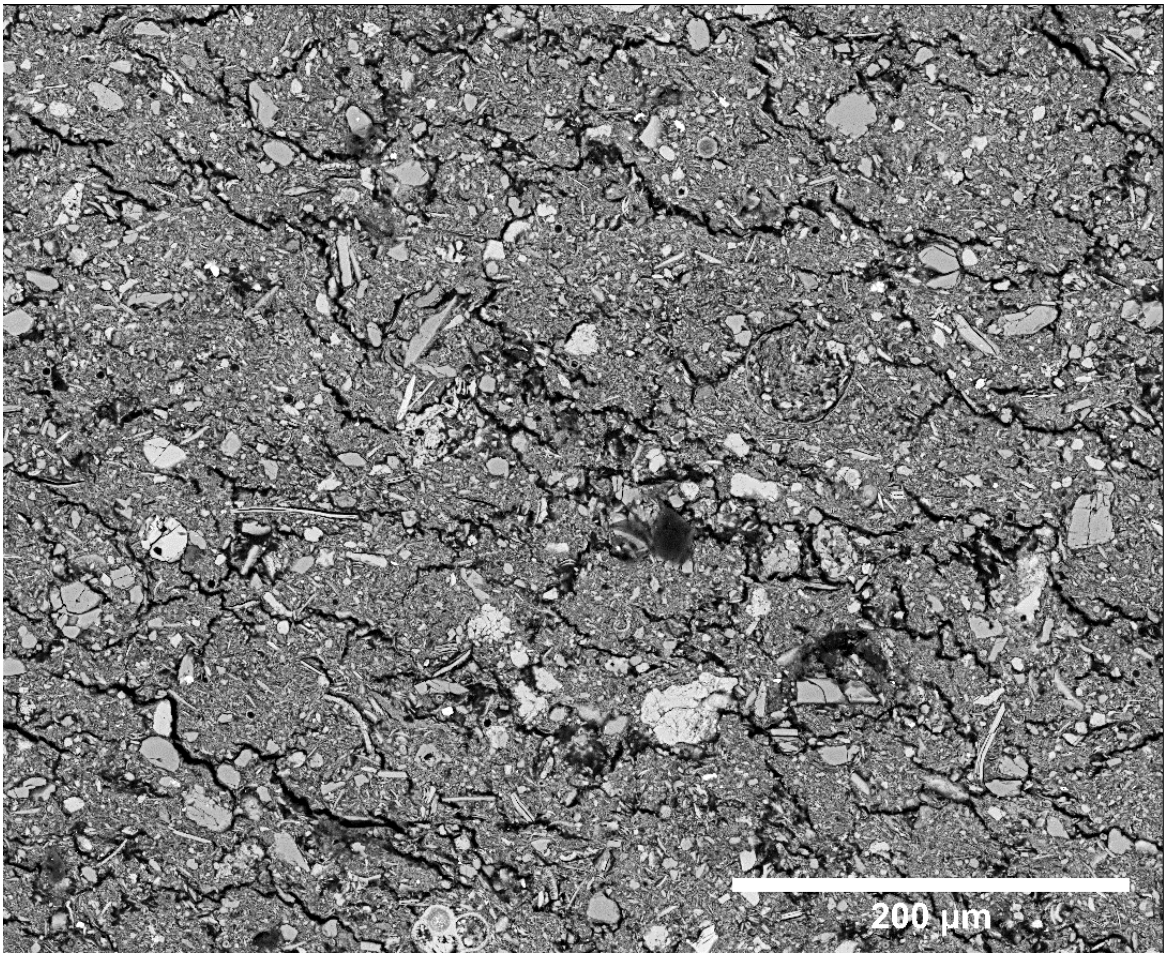

Figure 3.19. BSE SEM image of a polished thin-section of a freeze-dried sample. There are plenty of cracks or fracture in the polished thin-section and this are likely to have been artificially induced by ice crystals that formed during the freeze-drying process. Sample ID: 339-1385D-4H4-98-100.

3.2.2.3 Oven drying

Sub-samples (ca. 1 cm x 1cm x 2.5 cm) were steadily oven dried at a temperature of 60^0C until the weight of the samples remained constant regardless of further drying. The oven drying process took between 5 to 6 days. Prior to placing the samples in the oven, the weight of the samples was measured using an electric weighing device. The procedure for the oven drying is similar to the oven drying description of Houben (2013).

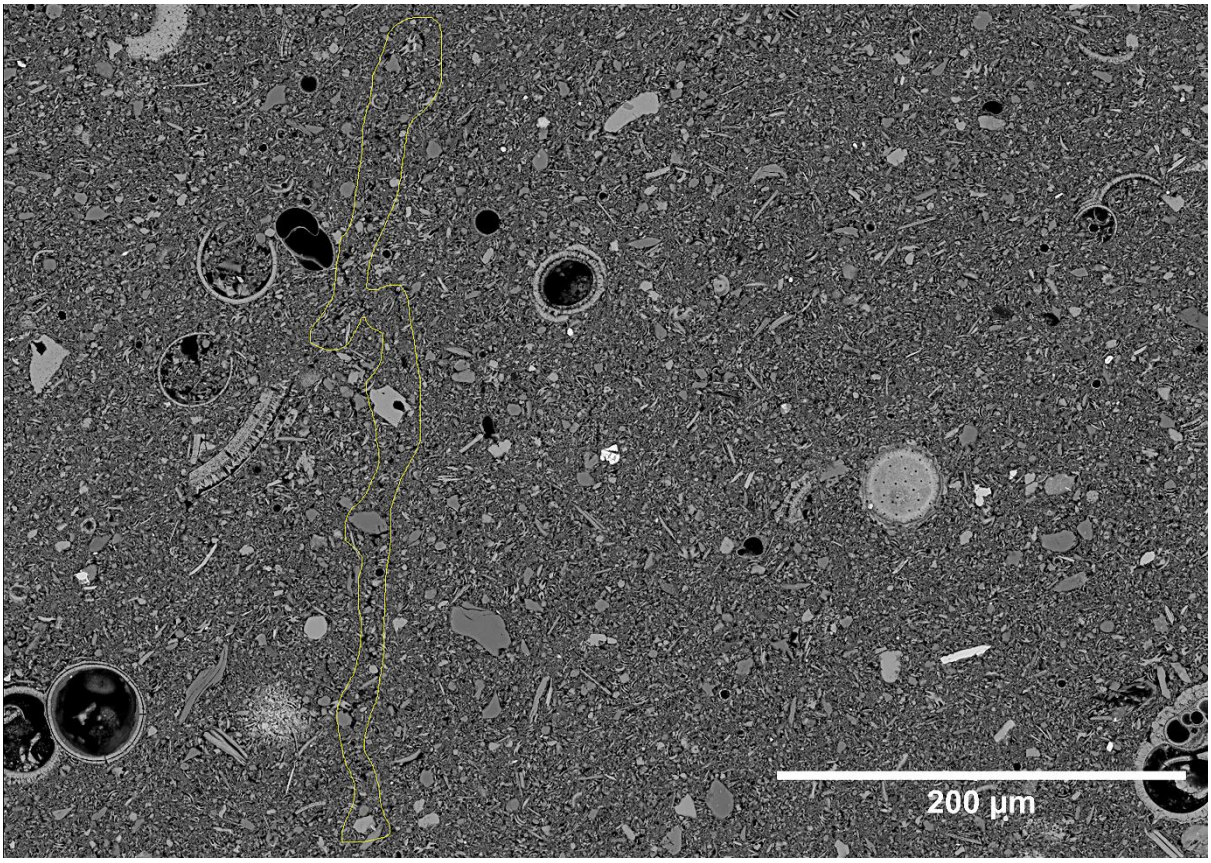

Figure 3.20. BSE-SEM image of a prepared polished thin-section in which the sample was oven dried. The yellow polygon surrounds a micro-fracture that runs down through the slide. The width of the micro-fracture is approximately 1.35 µm and this are thought to be natural rather than being artificially induced by the drying technique. Sample ID: 339-1385A-6H2-49-51.

3.2.2.4 Critical point drying

Critical point drying has been used in the field of biology to dry samples that are considered to have fragile microscopic structures (Cohen, 1979). It has also be employed in drying samples for microstructural studies of fine-grained sedimentary rocks to study specifically microscopic structures of tight reservoirs especially mudrocks (Suleimenova *et al.*, 2014). The method is used to avoid problems related to surface tension and ice formation associated with the freeze-

drying technique. The principle behind critical point drying is that at certain temperature and pressure (i.e. at a critical point), a liquid transform into gas without being accompanied by boiling.

At the critical temperature-pressure condition the density of the liquid and gaseous phases are similar and there is equal exchange of molecules between the two phases (Echlin, 2009). At that point the boundary between liquid and gas does not exist and therefore the surface tension is zero. The temperature and pressure at which different liquids reach the critical point condition is diverse. Most sedimentary samples have water residing within their pore spaces but due to the fact that the temperature at which water reach a critical point condition is too high (Table 3.1), the usual practice is to substitute water with a fluid which reaches critical point at a lower temperature. In principle, the replacement fluid should be miscible with water. Carbon dioxide is commonly used in some of the critical point driers as applicable here. Carbon dioxide reaches a critical point at 31^0C and 7.4 mPa temperature and pressure condition respectively. Due to the fact that carbon dioxide is immiscible with water a transitional fluid that is miscible with both water and carbon dioxide is used (e.g. acetone, ethanol and methanol).

Critical point drying performed in this study adopted acetone as the transitional fluid between water and carbon dioxide. The samples were immersed in acetone in increasing order of concentration; 30%, 50%, 70%, 90% and 100%. The samples were left for a period of 24 hours in each of the varying acetone concentration such that gradual water-acetone replacement was facilitated. At 100% acetone concentration, it is believed that all the pore water should have been replaced by acetone. After the water-acetone replacement, the samples were transferred to the chamber of the critical point drier (Figure 3.21).

The critical point drier was connected to liquid carbon dioxide cylinder through a high-pressure vessel which is cooled by running water. The acetone bearing sample was then placed inside the chamber of the critical point drier. Liquid carbon dioxide was delivered to the sample by opening the valve of the liquid carbon dioxide and the inlet valve of the chamber. After few minutes (10-15 mins) the outlet valve (vent valve) of the chamber was opened to allow fresh liquid carbon dioxide to flush through the sample. 10 to 15 minutes later both the inlet and outlet valve to the chamber were closed to allow infiltration of liquid carbon dioxide into the sample. The inlet valve was later opened while the outlet valve was slightly open to allow the chamber to be 75% filled with carbon dioxide. The running water serving as a cooling fluid was turned off and the chamber was heated gradually till it reaches 35^0C. The heating was

accompanied with pressure increase which is monitored through the pressure gauge and it is allowed to rise up to 7.4 mPa. The temperature is sustained at 35^0C and the outlet valve is slightly open to allow gaseous carbon dioxide to be discharged out of the chamber. There is a drop in the pressure and when it reaches 0.101 mPa (atmospheric pressure) the sample which must have been dried is then retrieved from the chamber. A micrograph of polished thin-section of a sample dried subjected to critical point drying is presented in Figure 3.22.

Table 3.1 Critical temperature and pressure of some liquids (From, Smart and Tovey, 1982)

Substance	Chemical formula	Critical Temp. (^{0}C)	Critical Press. (MPa)
Water	H_20	374	22.1
Benzene	C_6H_6	289	4.86
Carbon tetrachloride	CCl_4	283	4.5
Ethanol	C_2H_5OH	243	6.38
Methanol	CH_3OH	239	7.9
Acetone	$(CH_3)_2CO$	236	4.7
Ether	$(C_2H_5)_2O$	194	3.68
Propane	C_3H_8	97	4.2
Nitrous oxide	N_2O	37	7.26
Ethyne	C_2H_2	36	6.29
Ethane	C_2H_6	35	4.95
Carbon dioxide	CO_2	31	7.433
Freon 13	$CClF_3$	29	3.86
Hexafluoroethane	C_2F_6	20	3
Ethene	C_2H_4	10	5.13

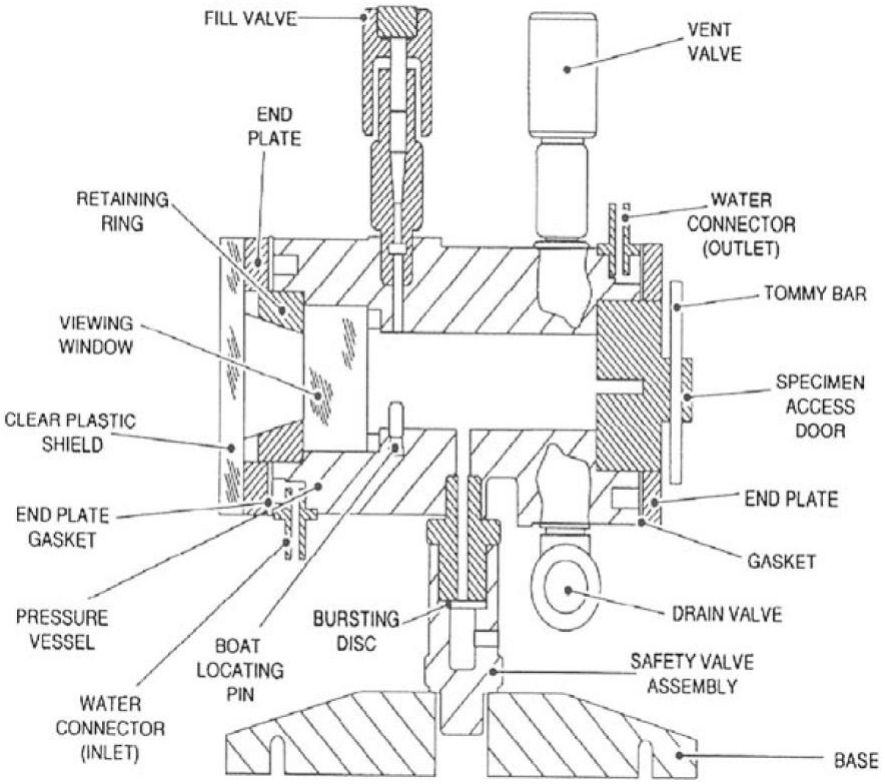

Figure 3.21. Schematic diagram of a critical point drier (Adapted from, Echlin, 2009).

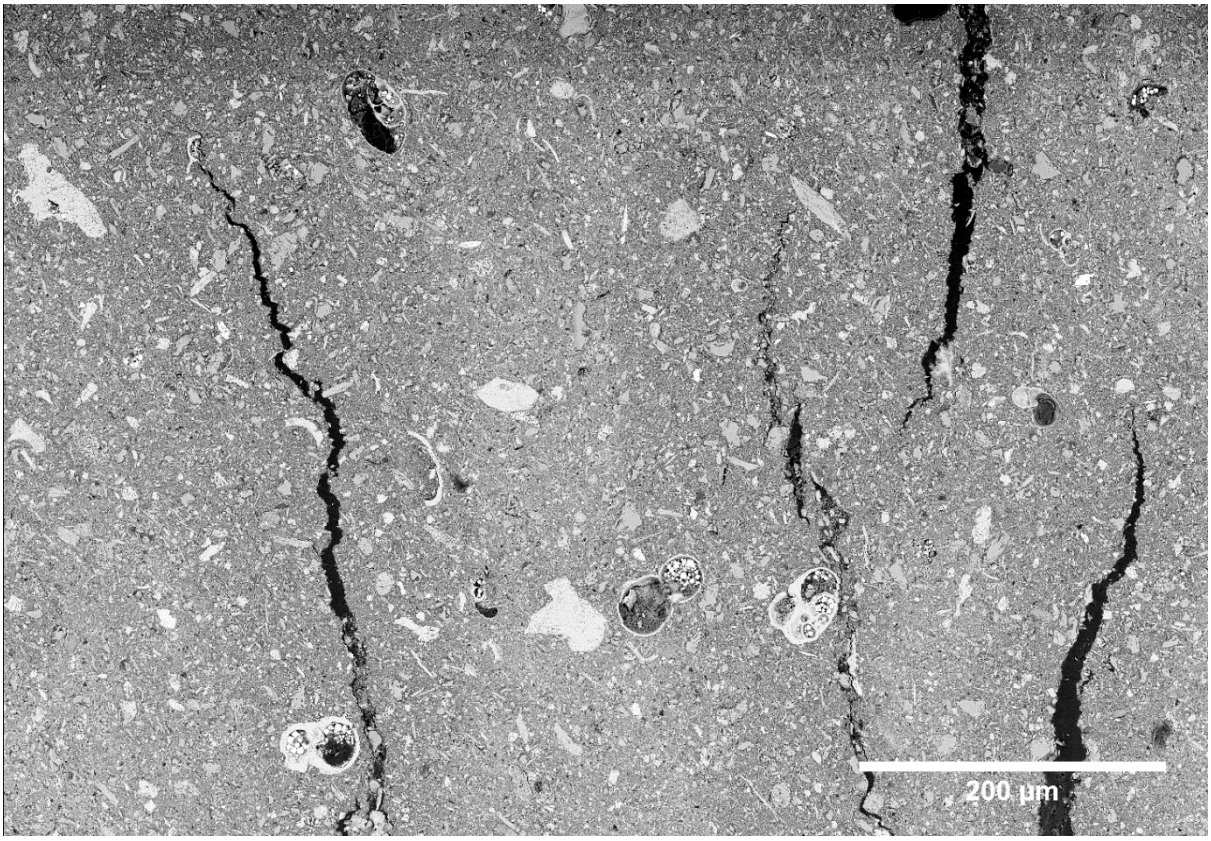

Figure 3.22. BSE SEM image of a polished thin-section that was dried with a critical point drier. The cracks in the slide ranges between 8 and 20 µm and these are suggested to be associated wih the dying technique. Sample ID: 339-1385D-5H4-41-43.

3.2.2.5 Low viscosity resin impregnation

Conventional resins have very high viscosity to infiltrate fine-grained sedimentary rocks (Jim, 1985; Swartz and Lindsley-Griffin, 1990), which therefore require low viscosity resin. Here, low viscosity impregnation procedures similar to those described by Swartz and Lindsley-Griffin (1990) were adopted.

Carefully wrapped samples with cling film and sealed in nylon during sample collection were kept inside a fridge at a temperature between 0^0-4^0C. The samples were left enclosed inside the fridge until low viscosity resin impregnation is to be performed.

During sampling, indelible marker was used to indicate the direction to the top of the bed on the sampling container. To perform the low viscosity impregnation, the samples were removed from the sealed nylon and unwrapped from the cling film. Subsample (ca. 1 cm X 1 cm x 2.5 cm) or the whole sample (ca. 5 cm x 2 cm x 2 cm) was placed in glass vials and acetone was introduced into the samples at approximated at a drop per second, in increasing order of concentrations; 30%, 50%, 70%, 90% and 100% for 24 hours.

The reason for immersing the sample in acetone is partly due to the high surface tension associated with water (Grimm, 1992) and the hygroscopic nature of resin (Jim, 1985; Swartz and Lindsley-Griffin, 1990). The slow introduction of acetone into the samples is to prevent osmotic shock which could destroy the original microstructure or destroy the semi-consolidated sample. The acetone-soaked samples were wrapped with cling film and aluminum foil with openings at the top and the bottom. The sample was wrapped to maximize the infiltration of resin directly through the sample and on the other hand to minimise the amount of resin wasted. The wrapped samples were hung on a plastic holder and placed in a dry lidded glass vial. The plastic holder ensures that the resin drips through the samples.

The low viscosity resin has four separate components (ERL 4221, NSA, DER 736 and DMAE). Mixing of the components was carried out following the formulation prescribed by Ellis (2006) for hard output (Table 3.2). The mixing process and other procedures of the resin impregnation were carried out in a fume cupboard. The acetone-soaked samples were covered with the low viscosity resin up to the top of the aluminum foil and the resin slowly penetrates the sample. Low viscosity resin was added to the sample on a regular basis until the resin fully replaced the acetone.

Complete replacement of acetone by low viscosity resin was achieved between 3-4 days. The samples were then transferred into a vacuum bell jar, uncapped and evacuated for one hour. This process allows further resin infiltration into the sample. The uncapped sample is left in a vacuum overnight. The next day the samples were transferred into an oven for curing. The operating temperature of the oven is 60^0C to allow polymerization of the resin in which the oven drying acts as thermal catalyst (Grimm, 1992). The curing process usually last up to 4 days. A backscattered image of a polished thin-section of a sample that was impregnated with low viscosity resin is shown in Figure 3.24.

Table 3.2 Hard and soft formulation of spurr low viscosity resin components (From, Ellis, 2006)

Formulation	ERL 4221	NSA	DER 736	DMAE
Hard	4.10	5.90	0.95	0.1
Soft	4.10	5.90	1.90	0.1

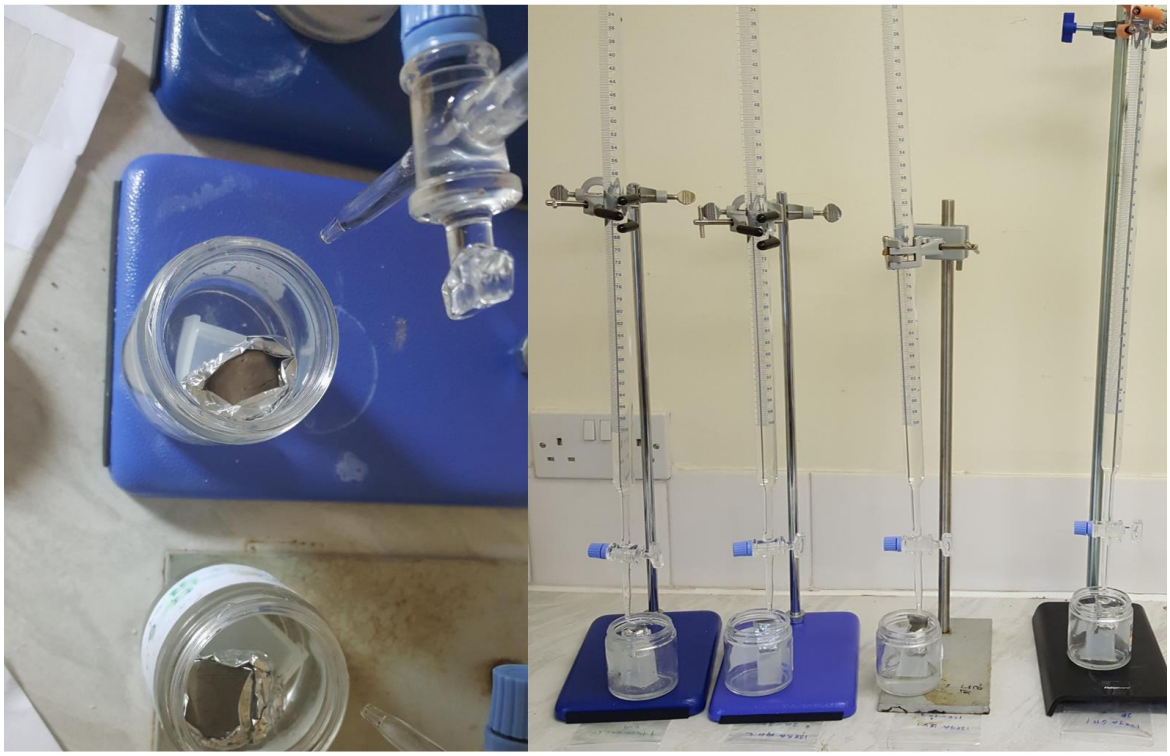

Figure 3.23. Picture showing gradual introduction of acetone into water bearing samples through burettes. The samples were wrapped in aluminium foil and placed in glass jars. Note that acetone was introduced into the samples at about 1 drop per second.

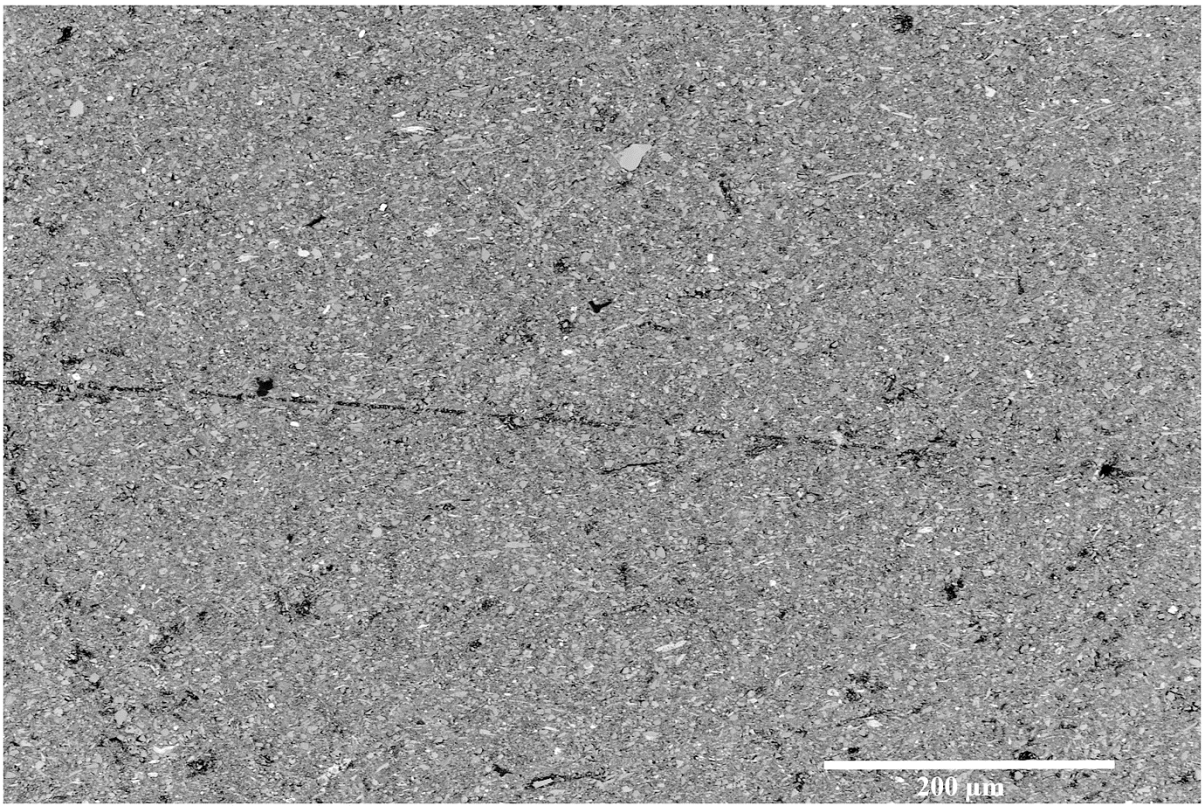

Figure 3.24 BSE SEM image of polished cross section for low viscosity resin impregnated sample. The black line running across the slide was imparted during polishing. Samples prepared through low viscosity resin impregnation showed the least damage in comparison to those dried through other techniques. Sample ID: 339-1385A-7H2-132-134.

3.2.2.6 Discussion on the Different Drying Techniques

There are micro-fractures in virtually all the polished thin-sections that were dried with the different techniques especially when the whole slides were imaged by scanning electron microscopy. While some of the micro-fracture can be associated with sample preparation due to the drying techniques, stress relaxation imparted by drilling cannot be ruled out (Corkum and Martin, 2007; Soe *et al.*, 2009).

However, the intensity of the micro-fracture varies from one drying technique to the other. The drying techniques in decreasing order of micro-cracks density are: freeze drying, critical point drying, room temperature drying, oven drying and low viscosity resin impregnated samples. The low viscosity resin impregnated sample showed the least micro-cracks/fractures while the freeze dried sample showed the highest degree of micro-fractures.

Large areas up to 1 mm by 1 mm were observed to be micro-crack free for the samples dried at room temperature, oven dried sample and resin impregnated samples. The critical point dried sample have area of up to 200 µm by 200 µm that are crack-free but are associated with big micro-cracks of up to 35 µm. It is suspected that the cracks seen from the backscattered image of the sample dried through critical point drying were because of the replacement of water by acetone because several wet samples disintegrated as soon as they were plunged into a vial containing acetone even at low concentration. It is also possible that the big micro-cracks observed from the backscattered image of the critically point dried sample might have been induced during vacuum impregnation in which resin was forced into the pore spaces to harden the sample prior to polishing. In view of the crumbling of the samples in acetone, for the resin impregnated samples, the varying concentrations of acetone were introduced to the sample gradually (a drop per second) via a burette. By this method, none of the samples disintegrate. Due to the fact that the freeze-drying reported here produced the most distorted microstructure in which it is difficult to achieve a representative area within the cracks, it is apparent that semi-unconsolidated samples similar to those used in this research are not recommended to be plunged in liquid nitrogen as the micro-cracks are suggested to have been imparted by the bubbling of the liquid nitrogen or ice formation.

Due to the foregoing, resin impregnation is the most recommended procedure for getting rid of water from semi-consolidated mudrocks when microstructural study is intended. The procedure involves a passive process that entails ordinary fluid displacement (water-acetone-resin) and the sample is not physically dried. The process requires no sophisticated equipment and can easily be carried out successfully in any laboratory. However, the technique is not suitable for dried semi-consolidated dried samples as they must be water saturated. Efforts to impregnate dried semi-consolidated samples were impaired as the samples crumble immediately after acetone was introduced (Figure 3.25).

Figure 3.25. Picture showing samples crumbling in acetone as soon as there were introduced to the vials containing acetone. The concentration of the acetone is 30% i.e. 70% of distilled water and 30% of acetone. The crumbling of the sample might have been cause by osmotic shock (Jim, 1985).

3.2.3 Scanning Electron Microscope

The scanning electron microscope (SEM) and its associated technologies have been in used to study fine-grained sediments and biological materials for many decades. The technology is a potentially non-destructive analysis involving interaction of electrons with the specimen. It is well suited to image the complexity in the distribution of clay minerals, organic matter and pore network in both nanoscale and microscale (Erdman and Drenzek, 2013). Recent development of shale gas as a way of meeting energy demands particularly in North America and to a lesser extent within Europe has increased SEM utilisation as physical properties pertinent to fluid flow in shale are determined using this technology.

SEM differs from traditional optical microscopy in that, it uses an electron beam instead of light (Houben, 2013). The resolution obtained through optical microscopy is unsuitable for microstructural characterisation of mudrock because most microstructural features are of a micron to submicron scale. SEM operates by producing raster images (Figure 3.26) through the interaction of an electron beam emanating from the electron gun with the surface of the

sample. Focusing of the electron beam on sample is achieved by series of electron lenses (Huang, Cavanaugh and Nur, 2013).

The electron beam emanating from the electron gun is usually too large to produce a sharp image at high-resolution. To maintain a sharp image and also a high-resolution, scanning electron microscopy utilises electron lenses that reduces the electron beam released from the source to a smaller spot size (Goldstein *et al.*, 2003). The spot size also known as probe size limits the maximum resolution obtainable in scanning electron microscopy. The spot size is proportional to the number of electron interacting with the surface of the sample. The final beam that reaches the sample being investigated depends on the size of the aperture and the strength of the condenser lens which is being focused by an objective lens to a point of interest.

The smallest magnified image produced by a scanning electron microscope is two orders of magnitude higher than the magnification of an optical microscope (Reichelt, 2007). The magnified image (magnification) is defined by the ratio of the length of the image produced on the monitor to the actual scanned length of the sample. The focal length of the objective lens determines the working distance (WD). Working distance is the distance between the lower piece of the objective lens and the sample on the stage. It ranges between 5mm and 30mm.

Modern SEMs are controlled on a computer system through installed software and mouse clicking. This allows easy switching between detectors. The signal varies as the electron beam scans from pixel to pixel due to the variation in topography and composition (Reichelt, 2007). Higher magnification is obtained by reducing the length of the specimen scanned but maintaining the length of the image displayed on the screen (monitor).

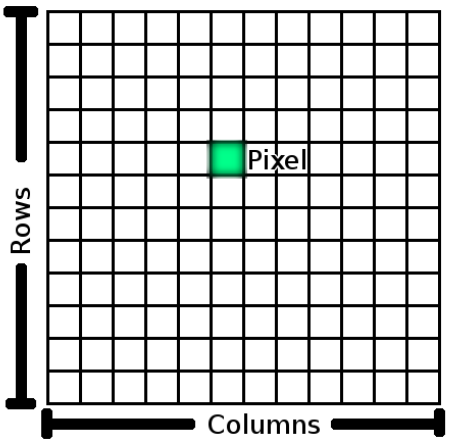

Figure 3.26 Diagram representing a raster data set running in rows and column.

The scanning electron microscopes scans the sample from one point to another producing a rectangular box with each point represented on the computer screen. This allows contrast in the image to be enhanced using deflection system control (Goldstein *et al.*, 2003). Note that each square box represents the obtained pixel during scanning. The system used here employs 768 x 512, 1536 x 1024, 3072 x 2048 or 6144 x 4096 pixels.

In scanning electron microscopy, there are a number of ways by which electrons from the source (electron gun) interact with the sample on the stage. Electron beam can interact inelastically with the sample by collision of incident electrons with the electrons of the atoms in the sample. Such interaction produces secondary electrons (SE), auger electron, bremsstrahlung x-rays and cathodoluminescence (CL). There is slight deflection in trajectory of the electron beam and little dissipation in kinetic energy before scattering event (Reichelt, 2007). Electron beam can also interact elastically with the sample to generate backscattered electrons (BSE) (Figure 3.27). In this case, there is deflection in the direction of electron beam after scattering event resulting from electrical field interaction of incident electron beam with the positive nucleus of the specimen (Reichelt, 2007).

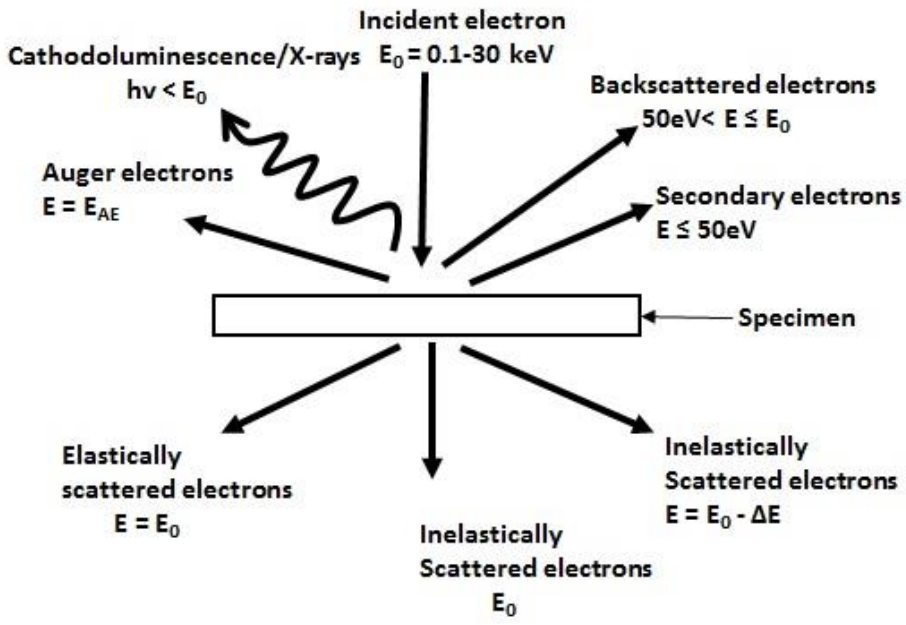

Figure 3.27 Different signal resulting from inelastic and elastic interaction of the incident electron with the specimen, E_0 = energy of signal electrons; E_{AE} = energy of auger electrons; ΔE = energy loss of inelastically scattered electrons; hv = energy radiation (Reichelt, 2007). There is no reduction in kinetic energy during elastic interaction of the electron with the specimen. Inelastic interaction such as secondary electrons, auger electrons and cathodoluminescence produces reduced kinetic energy.

Commonly used modes in scanning electron microscopy are the secondary mode and the backscattered mode (BSE). Figure 3.28 shows practically how secondary electron (SE) and backscattered electron interact with the specimen. In secondary electron mode, the primary electrons interact with the target material and some energy are loss which is a function of the angle of incidence between the primary electron and the target material (Reynolds and Gorsline, 1991). Secondary mode is generated close to the surface and therefore provides information about topographic features such as crystal morphology, topography and pores. In backscattered mode, electrons travel deeper into the specimen. Backscattered electrons are produced when the primary electrons strike the atom of the materials and subsequently produces a reflection of the electron beam. The intensity of the reflected electron is dependent on the atomic number of the material composition. Hence, there is an increase in the number of electrons reflected with increase in the atomic number of the material. Because the interaction between the electrons and the sample is elastic, there is minimal energy loss and the electron is scattered within the target material. The reflected electrons are eventually captured by the backscattered electron detector. Backscattered (BSE) mode is well suited for highlighting contrast in compositional variation.

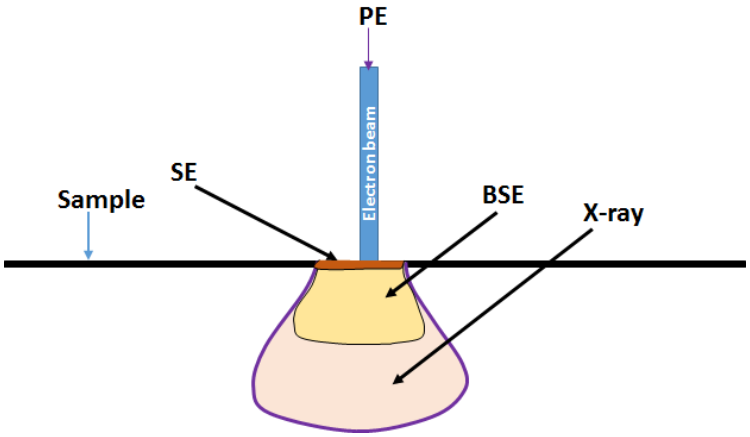

Figure 3.28 Cartoon of electron and sample interaction in scanning electron microscope. The elastic interaction of electron yield backscattered (BSE) while inelastic interaction yield secondary electron (SE), The X-ray penetrates deeper than both secondary electron (SE) and backscattered electron (BSE) and it is associated with absorption of electrons. (Modified after, Huang, Cavanaugh and Nur, 2013).

Scanning electron microscope (SEM) images are in gray-scale and the degree of grey in the image is proportional to the relief (in SE) or atomic number (BSE) of the sample components. Areas where features such as pores and fractures are located are dark in colour with ring of brightness surrounding the feature in secondary electron mode (Figure 3.29). Because backscattered mode is related to atomic number of the material, low atomic number are portrayed in dark shades compared to those with higher atomic number which would appear lighter. For example, kerogen (organic matter) would appear dark, silicate would be grey, carbonate would be light grey, and pyrite would appear as white (Figure 3.29).

In order to avoid charge build up from insulating (non-conductive) materials during imaging, such materials are coated in a thin layer of carbon or gold. The choice of coating material is dependent on the interest of the study. Carbon coating of the material is suitable for elemental analysis while if the interest is centered on acquisition of high-resolution images, gold coating is recommended (Swapp, 2016). In this research a Quanta 650 field emission scanning electron microscope and an XL30 environmental scanning electron microscope (ESEM) were used at low vacuum (0.83 Torr) in both gaseous secondary electron (GSE) and backscattered electron (BSE) modes at 15-20 kV, spot size of 4.5 and working distance of about 10 mm. The use of low-vacuum allows imaging without coating the sample with conductive medium.

Examples of a broken mudrock surface taken with the XL30 environmental scanning electron microscope (ESEM) are illustrated Figure 3.29. The left side images were obtained using GSE

while the right images were obtained using BSE. White arrow shows pores, blue arrow framboidal pyrite and yellow arrow depicts coccolith which is rich in calcite. Observation from images from the images that those collected with GSE mode (Figure 3.29) give little information regarding the compositional variation compared to backscattered electron. Pictures of the two SEM systems used in the current study are shown in (Figure 3.30).

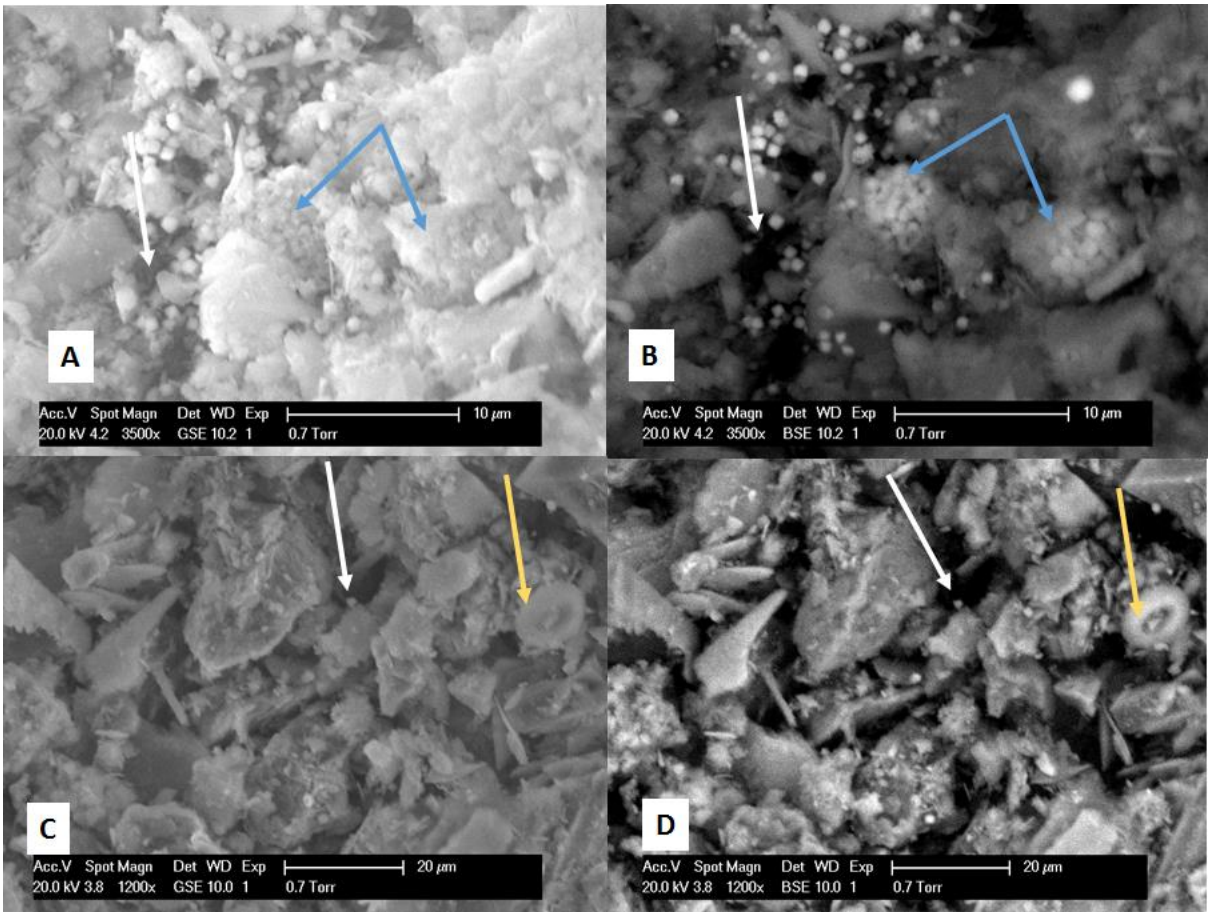

Figure 3.29 Micrograph of broken surfaces of clay particles in both secondary electron (SE) and backscattered modes (BSE).

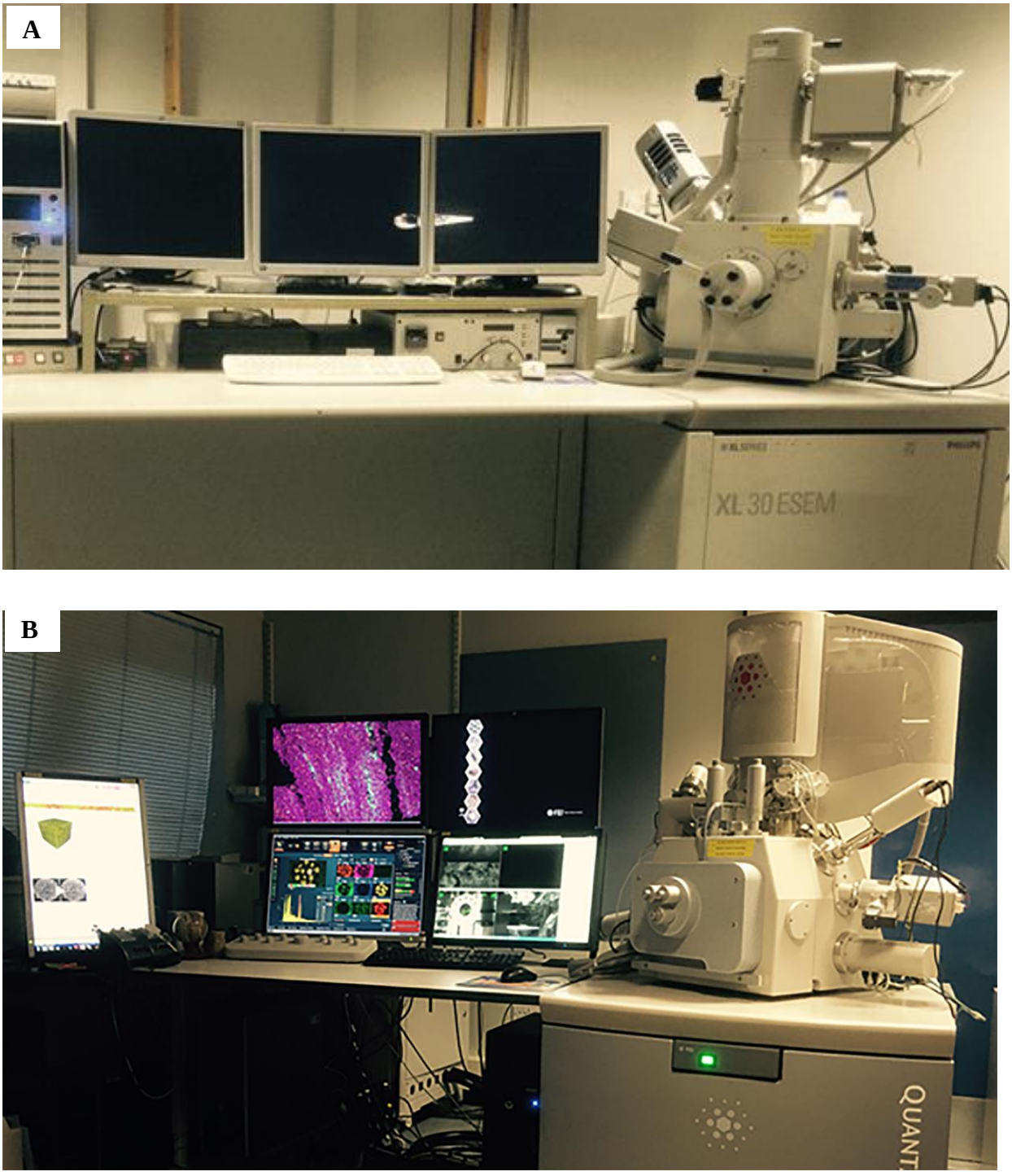

Figure 3.30. Picture showing (A) XL30 ESEM and (B) the FEG 650 scanning electron microscope and desktop computers used for collection of large scale montages of SEM images.

3.2.3.1 Mineralogy

Data on mineralogy were obtained through automated acquisition of elemental composition on polished-thin sections with the energy dispersive x-ray (SEM-EDX) component of the scanning electron microscopy. The elemental composition was determined from large area

(EDX) which is up to a millimeter horizontal field of view (HFOV). The large area EDX mapping was obtained using Oxford instrument 'Aztec (v3.3) Large Areas' (LAM) and was also used to construct phase maps by processing all the elemental data to yield associations of elements in which minerals or group of minerals present in each sample were then quantified. For few samples, mineralogical composition was determined from backscattered scanning electron microscopy (BSE-SEM) through multiple thresholding with Fiji-ImageJ and subsequently determining the percentage of the minerals. Mineral quantification from BSE image through thresholding has been recently employed and is detailed in Buckman *et al.* (2018).

3.2.4 Broad Beam Ion Milling (BBIM)

Microstructural studies of fine-grained sedimentary rocks with scanning electron microscopy is better carried out on polished sections rather than broken surface. Mechanical polishing of rocks are associated with uneven topography (Loucks *et al.*, 2009; Loucks *et al.*, 2012) and artificially created structures (artifacts) such as plucking, smearing etc. which have strong negative effect on the reliability of the results. Due to the fact that mudrocks have a variety of mineral compositions with disparate hardness, smearing and plucking of grains are common problems associated with mechanically polished cross-sections. Argon ion beam milling (broad ion beam) is the state of the art polishing method that produces a flat surface with minimum topography. Argon ion milling is similar to focused ion beam milling (FIB) but it has an advantage of milling a wider area (Desbois *et al.*, 2011; Reed, Loucks and Ruppel, 2014) that is more representative of the sample compared to the FIB. Subtle features for example hair line micro-fractures and narrow cracks which can be masked by mechanical polishing, can be preserved using argon ion milling. During ion milling the sample can be rotated to prevent striation from the irradiated argon ion beam bombarding the sample and this allows the material to be milled uniformly regardless of the disparity in the hardness of sample composition (Erdman, Campbell and Asahina, 2006). Hence, soft and hard components of the material are milled at the same rate.

For this study, a limited number of samples were ion milled at The University of Oklahoma, USA using a stand-alone argon ion milling cross polisher. The process involved cutting off a slice of about 3 mm thickness using a diamond saw blade with ethanol serving as the cooling fluid in order to prevent swelling of the clay minerals. The samples were then mounted on a 2.5 cm aluminum pin style stubs with an adhesive (CrystalbondTM 509). The samples were

then polished mechanically to reduce the surface roughness without using any fluid with sandpapers of progressively small grit sizes. Artifacts that might have been introduce through the mechanical polishing were removed during ion milling as the instrument is capable of removing more than 100 µm of the topmost layer. All the samples were ion milled with argon using Fischione Instruments model 1060 SEM ion mill at 5kV for 3 hours. All the sample ion milled were prepared through low viscosity resin impregnation of which the procedures are highlighted above. An example of broad ion milled sample imaged on a FEI Helios 650 FIB/SEM is presented in Figure 3.32.

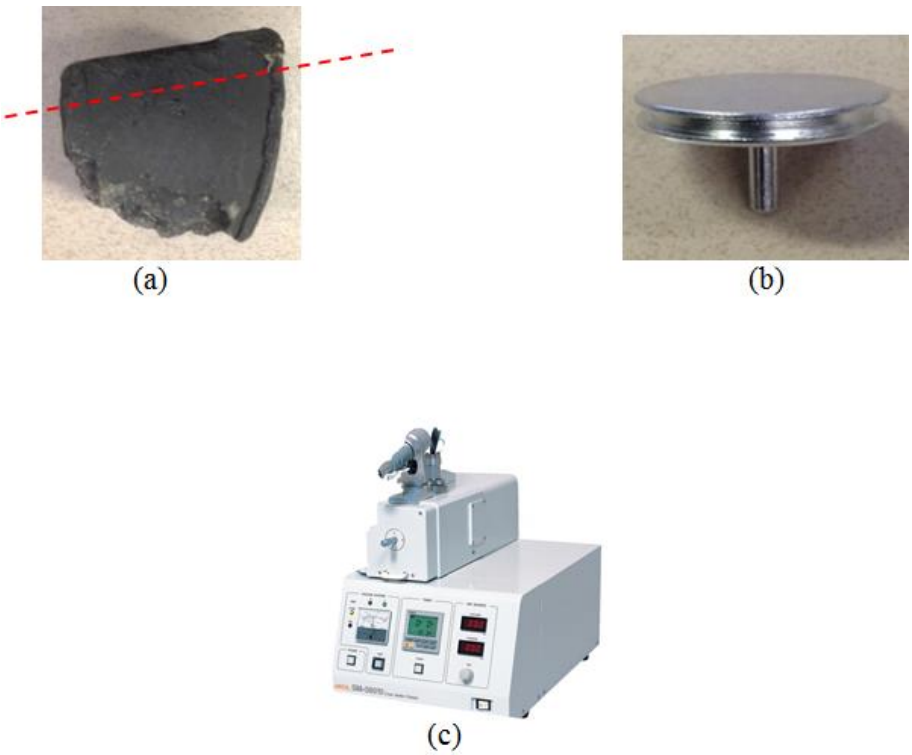

Figure 3.31. Procedure for ion milling sample through a stand-alone broad ion milling cross polisher (a) 3 mm of the sample was cut off using ethanol based diamond rock cutting machine at a slow speed (b) the cut off sample was mounted on a 2.5 cm diameter stub and mechanically polished without any fluid using sandpaper of progressively small grit sizes (c) the polished sample was placed in the sample holder milled with Argon using a Fischione Instruments model 1060 SEM ion mill for 3 hours. Note that the milling process is automated, the instrument requires no supervision as the milling progresses.

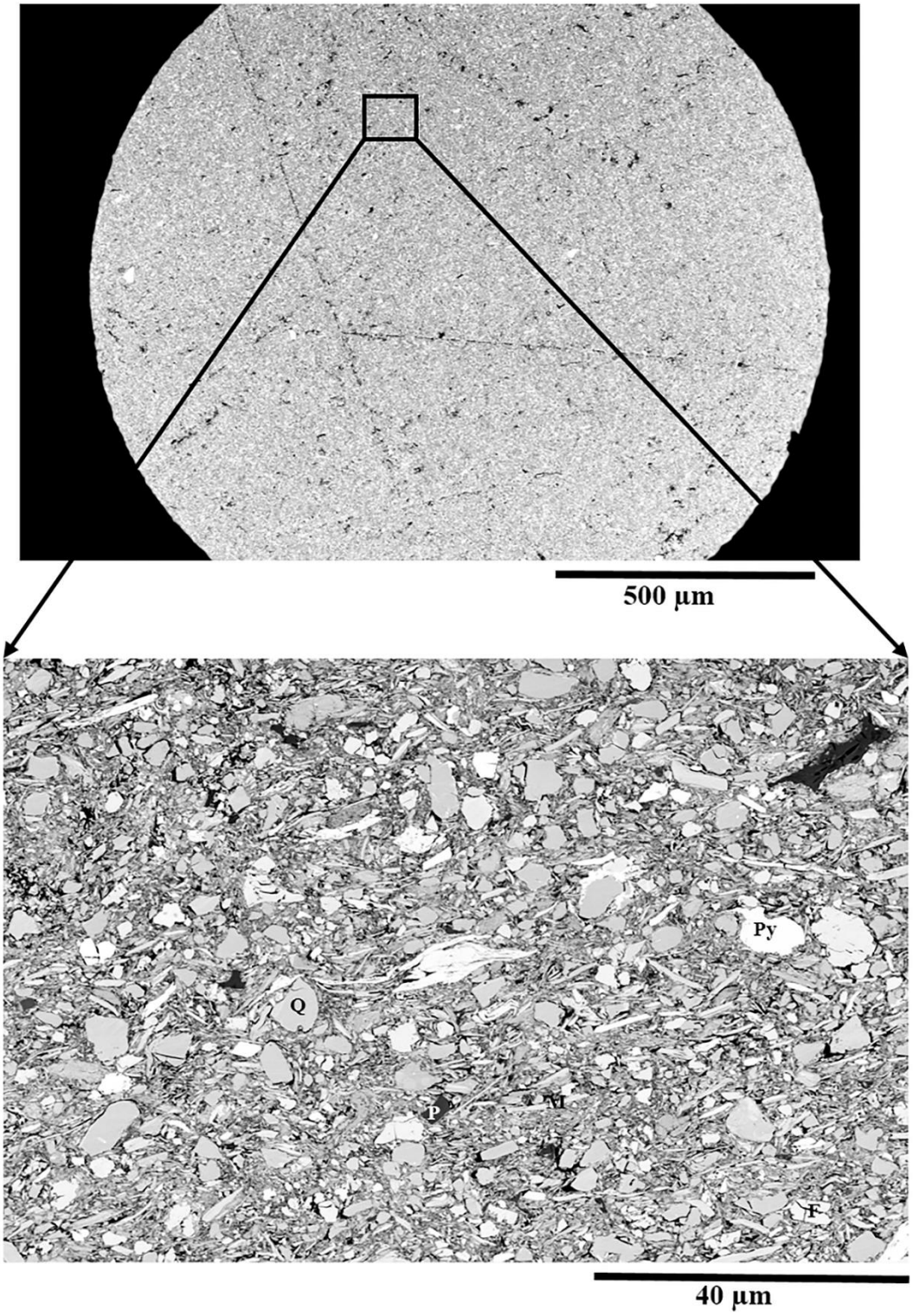

Figure 3.32. Backscattered SEM image of an ion milled sample on a FEI Helios 650 FIB/SEM at ca. 4 mm working distance, 2kV and with a concentric backscattered detector-CBS- (Courtesy of Mark Curtis of The University of Oklahoma, USA). Q=quartz, Py=pyrite, F=feldspar and M=mica.

3.2.5 High-resolution Large-scale imaging

High-resolution large-scale imaging with scanning electron microscopy employed in this research follows the procedures described by Buckman (2014) and Bankole *et al.* (2016). The procedure involves automated collection of multiple tiles and stitching from a regular grid across the surface of the sample using the FEI Maps software. The procedure can be applied to produce large montage SEM image of the whole slide. The only constraints to the large-scale high-resolution image are; time, storage and availability of software to process or analyse the big-data resulting from the process.

Both polished thin-sections and ion milled samples were imaged using a Quanta 650 field emission scanning electron microscope (Figure 3.30) in low vacuum mode (0.83 Torr). The settings for the SEM images involves using backscattered detector, 4.5 spot size and a working distance of about 10 mm. Once the SEM has been pumped, a specific area of interest is focused on with the number of tile and pixel resolution defined. In general, a low-resolution image was acquired with a horizontal tile width of 2 mm per tile to get an overview of the whole slide. This allows further higher resolution SEM images to be acquired within areas between cracks. The resolution of SEM images acquired is dependent on the interest of the study. Backscattered SEM images at a resolution of 45 nm per pixel were acquired for studying grain-size, microfabric and grain orientation and these are termed high-resolution, while for the determination of pore size distribution and porosity from 2-Dimensional SEM images, the resolution employed is approximately 3 nm per pixel (Figure 3.33). Further details on workflow for acquiring large-scale high-resolution SEM can be found in (Buckman *et al.*, 2018).

The intention was to collect several tiles and stich the whole polished thin-sections and the ion milled samples but due to cracks, imaging was limited to between cracks. Image acquisition through automated collection and stitching as employed here is also constrained by computer memory because most montages can be up to several gigabytes in which not only storage of the collected data is problematic but getting a software for image processing and analysing large SEM images is not practicable. A chart showing the time it takes to acquire backscattered SEM montages with respect to horizontal field of view, pixel resolution and scan time is presented in Figure 3.34.

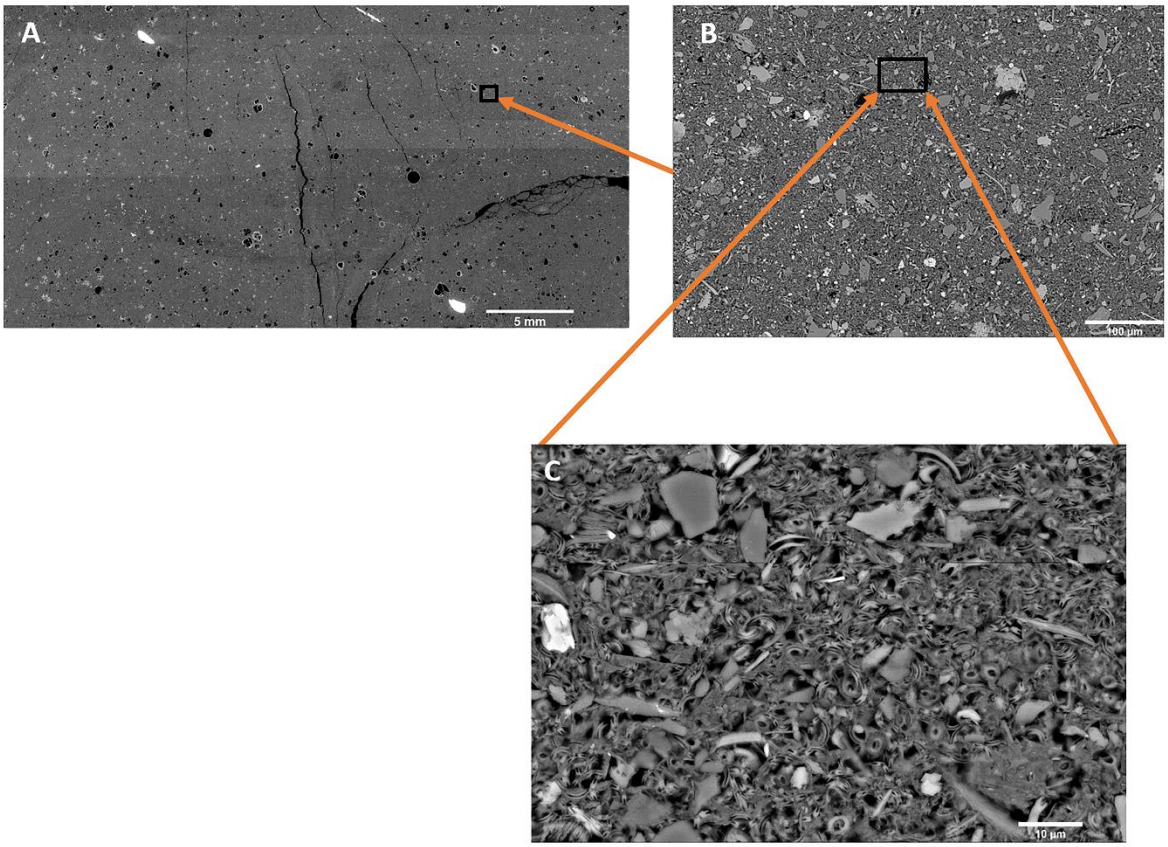

Figure 3.33. Multi-resolution images (a) low-resolution image of polished thin section to determine good area for higher resolution (b) high resolution image for grain orientation and particle size analysis (45 nm per pixel) (c) super-high-resolution image for porosity and pore size (3.2 nm per pixel).

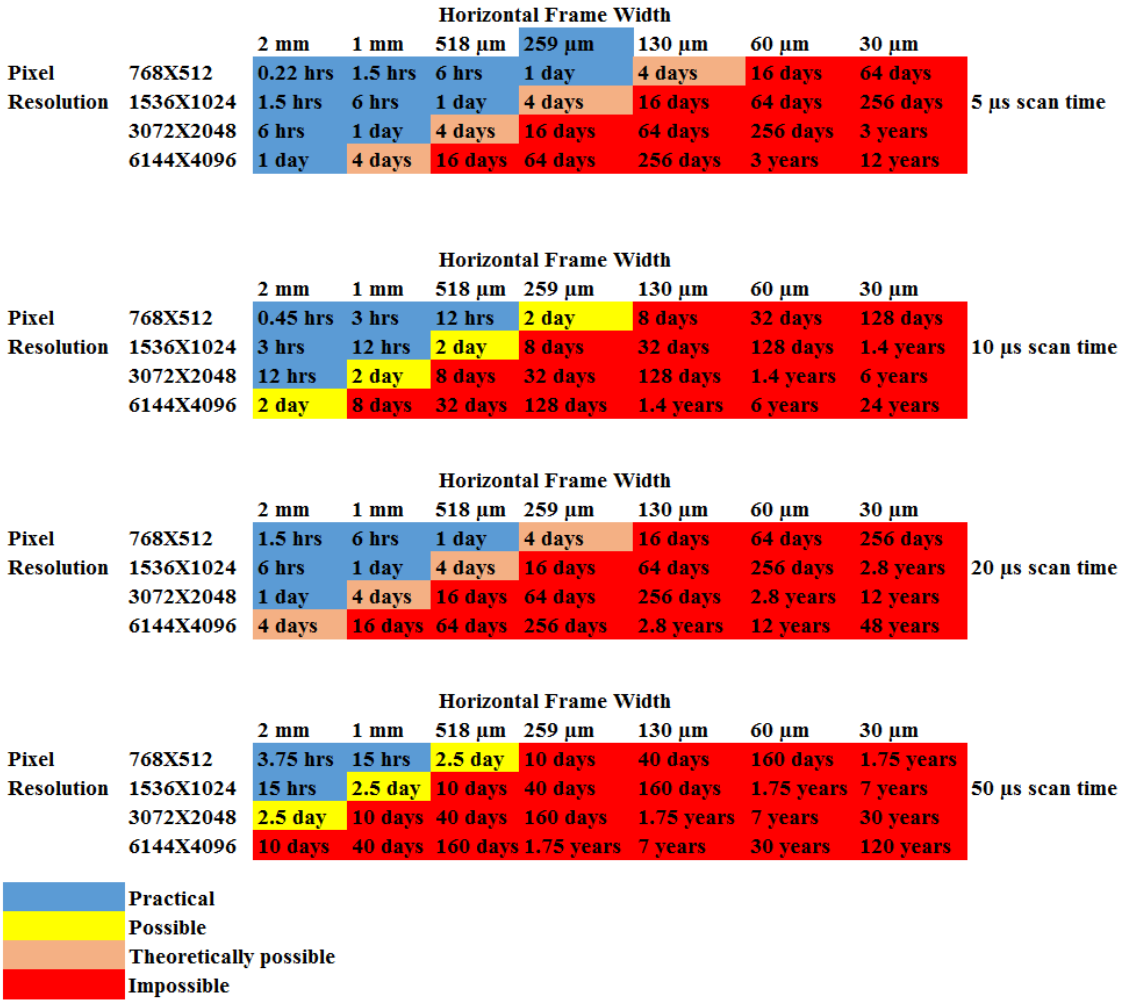

Figure 3.34. Relationship between pixel resolution, tile horizontal frame width and scan time, for time taken to acquire a whole slide image (Buckman *et al.*, 2018).

3.2.6 Low-pressure nitrogen gas adsorption

Gas adsorption is widely used for characterisation of pore size and specific surface area of materials (Busch *et al.*, 2017). Adsorption involves adherence of gas molecule to the surface of the solid phase. The process by which gas adsorption occurs is a multi-process in which the gas diffuses into the solid phase, the solid phase absorbs the gas and finally the gas interacts with the solid phase through a process called sorption.

The adsorption process can occur through physical adsorption (physisorption) or chemical adsorption (chemisorption). Physisorption involves attraction of gas molecules to the surface of the solid phase by a weak force of attraction i.e. van der Waals interaction (Thommes and Cychosz, 2014). In the case of chemical adsorption the gas molecules are adsorbed to the solid

phase through chemical bonding (Rouquerol *et al.*, 2014). The chemical bond is so strong such that adsorption is restricted to a monolayer and higher heat energy is released through the process in comparison with physisorption. Physisorption is thermodynamically reversible at isothermal condition whereas chemisorption is irreversible thermodynamically (Bertier *et al.*, 2016). Due to the fact that low-pressure nitrogen has little to do with chemisorption, further discussion on chemisorption is of no relevance.

Nitrogen gas at 77 K adsorbed to the surface of a solid material through physisorption is dependent on the relative pressure (p/p_o) of nitrogen gas which is at equilibrium with the surface of the material (Bertier *et al.*, 2016). To calculate the amount of gas adsorbed on the surface of an adsorbent (solid phase), the difference between the gas introduced to the sample cell and amount of gas in the free space is calculated (Thommes and Cychosz, 2014). An adsorption experiment yields an isotherm curve which indicates the amount of gas molecules adsorbed to the surface of a material as a function of relative pressure. In order to interpret the pore structure based on the isotherm curve, it is generally assumed that the pores are homogeneous and cylindrical (Bertier *et al.*, 2016), though this might be untrue in the real sense. Further information guides on the procedures and discussion on the method can be found elsewhere (Barrett, Joyner and Halenda, 1951; Sing, 1982; Rouquerol *et al.*, 1994; Sing, 2001; Rouquerol *et al.*, 2014).

The low-pressure Nitrogen sorption in this study was performed on a Gemini VII 2390t device through the static volumetric method and the isotherm curves were determined at 77.3 K. The adsorption and desorption curves were measured at 81 points in which the relative pressure ranges between 0.001 and 0.95. Samples for low pressure gas adsorption (LPNGA) requires crushing to less than 250 µm to attain the vacuum threshold prior to the gas adsorption experiment (Chalmers, Bustin and Power, 2012). Prior to the adsorption experiment, the samples were crushed to a size diameter of between 250 µm and 63 µm and then dried for about 24 hours at 100^0C. About 0.5 g to 0.7 g of the crushed samples were then degassed under vacuum with nitrogen gas for a minimum of 12 hours. The collected data on the crushed samples were interpreted for the specific surface area (SSA) based on the multi-layer model of Brunauer-Emmet-Teller (BET) (Brunauer, Emmett and Teller, 1938) while total pore volume was determined using Barrett-Joyner-Halenda (BJH) analysis (Barrett, Joyner and Halenda, 1951). The pore volume is in cm^3/g and to get the porosity value, which is the ratio of pore volume to bulk volume, additionally the grain density is required (Bertier *et al.*, 2016). Hence

the grain density derived through helium pycnometry which formed part of the data acquired on board during the expedition program, and provided by the IODP, were used. Information on how grain density is measured during International Ocean Discovery Program is provided in (Blum, 1997). The porosity values were calculated based on Gurvich's rule as employed by Bertier *et al.* (2016) and it is believed to give an approximation to the total porosity (Seemann *et al.*, 2017). Gurvirch rule is premised on two main assumptions and these include:

(i) The total pore system is filled up at the relative pressure close to the saturation pressure.

(ii) At the experimental temperature condition, the adsorbate in use has similar physical and chemical properties as in its liquid state.

The total pore volume of the samples was derived close to their maximum sorption capacity i.e relative pressure (P/P◦) is close to 1 by employing the Gurvirch rule and subsequently calculating the approximate total porosity based on the formulae provided below.

$$V_T = \frac{Q_{max}}{1000}.\ V_m \quad \text{..... Equation 3.1}$$

Where

V_T (cm^3/g) is the total specific pore volume determined based on the amount of gas adsorbed at relative pressure (P/P_o) close to 1 by assuming that all the pores are filled with the adsorbate (Gurvich principle).

Q_{max} is the maximum sorption capacity measured in mmol g^{-1}

V_m is the molar volume of the liquid adsorbate, which is 34.7 cm^3/mol for nitrogen at 77K.

$$ø = \frac{V_T}{\frac{1}{p_{grain}} + V_T.} \quad \text{..... Equation 3.2}$$

Where Ø is the porosity, which is unitless.

V_T is the total specific pore volume in cm^3/g derived from the Gurvich principle

ρ is the grain density derived from He-pycnometry in g/cm^3

Figure 3.35. Gemini VII 2390t micrometric instrument with the degassing unit and computer system for volumetric gas adsorption experiment.

3.2.7 Digital Rock Physics

Digital rock physics (DRP) involves imaging, digitizing pore space and numerical simulation of the physical processes to obtain salient rock properties (Andrä *et al.*, 2013a). DRP provided both qualitative and quantitative information about fluid transport and the geometric properties of the rocks (Fourier, 2017).

Most digital rock physics involves three procedures: (i) image acquisition be it in 3-dimensions or 2-dimensions (Hurley *et al.*, 2014) in which the resolution of the image should be high enough to capture the pore space; (ii) image processing and segmentation to extract the pores;

and (iii) computer simulation of physical processes to determine petrophysical properties including but not limited to porosity, permeability (both absolute and relative), electrical conductivity, elastic properties and pore network (Andrä *et al.*, 2013b).

High-resolution SEM images acquired from prepared polished thin-section at 3.2 nm per pixel were the input data for a three-dimensional stochastic pore reconstruction tool, to model pore architecture, and a flow/permeability simulation software. The steps involved in the sample preparation for the polished thin-sections; from drying, resin impregnation and automated acquisition and stitching of SEM images to form montages have been described explicitly in chapter 3 (3.2.2.5 and 3.2.5).

Image processing and segmentation were performed with an open source image analysis tool known as Fiji. The image segmentation employed machine learning segmentation which involved selecting training features such as pores, grains and undifferentiated grains. Detail on machine learning segmentation through Trainable Weka Segmentation incorporated into Fiji have been discussed in chapter 5 (5.2.3.1).

After segmentation, sub-regions of the high-resolution SEM images serve as input data for the 3-Dimensional reconstruction of the pores using the Pore Architecture Reconstruction tool (PAR). PAR is the recent version of Pore Architecture Modelling tool (PAM) which is an in-house tool for 3-Dimensional pore reconstruction at the Institute of Petroleum Engineering, Heriot-Watt University, United Kingdom.

The software employs Markov Chain Monte Carlo simulation in which small local conditions are used to predict global features (Wu *et al.*, 2007). In other words, it involves complex interaction of multiple voxels in order to produce individual realization that conforms with the input images (Wu *et al.*, 2006). The main input for PAR are SEM images acquired from thin-section in x, y and z directions (Figure 3.36). In this study, the high-resolution images acquired using scanning electron microscopy were used as the main input parameters and the x, y and z directions are sub-areas from the large-scale high-resolution SEM images of the individual polished thin-section representing the pore fabric (i.e. all within the same plane).

To perform the 3-D pore reconstruction, the length and breadth dimension for the individual input SEM images must must be equal, the SEM images must be binarised and not more than 600 by 600 pixel. In this research, the high-resolution SEM images were binarised and reduced to 400 by 400 pixel. The 3-D reconstructed output from PAR serves as input parameter for

another flow analysis tool referred to as Pore Analysis tool (PAT). The tool generates information on the pore system which include; pore size distribution, porosity, permeability, and pore connectivity function among other parameters that are significant to understanding fluid movement. Network models produced by PAT are useful input parameter for single and two-phase fluid flow simulation (Wu *et al.*, 2007; Otiede, Wu and Olafuyi, 2012).

In this thesis, the DRP technique employs a two-scale pore network extraction coupled with pore network simulation (Figure 3.37), due to the wide range in mudrock pores which are unlikely to be captured at a single resolution. The methodology involves pore network modelling at higher resolution (25 nm per pixel) and lower resolution (75nm -150nm per pixel) to describe the 3-D pore networks at the two resolutions and subsequently integrating the pore network into a single network with both resolution being honoured. The step by step in the two-scale pore network modelling and simulation follow the approach on multi-scale pore network extraction and simulation described by Jiang *et al.* (2013) and (Pak *et al.*, 2016). Further details on Pore Architecture modelling tool (PAM) and explicit information on the algorithm employed in PAT can be found elsewhere (Wu *et al.*, 2006; Wu *et al.*, 2007).

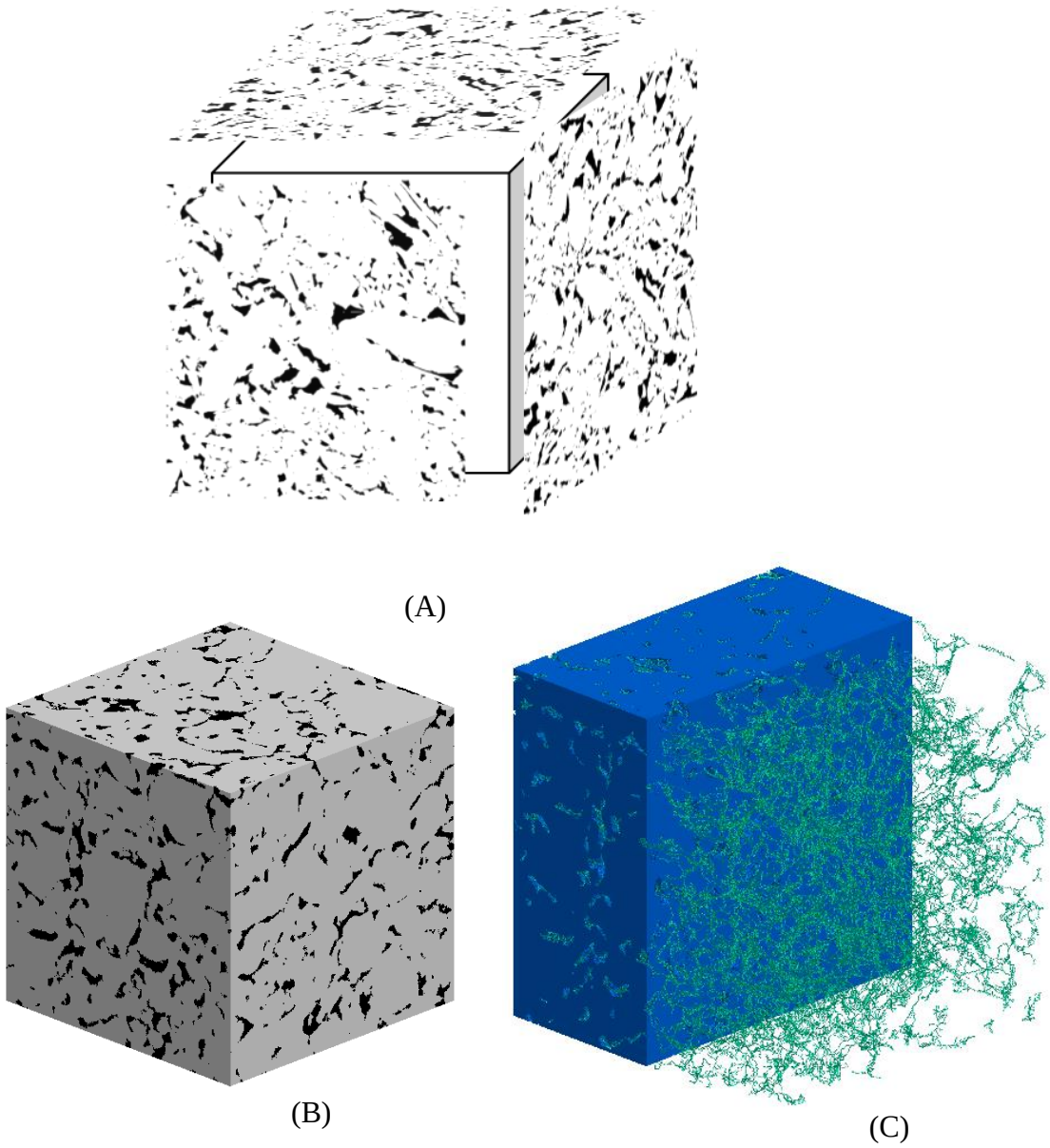

Figure 3.36. Sample of input and output derived using PAR and PAT (A) 2-D training images representing X, Y and Z directions (B) 3-D model of reconstructed pores by PAR (C) Pore network model derived from PAT.

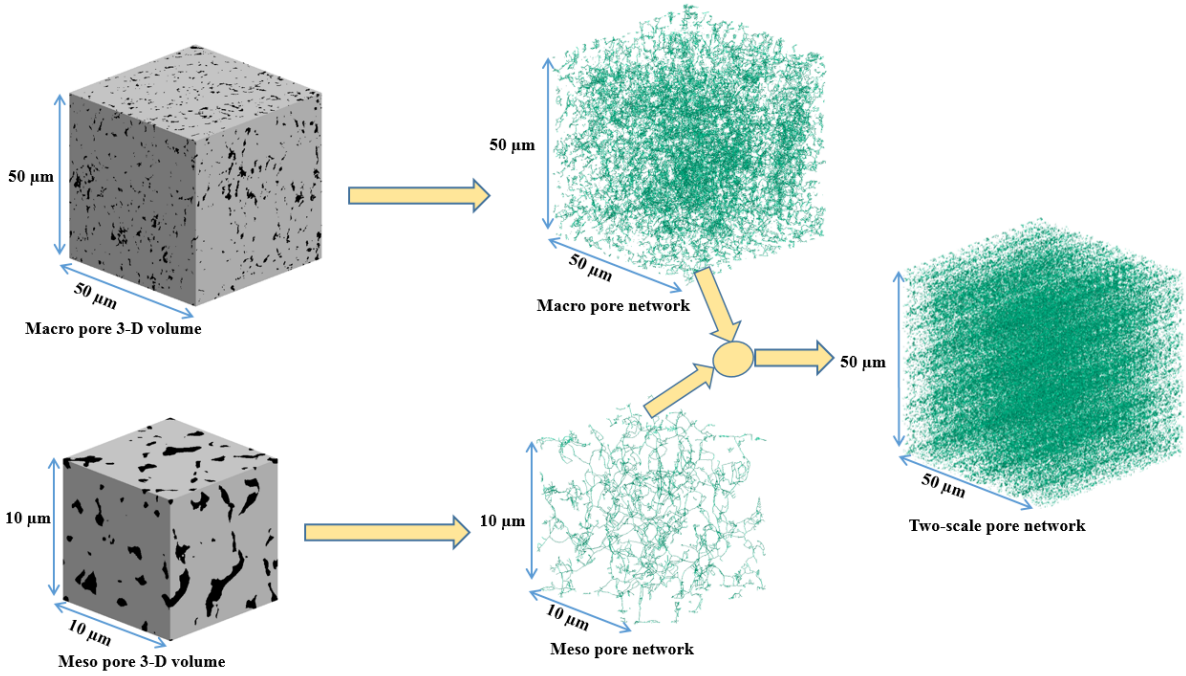

Figure 3.37. Workflow of two scale pore network extraction and simulation. The workflow involves pore network extraction at two different resolution, then integration of the extracted network into a single network.

3.2.8 Synchrotron powder diffraction

Hard synchrotron X-ray source provides a powerful technique for studying low scattering material such as mudrocks (Lonardelli, Wenk and Ren, 2007; Wenk *et al.*, 2008a). It has an advantage over the conventional X-ray goniometry technique due to its high energy and highly focused X-ray as well as very short wavelength that allow considerable sample penetration with limited X-ray absorption.

Powder X-ray diffraction was performed at the ID-11 beamline, European Synchrotron Radiation Facility (ESRF) at Grenoble, France. Prior to the experiment the samples were impregnated in resin to harden the samples and the resulting samples have approximate volume of about 2.5 cm X 2.5 cm X 1.5 cm. The blocky samples were later cut into slices of ca. 1.5 mm thickness with a rock cutting machine using oil based IsoCut as coolant to avoid swelling of clay minerals as well as destruction of the samples. In performing the experiment, a monochromatic X-ray beam of a short wavelength of approximately 0.30996 Å (energy ~40 KeV), beam size of 0.05 X 0.05 mm, radial diffraction geometry and recorded by a 2048 X 2048 pixels CCD (Charged Couple Device) detector at about 0.231 m away from the sample. The samples were mounted on a metal pin and placed on the goniometer (Figure 3.38). Data acquisition was carried

out at twelve different angles as the sample is being rotated about the horizontal axis from -75^0 to 75^0 at an increment of 15^0 for good statistics of textural analysis and to improve the pole figure coverage (Wenk *et al.*, 2008b). The bedding plane was placed perpendicular to the tilting axis in order to ensure that the X-ray beam hits the same layer during rotation.

Due to the inherent heterogeneity of mudrocks, data were acquired over three spots, spaced at about 1 mm interval in order to obtain a representative average (Wenk *et al.*, 2008a; Kanitpanyacharoen *et al.*, 2012). Th time for data acquisition per sample is approximately 45 mins per sample.

The difraction images are characterised by Debye rings, which correspond to different mineral phases and varying lattice planes. The variation in intensity along the Debye rings is an indication of preferred orientation (Wenk *et al.*, 2008b; Wenk *et al.*, 2014).

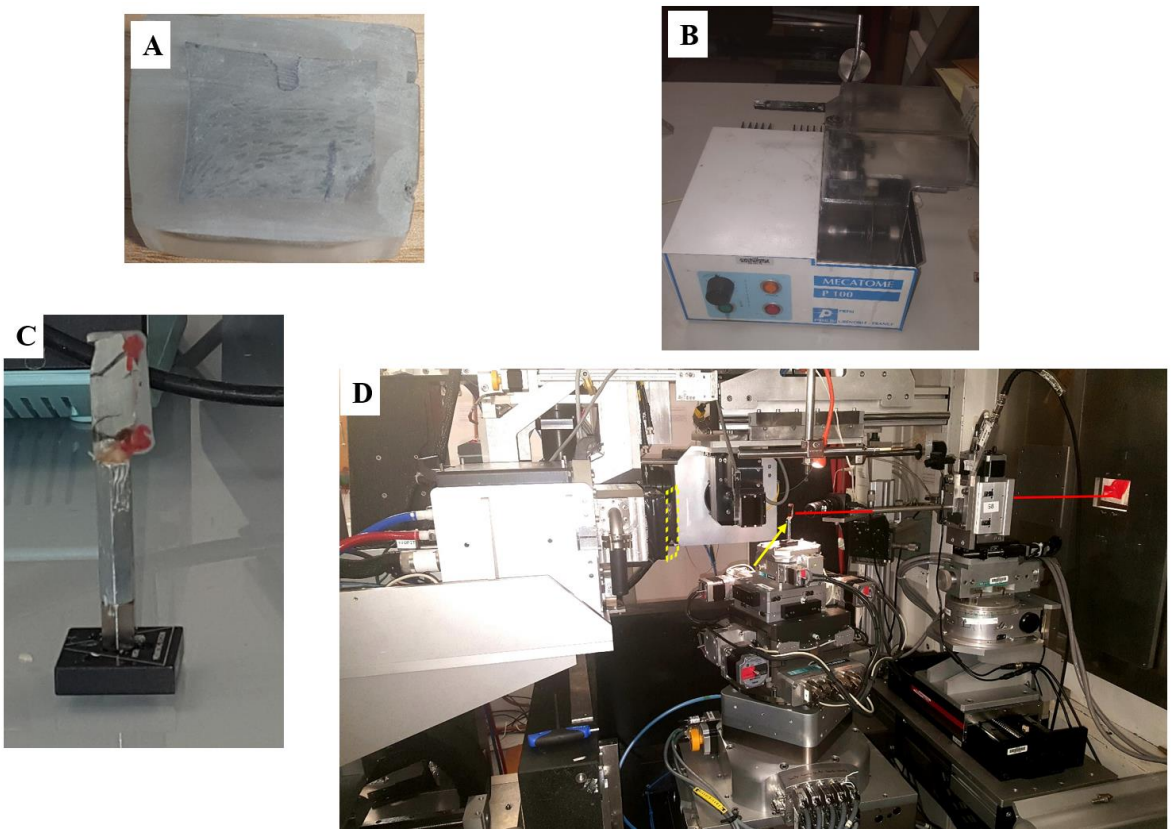

Figure 3.38. Sample preparation and and experimental set up for data acquisition for textural analysis at the European Synchrotron Radiation Facility, Grenoble (ID-11 beamline). (A). Block of mudrock impregnated in epoxy resin (thickness ca. 5 mm) (B) Rock cutting machine, which uses oil-based coolant (C) Mudrock slab mounted on a pin (thickness ca. 1.5 mm). The arrow mark on the slab is perpendicular to the bedding (D) Experimental set up at ESRF, ID-11 beamline. Read line is the direct X-ray beam, yellow arrow is the 1.5 mm thick sample mounted on the stage and the broken square indicates the position of the CCD detector.

3.2.9 Methodology development for studying microstructure

Mudrock microstructure is maturing, as an emerging field, and the renewed focus on mudrocks calls for development of methodology to better characterise their different properties. Charaterisation of mudrock microstructure is challenging as it requires special sample handling and preservation and limited amount of air exposure is recommended (Ewy, 2015).

Laboratory measurement is inevitable and remains a significant means of characterising unique properties of mudrocks, which include: grain size, macro/microfabric, mineral composition, porosity, permeability and preferred orientation among others. In fact, there are diverse techniques that are currently in use for measuring different aspects of mudrock microstructure.

There is a challenge of getting comparable measurements from different techniques due to difference in resolution.

Scanning electron microscopy is a commonly used technique for studying mudrock microstructure. Its high resolution is ideal for revealing fine scale features in mudrocks from micron to sub-micron scale. Current advancement in electron microscopy has resulted in improved images and analytical technique for better characterisation of mudrocks (Lemmens and Richards, 2013) but there is still room for methodological development. Hence, in this research, a new workflow for characterising mudrock properties via automated image analysis of large areas and high-resolution scanning electron microscopy coupled with image analysis have been developed. This is presented in chapters 4 and 5, and currently in press as Bankole *et al.* (2018a,b). The methods are very significant for improved understanding of subsurface mudrocks and their capacity for movement of fluid as well as their storage potential.

CHAPTER 4 – GRAIN-SIZE ANALYSIS OF MUDROCKS FROM SEM IMAGES

4 Grain size analysis of mudrocks from SEM images

This chapter is currently in press as: Bankole, S.A., Buckman, J., Stow, D. and Lever, H. (2018) 'Grain-size Analysis of mudrocks: A New Semi-Automated Method from SEM Images', *Journal of Petroleum Science and Engineering.* (In press). The work is 90% that of the first author.

4.1 Introduction

Grain-size is a fundamental property of rocks that has a significant impact on their petrophysical properties such as specific surface area, pore size distribution, porosity and permeability. It is a general belief that there is a positive correlation between grain-size and pore size distribution which in turn is imperative to fluid movement within the rock (Aplin, Fleet and Macquaker, 1999; Yang and Aplin, 2007). Grain-size distribution reflects the hydrodynamic condition of the depositional environment (Saner, Cagatay and Al Sanounah, 1996), hence it is a useful forensic technique to reconstruct the depositional processes and mode of transport of sediments (Blott *et al.*, 2004).

Numerous techniques have been developed for analysing the grain-size of sediments, including sieving, laser diffraction, dynamic light scattering, image analysis, sedimentation, and electro zone sensing. The choice of technique depends in part on the grain-size of the material, but in most cases should be inexpensive, fast, accurate and cover a wide range of grain-sizes (Jiang and Liu, 2011).

However, grain-size analysis of fine-grained sediment is especially difficult and time consuming. There is a strong possibility of underestimating the proportion of clay-size particles (< 4 um) due to the fact that clay particles are within the resolution limits of most technique (Røgen, Gommesen and Fabricius, 2001). Recognition of mudrocks as important hydrocarbon reservoirs (shale gas and shale oil), as potential storage containers for carbon dioxide in the subsurface and as repositories for nuclear waste has put into sharp focus a growing interest in studying mudrocks. This has prompted an on-going development of methods that are suitable for analysising this suite of rocks.

Electron microscopy has been employed in resolving features down to the nanometre scale and it is a common method utilised in studying both the nanostructure and microstructure of fine-grained sediments (Curtis *et al.*, 2010; Camp, Diaz and Wawak, 2013). These techniques can also be used in quantifying mudrock grain-size, although such application is relatively rare. The scarcity of utilising electron microscopy in estimating grain-size might be due in part to the limited area of coverage normally obtained by the scanning electron microscopy (SEM) method and hence, how representative the measurement is for the whole sample (Saraji and Piri, 2015; Sanei *et al.*, 2016).

In this study, in order to mitigate against a very small measurement, grain-size analysis was carried out with large-scale images (ca. 0.65 mm X 0.42 mm) acquired from polished thin-sections through backscattered electron (BSE) imaging by scanning electron microscopy and processed by image analysis. The grain analysis results from image analysis described herein, were compared with grain-size results using laser diffraction granulometry on the same section of core samples.

4.2 Principal methods of Grain-size Analysis

There are several principal techniques for measuring the grain-size of sediments (including soils) and sedimentary rocks. Each technique measures a different property of the sediment and then relates this property to the grain diameter (or grain volume) of constituent particles. The amount of sediment in each of the different size classes (as originally proposed by Wentworth, 1922) is reported as a fraction of the total amount of sediment analysed in one of three ways: (a) as a volume percentage of the total volume; (b) as a weight percentage of the total dry weight; or (c) as the absolute number of particles counted.

The principal techniques can be summarised as follows

1. *Laser diffraction*. Particle size analysis by laser diffraction is currently one of the most common methods employed in sedimentology. It is based on the premise that particle size determines the angle of light diffraction. There is a negative correlation between the diffracted angle and particle size, such that a small size particle produces a higher diffraction angle compared with a larger particle size.

A laser light source is generally directed through a small, dilute, liquid suspension of the sediment dispersed in distilled water and the diffraction angle of different grains is measured. Samples of about 100 - 500 mg are introduced into the water module of the laser equipment.

The technique is most appropriate for unconsolidated sediments and readily measures grain-sizes between 100 nm and 5 mm. The laser diffraction technique can also be used to analyse samples in a dry state.

2. *Image analysis*. This is the only method that makes direct measurement of grain diameter (known as the Feret or Calliper diameter). It is commonly performed in conjunction with analysis of microfabric and grain orientation. Grain-size through image analysis requires image acquisition, processing, measurement and then interpretation (Francus, 1998). The method can be performed on both sedimentary rocks (polished thin-section) and unconsolidated sediment. Images are acquired using a high-resolution camera in the field or lab for gravel size particles or with a camera attached to an optical microscope (for sandy sediments) and a scanning electron microscope (for sand to clay size particles). Sample sizes required for analysis can be as small as 2 to 5 g for polished thin-sections and < 100 mg for unconsolidated sediment. Image analysis generally refers to a computer-automated technique, and is therefore considered to be objective, precise and reproducible. It can measure accurately between 10 nm and 5 mm, but this is dependent on the equipment used (Bons and Jessell, 1996). Manual image analysis by direct observer measurement and point-counting of grains in thin sections or smear slides is typically used for grain-sizes between 0.03 mm and 1 mm.

3. *Sedimentation*. There are a number of techniques that apply sedimentation through a water column in analysing grain-size distribution in sediments and soils. These methods are all based on the principle of relating the settling velocity of grains in distilled water to the diameter of the grains. Sediments are introduced to the top of a tube containing water and the settling rate of the grains is monitored at the base. The coarsest grains settle most rapidly, whereas the finest grains settle more slowly. The shape of the grains is assumed to be spherical and the sphere diameter is calculated using Stoke's law. The settling velocity is dependent on the shape and density of the grains (Lewis and McConchie, 1994). The technique requires a sample size of about 1 - 10 g for sandy sediments and < 1 g for silt to clay-rich sediment and can accurately measure grain-sizes between 100 nm and 100 µm, depending on the particular techniques employed. The sediment must be unconsolidated or disaggregated.

4. *Sieving*. This is a common method used in analysing unconsolidated, coarse-grained sediments (0.05 mm to >50 mm). A sample size of between 30 - 70 g is introduced into a set of sieves, which are arranged in descending order of mesh size. The set of sieves containing the sample is mechanically shaken for 10 to 15 minutes, and the weight of the fraction retained

by each sieve size is then measured. Ultrasonic micro-sieving can be used with a particle analyser for the silt-size range (0.005 – 50 mm). Sieve analysis is only possible for unconsolidated sediments, or those that can be readily disaggregated prior to sieving.

Each method has clear advantages and disadvantages. Important considerations when selecting the appropriate technique include: sample size and how representative thes sample is of a heterogeneous sediment.

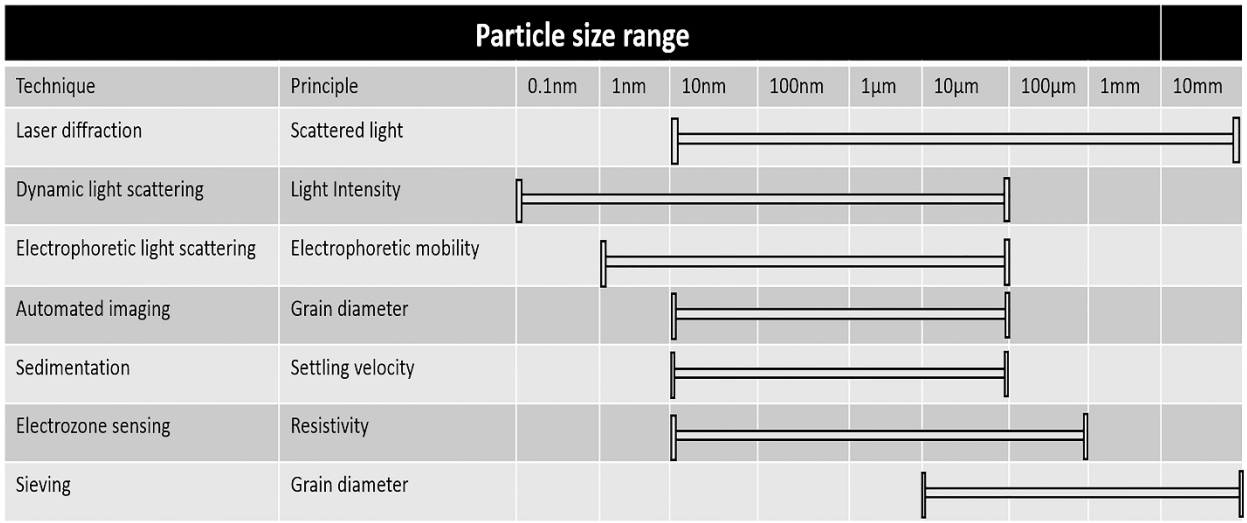

Figure 4.1. Principal grain-size techniques, their principles and resolution (From, Malverns Instruments Limited, 2012)

4.3 Materials and Methods

4.3.1 Samples

This study is part of a broader research programme investigating the microfabric of fine-grained sediments (mudrocks). It seeks to examine the relationship between microfabrics and depositional processes in deep-water. The samples used for this study are from core samples retrieved during Expeditions 317, 339 and 355 of the International Ocean Discovery Program (IODP), from the Canterbury continental margin off New Zealand, the Iberian continental margin off SW Portugal and Spain and Laxmi Basin, India which is part of the Indus fan respectively. The samples from expeditions 317 and 339 were selected from the mud-rich hemipelagic intervals while samples from 335 were from the turbidite intervals.

Two sets of sub-samples were taken from each of these 16 samples to allow replicate measurements, through image analysis and laser diffraction. The samples from Expedition 317 and 339 are from bioturbated, calcareous muds that are interpreted as the result of hemipelagic

sedimentation. In the case of the samples from Expedition 355, the samples were deposited by turbidity currents. The Canterbury margin sediments were of Pliocene age and partially consolidated by compaction (Fulthorpe *et al.*, 2010), the Iberian margin sediments were of Quaternary age and unconsolidated (Expedition 339 Scientists, 2012; Hodell *et al.*, 2013) and the Indus fan sediments were of Pleistocene to Miocene age (Pandey *et al.*, 2015).

4.3.2 Image Analysis

4.3.2.1 Sample preparation (Image analysis)

Sample preparation is the key to obtaining good results in analysis. Samples can be imaged in a disaggregated dispersed form (Fernlund, 2005), as a thin section (Francus, 1998) polished block (Sanei *et al.*, 2016) or after ion milling (Milner, McLin and Petriello, 2010). Fine-grained sediments are best imaged in polished thin sections, polished blocks or ion milled sections as this prevents overlapping of grains during imaging. The technique prevents grain breakage, which is likely to occur during sample disaggregation. It also preserves the original fabric and so allows the relationship among grains to be more accurately observed.

The two samples from Expedition 317 were allowed to dry naturally while being kept in air tight bags. The drying process was slow at room temperature. The five samples from expedition 339 and nine samples from expedition 355 were oven dried at a controlled temperature of 60^{0}C until the weight of the samples remained constant regardless of further drying. The samples were vacuum impregnated with low-viscosity resin, after which polished thin-sections were prepared.

4.3.2.2 Image acquisition

The next step after the sample has been prepared is image acquisition. The quality of the image acquired has a significant effect on image analysis end results. Accurate determination of grain-size and shape estimation are dependent on the magnification of the image (Heilbronner and Barrett, 2014) as well as effective pixel resolution. Images can be acquired with a stand-a-lone high-resolution camera or an optical microscope with an attached camera. The choice of equipment is a function of the grain size of the material being analysed. In geotechnical engineering, gravel-sized particles can be analysed using a high-resolution camera (Kwan, Mora and Chan, 1999; Lee, Smith and Smith, 2007). Imaging through an optical microscope is ideal for sandstone and coarse silt samples, whereas clay particles sizes are best resolved through electron microscopy. Acquired images must have a sharp contrast such that the boundaries between grains are clear and distinct.

Imaging of relatively large sample areas (approximately 0.65 mm by 0.42 mm) was achieved on the sixteen samples in this study through automated collection and stitching together of images using scanning electron microscopy (SEM) of the polished thin-sections. The imaging follows a two-step procedure: (i) low-resolution to get an overview of the whole polished thin-section; and (ii) higher-resolution of as wide an area as possible, being careful to avoid cracks

or other sample disturbances (Buckman, 2014; Bankole *et al.*, 2016). Images were acquired on a Quanta 650 FEG (field emission) SEM, operated in low vacuum (0.83 Torr), with a backscattered (BSE) detector, an operating voltage of 15 kV, spot size of 4.5 and a working distance of 10 mm. Six randomly selected areas (or subsets) were imaged at high-resolution for sample 1 to 7 (Figure 4.2) while four randomly selected areas were images for the polished thin-sections of sample 8 to 16. The dimension of each area is approximately 650 µm by 420 µm, which is believed to be sufficiently representative of the whole sample (Figure 4.2). Random selection of these areas was made in order to account for variability in the grain-size from one part of the polished thin-section to another. In order to more accurately analyse the very fine grain-sizes, the SEM images were taken at high-resolution with about 45 nm per pixel. The smallest grain that can be technically measured at such resolution is about 135 nm; a minimum cluster of three pixels are required to confidently delineate a feature. However, particles less than 150 nm were discounted as this is close to the lower end of the resolvable features. The choice of image resolution for the grain-size analysis was informed in part by the resolution (100 nm) of the laser diffractometer employed.

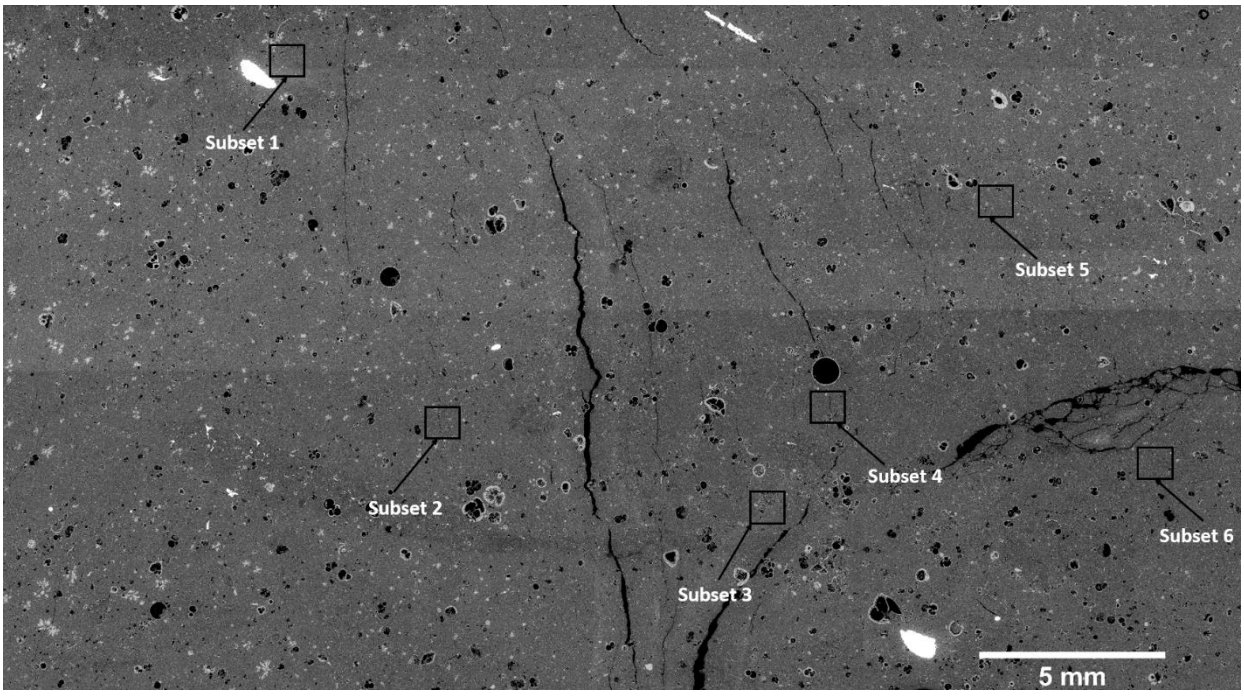

Figure 4.2. SEM image of sample 2 showing the six subsets of images analysed. Each subset has about 0.6 mm horizontal field of view.

4.3.2.3 Image Processing

Image Processing of the acquired images is required to enhance certain features of the image with respect to others (Bons and Jessell, 1996). It involves enhancing the image quality to allow clear derivation of the boundary between the features through brightness and contrast adjustment, segmentation and then filtering the unwanted features (noise). The penultimate step in image processing is segmentation. In this step, features of interest are delineated from unwanted features such that the feature of interest is rendered to the foreground while unwanted features are rendered to the background. Segmentation of an image is a very important and non-trivial process (Bankole *et al.,* 2016). For grain-size analysis, the image is segmented to delineate the grains. The grains are characterised by groups of pixels and likewise the boundaries between grains. The features between the boundaries are interpreted as the grains, which are then characterised by a unique grey value. Hence, the grey value can be used to define the region occupied by the grains.

In order to enhance the boundary between the grains in this study, the images were pre-processed through the application of smooth and enhanced contrast functions. After the pre-processing, each image was segmented using the default threshold. An adjustment (binarization) was made to render the grains into the foreground (black) while pores were rendered into the background (white). A median filter of the 4-pixel radius was then applied to reduce the noise and accentuate the grains (Figure 4.3).

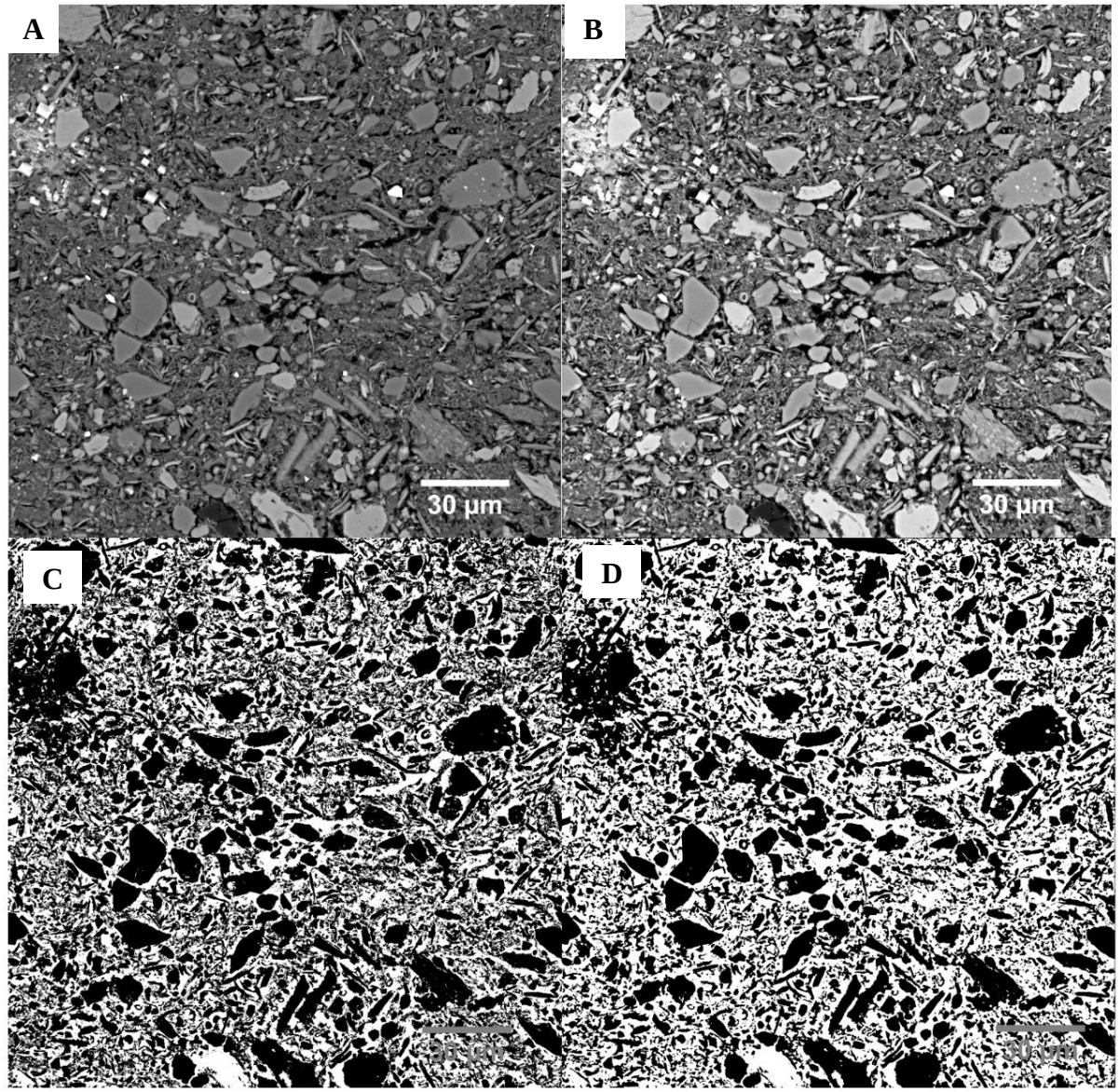

Figure 4.3. (A) Raw SEM image (B) SEM image after applying smoothing and contrast enhancement (C) Segmented (binarized) image of grains (D) segmented image after median filtering.

4.3.2.4 Grain-size measurement

Grain-size measurement (or data acquisition) requires taking measurements from the processed images. Most imaging software can swiftly measure the designated areas and return grain data such as diameter, area, orientation, perimeter and others.

In this study, data on grain-sizes were generated using Fiji software, which is an adaptation of *Image J*, an open software produced by the US National Institute of Health (NIH). This was first developed for analysing biological images (Schindelin *et al.*, 2012) and it was previously

known as *NIH image* software (Schneider, Rasband and Eliceiri, 2012). However, the usage is not limited to biological samples and the application of Fiji in the field of geoscience is gaining momentum, especially in analysing microstructure (Camp and Wawak, 2013; Hemes *et al.*, 2015; Buckman *et al.*, 2017).

The software is user-friendly and requires no prior knowledge of programming languages. It also provides a method for recording macros, which can be applied to several images through batch processing. Randomly selected areas (subsets) were imaged at high-resolution (45nm per pixel) for each of the sixteen polished thin-sections. The dimension of each area is approximately 650 µm by 420 µm, which is believed to be sufficiently representative of the whole sample. Random selection of these areas was made in order to account for variability in the grain-size from one part of the polished thin-section to another.

Raw images from the scanning electron microscope were processed with *Fiji* by first setting the scale of the image based on the horizontal field of view of the tiles in nanometres per pixel. Grain data were then acquired on diameter, perimeter, area, circularity, and aspect ratio. Data returned by Fiji were saved in Excel format and further data management were automated through some Excel functions and Visual Basic for Applications macros. A flowchart highlighting the steps employed in processing the image in Fiji is presented in Figure 4.4. Grain-size was determined by measuring the Feret diameter of every grain within a one phi size class interval. The percentage of thetotal diameter within each phi class was determined.

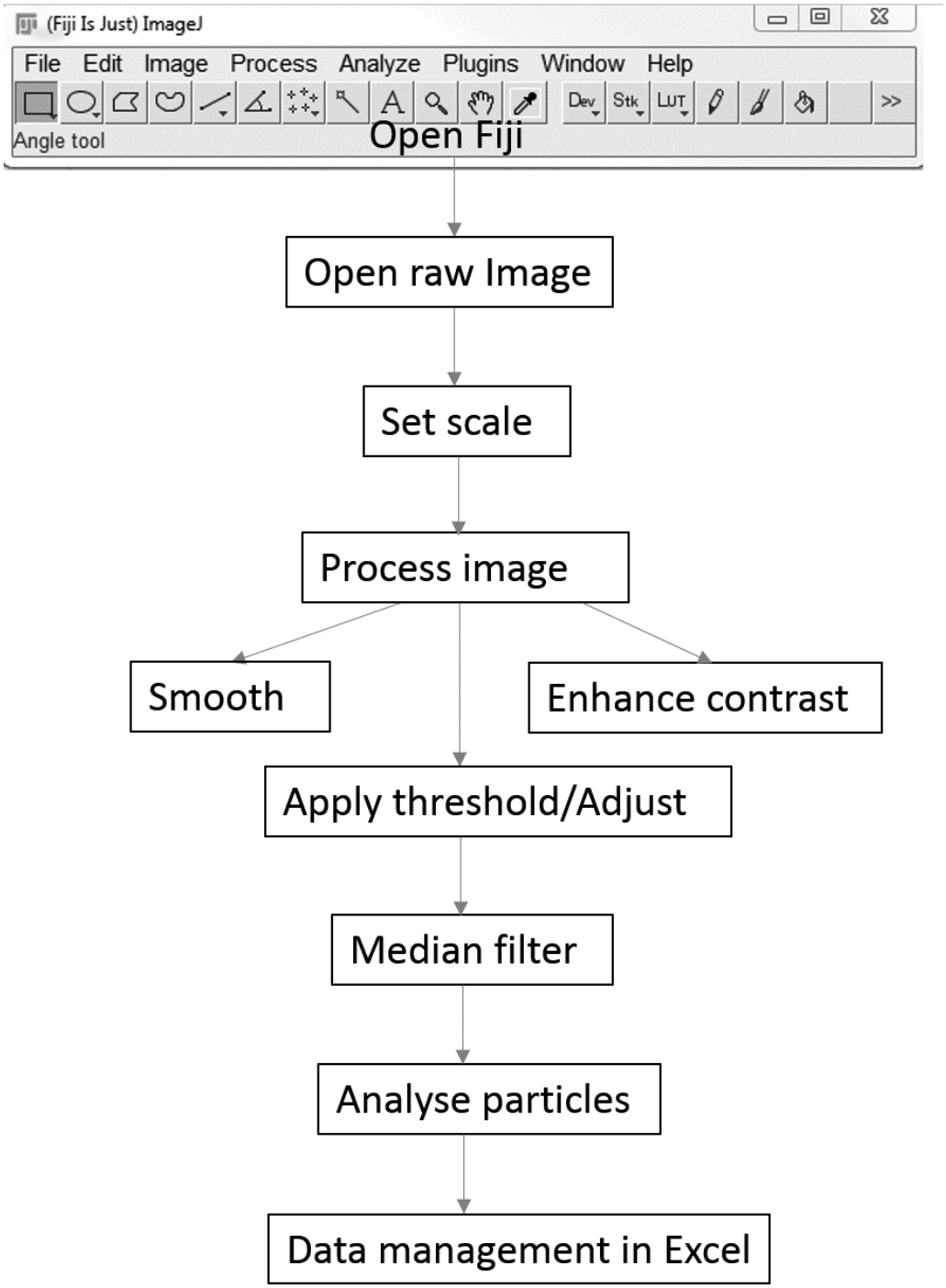

Figure 4.4. Flow chart highlighting the steps employed in analysing grain-size with Fiji ImageJ.

4.3.2.5 Analysis and Interpretation

The simplest method of representing grain-size through image analysis is by the number of particles (frequency) recorded in each size class. However, such an approach is not comparable

with most of the other methods, which record either weight or volume percentage of sediment in each size class.

Feret diameter using Fiji was measured by taking the average of multiple measurements along different grain axes. The Feret diameter is also known as caliper diameter and it is defined as the maximum particle diameter. However, in Fiji, the Feret diameter is determined diagonally across a particle rather than along the longest axis (Igathinathane *et al.*, 2008). This measurement is taken as a fair representation of the particle size. Feret diameters for grain-size at 1 phi intervals from 265 µm to 150 nm were calculated by summing up the diameter in each class interval. Subsequently the percentage of Feret diameter in the class interval were determined as a measurement of percentage for each grain-size class.

4.3.3 Laser diffraction analysis: comparative method

In order to validate the results of grain-size analysis by the automated imaging technique, sub-sections of the same samples were analysed by a standard alternative process – laser diffraction. Details on the procedures involved for grain-size measurement using laser diffraction granulometer is presented in chapter 3.

4.4 Results

4.4.1 Subset Comparison

The four/six subsets taken from the sixteen (16) samples for image analysis show closely comparable grain-size characteristics in most cases (Table 4.1), with little significant variation in the percentage of sand, silt and clay contents. This variation between subsets is between 1% and 6%, except for sample 3 subset 1 and 2, sample 4 subset 1 and sample 6 subset 2 in which both the silt and clay content show greater variation (up to 20%). Standard ternary grain-size plots for all the subsets in each image shows good clustering of all subsets within the silty-mud grain-size class (Figure 4.5). These results show relatively homogeneous sediment samples. It was therefore deemed reasonable to take an average value from the subsets for comparison with the laser diffraction technique.

4.4.2 Comparison between techniques

The ternary grain-size plots presented in Figure 4.5 show that the relative proportions of sand-silt-clay based on image analysis from most of the subsets and the laser technique fall within the same grain-size class. This is true for more than 55% of the samples (2, 3, 4, 9, 10, 11, 12,

14 and 16) where the difference in the proportion of clay is less than 12%. For samples 1, 5, 6, 7, 13 and 15 there is a wider variation apparent, with up to 30% difference in the clay content.

The laser diffraction results are similar to image analysis results with respect to grain size classes, but there are some variations in the grain-size statistical parameters between the two techniques (Figure 4.6). The summary results from both techniques (Table 4.2) indicate that all the samples are muds (within the silty-mud class) and that grain-size distributions are generally unimodal except for laser diffraction granulometry which showed that samples 8, 12 and 16 are bimodal. The mean grain-size ranges from very fine silt (7.98 phi) to coarse silt (4.311 phi) based on both methods. There are some variations in the mean size from both techniques but generally less are than 1 phi except in sample 1 in which the difference in the mean size is up to 2 phi. In most cases where the mean size varies, the mean size from the laser diffraction fall into the next coarsest grain fraction in comparison to the image analysis technique.

The standard deviation output from the Gradistat program, which was computed based on Folk and Ward (1957), shows that the samples are very poorly sorted to poorly sorted. There is no discrepancy in sorting class between the two techniques for about 70% of the analysed samples (Table 4.2). For the remaining 30% samples (2, 5, 6, 8 and 12) the nominal difference in sorting is in effect not more than 0.20 phi units. Computed skewness for all the sample ranges from -0.01 to 0.310. Skewness based on image analysis shows that the samples are symmetrical while laser diffraction shows that about 31% of the samples are symmetrical while others are skewed (Table 4.2). Kurtosis determined from both techniques has values between 0.852 and 1.24. In terms of Kurtosis image analysis reveals that all the samples are mesokurtic. This is true for about 60% when compared with laser diffraction granulometry. Those in which there are discrepancies in kurtosis determined based on image analysis and laser diffraction technique, the actual difference in kurtosis is less than 0.25 phi units.

The percentage of grain-size within different phi classes is plotted for both laser diffraction granulometry (x-axis) and image analysis average values (y-axis) for each sample (Figure 4.6). The plots show a strong linear positive correlation between the two techniques with an R-square value ranging between ca 0.5 and 0.96. However, the R-square value for sample 1 shows almost no correlation between the two techniques, with an R-square value of 0.083.

Table 4.1. Summary of the results on grain-size for the subset images for all the samples, from image analysis method.

Sample ID	Expedition Site/Hole	Depth (m)	Particle size	Subset1	Subset2	Subset3	Subset4	Subset5	Subset6
Sample 1	317 1352B-80X2-78-80	700	clay	42%	40%	43%	44%	45%	46%
			silt	52%	53%	51%	53%	53%	51%
			sand	6%	7%	6%	3%	2%	3%
Sample 2	317 1354C-10X-5-116-118	130	clay	33%	38%	35%	36%	32%	32%
			silt	65%	59%	61%	62%	65%	65%
			sand	2%	3%	4%	2%	3%	2%
Sample 3	339 1385A-6H2-36-38	50	clay	66%	47%	53%	54%	52%	53%
			silt	34%	53%	46%	45%	47%	47%
			sand	0%	0%	1%	1%	1%	0%
Sample 4	339 1385E-7H2-111-113	60	clay	51%	45%	43%	46%	46%	46%
			silt	48%	54%	55%	51%	52%	53%
			sand	1%	1%	1%	3%	1%	1%
Sample 5	339 1385E-2H5-72-74	10	clay	53%	50%	52%	50%	48%	52%
			silt	45%	47%	46%	48%	48%	47%
			sand	2%	2%	2%	2%	4%	1%
Sample 6	339 1385D-2H6-115-117	15	clay	50%	58%	50%	49%	51%	50%
			silt	48%	39%	49%	50%	48%	47%
			sand	2%	3%	1%	1%	1%	3%
Sample 7	339 1385E-10H2-74-76	80	clay	66%	65%	66%	70%	67%	67%
			silt	33%	34%	33%	28%	32%	32%
			sand	1%	1%	1%	2%	1%	1%
Sample 8	355 1457A-8H1-38-42	67	clay	55%	56%	58%	60%	-	-
			silt	44%	43%	41%	39%	-	-
			sand	1%	1%	1%	1%	-	-
Sample 9	355 1457A-17F1-20-22	130	clay	48%	47%	47%	48%	-	-
			silt	52%	53%	53%	52%	-	-
			sand	0%	0%	0%	0%	-	-
Sample 10	355 1457C-9R1-7-11	260	clay	45%	44%	44%	43%	-	-
			silt	55%	56%	56%	57%	-	-
			sand	0%	0%	0%	0%	-	-
Sample 11	355 1457C-18R2-6-10	348	clay	37%	36%	36%	36%	-	-
			silt	63%	64%	64%	64%	-	-

			sand	0%	0%	0%	0%	-	-
Sample 12	355 1457C-29R1-99-103	455	clay	40%	39%	39%	35%	-	-
			silt	60%	61%	61%	64%	-	-
			Sand	0%	0%	0%	1%	-	-
Sample 13	355 1457C-38R1-43-45	542	clay	43%	45%	44%	46%	-	-
			silt	57%	55%	56%	54%	-	-
			sand	0%	0%	0%	0%	-	-
Sample 14	355 1457C-38R2-124-126	542.5	clay	55%	54%	48%	53%	-	-
			silt	45%	46%	52%	47%	-	-
			sand	0%	0%	0%	0%	-	-
Sample 15	355 1457C-46R6-64-66	635	clay	48%	52%	49%	45%	-	-
			silt	52%	48%	51%	55%	-	-
			sand	0%	0%	0%	0%	-	-
Sample 16	355 1457C67R3-5-8	825	clay	40	39%	43%	44%	-	-
			silt	60%	59%	56%	55%	-	-
			sand	-	2%	1%	1%	-	-

Sample 1

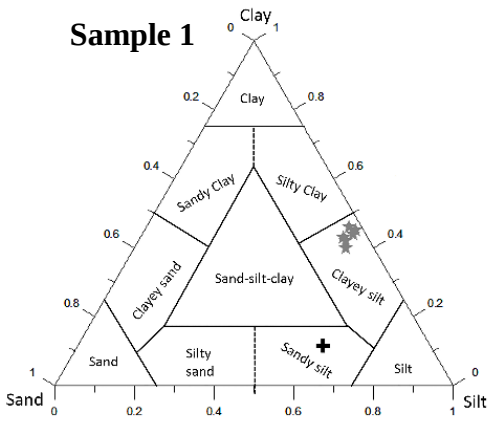

Sample 2

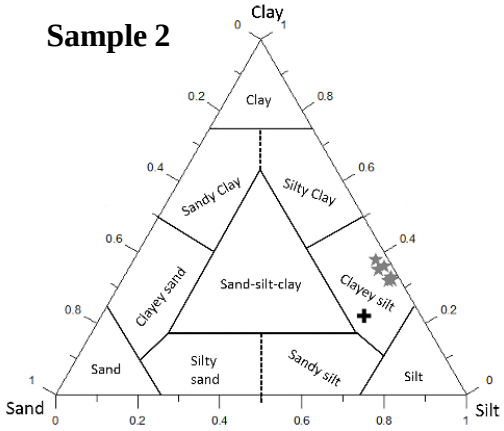

Sample 3

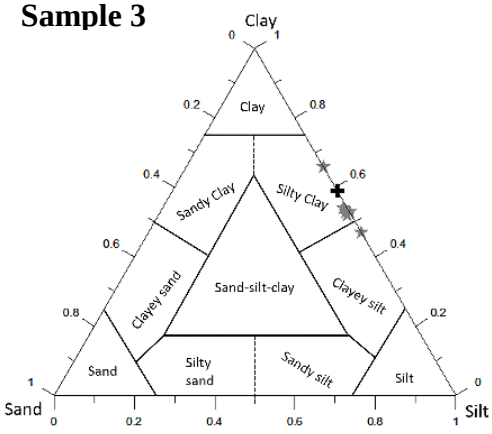

Sample 4

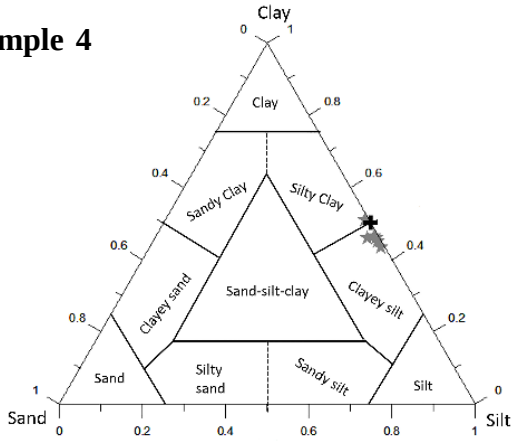

Sample 5

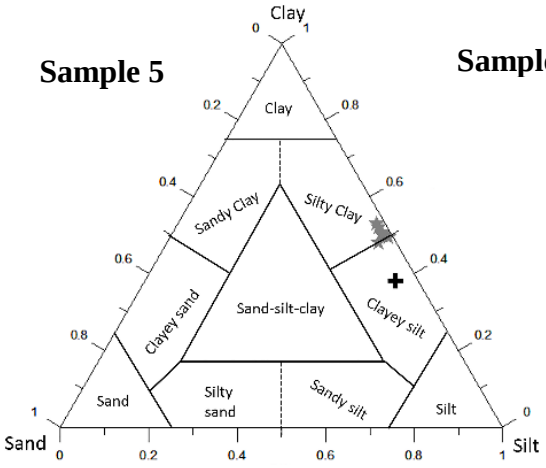

Sample 6

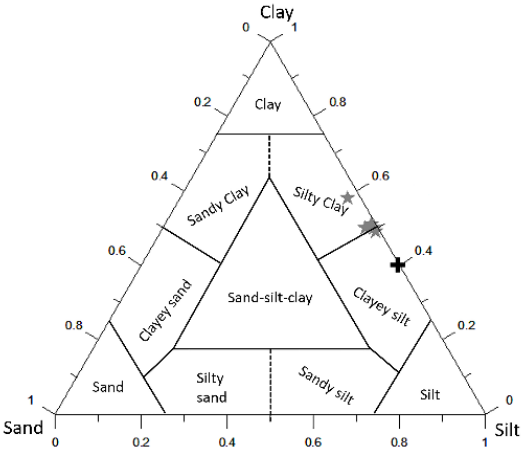

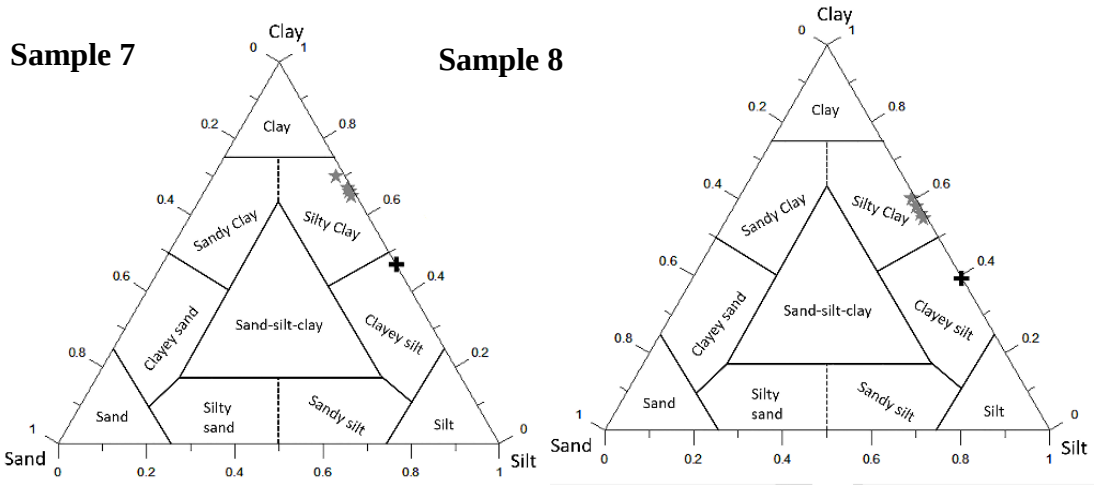

Figure 4.5. Sample of ternary plots of grain-size distribution based on Feret diameter percentage for the various image subsets analysed and laser diffraction granulometry (Modified from, Shepard, 1954). The ternary plots are for sample 1 to 8 respectively. Image analysis subsets are in grey while laser diffraction results are plotted as black cross. The plots indicate grain-size data from each subset within a sample, although there is subtle variation among the subsets however grain-size for the varying subsets in each sample form a cluster. Note that ternary plots for the other samples are presented in Appendix 1A.

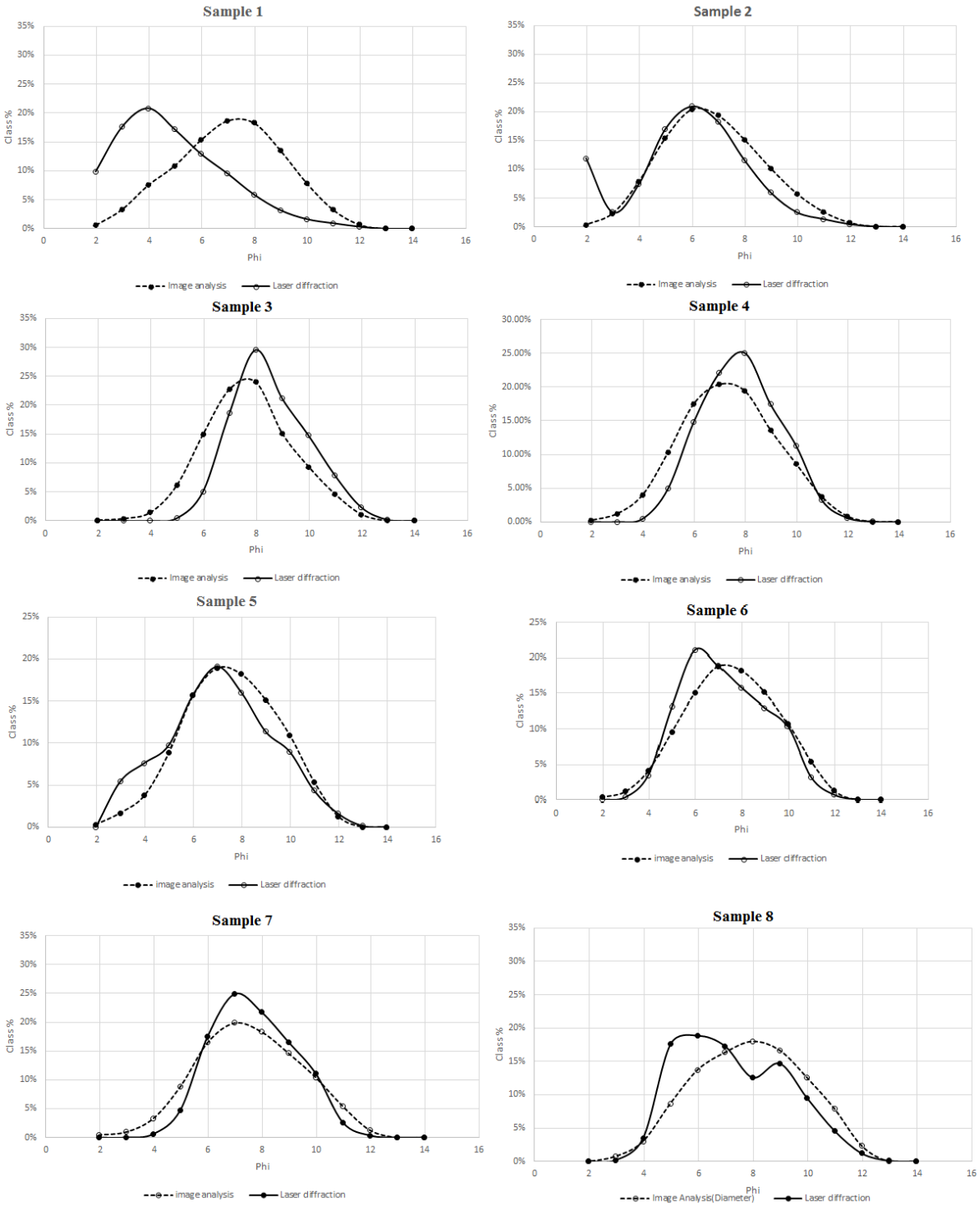

Figure 4.6. Grain-size distribution curves to compare the resulting distribution from laser diffraction granulometry and image analysis technique described herein. The rest of the distribution curves are presented in Appendix 1B. Note that for the image analysis cure, all the randomly slected areas were integrated.

Table 4.2. Statistical parameters for results obtained from image analysis (IMA) and laser diffraction (LSD) techniques using Gradistat software (Blott and Pye, 2001). The statistical parameters were calculated based on Folk and Ward (1957).

Sample	**Statistical parameters**						
	Textural group	Mean size (phi)	Median (phi)	Distribution	Sorting	Skewness	Kurtosis
1 LSD	Mud	Coarse silt (4.311)	4.10	Unimodal	Very poorly sorted (2.172)	Fine skewed (0.169)	Mesokurtic (1.044)
1 IMA	Mud	Fine silt (6.560)	6.60	Unimodal	Very poorly sorted (2.089)	Symmetrical (-0.0480)	Mesokurtic (0.965)
2 LSD	Mud	Medium silt (5.384)	5.50	Unimodal	Very poorly sorted (2.295)	Coarse skewed (-0.121)	Leptokurtic (1.24)
2 IMA	Mud	Fine silt (6.244)	6.15	Unimodal	Poorly sorted (1.956)	Symmetrical (0.0840)	Mesokurtic (0.980)
3 LSD	Mud	V. Fine silt (7.987)	7.80	Unimodal	Poorly sorted (1.492)	Fine skewed (0.159)	Mesokurtic (0.991)
3 IMA	Mud	V. Fine silt (7.180)	7.10	Unimodal	Poorly sorted (1.710)	Symmetrical (0.0450)	Mesokurtic (1.027)

4 LSD	Mud	V. Fine silt (7.294)	7.30	Unimodal	Poorly sorted (1.567)	Symmetrical (0.030)	Mesokurtic (0.919)
4 IMA	Mud	Fine silt (6.842)	6.80	Unimodal	Poorly sorted (1.859)	Symmetrical (0.0410)	Mesokurtic (0.950)
5 LSD	Mud	Fine silt (6.579)	6.50	Unimodal	Very poorly sorted (2.270)	Symmetrical (0.00100)	Mesokurtic (1.01)
5 IMA	Mud	V. Fine silt (7.058)	7.00	Unimodal	Poorly sorted (1.996)	Symmetrical (0.0180)	Mesokurtic (0.938)
6 LSD	Mud	Fine silt (6.775)	6.60	Unimodal	Poorly sorted (1.868)	Fine skewed (0.129)	Platykurtic (0.852)
6 IMA	Mud	V. Fine silt (7.043)	7.00	Unimodal	Very poorly sorted (1.980)	Symmetrical (0.0160)	Mesokurtic (0.930)
7 LSD	Mud	V. Fine silt (7.163)	7.10	Unimodal	Poorly sorted (1.560)	Symmetrical (0.0960)	Platykurtic (0.892)
7 IMA	Mud	V. Fine silt (7.050)	7.00	Unimodal	Poorly sorted (1.943)	Symmetrical (0.0580)	Mesokurtic (0.930)
8 LSD	Mud	Fine silt (6.71)	6.54	Bimodal	Poorly sorted (1.99)	Fine skewed (0.150)	Platykurtic (0.800)
8 IMA	Mud	V. Fine silt	7.38	Unimodal	Very poorly sorted	Symmetrical	Mesokurtic

		(7.37)			(2.06)	(-0.010)	(0.900)
9 LSD	Mud	Fine silt (6.02)	5.75	Unimodal	Poorly sorted (1.90)	Fine skewed (0.250)	Mesokurtic (1.070)
9 IMA	Mud	Fine silt (6.90)	6.85	Unimodal	Poorly sorted (1.57)	Symmetrical (0.050)	Mesokurtic (1.00)
10 LSD	Mud	Fine silt (6.74)	6.39	Unimodal	Poorly sorted (2.06)	Fine skewed (0.270)	Platykurtic (0.890)
10 IMA	Mud	Fine silt (6.79)	6.73	Unimodal	Poorly sorted (1.55)	Symmetrical (0.060)	Mesokurtic (0.980)
11 LSD	Mud	Fine silt (6.20)	5.95	Unimodal	Poorly sorted (1.85)	Fine skewed (0.250)	Mesokurtic (1.010)
11 IMA	Mud	Fine silt (6.47)	6.42	Unimodal	Poorly sorted (1.50)	Symmetrical (0.060)	Mesokurtic (0.930)
12 LSD	Mud	Fine silt (6.35)	5.96	Bimodal	Very poorly sorted (2.26)	Very Fine skewed (0.310)	Mesokurtic (1.040)
12 IMA	Mud	Fine silt (6.52)	6.46	Unimodal	Poorly sorted (1.60)	Symmetrical (0.060)	Mesokurtic 0.92
13 LSD	Mud	V. Fine silt (7.33)	7.04	Unimodal	Poorly sorted (1.91)	Fine skewed (0.210)	Mesokurtic (0.920)

13 IMA	Mud	Fine silt (6.80)	6.74	Unimodal	Poorly sorted (1.59)	Symmetrical (0.070)	Mesokurtic (0.970)
14 LSD	Mud	V. Fine silt (7.44)	7.40	Unimodal	Poorly sorted (1.85)	Symmetrical (0.04)	Mesokurtic (1.00)
14 IMA	Mud	V. Fine silt (7.11)	7.07	Unimodal	Poorly sorted (1.46)	Symmetrical (0.060)	Mesokurtic (0.970)
15 LSD	Mud	V. Fine silt (7.71)	7.56	Unimodal	Poorly sorted (2.00)	Symmetrical (0.10)	Platykurtic (0.840)
15 IMA	Mud	Fine silt (6.93)	6.90	Unimodal	Poorly sorted (1.49)	Symmetrical (0.030)	Mesokurtic (1.010)
16 LSD	Mud	Fine silt (6.71)	6.54	Bimodal	Poorly sorted (1.99)	Fine skewed (0.150)	Platykurtic (0.800)
16 IMA	Mud	V. Fine silt (7.10)	7.05	Unimodal	Poorly sorted (1.51)	Symmetrical (0.070)	Mesokurtic (0.980)

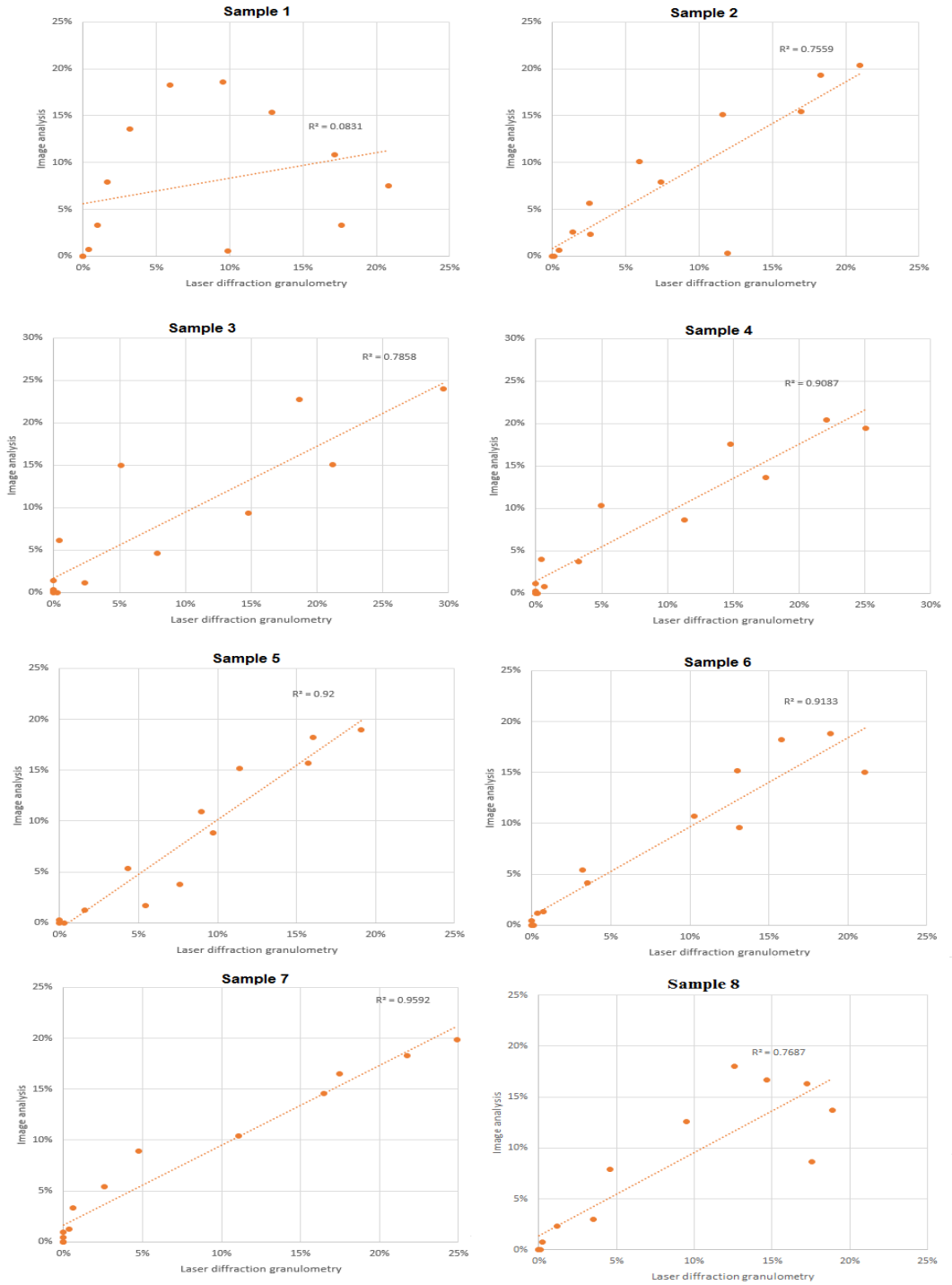

Figure 4.7. Plots of percentage of grain-size at specific phi intervals for laser diffraction granulometry vs image analysis based on Feret diameter. Note that the average Feret diameter from the subsets of SEM images per sample was used. Note that the plots are for sample 1 to 8 while others are presented in Appendix 1C.

4.5 Discussion

Grain-size measurement by image analysis is demonstrated here to be a robust and reliable technique, particularly for fine grained sediments in the clay-silt-sand size range. One possible criticism of the image analysis technique via SEM is the very small sample size that is analysed. However, the method employed in this study for image acquisition allowed for imaging of a relatively large sample area through automated collection and stitching together of images using scanning electron microscopy on the polished thin-sections. The grain-size was estimated from four to six subsets of SEM montages in each sample and the number of grains analysed from each subset was between 35000 to 45000. This number of grains would have been almost impossible to manage through manual measurement.

Earlier work on grain-size analysis, typically via point-counting of thin-sections, recommends measurement of about 50 to 500 grains to achieve grain-size results that are statistically significant (Sanei *et al.*, 2016 and references therein). However, this approach is only viable for coarser-grained sediments (sands and gravels), and a much larger number of grains must be analysed for silt and clay-sized sediment.

Image analysis is the only grain-size analysis method which has the advantage by providing a direct means of visualising grains in mudrocks with respect to the whole sediment, so that the grain shape and context (grain fabric) can also be determined at the same time. Grain-size analysis by other techniques mainly involve bulk analysis of disaggregated samples and yield only the percentage of grains in each size class, without having knowledge about the morphology and the number of grains considered.

The results generated in this study from image analysis were compared with samples analysed by laser diffraction granulometry. For the most part, all elements of the grain-size measured, including grain-size distribution curves, ternary sand-silt-clay plots, and statistical parameters (mean size, sorting, skewness and kurtosis) are closely comparable between the two techniques. Any variation noted was only subtle for nearly all samples. There is a strong positive correlation between results from the two techniques except for one sample (sample 1), for which the correlation is very poor.

The reason for the subtle variations in grain-size for most of the samples and conspicuous discrepancy in grain-size for sample 1 from laser diffraction granulometry and image analysis based on Feret diameter can be attributed to a number of reasons:

(a) Visual inspection of the SEM image for sample 1 shows that the silt particle size is dominant and embedded in the clay matrix, with very few sand grains (Figure 4.8). However, there are a number of conspicuous elongated particles. It is likely that the laser diffraction method overestimated the sand fraction due to the presence of the elongated particles. This is an acknowledged limitation of laser diffraction granulometry (Loizeau *et al.*, 1994; Hayton *et al.*, 2001; Blott *et al.*, 2004).

(b) The actual samples used for image analysis and laser diffraction granulometry were necessarily different. Fine grained sediments are known to be highly heterogeneous, from the metre scale (Macquaker and Howell, 1999; Macquaker and Jones, 2002) to nanometre scale (Bernard *et al.*, 2010; Clarkson, Jensen and Chipperfield, 2012; Silin and Kneafsey, 2012). There is a strong possibility, therefore, that a pair of samples adjudged to be similar visually in terms of their grain-size and sedimentary structures, were microscopically different.

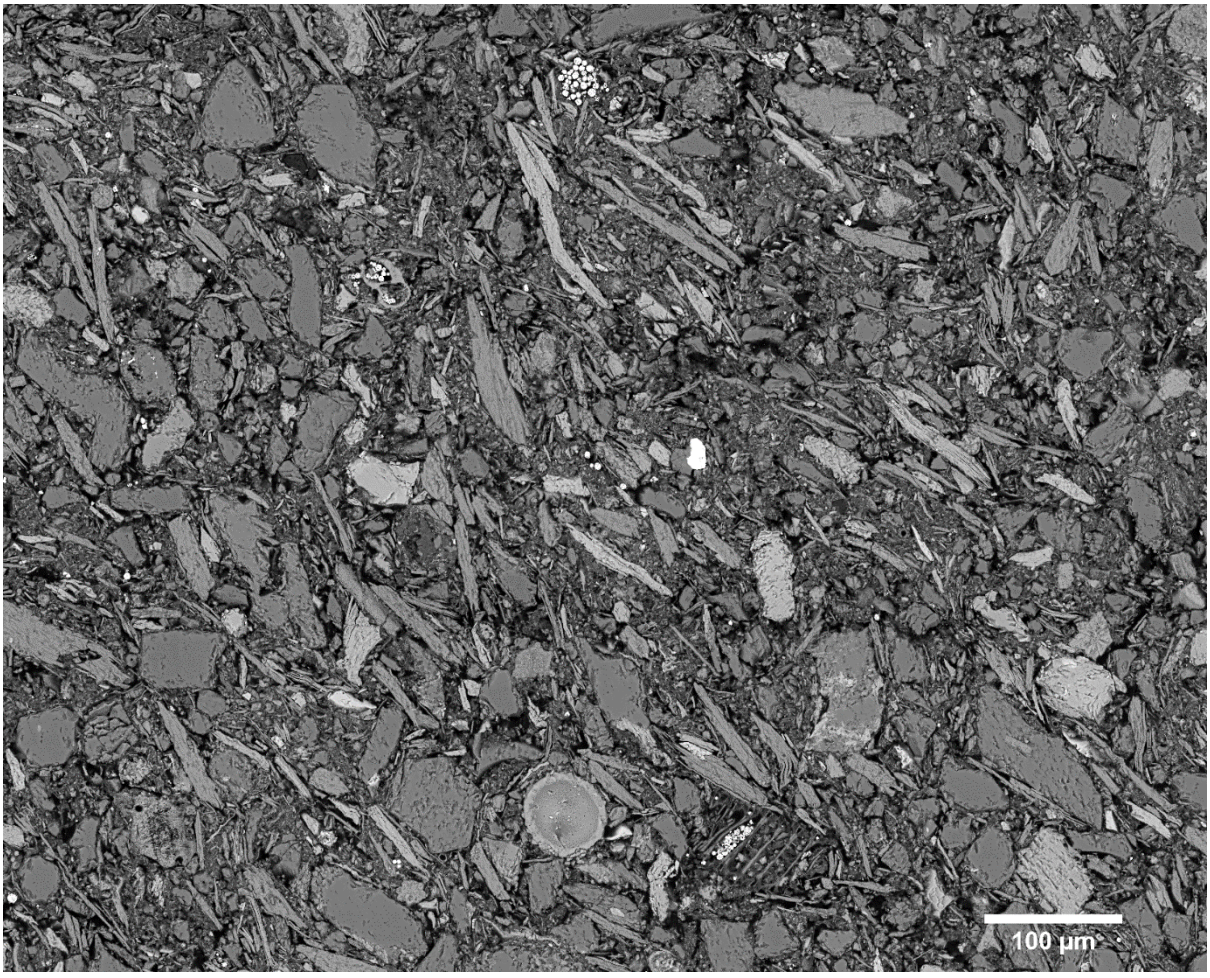

Figure 4.8. A subset image from sample one showing silt as the dominant grain. Sample ID: 317 1352B-80X2-78-80.

(c) It is also evident from the various subsets of images analysed herein that even in the small core plug, subtle variation exists. This is almost certainly due to sample heterogeneity at the small scale (micron to submicron scale). Laser diffraction also requires a small sample size of about 0.1g to 0.5g (Eshel *et al.*, 2004) such that representativeness without preferential subsampling can be equally difficult using this technique.

(d) Laser diffraction granulometry requires disaggregation and dispersion of the sample, using chemical and ultrasonic treatment. Overtreatment of the sample with the ultrasonic device can result in breakage of particles (particularly of coccolithphores), while insufficient dispersion of the sample ultrasonically can result in the reduced estimation of fine particle sizes. This might explain, in part, the common lower estimation of clay-size fraction via the laser technique.

All grain-size techniques have some draw backs, and the image analysis method as described herein also has some problems. Firstly, the technique requires adequate segmentation and definition of grain boundaries. This is not always easy to achieve, and in some instances two grains might appear inseparable and are then measured as a single grain. In this case, there is tendency for image analysis to overestimate the coarser grain-size. Secondly, image analysis in this study utilised polished thin-sections. There is possibility that individual particles might be plucked out during polishing. Thirdly, 2-dimensional SEM images are used for the method presented here, and there is a certainty that the diameter of grains as measured is not a true representation of their 3-dimensional diameter.

In fact, grain-size is a three-dimensional textural property and three-dimensional measurement is recommended for precise grain-size estimation (Rubin, 2004). Quantification of grain-size analysis through image analysis involves measurement in a two-dimensional image which limits measurement into two-dimensions. Efforts have been made to transform grain measurement in two-dimensions into three-dimensions (Sahagian and Proussevitch, 1998; Fernlund, 2005). However, most transformations from two-dimensions into three-dimensions remain a best guess (Sanei *et al.*, 2016), inconclusive and fraught with disagreement (Zhao, 1998; Kong *et al.*, 2005; Fernlund, Zimmerman and Kragic, 2007). Most of the transformation techniques are limited to loose and coarse-grained sediments (Fernlund, Zimmerman and Kragic, 2007) and are also susceptible to systematic error (Zhao, 1998). Adding to the degree of uncertainty associated with the transformation is the shape of the grains, which can introduce bias into the end result (Buscombe, Rubin and Warrick, 2010). Common practice involves determination of grain volume based on an assumption that the shape of the grains is spherical. However grains in sediments are irregular and as the irregularity increases, there is a growing error between the actual diameter and estimated diameter relying on such assumption (Syvitski, Leblanc and Asprey, 1991). This is especially demonstrated in the case of elongated, flaky, mica grains.

4.6 Conclusion

This study clearly demonstrates that image analysis of polished thin-sections with scanning electron microscopy is a rapid, reliable and robust method for grain-size analysis of fine-grained (mud-rich) sediments. By using automated collection and stitching together of images it is possible to analyse relatively larger sample sizes.

The proposed method has the advantage of being fully automated, objective and reproducible, and relatively free from human error or bias. Measuring several different subsets on one sample also reveals the nature and degree of heterogeneity in grain-size distribution of the sample. The same samples can also be assessed for microstructure and fabric. By combining these different observations, the technique becomes highly cost-effective.

Comparison of data from image analysis and those gained from laser diffractometry yield comparable results. Minor differences are readily accounted for in terms of sediment heterogeneity and in the erroneous measurement of elongate particles. Image analysis, like every other technique, has its flaws and limitations, and it is always important to be cognisant of these.

CHAPTER 5 – AUTOMATED IMAGE ANALYSIS OF MUDROCK MICROSTRUCTURE AND CHARACTERISATION OF HEMIPELAGIC SEDIMENTS: IODP EXPEDITION 339

5 Automated Image Analysis of Mudrock Microstructure and Characterisation of Hemipelagic Sediments: IODP Expedition 339

This present chapter is currently in press as: Bankole, S.A., Buckman, J., Stow, D., Lever, H. (2018) 'Automated Image Analysis of Mud and Mudrock Microstructure and Characteristics of Hemipelagic Sediments: IODP Expedition 339', *Journal of Earth Science. (*in press). And about 90% of work is that of the first author.

5.1 Introduction

Microstructure is an important feature that affects many physical properties such as porosity, pore connectivity and permeability of mudrocks. The renewed interest in microstructural study has a link to the growing interest in the development of shale gas, carbon storage and radioactive disposal (Bustin and Bustin, 2012; Curtis *et al.*, 2012b; Hemes *et al.*, 2015). Due to the small grain size of particles in mudrocks, their characterisation is challenging and conventional equipment such as optical microscopy cannot quantify their microstructure. The use of high-resolution instruments such as scanning electron microscopy (SEM) is well suited for studying the complex mudrock microstructure (Erdman and Drenzek, 2013), but there is a trade-off between resolution and coverage area of the SEM.

The present study utilised scanning electron microscopy and its aims are twofold: (1) to present an improved methodology for investigating the microstructure of mudrocks; and (2) to apply this methodology to better understand the characterisation of hemipelagic sediments on the Iberian continental margin.

The microstructural methodology presented here includes analysis of grain size, grain orientation and arrangement, porosity, and pore-size distribution, and mineral composition. Such studies are extremely challenging because the very small grain size and even smaller pore sizes are at the resolution limit of most conventional techniques (Camp et al., 2013). However, mudrock microstructure has a significant effect on understanding the petrophysical properties, geotechnical characteristics and diagenesis of fine-grained sediments (Douglas et al., 2016; Janssen et al., 2012; Josh et al., 2012). These are important properties that control hydrocarbon storage and migration in shale reservoirs, primary migration from shale source rocks, sealing

integrity of cap rocks, and hydraulic fracking properties of shale reservoirs. They are also significant for storage of nuclear waste in fine-grained sediments (Houben et al., 2013; Keller et al., 2013). Furthermore, the preferred orientation of clay particles causes seismic elastic anisotropy (Lonardelli et al., 2007; Wenk and Houtte, 2004; Wenk et al., 2008, 2014), and also has implications for the deformation history of mudrocks (DeVasto et al., 2012).

Electron microscopy, especially scanning electron microscopy (SEM), is the principal method to directly investigate the microstructure of mudrocks at high-resolution (micrometre to nanometre scales), both qualitatively and quantitatively. There are two key problems associated with electron microscopy: (1) the acquisition of images is limited to a very small sample area, which might not be representative of a larger sample size (Hemes et al., 2013; Saraji and Piri, 2015); and (2) mudrocks are noted to be heterogeneous at a variety of scales (Aplin and Macquaker, 2011; Macquaker and Howell, 1999). Recently, methods that involve the automated collection and stitching of thousands of image tiles at high-resolution using scanning electron microscopy have been presented (Bankole et al., 2016; Buckman, 2014; Lemmens and Richards, 2013). However, the images produced through this process may run to gigabytes of memory and are therefore difficult to handle manually. Hence, here, a workflow involving an automated method of handling such large data sets is presented, which is crucial for efficient time management in interpreting petrophysical properties of mudrocks.

The methods presented herein are applied to a uniform mid-slope series of hemipelagic sediments that were retrieved during Expedition 339 of the International Ocean Discovery Program (IODP) at Site1385 on the Iberian continental margin off SW Portugal. This is known as the ‘Shackleton Site’ in honour of Sir Nick Shackleton, whose pioneering work on earlier cores from this location has been pivotal in the understanding of millennial-scale climatic variation over the past glacial cycle (Shackleton et al., 2000, 2004). Following careful shore-based study of the cores, a total of five representative samples were selected for this study from the bioturbated, calcareous and unconsolidated mud rich intervals, interpreted as hemipelagites by the shipboard scientists. The age of the sediments retrieved from the Iberian margin site is Quaternary (Hodell et al., 2013; Stow et al., 2013). Further details on the samples used are presented in Table 5.1.

Hemipelagites are fine-grained sediments, typically muds and mudrocks, which comprise mixtures of terrigenous and biogenic material, of which the terrigenous component is silt-rich. They are deposited by a combination of vertical settling and slow lateral advection (Stow and

Tabrez, 1998). Hemipelagites are one of the principal marine sediment types covering large tracts of continental margins worldwide, and forming the ‘background’ facies of many deep-water successions (Pickering and Hiscott, 2015; Stow, 1985; Stow et al., 2001). Many black-shale source rocks and organic-rich shale-gas reservoirs are largely of hemipelagic origin, although other processes may also be involved (Stow et al., 2001). However, documentation of the detailed sedimentary characteristics of hemipelagites is still quite rare (see summary in Stow and Tabrez, 1998). Hence, both lithological and microstructural characteristics for the hemipelagites is presented in this chapter.

Table 5.1. Brief description of samples analysed for this study

S/No	Expedition	Site	Sediment type	Water depth	Depth (MBSF)
1	IODP 339	1385	Hemipelagite	2589	50
2	IODP 339	1385	Hemipelagite	2589	60
3	IODP 339	1385	Hemipelagite	2589	10
4	IODP 339	1385	Hemipelagite	2589	15
5	IODP 339	1385	Hemipelagite	2589	80

5.2 Materials and Methods

5.2.1 Core description and sampling

Detailed visual core description was carried out on board the *Joides Resolution* during IODP Expedition 339 by the Expedition scientists. This was augmented by petrographic analysis of smear slides, selected X-ray diffraction analysis of powdered bulk samples, and geochemical analysis of total carbonate content (organic and inorganic). Physical properties measurements on whole cores included sediment colour and reflectance spectrometry, magnetic susceptibility, natural gamma radiation, grain density and sediment strength. A post-cruise review of the cored section at the core repository in Bremen was carried out.

Five samples identified as hemipelagites were selected for microstructural analyses. These were oven dried slowly at a temperature of 60^0C until the weight of the sample became constant regardless of further drying. The dried samples were vacuum impregnated prior to the preparation of well-polished thin-sections and ion milled samples.

5.2.2 Automated Large Area SEM high-resolution montages

The procedure for acquisition of large-scale montage images as employed here is similar to previous method presented by Lemmens and Richards (2013) and further details can be found elsewhere (Buckman, 2014; Bankole *et al.*, 2016). A field emission Quanta 650 SEM equipped with a backscattered (BSE) detector was used to acquire the SEM images. The operational settings for the equipment are; low vacuum mode (0.83 Torr), 15 kV, 4.5 spot size and 10 mm working distance.

A step-wise scanning procedure was adopted (Figure 5.1) and this involves: (1) SEM image of the whole polished thin-section at low-resolution to obtain information on the distribution of the mineral phases and cracks. (2) High-resolution SEM image tiles at 45 nm per pixel, for orientation analysis (3) super high-resolution at 3.2 nm per pixel, for porosity and pore size determination. Randomly selected areas were imaged at both high-resolution and super high-resolution for grain orientation and porosity (Table 5.2).

Table 5.2. Number of SEM images and EDX acquired at randomly selected areas (subsets) per sample.

Sample ID	Subsets		
	High-resolution	Super high-resolution	EDX
1	6	5	4
2	6	6	4
3	6	4	4
4	6	6	4
5	6	6	4

*The high-resolution image (45 nm/pixel) were used for orientation analysis while the super high-resolution images were used to estimate the porosity and pore size distribution.

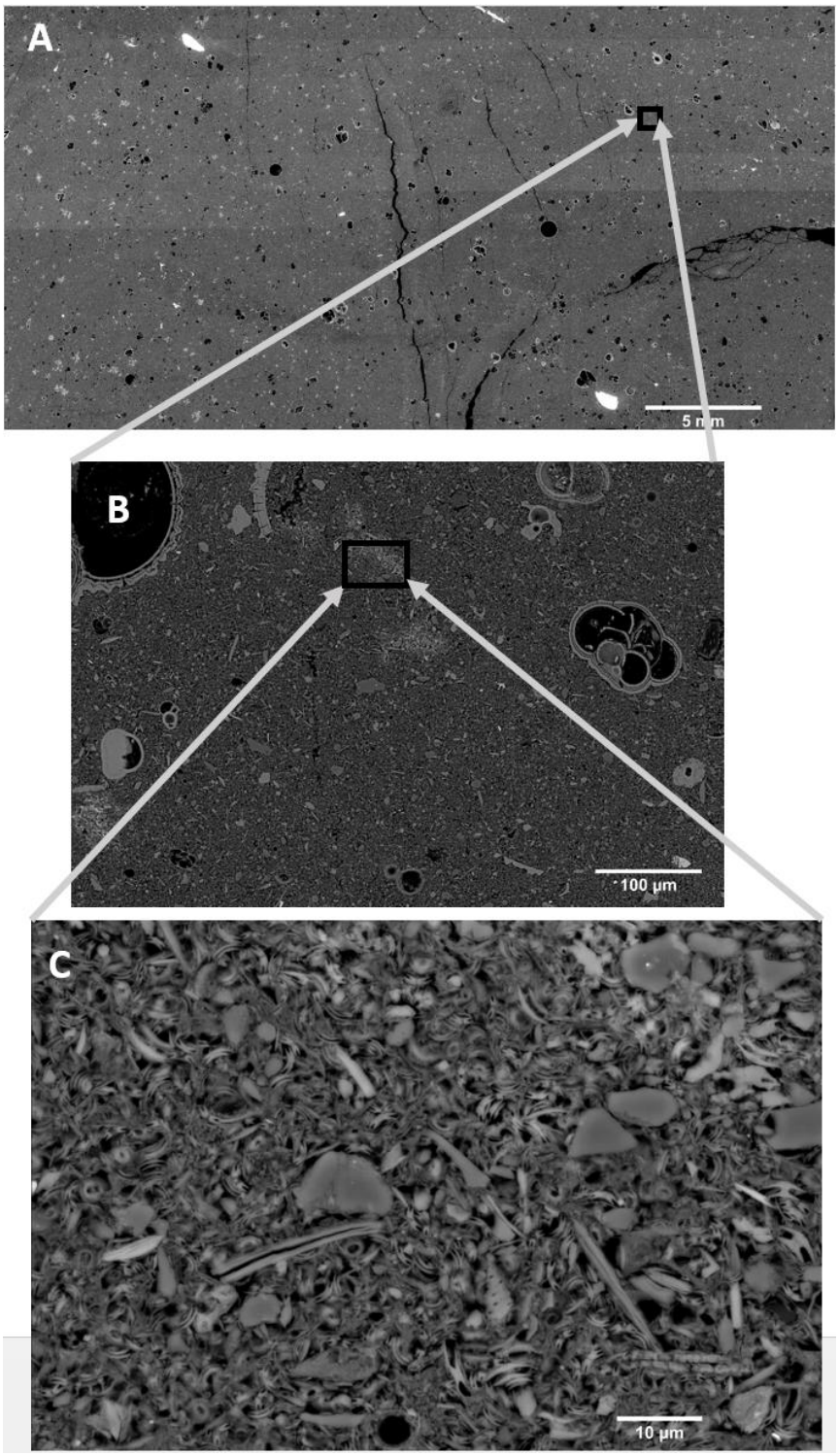

Figure 5.1 A step-wise method of SEM imaging of polished thin-sections (A) low-resolution image of the whole polished thin-section with resolution of 2 µm per pixel (B) High-resolution SEM image at 45 nm per pixel (C) super high-resolution SEM image at about 3.2 nm per pixel.

5.2.3 Image analysis

Image analysis was performed with *Fiji* (version 1.51 for window 64 bits), an adaptation of imageJ. *Fiji* is an open source software developed by the National Institute of Health (NIH), United States of America. Fiji hosts a library of algorithms for practically handling image analysis. The software was initially developed as a platform to iteratively handle and analyse biological images (Schindelin *et al.*, 2012). The usage of the software is not limited to biology but cuts across several disciplines, and is particularly suited to geological materials.

The SEM images were processed through contrast and brightness enhancement and application of median filter with radius value of 4. There are numerous segmentation methods in the literature (Pal and Pal, 1993; Zaitoun and Aqel, 2015), the simplest is manual thresholding which is based on visual judgement.

5.2.3.1 Trainable Weka Segmentation

Due to the intricacy involved in segmenting clay platelets and silt-size particles, Trainable Weka segmentation (TWS) was employed. TWS is a form of pattern recognition by the system through supervised machine learning segmentation. This process requires manual annotation of features of interest to train the classifier. The image is segmented based on the selected classifier. The segmentation may require several iterations until the user is satisfied with the result. TWS was applied and the classifier was trained to identify the following classes: grains (quartz, feldspar, muscovite, calcite and clay platelets), undifferentiated grains and pores (Figure 5.2 B, E). In the final binarised image, grains were rendered to the foreground (background) while undifferentiated grains and pores were rendered to the background (white) (Figure 5.2 C, F). The setting up employed with TWS involves the selection of minimal but reasonable training features that are appropriate for the segmentation. The features selected are sobel filter, Gaussian blur and median. Once the classified image is satisfactory, the classifier is saved and later applied to several other images in order to reduce running time.

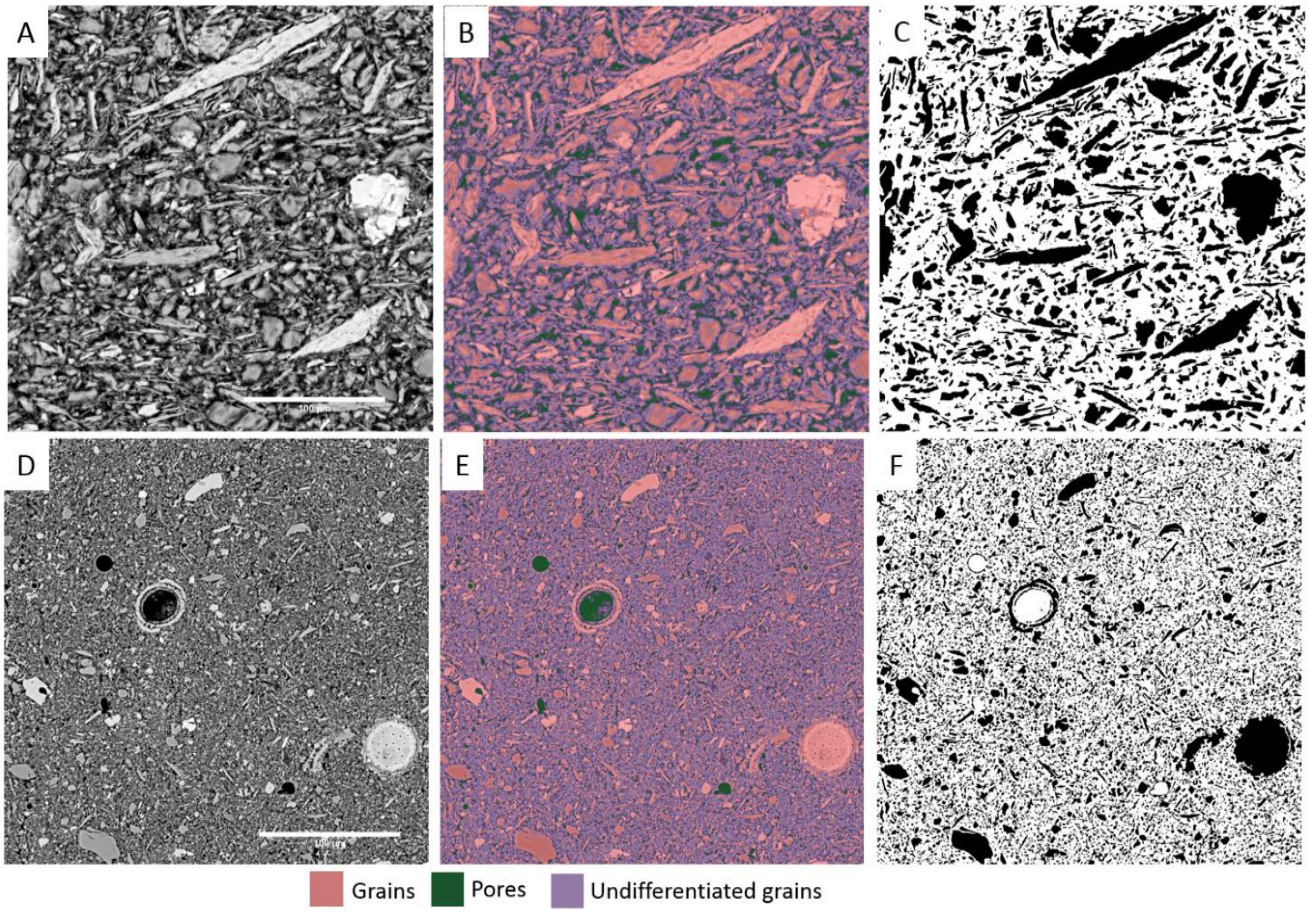

Figure 5.2. Sample of SEM images segmented through Trainable Weka segmentation (A,D) processed SEM image (B,E) Output of Trainable Weka Segmentation (C,F) binarised images. The horizontal field of view (HFOV) of the images is 300 µm. Note the outputs of the Trainable Weka contain three classes; pores, grains and undifferentiated grains. In the binarised image, the grains were rendered to foreground. Note than the undifferentiated grains are aggregates of grains which cannot be separated into individual grains during thresholding.

5.2.3.2 Grain size

Grain-size measurements were made from the processed images using *Fiji* software. Six randomly selected areas (or subsets) were imaged at high-resolution (45 nm per pixel) for each of the five polished thin-sections. The dimension of each area is approximately 650 µm by 400 µm, which is believed to be sufficiently representative of the whole sample. Random selection of these areas was made in order to account for heterogeneity in the grain size within the sample. Raw images from the scanning electron microscope were processed with *Fiji* by first setting the scale of the image based on the horizontal field of view of the tiles in nanometres per pixel. The grains were then analysed and data acquired on grain diameter, perimeter, area, circularity, and aspect ratio. Data returned by *Fiji* were saved in Excel format and further data management were automated through some Excel functions and Visual Basic for Applications macros. Grain size was determined based on percentage Feret diameter by summing up the diameters in each sediment class.

5.2.3.3 Silt and clay orientation

Particle orientation of both silt and clay-sized grains was analysed using the particle size analysis function in Fiji. The orientation of each grain was measured through the best fit ellipse drawn around that grain. In order to focus only on the silt and clay-size particles separately, a macro was run on the orientation data in Excel in order to examine only particle sizes 4-63 µm (i.e. silt-size) in the first instance, and then < 4 µm (i.e. clays). A further filter was applied to exclude particles with an aspect ratio less than 2. This guaranteed that only silt and clay size particles that are elongated (typically mica and clay platelets) were used for the orientation analysis. Orientation data were divided into 18 bins and rose diagrams were constructed with Georient 9.5.1 software (Holcombe, 2011). In addition to the rose diagrams produced by Georient, the software gives as an output of circular statistical parameters, including circular variance, circular standard deviation, kappa coefficient, and circular skewness, among others.

To reduce subjectivity that might arise based on visual judgment, circular statistical parameters mentioned above as well as entropy were applied. Kappa values greater than 0.5 signify preferred orientation direction but due to the fact that kappa is only suitable for unimodal distributed data which is not the case here (visual observation) kappa and entropy were used to interpret the orientation output derived from Georient (Holcombe, 2011). The higher the entropy value the greater the randomness, values lower than 2.83 represent preferred alignment

of grains (which can either be oblique or parallel to bedding), values between 2.83 and 2.86 were interpreted as semi-random while values higher than 2.86 suggest random orientation.

5.2.3.4 Pore size and porosity

Determination of pore sizes was based on Feret diameter and porosity was estimated as an area percentage using the Fiji software. In this chapter, manual segmentation was employed for analysis of pores such that the feature of interest (pores) were rendered to the foreground and the scale of the image resolution was set based on the horizontal field of view. The scale was in nanometres per pixel. To fully automate the workflow, a subset of images that is adjudged representative of several images is first analysed in order to set certain parameters, such as contrast and brightness and thresholding in grayscale.

Data on pore size were obtained via the particle analysis function with Fiji. Information produced on pores in this way include Feret diameter, pore area, circularity, aspect ratio and orientation angles. All the steps involved were turned into script via macro recording and then run on a folder containing several images through batch processing. The macro recording produces a script of all the steps involved. The recorded macro is like script writing but it has the advantage that it requires no prior knowledge about scripting or any programming language. Further information on operations of Fiji can be found elsewhere (Schindelin *et al.*, 2012; Schneider, Rasband and Eliceiri, 2012). Information retrieved on pore size, porosity and grain orientation through Fiji were saved in Excel format. Pores less than 15 nm were filtered out in Excel through Visual Basic Application (VBA). Further analysis and plotting were performed in Excel 2014 and Matlab R2016b for graphical presentations. Estimation of pore size and porosity was performed by progressively increasing the area of the image to achieve a less statistically varied value (Bosl, Dvorkin and Nur, 1998; Kameda *et al.*, 2006).

To investigate whether pore size distribution among subsets of the same sample varied, empirical quantile-quantile plots (Q-Q plots) were constructed. A Q-Q plot is a non-parametric statistical test to determine if two sets of data have common distribution. The quantile of subset A was plotted against the quantile of other subsets for each of the samples on a log-log graph. A common distribution between two data sets is indicated by the Q-Q plot when it falls close to a reference line y= x. Further explanation of Q-Q plots can be found elsewhere (Chambers, 1983; Lovie, 2005).

To display variation in porosity at the microscale, hundreds of tiles of SEM images were analysed for porosity and subsequently turned into coloured contour maps. The maps express variation in pore distribution among tiles from each montage (Buckman *et al.*, 2017). Because the polished thin-sections were prepared perpendicular to the bedding both vertical and horizontal pore distribution were visually observed.

5.2.4 Mineralogy

Mineralogical composition was analysed via energy dispersive X-ray (EDX) analysis, within the scanning electron microscope. The EDX can provide information about the mineral phases through elemental composition. Mineralogical information through EDX were acquired on carbon-coated, polished thin-sections at 20 kV, high vacuum mode. EDX maps were acquired at 2 µm per pixel and 69 nm per pixel, such that the total horizontal fields of view were 1 mm and 70 µm respectively. A total of 75 frames per map, with a scan time of 10 µs, were taken in order to maximise data quality at both resolutions. Mineralogical phase maps were constructed and quantified using AZtec software. The derived mineralogy from EDX requires observer intervention by interrogating several areas of the map to determine the elemental composition. A combination of elemental composition and mineralogical morphology form the basis for identifying minerals present in the EDX maps.

To directly compare the result of the EDX analysis with another technique, bulk X-ray diffraction was performed on all the samples. The samples for XRD analysis were oven dried at 60^0C, ground with mortar and pestle and then mounted on a glass slide with acetone, similar to the smear mount method described by Munson *et al.* (2016). X-ray diffraction data were collected at room temperature on a Bruker D8 advance powder diffractometer, operating with Ge-monochromatic Cu Kα1 radiation. The mineralogical composition was semi-quantified from the diffraction pattern using the intensity peak ratio and corrected with the multiplication factor presented in Piper (1977).

5.3 Results

5.3.1 Lithological characteristics

The sediments recovered from Site 1385 on the Portuguese continental slope are a very uniform series of nannofossil muds, with variable proportions of biogenic carbonate and terrigenous material. Bedding is very indistinct to non-existent, but a more or less distinct colour variation is evident throughout, from paler to darker greyish hues. These colour cycles correspond with more biogenic content (paler) and more terrigenous content (darker), respectively. The same

cyclicity is also observed in physical property measurements, including natural gamma radiation, magnetic susceptibility, and density, as well as sediment colour spectral indices. The minor lithologies present include more carbonate-rich nannofossil ooze, and more clay-rich mud with biogenic grains.

There are no primary sedimentary structures present, and no discernible variation in the very fine grain size. Bioturbation and burrowing is pervasive, and the bioturbation index ranges from moderate to intense. The trace fossil assemblage comprises abundant *Planolites*, common *Paleophycus*, *Thalassinoides* and *Taenidium*, and rare *Chondrites* and *Zoophycos*. Other non-specific traces are also present together with abundant biodeformation. Small-scale, sub-vertical microfaults are present at relatively few restricted intervals, and one thin interval of contorted strata was observed during the expedition (Expedition 339 Scientists, 2012). Typical facies photographs with trace fossils and bioturbation are shown in Figure 5.3.

The Shackleton Site 1385 was drilled in order to provide a continuous marine record of Pleistocene millennial-scale climatic variability that can be correlated with both polar ice cores and European terrestrial records. For this reason, it has been intensively studied and has thus far yielded four separate age models, all of which are in very good agreement (Hodell *et al.*, 2015). These show that sediment accumulation rates have been extremely uniform over the past 1.5 Myr, averaging around 11 cm/ky.

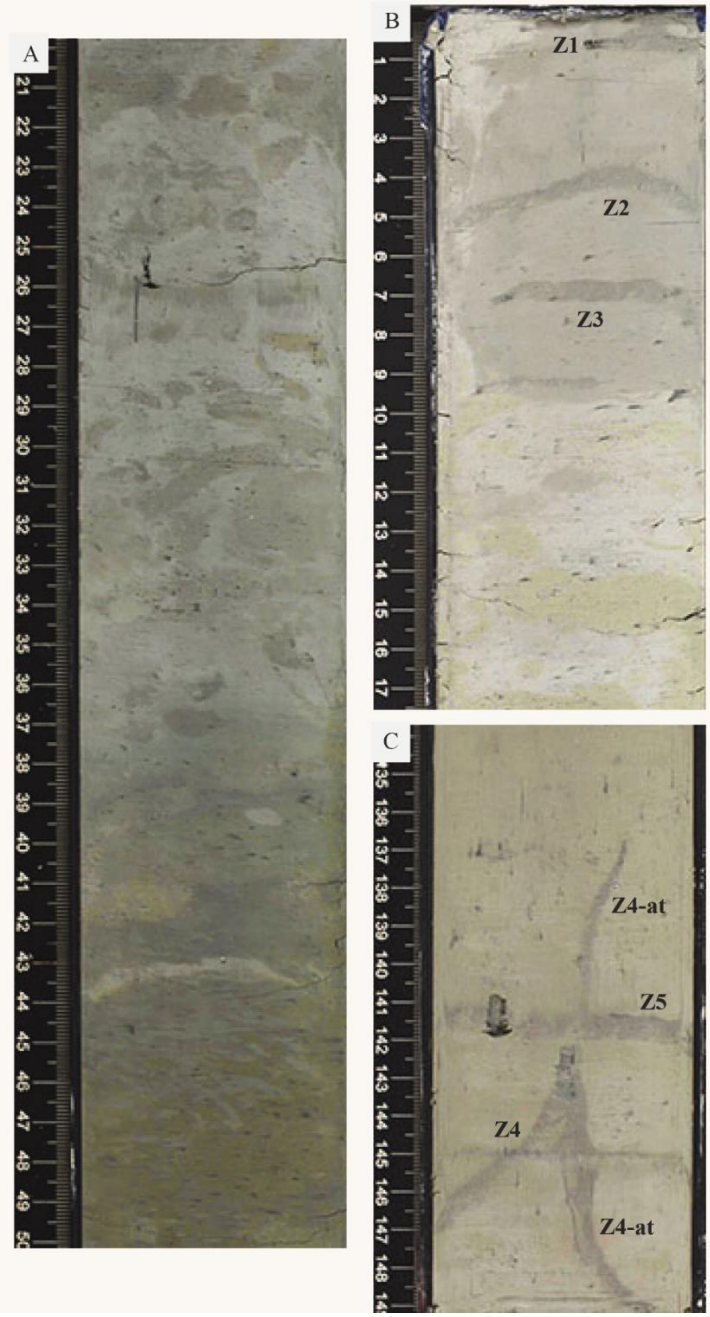

Figure 5.3. Selected core sections representative of hemipelagite facies at IODP Site 1385. A) Core shows part of colour cycles from light grey (more biogenic carbonate) to dark grey (more terrigenous clay). Intense multi-tiered bioturbation and burrowing throughout. Larger trace fossils observed include: *Planolites*, *Zoophycos*, *Scolicia* and *Thalassinoides*. Small-scale burrows in mottled background are probably *Phycosiphons*. B) Detail of Zoophycos, displaying three levels of a single specimen (Z1-Z3). (C) *Zoophycos* (Z4), with axial tube (Z4-at), indicating a minimum burrow depth of 120 mm. Z4 cross cut by a second *Zoophycos* (Z5) (From IODP database).

5.3.2 Grain size

The results of the grain size analysis are presented more fully in another publication and further details on the procedures, results and discussion are given therein (Bankole *et al.*, 2018b). In brief, the samples are all within the mud-size field (Stow, 2005), ranging from silty clays to clayey silts. The mean size for all samples ranges from 7.6-6.8 phi (i.e. about 6-9 um), with unimodal size distributions. They are very well to moderately well sorted, symmetrical to fine skewed. Significantly, from the methodological viewpoint, there is no substantial variation in the grain size among the subsets for any one sample (Figure 5.4).

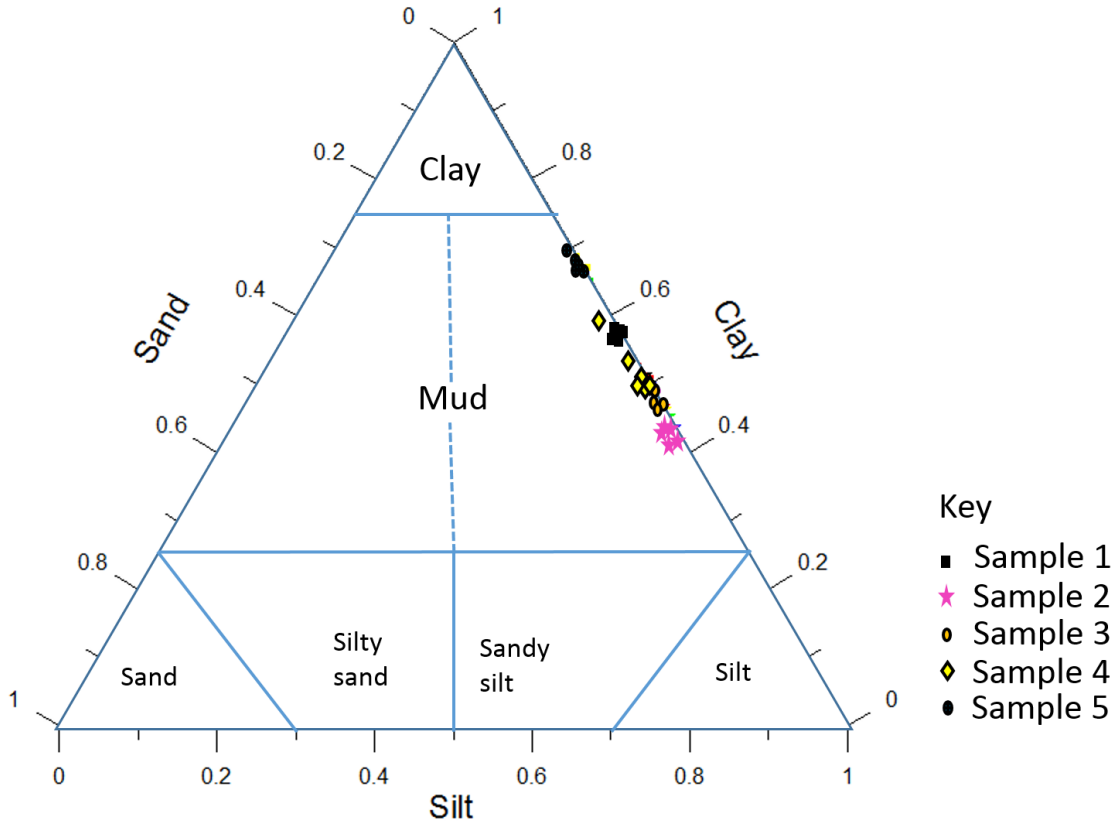

Figure 5.4. Ternary plot of grain-size for several subsets. Mudrock classification in both ternary plots is based on Stow (2005). The varying subsets from each sample plot within a cluster.

5.3.4 Particle orientation

Particle orientation (silt and clay) in the vertical plane (i.e. approximately perpendicular to bedding) is shown as a series of rose diagrams. The full collection of particle orientation measurements is presented as rose diagrams for each of the sample subsets, and for silt and clay fractions separately, in Table 5.3. Sample 1 is dominated by random or mixed alignment, with two subsets that show oblique preferred alignment. Sample 2 is typical of a more or less random or less completely random particle orientation for both silt and clay fractions separately. Only two of the subset samples show a more oblique alignment to mixed orientation that appears at a high angle to the horizontal. Of the 60 individual orientation measurements from the 5 samples, approximately 48% show random orientation, 41% display oblique preferred alignment, and approximately 1% shows a mixed (or polymodal) alignment that is classifed as semi-random. The samples that show oblique alignment, are mostly horizontal or nearly perpendicular, whereas a further 4 rose plots show 'anomalous' orientations at a high oblique angle to the horizontal. In almost all cases, orientation of clays versus that of silt particles were found to be similar.

In order to validate our visual observation of random versus preferred grain alignment, circular statistical parameters and entropy values were calculated (Table 5.4). Circular variance measures dispersion of the orientation data and its value ranges between 0 and 1. Values close to 0 suggest distribution of data are well aligned with small dispersion, whereas values close to 1 suggest more random distribution (Davis, 1986; Berens, 2009). The Kappa coefficient (k) is inversely proportional to dispersion, such that high Kappa values ($k > 0.5$) suggests the angular data are restricted to a narrow arc of the circle with little dispersion i.e. preferred orientation (Davis, 1986; Mardia and Jupp, 2000; Suttle, Genge and Russell, 2017). Entropy is a different parameter for determining orientation of fabric for both unimodal and multimodal data, for which a high value signifies randomness, whereas a low value signifies greater alignment. Suttle, Genge and Russell (2017) used a value of 2.80 to differentiate random and preferred alignment in fine-grained meteorites.

The data presented in Table 5.4 are based on averages of all subsets for each sample and, therefore, the ranges shown for circular variance, kappa coefficient and entropy include what has been interpreted as both random and oblique preferred fabrics. These ranges typically span the random/preferred fabric values. Individual subset measurements, however, show better correlation (Table 5.3).

Furthermore, a plot of entropy values for clay size particles against that of silt particles shows strong correlation between the two which is also supported by a high value of Pearson correlation coefficient (0.91) (Figure 5.5). This agrees with visual inspection of the rose diagrams which show that silt and clay orientations for each subset are very similar. At a 95% confidence interval, F-test statistics computed from the entropy values of silt and clay size particles showed that the null hypothesis can be accepted, which means that the calculated entropy for silt particles and clay size particles have equal variance (Table 5.5). All the statistical parameters, therefore, indicate that orientation analysis of silt particles is a proxy for clay size particle orientation.

Table 5.3. Rose plots for silt and clay orientation for all the samples and their varying subsets.

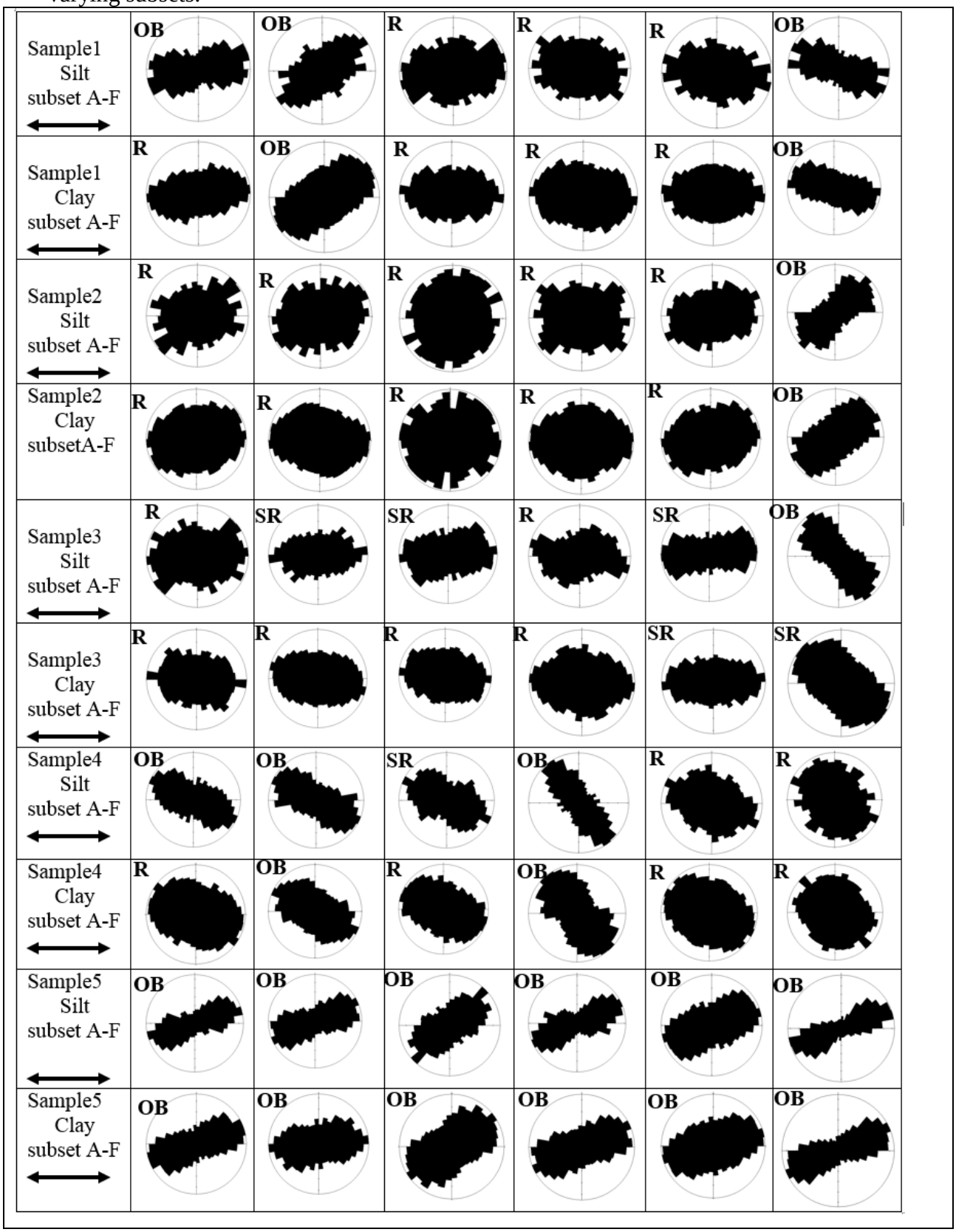

- Arrow indicates direction parallel to the bedding.
- OB= oblique orientation to the bedding, P= bedding parallel, SR=Semi-random
- R= random orientation

Table 5.4. Summary of circular statistical parameters

Sample no	Particle size	Cir. variance	Cir. STD	Dispersion	Cir kurtosis	Cir. skewness	Kappa	entropy
1	Silt	0.24-0.47	43^0-65^0	4.32-76.32	-0.03 - 0.22	-4.09 -0.22	0.16-0.69	2.77-2.88
	Clay	0.31-0.61	49^0-78^0	9.47 - 848.1	-0.1 - 0.05	-2.05--0.08	0.05-0.46	2.83-2.88
2	Silt	0.13-0.24	30^0-42^0	1.13 -4.08	-0.92--0.13	-21.69 - -4.92	0.71-1.44	2.51-2.77
	Clay	0.2-0.32	38^0-51^0	2.53-10.97	-0.37-0.11	-7.21 - -1.6	0.43-.91	2.70-2.84
3	Silt	0.27-0.44	46^0-62^0	6 - 50	-0.19 - 0.17	-3.27 - -0.46	0.2 - 0.59	2.81-2.88
	Clay	0.3-0.42	48^0-60^0	7.86 - 40.77	-0.05 - 0.1	-2.23 - -0.51	0.22-0.51	2.83-2.88
4	Silt	0.28 - 0.57	47^0-75^0	6.97-427.21	-0.07 - 0.07	-3.22 - -0.07	0.26-0.55	2.63-2.74
	Clay	0.34 - 0.55	52^0-73^0	13.53 - 302.43	-0.04 - 0.11	-1.66 - -0.17	0.08 - 0.39	2.66 - 2.71
5	Silt	0.26-0.42	45^0-59^0	5.6 - 35.76	-0.32-0.12	-3.79 - -0.64	0.23-0.61	2.60-2.68
	Clay	0.35-0.45	53^0-63^0	15.01-59.22	-0.1-0.04	-1.15--0.3	0.18-0.36	2.65-2.71
6	Silt	0.26-0.49	45^0-66^0	5.12-107.42	-0.17-0.08	-3.11--0.31	0.14-0.63	2.63-2.71
	Clay	0.33-0.53	51^0-70^0	11.62-196.45	-0.01-0.1	-2.1--0.21	0.1-0.42	2.69-2.72
7	Silt	0.18-0.33	36^0-51^0	2.11-12.07	-0.02-0.48	-8.52--1.59	0.41-0.99	2.45-2.67
	Clay	0.22-0.37	40^0-55^0	3.23-18.19	-0.13-0	-5.9--0.93	0.33-0.81	2.51 - 2.67

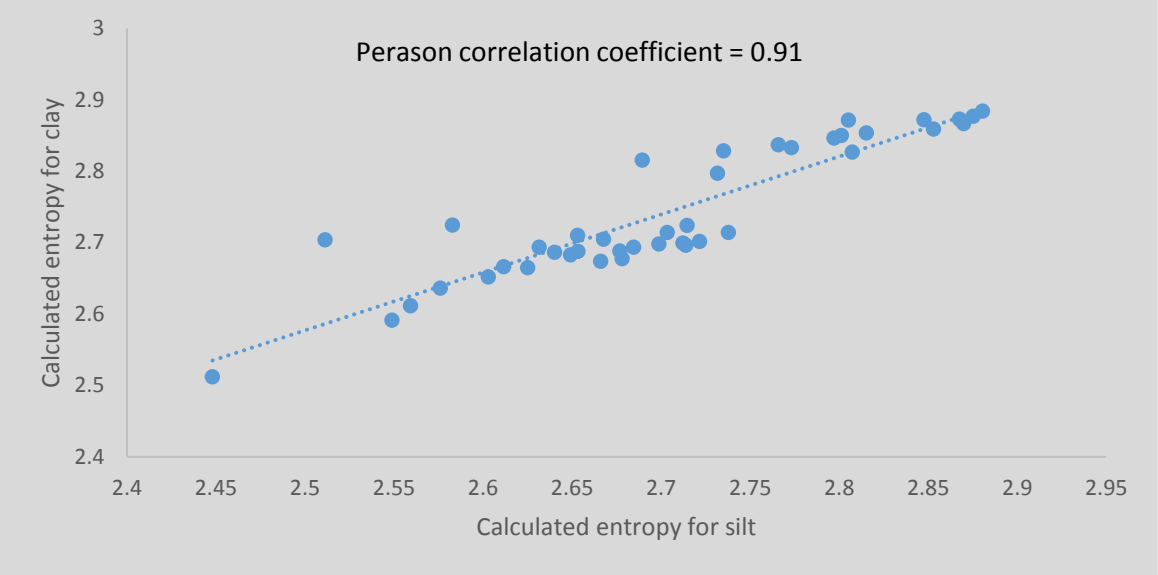

Figure 5.5. Plot of entropy values for silt against entropy for clay. The graph shows a strong correlation between the two set of values which is an indication that the silt and clay particles have similar orientation.

Table 5.5. F-test two sample variances for entropies of clay and silt

	Silt entropy	*Clay entropy*
Mean	2.70	2.74
Variance	0.01	0.01
Observations	42	42
df	41	41
F	1.25	
P(F<=f) one-tail	0.24	
F Critical one-tail	1.68	

5.3.5 Mineralogy

The composition of sediments at site 1385 is a distinctive mixture of biogenic and terrigenous components. Smear-slide petrography reveals the biogenic fraction to comprise dominantly calcareous nannofossils, with minor to rare foraminifera, diatoms and sponge spicules. The terrigenous fraction is dominated by quartz silt, clay minerals and detrital carbonate silt, with minor to rare feldspar, accessory heavy minerals and authigenic dolomite. There is a notable difference in biogenic/terrigenous proportions between the dark and light-coloured cycles, as well as a slight increase in terrigenous fraction in the upper 40 m of section. The shipboard measurement of total carbonate content ranged between about 20% and 40% by weight.

The mineral composition determined by automated image analysis with EDX measurement is shown in Table 5.6, and compared with results from our own XRD analysis. Broadly speaking, the same minerals are identified by the different techniques, in the different subsets, and at the different EDX resolution settings used (i.e. 2 μm per pixel and 69 nm per pixel). However, the quantified measurements obtained may vary significantly for each of the three principal components – calcite, clay minerals (illite-kaolinite-smectite), and silt minerals (quartz-feldspar-mica).

There is a systematic difference between the coarser and finer resolution measurements by EDX, with the finer resolution always being closer in amount to that determined by XRD. The difference between subsets in one sample is typically within 10 percentage points, rarely more. However, the difference between techniques is more marked, with the amounts of principal components varying by a factor of 2 or more.

Table 5.6. EDX average mineral composition from different subsets and bulk mineral composition

	Mineral	Calcite	Clay	Silt Index	Dolomite	Halite	Anatase	pyrite
Sample 1	2 µm per pixel	93.00%	-	1.71%	0.33%	0.25%	-	-
	69 nm per pixel	80.73%	8.35%	9.05%	1.03%	-	0.03%	0.03%
	XRD	63.29%	12.11%	16.03%	-	2.91%	-	-
Sample 2	2 µm per pixel	89.65%	0.55%	5.43%	0.53%	0.55%	-	0.23%
	69 nm per pixel	69.13%	13.78%	9.71%	0.55%	0.15%	0.08%	0.08%
	XRD	17.96%	22.41%	39.98%	3.22%	1.33%	-	-
Sample 3	2 µm per pixel	7.98%	64.00%	17.95%	1.10%	2.38%	-	0.03%
	69 nm per pixel	11.75%	61.60%	22.19%	2.53%	0.13%	0.03%	0.03%
	XRD	24.68%	40.28%	29.37%	2.94%	2.73%	-	-
Sample 4	2 µm per pixel	9.33%	68.43%	15.16%	0.48%	3.50%	0.03%	0.35%
	69 nm per pixel	16.93%	60.95%	19.74%	0.25%	0.18%	0.18%	0.18%
	XRD	49.13%	20.82%	24.77%	2.04%	3.23%	-	-
Sample 5	2 µm per pixel	9.40%	76.33%	10.01%	0.53%	0.13%	0.03%	0.25%
	69 nm per pixel	17.98%	57.50%	21.53%	0.83%	0.33%	0.55%	0.55%
	XRD	45.32%	15.75%	33.17%	2.69%	3.06%	0.00%	-

*Silt Index = Quartz, Feldspar and Mica. Grey colour indicates clay-rich, brown; calcite-rich and yellow shows where there is discrepancy between XRD and EDX result in terms of the dominant mineral.

5.3.6 Pore size and porosity

The mean pore size are within the macropore range (Sing *et al.*, 1985), with actual values from 541 nm to 1000 nm (i.e. 0.54-1.0 µm) (Table 5.7). They vary significantly among subsets of the same sample, typically by between 10-30%. The median pore sizes are systematically lower, wheras the modal pore sizes for all the samples are much less (21-177 nm) and fall within the mesopore (2 -50 nm) and macropore range (> 50 nm). Computed skewness for the pore size distributions indicate that all the samples are positively skewed. Pore size distributions for the subsets in each sample shows that all samples have a unimodal distribution and are log-normally distributed (Figure 5.6 and Figure 5.7).

Samples of the Q-Q plots are presented in Figure 5.8. Most of the Q-Q plots constructed showed that the subsets in each sample have similar pore size distributions with only few having slightly varied pore size distributions (Figure 5.8). However, the number of pores per subset differs substantially.

A summary on pore size and porosity with respect to the subsets are presented in Table 5.8. These show the full range of subset values obtained as well as the values at progressively increasing areas of measurement from 900 μm^2 to 5400 μm^2. The representative area is taken as the area for which variation in porosity is less than 10% (Figure 5.9) indicating that the change is statistically insignificant (VandenBygaart and Protz, 1999). Although this is subset specific, it was noted that an area of 3600 μm^2 can be considered a representative area for all the subsets. For this area, porosity across the subsets typically varies by 10-15% of the value, but can be much more in some cases (i.e. > 50% variation).

In general, the distribution of porosity varies from one subset to the other within individual samples, as well as within individual subsets. Based on porosity distribution maps (Figure 5.10,

Figure 5.11 and Appendix 2B), the subsets are classified into three groups: highly porous, partially porous and tightly porous (Table 5.9). Highly porous samples are those, in which more than half of the area shows values of more than 15% porosity. Porosity in this group is evenly distributed and well-connected in 2-dimensions (Figure 5.10C). The second group are those, in which less than half of the area shows 15% porosity, and the pore spaces are either poorly linked or disconnected. This group are considered partially porous and characterised by clear separation between porous and non-porous areas (Figure 5.10A, B and

Figure 5.11C). The last group are those in which more than half of the area shows less than 10% porosity (

Figure 5.11 A and B). These are considered tightly porous.

Table 5.7. Computed statistical parameter for the pore sizes. There is wide disparity between the mean and the median because the pore sizes are highly skewed.

Sample No	Mean (nm)	Median (nm)	Mode (nm)	Min (nm)	Max (nm)	Skewness	Kurtosis
Sample 1	581-686	367-441	32-163	15-17	5383-14117	2.7-4.6	10.4-46.7
Sample 2	731-1000	451-574	58-126	17-19	8379-13371	3.12-4.24	3.12-26
Sample 3	541-692	275-420	20-102	15-17	8012-1785	3.0-6.1	14.8-53.8
Sample 4	623-842	365-447	52-132	15-25	6835-16489	2.87-6.5	11.85-75.16
Sample 5	564-670	323-434	24-177	15-17	6027-47741	2.68-24.1	2.69-804

Table 5.8. Summary of porosity values from different subsets

Sample No	Porosity (%)							
		900 μm^2	1600 μm^2	2500 μm^2	3600 μm^2	4200 μm^2	4800 μm^2	5400 μm^2
Sample 1	Subset A	10.81%	9.73%	9.55%	9.40%	9.55%	9.57%	9.53%
	Subset B	11.22%	10.30%	9.64%	9.57%	9.67%	9.53%	9.48%
	Subset C	11.04%	11.84%	12.42%	12.37%	12.16%	12.33%	12.64%
	Subset D	10.40%	9.76%	9.97%	10.25%	10.32%	10.38%	10.58%
	Subset E	11.39%	11.29%	11.20%	11.15%	11.16%	11.31%	11.30%
Sample 2	Subset A	8.37%	9.10%	10.21%	10.42%	10.38%	10.48%	10.47%
	Subset B	10.31%	10.72%	10.42%	10.31%	10.25%	10.29%	10.58%
	Subset C	14.59%	15.20%	15.73%	15.32%	14.73%	14.52%	13.83%
	Subset D	11.35%	11.28%	11.78%	11.46%	11.61%	11.82%	11.73%
	Subset E	11.86%	12.29%	12.92%	12.44%	12.64%	13.22%	13.62%
	Subset F	9.74%	9.12%	8.92%	9.20%	9.47%	9.32%	9.22%
Sample 3	Subset A	8.64%	7.29%	6.50%	7.32%	7.56%	7.30%	7.16%
	Subset B	10.24%	10.61%	10.97%	10.62%	10.68%	10.94%	11.07%
	Subset C	8.78%	8.53%	8.79%	8.53%	8.47%	8.42%	8.47%

	Subset D	12.94%	13.26%	13.22%	13.56%	13.57%	14.18%	14.22%
Sample 4	Subset A	7.89%	7.66%	7.83%	8.55%	8.32%	8.36%	8.40%
	Subset B	6.63%	7.30%	7.73%	8.05%	8.14%	8.11%	8.00%
	Subset C	16.48%	14.54%	13.97%	13.58%	12.94%	12.49%	12.51%
	Subset D	7.37%	8.24%	8.72%	8.84%	9.09%	9.11%	8.97%
	Subset E	8.51%	8.35%	8.25%	8.29%	8.38%	8.44%	8.29%
	Subset F	13.35%	12.35%	11.22%	10.39%	10.26%	10.77%	10.68%
Sample 5	Subset A	8.30%	8.43%	9.00%	9.03%	9.10%	9.45%	9.39%
	Subset B	8.37%	8.58%	8.35%	8.51%	8.54%	8.50%	8.35%
	Subset C	14.20%	13.39%	13.00%	12.88%	12.73%	12.61%	12.31%
	Subset D	11.59%	11.61%	11.99%	11.89%	11.94%	12.24%	12.31%
	Subset E	8.74%	9.13%	9.73%	9.81%	10.11%	10.02%	10.10%
	Subset F	9.97%	10.26%	10.06%	10.38%	10.92%	10.92%	10.79%

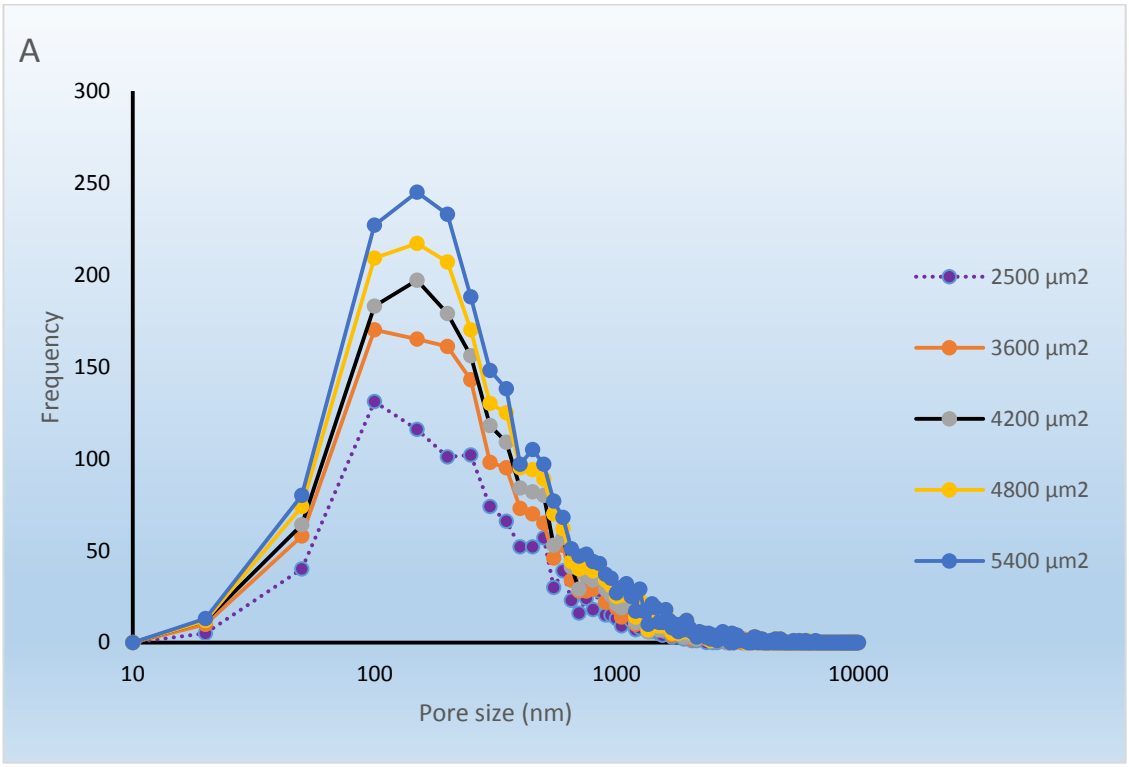

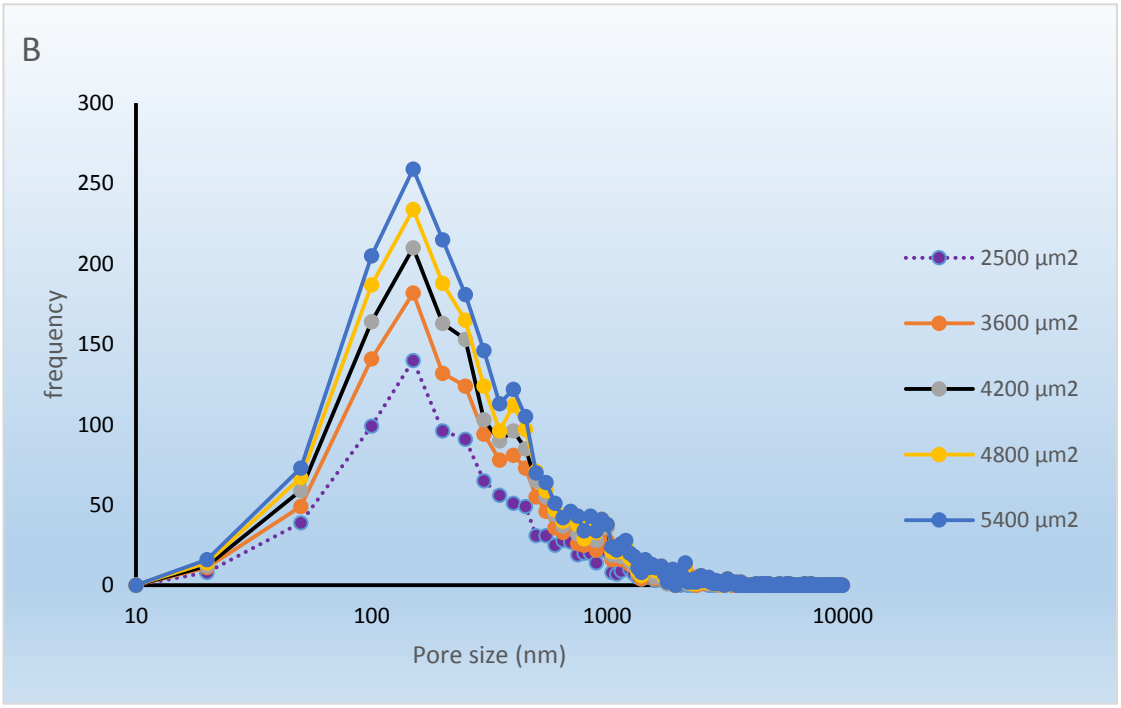

Figure 5.6. Pore size distribution for sample 5 at different size of areas (A) Subset A (B) Subset B. The distribution of pores in both graphs indicate increase in number of pores with progressive increase in area analysed. The modal distribution in subset A varies with the size of the area while in subset B, the modal pore is with a sharp peak and consistent all through as the area analysed increases.

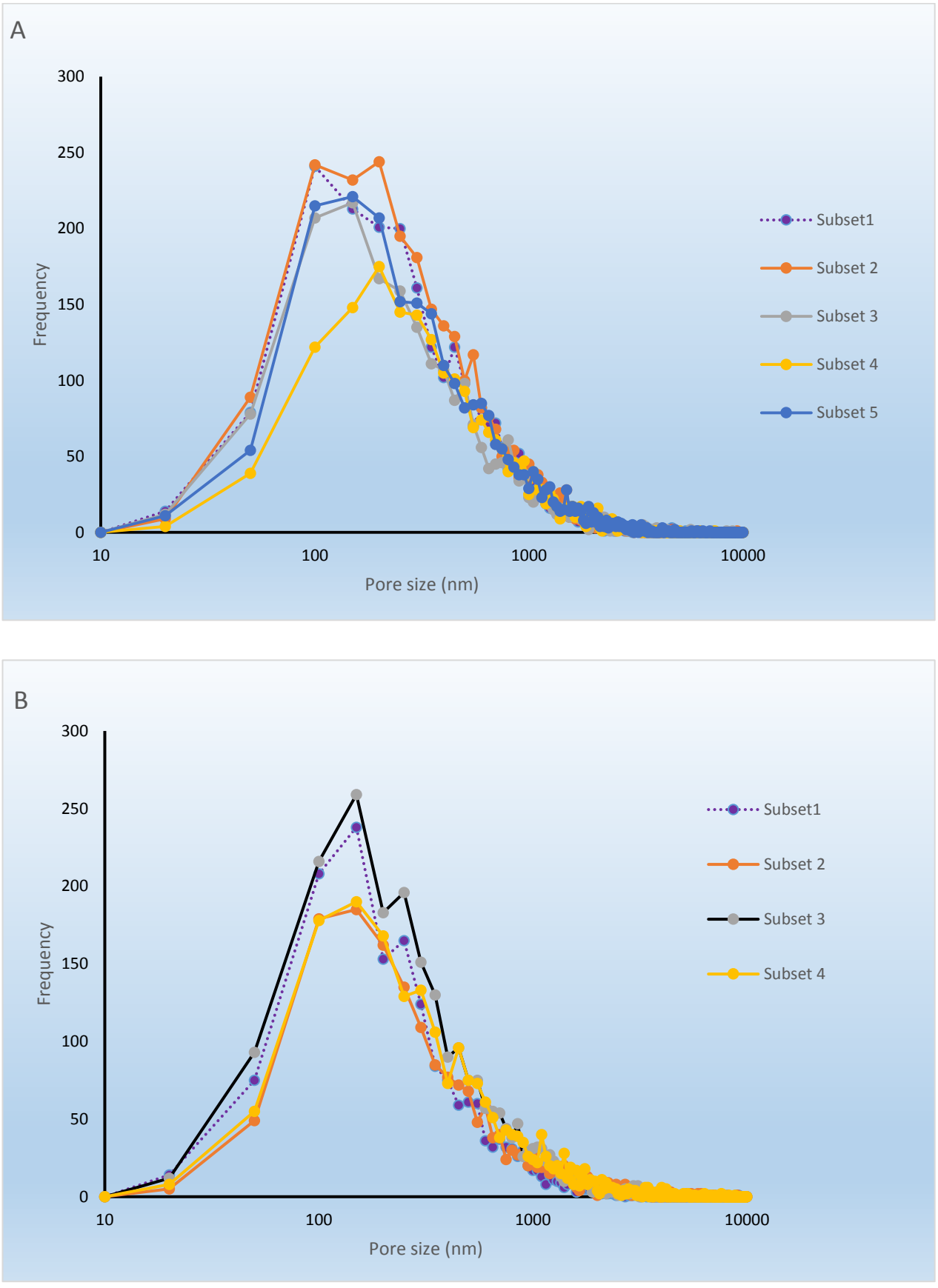

Figure 5.7. Log-normal plot of frequency vs pore size (A) sample 1 (B) sample 3. All subsets in both sample have unimodal distribution.

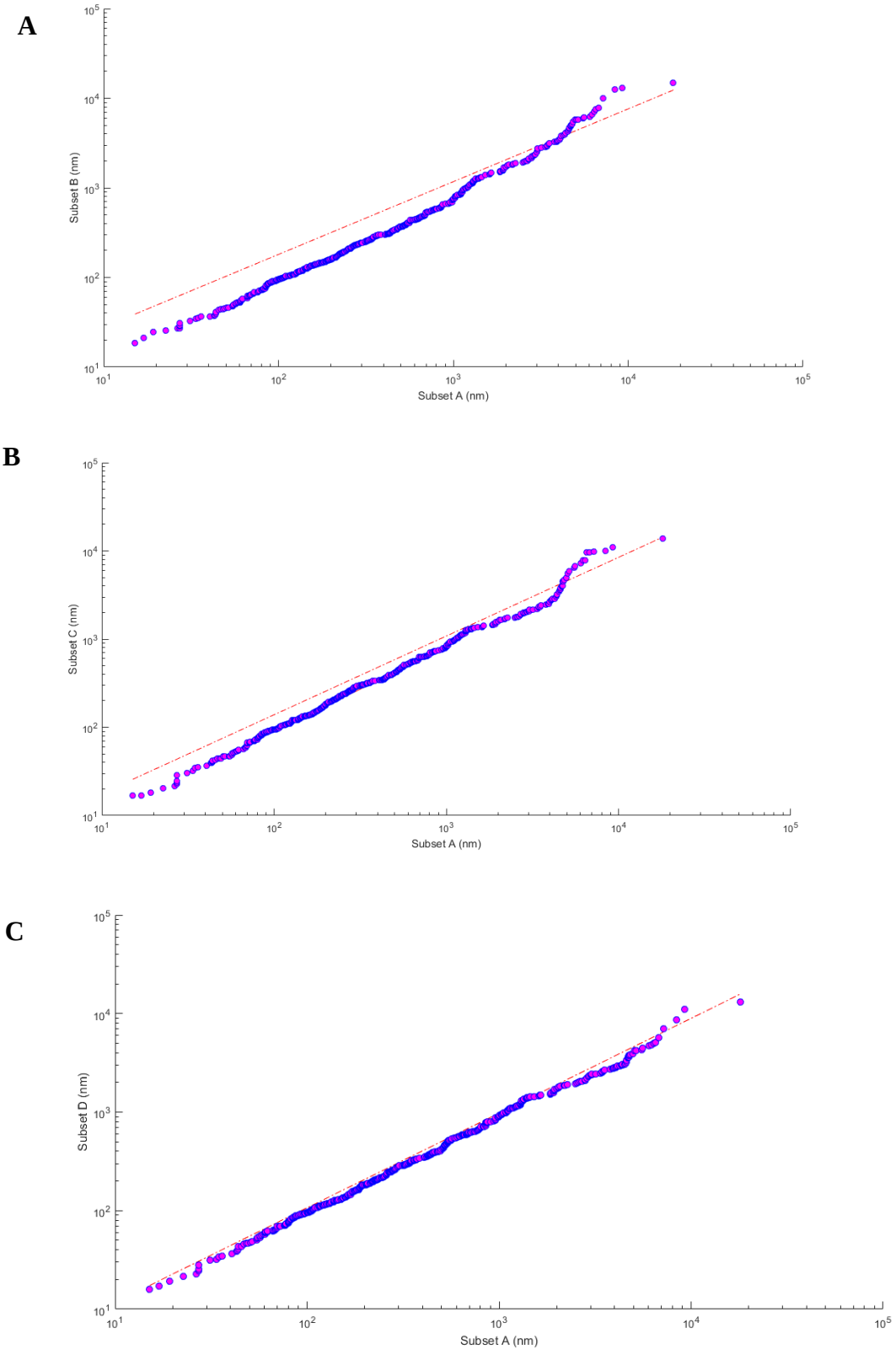

Figure 5.8. Empirical Q-Q plots for pore size distribution for Sample 1. A and B showed slightly varied distribution while C showed that the pore distribution between the two subsets are similar. The red line is the reference line and a well aligned plots along the red line signifies similar distribution for the two subsets that are compared.

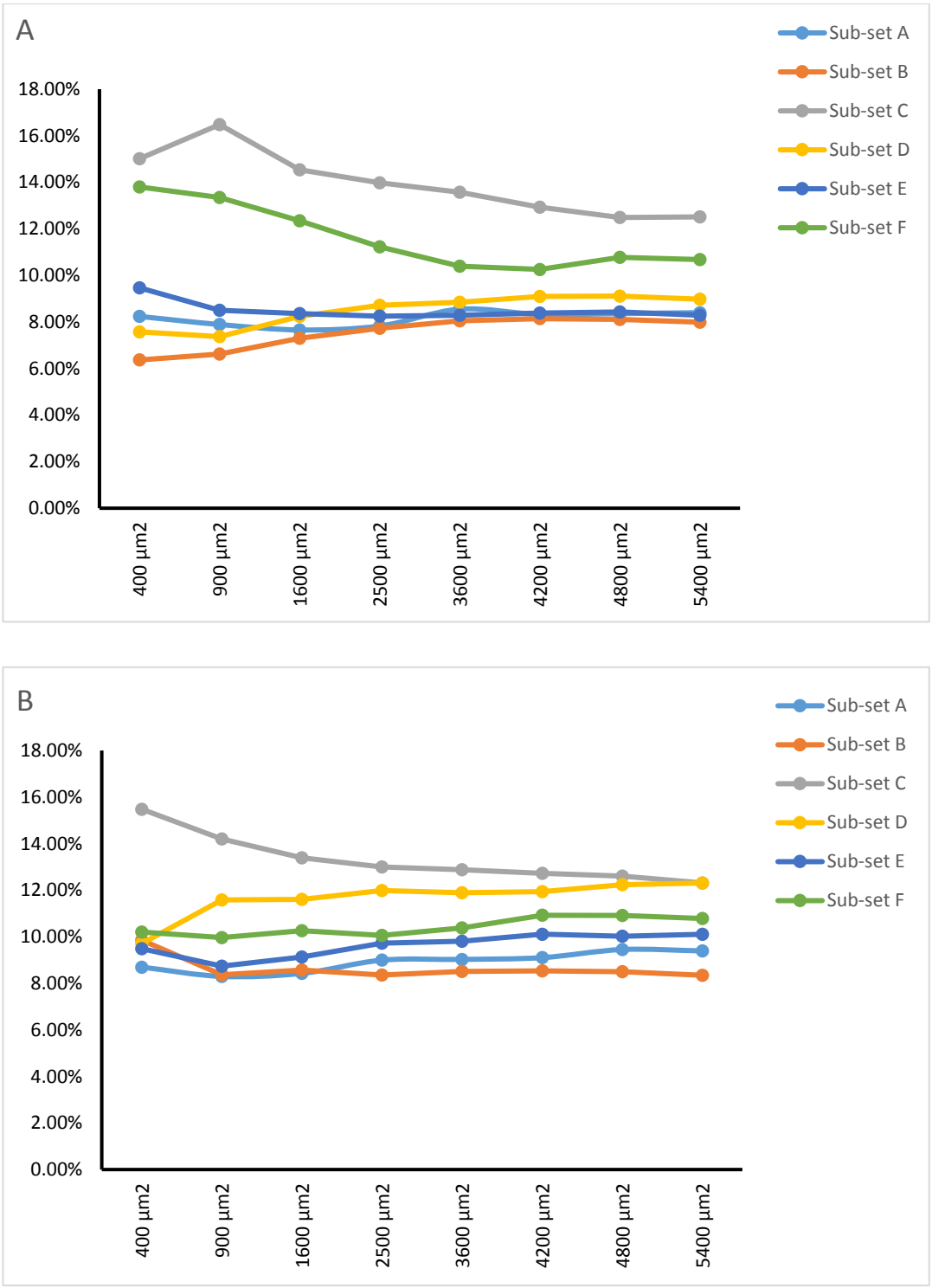

Figure 5.9. Plot of porosity values for different subsets in (A) sample 4 (B) sample 5. Note that the distribution of porosity across the subsets varies.

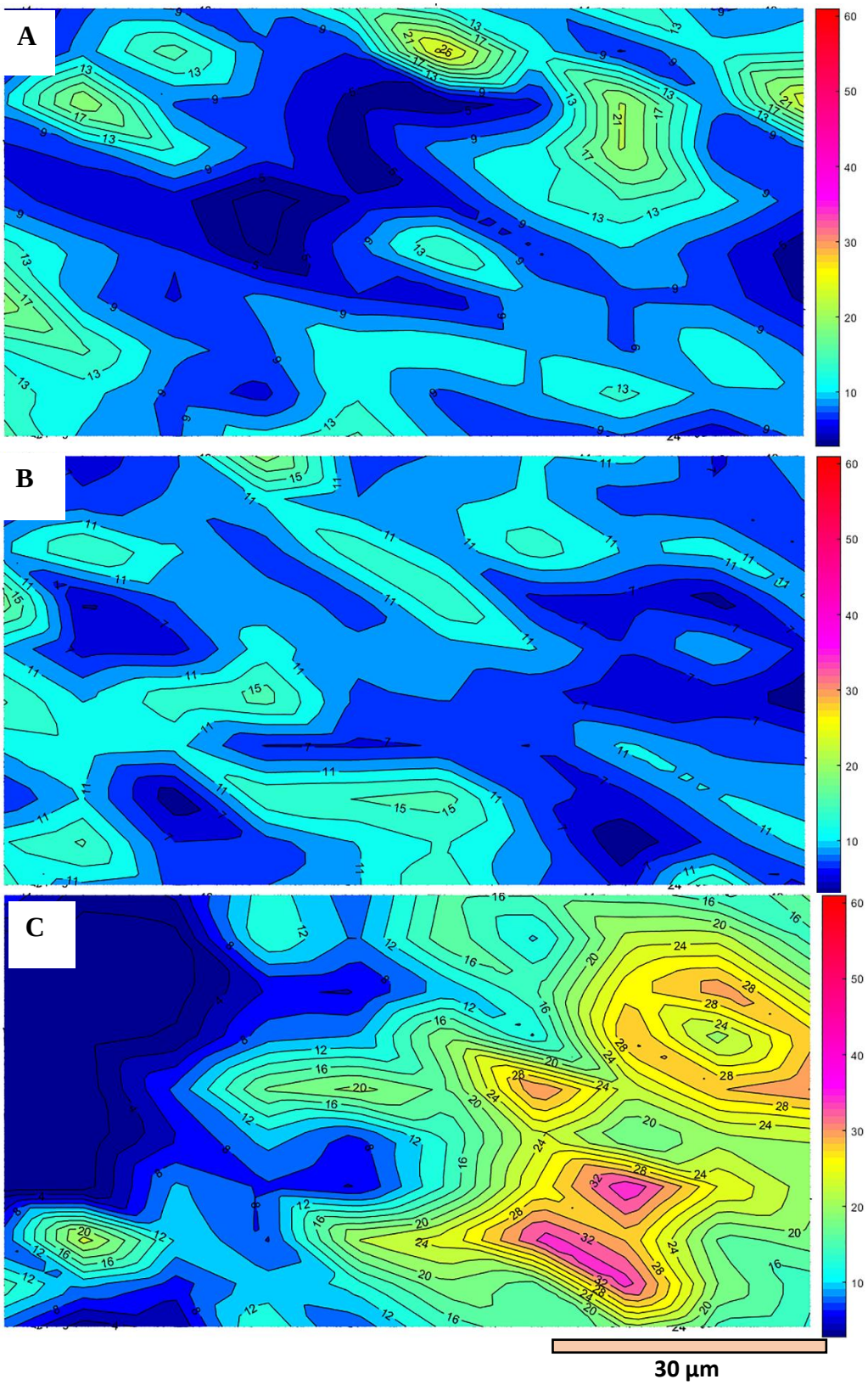

Figure 5.10. Contour maps showing variation in porosity for sample 2, A-C are subset A to C. Subset A and B are examples of partially porous while C is highly porous. Total horizontal field of view (HFOV) is 95 µm

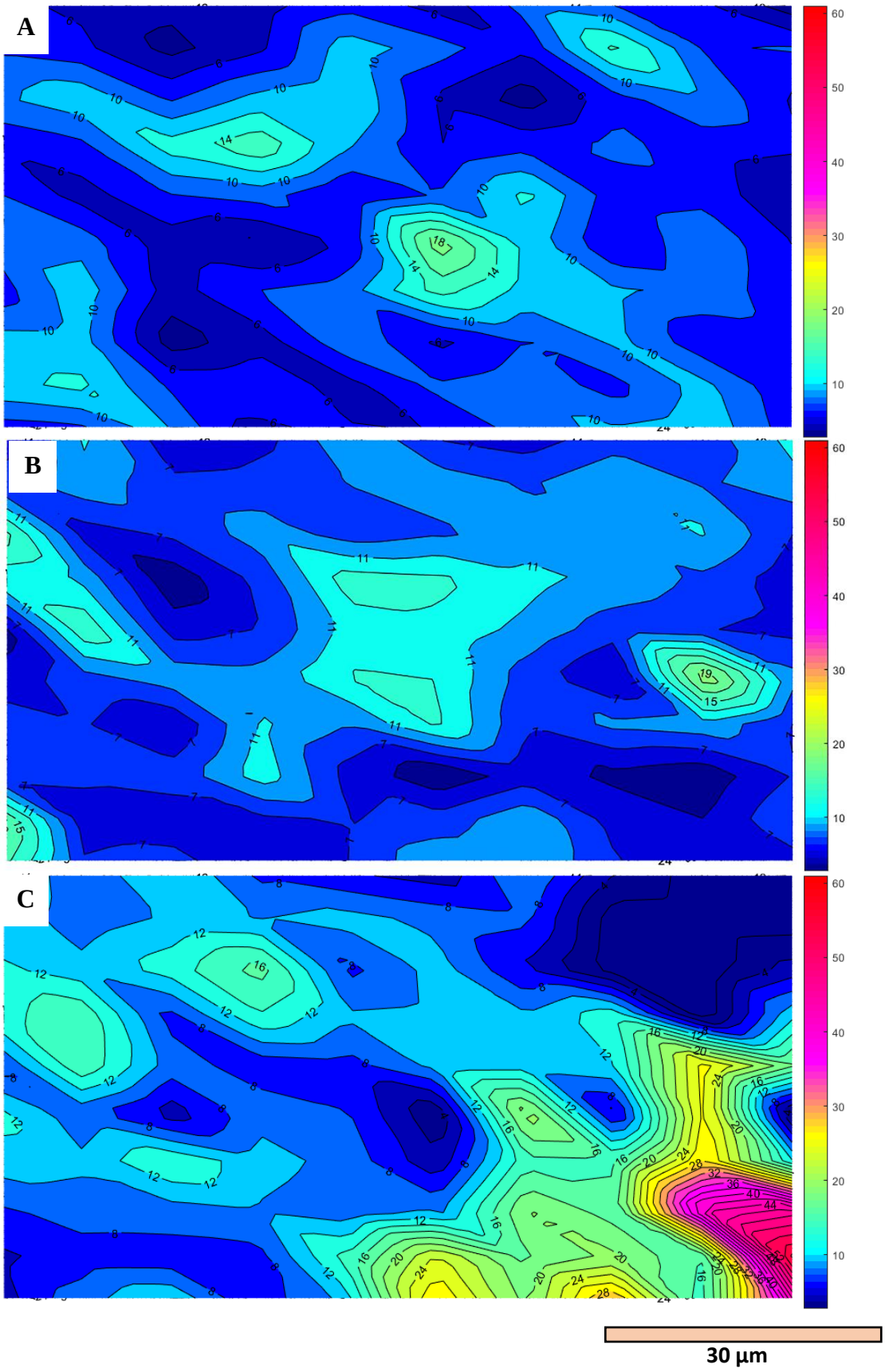

Figure 5.11. Contour maps showing pore distribution for sample 1, A-C are subset A to C. Subset A and B are tightly porous while C is partially porous. Total horizontal field of view (HFOV) is 95 µm.

Table 5.9. Classification of subsets per sample based on porosity distribution. It is apparent that no single sample has the same porosity distribution across all the subsets.

Sample ID	Highly porous	Partially porous	Tightly porous
1	Subset D	Subset C,F	Subset A,B E
2	Subset C, D, E	Subset A, B	Subset F
3	D, E	Subset B	Subset A, C, F
4	-	Subset F	Subset A, B, C, D, E
5	Subset C, D	Subset E, F	Subset A,B

5.4 Discussion

This discussion is divided into two parts: (1) critical assessment of the new methodology introduced here for the characterisation of mudrocks in general; and (2) consideration of the new data presented on hemipelagic sediments from the Shackleton Site on the Iberian continental slope, and of how these compare with hemipelagites more broadly.

5.4.1 Methodology

The automated image acquisition analysis (AIAA) technique presented here differs from prior work in two important respects. Firstly, it images relatively large areas by a process of automated acquisition and stitching and, secondly, it incorporates multiple areas that have been randomly selected from the available polished thin-section or ion-milled sample. Both these aspects help mitigate against relying on data from too small a sample area of a heterogeneous sediment. The methodology minimises human subjectivity and bias, but does require selected manual thresholding by image segmentation. This is non-trivial and may lead to varied results among different operators. It is likely that the discrepancies in results among users is minimal and for an individual, the process is expected to be reproducible. These factors can be quantified (Francus and Pirard, 2004; Grove and Jerram, 2011) but are not addressed here.

For the different attributes investigated, the following observations and assessment of the AIAA method were made.

5.4.1.1 Grain Size analysis

AIAA provides an important and reliable technique for grain size analysis of very fine-grained sediments, for which high-resolution measurement is required. It measures actual grain diameters (Feret diameter) for tens of thousands of grains, and is effective over a wide range of sizes from 10 nm to 5 mm. However, for most SEM measurements of mudrocks, a preferred range of 100 nm to 100 μm is suggested. The results obtained here were found to be closely comparable to those obtained by laser diffraction on the same samples (Bankole *et al.*, 2018b), and broadly comparable with the results of laser diffraction analysis carried out by Nishida (2016) on other samples from the same site. A significant advantage of the AIAA methodology is that it can be applied equally to unconsolidated and consolidated sediments, as well as to compacted and cemented sedimentary rocks.

5.4.1.2 Particle orientation

Visual inspection of grain alignment is the only effective method of determining particle orientation in mudrocks. AIAA, therefore, provides a fast, effective and objective method of measuring a large dataset and deriving meaningful quantification. The majority of previous works on the application of SEM to the orientation of clay particles are descriptive. There have been some attempts to quantify orientation of clay particles automatically, although these earlier efforts involve deduction of particle orientation from certain proxies (Sokolov and O'Brien, 1990; Tovey *et al.*, 1992; Martínez-Nistal *et al.*, 1999).

It is important to separate out measurements for silt and clay-size particles and to filter for elongate grains. It is also important to use circular statistical and entropy measures in conjunction with visual observation, as the circular statistical parameters are less reliable with multimodal orientation data (Fisher, 1993; Mardia and Jupp, 2000). An important result of this study is to demonstrate that silt orientation is a very good proxy for clay orientation. The results show an approximately equal spread of random and preferred fabrics (oblique), which is suggested characteristic for hemipelagites (see discussion below). The slightly oblique to horizontal orientation, common to a number of subsets, may in some cases be due to a bedding curvature induced by the coring process, which is especially common at the very edge of cores. However, in most cases it is suggested that the grain alignment is due to the bioturbational fabric.

5.4.1.3 Mineralogy

By contrast, AIAA does not appear to be such a good method for determining the sediment composition or, at least, not by using the SEM-EDX methodology in this study. There is poor agreement between subsets of the same sample as well as significant differences in mineral composition at the two scales of resolution used (i.e. 2 µm and 63 nm per pixel). There is also poor agreement with the composition data obtained from the same samples by XRD measurement. Problems encountered with the AIAA technique include: (a) an over-estimation of the dominant minerals present; (b) separation of calcite grains encased within a clay matrix; and (c) the separation of detrital mica silt grains (muscovite, biotite) from clay-fraction illite. Furthermore, high-resolution EDX maps of large areas is time-consuming and runs to several gigabytes of data, which is difficult to handle. The high-resolution EDX maps presented here are limited to about 4200 μm^2 and these are unlikely to be representative.

SEM-EDX does have the advantage of determining the mineralogy of specific grains and of making a visual assessment of their morphology or crystallinity and likely diagenetic or detrital origin. It can be used to pick out important heavy mineral components, such as the anatase and pyrite as observed in this study, which may be useful for provenance or digenetic studies. However, further work is needed to enable the effective application of AIAA. This should also include calibration of results with whole-rock x-ray fluorescence techniques.

5.4.1.4 Porosity

The usage of image analysis for determining porosity and pore size distribution is not well established compared to the more traditional methods, but the process involved is both easy and highly effective. Whereas previous work on pores and pore networks has mostly been qualitative (Desbois, Urai and Kukla, 2009; Loucks *et al.*, 2009; Curtis *et al.*, 2010; Curtis *et al.*, 2012a; Loucks *et al.*, 2012), here AIAA was used for quantitative analysis, with minimal user-bias, using high-resolution SEM images. From the results presented here, there is relatively little variation between subsets of pore size distribution, which suggests repeatable results. The normal to slightly skewed distribution curves most likely reflect a close link to the grain-size distribution. The variation in porosity evident among subsets of the same sample is likely to be due to mudrock heterogeneity. Mapping the geometry of porosity distribution allows an inference about the connectivity of porosity and therefore provides a qualitative measure of permeability.

The majority of pores in mudrocks are within the microscale (< 2nm) and mesoscale (2-50 nm) (Kuila and Prasad, 2013; Wang *et al.*, 2014). Microporous mudrocks have a high capacity for gas adsorption (Yang, Ning and Liu, 2014). For this study by AIAA, due to the spatial resolution limit of the SEM image, pores less than 15 nm were discounted in order to improve the signal to noise ratio. This technique, therefore, misses the percentage of the pores within micropore (< 2 nm) range, as well as some of the mesopores. The most common techniques currently used to determine pore size and porosity of mudrocks also have limitations in their measuring capabilities (Figure 5.12). Nitrogen or carbon dioxide gas adsorption and NMR are suitable for measuring at the mesopore scale, whereas helium porosimetry and water intrusion porosimetry can measure the full range of pore sizes (Figure 5.12).

The AIAA technique with SEM, however, has the added benefit of being able to place pores within their spatial context, which cannot be done with other techniques. Higher resolution

SEM than the one used for this study and helium ion beam microscopes (HIM) can provide some useful data on smaller pores, and HIM has better image clarity especially at lower kV.

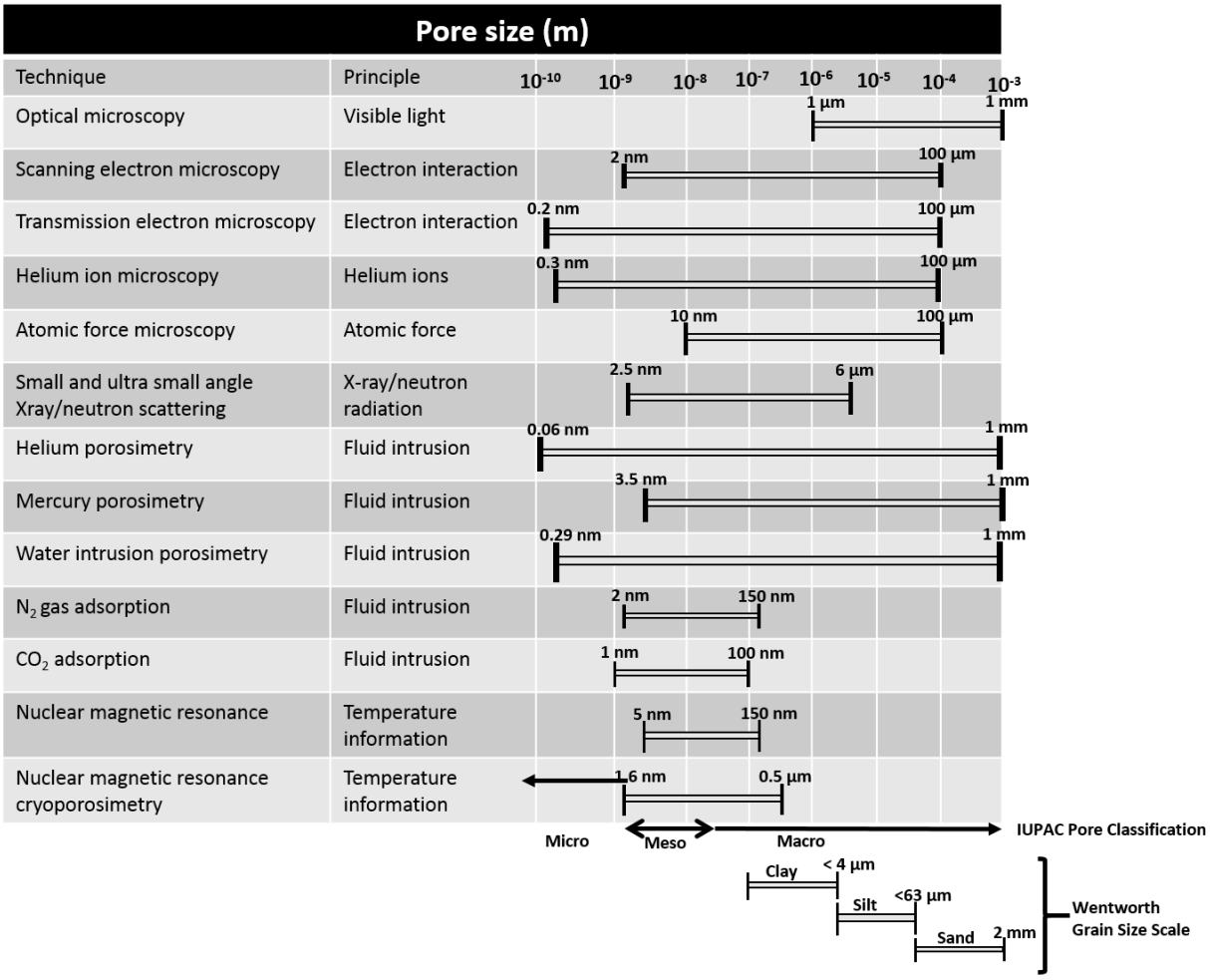

Figure 5.12. Array of techniques for determining pore size and porosity. The variation in the measuring capabilty of one technique to the order is several orders of magnitude. The technique applied in the research for measuring pores and porosity is the scanning electron microscopy and its spacial resolution is limited to 5 nm (Bankole *et al.*, 2018a).

5.4.2 Hemipelagites

The Shackleton Site 1385 was originally selected for construction of a marine reference section of Quaternary millennial-scale climate variability (Hodell *et al.*, 2013; Stow *et al.*, 2013). What was required was a site with a continuous sedimentary record and relatively 'high' rates of hemipelagic sedimentation to allow better resolution. Site 1385 was located at a water depth of 2589 m on a spur of the Iberian margin, away from any potential turbidity current pathways and outside the slope region affected by the Mediterranean Outflow Water bottom currents.

The 160 m section cored satisfied the criteria of a continuous sedimentary record, but it is also important to understand in detail the nature of sediments recovered at this marine reference site.

5.4.2.1 Classical Hemipelagites

The entire section is made up of classical hemipelagites of mixed terrigenous-biogenic composition and a silt-rich terrigenous fraction – the marl-hemipelagite category of Stow and Tabrez (1998) and (Stow, Huc and Bertrand, 2001). They show no primary sedimentary structures, but pervasive bioturbation. The trace fossil assemblage documented here is characteristic of the deep-water *Zoophycos* ichnofacies (Uchman and Wetzel, 2011; Wetzel and Uchman, 2012) an indicator of well-oxygenated bottom waters and pore waters as well as good availability of organic matter and other nutrients. Several tiers of burrowing are evident, which suggests the thorough mixing of sediment over a few cm of section and partial mixing up to tens of cm. Two earlier papers (Rodríguez-Tovar and Dorador, 2014; Rodríguez-Tovar *et al.*, 2015) have presented the results of more detailed studies of trace fossils at the Shackleton Site. They note a very similar ichnofacies assemblage and tiering structure to that presented here, with the addition of *?Scolicia* and *?Nereites* traces, as well as evidence for periods with less well-oxygenated conditions.

The mean sedimentation rate at the Shackleton Site of just over 11 cm/kyr for the past 1.4 Myr is typical of open slope hemipelagites with moderate fluvial/eolian supply of terrigenous material. The Holocene rate is slightly higher, about 20-25 cm/kyr, which may reflect an increase in both biogenic and terrigenous supply during this period. The sediments are all very fine clayey silts and silty clays and moderately well sorted with a unimodal grain-size distribution, which is compatible with the mixed biogenic-terrigenous model of Stow and Tabrez (1998) and similar to the results obtained by (Nishida, 2016).

5.4.2.2 Microstructures

The sediment microstructures observed are mainly of random or mixed (polymodal) particle alignment and a secondary preferred grain alignment. There are few prior observations in the literature, but those summarised in Stow and Tabrez (1998) suggest that open-water hemipelagites are characterised by a partially sub-parallel (preferred) alignment that is disrupted into a random or mixed fabric by bioturbation and by the presence of larger grains, such as foraminifera. The results presented here would tend to support this interpretation, although the high-angle preferred grain alignment in four subset samples is interpreted as the

re-alignment of particles along the walls of sub-vertical burrows. The slightly oblique grain alignment may also reflect the bioturbational fabric. However, (Nishida, 2016) found only random fabrics in the Shackleton Site hemipelagites, which he interprets as the result of the vertical aggregation of loosely-bound flocs in the absence of current shear caused by either bottom currents or turbidity currents (Moon and Hurst, 1984).

The results presented herein clearly demonstrate the small-scale and micro-scale heterogeneity of mudrock properties. This can only be effectively elucidated by large-area imaging of multiple subsets. Further work is required, particularly to compare hemipelagite, contourite and turbidite mud fabrics (Nishida, 2016) and to consider the nature of fabric re-orientation with burial compaction (Douglas, Gerhard and Alyssa, 2016). The samples used range in burial depth from 10 m to 80 m, so that little obvious compaction effect is expected. However, it is noted that the deepest sample (number 5) does show the most consistent parallel grain alignment of all the samples.

5.4.2.3 Hemipelagic Deposition

The lithology, ichnofacies, composition, grain size and microstructural character of the hemipelagites at the Shackleton Site all support their deposition by vertical settling coupled with very slow lateral advection, as invoked by previous studies (Hesse, 1975; Stow and Tabrez, 1998; Hoogakker *et al.*, 2004). The vertical settling component comprises biogenic planktonic material, wind-derived or storm-stirred terrigenous material, and material eroded from the seafloor by the action of internal tides and waves. The lateral advection of largely terrigenous material within the water column occurs as cross-shelf nepheloid-layer transport, eddies that peel off from along-slope bottom currents, and from the finest portions of low-concentration turbidity currents that become detached along density discontinuities. Progressive seaward distribution can occur via a process of suspension cascading.

The colour cyclicity observed, which reflects variation in the detrital/biogenic ratio in the sediments, is probably caused by variation in the flux of silt and clay material from the continent rather than by changes in carbonate productivity (Hodell *et al.*, 2015). These cycles are non-regular in thickness, but on average are close to 20 kyr in duration – i.e. precession cycles (Hodell *et al.*, 2015).

5.5 Conclusion

Microstructure is an important attribute that controls petrophysical properties of mudrocks and consequently the movement of fluid within them as well as their seismic elasticity. Scanning electron microscopy has advanced knowledge of microstructural characteristics, but understanding this complex and highly heterogeneous sediment type is still limited. Hemipelagic muds are very common in the marine environment, and one of the principal sediment types in deep-water. This study, therefore, has used samples of hemipelagites from the Iberian margin (Shackleton Site) to both develop an improved methodology for their microstructural characterisation, and advance the knowledge of hemipelagic sedimentation in general.

This study has developed a new methodology for the fast, reliable and effective characterisation of microstructure in mudrocks. Good sample preparation techniques are the first important step. The method has the following principal advantages: (a) a high degree of automation, which increases efficiency and reduces user-input and bias; (b) maximum areal coverage by using automated tiling and stitching of images; (c) quantification of orientation measurements; and (d) the ability to derive high quality data on grain size, grain orientation, pore size and porosity at the same time.

There are some disadvantages, which include: (a) the requirement for very large datasets (gigabytes per image), which has implications for computer memory and data handling; (b) the need for image segmentation, which is a non-trivial exercise requiring user input; (c) lack of resolution at the nano-scale for micropore characterisation. Further refinement of the technique and the use of higher-resolution instrumentation should help resolve these issues. The method also requires development to allow better compositional analysis.

The study has also provided important data on the nature of hemipelagic sedimentation at the Shackleton Site (IODP Site 1385) on the Iberian margin, and their deposition from a combination of vertical settling and very slow lateral advection. The sediments are typical mixed biogenic-terrigenous, silt-rich hemipelagites, with a tiered and diverse trace fossil assemblage of the deep-water *Zoophycos* ichnofacies. Sedimentation has been continuous at the site at an average rate of accumulation of 11 cm/kyr over the past 1.4 Myr, and showing a pronounced but non-regular colour cyclicity. The site is well-placed to become a valuable

marine reference section for Quaternary climate change (Hodell et al., 2015). The sediment microstructures show small-scale heterogeneity in all properties, and an overall random fabric with secondary preferred grain-alignment. These results on the fabric differ, in part, from previous studies and suggest that further work is required on the microstructure of hemipelagites and their comparison with different deep-water sediment facies.

CHAPTER 6 – DEEP-WATER MUDROCK MICROSTRUCTURE

6 Deep-water mudrock microstructure results

6.1 Introduction

The microstructure of mudrocks includes a range of microscopic characteristics, including grain size, microfabric (grain orientation and arrangement), mineralogical composition, and petrophysical properties – porosity, pore volume, permeability and specific surface area. In mudrocks, the diameter of grains ranges between submicron and 63 microns. It is this very fine grain size that makes their study so challenging, and for which high-resolution instrumentation and careful, time-consuming analyses are required.

In the deep-water, sediments are deposited via three principal mechanisms and commonly occur in complex associations of three facies; turbidites generated from downslope process, contourites produced by bottom currents, and hemipelagites deposited by slow vertical settling coupled with very slow lateral advection. There is a great challenge associated with distinction between end-members of the deep-water facies (Stow *et al.*, 1998) especially from a lithological point of view, with each end-member failing to exhibit unique sedimentary features (Dall'Olio, Felletti and Muttoni, 2013 and reference therin). In part, this lack of distinction may be due to the process continuum that exists between turbidity currents, bottom currents and vertical settling out of suspension (Stow, 1985b; Mulder, Faugères and Gonthier, 2008).

Whereas many previous researchers have investigated clay orientation microfabric, relying on either visual judgement or more quantitative approaches (Ho, Peacor and van Der Pluijm, 1999; Charpentier *et al.*, 2003; Aplin *et al.*, 2006; Janssen *et al.*, 2012; Day-Stirrat, 2014), few have considered mudrock microfabric in the context of depositional process. In this study, mudrocks of different facies and depositional processess (bottom currents, hemipelagic processes and turbidity currents) were assessed for their microstructure using high-resolution scanning electron microscopy, and low-pressure nitrogen gas adsorptiom in combination with digital rock physics, in order to differentiate among them based on their microstructure and also to understand the important factors that affect microstructure of mudrocks in the deep-water setting.

Having developed the methodology and workflow for mudrock investigations, preliminary results on grain-size analysis were presented in Chapter 4 (Bankole *et al.*, 2018b), and on microstructure of hemipelagites in Chapter 5 (Bankole *et al.*, 2018a). This chapter collates all the results on the microstructure of the different deep-water mudrock facies examined. It also presents the first preliminary results from an ultra-high-resolution experiment using the European synchrotron facility in Grenoble, France. The aim of this experiment was to use whole-rock, x-ray powder-diffraction patterns to characterise the crystallographic axes of component minerals, and so complement the SEM microfabric analyses. Full discussion of the results is provided in chapter 7.

6.2 Results

6.2.1 Lithological characteristics

6.2.1.1 Contourites

During expedition 339, sediments of contourite deposits were recovered from six sites (1386 to 1391) in the Gulf of Cadiz. Overall, the contourites from these sites are uniform in colour and composition. They comprise an admixture of biogenic components (mainly nannofossils and foraminifera) and terrigenous particulates (mainly clay minerals, quartz and detrital carbonate). Other components are present in minor or trace amounts (Expedition 339 Scientists, 2013). They show a distinctive, though often subtle, cyclicity in grain size, from mud to silty mud to silty sand, then back to silty mud and mud. This is the characteristic bi-gradational sequence of a typical contourite (Gonthier, Faugères and Stow, 1984). A range of partial bi-gradational sequences are also present, as well as sandier contourites at the more proximal site.

Bedding is very indistinct and most contacts between individual sequences and parts of the sequence are wholly gradational. In general, there are no primary sedimentary structures observable in the contourite facies but there is conspicuous mottling throughout caused by moderate bioturbation (Figure 6.1). The sediment accumulation rate varies from one site to another, averaging 35 cm/ky at site 1387, 25-27 cm/ky, at sites 1386 and 1391, 25-40 cm/ky at site 1389, and more than 100 cm/k.y at site 1389. Site 1388 is the most proximal site with abundant sandy contourites, and so was not examined for this thesis.

6.2.1.2 Hemipelagites

The hemiplegic facies were recovered from site 1385 (IODP Expedition 339) along the continental slope of the Iberian margin. Detailed lithological characteristics of the hemipelagic facies from this site are documented in Chapter 5 (section 5.3.1). In summary, the hemipleagite

facies are uniform consisting of admixture of calcareous nannofossils and terrigeneous material and are extensively bioturbated (Figure 6.2). Typical trace fossils recognized from these facies are: *Chondrites, Thalassinoides, Planolites and Zoophycos* among others.

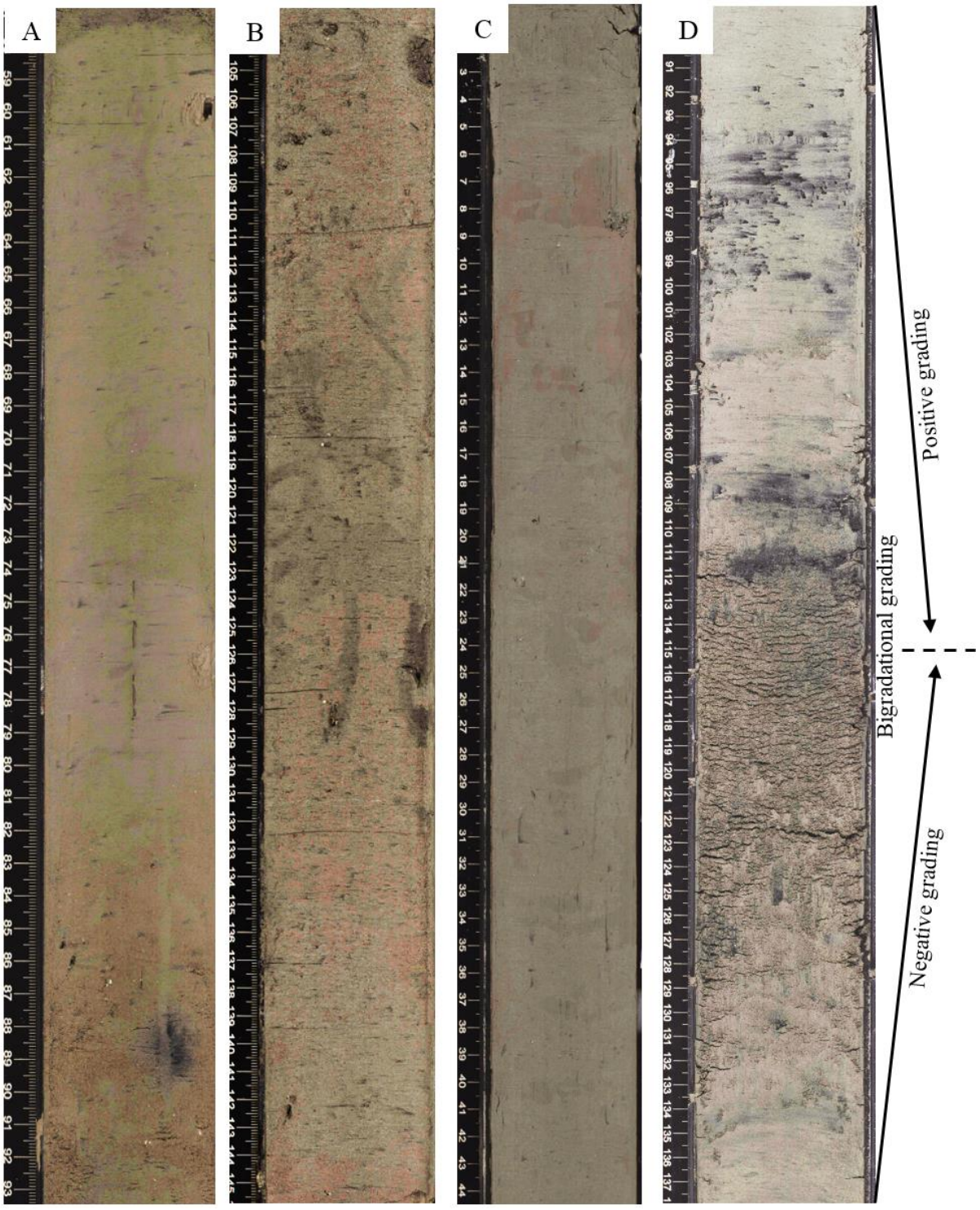

Figure 6.1. Muddy contourite facies showing varying degree of mottling due to bioturbation. All the core photographs are from expedition 339 of the IODP (A) site 1387B-2H-5A (B)1389A-2H-6A (C) 1389A-7H-1A (D) 1390A-7H-4A. Note that the the presence of bigradational grading in core 1390A-7H-4A.

Figure 6.2. Core photographs showing typical hemipelagite facies from site 1385 of expedition 339 with pervasive mottling. The core photos display intense bioturbations and distinct colour cyclicity, in which lighter grey intervals have more of biogenic carbonate and darker grey intervals are rich in terrigenous components. Ch- *Chondrites*, Pl-*Planolites*, Tha-*Thalassinoides*, Z-*Zoophycos*. (A)1385E-6H1-A (B)1385A-10H-7A (C) 1385E-6H-1A (D) 1385A-7H-1A (E) 1385A-11H-3A.

6.2.1.3 Turbidites

Turbidite facies recovered from site 1457 of expedition 355 are part of the Indus fan. The sediments are made up of terrigeneous sediments (silty clay and silty sand). The sequence of turbidites from the Indus fan are thin-bedded or medium bedded. Much of the succession comprises mud-rich distal turbidites, whereas parts are more sand-prone. Most of the turbidites have a sharp erosive base and show clear normal grading. The silt-mud turbidites are generally structureless, at least under visual inspection, but typically show very thin to thin sandy silt layers at the base. The common primary structures in these lower divisions are parallel lamination, lenticular lamination and micro-cross-lamination. The turbidite facies are mostly non-bioturbated, but with rare bioturbation restricted to the upper parts of beds.

Figure 6.3. Core photograph of typical turbidite facies from site 1457 of expedition 355.The turbidite sequences are characterised by dark gey sandy silt or silt and normal grading to pale grey mud. Ts- Thin layer of silty sand, Es- Erosional surface. (A) 1457A-8H-2A (B) 1457A-1F-1A (C) 1457C-9R-1A (D) 1457C-38R-2A.

6.2.2 Grain-size results

Grain size analyses were carried out on 196 samples from the three locations – Gulf of Cadiz (contourites), SW Iberian margin (hemipelagites) and the Indus Fan (turbidites). Of these, 38 samples were selected for microstructural analyses using scanning electron microscopy and image analysis. For each sample, between 4-6 separate areas were selected at random, for analysis, so that a total of nearly 350 automated image analysis results were obtained. The complete grain size results including statistical parameters are presented in Appendix 3A. Grain size results for the samples analysed with both techniques are presented in Table 6.1.

Contourite facies are medium silt to coarse clay with mean size ranging between 5.96 and 8.91 phi values. Out of the 64 samples of contourite facies analysed, about 28% are coarse clay, 53% very fine silt, 17% fine silt, and approximately 2% are medium silt. The contourite facies are generally very poorly sorted but with occasional poor sorting. The skewness varies from symmetrical to very fine skewed. Most samples are platykurtic, but some are mesokurtic.

Hemipelagites are very fine grained, with a mean size between very fine silt and very fine clay, i.e. between 7.63 and 12.27 phi. Based on the number of samples analysed, most of the hemipelgite facies fall within the coarse clay grain size (63%), 15% are very fine silt, 14 % are fine clay, and 8% are medium clay. In terms of sorting characteristics, they are generally poorly sorted, while a few samples of the hemipelagites are moderately well sorted and very poorly sorted. In terms of skewness, the hemipelagite facies are mostly fine skewed but symmetrical distribution is also common. Results of kurtosis show that a large percentage of hemipelagites are mesokurtic and the rest platykurtic.

The mean grain size of turbidite facies ranges between medium silt (5.43 phi) and very fine clay (11.22 phi). About 50% of the samples fall within the silt grain size, whereas the other 50% are clay size (Table 6.2). Most are poorly sorted while a few are moderaletly sorted or very poorly sorted. In terms of skewness, they are rather diverse but generally fine skewed and symmetrical. More than 60% of the turbidite facies are platykurtic and the rest are mesokurtic.

Table 6.1. Grain size statistics for those selected samples that were analysed using automated image analysis technique.

S/N	Sample ID	Sediment type	Mean size	Sorting	Skewness	Kurtosis
1	339-1387B-2H1 032-034	Contourite	V. Fine Silt (7.57)	Very Poorly Sorted	Fine Skewed	Mesokurtic
2	339-1387B-2H1 128-130	Contourite	V. Fine silt (7.31)	Poorly Sorted	Fine Skewed	Mesokurtic
3	339-1390B-2H4 7-9	Contourite	Fine silt (6.17)	Very Poorly Sorted	Very Fine Skewed	Platykurtic
4	339-1390B-2H5 22-24	Contourite	Fine Silt (6.23)	Very Poorly Sorted	Very Fine Skewed	Platykurtic
5	339-1387B-2H5 67-69	Contourite	Coarse Clay (8.21)	Very Poorly Sorted	Very Fine Skewed	Mesokurtic
6	339-1389A-6H1 28-30	Contourite	Coarse Clay (8.17)	Poorly Sorted	Symmetrical	Platykurtic
7	339-1389A-18X1 125-127	Contourite	V. Fine Silt (7.5)	Very Poorly Sorted	Fine Skewed	Platykurtic
8	339-1389A-28X5 130-132	Contourite	V. Fine Silt (7.32)	Very Poorly Sorted	Symmetrical	Platykurtic
9	339-1389A-38X2 112-114	Contourite	V. Fine Silt (7.32)	Very Poorly Sorted	Fine Skewed	Platykurtic
10	339-1386C-17R1 46-47	Contourite	Coarse Clay (8.21)	Very Poorly Sorted	Fine Skewed	Platykurtic
11	339-1389E-26R3 61-63	Contourite	V. Fine Silt (7.78)	Very Poorly Sorted	Fine Skewed	Platykurtic

12	339-1389E-35R5 60-61.5	Contourite	Fine Silt (6.97)	Very Poorly Sorted	Fine Skewed	Platykurtic
13	339-1387C-48R3 33-35	Contourite	Coarse Clay (8.04)	Poorly Sorted	Fine Skewed	Mesokurtic
14	339-1389E-47R2 22-24	Contourite	V. Fine Silt (7.28)	Very Poorly Sorted	Fine Skewed	Platykurtic
15	339-1387C-56R1 8-10	Contourite	Coarse Clay (8.17)	Poorly Sorted	Fine Skewed	Platykurtic
16	339-1389E-57R3 12-13.5	Contourite	V. Fine Silt (7.60)	Very Poorly Sorted	Symmetrical	Mesokurtic
17	339-1389E-66R1 18-21	Contourite	V. Fine Silt (7.99)	Very Poorly Sorted	Symmetrical	Mesokurtic
18	339-1385A-2H6 13-15	Hemipelagite	V. Fine Silt (7.63)	Poorly Sorted	Fine Skewed	Mesokurtic
19	339-1385E-2H5 74-76	Hemipelagite	V. Fine silt (7.63)	Very Poorly Sorted	Symmetrical	Mesokurtic
20	339-1385D-2H6 115-117	Hemipelagite	V. Fine silt (7.64)	Poorly sorted	Fine skewed	Mesokurtic
21	339-1385A-6H2 49-51	Hemipelagite	Coarse Clay (8.99)	Poorly Sorted	Symmetrical	Mesokurtic
22	339-1385A-7H6 54-56	Hemipelagite	Coarse Clay (8.74)	Poorly sorted	Fine skewed	Platykurtic
23	339-1385E-7H2 113-115	Hemipelagite	Coarse Clay (8.27)	Poorly Sorted	Fine Skewed	Platykurtic

24	339-1385E 10H2 80-82	Hemipelagite	Coarse Clay (8.06)	Poorly Sorted	Fine Skewed	Platykurtic
25	339-1385A- 14H2 30-32	Hemipelagite	Coarse Clay (8.42)	Poorly sorted	Symmetrical	Mesokurtic
26	355-1457A- 8H1 38-42	Hemipelagite	V. Fine silt (7.28)	Poorly sorted	Fine skewed	Mesokurtic
27	355-1457A- 8H2 27-31	Turbidites	Coarse Clay (8.36)	Very Poorly Sorted	Very Fine Skewed	Platykurtic
28	335-1457A- 17F1 124-128	Turbidites	Fine silt (6.94)	Poorly Sorted	Fine Skewed	Platykurtic
29	355-1457C- 9R1 7-11	Turbidites	V. Fine Silt (7.68)	Poorly Sorted	Fine Skewed	Mesokurtic
30	355-1457C- 18R2 6-10	Turbidites	V. Fine Silt (7.13)	Poorly Sorted	Very Fine Skewed	Platykurtic
31	355-1457C- 29R1 99-103	Turbidites	V. Fine Silt (7.24)	Poorly Sorted	Fine Skewed	Mesokurtic
32	355-1457C- 38R1 43-45	Turbidites	Coarse Clay (8.27)	Very Poorly Sorted	Very Fine Skewed	Mesokurtic
33	355-1457C- 38R2 124-126	Turbidites	Coarse Clay (8.33)	Poorly Sorted	Symmetrical	Mesokurtic
34	355-1457C- 49R6 30-34	Turbidites	Coarse Clay (8.6)	Poorly Sorted	Fine Skewed	Platykurtic
35	355-1457C- 61R3 11-15	Turbidites	Medium Clay (9.17)	Poorly Sorted	Fine Skewed	Platykurtic

36	355-1457C-67R3 4-8	Turbidites	V. Fine Silt (7.66)	Poorly Sorted	Fine Skewed	Platykurtic
37	355-1457C-71R4 63-67	Turbidites	Medium Clay (9.5)	Poorly Sorted	Symmetrical	Platykurtic
38	355-1457C-83R6 5-6	Turbidites	V. Fine Silt (7.98)	Very Poorly Sorted	Symmetrical	Platykurtic

Table 6.2. Grain size data based pon all analysed samples.

Grain size	Contourites (%) Gulf of Cadiz	Hemipelagites (%) Iberian Margin	Turbidites (%) Indus Fan
Coarse silt	-		
Medium silt	2		4
Fine silt	17	14	7
Very fine silt	53	15	42
Coarse clay	28	63	21
Medium clay	-	5	12
Fine clay	-		12
Very fine clay	-	3	2

Although these data show that contourite facies analysed are, on average, slightly coarser grained, and the hemipelagites are slightly finer grained, the grain sizes are sufficiently similar that valid comparisons of microstructures can be made. The turbidites span the grain size range of both contourites and hemipelagites. A plot of the clay, silt and sand fractions on a ternary diagram show the three facies plot within the silt-clay region (Figure 6.4). This also illustrates the slight differences in grain size among the three sediment types, and the overall range of mean size.

Bivariate plots of grain size statistical parameters, including mean size versus sorting, kurtosis and skewness, present interesting results, in which some differences are clearly depicted on the graphs. Turbidite facies plot across both contourites and hemipelagites. However, plots of these statistical parameters excluding turbidite samples show a more distinct boundary between countourites and hemipelagites, but still with a region of overlap (Figure 6.5B, Figure 6.6B, and Figure 6.7B). More significant are the trends between different variables, which apply to all three facies. Mean size and sorting show a strong positive correlation, with a marked

improvement in sorting for finer grain sizes. There is a less good positive correlation between mean size and skewness, but no apparent correlation between mean size and kurtosis.

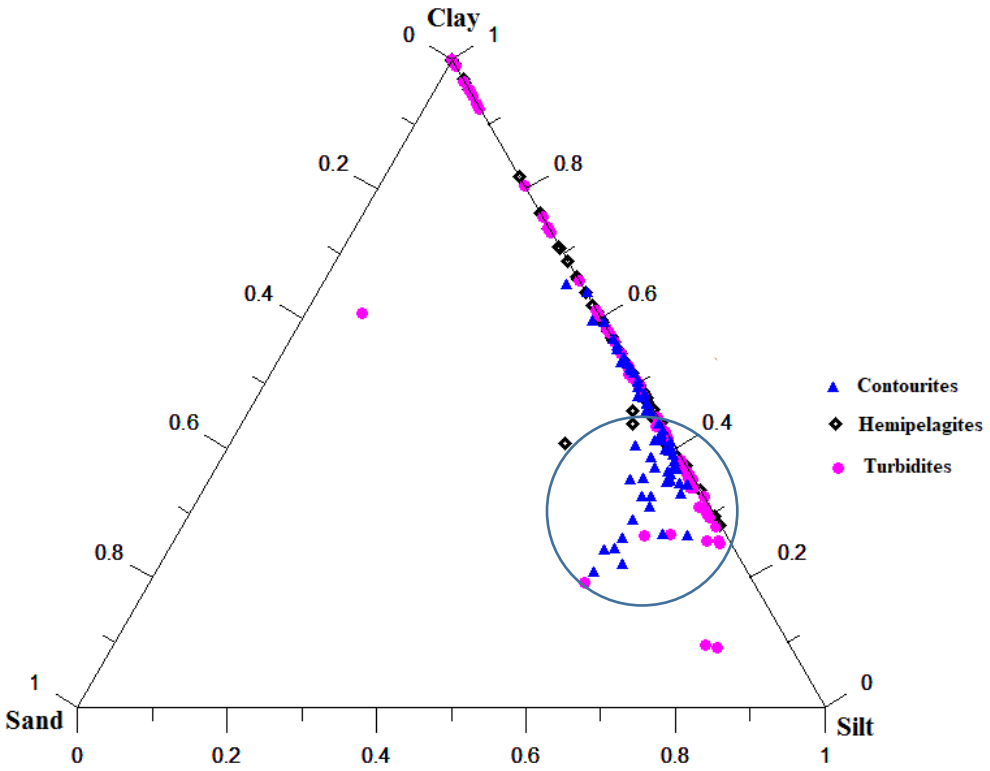

Figure 6.4. Ternary plot of percentage clay, silt and sand size percentage. The plot shows the subtle grain size difference among contourites, hemipelagites and turbidites. There is progressive increase in grain size from hemipelagites to turbidites to contourite, as shown within the circle, but many turbidites are also very fine gained. The number samples plot on the ternary diagram are 196.

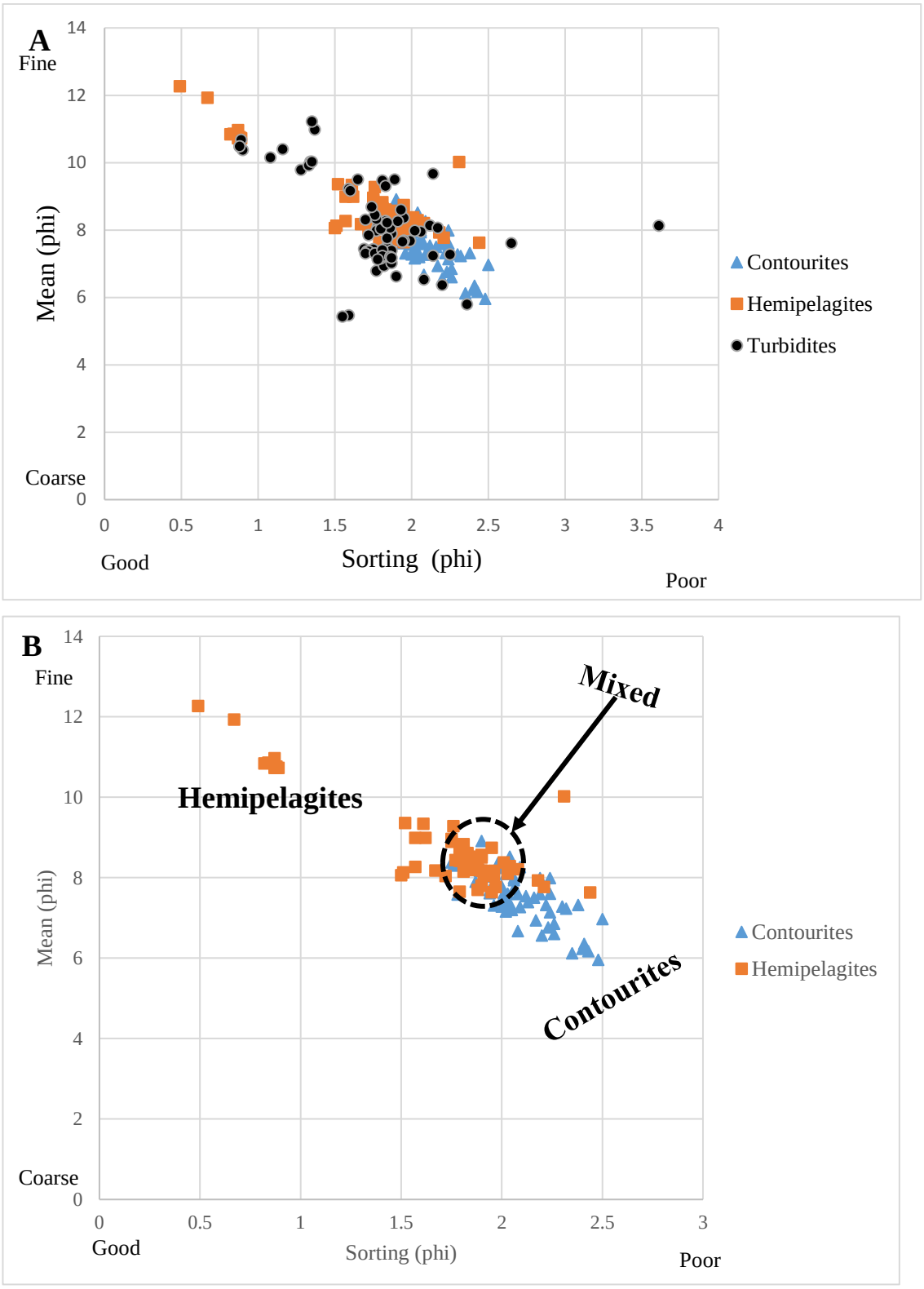

Figure 6.5. Bivariate plot of sorting (inclusive standard deviation) versus mean. In (A) Turbidite facies are plot in both contourite and hemipelagite areas. (B) When turbidite is excluded from the plot, there is a distinct boundary between contourites and hemipelagites but with a mixed region of contourites and hemipelagites.

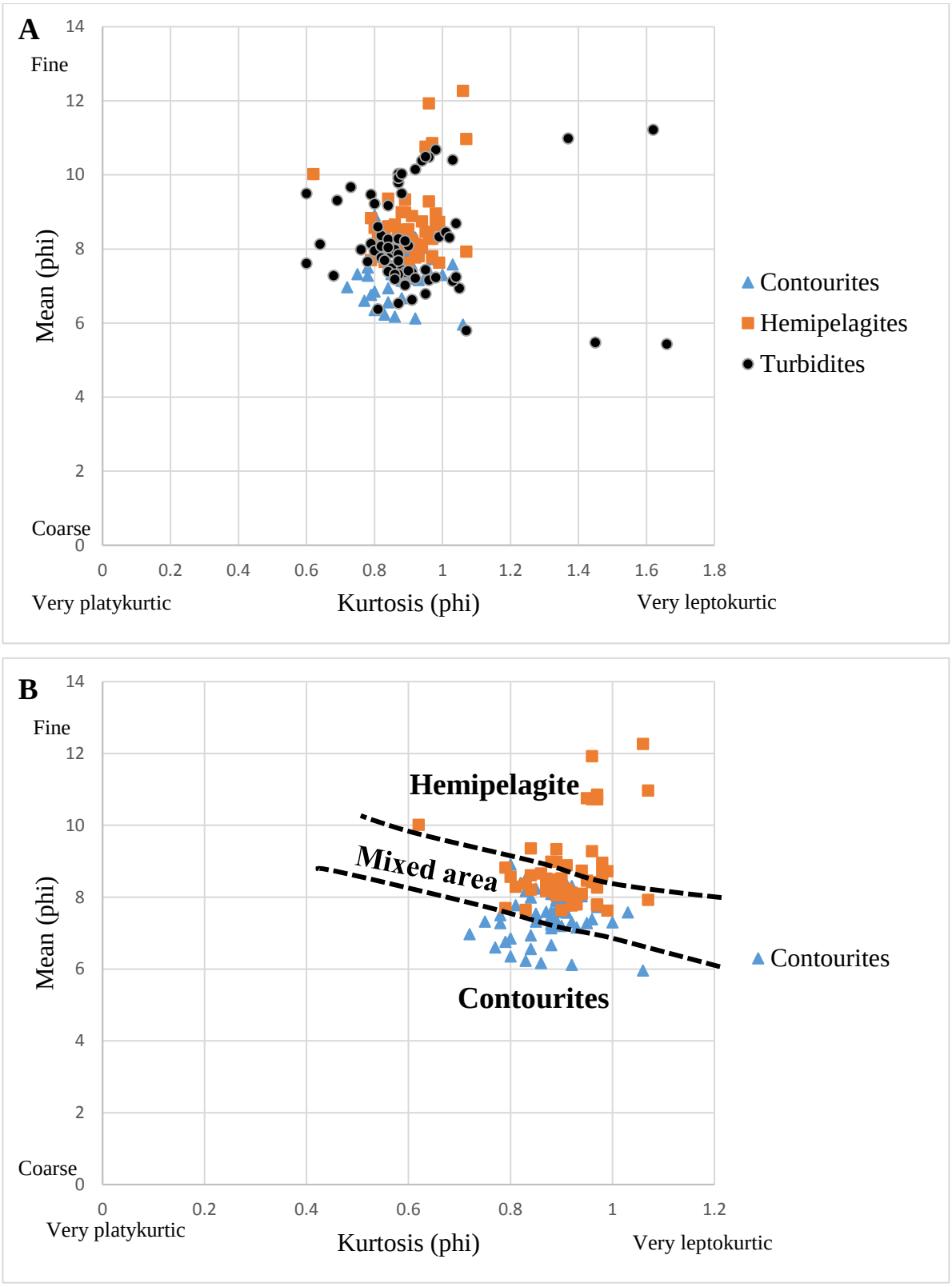

Figure 6.6. Cross plot of Kurtosis versus mean grain size. (A). There is no clear boundary between turbidites and contourites and between turbidites and hemipelagite. (B) There is a unique boundary between contourites and hemipelagites.

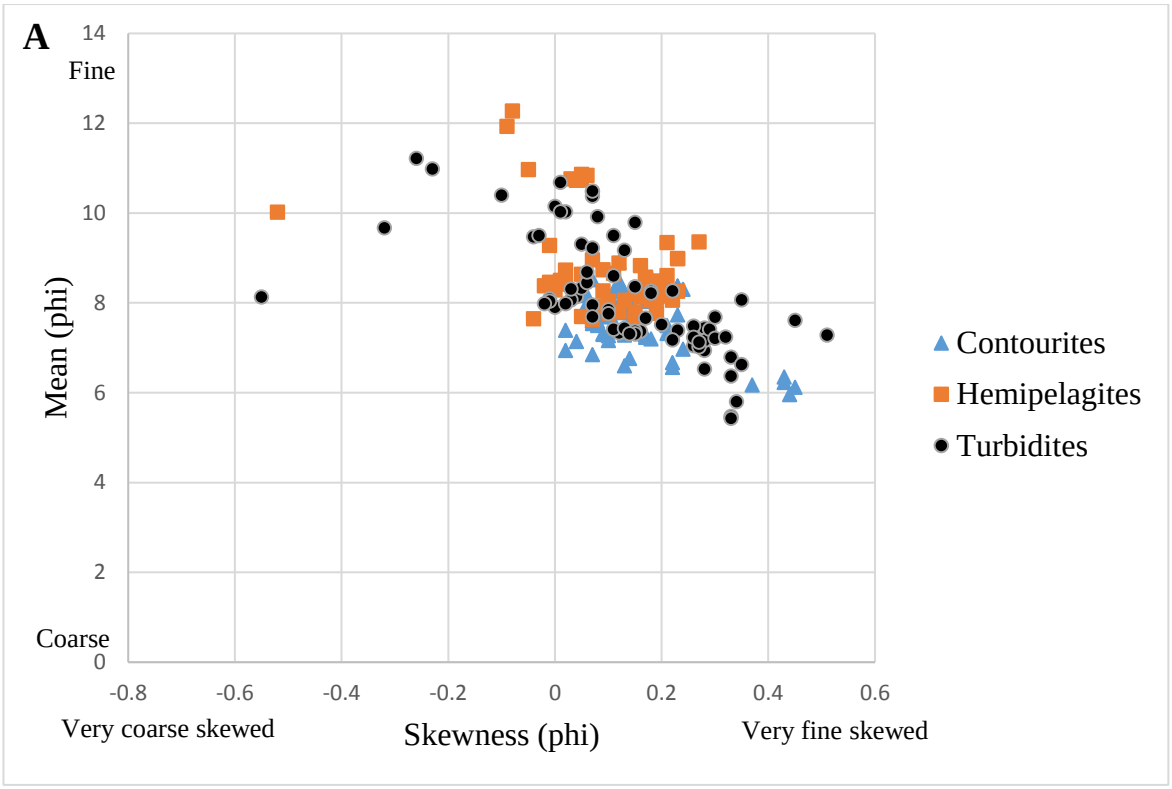

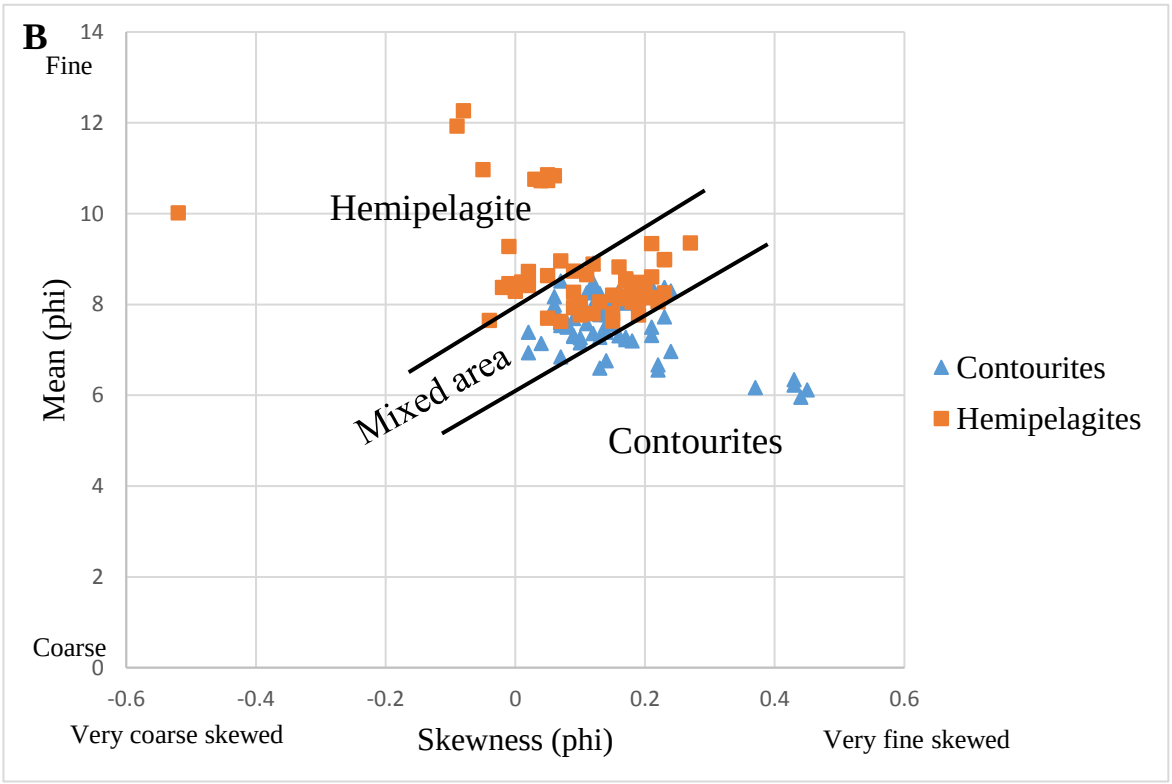

Figure 6.7. Bivariate plot of skewness versus mean (A) for all the three facies with turbidites plotting in both contourites and hemipelagites regions (B) for contourites and hemiplegite which shows obvious boundary between the two sediment types and a mixed area of both contourites and hemipelagites.

6.2.3 Visual estimation based on SEM images

The summary of the microfabric and composition estimated through visual inspection of the randomly selected large areas (ca. approximately 0.65 mm by 0.42 mm) high resolution SEM (45 nm per pixel) is presented in Table 6.3 while the SEM images for the different facies are given in Appendix 3B.

Contourites generally have coarse grains embedded within the matrix. The coarse grains in the contourite facies form a grain supported pattern in which the coarser grains are in contact with each other, but matrix supported pattern are not also uncommon. The microfabric of contourite facies is generally random (Figure 6.8) but occasionally exhibits oblique pattern that is nearly perpendicular to bedding at shallow depth Figure 6.8. At greater depth, more than 500 m, the microfabric of contourite facies show a combination of random fabric and bedding parallel. Mudclasts are ubibiquitous within the contourite facies ranging between 1 and 3% (Table 6.3 and Figure 6.8). The percentage composition of coccoliths in contourites varied widely between 1 and 15%. Estimated percentage for pyrite is generally low which is not more than 2%, but more common within matrix and foram chambers than in other facies. The silt size particles are very coarse (up to 60 μm in diameter) and they varied from ca. 16 % to 52 %. Contourite facies are characterised by burrows which are filled with pyrite. Other micro features present in the contourite facies are tunicate spicules and algae borings (Figure 6.9).

Hemipelagites are either siliciclastic dominated (Figure 6.10) or calcareous biogenic dominated (Figure 6.11). The differentiation is based on prevailing components. The hemipelagic facies are rich in calcareous nannofosils especially coccoliths which is not generally less than 7 % in the siliciclastic dominated hemipelagites but more than 50% in the calcareous biogenic dominated samples (Table 6.3). Hemipelagic sediments are thoroughly bioturbated and they have random microfabric but some show oblique pattern. At shallow burial depth close to the seafloor, the platy grains in the hemipelagites are nearly vertical to the bedding (Figure 6.10). The hemipelagic sediments are burrowed which are then filled by framboidal pyrites or with coarse silty grains (Figure 6.10B and Figure 6.11B). The hemipelagites generally consist of floating grains within the matrix in which case they are usually matrix supported except within burrows in which there might be in-filling of the burrows with coarse grained particles that are in contact with each other (Figure 6.11B). The rounded to angular grains within the hemipelagites are nearly of same size (Figure 6.10 and Figure 6.11). Forams are ubiquitous in the hemipelagites as well as other biogenic calcareous

materials. The silty grains can be up to 30 μm but they are dispersed within the finer grains and are not more than 30% of the material composition (Table 6.2 and Figure 6.10). Tunicate spicules is less common in hemipelagite facies and when present its structural pattern is different from those present within the contourite facies (Figure 6.12). The tunicate spicules recognised from hemiplegite is smaller in size (ca. 10 μm in diameter) when compared to those identified from contourites (ca. 20 μm in diameter).

Turbidite facies show well aligned fabric that is parallel to bedding and oblique pattern (Figure 6.13) but sub areas that are random are occasional present. Siliciclastic components dominate in the turbidite facies and they are associated with numerous platy like materials that are usually mica and clay platelets. Calcareous nanofossils (coccoliths) are not common within the turbidite facies and when they are present, they are usually less than 1%. Forams are not common components within the turbidite facies, but they were seen in some samples as part of the accessory components. Silt size particles in turbidite facies embedded within the matrix are finer than that of the contourites and the hemipelagites but show some level of uniformity and have closed contacts with each other which therefore impart grain-supported pattern. The silt size grains are generally not more than 15 μm and their percentage varies between ca. 6% and 59 %.

Table 6.3. Microfabric and estimated composition by paticle area based on visual inspection using chart for visual estimation of percentage (Terry and Chilingar, 1955).

S/N	Sample ID	Sediment type	Microfacric	Coccolith (%)	Mudclast (%)	Pyrite (%)	Forams (%)	Silt size grains (%)
1	339-1387B-2H1 032-034	Contourite	Random	1	2	-	1	41.6
2	339-1387B-2H1 128-130	Contourite	Random	2	2	< 1	< 1	46.5
3	339-1390B-2H4 7-9	Contourite	Random	3	1	< 1	1	50.1
4	339-1390B-2H5 22-24	Contourite	Random	2	2	<1	< 1	52.3
5	339-1387B-2H5 67-69	Contourite	Random-oblique	3	3	-	1	42.2
6	339-1389A-6H1 28-30	Contourite	Random	7	2	< 1	< 1	29.9
7	339-1389A-18X1 125-127	Contourite	Random	5	2	< 1	2	46.1
8	339-1389A-28X5 130-132	Contourite	Random	7	3	< 1	2	42.6
9	339-1389A-38X2 112-114	Contourite	Random	2	2	1	1	47.3
10	339-1386C-17R1 46-47	Contourite	Random	10	1	2	3	30.6
11	339-1389E-26R3 61-63	Contourite	Random-bedding parallel	5	3	1	2	39.1

12	339-1389E-35R5 60-61.5	Contourite	Random	7	2	2	3	46.4
13	339-1387C-48R3 33-35	Contourite	Random	15	< 1	1	< 1	28.2
14	339-1389E-47R2 22-24	Contourite	Random-bedding parallel	10	2	3	2	16.2
15	339-1387C-56R1 8-10	Contourite	Bedding parallel	15	2	-	5	30.3
16	339-1389E-57R3 12-13.5	Contourite	Bedding parallel	10	3	-	5	38.1
17	339-1389E-66R1 18-21	Contourite	Random	15	3	< 1	2	38.1
18	339-1385A-2H6 13-15	Heimelagite	Random	10	< 1	<1	2	25.1
19	339-1385E-2H5 74-76	Hemipelagite	Random	7	< 1	1	2	27.9
20	339-1385D-2H6 115-117	Hemipelagite	Random	12	-	-	1	40.6
21	339-1385A-6H2 49-51	Hemipelagite	Random	> 50	< 1	2	1	7.9
22	339-1385A-7H6 54-56	Hemipelagite	Oblique	7	-	-	7	18.1
23	339-1385E-7H2 113-115	Hemipelagite	Random	> 50	-	3	-	21.5
24	339-1385E 10H2 80-82	Hemipelagite	Random	>50	-	-	< 1	22
25	339-1385A-14H2 30-32	Hemipelagite	Random	> 50	-	< 1	3	25.1
26	355-1457A-8H1 38-42	Hemipelagite	Random	15	-	< 1	5	23
27	355-1457A-8H2 27-31	Turbidites	Oblique	< 1	< 1	1	2	58.7

28	335-1457A-17F1 124-128	Turbidites	Bedding parallel-Random	< 1	< 1	< 1	-	56.6
29	355-1457C-9R1 7-11	Turbidites	Bedding parallel	-	-	< 1	1	44.7
30	355-1457C-18R2 6-10	Turbidites	Random–bedding parallel	-	-	<1	-	53
31	355-1457C-29R1 99-103	Turbidites	Bedding parallel	-	< 1	< 1	-	51.9
32	355-1457C-38R1 43-45	Turbidites	Bedding parallel- oblique	-	< 1	-	-	27.4
33	355-1457C-38R2 124-126	Turbidites	Bedding parallel	-	-	< 1	-	28
34	355-1457C-49R6 30-34	Turbidites	Bedding parallel	-	-	< 1	< 1	53.4
35	355-1457C-61R3 11-15	Turbidites	Bedding parallel	< 1	< 1	-	-	6.6
36	355-1457C-67R3 4-8	Turbidites	Bedding parallel	-	<1	< 1	-	42.4
37	355-1457C-71R4 63-67	Turbidites	Bedding parallel	< 1	-	< 1	< 1	5.6
38	355-1457C-83R6 5-6	Turbidites	Bedding parallel	-	-	< 1	< 1	35.1

Note that the silt size percentage was quantitatively derived from grain size analysis through laser diffraction granulometry. Other features are from visual estimation based on average value derived from 4-6 large scale high resolution SEM images with approximate area of about 0.65 mm by 0.42 mm.

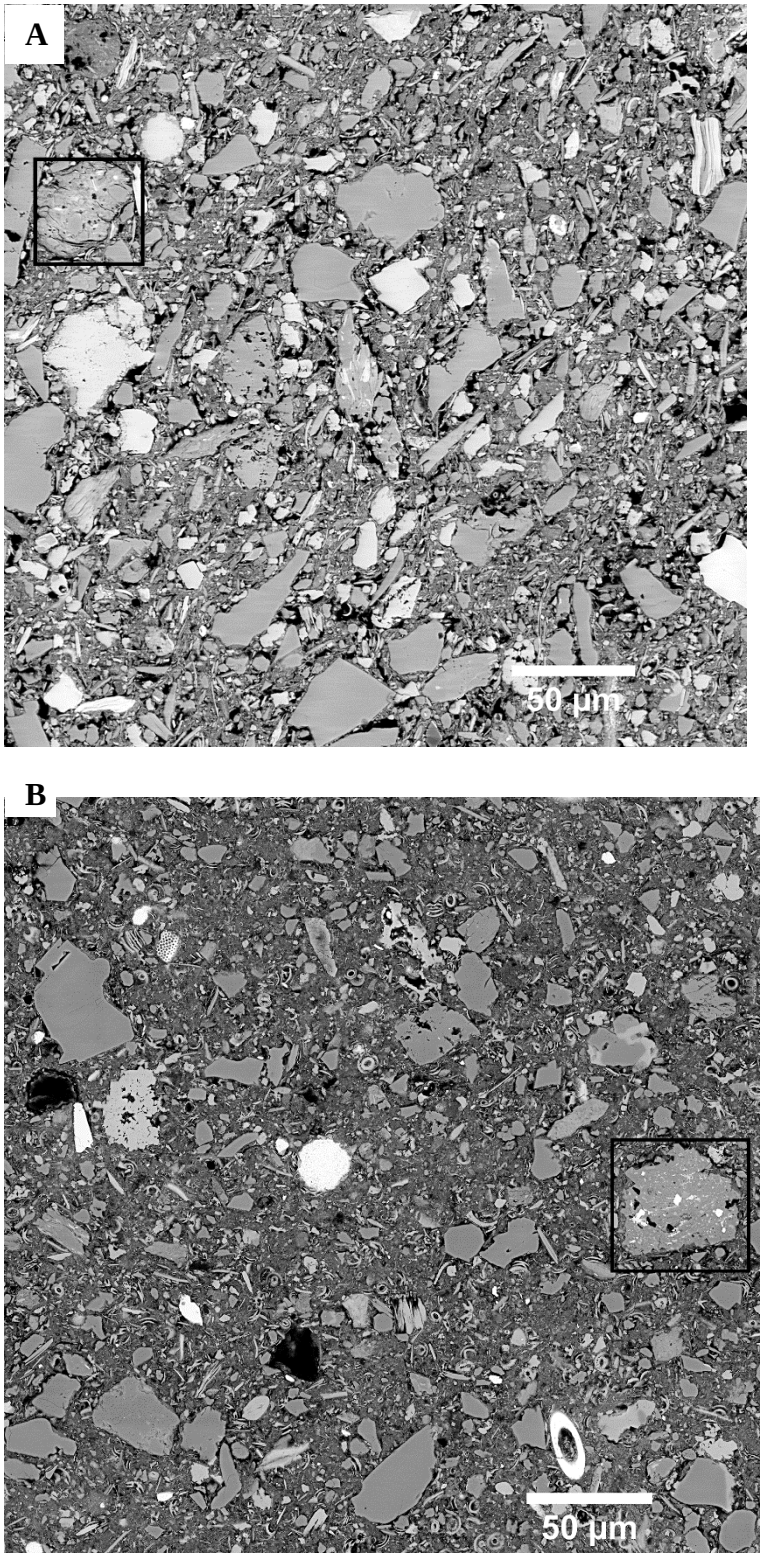

Figure 6.8. BSE-SEM images of typical contourite facies showing their microfabric. In both A (sample 1) and B (sample 10) the fabric is chaotic, while A displays grain-supported fabric, B shows matrix supported. Mudclast associated with contourite facies are marked within the square boxes in both A and B.

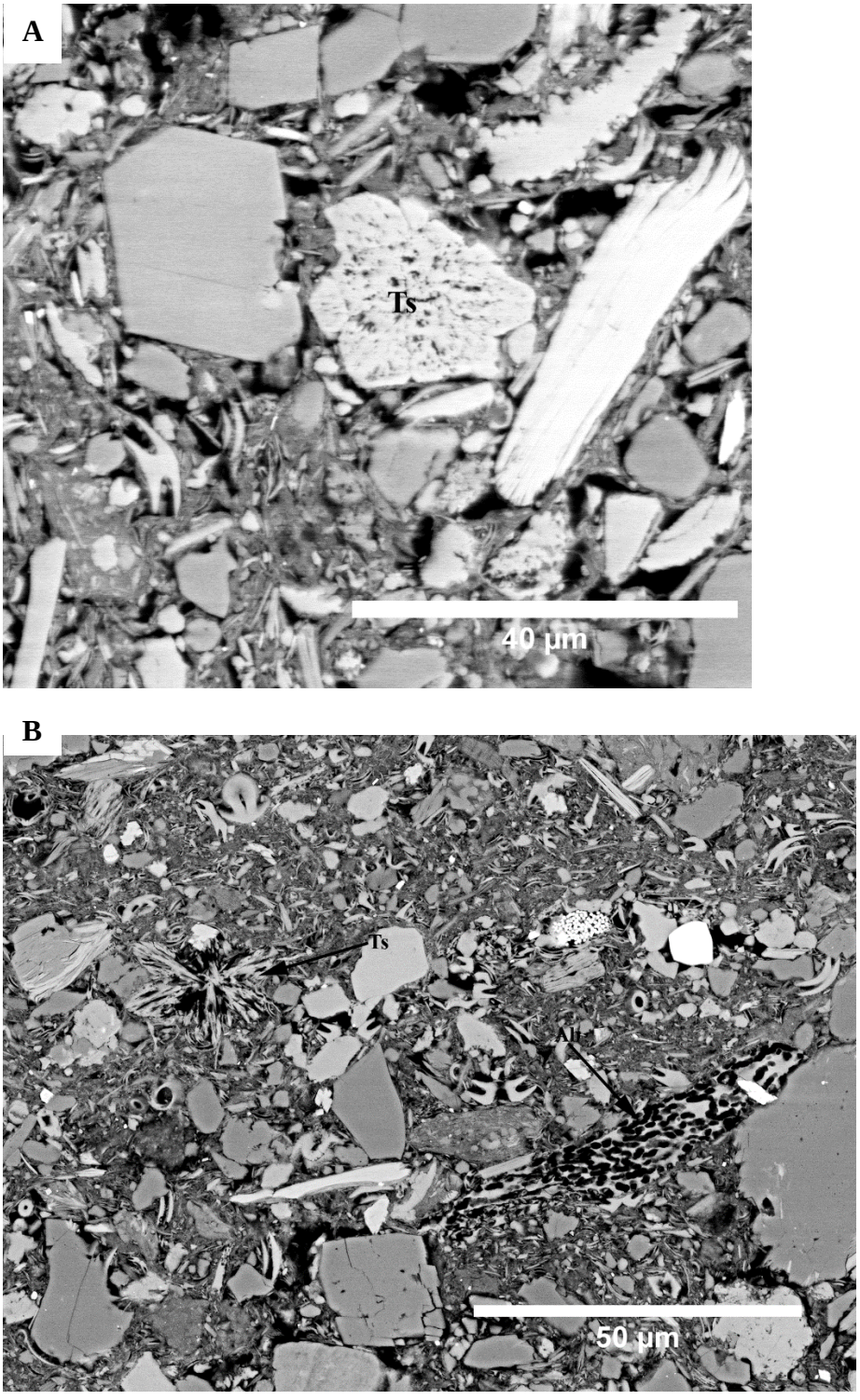

Figure 6.9. BSE-SEM images contourite showing Tunicate spicules (Ts) in A (from sample 1) and B and Algal borings (Ab) in B.

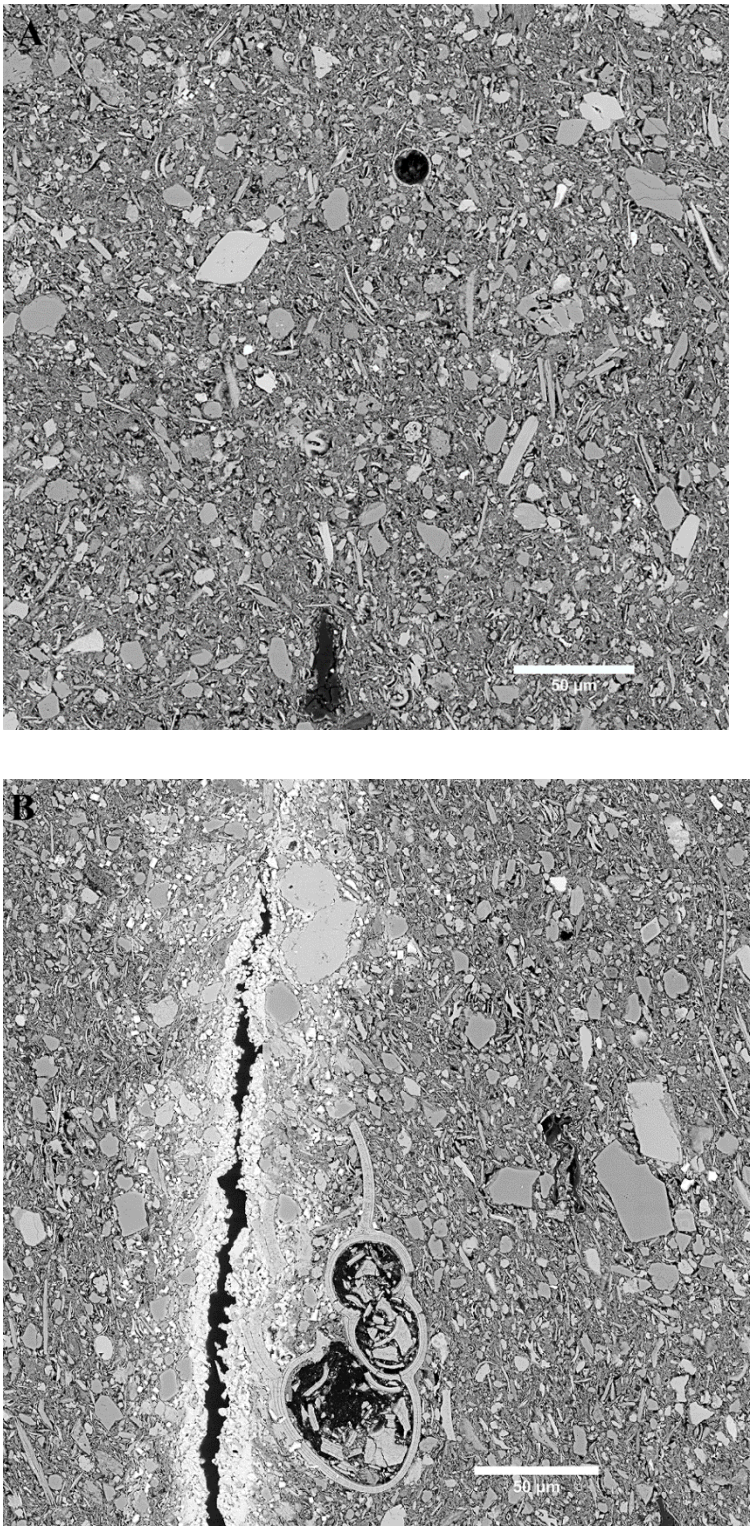

Figure 6.10. BSE-SEM image of siliciclastic dominated hemipelagites showing the microfabric in sample 18 (A) Random fabric (B) vertical burrow filled with pyrite and the grains here are obliquely oriented that are nearly perpendicular to the bedding. The relationship between the matrix and coarse-grain typified matrix-supported fabric. Note that the direction of bedding is along the horizontal scale. Both Figure A and B are from different sub areas in sample 18.

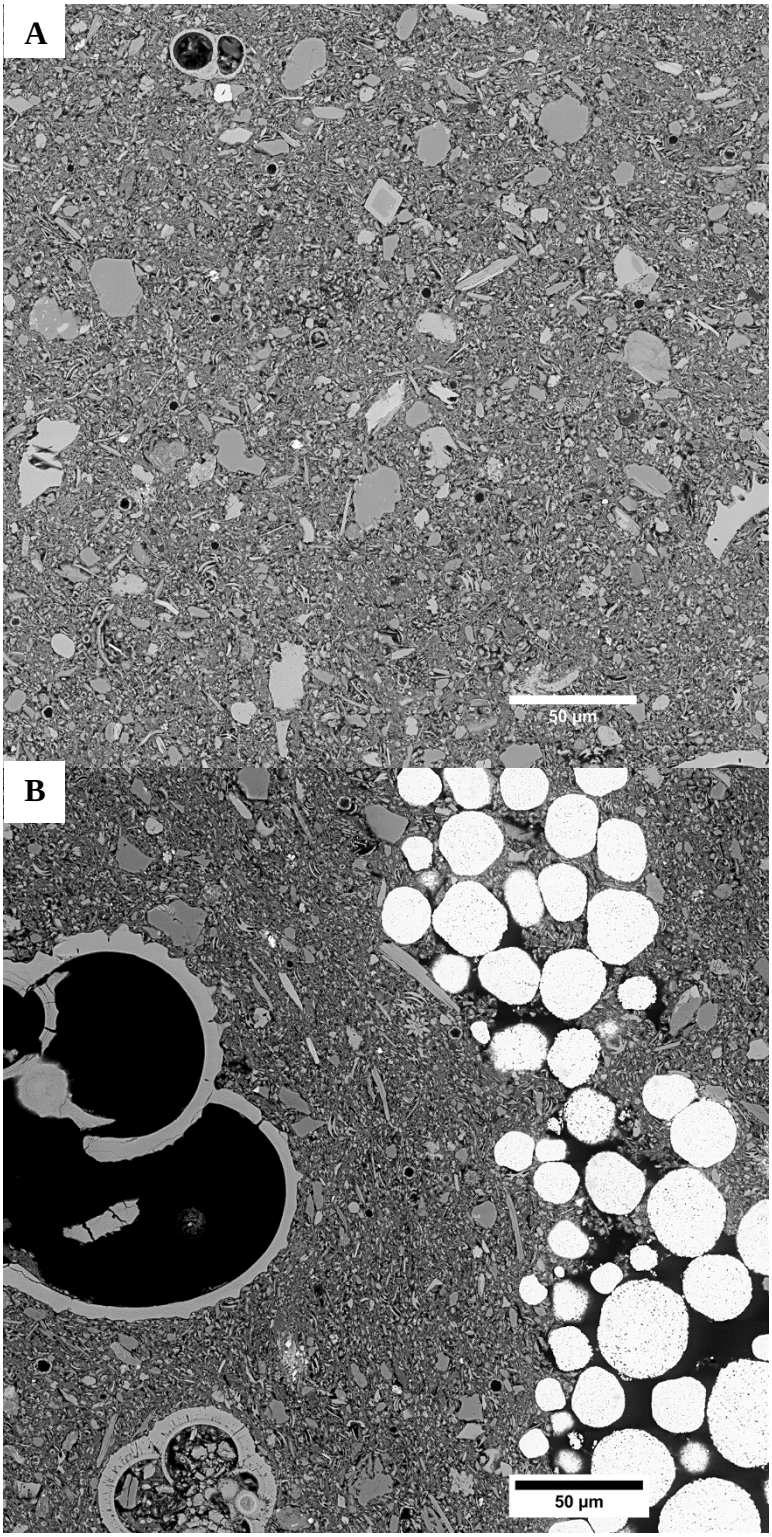

Figure 6.11. BSE-SEM image for of coccoliths dominated hemipelagites (sample 20) showing the random fabric in (A) and framboidal pyrite filled burrow in (B). The fabric in B shows nearly vertical grains and large forams. Both A and B are matrix supported.

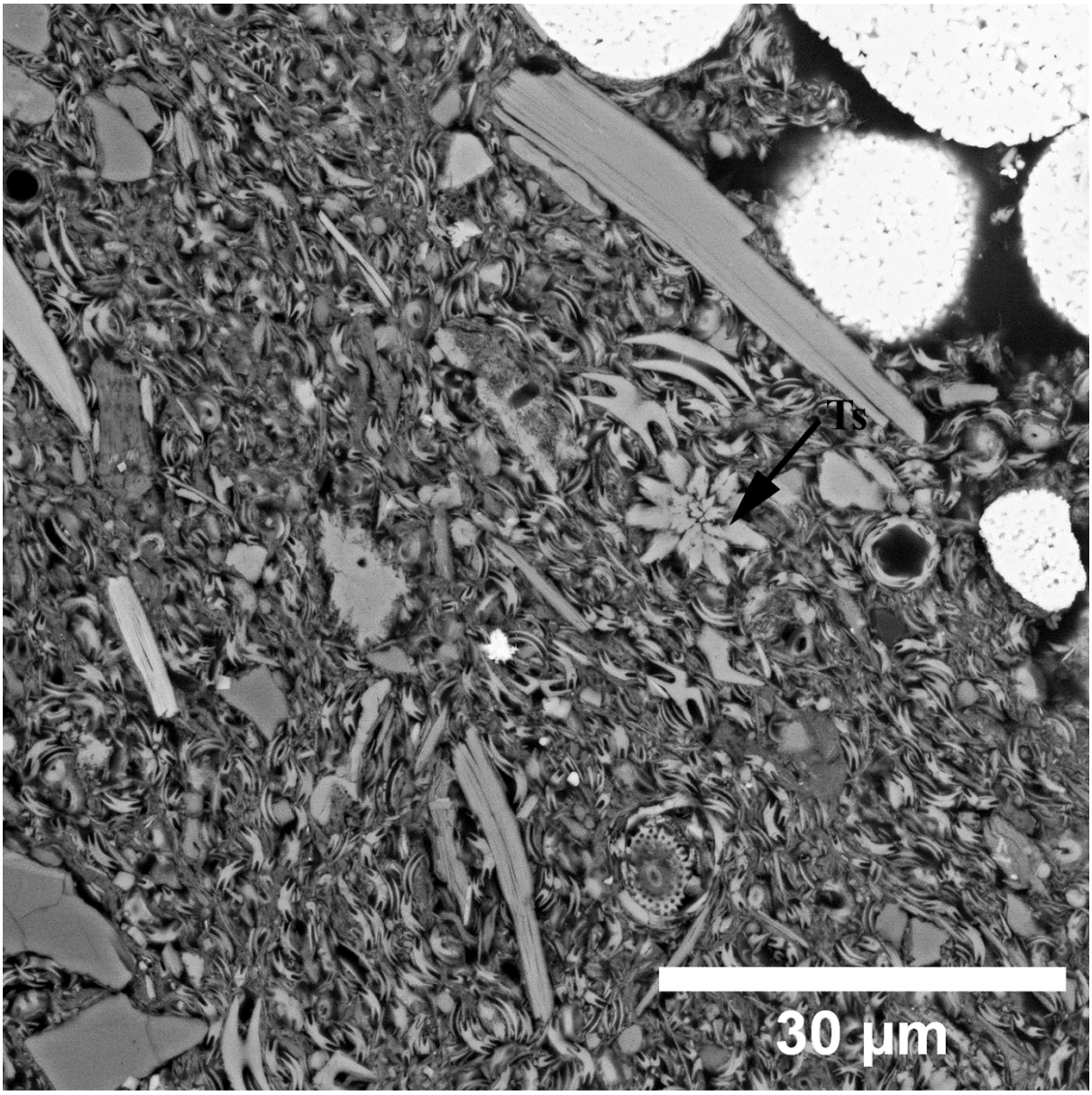

Figure 6.12. BSE-SEM image showing the the structure of tunicate spicules (Ts) found within hemipelagite (sample 20). Note that the structural pattern of the tunicate spicule here is different from those found within the contouritic facies. In hemiplagite facies, the spicules are longer than those found within contourites.

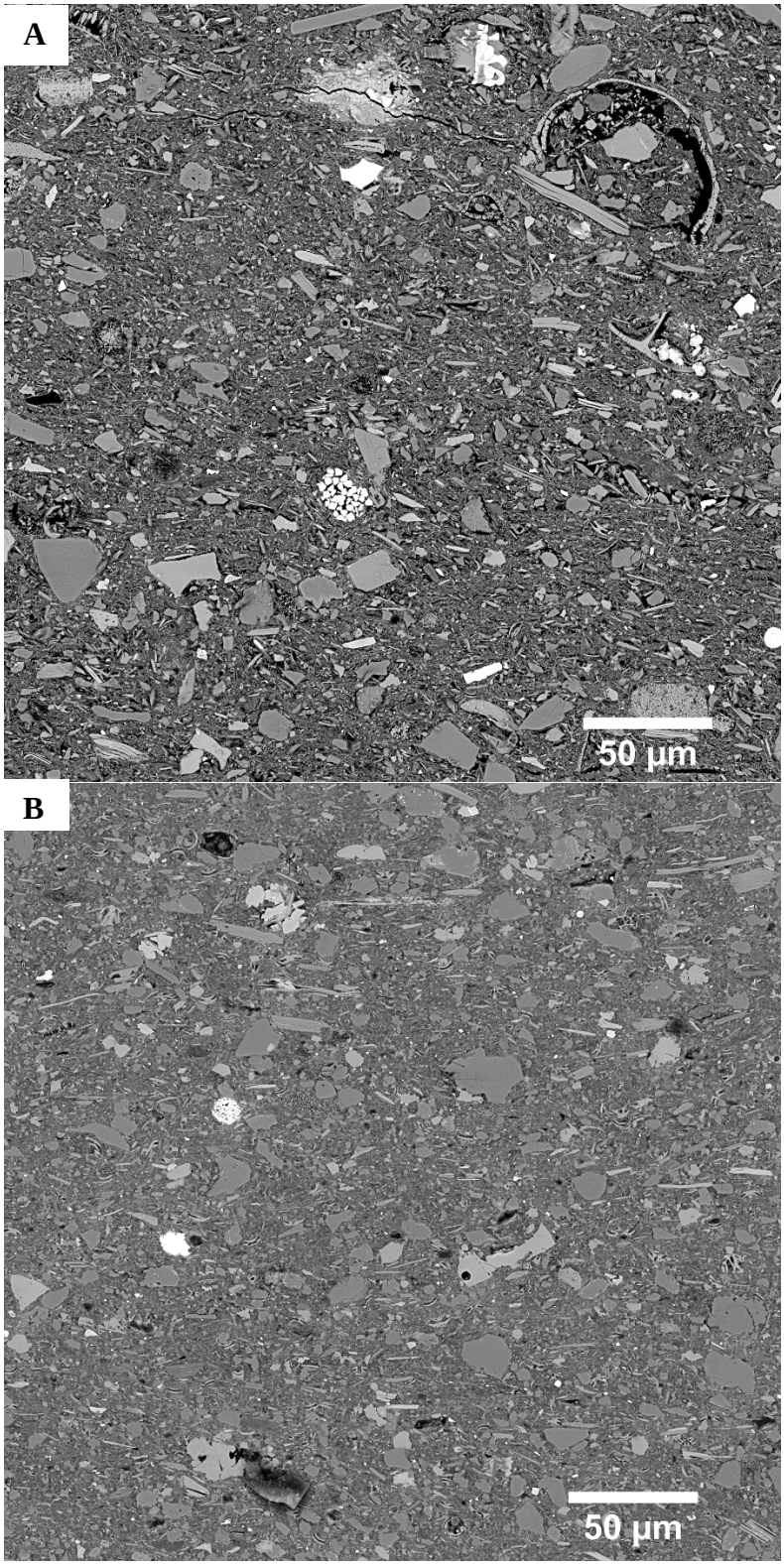

Figure 6.13. BSE-SEM images show typical microfabric of turbidite facies (A) Oblique parallel (B) Bedding parallel. Both SEM images show matrix supported fabric.

6.2.4 Silt and Clay Orientation

To reduce subjectivity resulting from visual interpretation, microfabrics of the different facies were interpreted by constructing rose diagrams and using parameters such as circular variance, von Mises distribution parameter (kappa) and entropy parameter as complementary. Discussion on circular statistics parameters utilized here has been described chapter 5.

The overall orientation patterns displayed in rose diagrams for the different facies are presented in Table 6.4 while the statistical parameters are presented in Appendix 3C.

Contourite facies are typically random to semi random in orientation with ocassional parallel bedding pattern. One hundred and fifty rose diagrams were constructed for the contourite facies out of which about 42% of the rose plots indicate random orientation, 30% and 23% of the rose plots showed semi-random and parallel to bedding pattern respectively while the obique pattern is negligible (Figure 6.14).

One hundred rose diagrams were constructed for the hemipelagites in which most of the plots show a combination of random orientation and oblique orientation of grains. Approximately 43 % of these rose plots shows that hemipelagic facies are randomly oriented while 48% and 9 % show oblique orientation and semi-random orientation respectively. In some cases, the oblique to bedding characteristics exhibited by the hemipelagites are nearly perpendicular to bedding plane (Table 6.4 and Figure 6.14).

Turbidite facies show the most preferred orientation which is either oblique to bedding or parallel to bedding. Virtually all the rose diagrams constructed for the silt and clay size particles indicate preferred orientation while in some instances weak random orientation is not uncommon. Out of the ninety-six rose plots constructed for the turbidite facies, 14% are oblique parallel, 81% of the rose diagrams show bedding parallel, while negligible percentage show semi-random orientation. Beyond burial depth more 800 m, both the silt and the clay size particles for the turbidite facies exhibit preferred orientation that is bedding parallel.

Table 6.4. Rose diagrams showing orientation patterns for contourite, hemipelagite and turbidites. The arrow indicates the direction of the bedding. Contourites are generally random but can show parallel to bedding. Hemipelagites are characterised by a mixture oblique and random orientations while turbidite are dominantly parallel to bedding.

S/N	Sediment type/Depth/ Sed. rate	Subset A	Subset B	Subset C	Subset D	Subset E	Subset F
1	Contourite 9 m 25 cm/ky Silt	P	SR	P	P		
1	Contourite 9 m 25 cm/ky Clay	P	SR	P	P		
2	Contourite 10 m 25 cm/ky Silt	P	P	P	P		
2	Contourite 10 m 25 cm/ky Clay	P	P	P	P		
3	Contourite 14 m 100 cm/ky Silt	OB	SR	SR	OB		
3	Contourite 14 m 100 cm/ky Clay	SR	SR	SR	SR		
4	Contourite 15 m 100 cm/ky Silt	OB	SR	SR	P		
4	Contourite 15 m 100 cm/ky Clay	SR	P	SR	P		

Arrow indicates direction parallel to the bedding.

OB= Oblique P= bedding parallel R= random orientation SR= Semi random

5	Contourite 16 m 25 cm/ky Silt	OB 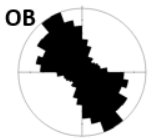	P 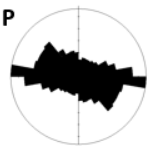	OB 	P 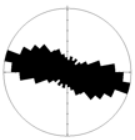		
5	Contourite 16 m 25 cm/ky Clay	SR 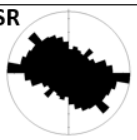	P 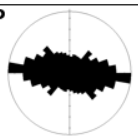	SR 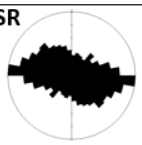	P 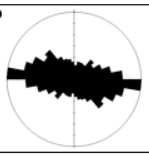		
6	Contourite 42 m 40 cm/ky Silt	R 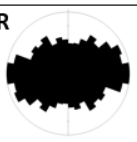	SR 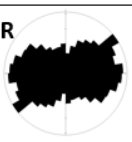	SR 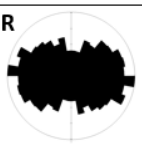	R 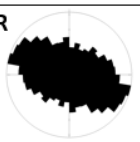	SR 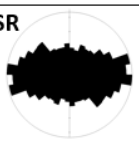	P 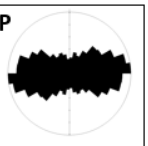
6	Contourite 42 m 40 cm/ky Clay	R 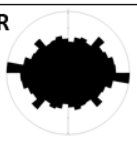	SR 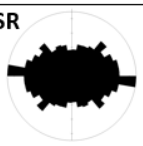	R 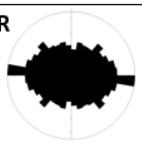	R 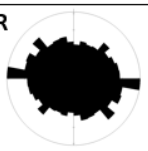	SR 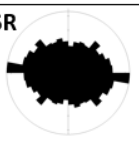	SR 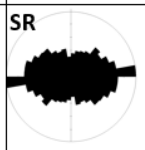
7	Contourite 151 m 40 cm/ky Silt	SR 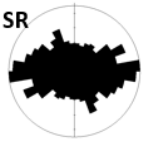	SR 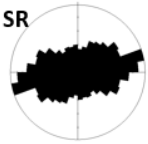	SR 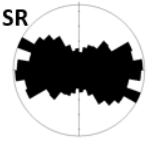	P 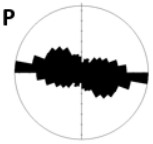	R 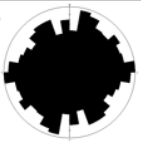	
7	Contourite 151 m 40 cm/ky Clay	R 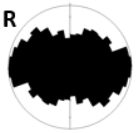	R 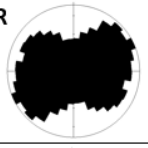	R 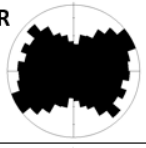	R 	R 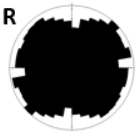	
8	Contourite 253 m 40 cm/ky Silt	SR 	R 	OB 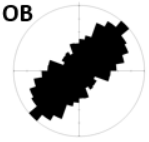	R 		
8	Contourite 253 m 40 cm/ky Clay	R 	R 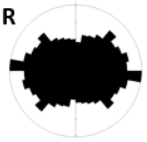	R 	R 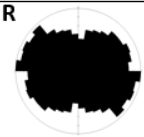		
9	Contourite 343 m 40 cm/ky Silt	P 	OB 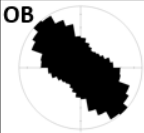	SR 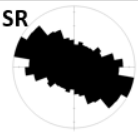	SR 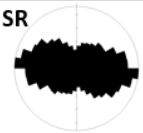		
9	Contourite 343 m 40 cm/ky Clay	SR 	SR 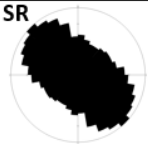	SR 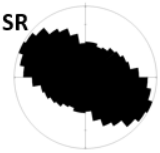	R 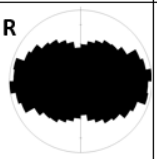		
10	Contourite 510 m 35 cm/ky Silt	R 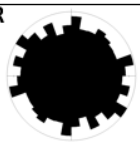	R 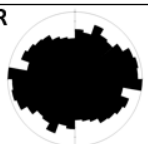	R 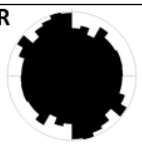	R 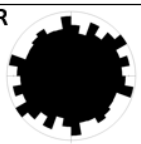		
10	Contourite 510 m 35 cm/ky Clay	R 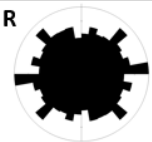	R 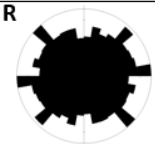	R 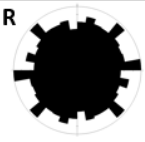	R 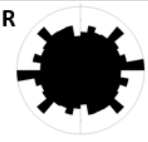		

11	Contourite 563 m 40 cm/ky Silt	P	SR	R	SR		
11	Contourite 563 m 40 cm/ky Clay	SR	SR	SR	SR		
12	Contourite 653 m 40 cm/ky Silt	R	R	R	R		
12	Contourite 653 m 40 cm/ky Clay	R	R	R	R		
13	Contourite 734 m 25 cm/ky Silt	R	R	R	R	R	
13	Contourite 734 m 25 cm/ky Clay	R	R	R	R	R	
14	Contourite 763 m 40 cm/ky Silt	P	R	P	P	P	
14	Contourite 763 m 40 cm/ky Clay	SR	SR	SR	R	SR	
15	Contourite 808 m 25 cm/ky Silt	SR	P	P	P	P	
15	Contourite 808 m 25 cm/ky Clay	SR	P	SR	SR	SR	

16	Contourite 860 m 40 cm/ky Silt	P					
16	Contourite 860 m 40 cm/ky Clay	P	P	SR	R	R	
17	Contourite 943 m 40 cm/ky Silt	SR	R	R	R		
17	Contourite 943 m 40 cm/ky Clay	R	R	R	R		
18	Hemipelagites 8 m 10 cm/ky Silt	OB	OB	R	OB	OB	
18	Hemipelagites 8 m 10 cm/ky Clay	R	R	R	OB	R	
19	Hemipelagites 10 m 10 cm/ky Silt	R	SR	SR	R	SR	OB
19	Hemipelagites 10 m 10 cm/ky Clay	R	R	R	R	SR	R
20	Hemipelagites 15 m 10 cm/ky Silt	OB	OB	SR	OB	R	R
20	Hemipelagites 15 m 10 cm/ky Clay	R	SR	R	OB	R	R
21	Hemipelagites 50 m 10 cm/ky Silt	OB	OB	R	R	R	OB
21	Hemipelagites 50 m 10 cm/ky Clay	R	R	R	R	R	OB

22	Hemipelagites 57 m 10 cm/ky Silt	R	R	OB	OB	OB	
22	Hemipelagites 57 m 10 cm/ky Clay	R	R	R	R	OB	
23	Hemipelagites 60 m 10 cm/ky Silt	R	R	R	R	R	OB
23	Hemipelagites 60 m 10 cm/ky Clay	R	R	R	R	R	OB
24	Hemipelagites 80 m 10 cm/ky Silt	OB	OB	OB	OB	OB	OB
24	Hemipelagites 80 m 10 cm/ky Clay	OB	R	OB	OB	OB	OB
25	Hemipelagites 117 m 10 cm/ky Silt	R	OB	OB	OB		
25	Hemipelagites 117 m 10 cm/ky Clay	R	OB	OB	SR		
26	Hemipelagite 68 m 10 cm/ky Silt	OB	OB	OB	OB	OB	OB
26	Hemipelagite 68 m 10 cm/ky Clay	OB	SR	OB	OB	SR	OB
27	Turbidite 66 m Silt	OB	P	OB	OB		
27	Turbidite 66 m Clay	OB	P	OB	OB		

28	Turbidite 132 m Silt	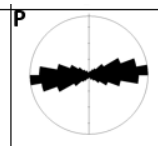	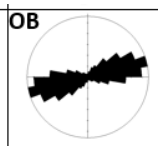	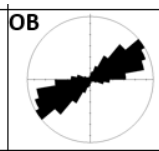	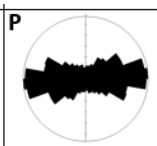		
28	Turbidite 132 m Clay	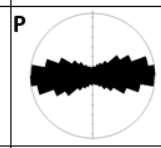	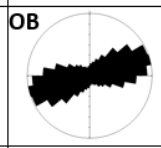	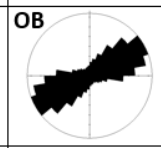	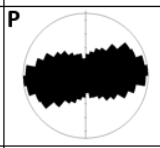		
29	Turbidite 260 m Silt	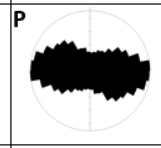	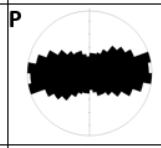	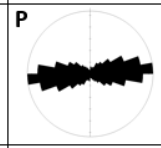	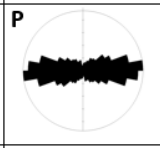		
29	Turbidite 260 m Clay	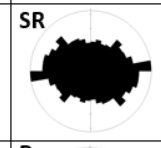	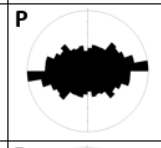	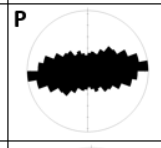	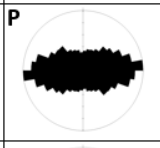		
30	Turbidite 348 m Silt	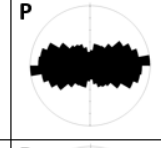	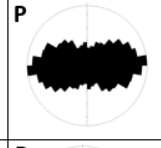	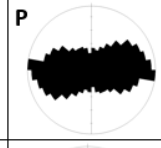	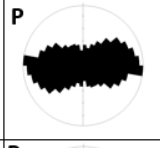		
30	Turbidite 348 m Clay	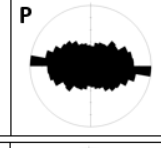	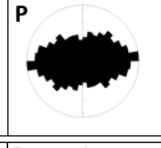	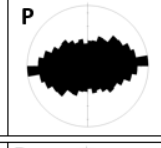	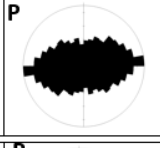		
31	Turbidite 455 m Silt	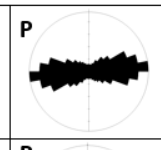	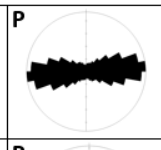	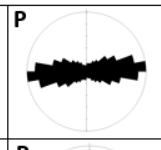	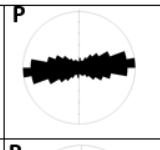		
31	Turbidite 455 m Clay	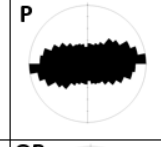	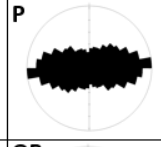	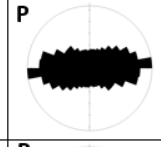	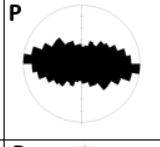		
32	Turbidite 541 m Silt	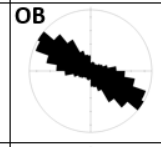	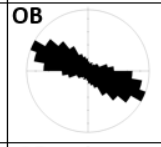	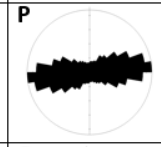	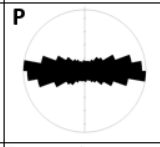		
32	Turbidite 541 m Clay	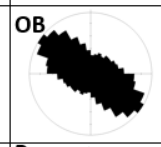	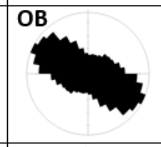	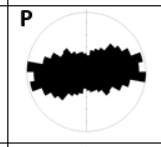	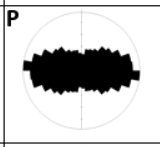		
33	Turbidite 543 m Silt	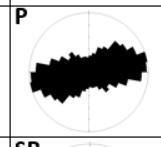	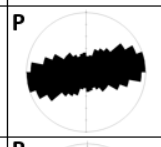	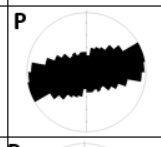	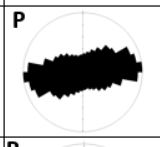		
33	Turbidite 543 m Clay	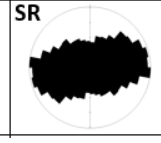	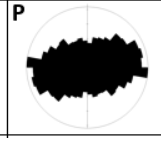	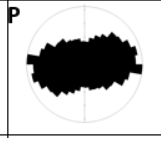	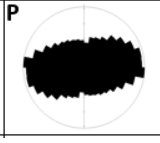		

34	Turbidite 655 m Clay	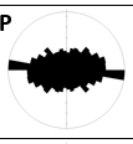	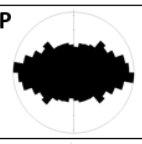	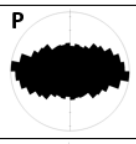	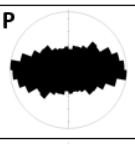		
35	Turbidite 766 m Silt		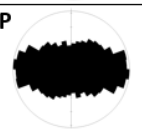	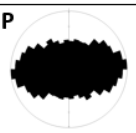	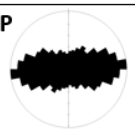		
35	Turbidite 766 m Clay		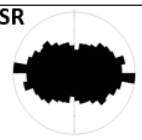	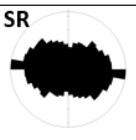	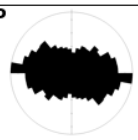		
36	Turbidite 825 m Silt	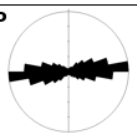	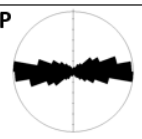	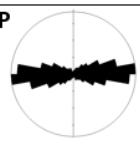	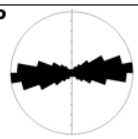		
36	Turbidite 825 m Clay	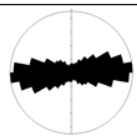	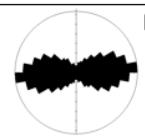	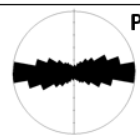	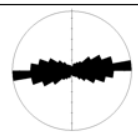		
37	Turbidite 866 m Silt	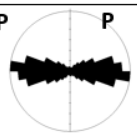	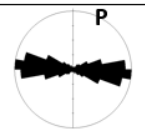	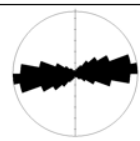	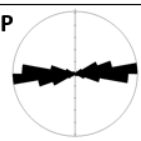		
37	Turbidite 866 m Clay	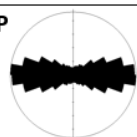	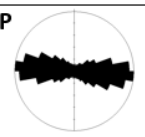	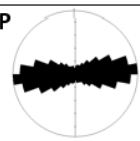	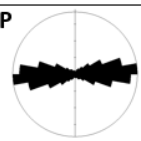		
38	Turbidite 985 m Silt	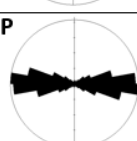	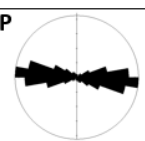	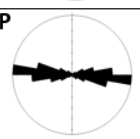	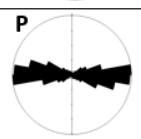		
38	Turbidite 985 m Clay	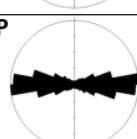	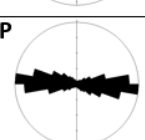	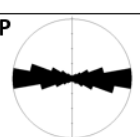	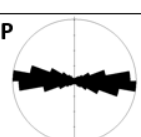		

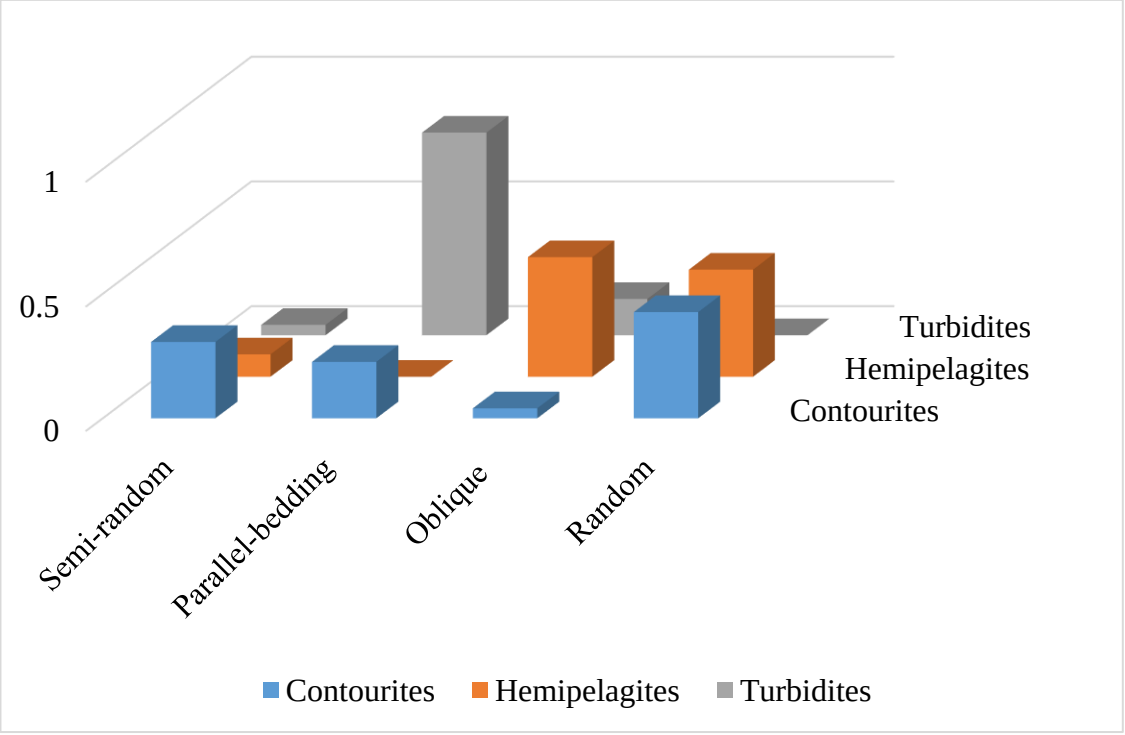

Figure 6.14. Percentage of orientation patterns for contourites, hemipelagites and turbidites facies. Contourite facies are characterised by a combination of random and semi-random orientation with ocassional parallel to bedding pattern. Hemipelagites display dominantly oblique and random orientation while turbidites are generally parallel to bedding but sometimes with oblique orientation.

6.2.5 Mineralogical composition

Synopsis of the mineralogical composition determined by EDX for the three sediment types i.e contourites, hemipelagite and turbidites is presented in Table 6.5.

The carbonate mineral percentage is lowest in the turbidite facies (4 - 16.5%), followed by contourites (4 – 37%) while hemipelagites are the most carbonate dominated when compared to turbidites and contourites. In terms of clay minerals, turbidites have the highest percentage of clay minerals with an approximate average of about 76%, contourites has moderate clay mineral percentage (ca. average 59%) while hemipelagites contain the least amount of clay (ca. avaerage 50%).

The silt index (mainly quartz plus feldspar content) is highest for the contourite facies (mean value ca. 24%) while both hemipelagites and turbidites contain average silt index of 14% and 15% respectively.

Table 6.5. Summary of the average mineralogical composition determined through energy dispersive X-ray analysis.

Sample No	Sample ID	Sediment type	Carbonate %	Clay%	*Silt index %	Others %
1	339-1387B-2H1 032-034	Contourite	8.9	60.5	28.5	2.1
2	339-1387B-2H1 128-130	Contourite	9	60	30.5	0.4
3	339-1390B-2H4 7-9	Contourite	6.4	56.7	33.2	3.7
4	339-1390B-2H5 22-24	Contourite	4	56.5	29.8	9.7
5	339-1387B-2H5 67-69	Contourite	5.4	61.2	32.3	1.1
6	339-1389A-6H1 28-30	Contourite	14.7	73.6	7	4.7
7	339-1389A-18X1 125-127	Contourite	8.9	56	30.5	4.6
8	339-1389A-28X5 130-132	Contourite	16.0	54.1	20	9.9
9	339-1389A-38X2 112-114	Contourite	19.6	58	20.1	
10	339-1386C-17R1 46-47	Contourite	19.7	57.7	15.3	7.3
11	339-1389E-26R3 61-63	Contourite	7.1	62.6	28	2.3

12	339-1389E-35R5 60-61.5	Contourite	8.7	60.4	26.8	4.1
13	339-1387C-48R3 33-35	Contourite	8.7	62.5	25.4	3.4
14	339-1389E-47R2 22-24	Contourite	7.1	62.8	28.6	1.5
15	339-1387C-56R1 8-10	Contourite	4.1	72.6	18.2	5.1
16	339-1389E-57R3 12-13.5	Contourite	24.6	56	11.5	7.9
17	339-1389E-66R1 18-21	Contourite	37.1	34.1	24.1	4.7
18	339-1385A-2H6 13-15	Hemipelagite	12.0	71.7	13.5	2.8
19	339-1385E-2H5 74-76	Hemipelagite	11.8	61.6	22.2	4.5
20	339-1385D-2H6 115-117	Hemipelagite	16.9	60.9	19.7	2.5
21	339-1385A-6H2 49-51	Hemipelagite	80.7	8.4	9.	1.9
22	339-1385A-7H6 54-56	Hemipelagite	82.9	14.7	-	2.4
23	339-1385E-7H2 113-115	Hemipelagite	69.1	13.7	9.8	7.4

24	339-1385E 10H2 80-82	Hemipelagite	17.9	57.5	21.5	3.1
25	339-1385A-14H2 30-32	Hemipelagite	12.1	76.1	8.2	3.6
26	355-1457A-8H1 38-42	Hemipelagite	15.3	64	17.8	2.9
27	355-1457A-8H2 27-31	Turbidites	11.6	69.3	15.8	3.3
28	335-1457A-17F1 124-128	Turbidites	3.9	71.7	22.1	2.3
29	355-1457C-9R1 7-11	Turbidites	1.5	78.7	17.3	2.5
30	355-1457C-18R2 6-10	Turbidites	2	80	16.8	1.2
31	355-1457C-29R1 99-103	Turbidites	3.5	62.5	32.2	1.8
32	355-1457C-38R1 43-45	Turbidites	11.1	81.2	7.1	0.6
33	355-1457C-38R2 124-126	Turbidites	11.2	81.0	6.1	1.7
34	355-1457C-49R6 30-34	Turbidites	2.3	73.1	22.7	1.9
35	355-1457C-61R3 11-15	Turbidites	10.6	76.0	9.9	3.5

36	355-1457C-67R3 4-8	Turbidites	16.5	65.6	16	1.9
37	355-1457C-71R4 63-67	Turbidites	9.1	81.5	5.5	3.9
38	355-1457C-83R6 5-6	Turbidites	1.2	87.6	9.3	1.9

* The silt index is the percentage of quartz plus that of feldspar.

6.2.6 Petrophysical properties

The results on pore volume, porosity and specific surface area derived through LPNGA are presented in Table 6.6. The values of pore volume for contourites (0.021- 0.0318 cm^3/g) and hemipelagite (0.0318 – 0.0478 cm^3/g) are within a similar range, while that for the turbidite facies is wider (0.025 – 0.0616 cm^3/g). Porosity and specific surface area follow a similar trend to the pore volume with respect to the three sediment types, but the mean porosity values for contourite, hemipelagite and turbidite facies are 11.08, 14.78 and 12.59% respectively. Variability in mean porosity values represent about 33% increase in value for that of contourite to hemipelagite and approximately 15% decrease in value from hemipalgite to turbidite. In terms of specific surface area, turbidite facies have the maximum value with an average of 31.05, followed by hemipelagites which have a mean value of about 28.97, while the average specific surface area for the contourites stands at 26.83

Plot of specific surface area against porosity indicate that about 50% of turbidite facies plot within similar area which can be differentiated from other sedimentary facies (contourites and hemipelagites) while both contourites and hemipelagites plot within a cluster as there is no unique boundary between them (Figure 6.15).

Table 6.6. Petrophysical properties contourite, hemipelagite and turbidite facies derived from LPNGA

Sample No	Sediment type	Pore volume (cm^3/g)	Porosity (%)	Specific specific surface area (m^2/g)

1	Contourite	0.0302	10.45	27.84
2	Contourite	0.0287	10.05	25.35
3	Contourite	0.0210	7.42	17.18
4	Contourite	0.0322	10.82	26.56
5	Contourite	0.0222	7.72	17.50
6	Contourite	0.0333	11.36	27.97
7	Contourite	0.0350	11.86	28.5
8	Contourite	0.0345	12.34	26.44
9	Contourite	0.0331	11.65	30.44
10	Contourite	0.0323	11.40	32.64
11	Contourite	0.0463	17.96	28.90
12	Contourite	0.0351	12.62	27.25
13	Contourite	0.0248	9.65	28.69
14	Contourite	0.0350	13.08	27.34
15	Contourite	0.0376	10.05	32.92
16	Contourite	0.0283	10.03	25.70
17	Contourite	0.0282	10.05	24.90
18	Hemipelagite	0.0369	13.00	25.36
19	Hemipelagite	-	-	-
20	Hemipelagite	-	-	-
21	Hemipelagite	-	-	-

22	Hemipelagite	0.0318	11.81	21.92
23	Hemipelagite	-	-	-
24	Hemipelagite	-	-	-
25	Hemipelagite	0.0478	18.49	32.71
26	Hemipelagite	0.0403	15.82	35.89
27	Turbidites	0.0402	14.40	43.58
28	Turbidites	0.0272	11.07	16.79
29	Turbidites	0.0250	10.49	17.18
30	Turbidites	0.0253	9.86	16.54
31	Turbidites	0.0267	10.49	16.92
32	Turbidites	0.0360	10.42	27.60
33	Turbidites	0.0299	10.39	23.99
34	Turbidites	0.0377	13.35	34.51
35	Turbidites	0.0351	13.03	30.87
36	Turbidites	0.0276	9.88	28.20
37	Turbidites	0.0533	17.67	57.23
38	Turbidites	0.0616	20.1	59.19

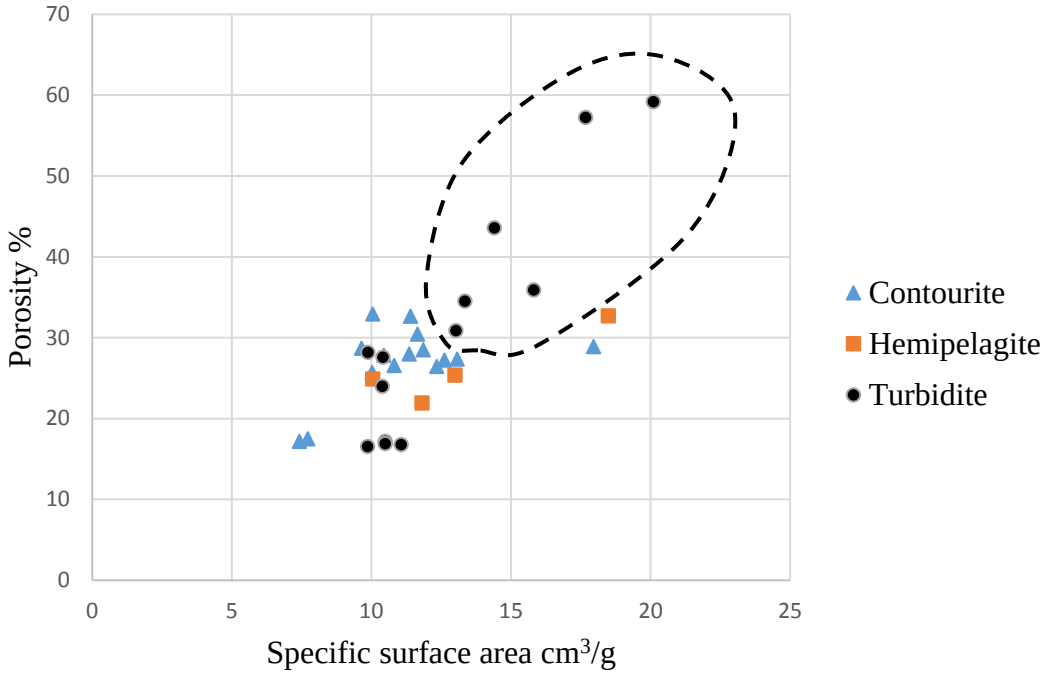

Figure 6.15. Cross plot of porosity against specific surface area. 50% of turbidite facies are distinctively differentiated based on this plot. However, both contourite and hemipelagites plot within similar region of the graph and are unlikely to be differentiated based on the cross plot. Note that the porosity for low-pressure nitrogen gas adsorption is not total porosity but meso-porosity.

Porosity and permeability values generated through digital rock physics is presented in Table 6.7. The average porosity and permeability value for contourite facies is 14.14 % and 9.38 µD respectively. The hemipelagite facies has an overall mean of 22.42% porosity and 47 µD permeability. The mean porosity value for tubidite facies show that the mean porosity value stands at 18.71 % while the average permeability is approximately 31 µD. Porosity versus permeability curve shows that hemipelagite are the most permeable muddy facies. Turbidite facies have intermediate permability values lying between contourites and hemipelagites permeability values while contourites are the least permeable among the three sedimentary types.

Table 6.7. Output of digital rock physics simulation of pore network.

Sample No	Sediment type	Porosity (%)	Absolute permeability (μD)
1	Contourite	26.0	19.4
2	Contourite	18.2	18.1
3	Contourite	-	-
4	Contourite	-	-
5	Contourite	12.4	18.2
6	Contourite	12.1	5.9
7	Contourite	18.6	9.9
8	Contourite	15.6	10.5
9	Contourite	12.9	6.8
10	Contourite	4.1	-
11	Contourite	17.9	10.2
12	Contourite	15.5	7.5
13	Contourite	1.92	0
14	Contourite	15.4	7.7
15	Contourite	9.9	0.033
16	Contourite	15.8	9.7
17	Contourite	15.8	7.4
18	Hemipelagite	24.6	48.0

19	Hemipelagite	20.1	25.7
20	Hemipelagite	21.2	9.2
21	Hemipelagite	24.7	129
22	Hemipelagite	19.1	13.2
23	Hemipelagite	22.3	34.5
24	Hemipelagite	18.7	23.3
25	Hemipelagite	31.3	127.9
26	Hemipelagite	19.8	12.3
27	Turbidites	11.3	1.3
28	Turbidites	20.1	36.4
29	Turbidites	19.1	30.7
30	Turbidites	13.6	1.65
31	Turbidites	-	-
32	Turbidites	13.7	2.9
33	Turbidites	14.3	4.3
34	Turbidites	29.9	119.9
35	Turbidites	12.2	0.52
36	Turbidites	15.1	6.2
37	Turbidites	7.9	.012
38	Turbidites	12.2	1.9

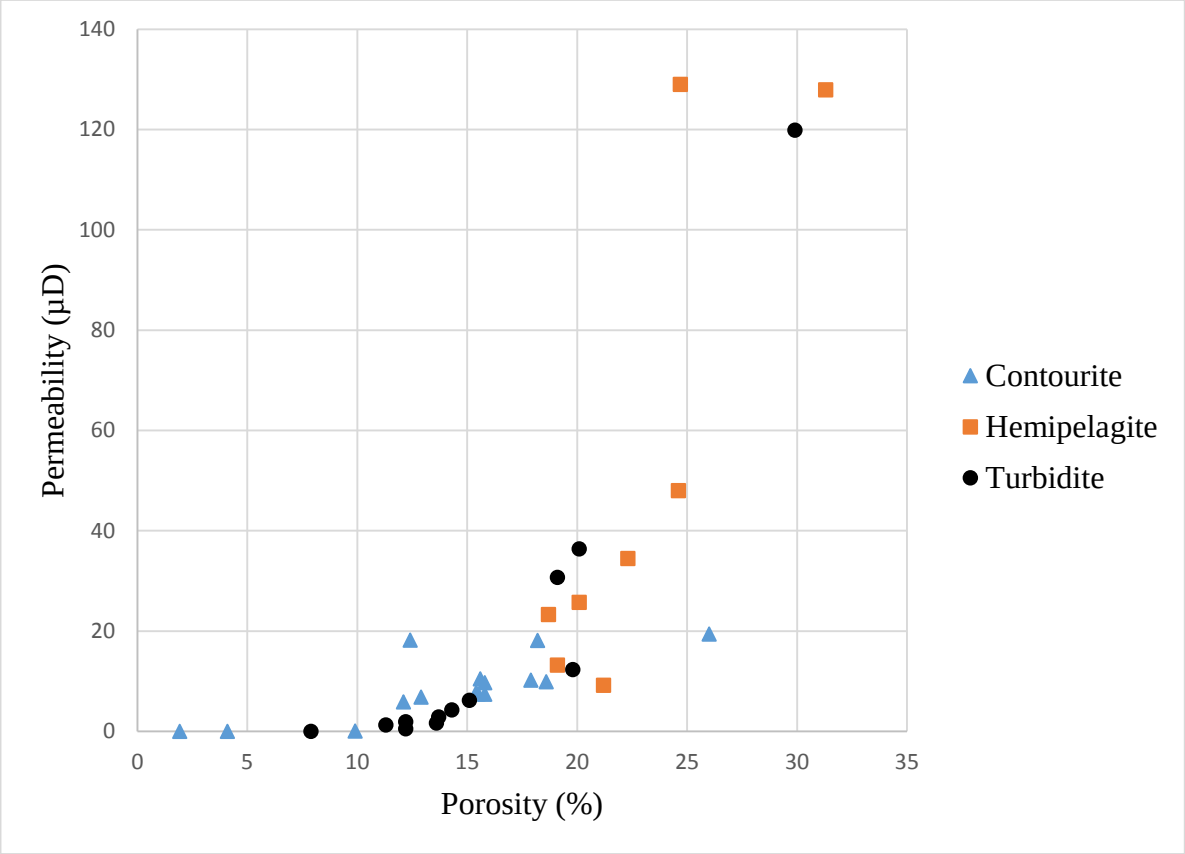

Figure 6.16. Cross plot of porosity versus permeability. The plot shows overlap in porosity and permeability value for the three sedimentary facies, but hemipelagites are the most permeable while contourites are the least permeable and turbidite are fairly permeable.

The pore size distribution derived through digital rock physics shows that for contourites, hemipelagite and turbidites the distribution is unimodal. The pore size distribution for contourite facies is nearly symmetrical, while hemipelagite and turbidites are slightly negatively skewed. The modal pore size for contourite facies stands between 250 nm and 750 nm. The modal pores for hemipelagites and turbidite facies is between 250 nm and 1000 nm.

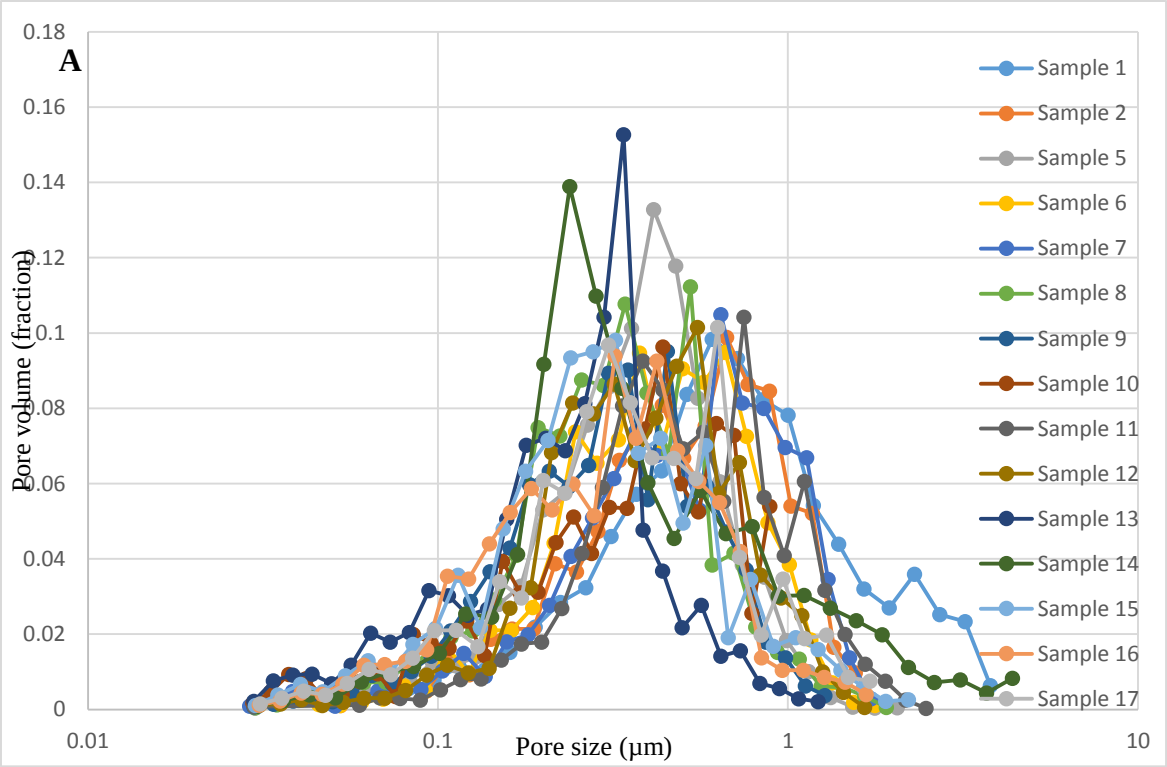

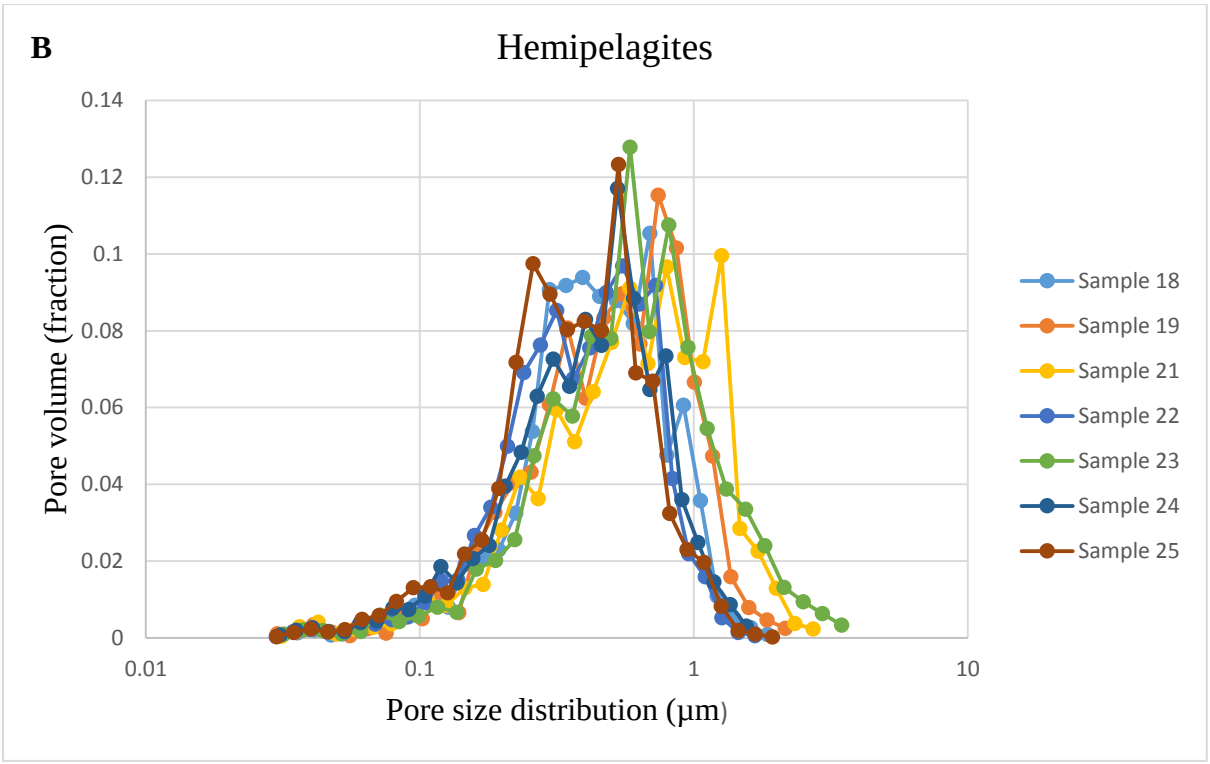

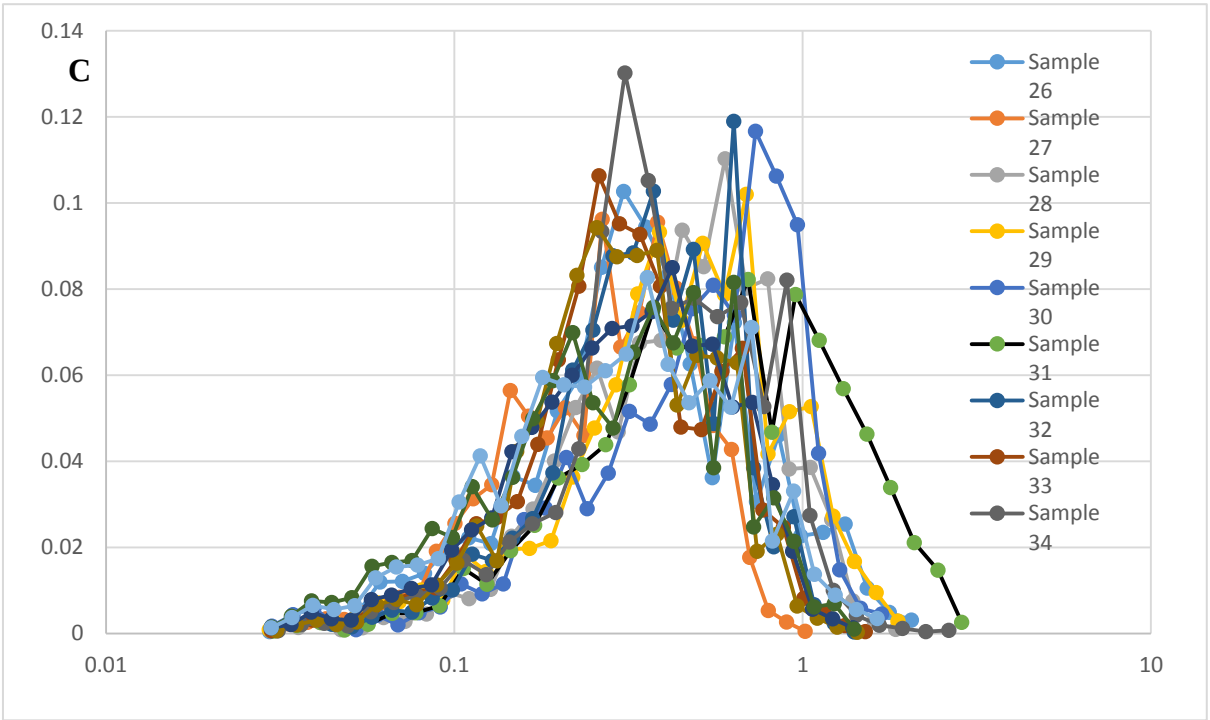

Figure 6.17. Pore size distribution derived from digital rock physics (A) Contourite shows a relatively unimodal distributions on a log-normal graph and are nearly symmetrical (B) Hemipelagite portrays a unimodal distribution and slightly negatively skewed (C) Turbidite displays fairly unimodal distribution and are negatively skewed.

Plots of key parameters such as average grain size, porosity (derived from helium pycnometry), sedimentation rate and general microfabric against burial depths are presented in Figure 6.18 to Figure 6.23. In all the sites, there is no obvious link between microfabric and depth, as there is no clear trend between the two parameters (Figure 6.18 to Figure 6.23). In the case of porosity, decrease in porosity along the depth profile was noticed from all the sites (Figure 6.18 to Figure 6.23). However, in order to quantify the variation in porosity along burial depth, some statistical parameters were computed (Table 6.8). The computed statistics indicate low standard deviation for the porosity values, which is an indication of minimal dispersion of data around the mean value. The values of correlation coefficient when depth is compared against porosity through Pearson function suggest low (PCC< 0.5) to strong negative correlation (PCC =0.7-0.9) exists between the two parameters.

Recent studies aimed at characterising porosity-depth curve for deep-water sediments (Kominz, Patterson and Odette, 2011; Kominz *et al.*, 2016) employ correlation coefficient (R) through regression analysis rather than the PCC. However, both coefficients give similar results (Table 6.8) except that the PCC has a further advantage, as a negative value indicates negative correlation between two varaibles while positive correlation coefficient suggests otherwise.

Table 6.8. Summary of statistical parameters for porosity changes with depth for all the six sites. The Perason correctaion coefficient indicates presence of negative moderate to strong correlation between depth (< 1 km) and porosity.

Expedition	Site	Maximum depth (mbsf)	Mean (vol. %)	Median (vol. %)	Range (vol. %)	Standard deviation (vol. %)	Pearson Correlation Cofficient (PCC)	R Correlation coefficient
399	1385	150	56.9	56.3	19.8	4.8	-0.83	0.83
399	1386	520	45.7	45.6	52.3	5.6	-0.41	0.41
399	1387	550	46.5	46.3	41.2	0.33	-0.44	0.39
399	1389	980	45.3	44.9	65.3	0.34	-0.38	0.33
399	1390	350	47.2	47.3	34.3	6.1	-0.68	0.70
355	1457	1000	45.6	43.3	45.9	0.76	-0.81	0.81

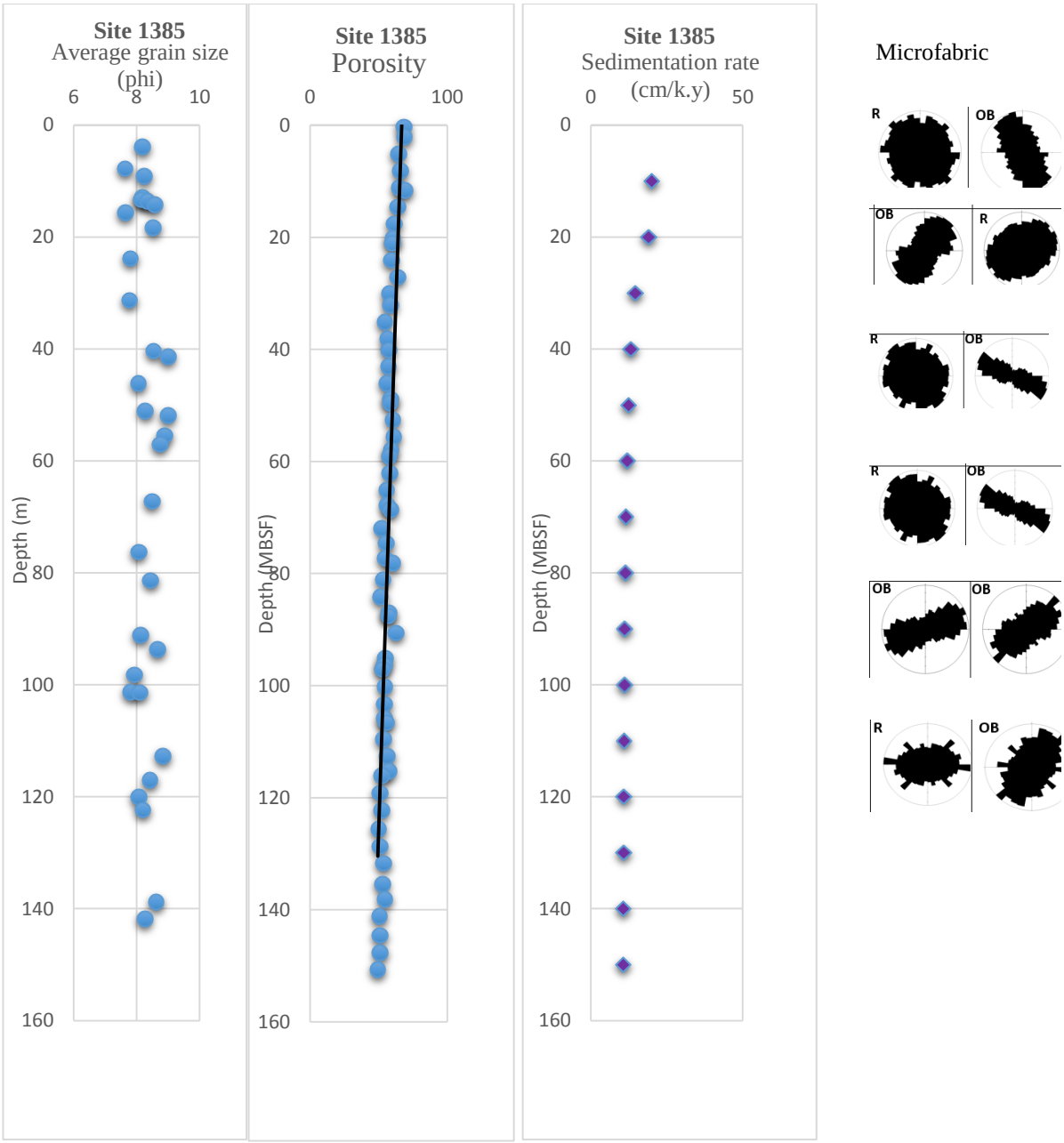

Figure 6.18. Plot of average grain size, porosity (from IODP database), sedimentation rate and microfabric along the depth profile in site 1385.

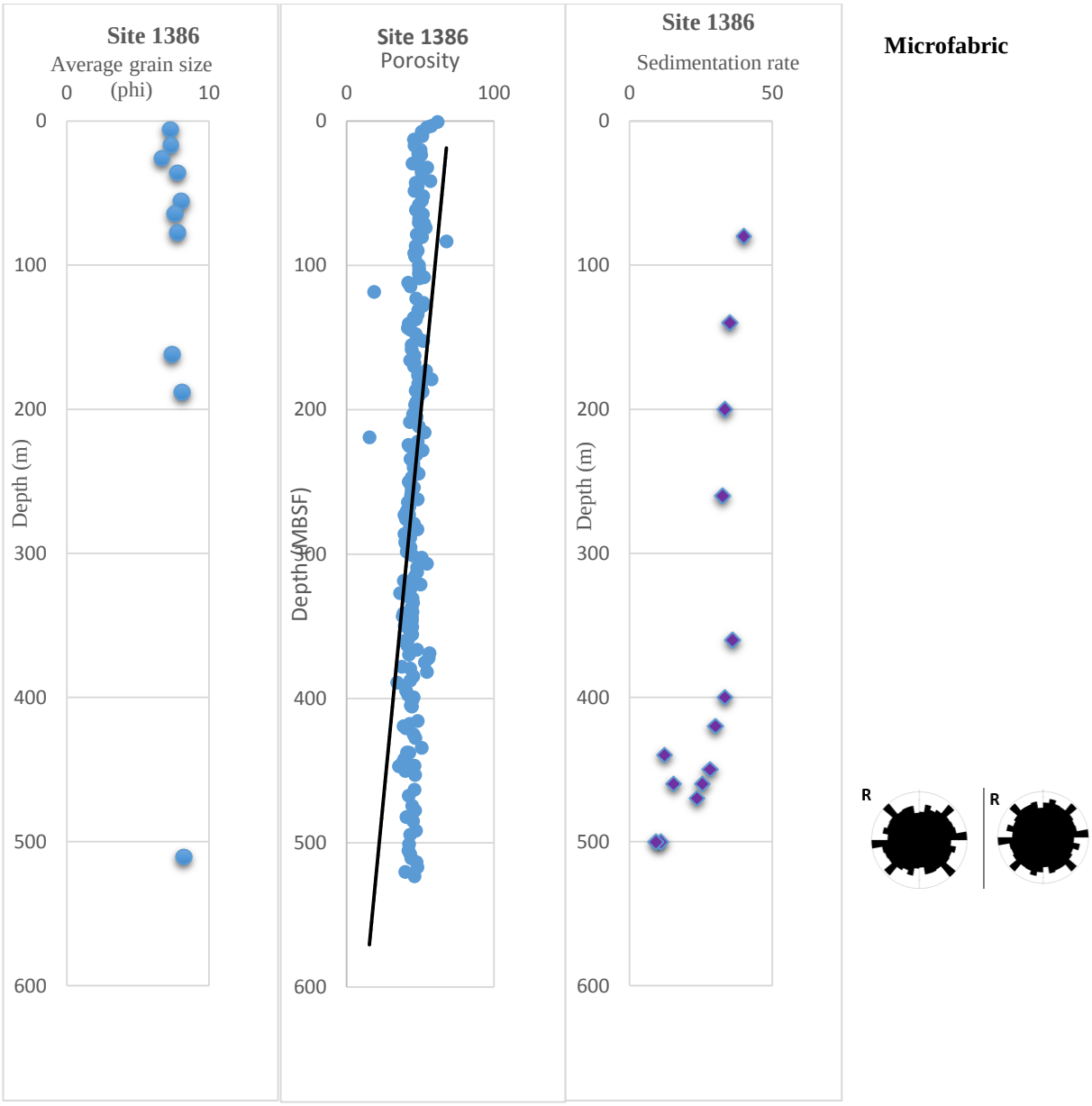

Figure 6.19. Plot of average grain size, porosity (from IODP data), sedimentation rate and microfabric along the depth profile in site 1386.

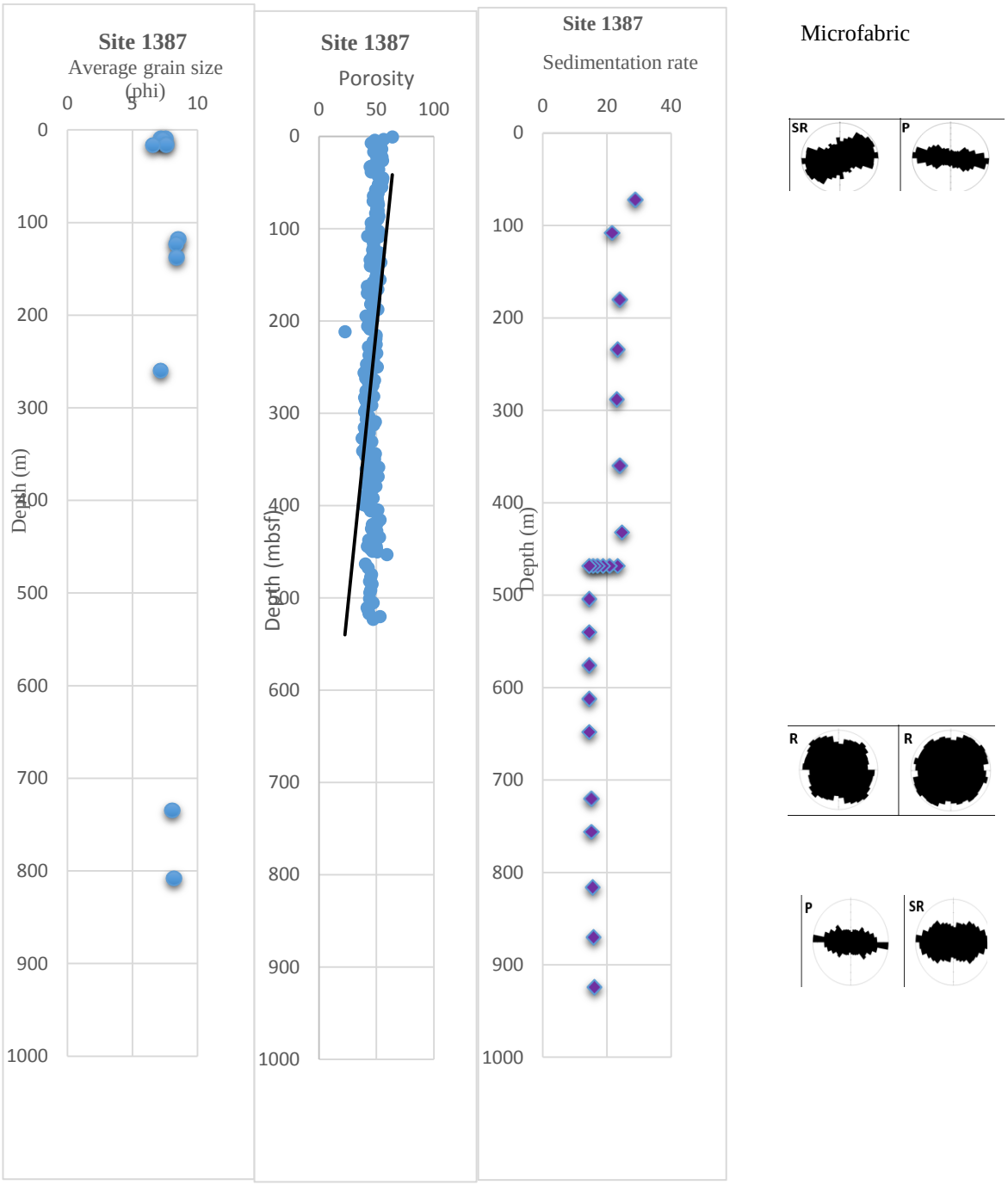

Figure 6.20. Plot of average grain size, porosity (from IODP data), sedimentation rate and microfabric along the depth profile in site 1387.

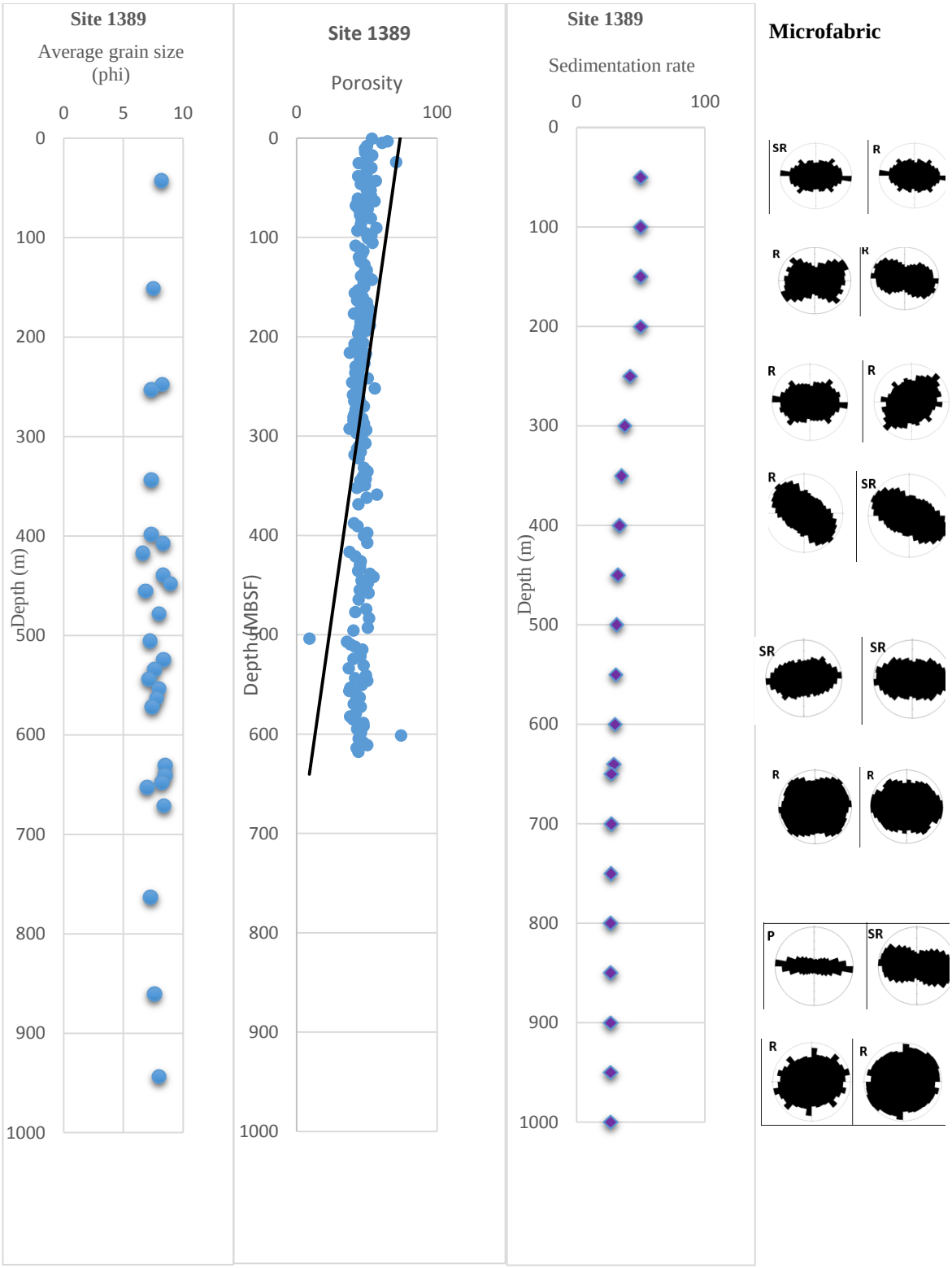

Figure 6.21. Plot of average grain size, porosity (from IODP data), sedimentation rate and microfabric along the depth profile in site 1389.

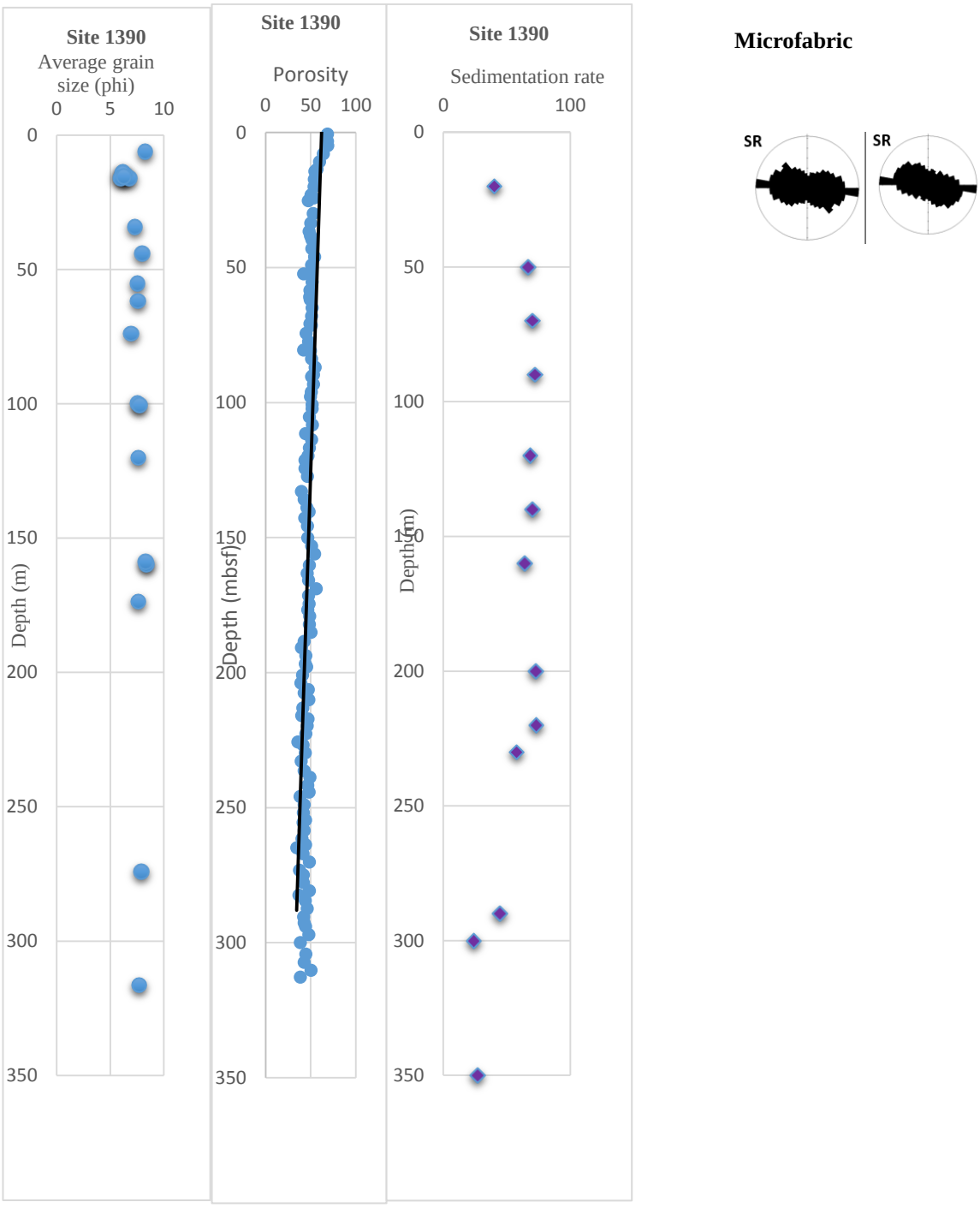

Figure 6.22. Plot of average grain size, porosity (Helium pycnometry), sedimentation rate and microfabric along the depth profile in site 1390.

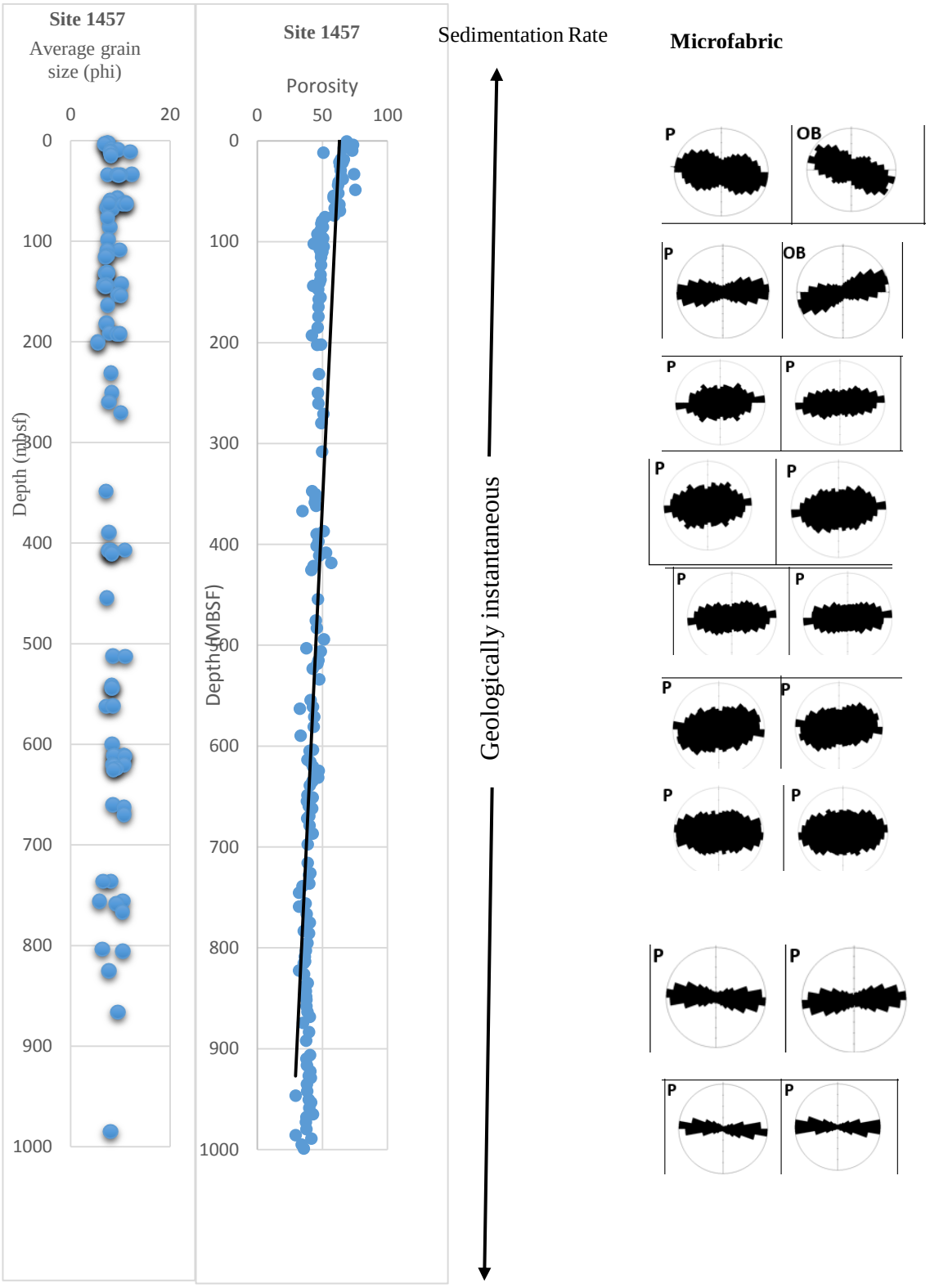

Figure 6.23. Plot of average grain size, porosity (from IODP data), sedimentation rate and microfabric along the depth profile in site 1457.

6.2.7 Synchrotron X-ray powder diffraction

Preferred orientation from synchrotron powder diffraction were inferred based on intensity variation along the Debye rings (Janssen *et al.*, 2012). A diffraction image in which some minerals are indexed is presented in Figure 6.24. The diffraction images for contourite, hemipelagite and turbidite samples are presented in Table 6.9. Virtually all the diffraction images for the contourite facies display lack of preferred orientation as accentuated by lack of azimuthal intensity variation except in one sub area in sample 1 where there is a slight intensity variation in the innermost Debye ring. The Debye rings for the turbidite facies show variation in intensity at the innermost Debye rings, which is an indication of preferred orientation. 50% of the diffraction images for the hemipelagites indicate some element of preferred orientation while the other 50% are characterized by random orientation.

The prevailing crystallographic orientation in contourite facies is random, admixture of random and preferred orientation for hemipelagites as well as very strong preferred orientation for turbidites from the diffraction image. These results are consistent with grain orientation from the image analysis of the SEM images.

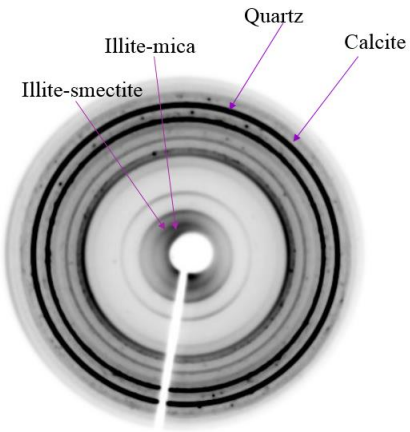

Figure 6.24. Diffraction image from an area of 1 mm x 1mm of a turbidite sample with diffraction rings of illite-smectite, illite-mica and quartz indexed.

Table 6.9. Diffraction images for selected samples of contourites, hemipelagites and turbidites. The diffraction images for each sample represent analysis on three separate spots, in which each spot is about 1 mm X 1 mm and situated 1 mm apart.

Countourites Depth 9m 339-1387B- 2H1 32-34	P 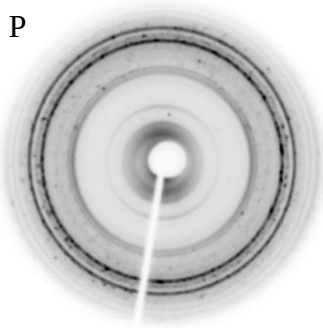	R 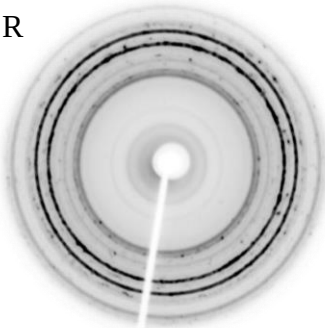	R 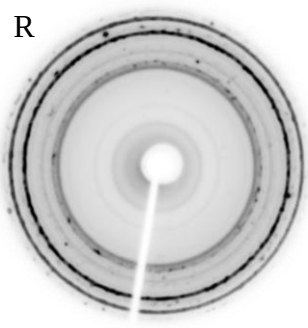
Countourites Depth 253 m 339-1389A- 28X5 130-132	R 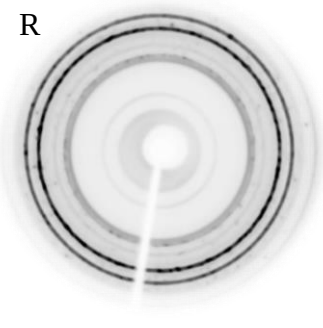	R 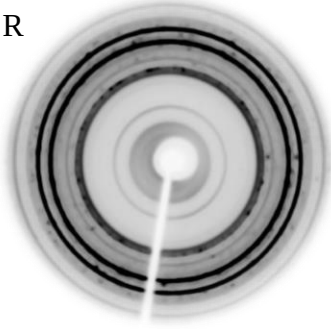	R 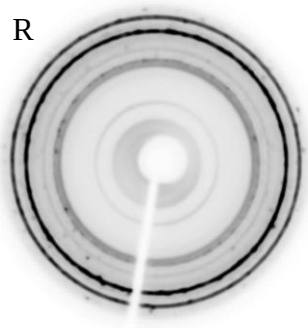
Countourites Depth 943 m 339-1389E 66R1 18-21	R 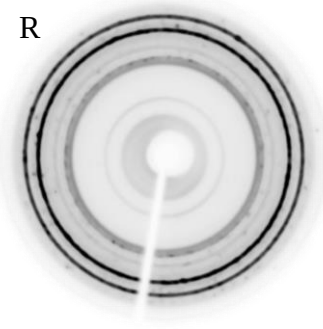	R 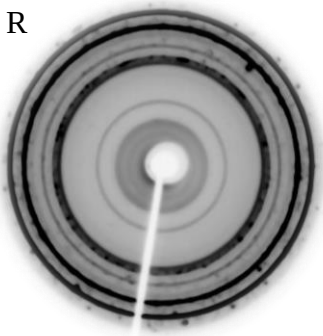	R 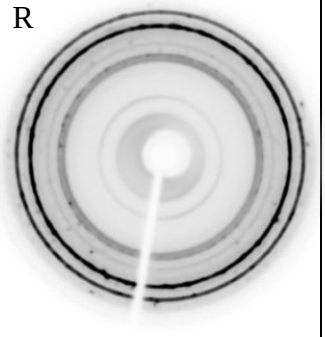
Hemipelagites Depth 8 m 339-1385A 2H6 13-15	R 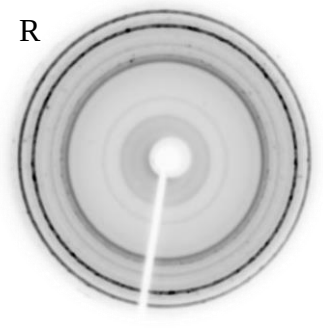	R 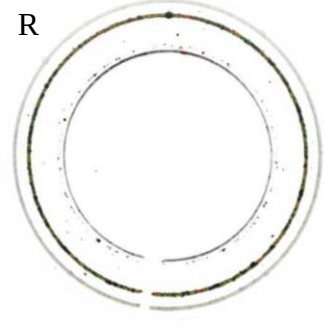	R 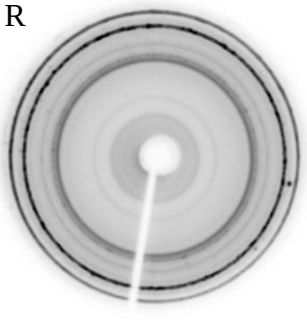

Hemipelagites Depth 57 m 339-1385A 7H6 54-56	P 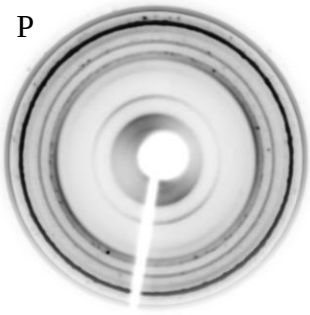	P 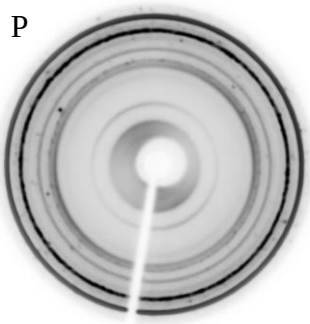	R 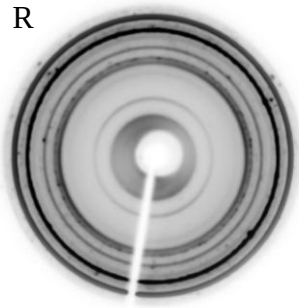
Hemipelagites Depth 117 m 339-1385A 14H2 70-72	P 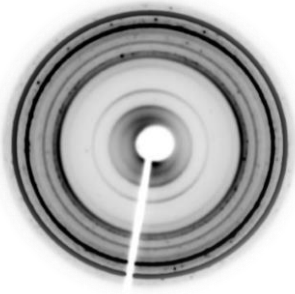	P 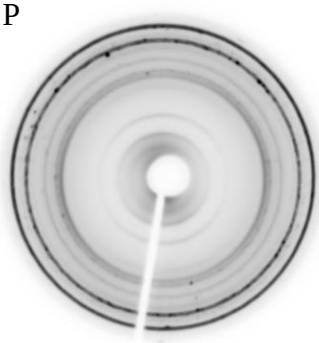	P 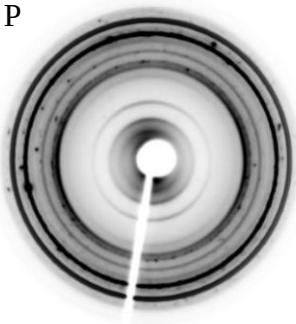
Turbidites Depth 68 m 355-1457A 8H2 27-31	P 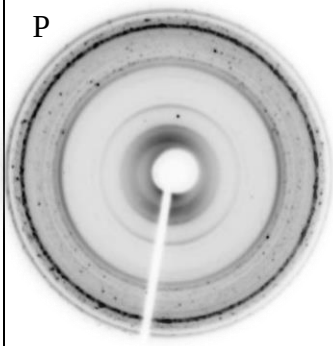	P 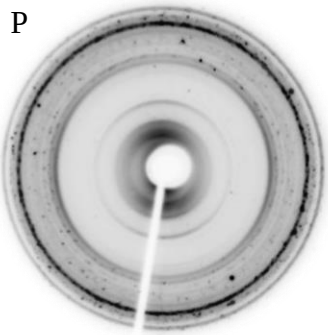	P 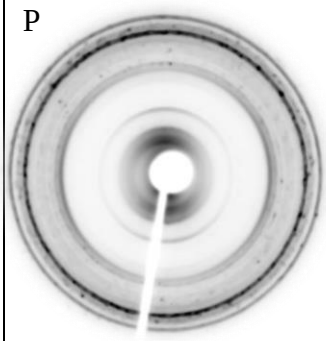
Turbidites Depth 260 m 355-1457C 9R1 7-11	P 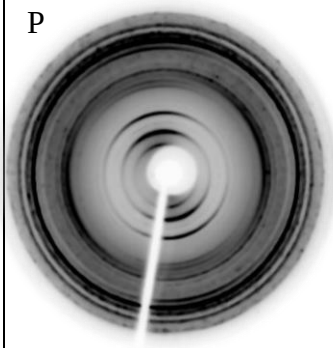	P 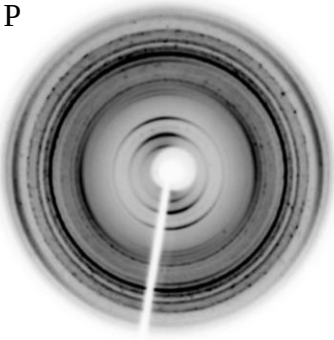	P 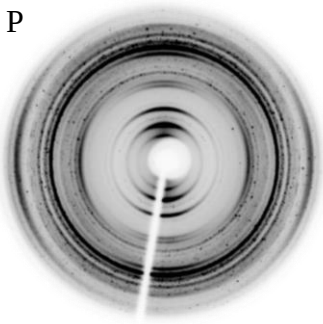

Turbidites Depth 985 m 355-1457C 83R6 5-6	P 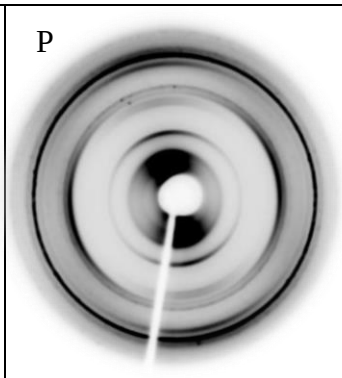	P 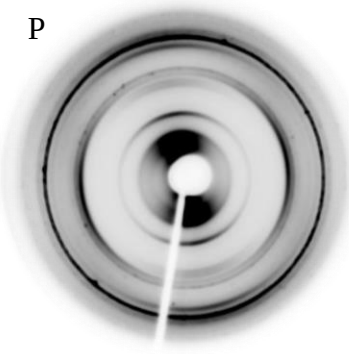	P 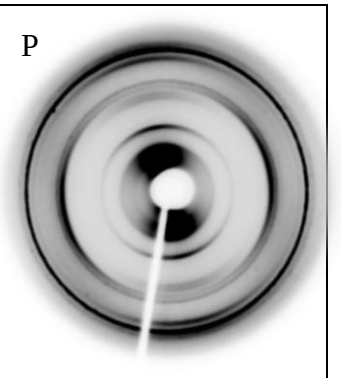

P= Preferred orientation R= Random orientation

CHAPTER 7 – DISCUSSION

7 Discussion

7.1 Introduction

The overall aims of this research, as set out in Chapter 1, are to: (1) develop an improved methodology and workflow for the study of mudrock microstructure; and (2) document and compare the microstructural characteristics of different deep-water mudrock facies, and assess to what extent the depositional process is a causal factor in their microstructure.

The new methodology and an appropriate workflow has been fully developed and discussed in Chapters 4 (Bankole *et al.*, 2018b) and 5 (Bankole *et al.*, 2018a) and are currently in press. That discussion, therefore, is only briefly summarised below. Two other publications, in which I made significant contribution are highlighted under list of publications. One of the published paper entails part of the workflow presented in chapter 5 on quantification of microporosity, but applied to carbonate rocks (Buckman *et al.*, 2017) while the other is a methodology applied to mudrocks (Buckman *et al.*, 2018).

The main focus of this chapter is to discuss progress made towards the second principal aim. For this purpose, microstructure is considered in its three main components – grain size, microfabric, and petrophysical properties – and, for each of these, the differences between turbidites, contourites and hemipelagites are discussed.

Microstructure is a specific characteristic of mudrocks that is believed to be influenced by a range of factors including: depositional environment, depositional processes, mineralogical composition, grain-size distribution, diagenetic history (cementation), sediment compaction (burial), and post-depositional deformation processes (other than compaction). Salient properties such as porosity, permeability and seismic anisotropy have been linked to the microstructural characteristics of rocks (Berge, Berryman and Bonner, 1993; Dvorkin and Nur, 1996; Noiriel, Gouze and Bernard, 2004). There is currently much interest in understanding the microstructure of low permeability rocks, including mudrocks, due to the growing interest in their potential as seals for carbon-dioxide storage, as suitable repositories for nuclear waste, and as from unconventional reservoir rocks for the production of hydrocarbons (shale oil and shale gas). One aspect of mudrock microstructure of particular interest is that of clay mineral orientation (or microfabric) as it causes seismic anisotropy and also affects the elastic properties of the rocks (Kanitpanyacharoen *et al.*, 2014; Wilkinson and Fenton, 2015).

The findings of this thesis contribute to these several important applications.

7.2 Methodology

This study has developed a new methodology for the fast, reliable and effective characterisation of microstructure in mudrocks, using a semi-automated image analysis of SEM images in backscatter mode. This is referred to as the automated image acquisition and analysis (AIAA) technique (Bankole *et al.*, 2018a). It differs significantly from prior work in two respects: (1) it images relatively large areas by a process of automated acquisition and stitching and, (2) it incorporates multiple areas that are randomly selected from the sample. Both of these aspects help mitigate against relying on data from too small a sample area of a heterogeneous sediment.

Good sample preparation techniques are the first important step, in order to ensure a high degree of polish and minimal sample disturbance. This can be by polished thin section or ion-milling. The AIAA technique then has the following principal advantages: (a) a high degree of automation, which increases efficiency and reduces user-input and bias; (b) maximum area coverage by using automated tiling and stitching of images; and (c) the ability to derive high quality data on grain size, grain orientation, pore size and porosity at the same time.

In Chapter 4 (Bankole *et al.*, 2018b), the method is specifically used for grain-size analysis. This is the first application, known to the author, of the image analysis technique for grain-size measurement. It has all the advantages listed above, as well as being the only method that directly images and measures individual grains in mud-grade sediments. Between 35000 to 45000 measurements are made in each of six subset images from one sample. This number of grains would be impossible to manage through manual measurement. Because this provides a direct means of visualising grains in mudrocks with respect to the whole sediment, the grain shape and context (grain fabric) can also be determined at the same time. Whereas, grain-size analysis by other techniques mainly involve bulk analysis of disaggregated samples and yields only the percentage of grains in each size class, without having knowledge about the morphology and the number of grains considered.

There are, however, some clear disadvantages in the methodology developed for both microstructural and grain-size analysis. These include: (a) the requirement for very large datasets, typically up to many gigabytes per image, which need long scanning times and very large computer memory; and (b) there is always a need for higher-resolution instrumentation at the nano-scale, especially for micropore characterisation.

The grain-size technique has been compared with one of the most common grain-size analysis methods in current use – that of laser diffraction analysis. The two methods yielded closely comparable results for the majority of samples, which therefore provides a high level of confidence in the new technique proposed here. There are, of course, some differences, which would be expected in techniques that are measuring different grain properties – i.e. actual feret diameter of grains for AIAA versus a light-scattering parameter for laser diffraction. These have been further discussed in Chapter 4.

Few other methods exist for microfabric determination, so that it is difficult to make any reliable comparison with the AIAA technique developed here. Recent work by Nishida (2016) uses the anisotropy of magnetic susceptibility as a proxy for the microfabric of muddy contourites in the Gulf of Cadiz. In this thesis, I have also attempted a completely new method of microstructural analysis using the European synchrotron facility in Grenoble, France. This used a highly focussed x-ray beam directed on a polished sample surface to produce an x-ray powder diffraction pattern. This revealed the orientation of crystallographic axes for the different minerals present, which could then be compared with results on grain orientation using the AIAA technique. Very preliminary results from this work appear to validate the AIAA study. This is discussed further in the microfabric section below (7.4).

7.3 Grain size

The original sample selection of mud-rich sediments has ensured that all are fine-grained, with mean size mostly in the fine silt to fine clay range (6-11 phi), with one or two medium silt and very fine clay sizes. An effort was made to select the finer mud-rich parts of contourite sequences from the Gulf of Cadiz cores, the upper mud-rich parts of distal turbidites from the Indus Fan cores, and normal slope hemipelagites with an admixture of terrigenous mud and fine bioclastics. There is, therefore, relatively little difference in the range of mean size for each of the three deep-water facies, although the hemipelagites are slightly finer-grained overall, the contourites slightly coarser grained, and the turbidites span the spectrum of both other facies. This allows for reasonable comparison to be made between the facies without any significant influence of grain size.

The actual mean size of deep-water sediments is controlled by three principal factors: (a) sediment supply – i.e. the grain size distribution of the original source material; (b) distance from source – i.e. the distance travelled in the turbidity current or bottom current, or the

distance from shore for hemipelagites; and (c) current velocity – in that this affects the current's capacity to transport and/or winnow sediment.

Because both the turbidite and contourite facies sampled are closely associated with similar but coarser-grained facies (commonly in the same bed), neither the sediment supply nor the distance travelled are likely to exert significant control. Rather, it is the current velocity at the time of deposition and within that particular part of the depositing current that was most important. This is likely to have been very low for both types of current – i.e. around 10 cm/s or less (Brackenridge *et al.*, 2018; Stow and Omoniyi, 2018). Hemipelagite grain size, by contrast, is controlled by sediment supply, including primary productivity of biogenic material, and by distance from source, for the wind-blown and surface-current transported terrigenous fraction.

Cross plots of textural statistical parameters to differentiate between river, dune and beach environments has been in used for some decades (Friedman, 1961; Moiola and Weiser, 1968) but there is very little application of this approach to distinguish between deep-water sediments. Early work on distinguishing turbidites from contourites is reported by Stow (1979) and, more recently, Alonso *et al.* (2016) and Brackenridge *et al.* (2018) have presented much recent data on grain-size characteristics from Gulf of Cadiz contourites, including some very interesting bivariate cross plots. The bivariate cross plots of average grain size versus sorting, kurtosis and skewness, presented in this thesis (Chapter 6), complement those of Brackenridge *et al.* (2018) and confirm that, in general, these textural statistical parameters are sensitive to depositional processes occurring within deep-water. The plot of mean size versus sorting (see Figure 6.5) shows a well-defined trend, albeit with some scatter, of improved sorting with decrease in mean size for all three facies types. Although this trend is noted by Brackenridge *et al.* (2018), these authors focus primarily on the coarse silt to sand facies and have little to say about the finer muds. They do suggest that low current velocity and extensive bioturbation has induced the very poorly sorted nature of the fine and medium silts.

However, the controls on this trend, which includes all facies, must be more complex. The hemipelagites were deposited in the absence of current action and are intensely bioturbated throughout, whereas the turbidites were deposited by low velocity currents without significant bioturbation, and the contourites also show weak current action but with much bioturbation. It is therefore proposed that the mean-size/sorting trend observed is due to a combination of: (a) decreasing current velocity and hence lower carrying capacity for both contourite and turbidite

facies; (b) natural heterogeneity in the hemipelagites, in part caused by bioturbation, with areas dominated by only nannofossils and clays; (c) effective sorting within the fine-grained portion of a turbidity current; and (d) an effective lower limit to the grain size of weathered terrigenous particulates in natural systems. Based on the data in this thesis, such a limit may be around 13-14 phi (0.125-0.063 microns).

The skewness/mean-size cross plot also reveals a pronounced trend, in which the finer grain sizes show low or zero skewness (symmetrical size distribution) and the coarser grain sizes show increasingly fine to very fine skew. This pattern reflects deposition dominated by vertical settling for the finest sediments, and by increased, but still low, current velocity as the grain size increases. The kurtosis/mean size cross plot shows very little evidence of a systematic trend. Overall, the combination of the grain size statistical parameters provides useful information about depositional process as shown in Figure 7.1. However, it is less useful for differentiation between the three sediment types – contourites, hemipelagites and turbidites – because of significant overlap in the data points. There is some better separation between contourites and hemipelagites, which may be able to inform their distinction in some instances. However, it is believed there is a natural continuum between the two processes.

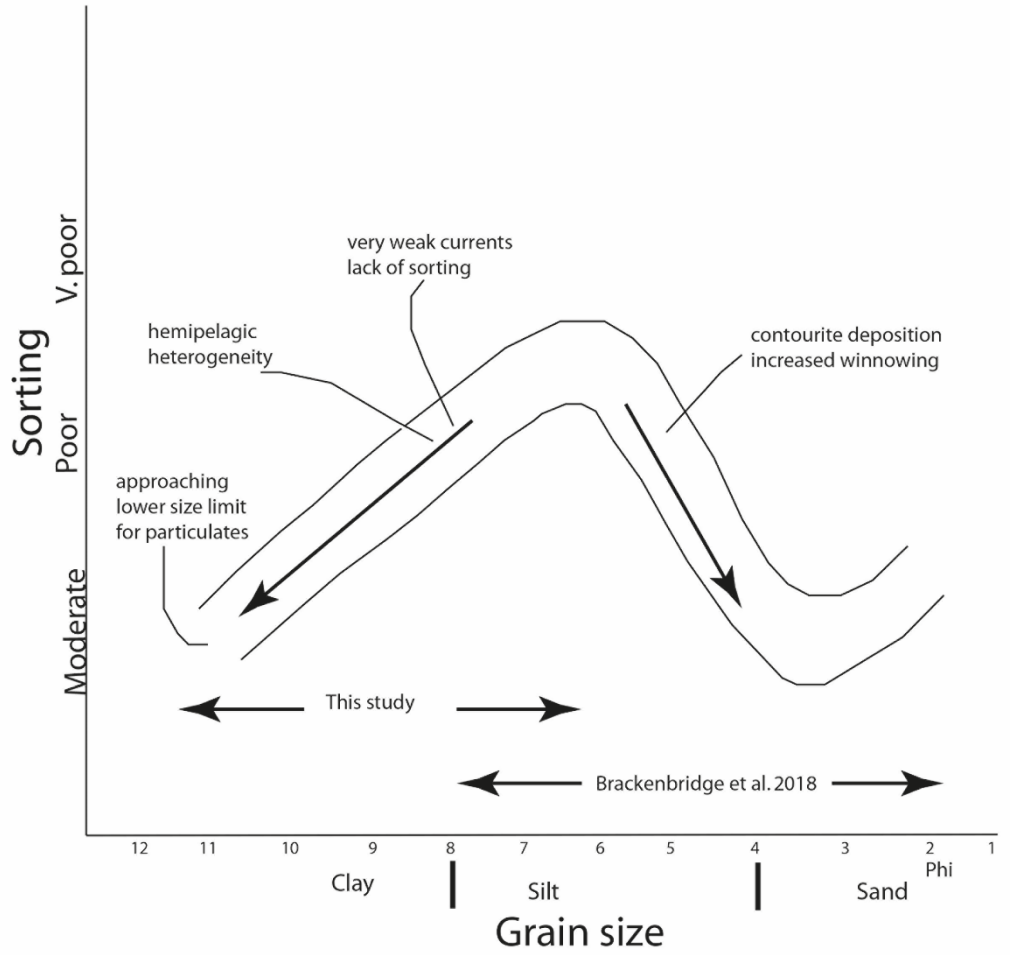

Figure 7.1. Cross plot of grain size agrainst sorting. The plot shows two end-members (sand rich and mud rich) of grains size displaying better sorting while the silt grain size is poorly sorted.

7.4 Petrophysical properties

Characterisation of the petrophysical properties based on low pressure nitrogen gas adsorption (LPNGA) shows existence of weak correlation between specific surface area and average grain size in which specific surface area increases with decrease in grain size (Figure 7.2 A). It is well documented in the literature that specific surface area increases with decrease in the grain size and specific surface area has been considered as a proxy to grain size (Horowitz and Elrick, 1987; Lowell *et al.*, 2012). Apart from the grain size, previous works have shown that there is positive correlation between specific surface area and the total organic carbon content in addition to the smectite content (Kaufhold *et al.*, 2010; Cao *et al.*, 2015). In this study, the clay content was not routinely differentiated between the different clay minerals. However, limited shipboard analyses for both the contourite and hemipelagite cores show relatively little if any

smectite (Stow *et al.*, 2013). Nevertheless, the results show that specific surface area increases progressively with the clay content (Figure 7.2 B). The specific specific surface area is higher in samples with higher clay content in comparison with the others due to the fine grain size and platy morphology of the clay minerals (Kuila *et al.*, 2012) .

Porosity value determined through LPNGA shows weak negative correlation (Pearson Correlation Coefficient (PCC) = 0.35) between grain size and porosity (Figure 7.3 A), whereas plots of grain size against porosity determined through digital rock physics show no correlation (PCC = -0.07) (PCC = -0.07) (Figure 7.3 B). The discrepancy between the two techniques is due to the fact that porosity values derived from LPNGA are mainly within the mesopore range (50 nm – 2 nm) and the technique is most accurate for measuring less than 200 nm diameter pores (Kuila *et al.*, 2014; Bertier *et al.*, 2016). On the other hand, digital rock physics utilizing high-SEM images as employed in this study yields results on porosity limited to the macropores (> 25 nm to > 1 μm). Hence, the technique misses significant number of pores within the mesopore range (50 nm – 2 nm) and the micropores (< 2 nm).

Porosity measurement through LPNGA shows that samples with high clay contents, and correspondingly fine grain size, have higher porosity values, which is an indication that the measured pores are restricted to small pores. In fact, this result is in agreement with previous works. In which high content of clay is suggested to produce hight amount of mesopores (Chalmers, Bustin and Power, 2012; Kuila *et al.*, 2012; Cao *et al.*, 2015).

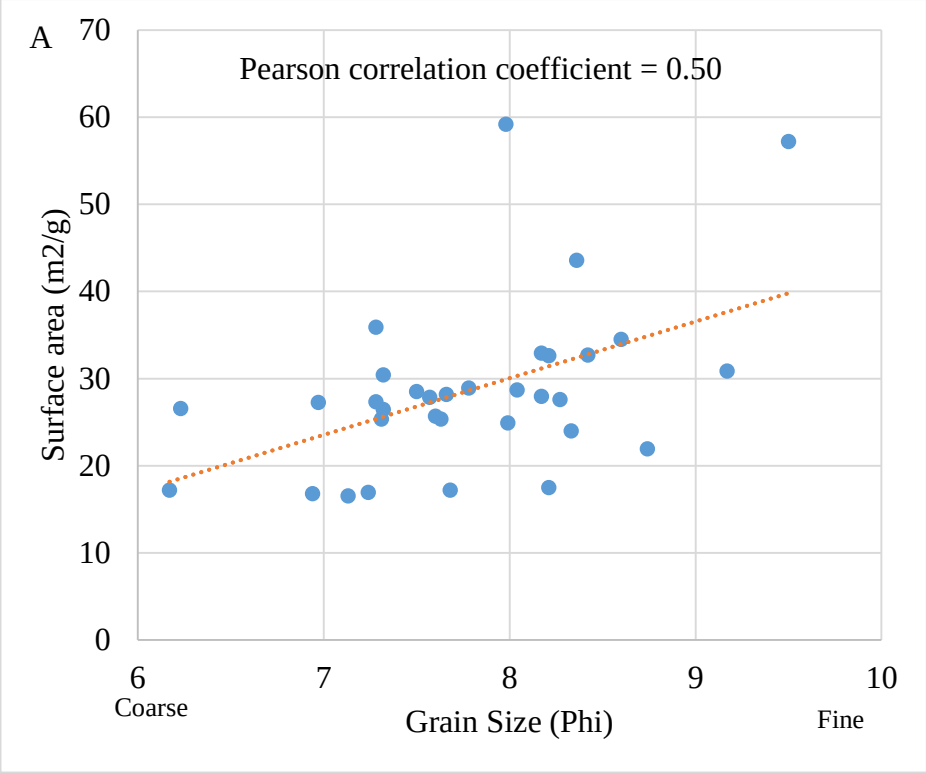

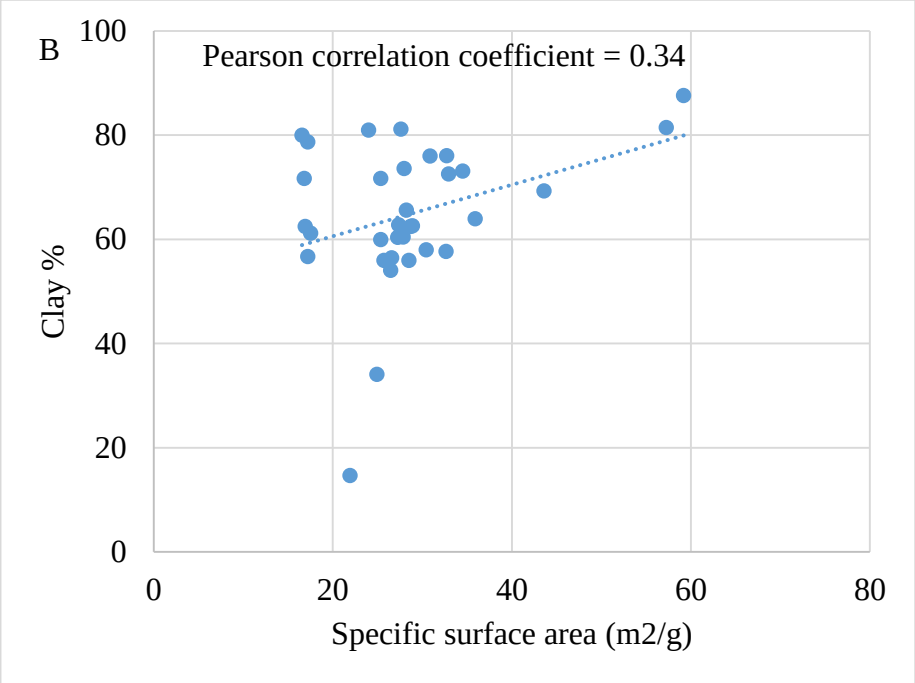

Figure 7.2. Plot of specific specific surface area against grain size (A) and clay content (B). There is a moderate negative correlation between specific surface area and grain size and a weak positive correlation between specific surface area and clay content. The correlation bettwen specific surface area and grain size and clay content indicate that both parameters clay and grain size have influence adsorption properties of the material. Note that the grain size in figure A decreases to the right of the x-axis.

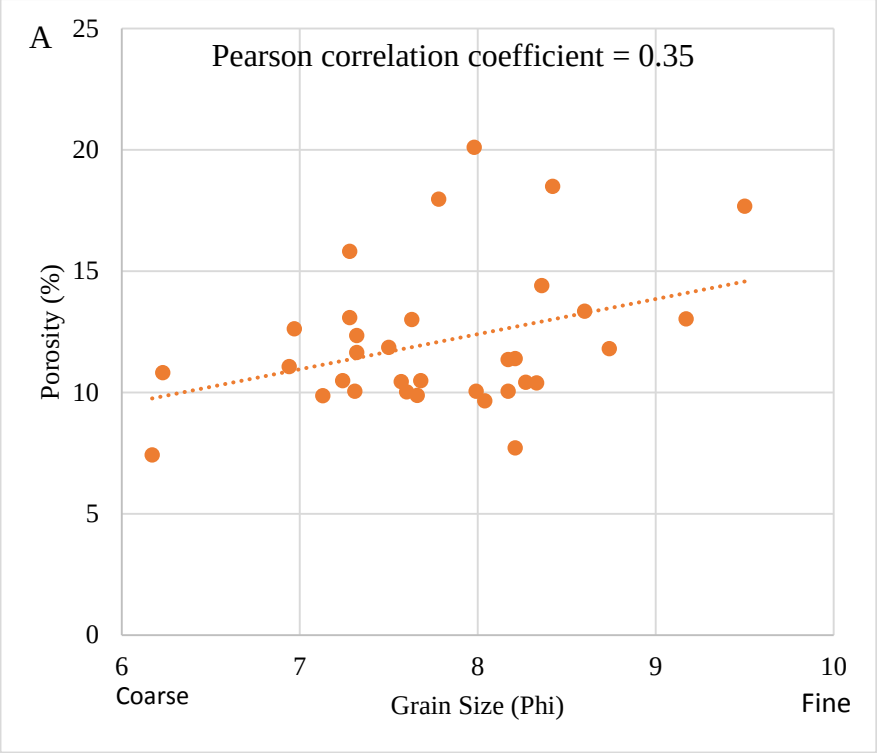

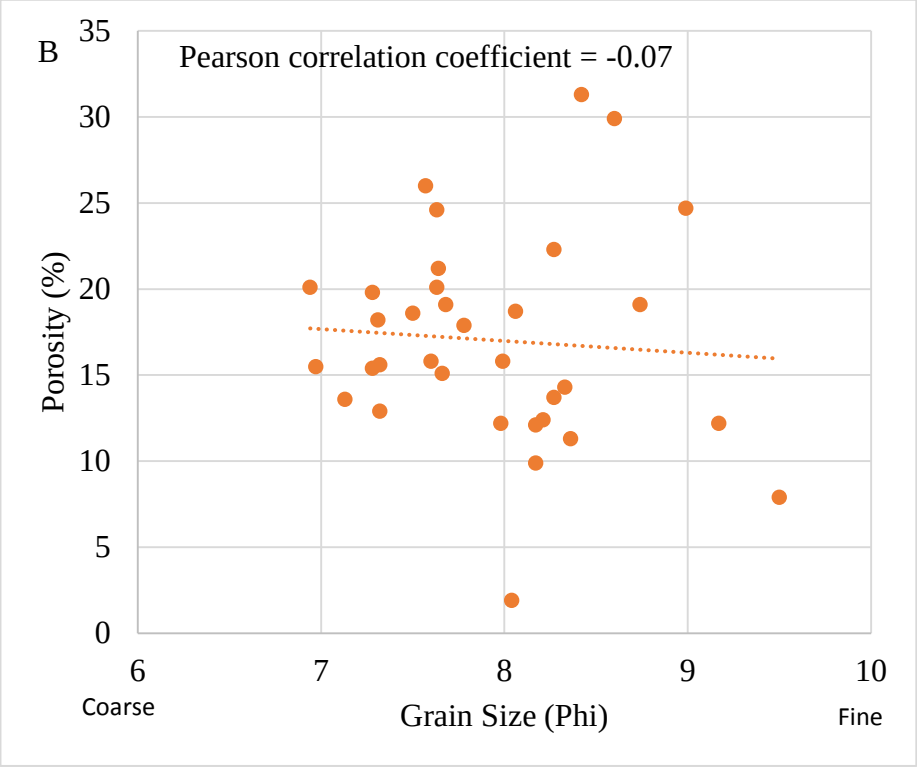

Figure 7.3. Plot of average grain-size against porosity (A) Porosity values determined from low pressure nitrogen gas adsorption (B) Digital rock physics (DRP). Note the variation between the two correlations which is due to the fact that low pressure nitrogen gas adsorption is measuring the mesopores while macropores are measured by the DRP.

Infact, cross plots of porosity versus depth reveal that the porosity measured through LPNGA increases with depth whereas porosity measurement derived from DRP decreases with depth (Figure 7.4). The dissimilar trends between the two porosity measurements can be attributed to compaction effect, in which many macropores (both interparticle and intraparticle pores) in mudrocks are collapsed and reduced in sizes through cementation and compression. As compaction progresses, finer grained materials especially clay minerals and pyrites are squeezed within the pores spaces as this process eventually destroys or reduces the pore sizes (Loucks *et al.*, 2012).

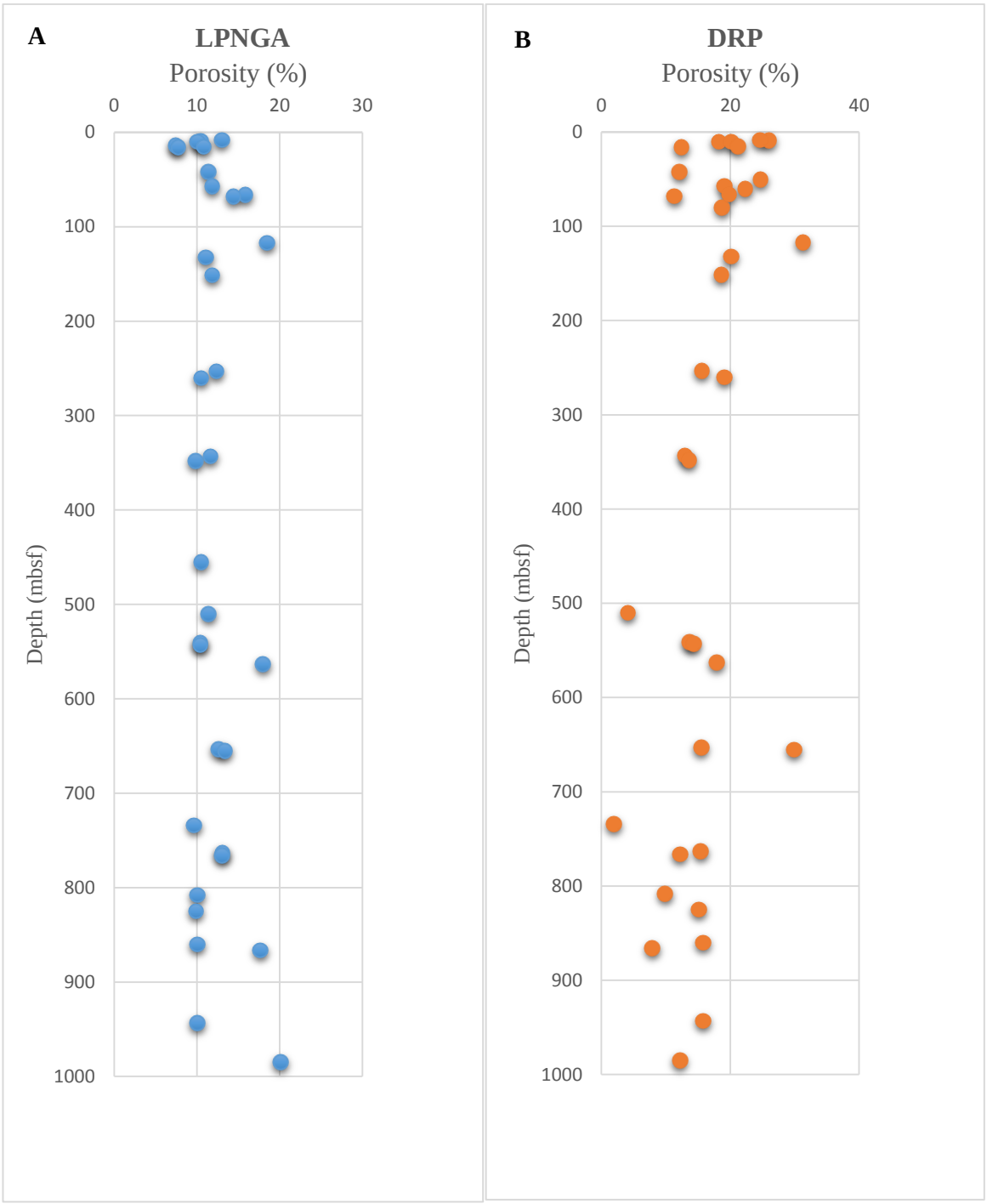

Figure 7.4. Cross plots of porosity against depth (A) LPNGA and (B) DRP. There is progressive increase in the porosity along the depth profile for porosity measurements through LPNGA while DRP shows an opposite trend. The discrepancy in both trends is due to destruction and reduction in size of the larger pore sizes along the depth profiles, resulting from compaction.

The petrophysical properties derived in this study (porosity, pore volume and surface area), using LPNGA technique and digital rock physics, show no very strong differences between the three deep-water sediment types. However, there is some indication from the cross plot of porosity versus permeability, which suggests that hemipelagites are the most permeable, followed by turbidites, whereas contourites have the lowest permeability values. This observation, coupled with microfabric analysis, in which hemipelagites show a combination of random and oblique microfabrics, suggests that permeability and pore connectivity is enhanced by a multi-directional orientation. A preferred orientation, as characteristic of the turbidite facies, has higher permeability restricted to the preferred bed-parallel orientation. Contourites have a less well-defined preferred bed-parallel alignment and less distinctive multi-directional microfabric, and therefore have the lowest permeability values (Figure 7.5).

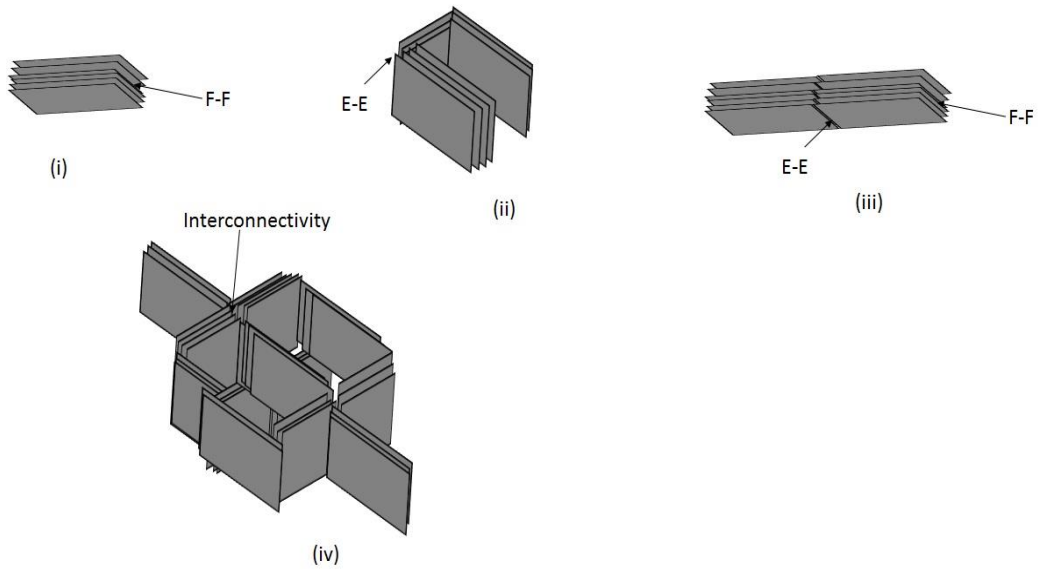

Figure 7.5. Schematic diagrams showing alignment of fine grain particles (i) Face to Face grain along a preferred orientation (ii) Face to Face and Edge to Edge indicating dual orientation directions (iii) Face to Face and Edge to Face indication a single preferred orientation direction (iv) Multiple Face to Face, Edge to Edge and Face to Face packets having multi-direction. Note that the multi-directional configuration is likely to enhance pore connectivity and permeability.

7.5 Microfabric

7.5.1 General controls on microfabric

Several different controls have been proposed for the origin and nature of microfabric in mudrocks, as reviewed in Chapter 2. In summary, these include:

(a) Primary orientation of grains during deposition either as dispersed or flocculated particles, which may be linked to depositional process and/or environment (O'Brien, Nakazawa and Tokuhashi, 1980; O'Brien, 1987; O'Brien and Pietraszek-Mattner, 1998);
(b) Primary and secondary orientation of grains as a result of organic matter content of the sediment, whereby greater organic-matter content leads to greater fissility and parallel grain orientation (Odom, 1967; Moon and Hurst, 1984);
(c) Primary and secondary orientation of clay minerals as a result of the silt content, with more silt leading to more random orientation (Day-Stirrat, 2014);
(d) Re-orientation of clay minerals during the smectite to illite transformation (Ho, Peacor and van Der Pluijm, 1999; Aplin, Matenaar and van der Pluijm, 2003)
(e) Re-orientation of grains as the result of mechanical compaction (Sintubin, 1994; Aplin *et al.*, 2006), fault gouge (Solum and van der Pluijm, 2009), and low-grade metamorphsm (Jacob, Kisch and van der Pluijm, 2000).

This study has focussed mainly on assessing the role of depositional processes in microfabric development of deep-water sediments, with a secondary comment on the role of mineralogy, grain-size (silt content), and burial compaction.

7.5.2 Process controls: this study

Over 340 measurements of microfabric have been documented (Chapter 6) and plotted as individual rose diagrams of grain orientation (Table 6.4) – 150 contourites, 100 hemipelagites and 96 turbidites. These clearly show two important points: firstly, visual observation of the rose plots coupled with quantitative statistical analysis provides robust data; and, secondly, the microfabric data derived from silt orientation is nearly always exactly the same as that for clay orientation, so that one can be used as the proxy for the whole sediment.

They also reveal very distinct differences between the three facies types. Turbidites show a dominance of *preferred orientation* parallel to bedding (81%), with 5% semi-random and 14% preferred, oblique plots. Hemipelagites, by contrast, show a dominance of *random* (43%) and

semi-random (9%) orientations, but with 48% oblique orientation. Contourites lie somewhere between the two, having 26% preferred orientation parallel to bedding, 31% semi-random, and 40% random. Only 3% are considered as oblique to bedding.

These pronounced differences are interpreted as being due to the different depositional processes. The *preferred microfabric* in turbidites reflects deposition from a relatively low-velocity and low-concentration turbidity current. Estimates of flow properties for such currents (Stow and Omoniyi, 2018) suggest velocity < 20 cm/s and concentration between 25-250 mg/l. The actual rate of sedimentation would be geologically instantaneous – with deposition occurring over a few days for a 10 cm mud turbidite. Many of the oblique orientation plots for the turbidites are only slightly deviated from parallel to bedding and may therefore reflect slight draw-down at the edge of the core due to the coring process. The very few semi-random plots might be influenced by draped fabric around coarser silt grains. Some minor bioturbation is also possible but was not observed in the cores studied.

Hemipelagic sedimentation have been proposed to result from very slow sedimentation, augmented by pelletization (Stow, 1985b) Subsequent research focused on trace fossils in hemipelagites (Uchman and Wetzel, 2011) as well a recent study focused on porosity characteristics in deep-water mudrocks have identified pellets within them (Slatt and O'Brien, 2011). However, in the current study no pellet was observed through thin-section petrography and scanning electron microscopy. The reason for the lack of pellets in hemipelagites remains an enigma but one possibility is bacterial degradation (Bąk *et al.*, 2014)

The *random microfabric* of hemipelagites, and complete absence of a preferred bedding parallel fabric, reflects deposition in the absence of any current influence, and results from ultra-low-concentration settling through the water column mainly as flocs and possibly as pellets. The rate of sedimentation is more or less uniformly very slow, and has been calculated as 11 cm/ky for the study site on the basis of very careful dating (Stow *et al.*, 2013). The co-dominance of an *oblique microfabric*, often highly oblique to bedding and with more or less distinct grain alignment, is believed to result from bioturbation (Figure 7.6). Distinctive large-scale burrowing and overall bioturbational mottling is a notable feature of the study cores, and of hemipelagites in general. The oblique microfabric observed is therefore considered to be a secondary preferred alignment, which is at various oblique angles or nearly vertical to bedding, in some cases, and which is caused by burrowing organisms that align the grains along the length of the burrow, particularly along the cavity walls. Because hemipelagites are more

ubiquitously bioturbated and characterised by large scale burrows compared to contourites, the oblique orientation is more common in them compared to the latter.

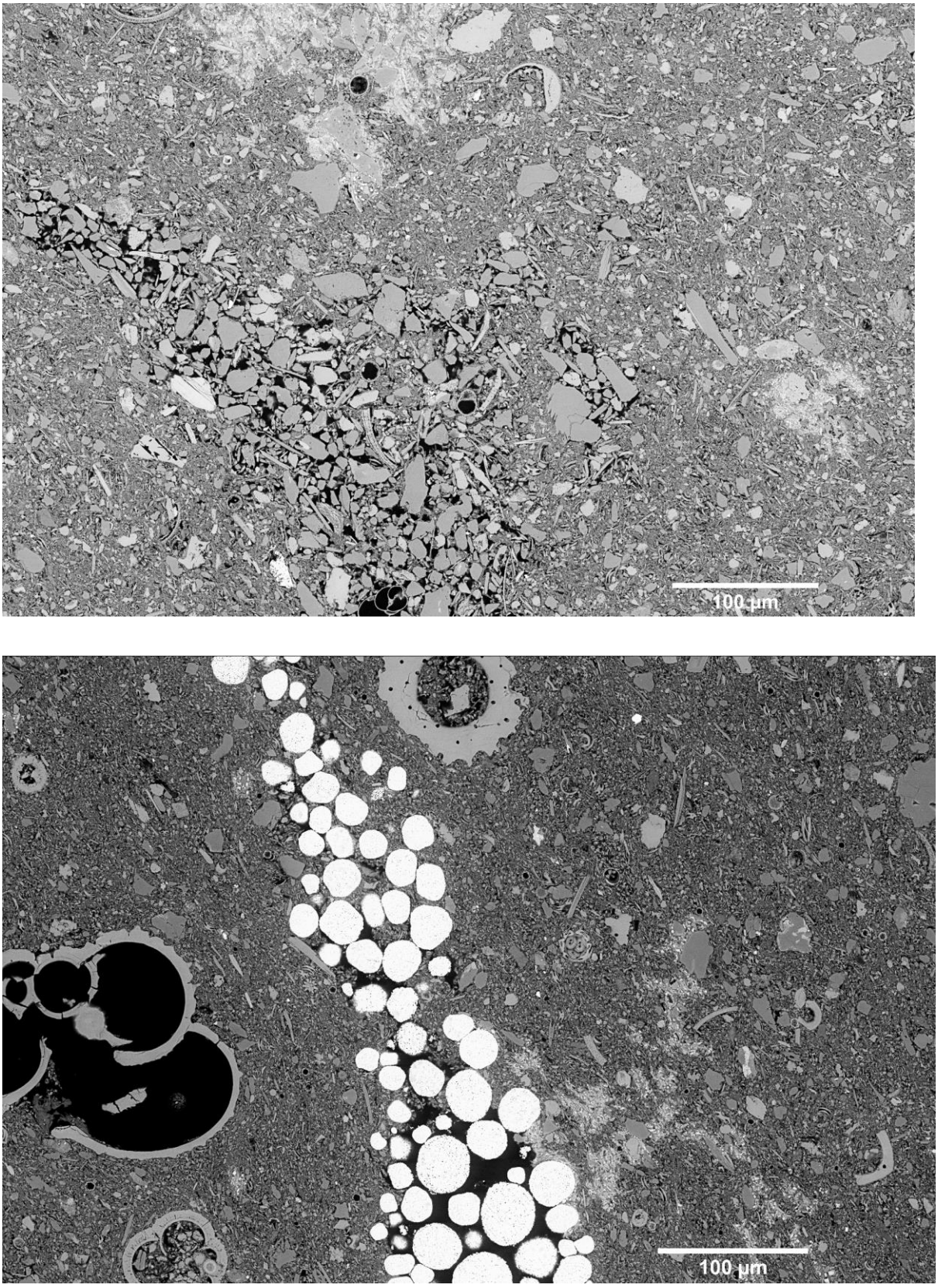

Figure 7.6. Burrows imparting preferred orientation directions on grains in hemipelagite facies (A) Sample 1 subset 2 (B) Sample 11 subset 5. Note the oblique orientation close to the burrows and rather chaotic fabric away from the burrows.

The *mixed microfabric* in contourites is a close mix between the turbidite and hemipelagite microfabric styles – part preferred, part semi-random and part random. This indicates deposition from low velocity and very low-concentration bottom currents, which would tend to produce a preferred to weakly-preferred microfabric, together with an overprint of bioturbation, which yields the random to semi-random microfabric. Flow properties for such bottom currents, based on data synthesised by (Stow *et al.*, 2008), are likely to be in the order of flow velocity 10-15 cm/s and concentration between 0.02-0.2 mg/l. The rate of sedimentation is considered to be more or less uniformly slow, and has been calculated as mostly between 25-40 cm/ky for the study sites on the basis of careful dating (Stow et al., 2013). Two samples are from a site with sedimentation rates of 100 cm/ky. With the slower rates of sedimentation, bioturbation is continuous throughout, although it is not generally quite as intense nor large-scale as for hemipelagites (Stow *et al.*, 2008; Wetzel, Werner and Stow, 2008). At the higher rates of sedimentation, there is evidence in the cores that some primary lamination has been preserved and that bioturbation is not as intense. However, within the contourite facies, there is no clear link between the rates of sedimentation and microfabric.

The null hypothesis set up in Chapter 1 (section 1.4) that 'there is no significant difference in microstructure among the various fine-grained sediment facies in deep-water' is therefore refuted. Marked differences do exist and those differences are due to depositional process. A further null hypothesis set up in Chapter 1, that 'variation in sedimentation rate does not cause modification in mudrock microstructure' is also refuted. Sedimentation rate affects the nature and degree of bioturbation in the different facies and hence the nature of the microfabric. This is true for the large differences in rate between turbidites, contourites and hemipelagites, but is not seen for subtle rate changes within the contourite facies.

7.5.3 Other controls: this study

Grain size: The grain size analysis data have been documented in Chapter 6 and discussed above (section 7.3), especially with regard to the information they provide with respect to the nature of deep-water depositional processes. With regard to the potential grain size influence on microfabric, there appears to be no systematic correlation between the two. The mean grain size classes represented in the studied samples include fine silt, very fine silt, coarse clay and medium clay, and across this spectrum of grain sizes there is an irregular variation between all the microfabric types observed. This is true both for all facies taken together and for each facies separately. For example, the data for contourites are shown in Table 7.1.

Table 7.1. Correlation of mean grain size class with microfabric

Microfabric	Fine Silt		
	Contourites (%)	Hemipelagites (%)	Turbidites (%)
Parallel bedding	12.5	-	50
Semi-random	42	-	-
Random	33	-	-
Oblique	12.5	-	50
	Very fine Silt		
Parallel bedding	36	0	97.5
Semi-random	31	16	2.5
Random	31	48	-
Oblique	3	36	-
	Coarse clay		
Parallel bedding	21	-	66
Semi-random	28	3.5	3
Random	49	44	-
Oblique	2	52.5	31
	Medium clay		
Parallel bedding	-	-	87.5
Semi-random	-	-	12.5
Random	-	-	-
Oblique	-	-	-

The null hypothesis set up in Chapter 1 (section 1.4) that 'variation in grain-size has no significant effect on microstructure of fine-grained sediments' is therefore upheld.

Mineralogy: The three dominant components present in all facies examined in this study are carbonate (biogenic and detrital), clay minerals, and quartz. Minor feldspars, heavy minerals, and lithic grains also occur in very low amounts. Comparison of mineralogy with microfabric shows no systematic trends, either within a single facies type or across all facies. For example, the carbonate percent ranges between 4-83% for all facies, and 12-83% for hemipelagites. But, regardless of the carbonate content, hemipelagites show the same admixture random and

oblique microfabric. The same lack of correlation is true for the contourite facies, with a carbonate range of 4-37%.

The null hypothesis set up in Chapter 1 (section 1.4) that 'mineralogical composition does not affect mudrock microstructure' is therefore upheld.

Burial depth: The burial depths from which samples were analysed for microfabric ranges from 8-985 m below seafloor. Those sediments recovered from near the surface are soft and unconsolidated, whereas those from 700m and below are hard, compact and semi-consolidated. Certain horizons even above 700 m are cemented as hard rocks, but samples from these were not included in this study. It is therefore reasonable to assume that any pronounced effects of compaction and consolidation on microfabric would be evident in the deeper samples. In particular, one might anticipate a high degree of preferred grain alignment with bedding as an effect of compaction.

However, the two contourite samples closest to the surface (within 10 m below the seafloor) show 87% strongly-preferred orientation that is parallel to the bedding, whereas the two deepest samples (at 763 m and 808 m depth below seafloor) show only 45% preferred, bed-parallel orientation. There is no systematic variation between these upper and lower samples.

Hemipelagites are characterised by dominantly random and oblique orientations at all depths, whereas turbidites show mostly preferred bed-parallel microfabric at all depths. However, in the case of the turbidites, the samples below 750 m show > 95% preferred bed-parallel fabric, whereas the samples above 150 m show 40% preferred bed-parallel and 60% preferred oblique to bedding. These oblique fabrics are mostly well aligned and only slightly oblique to bedding, so that they may be a result of core-margin bending during retrieval.

As earlier described in chapter 1 (section 1.5), mudrock microstructure entails the summation of all observations made on mudrocks at a nanometre to micrometre scale, which includes the relationship among grains (microfabric), grain orientation and alignment, pore shape and morphology, porosity and its connectivity, mineralogical composition and other small micron to submicron features that are present in them (e.g. microfractures and microbioturbation). The results presented in this study reveal no systematic variation in microfabric and grain size along the depth profile (Figure 6.18 - Figure 6.23). However, for each of the sites, there is systematic decrease in the total porosity values with increasing depth and Pearson correlation coefficient indicating low to strong correlation between the two parameters. Therefore, overall, the null

hypothesis set up in Chapter 1 (section 1.4) that ‘burial depth and physical compaction have no tangible effect on the microstructure of fine-grained sediment at depths less than 1000 m’ is therefore refuted.

7.5.4 Towards a microfabric model for deep-water sediments

Very few previous studies have specifically addressed the microfabric of deep-water sediments (O'Brien, Nakazawa and Tokuhashi, 1980; Stow and Tabrez, 1998) and these demonstrate rather inconclusive results. O'Brien, Nakazawa and Tokuhashi (1980) suggest turbidites are characterised by randomly oriented clays due to clay flocculation within more concentrated turbidity currents, whereas hemipelagites have a more preferred clay orientation. This conclusion is supported by Stow and Tabrez (1998, Table 3), who further report that contourites may show parts with particle clusters (random fabric) and parts with a more aligned fabric, where not bioturbated. They further report on 30 samples of hemipelagites from the Oman margin that were examined for microstructure. These results are rather mixed, but mostly indicate a random fabric.

These early studies utilised broken surfaces in combination with scanning electron microscopy, which had rather poorer resolution at the micron-scale than today's instruments. However, retrieving information on mudrock microstructures from broken surfaces is elusive and is no more recommended (Schieber, 2014), and the routinely higher resolution that can be achieved today should permit more definitive observations.

Two more recent studies have reported no difference between microfabric of turbidites and hemipelagites, and that both facies are characterised by random orientation (Ochoa, Wolak and Gardner, 2013; Kase *et al.*, 2016). Most recently, a single study by Nishida (2016) presented results on microfabric from the Gulf of Cadiz contourites, which indicate that these contourites, in general, have a sub-parallel clay microfabric (Nishida, 2016).

The results presented in this thesis represent the most detailed study to date, using 38 samples of mud-rich contourites, hemipelagites and turbidites, and a total of 346 high-resolution SEM images of microfabric. Furthermore, the study has pioneered a new methodology, utilising semi-automated image acquisition and analysis of multiple, large, high-resolution SEM images from randomly selected areas of the selected samples. It is also supported by synchrotron X-ray powder diffraction images from which there is remarkable consistency between the results from both techniques.

In the data presented here, the microfabric of deep-water mudrocks is interpreted as closely linked to the depositional process coupled with modification by syn-depositional and early post-depositional bioturbation processes. The grain size, mineralogy and depth of burial appear

to have little effect, certainly for burial depths of less than 1 km as examined for this thesis. The depositional controls are threefold: flow velocity, sediment concentration, and sedimentation rate. These are illustrated in Figure 7.7 with respect to the microfabric type found in turbidites, contourites and hemipelagites.

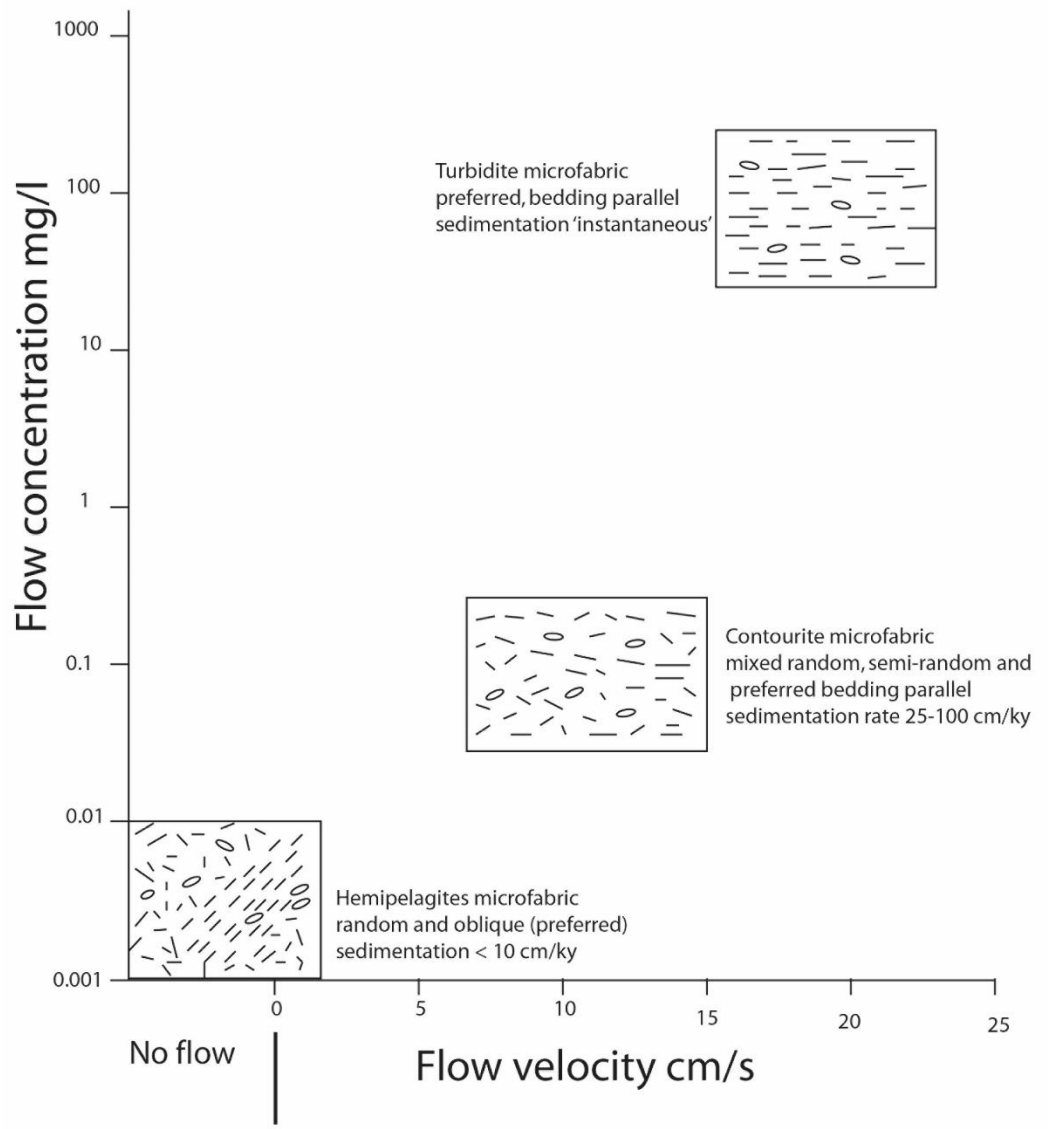

Figure 7.7. Microfabric model for deep-water fine-grained sediments. Hemipelagites are associated with no current flow and very low sedimentation rate (< 10 cm/ky) and their typical microfabric is random to oblique. Contourites are characterised with mixed fabric (random, semi-random and parallel to bedding), the sedimenation rate is also low and associated with low flow concentration. Turbidites are typically bedding parallel associated with very rapid semimentation.

In muddy turbidity currents, with low to moderate velocity and low sediment concentration, clay flocs and silt grains become progressively more concentrated as they settle out of suspension towards the seafloor. The randomly-oriented clay fabric within the flocs, now much more concentrated near the base of the flow, is then broken up by *flow shear* as final deposition occurs through the benthic boundary layer. This leads to the preferred bed-parallel microfabric (Figure 7.8). In more silt-rich muddy turbidity currents, it is shear sorting through the benthic boundary layer that has been invoked for the origin of alternating silt-mud laminae (Stow and Bowen, 1978; Stow and Bowen, 1980). But the same flow shear process will operate to yield a preferred microfabric. The actual rate of deposition is very rapid – i.e. hours to days.

Bottom currents, in the process of depositing muddy contourites, have slightly lower flow velocity and much lower levels of sediment concentration than muddy turbidity currents. The same flow shear process will operate as sediment settles through the benthic boundary layer, thereby yielding a preferred bed-parallel microfabric, but this is likely to be less pronounced than in turbidites (Figure 7.8). In particular, the lower concentration of flocs passing through the boundary layer at any one time will result in less particle interference and, therefore, a microfabric somewhere between parallel and semi-random. The rate of sedimentation is low, so that bioturbation is continuous throughout deposition and disruption of the fabric will occur to a greater or lesser extent, yielding a partially random and semi-random microfabric.

Hemipelagic sedimentation occurs in the absence of current activity and with a very sparse distribution of flocs and particles in the water column. Without flow shear, the default microfabric is random. The rate of sedimentation is mostly still lower than for contourites and the bioturbation is more intense and continuous (Figure 7.8). Rather than making an already random fabric more random, the burrowing activity can serve to re-align clay (and other) particles, yielding a preferred oblique or semi-preferred microfabric that is typically inclined to the bedding.

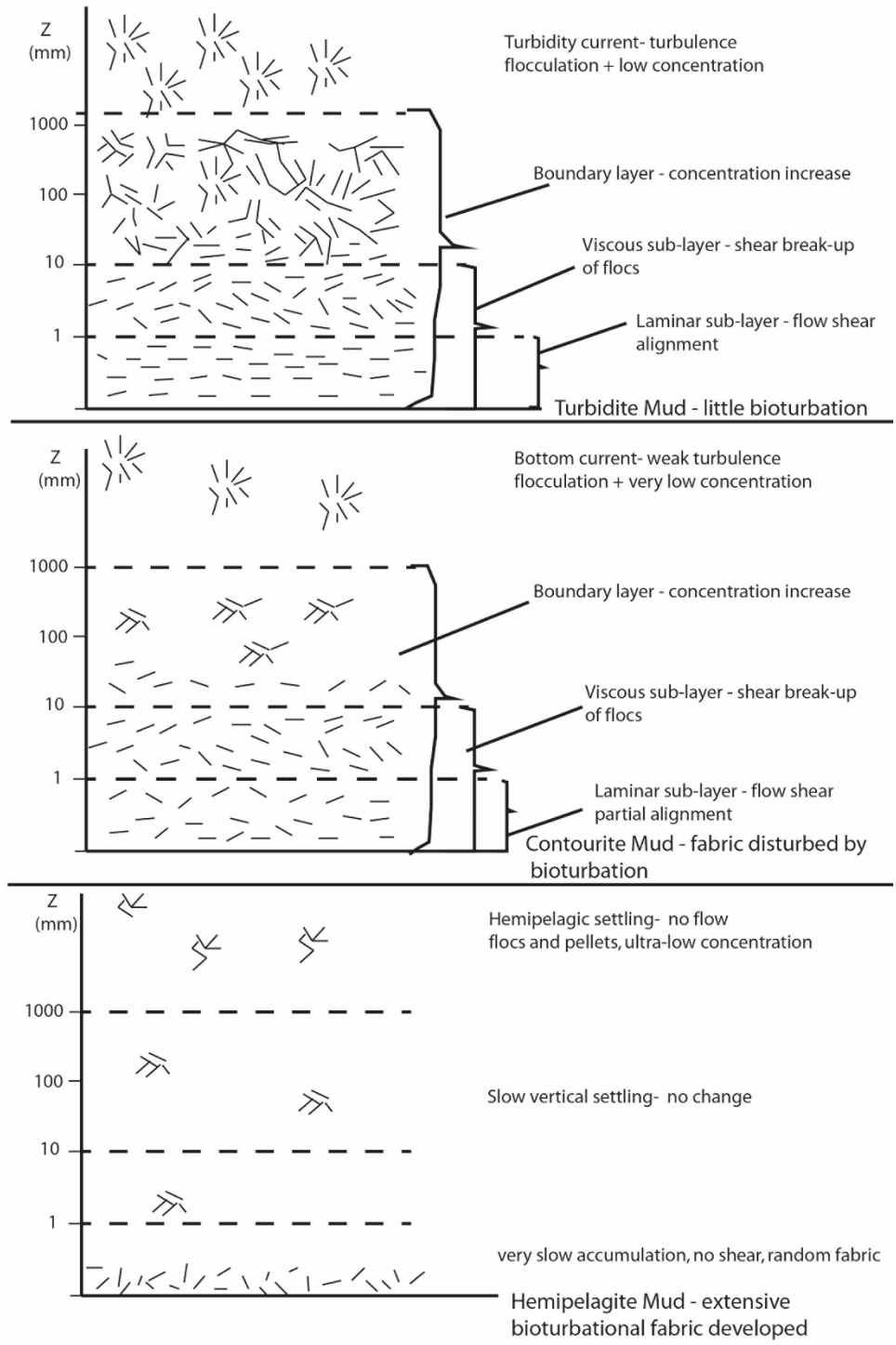

Figure 7.8. Diagramatic scheme showing development of microfabric in deep-water for fine grained sediments. In hemipelagic sedimentation, there is zero flow and sediments settle down thorugh vertical setting. The resultant product is a random fabric with extensive bioturbation. Contourites are produced by weak flow and as the flocculated sediments transit from the boundary layer towards the viscous sub-layer, the flocs are dispersed with grains partially aligned and distortion is caused by bioturbation. Turbidites are associated with high turbulence and the flocs break up as it transit between boundary layer to the viscous sub-layer due to shearing, which results into well aligned grains with little bioturbation.

CHAPTER 8 – SUMMARY, KEY FINDINGS, FURTHER WORK AND CONCLUSION

8 Summary, Key findings, Further work and Conclusion

Mudrocks are ubiquitous in all sedimentary environments including continental, marginal and deep-marine environments. They make up more than 60% of the Earth's sedimentary record and they hold significant information about the history of the Earth. Mudrocks being the general name for fine-grained sedimentary rocks without recourse to their inorganic and organic carbon content. In petroleum systems, mudrocks are well established as source rocks, seal and recently due to technological advancement in drilling, they are noted as unconventional reservoirs.

The aim of this research is twofold: (i) Development of methodologies for determining mudrock microstructure and (ii) application of the developed methodology to fine grained sediments from the deep-water setting (contourites, hemipelagites and turbidites).

8.1 Methodology

Technological advancement in scanning electron microscopy has advanced knowledge on mudrock, but development of fast and cost-effective techniques to study their microstructure is still emerging. In this research, two methodologies were developed: (i) grain size measurement of mudrocks through automated scanning electron microscopy; and (ii) automated imaging analysis of mudrock microstructure.

8.1.1 Drying technique for microstructural studies

Induced micro-fractures related to drying techniques are present in samples subjected to freeze drying, critical point drying, room temperature drying, oven drying and low viscosity resin impregnation. The intensity of the micro-fractures varies from one technique to the other. Low viscosity resin impregnation showed minimal sample damage. Although, critical point drying is commonly recommended for microstructural study of mudrocks (Schieber, 2014), the current study suggests that the critical point drying technique produces conspicuous artificial micro-fractures especially when dealing with semi-consolidated mudrocks. Few earlier studies on fine-grained sedimentary rocks had shown that particle breakage accompanies critical point drying (Lin and Cerato, 2014). For semi-consolidated mudrocks, low viscosity resin impregnation is recommended for getting rid of the pore fluid. The procedure involved is passive, in that the sample is not physically dried, but pore water is removed through ordinary

fluid displacement. The process is inexpensive and does not require any sophisticated equipment, but it is unsuitable for partially dried samples.

8.1.2 Grain size analysis of Mudrocks from SEM images

In chapter 4, the developed methodology for grain size measurement using scanning electron microscopy is presented and has been accepted for publication (Bankole *et al.*, 2018b). The methodology is fast, robust, precise, economical, reliable and suitable for analyzing 100 nm to 100 μm (i.e. clay to very fine sand size particles). The methodology benefits from automated acquisition of SEM images and stitching, which produces relatively large area high-resolution SEM images. Measurement of grain size as presented in chapter 4 was based on percentage Feret diameter and it was compared with laser diffraction granulometry. For most of the parameters deduced including grain size statistical parameters (mean, kurtosis, skewness and sorting), clay, silt and sand percentages, the technique compares well with the laser diffraction granulometry, but with some small disparities.

8.1.3 Automated imaging analysis of mudrock microstructure

Scanning electron microscopy is one of the commonly used techniques for studying microstructure in mudrocks. Widespread practice in scanning electron microscopy involves manual acquisition and stitching of SEM images, which are usually limited in area. The methodology on automated image analysis on microstructure presented in Chapter 5 is currently in press (Bankole *et al.*, 2018a).The methodology is unique and different from previous studies on mudrock microstructure via scanning electron microscopy in that the SEM images are relatively large, and are acquired through automated tiling and stitching. It employs multiple randomly selected areas within polished thin-section and ion-milled samples. These diminish any inaccuracy that might result from relying on data from too small an area, as mudrocks are noted to be highly heterogeneous. The methodology reduces human bias and applies supervised machine learning segmentation. The methodology highlights the varying measurements that can be deduced effectively through scanning electron microscopy, which include: grain size, porosity, pore size distribution, particle orientation (silt and clay size orientation) and mineralogy.

Significant outcomes from the chapter include, similar orientation direction for both silt and clay size particles and incorporation of statistical analysis together with visual observation from rose diagrams to yield unbiased and better interpretation that is devoid of human subjectivity. With respect to mineralogical analysis, energy dispersive x-ray analysis (EDX) displays

significant differences in mineralogy of a given sample at two different resolutions. It is also in poor agreement with whole rock X-ray diffraction techniques.

Overall the technique presented is reliable for analyzing mudrock microstructure, but a good sample preparation is required. The principal disadvantages of the technique include: data acquisition time, very large images running to several gigabytes, high storage computer memory, and lack of resolution at few nano-scales to capture the missed meso-pores and micro-pores.

The field of electron microscopy is still advancing, especially with the recent development of multi-beam scanning electron microscopy, which utilizes 61 to 91 beams and detectors (Crosby, Eberle and Zeidler, 2016) to produce large area images with a throughput of more than one order of magnitude at a very high speed (Eberle *et al.*, 2015). Hence, further refinement of the technique with multi-beam high resolution scanning electron microscopy, with appropriate handling of the data, will yield equally robust data in a still shorter time.

Although the automated process developed yields reduced run-time and helps to avoid user subjectivity, there is often a need to complement the automated process with visual judgement in order to serve as a quality check and produce reliable results.

8.2 Microstructural Characteristics of Deep-water Mudrocks.

In chapter 6 results of different microstructural properties including grain size, mineralogical composition and petrophysical properties were presented to differentiate between contourites, hemipelagites and turbidites. The discussion of the results was presented in chapter 7.

The chapter reveal two significant points that are applicable to mudrock microstructure in general: (i) orientation analysis through visual judgement of rose diagrams coupled with statistical analysis provide unbiased and reliable data; and (ii) orientation of silt size particles is generally closely comparable to that of clay particle orientation, so that one can be used as a reliable proxy for the other. More specifically, with respect to deep-water fine-grained sediments, the contribution also gives a new insight to their microstructure and differs significantly from previous works. It shows that turbidites are generally characterised by preferred parallel to bedding orientation, produced by a rapid sedimentation from turbulent suspension and flow shear during deposition through the benthic boundary layer. Hemipelagites, by contrast, show random or oblique orientation, which is suggested to be associated to the absence of current influence and a strong bioturbation effect. The oblique

orientations, which are mostly at high angle and nearly perpendicular are considered as secondary alignments resulting from burrowing. Contourites, on the other hand, show part alignment resulting from low concentration bottom currents coupled with weaker flow shear, and part random orientation imparted by bioturbation. Hence, the conclusions reached as against the null hypothesis set in chapter 1, section 1.4 are:

1. Microstructure of deep-water fine grained sediments is linked to depositional processes and sedimentation rate.

2. Based on the available data, variation in grain size yields no tangible difference in mudrock microstructure.

3. Mineralogical variation does not produce significant difference in the microstructure of mudrocks.

4. There is a link between burial depth and microstructure of fine grained sediments in the deep-water at burial depths less than 1000m, especially the porosity (but not the microfabric).

8.3 Recommendations for Future work

The research work presented in this thesis attempted to answer some questions related to microstructural characteristics of mudrocks using samples from deep-water settings. The research is believed to be the first of its kind to specifically focus on the microstructure of deep-water facies, and differs significantly from previous work in terms of methodology, results and interpretations. It is hoped that the findings presented in this research will lead to new ways of thinking about deep-water facies microstructure. Future areas that need to be researched to throw more light on deep-water mudrocks and mudrocks in general are highlighted below:

1. One of the problems that is paramount to mudrock study is the proliferation of terminologies. There is lack of standardised terminologies among mudrock researchers and this has a negative effect on comparing research on similar topics. As the publication on mudrock increases, there is a growing confusion in terminologies. It is necessary that mudrock terminologies are standardised so that uniform terms are used by both the industry and academia.
2. Future work on mudrock microstructure should employ higher-resolution electron microscopy, with still larger area of coverage than presented in this work. The high-resolution, large-scale reveals a more representative area, which in turn reveals greater

information on microstructure. Taking advantage of high-resolution electron microscopy, such as multi-beam scanning electron microscopy, will provide larger data sets, which would be more representative, acquired at a shorter time than using single beam scanning electron microscopy.

3. Hemipelagites have a wide range of composition ranging from siliciclastic dominated to biogenic materials. Additional work to understand the difference in microstructure of the two end-members of hemipelagites will give an insight about hemipelagic sedimentation processes.
4. In this research, digital rock physics have been using stochastic simulation to determine flow properties; porosity and permeability. The technique involves relatively small areas (100 μm^2 to 2500 μm^2). There is need for future work to compare results derived from digital rock physics with other experimental methods.
5. A general microstructure of deep-water fine-grained sediments have been presented but the samples analysed have not been buried to beyond 1 km. At such burial depths, mechanical compaction is not intense. There is need for future work to address the effect of greater mechanical compaction (i.e. greater burial depths) on the different sediments types from the deep-water setting. Previous studies have recognized that fine grained turbidites facies are of four types namely: silt, mud, biogenic and disorganized turbidites (Stow, 1985b). Fine grained contourites and hemipelagites are also likely to be of varying types, hence, detail microstructural studies of the sequence of beds belonging to each facies types is recommended.

APPENDICES

Appendix 1A

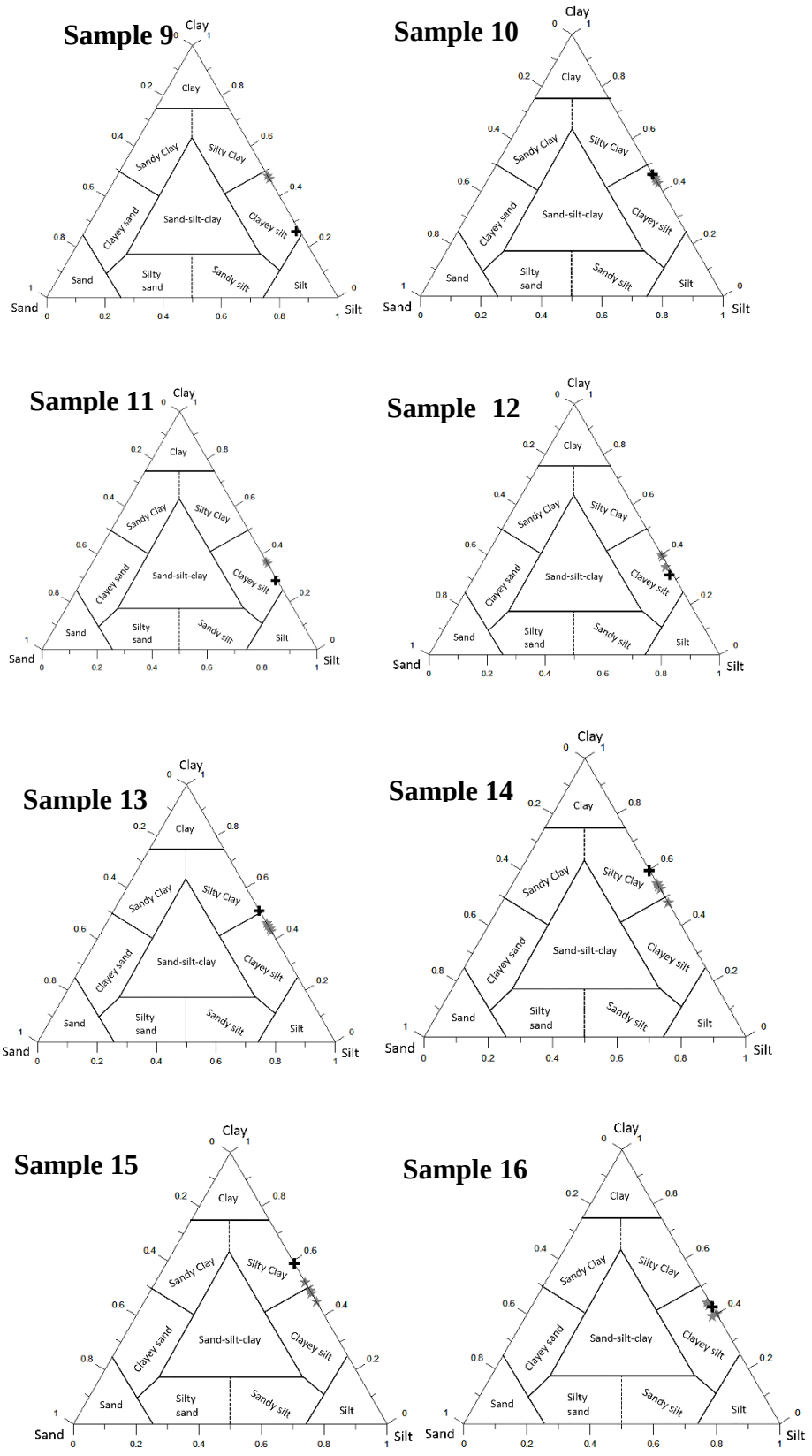

Ternary plot of grain-size distribution (Modified from, Shepard, 1954) based on Feret diameter percentage for the various image subsets analysed and laser

diffraction granulometry. The ternary plots are for sample 9 to 16 respectively. Image analysis subsets are in grey while laser diffraction results are plotted by a black cross. The plots indicate grain-size data from each subset within a sample, although there is subtle variation among the subsets however grain-size composition for the varying subsets in each sample form a cluster.

Appendix 1B

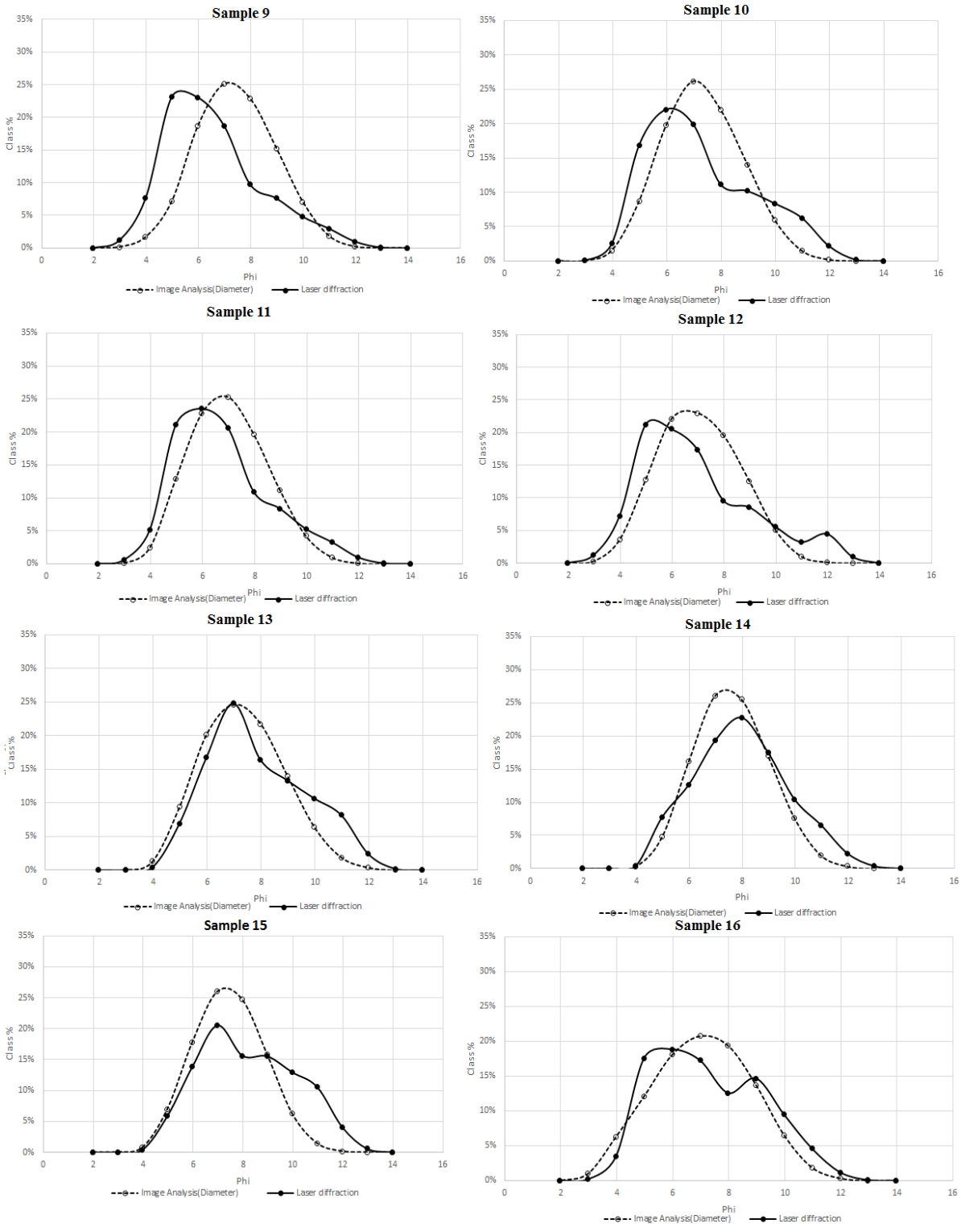

Grain-size distribution curves to compare the resulting distribution from laser diffraction granulometry and image analysis technique described herein.

Appendix 1C

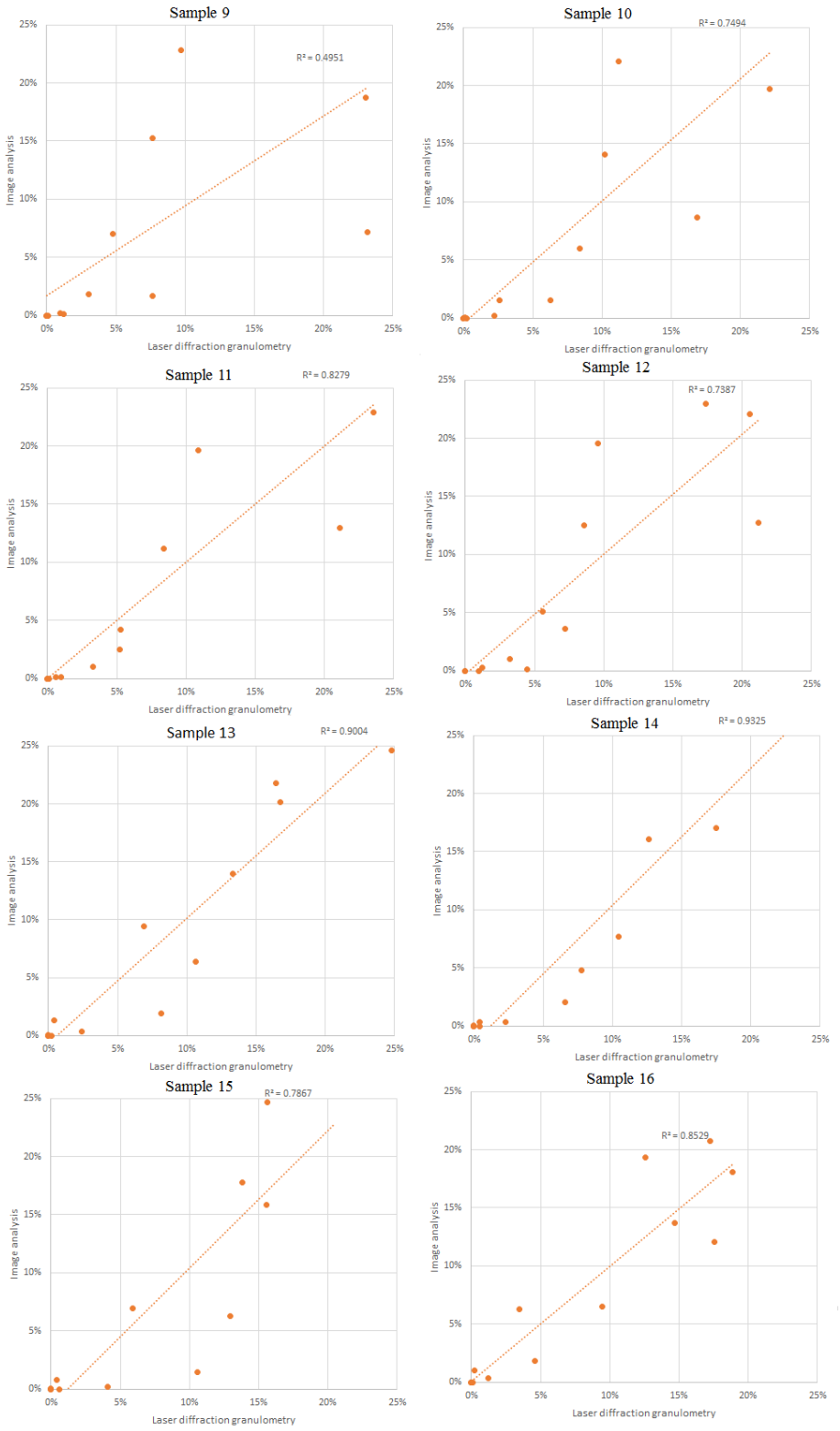

Plots of percentage of grain-size within different phi classes for laser diffraction granulometry vs image analysis based on Feret diameter. Note that the average feret diameter from the subsets of SEM images per sample was used.

Appendix 2A

Empirical Q-Q plots for pore size distribution for Sample 1 to 7

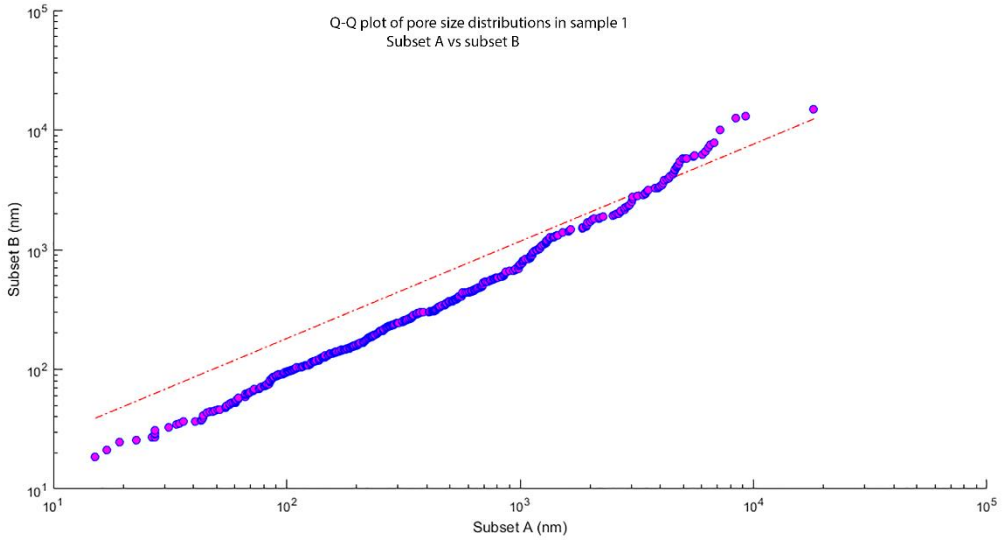

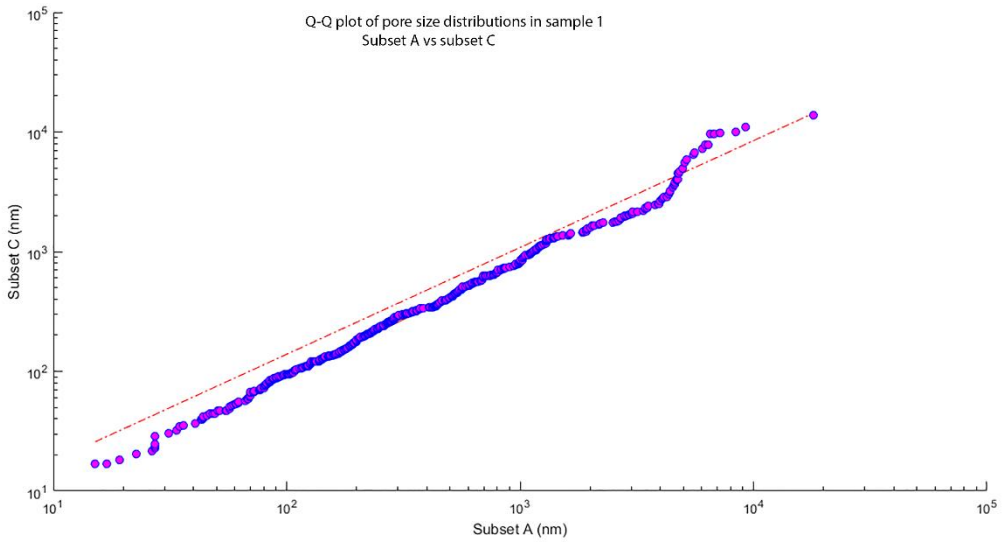

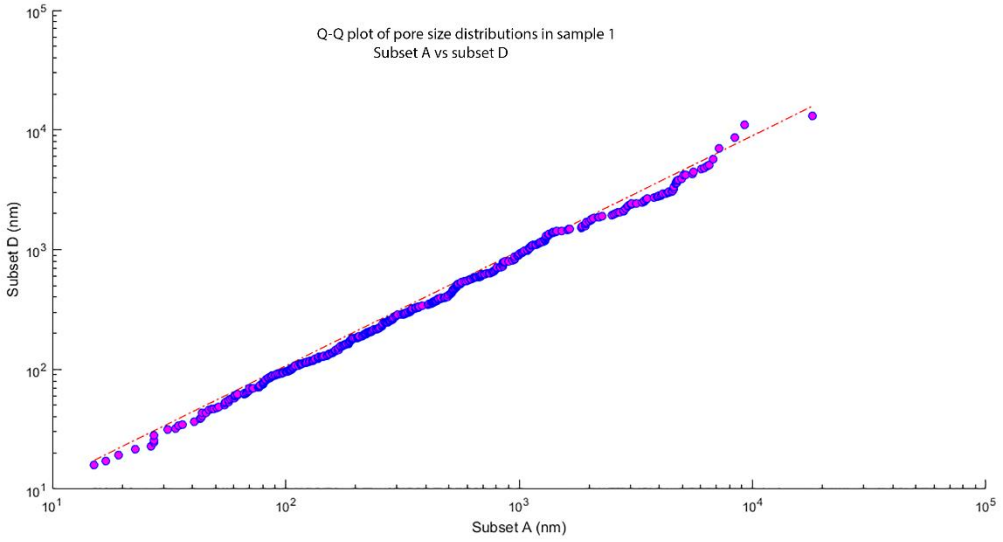
Q-Q plot of pore size distributions in sample 1
Subset A vs subset D
Subset D (nm)
Subset A (nm)

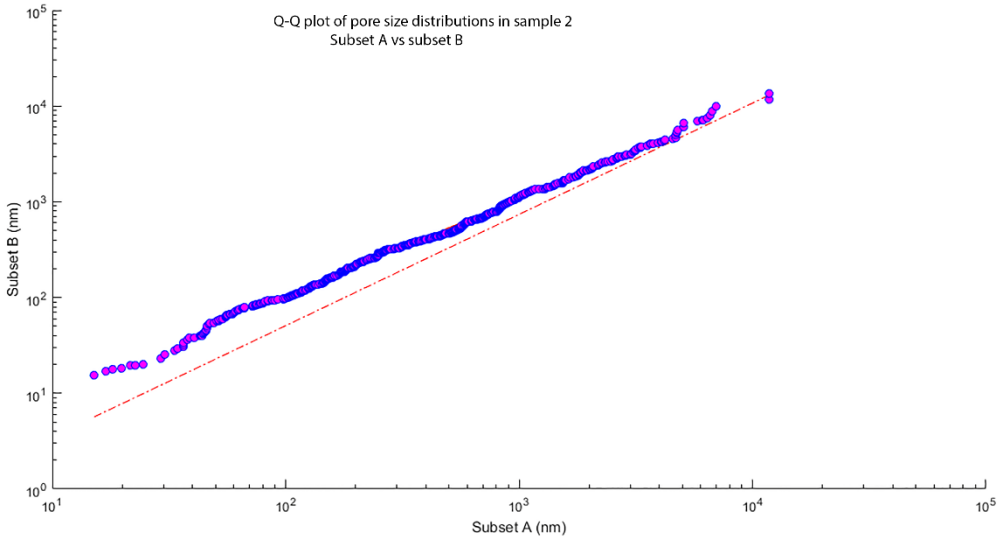
Q-Q plot of pore size distributions in sample 2
Subset A vs subset B
Subset B (nm)
Subset A (nm)

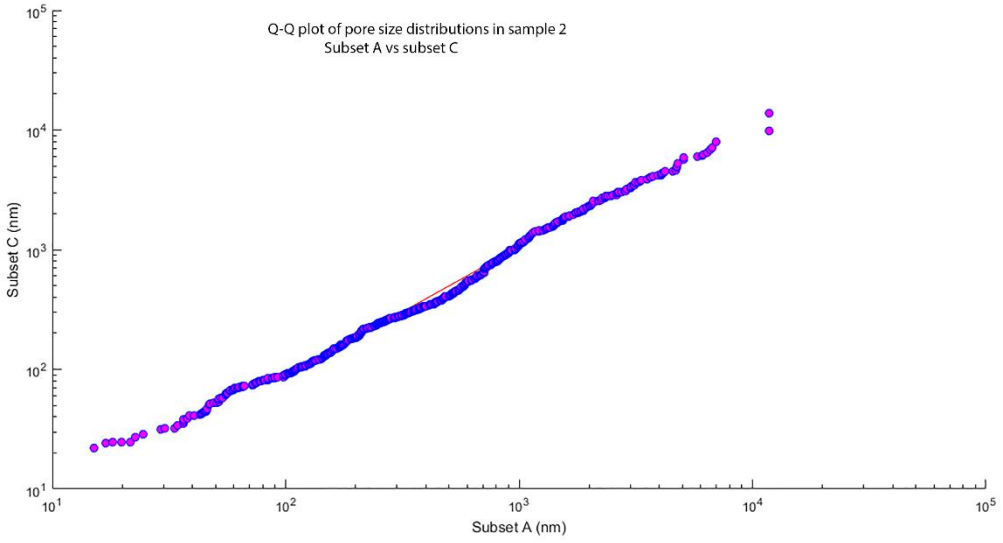
Q-Q plot of pore size distributions in sample 2
Subset A vs subset C
Subset C (nm)
Subset A (nm)

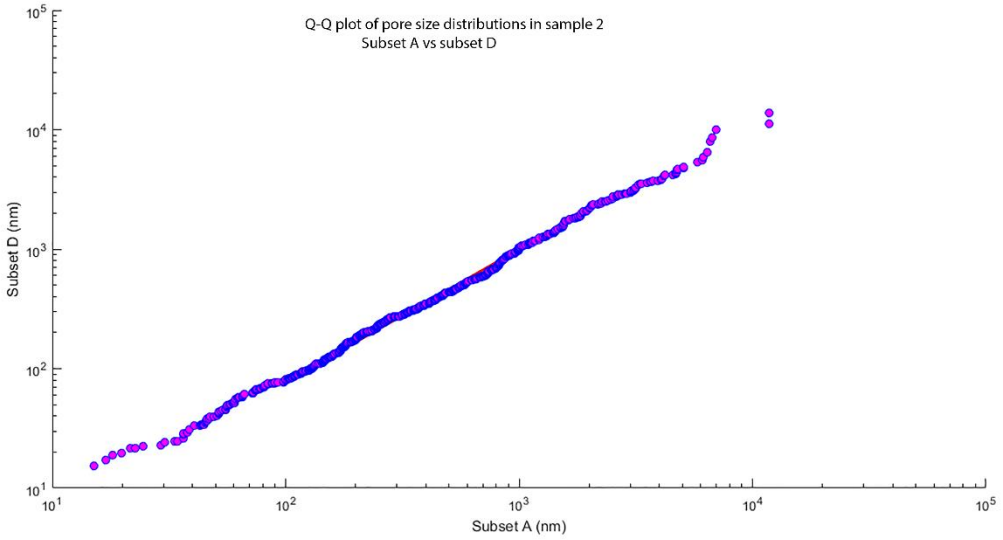
Q-Q plot of pore size distributions in sample 2
Subset A vs subset D
Subset D (nm)
Subset A (nm)

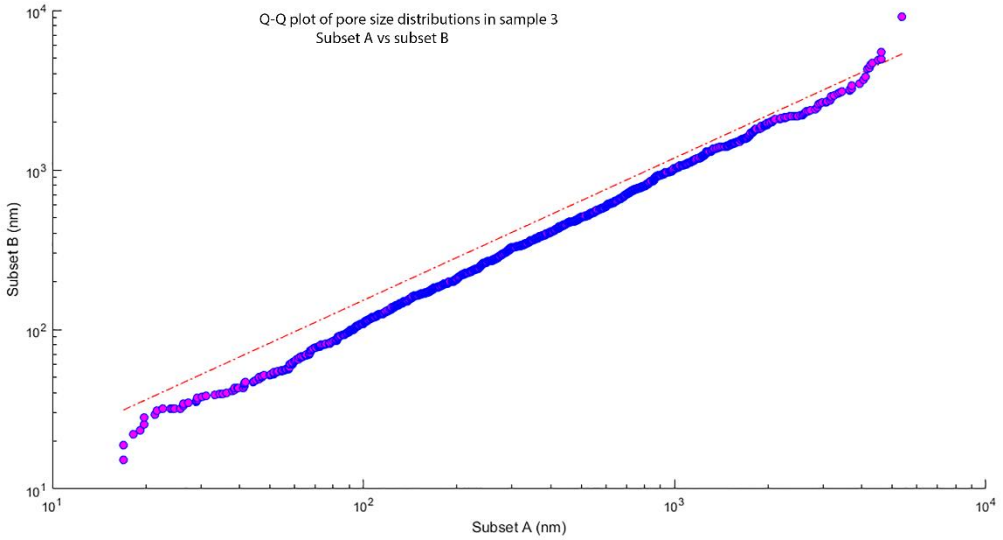
Q-Q plot of pore size distributions in sample 3
Subset A vs subset B
Subset B (nm)
Subset A (nm)

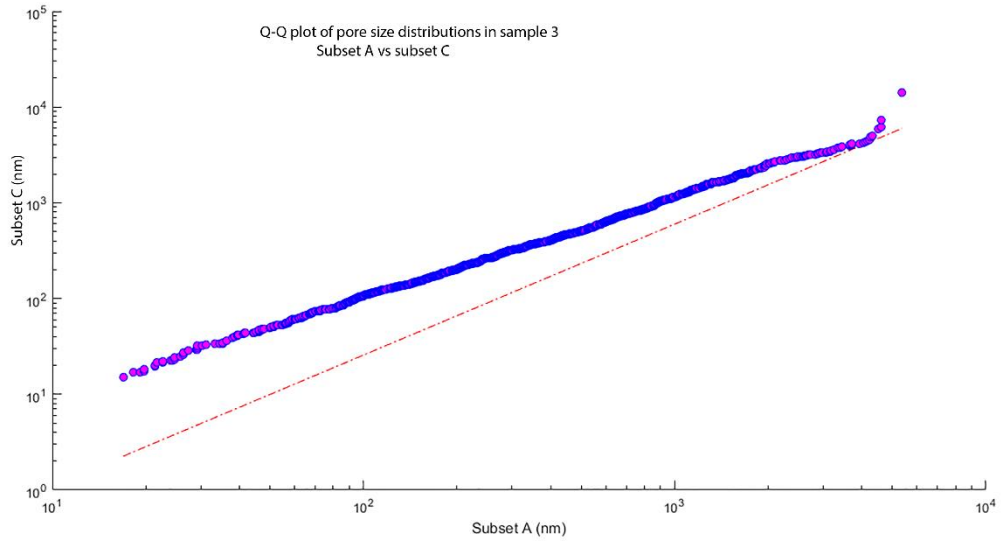
Q-Q plot of pore size distributions in sample 3
Subset A vs subset C
Subset C (nm)
Subset A (nm)

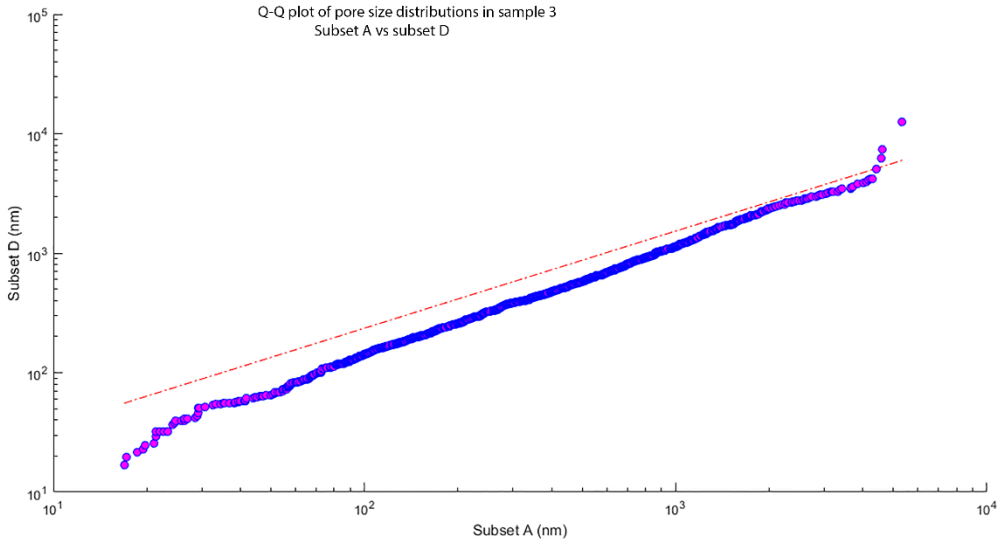
Q-Q plot of pore size distributions in sample 3
Subset A vs subset D
Subset D (nm)
Subset A (nm)

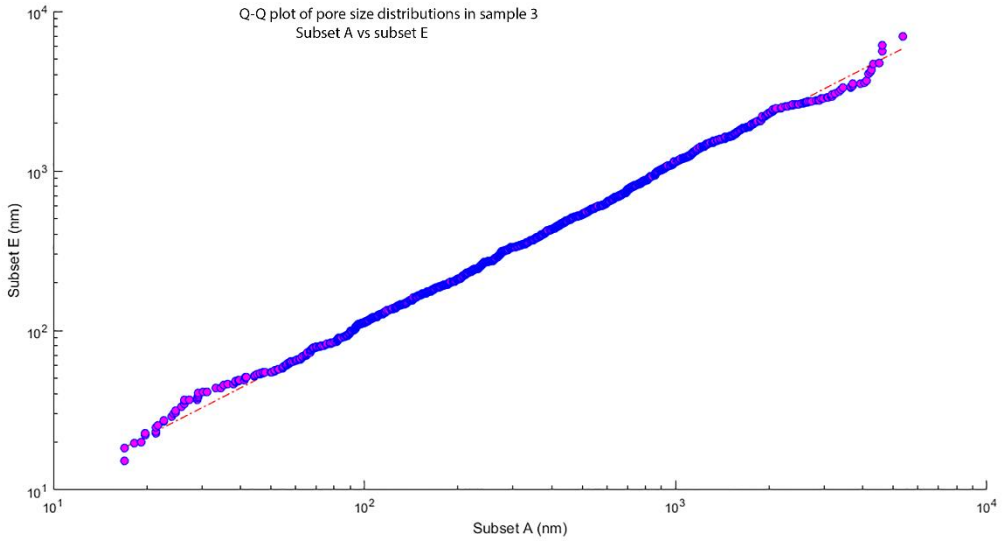
Q-Q plot of pore size distributions in sample 3
Subset A vs subset E
Subset E (nm)
Subset A (nm)

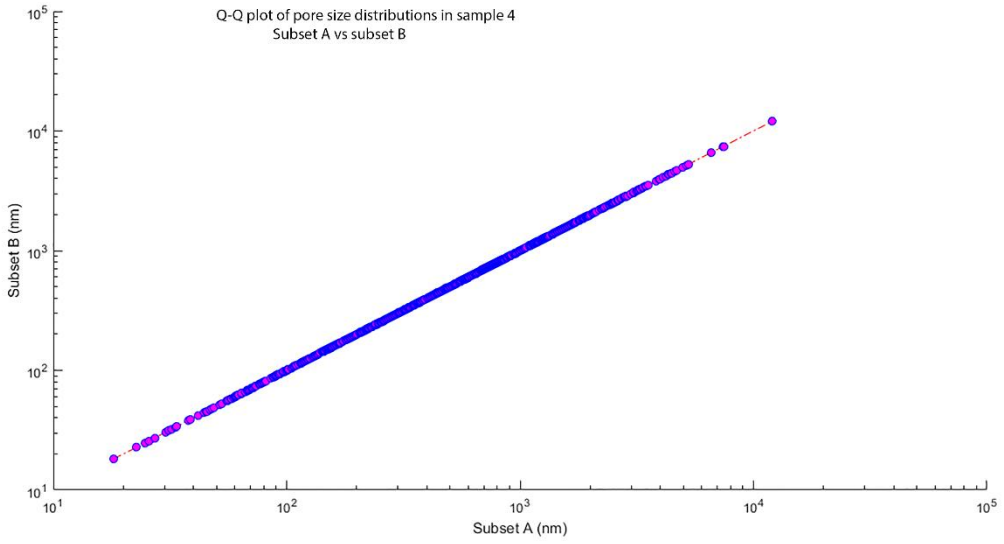
Q-Q plot of pore size distributions in sample 4
Subset A vs subset B
Subset B (nm)
Subset A (nm)

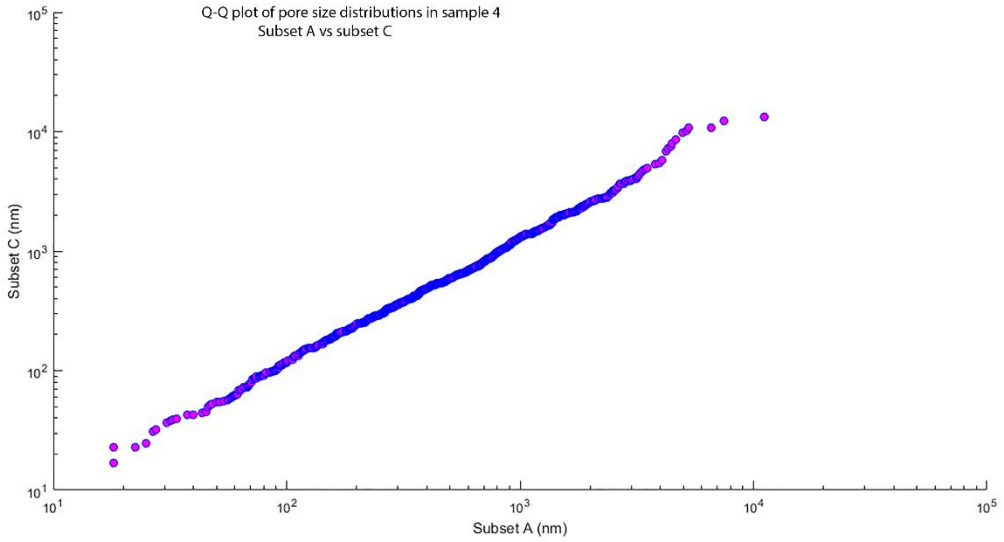
Q-Q plot of pore size distributions in sample 4
Subset A vs subset C
Subset C (nm)
Subset A (nm)

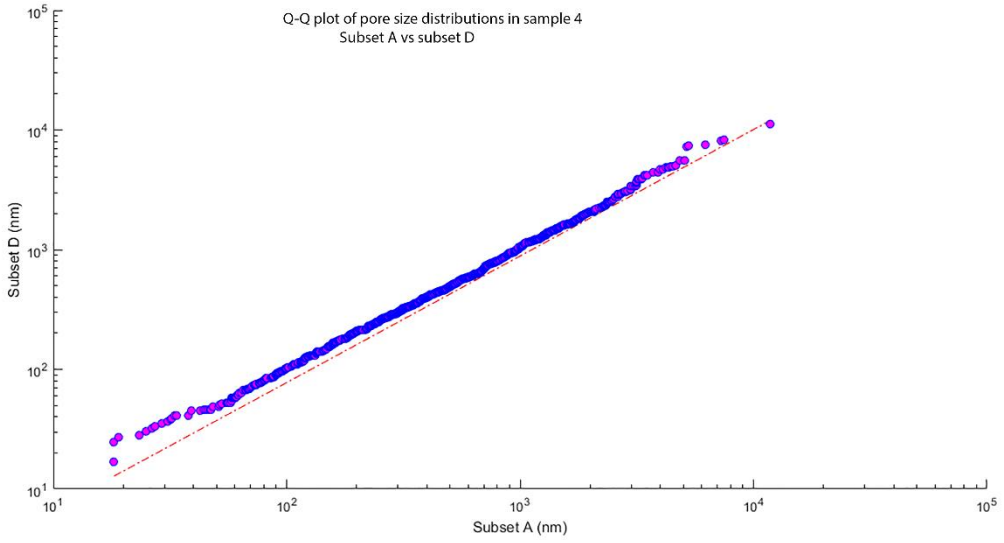
Q-Q plot of pore size distributions in sample 4
Subset A vs subset D
Subset D (nm)
Subset A (nm)

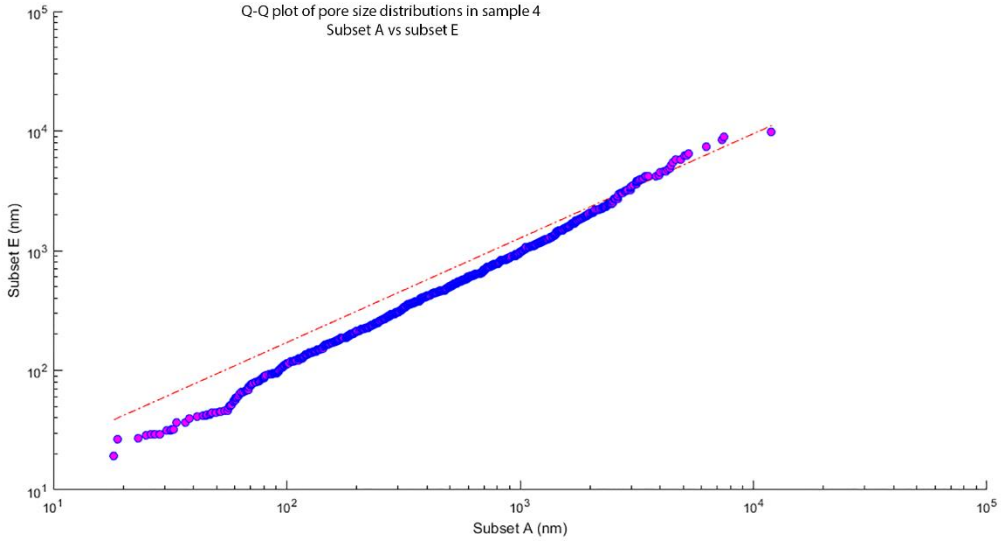
Q-Q plot of pore size distributions in sample 4
Subset A vs subset E
Subset E (nm)
Subset A (nm)

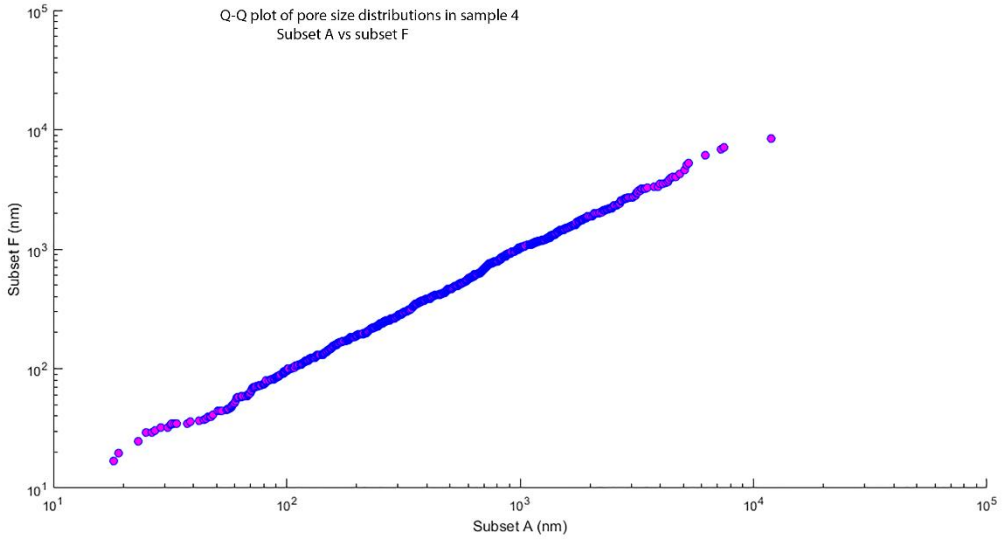
Q-Q plot of pore size distributions in sample 4
Subset A vs subset F
Subset F (nm)
Subset A (nm)

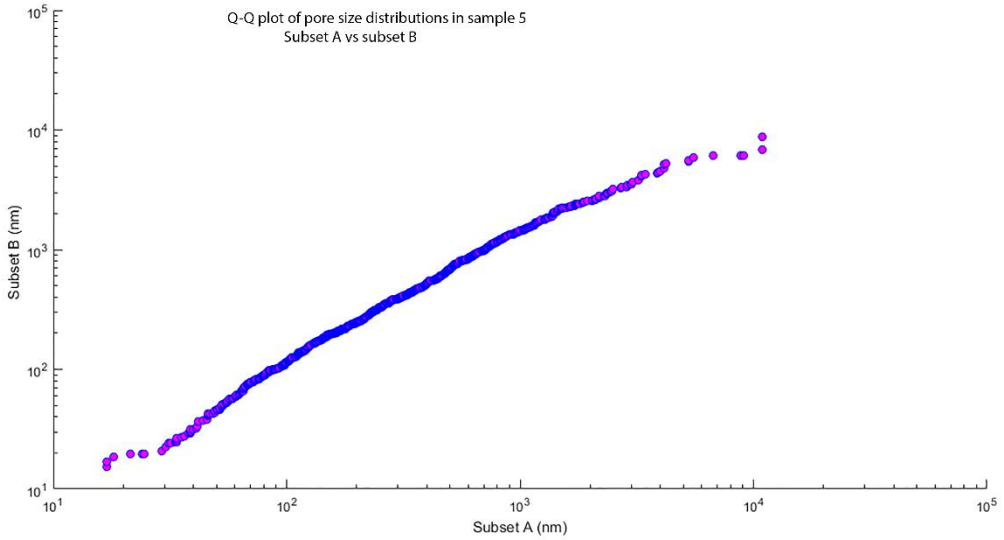
Q-Q plot of pore size distributions in sample 5
Subset A vs subset B
Subset B (nm)
Subset A (nm)

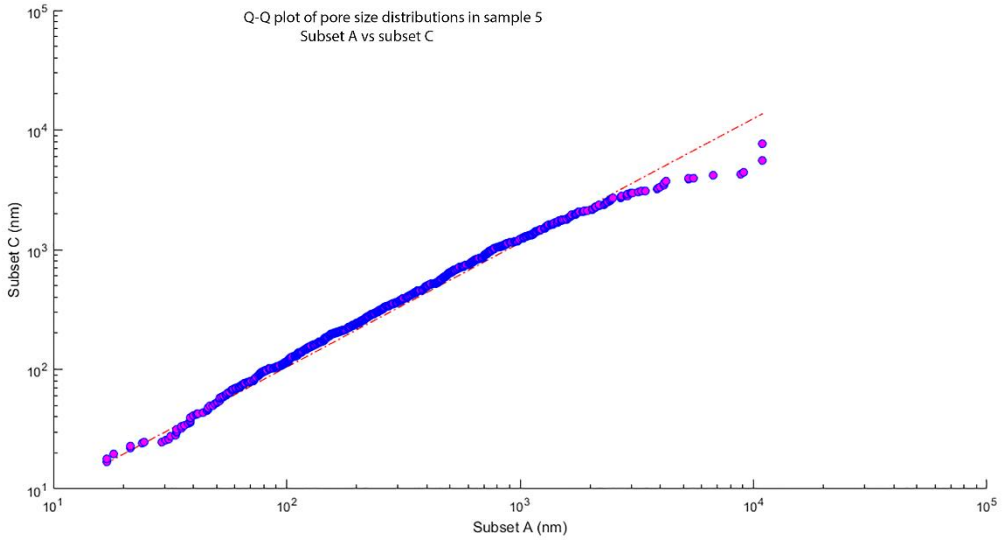
Q-Q plot of pore size distributions in sample 5
Subset A vs subset C
Subset C (nm)
Subset A (nm)

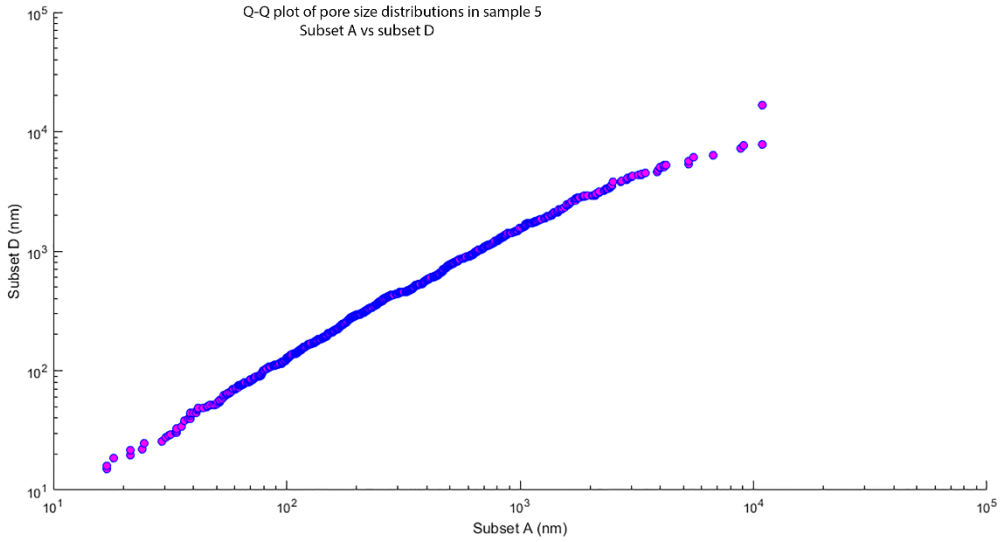
Q-Q plot of pore size distributions in sample 5
Subset A vs subset D
Subset D (nm)
Subset A (nm)

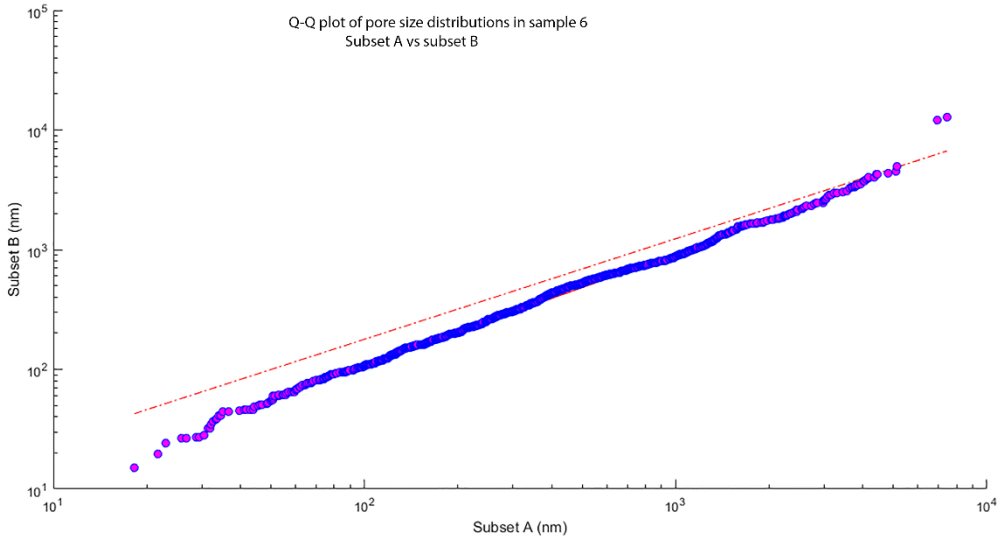
Q-Q plot of pore size distributions in sample 6
Subset A vs subset B
Subset B (nm)
Subset A (nm)

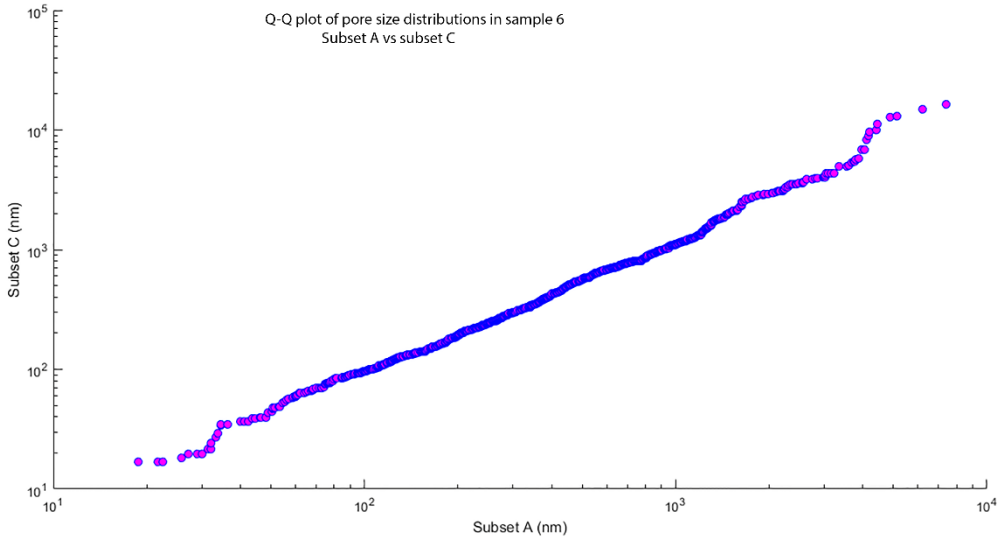
Q-Q plot of pore size distributions in sample 6
Subset A vs subset C
Subset C (nm)
Subset A (nm)

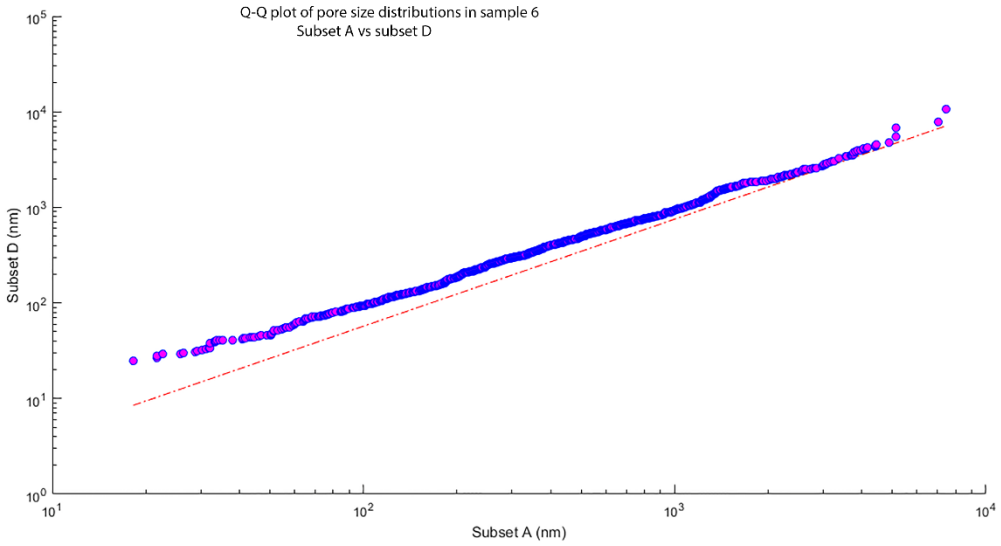
Q-Q plot of pore size distributions in sample 6
Subset A vs subset D
Subset D (nm)
Subset A (nm)

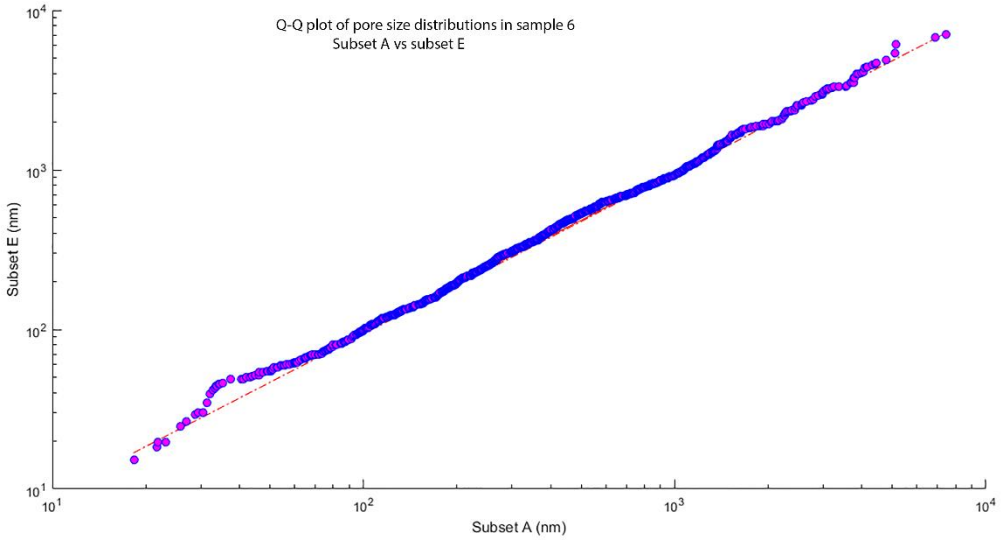
Q-Q plot of pore size distributions in sample 6
Subset A vs subset E
Subset E (nm)
Subset A (nm)

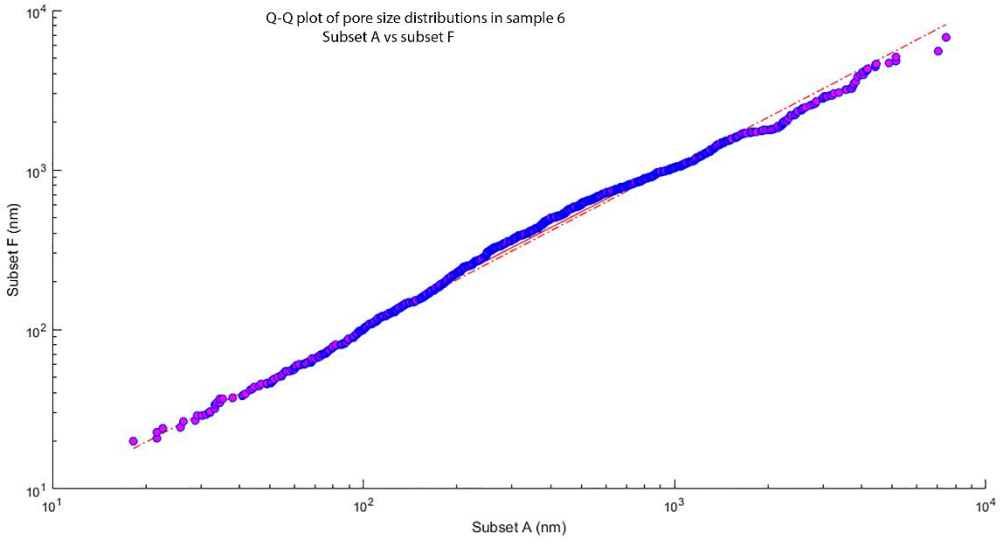
Q-Q plot of pore size distributions in sample 6
Subset A vs subset F
Subset F (nm)
Subset A (nm)

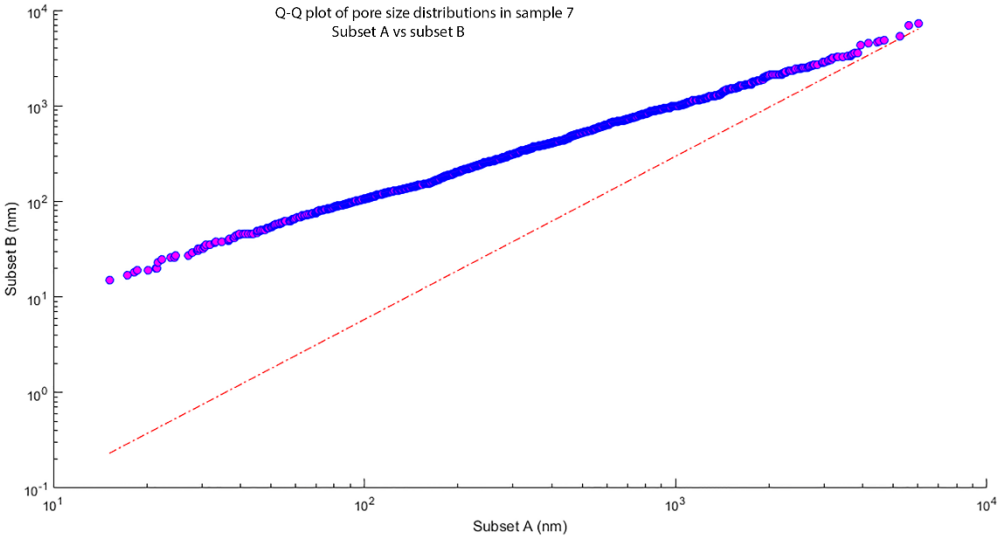
Q-Q plot of pore size distributions in sample 7
Subset A vs subset B
Subset B (nm)
Subset A (nm)

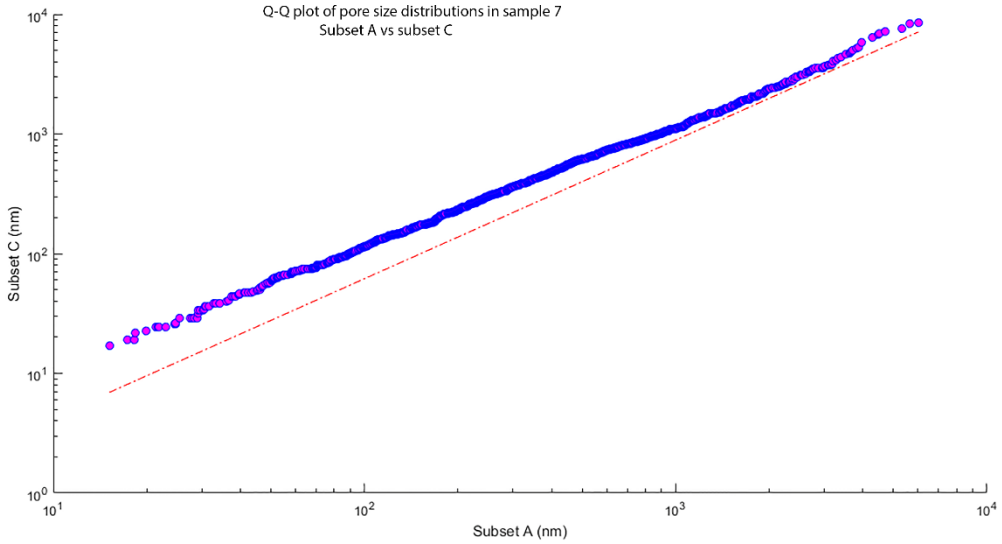
Q-Q plot of pore size distributions in sample 7
Subset A vs subset C
Subset C (nm)
Subset A (nm)

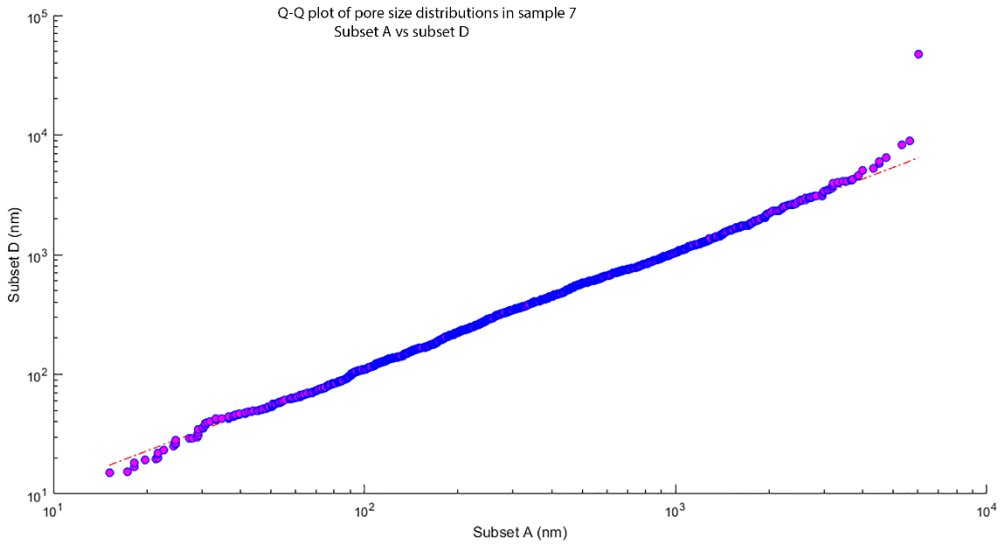
Q-Q plot of pore size distributions in sample 7
Subset A vs subset D
Subset D (nm)
Subset A (nm)

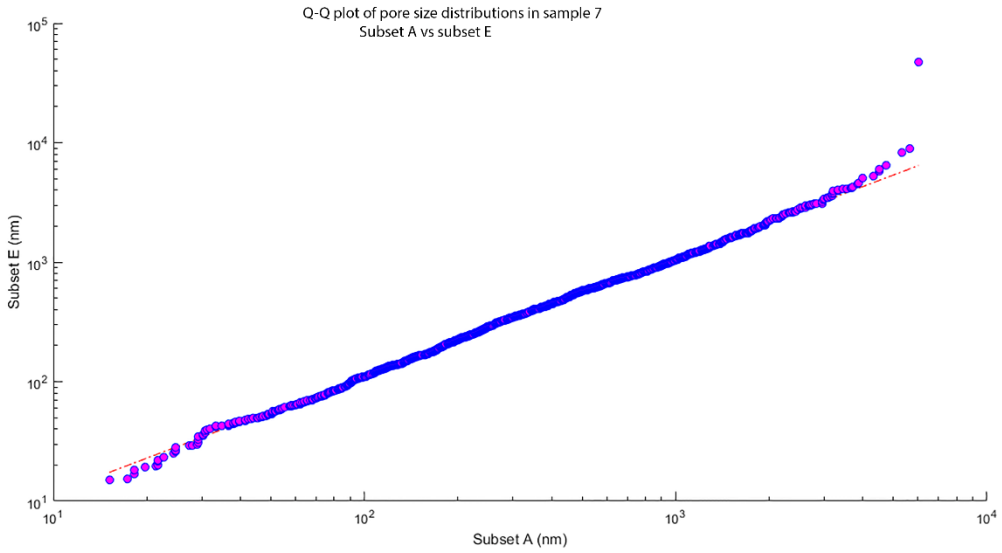
Q-Q plot of pore size distributions in sample 7
Subset A vs subset E
Subset E (nm)
Subset A (nm)
10^1
10^2
10^3
10^4
10^5

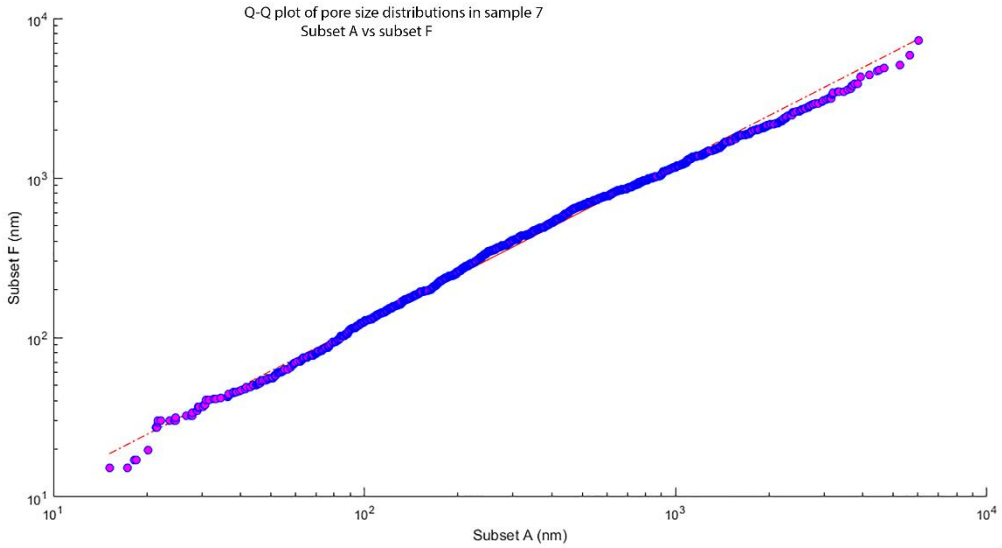
Q-Q plot of pore size distributions in sample 7
Subset A vs subset F
Subset F (nm)
Subset A (nm)
10^1
10^2
10^3
10^4

Appendix 2B

Contour maps showing variation in porosity for subsets in sample 1 to 7

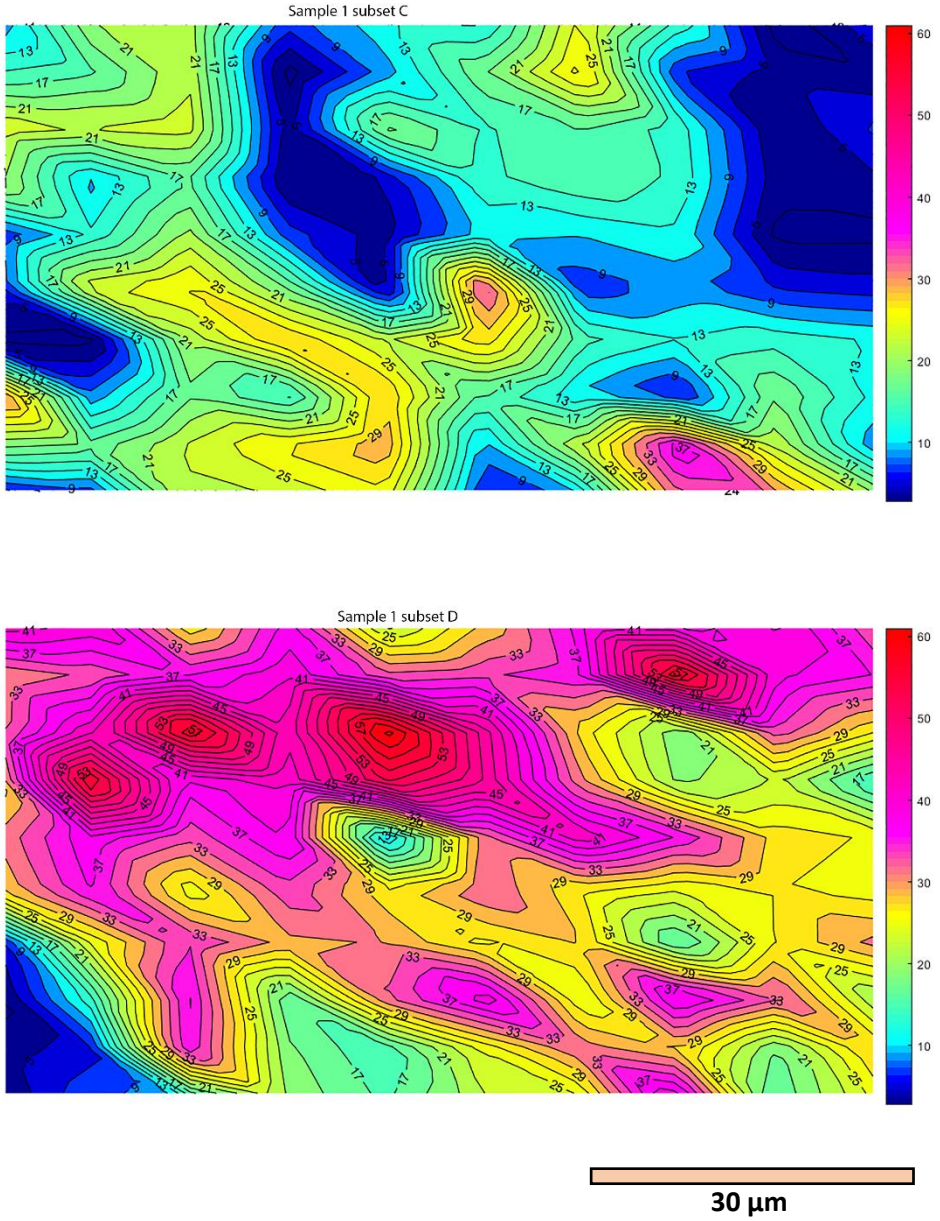

Sample 2 subset A

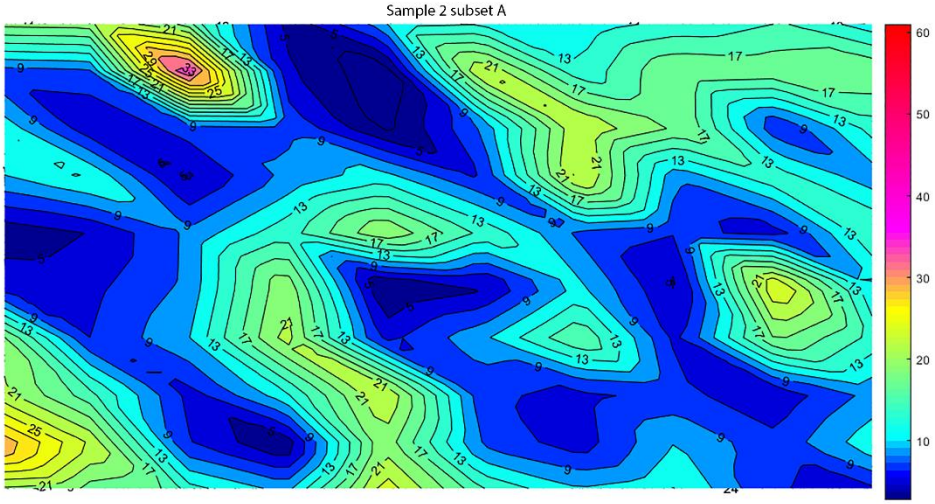

Sample 2 subset B

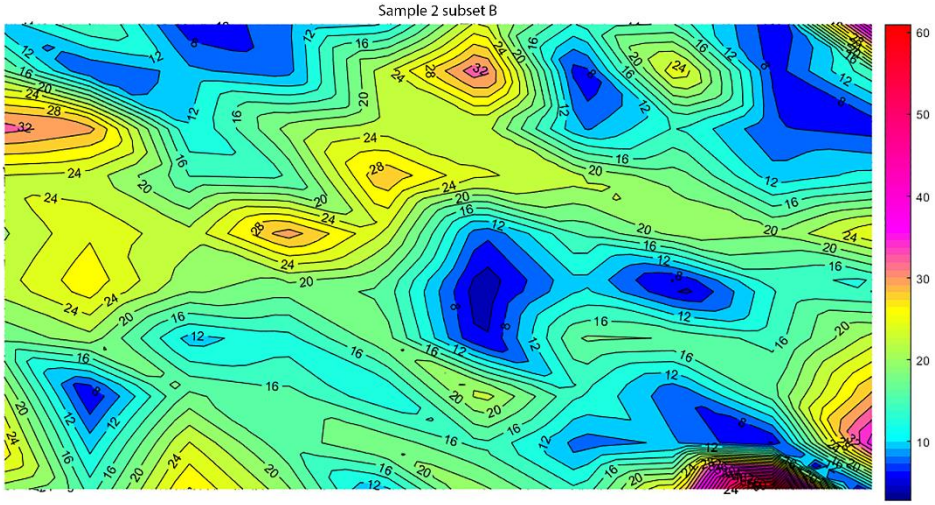

Sample 2 subset C

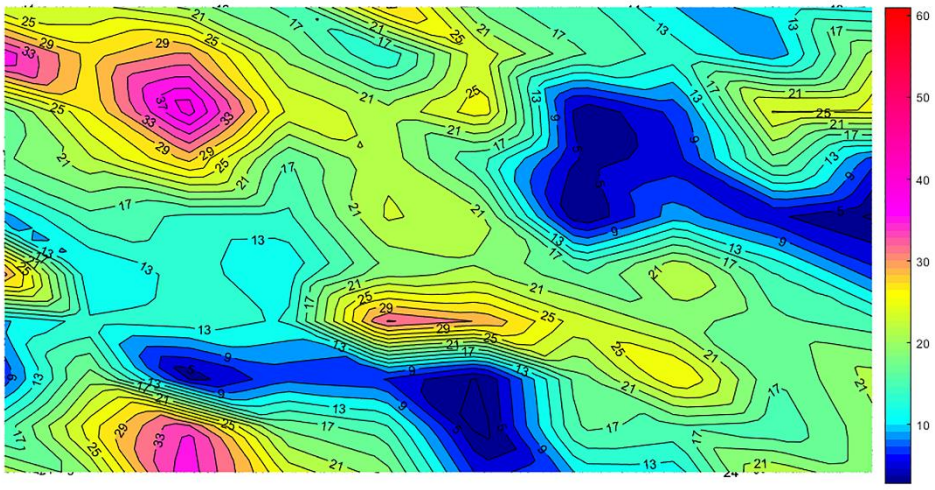

30 µm

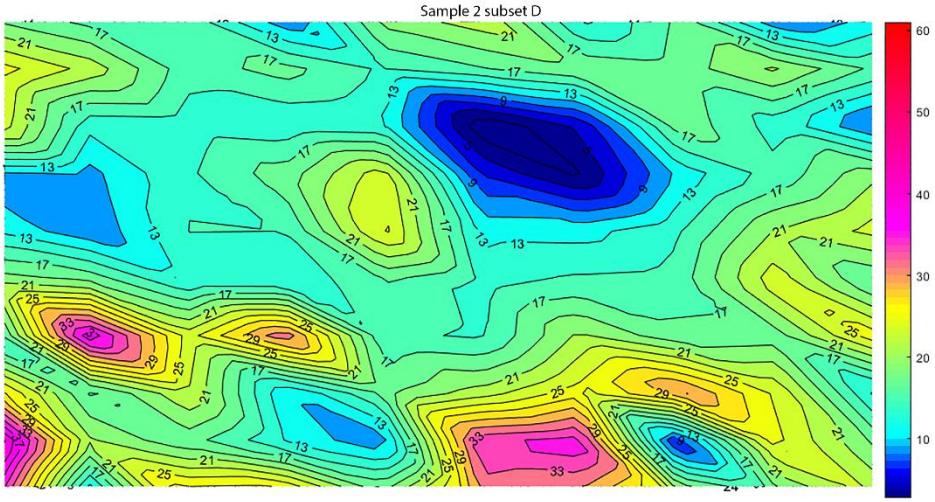
Sample 2 subset D
60
50
40
30
20
10

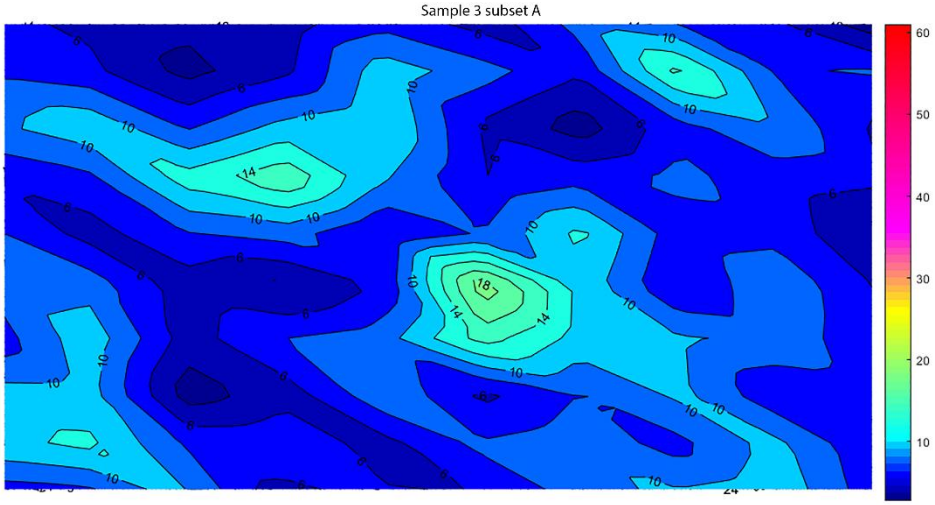
Sample 3 subset A
60
50
40
30
20
10

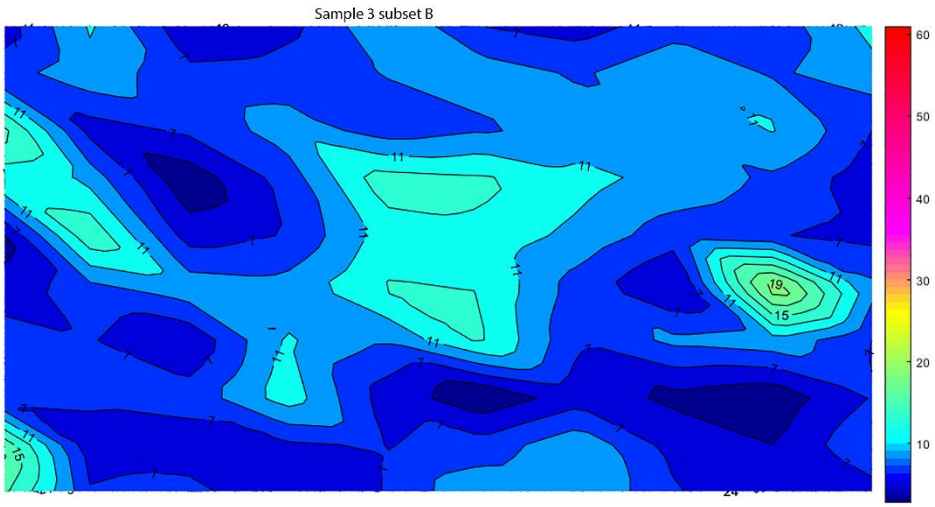
Sample 3 subset B
60
50
40
30
20
10

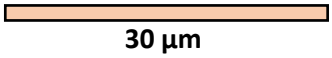
30 µm

Sample 3 subset C

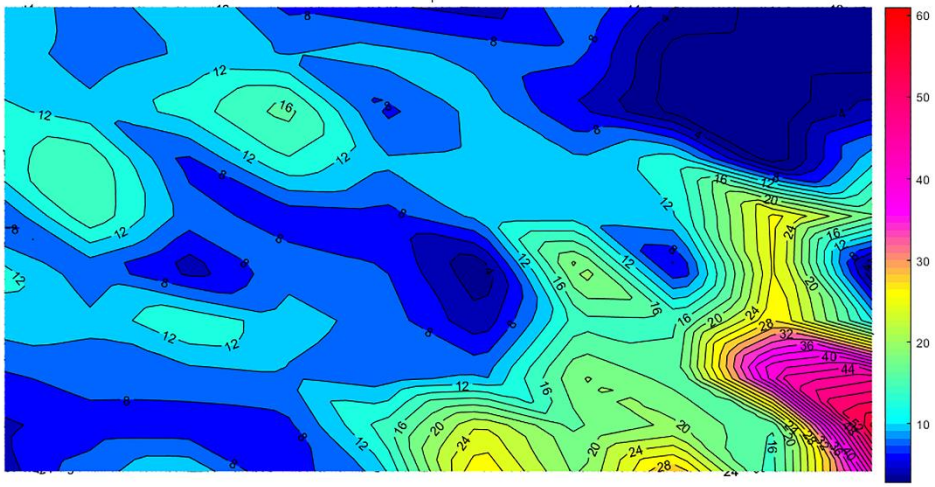

Sample 3 subset D

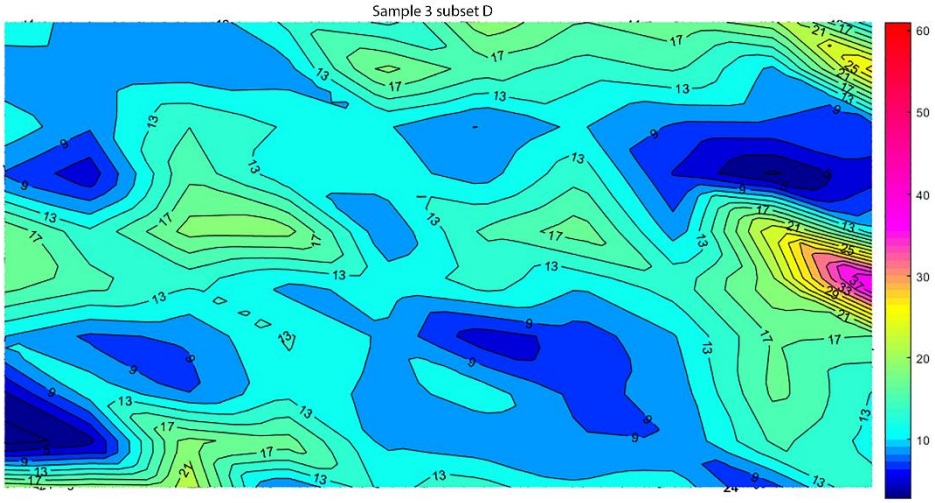

Sample 3 subset E

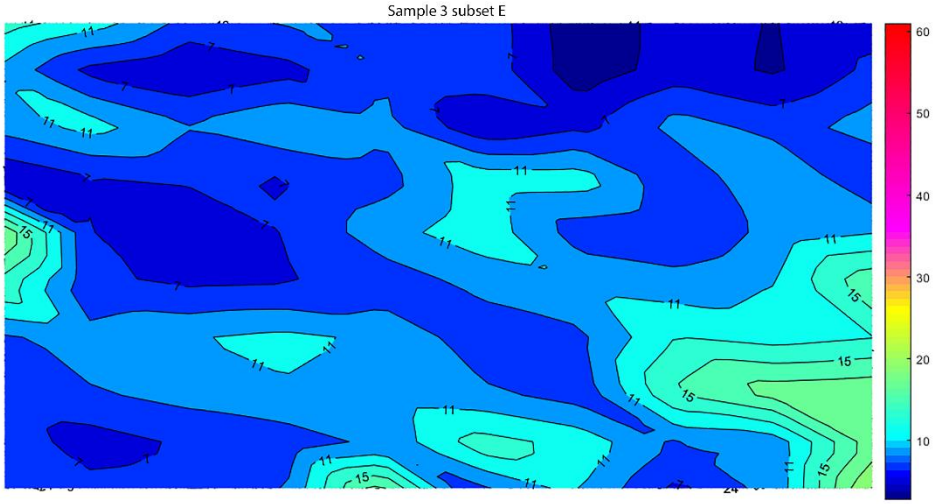

30 µm

Sample 3 subset F

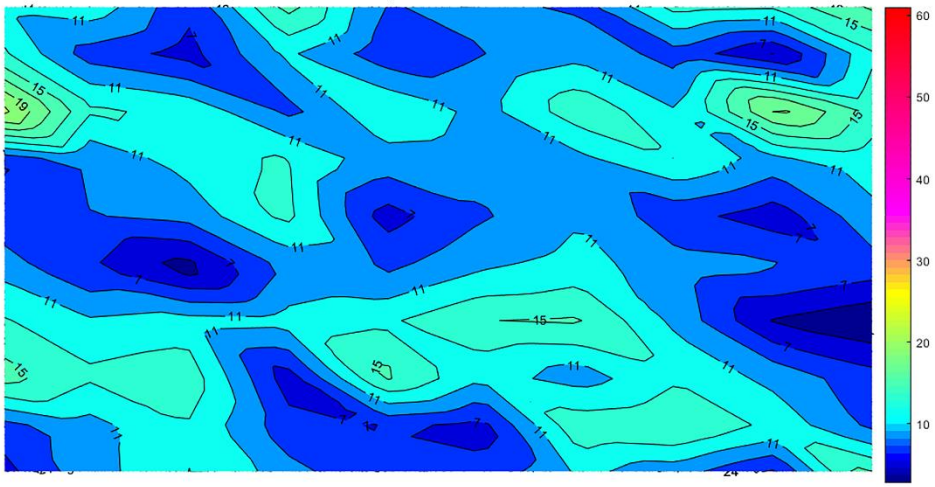

Sample 4 subset A

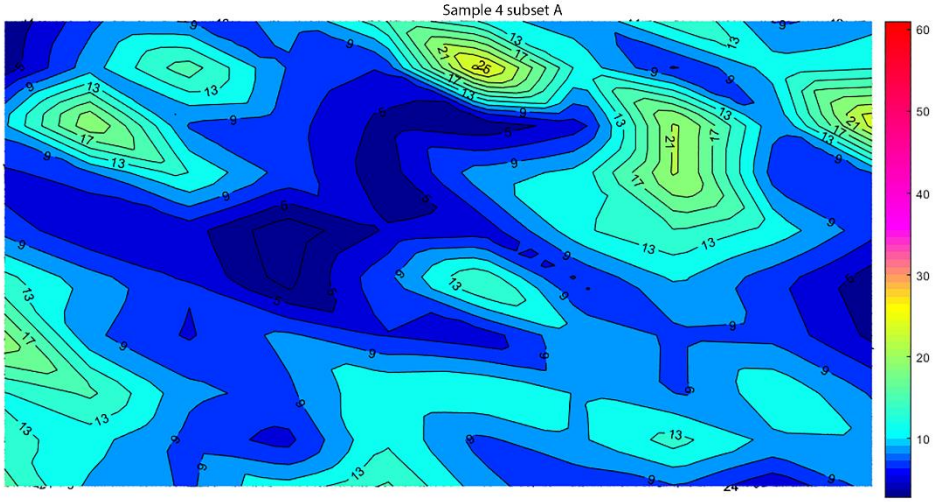

Sample 4 subset B

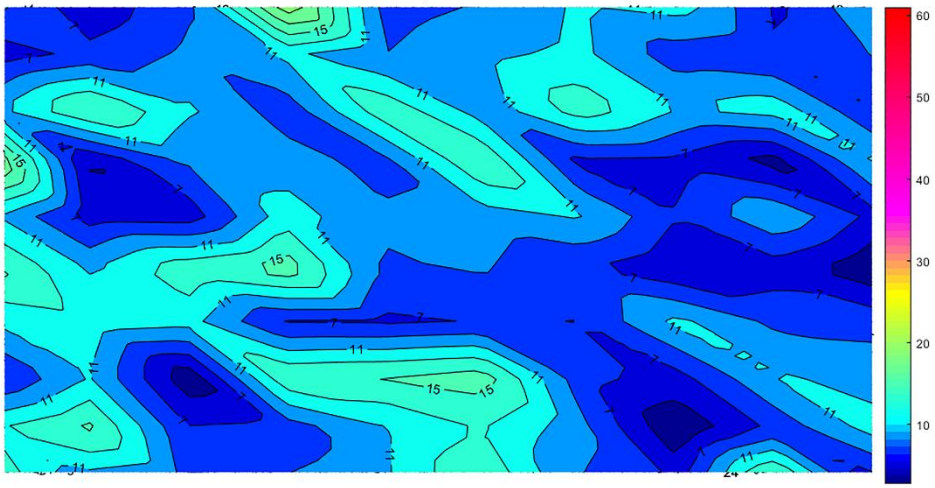

30 µm

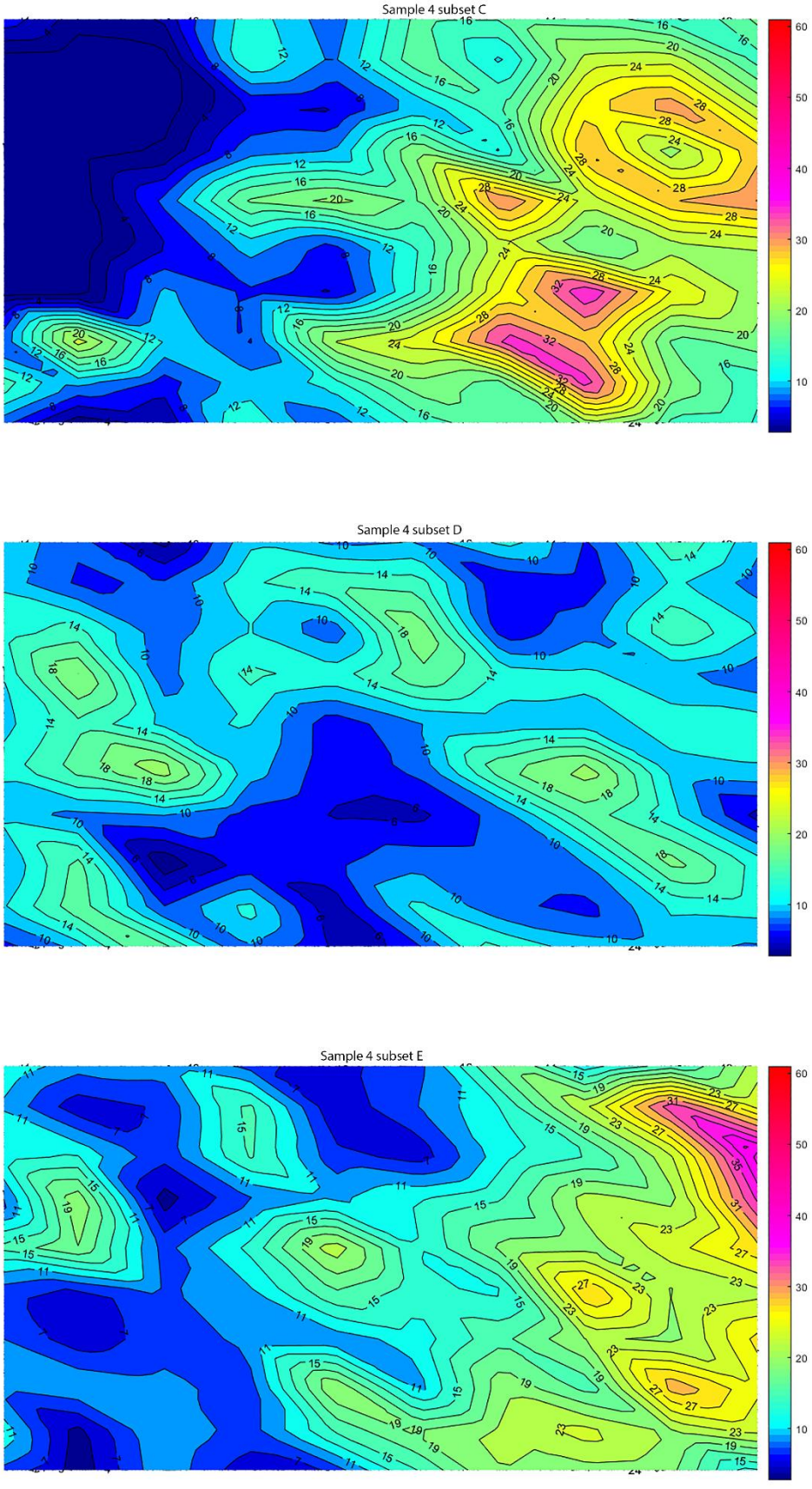
Sample 4 subset C
Sample 4 subset D
Sample 4 subset E
60
50
40
30
20
10
30 µm

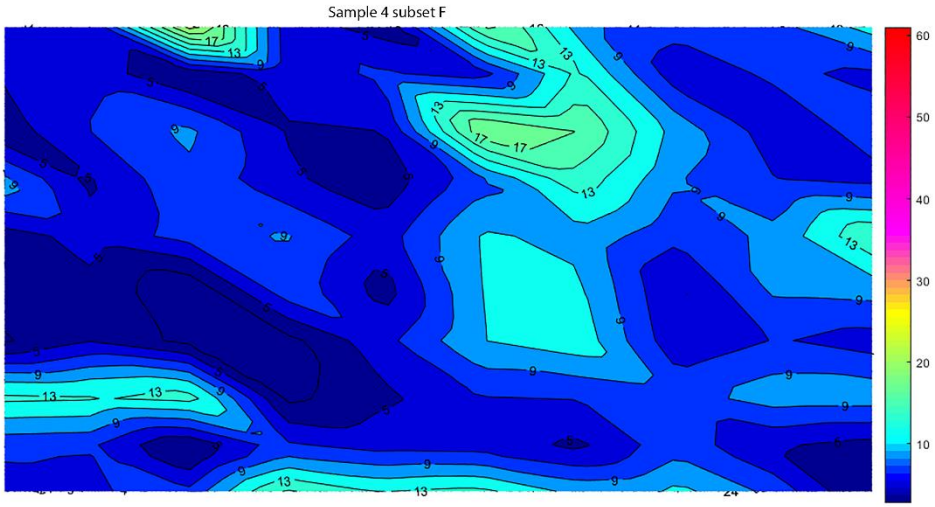
Sample 4 subset F
60
50
40
30
20
10

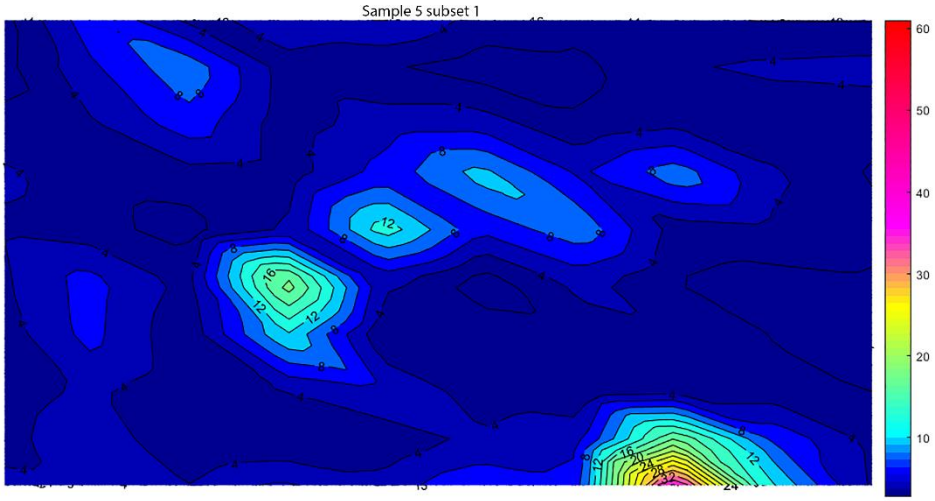
Sample 5 subset 1
60
50
40
30
20
10

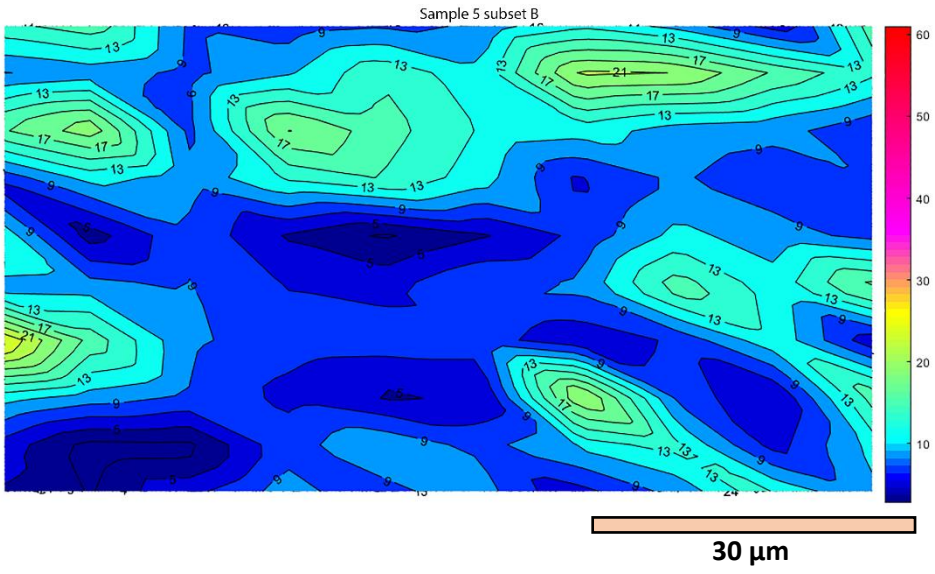
Sample 5 subset B
60
50
40
30
20
10
30 µm

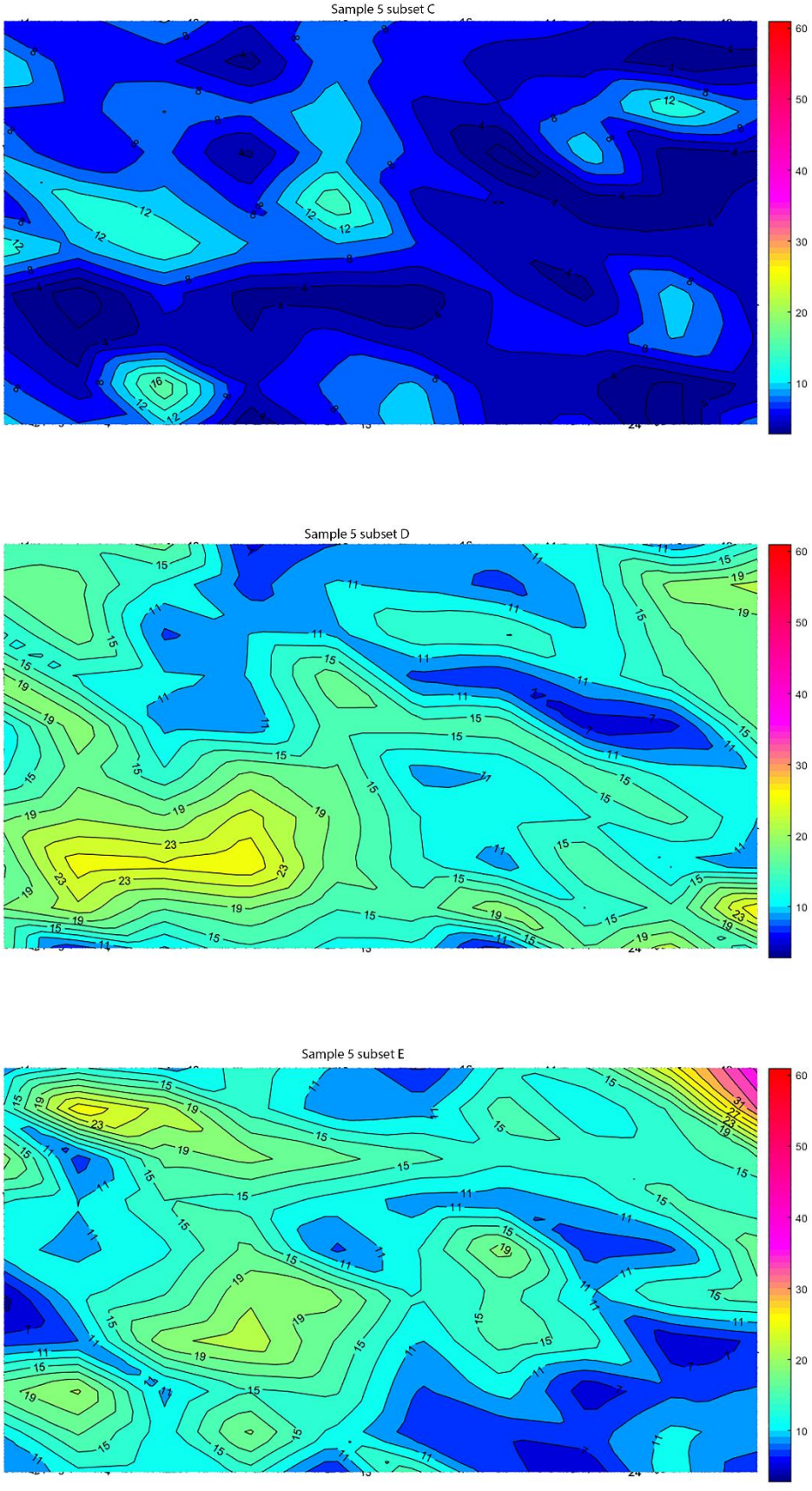
Sample 5 subset C
Sample 5 subset D
Sample 5 subset E
60
50
40
30
20
10
30 µm

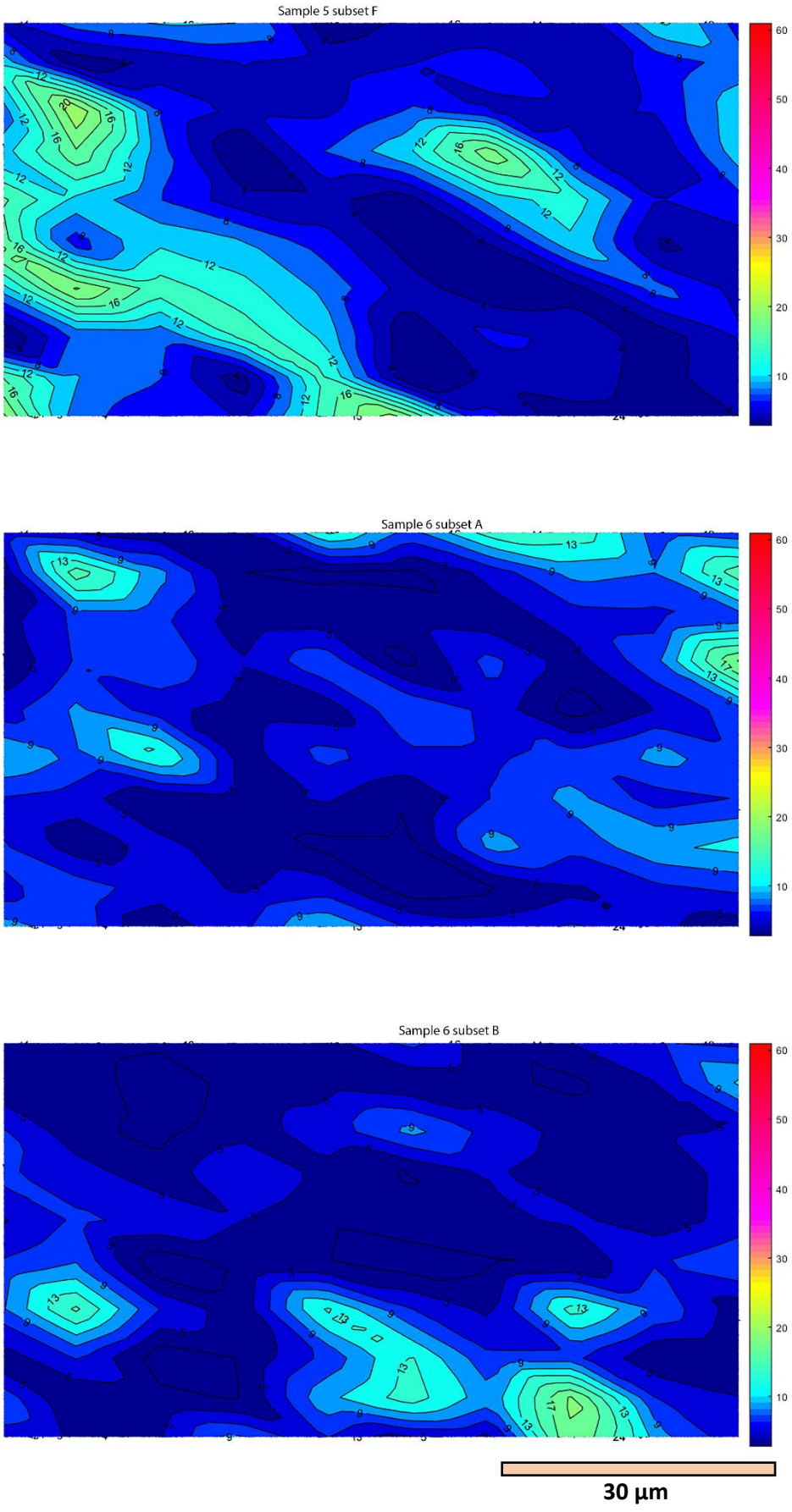
Sample 5 subset F
Sample 6 subset A
Sample 6 subset B
60
50
40
30
20
10
30 µm

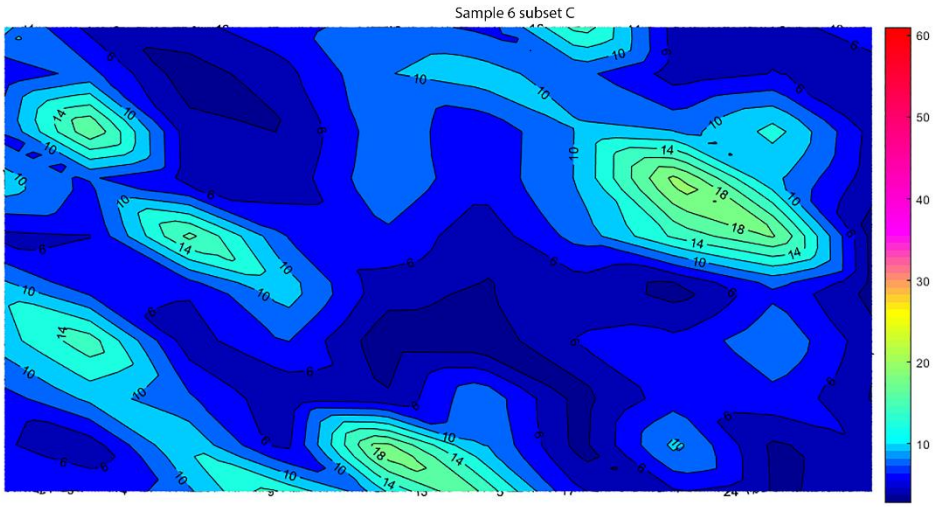
Sample 6 subset C
60
50
40
30
20
10

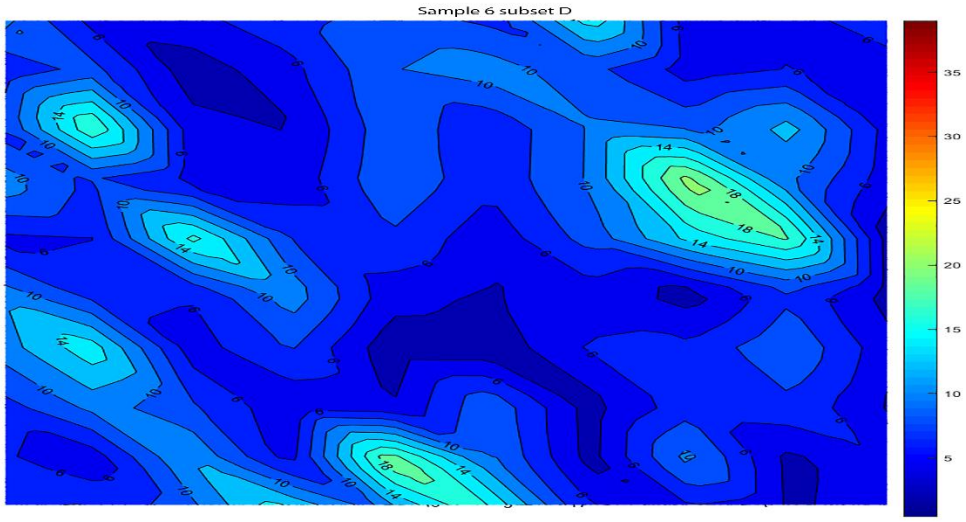
Sample 6 subset D
35
30
25
20
15
10
5

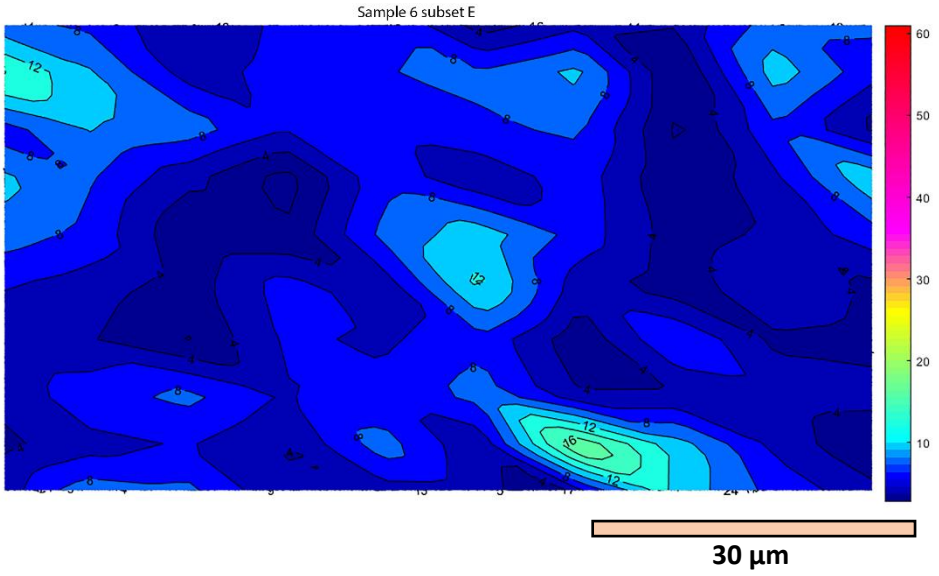
Sample 6 subset E
60
50
40
30
20
10
30 µm

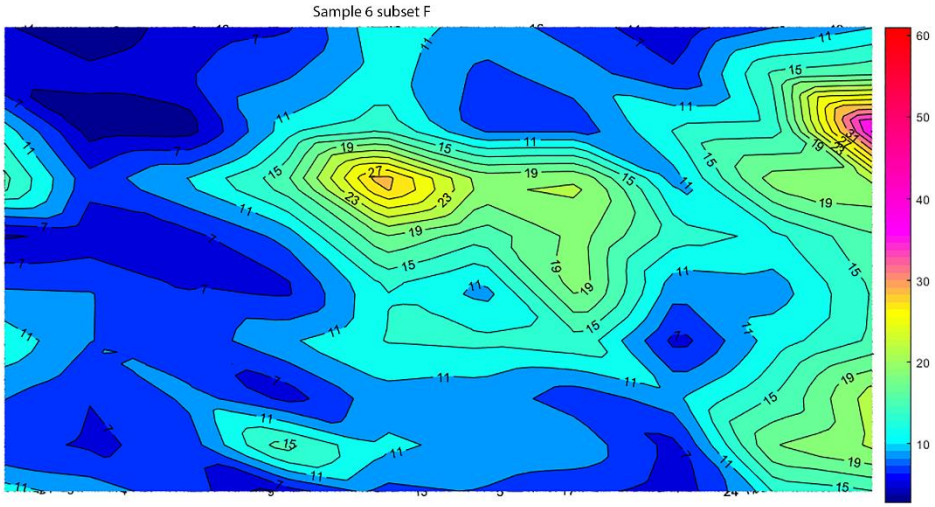
Sample 6 subset F
60
50
40
30
20
10

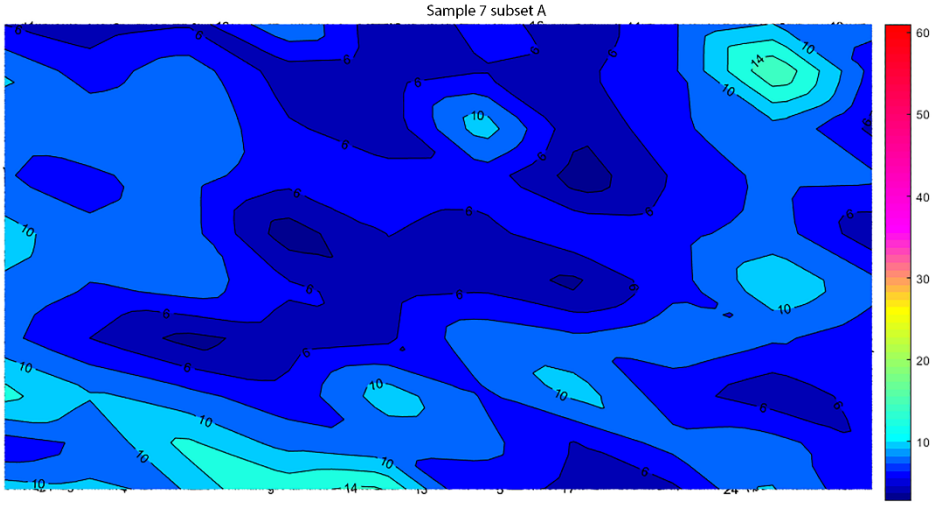
Sample 7 subset A
60
50
40
30
20
10

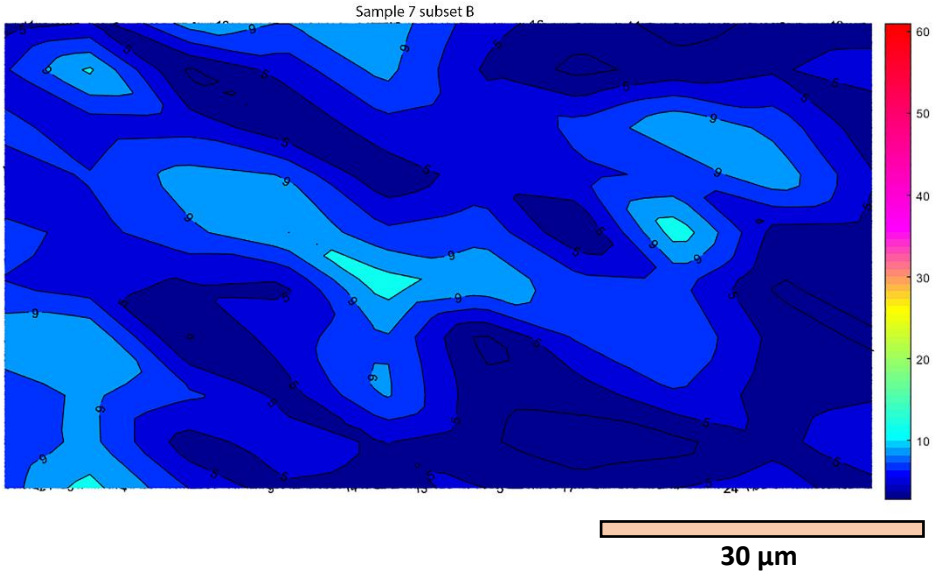
Sample 7 subset B
60
50
40
30
20
10
30 µm

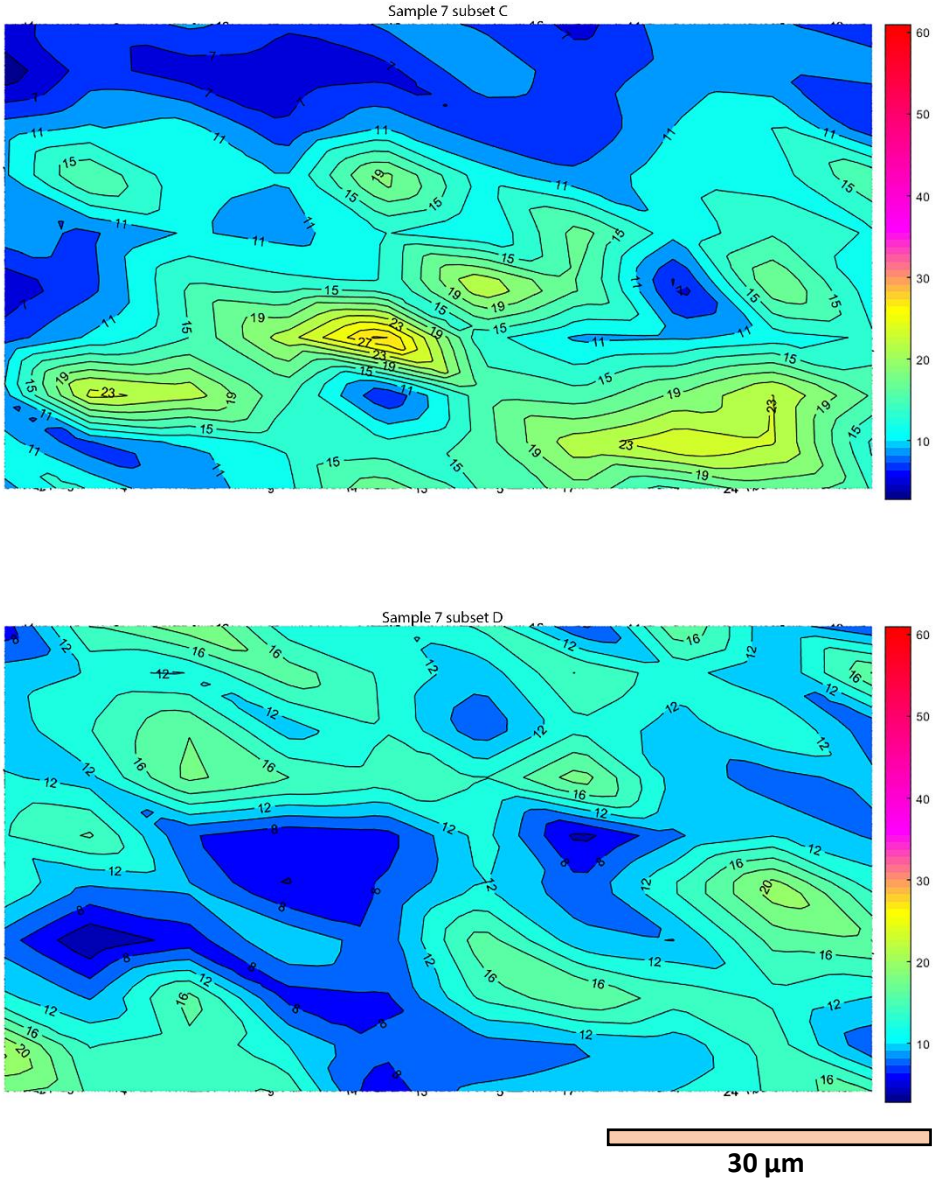
Sample 7 subset C
Sample 7 subset D
60
50
40
30
20
10
30 µm

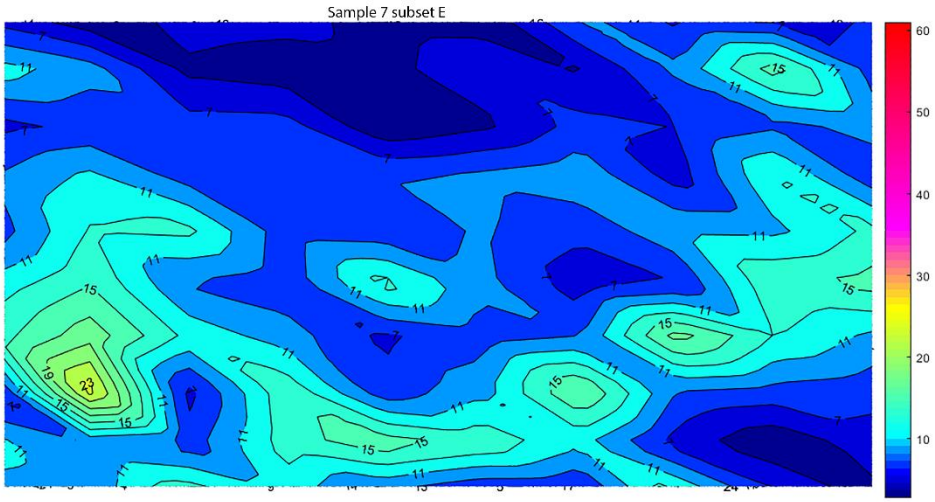
Sample 7 subset E
60
50
40
30
20
10

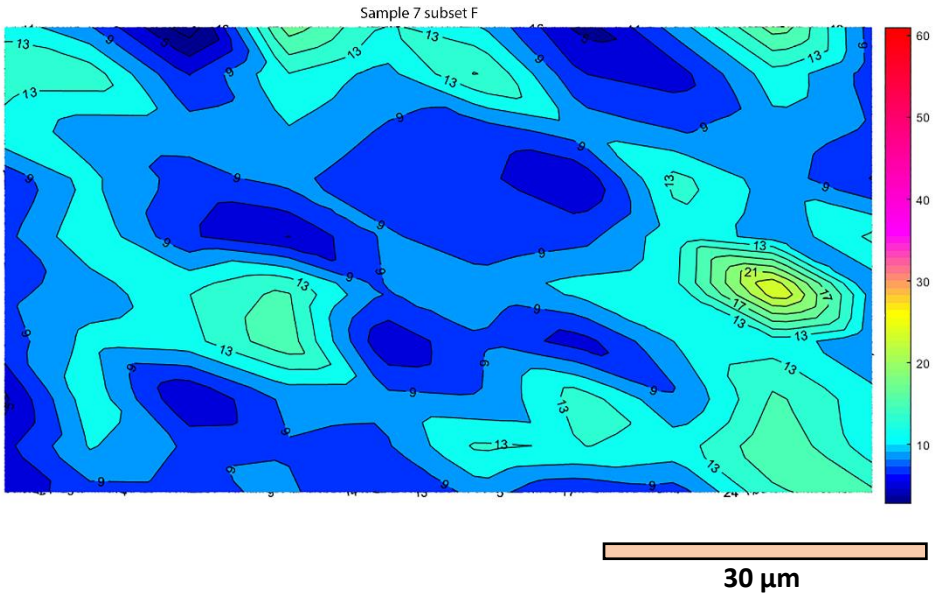
Sample 7 subset F
60
50
40
30
20
10
30 µm

Appendix 3A

Summary of the grain size results obtained from laser diffraction (LSD) granulometry. The data were analysed with using Gradistat software (Blott and Pye, 2001) and the staistical parameters were calculated based on Folk and Ward (1957) grain-size statistical description.

S/N	Sample ID	Sediment type	Depth (m)	Mean size (phi)	Sorting (phi)	Skewness (phi)	Kurtosis (phi)	Mean size	Sorting	Skewness	Kurtosis
1	1386A 2H2 32-34	Contourite	5.62	7.28	2	0.13	0.95	V. Fine Silt	Very Poorly Sorted	Fine Skewed	Mesokurtic
2	1390A 2H2 90-92	Contourite	6.02	8.26	2.09	0.11	0.87	M. Clay	Very Poorly Sorted	Fine Skewed	Platykurtic
3	1387B 02H1 006-008	Contourite	8.96	7.2	2.05	0.18	0.9	V. Fine Silt	Very Poorly Sorted	Fine Skewed	Mesokurtic
4	1387B 02H1 032-034	Contourite	9.22	7.57	2.01	0.14	0.91	V. Fine Silt	Very Poorly Sorted	Fine Skewed	Mesokurtic
5	1387B 02H1 128-130	Contourite	10.18	7.31	1.96	0.16	0.92	V. Fine Silt	Poorly Sorted	Fine Skewed	Mesokurtic
6	1390B 2H4 007-009	Contourite	13.67	6.17	2.43	0.37	0.86	Fine Silt	Very Poorly Sorted	Very Fine Skewed	Platykurtic
7	1390B 2H4 40-42	Contourite	14	6.12	2.35	0.45	0.92	Fine Silt	Very Poorly Sorted	Very Fine Skewed	Mesokurtic
8	1390B 2H4 088-090	Contourite	14.48	6.35	2.41	0.43	0.8	Fine Silt	Very Poorly Sorted	Very Fine Skewed	Platykurtic

9	1390B 2H5 22-24	Contourite	15.32	6.23	2.4	0.43	0.83	Fine Silt	Very Poorly Sorted	Very Fine Skewed	Platykurtic
10	1387B 02H5 067-069	Contourite	15.57	7.59	2.19	0.15	0.87	V. Fine Silt	Very Poorly Sorted	Fine Skewed	Platykurtic
11	1390A 3H2 133-135	Contourite	15.94	6.76	2.23	0.14	0.79	Fine Silt	Very Poorly Sorted	Fine Skewed	Platykurtic
12	1390B 2H5 094-096	Contourite	16.04	5.96	2.48	0.44	1.06	Medium Silt	Very Poorly Sorted	Very Fine Skewed	Mesokurtic
13	1387B 02H5 127-129	Contourite	16.17	6.56	2.2	0.22	0.84	Fine Silt	Very Poorly Sorted	Fine Skewed	Platykurtic
14	1386A 3H3 30-32	Contourite	16.61	7.3	2.02	0.09	1	V. Fine Silt	Very Poorly Sorted	Symmetrical	Mesokurtic
15	1386A 4H2 130-132	Contourite	25.6	6.67	2.08	0.22	0.88	Fine Silt	Very Poorly Sorted	Fine Skewed	Platykurtic
16	1390A 5H3 82-84	Contourite	34.15	7.27	2.09	0.1	0.88	V. Fine Silt	Very Poorly Sorted	Fine Skewed	Platykurtic
17	1386A 5H3 50-52	Contourite	35.81	7.78	1.97	0.13	0.91	V. Fine Silt	Poorly Sorted	Fine Skewed	Mesokurtic
18	1389A 06H1 028-030	Contourite	42.58	8.17	1.89	0.06	0.83	Coarse Clay	Poorly Sorted	Symmetrical	Platykurtic

19	1390A 6H2 100-102	Contourite	44.1	7.94	2.06	0.13	0.89	V. Fine Silt	Very Poorly Sorted	Fine Skewed	Platykurtic
20	1390A 7H3 125-127	Contourite	55.15	7.5	2.02	0.08	0.88	V. Fine Silt	Very Poorly Sorted	Symmetrical	Platykurtic
21	1386A 7H3 101-103	Contourite	55.31	8.03	1.96	0.17	0.94	Coarse Clay	Poorly Sorted	Fine Skewed	Mesokurtic
22	1390A 8H1 110-112	Contourite	61.7	7.59	2.08	0.08	0.9	V. Fine Silt	Very Poorly Sorted	Symmetrical	Mesokurtic
23	1386A 8H3 44-46	Contourite	64.25	7.58	1.78	0.11	1.03	V. Fine Silt	Poorly Sorted	Fine Skewed	Mesokurtic
24	1390A 9H3 85-87	Contourite	73.88	6.94	2.17	0.02	0.84	Fine Silt	Very Poorly Sorted	Symmetrical	Platykurtic
25	1390A 12X5 70-72	Contourite	99.8	7.54	2.12	0.07	0.85	V. Fine Silt	Very Poorly Sorted	Symmetrical	Platykurtic
26	1390C 12H1 110-112	Contourite	100.5	7.73	2.06	0.23	0.97	V. Fine Silt	Very Poorly Sorted	Fine Skewed	Mesokurtic
27	1387A 14X3 117-119	Contourite	117.27	8.52	2.04	0.07	0.9	Coarse Clay	Very Poorly Sorted	Symmetrical	Mesokurtic
28	1390C 14H2 20-22	Contourite	120.01	7.61	2.01	0.07	0.89	V. Fine Silt	Very Poorly Sorted	Symmetrical	Platykurtic
29	1387A 15X1 52-54	Contourite	123.12	8.35	1.98	0.12	0.91	Coarse Clay	Poorly Sorted	Fine Skewed	Mesokurtic

30	1387A 16X4 113-115	Contourite	137.7	8.39	1.8	0.18	0.9	Coarse Clay	Poorly Sorted	Fine Skewed	Mesokurtic
31	1389A 18X1 125-127	Contourite	150.75	7.5	2.16	0.21	0.78	V. Fine Silt	Very Poorly Sorted	Fine Skewed	Platykurtic
32	1390C 18H2 82-84	Contourite	158.7	8.3	1.76	0.24	0.9	Coarse Clay	Poorly Sorted	Fine Skewed	Mesokurtic
33	1390B 18H3 100-102	Contourite	159.8	8.37	1.77	0.2	0.88	Coarse Clay	Poorly Sorted	Fine Skewed	Platykurtic
34	1386A 19H1 135-137	Contourite	161.85	7.39	2.13	0.02	0.96	V. Fine Silt	Very Poorly Sorted	Symmetrical	Mesokurtic
35	1390B 19H7 70-72	Contourite	173.54	7.61	1.94	0.15	0.9	V.Fine Silt	Poorly Sorted	Fine Skewed	Mesokurtic
36	1386A 23X2 130-132	Contourite	188.11	8.09	2.02	0.14	0.88	Coarse Clay	Very Poorly Sorted	Fine Skewed	Platykurtic
37	1389A 28X2 064-066	Contourite	247.44	8.24	2	0.13	0.85	Coarse Clay	Very Poorly Sorted	Fine Skewed	Platykurtic
38	1389A 28X5 130-132	Contourite	252.6	7.32	2.38	0.09	0.75	V. Fine Silt	Very Poorly Sorted	Symmetrical	Platykurtic
39	1387A 29X3 72-74	Contourite	259.47	7.16	2.02	0.1	0.93	V. Fine Silt	Very Poorly Sorted	Fine Skewed	Mesokurtic
40	1390A 30X7 74-76	Contourite	274.02	7.9	1.87	0.06	0.89	V. Fine Silt	Poorly Sorted	Symmetrical	Platykurtic
41	1390A 35X3 28-30	Contourite	316.22	7.69	1.94	0.09	0.89	V. Fine Silt	Poorly Sorted	Symmetrical	Platykurtic

42	1389A 38X2 112-114	Contourite	343.62	7.32	2.22	0.21	0.85	V. Fine Silt	Very Poorly Sorted	Fine Skewed	Platykurtic
43	1389E 9R2 30-32	Contourite	398.5	7.36	2.04	0.12	0.89	V. Fine Silt	Very Poorly Sorted	Fine Skewed	Platykurtic
44	1389E 10R1 100-102	Contourite	407.3	8.31	1.82	0.16	0.92	Coarse Clay	Poorly Sorted	Fine Skewed	Mesokurtic
45	1389E 11R1 108-110	Contourite	416.98	6.6	2.26	0.13	0.77	Fine Silt	Very Poorly Sorted	Fine Skewed	Platykurtic
46	1389E 13R3 80-82	Contourite	438.9	8.32	1.88	0.19	0.88	Coarse Clay	Poorly Sorted	Fine Skewed	Platykurtic
47	1389E 14R3 027-029	Contourite	447.97	8.91	1.9	0.12	0.8	Coarse Clay	Poorly Sorted	Fine Skewed	Platykurtic
48	1389E 15R1 98-100	Contourite	455.28	6.85	2.26	0.07	0.8	Fine Silt	Very Poorly Sorted	Symmetrical	Platykurtic
49	1389E 17R4 20-22	Contourite	478	7.99	2.06	0.19	0.9	V. Fine Silt	Very Poorly Sorted	Fine Skewed	Mesokurtic
50	1389E 20R 55-57	Contourite	505.35	7.23	2.32	0.17	0.88	V. Fine Silt	Very Poorly Sorted	Fine Skewed	Platykurtic
51	1389E 22R3 58-62	Contourite	524.38	8.38	1.75	0.23	0.88	Coarse Clay	Poorly Sorted	Fine Skewed	Platykurtic
52	1389E 23R3 118-122	Contourite	534.43	7.6	2.03	0.07	0.88	V. Fine Silt	Very Poorly Sorted	Symmetrical	Platykurtic

53	1389E 24R3 85-87	Contourite	543.95	7.14	2.24	0.04	0.88	V. Fine Silt	Very Poorly Sorted	Symmetrical	Platykurtic
54	1389E 25R3 48-52	Contourite	553.28	7.99	2.24	0.12	0.84	V. Fine Silt	Very Poorly Sorted	Fine Skewed	Platykurtic
55	1389E 26R3 061-063	Contourite	563.01	7.78	2	0.14	0.81	V. Fine Silt	Very Poorly Sorted	Fine Skewed	Platykurtic
56	1389E 27R2 117-119	Contourite	571.67	7.39	2.03	0.14	0.88	V. Fine Silt	Very Poorly Sorted	Fine Skewed	Platykurtic
57	1389E 33R3 099-101	Contourite	630.59	8.51	1.81	0.18	0.83	Coarse Clay	Poorly Sorted	Fine Skewed	Platykurtic
58	1389E 34R397-99	Contourite	640.27	8.49	1.84	0.12	0.83	Coarse Clay	Poorly Sorted	Fine Skewed	Platykurtic
59	1389E 35R2 48-50	Contourite	647.98	8.19	1.91	0.16	0.87	Coarse Clay	Poorly Sorted	Fine Skewed	Platykurtic
60	1389E 35R5 60-61.5	Contourite	652.62	6.97	2.5	0.24	0.72	Fine Silt	Very Poorly Sorted	Fine Skewed	Platykurtic
61	1389E 37R5 50-53	Contourite	670.93	8.4	1.86	0.21	0.82	Coarse Clay	Poorly Sorted	Fine Skewed	Platykurtic
62	1389E 47R2 022-024	Contourite	762.82	7.28	2.3	0.17	0.78	V. Fine Silt	Very Poorly Sorted	Fine Skewed	Platykurtic
63	1389E 57R3 012-013.5	Contourite	860.22	7.6	2.24	0.07	0.9	V. Fine Silt	Very Poorly Sorted	Symmetrical	Mesokurtic

64	1389E 66R1 018-021	Contourite	943.68	7.99	2.19	0.06	0.91	V. Fine Silt	Very Poorly Sorted	Symmetrical	Mesokurtic
65	1457B 02H6 036-038	Hemelagites	10.9	11.93	0.67	-0.09	0.96	V. Fine Clay	Moderately Well Sorted	Symmetrical	Mesokurtic
66	1457B 05H2 010-012	Hemelagites	33.32	12.27	0.49	-0.08	1.06	V. Fine Clay	Well Sorted	Symmetrical	Mesokurtic
67	1457A 07H1 093-095	Hemelagites	57.13	9.36	1.52	0.27	0.84	Medium Clay	Poorly Sorted	Fine Skewed	Platykurtic
68	1457A 07H1 140-142	Hemelagites	57.59	9.34	1.61	0.21	0.89	Medium Clay	Poorly Sorted	Fine Skewed	Platykurtic
69	1385D 1H3 80-82	Hemipelagite	3.82	8.18	1.67	0.17	0.88	Coarse Clay	Poorly Sorted	Fine Skewed	Platykurtic
70	1385E 2H5 72-74	Hemipelagite	7.76	7.63	2.44	0.07	0.99	V. Fine Silt	Very Poorly Sorted	Symmetrical	Mesokurtic
71	1385A 02H6 013-015	Hemipelagite	9.13	8.23	1.88	0.18	0.91	Coarse Clay	Poorly Sorted	Fine Skewed	Mesokurtic
72	1385A 3H2 41-43	Hemipelagite	12.91	8.18	1.9	0.19	0.88	Coarse Clay	Poorly Sorted	Fine Skewed	Platykurtic
73	1385A 3H2 110-112	Hemipelagite	13.3	8.15	1.81	0.21	0.9	Coarse Clay	Poorly Sorted	Fine Skewed	Mesokurtic
74	1385A 5H3 114-116	Hemipelagite	13.6	8.33	1.84	0.2	0.88	Coarse Clay	Poorly Sorted	Fine Skewed	Platykurtic
75	1385E 3H3 62-64	Hemipelagite	14.14	8.57	1.9	0.17	0.8	Coarse Clay	Poorly Sorted	Fine Skewed	Platykurtic

76	1385D 2H6 115-117	Hemipelagite	15.6	7.64	1.95	0.15	0.9	V. Fine Silt	Poorly Sorted	Fine Skewed	Mesokurtic
77	1385D 3H2 44-46	Hemipelagite	18.34	8.52	1.86	0.17	0.87	Coarse Clay	Poorly Sorted	Fine Skewed	Platykurtic
78	1385E 4H3 82-84	Hemipelagite	23.83	7.8	1.9	0.15	0.93	V. Fine Silt	Poorly Sorted	Fine Skewed	Mesokurtic
79	1385D 04H4 94-96	Hemipelagite	31.31	7.77	2.21	0.1	0.97	V. Fine Silt	Very Poorly Sorted	Fine Skewed	Mesokurtic
80	1457B 05H2 044-046	Hemipelagite	33.66	10.02	2.31	-0.52	0.62	Fine Clay	Very Poorly Sorted	Very Coarse Skewed	Very Platykurtic
81	1385D 5H4 41-43	Hemipelagite	40.32	8.53	1.79	0.17	0.9	Coarse Clay	Poorly Sorted	Fine Skewed	Mesokurtic
82	1385A 6H2 36-38	Hemipelagite	41.36	8.99	1.57	0.23	0.88	Coarse Clay	Poorly Sorted	Fine Skewed	Platykurtic
83	1385D 6H3 118-120	Hemipelagite	46.09	8.05	1.91	0.18	0.89	Coarse Clay	Poorly Sorted	Fine Skewed	Platykurtic
84	1385E 7H2 111-113	Hemipelagite	51.11	8.27	1.57	0.09	0.97	Coarse Clay	Poorly Sorted	Symmetrical	Mesokurtic
85	1385A 7H2 136-138	Hemipelagite	51.86	8.99	1.62	0.23	0.89	Coarse Clay	Poorly Sorted	Fine Skewed	Platykurtic
86	1385A 07H5 042-044	Hemipelagite	55.42	8.89	1.75	0.12	0.91	Coarse Clay	Poorly Sorted	Fine Skewed	Mesokurtic
87	1385A 07H6 054-056	Hemipelagite	57.04	8.74	1.95	0.09	0.94	Coarse Clay	Poorly Sorted	Symmetrical	Mesokurtic
88	1385E 9H2 122-124	Hemipelagite	67.17	8.49	1.81	0.19	0.87	Coarse Clay	Poorly Sorted	Fine Skewed	Platykurtic

89	1385E 10H2 74-76	Hemipelagite	76.24	8.06	1.5	0.13	0.93	Coarse Clay	Poorly Sorted	Fine Skewed	Mesokurtic
90	1386A 9H5 100-102	Hemipelagite	77.35	7.77	1.97	0.19	0.92	V. Fine Silt	Poorly Sorted	Fine Skewed	Mesokurtic
91	1385A 10H3 80-82	Hemipelagite	81.31	8.44	1.77	0.19	0.89	Coarse Clay	Poorly Sorted	Fine Skewed	Platykurtic
92	1385A 11H3 115-117	Hemipelagite	91.15	8.13	1.51	0.16	0.92	Coarse Clay	Poorly Sorted	Fine Skewed	Mesokurtic
93	1385D 11H3 124-126	Hemipelagite	93.67	8.66	1.81	0.11	0.86	Coarse Clay	Poorly Sorted	Fine Skewed	Platykurtic
94	1385A 12H2 19-21	Hemipelagite	98.19	7.93	2.18	0.09	1.07	V. Fine Silt	Very Poorly Sorted	Symmetrical	Mesokurtic
95	1385D 12H2 90-92	Hemipelagite	101.3	7.8	1.9	0.12	0.97	V. Fine Silt	Poorly Sorted	Fine Skewed	Mesokurtic
96	1385D 12H2 96-98	Hemipelagite	101.36	8.1	2.03	0.19	0.94	Coarse Clay	Very Poorly Sorted	Fine Skewed	Mesokurtic
97	1385D 13H3 125-127	Hemipelagite	112.69	8.83	1.81	0.16	0.79	Coarse Clay	Poorly Sorted	Fine Skewed	Platykurtic
98	1385A 14H2 030-032	Hemipelagite	117	8.42	1.87	0.19	0.89	Coarse Clay	Poorly Sorted	Fine Skewed	Platykurtic
99	1385D 14H2 62-64	Hemipelagite	120.02	8.06	1.96	0.22	0.91	Coarse Clay	Poorly Sorted	Fine Skewed	Mesokurtic
100	1385E 15H2 34-36	Hemipelagite	122.34	8.19	1.86	0.19	0.91	Coarse Clay	Poorly Sorted	Fine Skewed	Mesokurtic

101	1385E 17H1 66-68	Hemipelagite	138.76	8.61	1.83	0.21	0.84	Coarse Clay	Poorly Sorted	Fine Skewed	Platykurtic
102	1385D 16H4 38-40	Hemipelagite	141.83	8.26	1.85	0.23	0.89	Coarse Clay	Poorly Sorted	Fine Skewed	Platykurtic
103	1457C 24R2 041-043	Hemipelagite	406.81	7.7	1.88	0.05	0.79	V. Fine Silt	Poorly Sorted	Symmetrical	Platykurtic
104	1386C 17R1 046-047.5	Hemipelagite	510.56	8.21	2.08	0.15	0.84	Coarse Clay	Very Poorly Sorted	Fine Skewed	Platykurtic
105	1457C 35R1 033-035	Hemipelagite	512.04	8.5	1.9	0.01	0.89	Coarse Clay	Poorly Sorted	Symmetrical	Platykurtic
106	1457C 35R1 97.5-99.5	Hemipelagite	512.68	10.97	0.87	-0.05	1.07	Fine Clay	Moderately Sorted	Symmetrical	Mesokurtic
107	1457C 45R2 054-056	Hemipelagite	610.67	8.96	1.75	0.07	0.98	Coarse Clay	Poorly Sorted	Symmetrical	Mesokurtic
108	1457C 45R2 085-087	Hemipelagite	610.98	10.73	0.89	0.04	0.97	Fine Clay	Moderately Sorted	Symmetrical	Mesokurtic
109	1457C 45R2 089-091	Hemipelagite	611.02	8.64	1.81	0.05	0.98	Coarse Clay	Poorly Sorted	Symmetrical	Mesokurtic
110	1457C 45R2 127-129	Hemipelagite	611.4	10.86	0.84	0.05	0.97	Fine Clay	Moderately Sorted	Symmetrical	Mesokurtic
111	1457C 46R2 026-028	Hemipelagite	620.07	8.42	1.79	0.02	0.96	Coarse Clay	Poorly Sorted	Symmetrical	Mesokurtic
112	1457C 46R4 081-082	Hemipelagite	623.62	9.28	1.76	-0.01	0.96	Medium Clay	Poorly Sorted	Symmetrical	Mesokurtic
113	1457C 50R2 126-128	Hemipelagite	659.93	8.46	1.87	-0.01	0.95	Coarse Clay	Poorly Sorted	Symmetrical	Mesokurtic
114	1457C 50R4 069-071	Hemipelagite	662.37	10.73	0.87	0.05	0.96	Fine Clay	Moderately Sorted	Symmetrical	Mesokurtic
115	1457C 51R2 124-126	Hemipelagite	669.64	10.73	0.88	0.04	0.97	Fine Clay	Moderately Sorted	Symmetrical	Mesokurtic

116	1387C 48R3 033-035	Hemipelagite	734.53	8.04	1.72	0.1	0.93	Coarse Clay	Poorly Sorted	Fine Skewed	Mesokurtic
117	1387C 56R1 008-010	Hemipelagite	808.08	8.17	1.96	0.18	0.87	Coarse Clay	Poorly Sorted	Fine Skewed	Platykurtic
118	1457C 22R3 079-081	Hemipelagite	389.41	7.65	1.79	-0.04	0.83	V. Fine Silt	Poorly Sorted	Symmetrical	Platykurtic
119	1457C 24R2 029-031	Hemipelagite	406.69	10.84	0.82	0.06	0.97	Fine Clay	Moderately Sorted	Symmetrical	Mesokurtic
120	1457C 24R3 109-111	Hemipelagite	408.89	8.38	2.01	-0.02	0.83	Coarse Clay	Very Poorly Sorted	Symmetrical	Platykurtic
121	1457C 24R4 141-143	Hemipelagite	410.37	8.29	2.04	0	0.81	Coarse Clay	Very Poorly Sorted	Symmetrical	Platykurtic
122	1457C 45R2 045-047	Hemipelagite	610.58	10.76	0.88	0.03	0.95	Fine Clay	Moderately Sorted	Symmetrical	Mesokurtic
123	1457C 45R2 076-078	Hemipelagite	610.89	8.73	1.79	0.02	0.99	Coarse Clay	Poorly Sorted	Symmetrical	Mesokurtic
124	1457A 01H3 013-015	Turbidites	2.34	7.52	1.84	0.2	0.86	V. Fine Silt	Poorly Sorted	Fine Skewed	Platykurtic
125	1457A 01H3 050-052	Turbidites	2.72	7.33	1.85	0.12	0.85	V. Fine Silt	Poorly Sorted	Fine Skewed	Platykurtic
126	1457A 01H3 052-054	Turbidites	2.74	7.41	1.74	0.11	0.84	V. Fine Silt	Poorly Sorted	Fine Skewed	Platykurtic
127	1457A 01H3 097-099	Turbidites	3.19	6.79	1.77	0.33	0.95	Fine Silt	Poorly Sorted	Very Fine Skewed	Mesokurtic

128	1457A 01H7 028-030	Turbidites	8.17	8.14	2.12	0.04	0.79	Coarse Clay	Very Poorly Sorted	Symmetrical	Platykurtic
129	1457A 02H2 039-041	Turbidites	9.11	9.47	1.81	-0.04	0.79	Medium Clay	Poorly Sorted	Symmetrical	Platykurtic
130	1457A 02H2 123-125	Turbidites	10.61	8.09	1.78	-0.01	0.9	Medium Clay	Poorly Sorted	Symmetrical	Mesokurtic
131	1457A 02H2 143-145	Turbidites	11.65	7.9	1.87	0	0.85	V. Fine Silt	Poorly Sorted	Symmetrical	Platykurtic
132	1457A 02H6- 054-056	Turbidites	14.7	8.07	2.17	0.03	0.83	Coarse Clay	Very Poorly Sorted	Symmetrical	Platykurtic
133	1457B 05H2 034-036	Turbidites	33.56	7.43	1.75	0.13	0.88	V. Fine Silt	Poorly Sorted	Fine Skewed	Platykurtic
134	1457B 05H2 079-081	Turbidites	34.01	9.31	1.83	0.05	0.69	Medium Clay	Poorly Sorted	Symmetrical	Platykurtic
135	1457B 05H2 142.5-144.5	Turbidites	34.64	9.67	2.14	-0.32	0.73	Medium Clay	Very Poorly Sorted	Very Coarse Skewed	Platykurtic
136	1457A 07H3 025-027	Turbidites	59.4	7.95	2.06	0.07	0.8	V. Fine Silt	Very Poorly Sorted	Symmetrical	Platykurtic
137	1457B 08H2 016-018	Turbidites	61.88	10.98	1.37	-0.23	1.37	Fine Clay	Poorly Sorted	Coarse Skewed	Leptokurtic
138	1457B 08H2 82-84	Turbidites	62.54	11.22	1.35	-0.26	1.62	V. Fine Clay	Poorly Sorted	Coarse Skewed	Very Leptokurtic

139	1457B 08H2 102-104	Turbidites	62.74	7.61	2.65	0.45	0.6	V. Fine Silt	Very Poorly Sorted	Very Fine Skewed	Very Platykurtic
140	1457B 08H2 137-139	Turbidites	63.09	10.4	1.16	-0.1	1.03	Fine Clay	Poorly Sorted	Coarse Skewed	Mesokurtic
141	1457A 08H1 038-042	Turbidites	66.11	7.28	2.25	0.51	0.68	V. Fine Silt	Very Poorly Sorted	Very Fine Skewed	Platykurtic
142	1457A 08H1 130-132	Turbidites	67	7.98	1.77	0.02	0.86	V. Fine Silt	Poorly Sorted	Symmetrical	Platykurtic
143	1457A 8H2 027-031	Turbidites	67.52	8.36	1.95	0.15	0.82	Coarse Clay	Poorly Sorted	Fine Skewed	Platykurtic
144	1457B 09H5 104-106	Turbidites	76.6	7.44	1.69	0.28	0.95	V. Fine Silt	Poorly Sorted	Fine Skewed	Mesokurtic
145	1457A 10H1 107-109	Turbidites	85.76	7.85	1.72	0.1	0.87	V. Fine Silt	Poorly Sorted	Fine Skewed	Platykurtic
146	1457A 11H3 110-112	Turbidites	98.32	7.48	1.84	0.26	0.85	V. Fine Silt	Poorly Sorted	Fine Skewed	Platykurtic
147	1457A 12H5 013-015	Turbidites	108.62	9.79	1.28	0.15	0.87	Medium Clay	Poorly Sorted	Fine Skewed	Platykurtic
148	1457A 12H5 053-055	Turbidites	109.01	7.37	1.71	0.16	0.91	V. Fine Silt	Poorly Sorted	Fine Skewed	Mesokurtic
149	1457A 13F3 016-018	Turbidites	114.38	7.37	1.72	0.15	0.89	V. Fine Silt	Poorly Sorted	Fine Skewed	Platykurtic
150	1457A 13F3 101-103	Turbidites	115.23	7.05	1.82	0.26	0.89	V. Fine Silt	Poorly Sorted	Fine Skewed	Platykurtic

151	1457A 17F1 020-022	Turbidites	130.62	7.39	1.87	0.23	0.84	V. Fine Silt	Poorly Sorted	Fine Skewed	Platykurtic
152	1457A 17F1 083-085	Turbidites	131.25	7.31	1.7	0.15	0.87	FV. ine Silt	Poorly Sorted	Fine Skewed	Platykurtic
153	1457A 17F1 124-128	Turbidites	131.64	6.94	1.82	0.28	1.05	Fine Silt	Poorly Sorted	Fine Skewed	Mesokurtic
154	1457A 17F1 138-140	Turbidites	131.8	7.31	1.76	0.14	0.86	V. Fine Silt	Poorly Sorted	Fine Skewed	Platykurtic
155	1457A 19F2 050-052	Turbidites	142	10.15	1.08	0	0.92	Fine Clay	Poorly Sorted	Symmetrical	Mesokurtic
156	1457A 19F2 139-141	Turbidites	142.89	7.16	1.8	0.28	0.96	V. Fine Silt	Poorly Sorted	Fine Skewed	Mesokurtic
157	1457B 21F1 05-07	Turbidites	143.66	6.63	1.9	0.35	0.91	Fine Silt	Poorly Sorted	Very Fine Skewed	Mesokurtic
158	1457B 21F2 072-074	Turbidites	145	7.02	1.87	0.27	0.89	V. Fine Silt	Poorly Sorted	Fine Skewed	Platykurtic
159	1457B 23F1 010-012	Turbidites	153.11	9.5	1.89	0.11	0.6	Medium Clay	Poorly Sorted	Fine Skewed	Very Platykurtic
160	1457B 23F1 103-105	Turbidites	154.04	10.03	1.34	0.02	0.87	Fine Clay	Poorly Sorted	Symmetrical	Platykurtic
161	1457B 25F1 103-105	Turbidites	163.39	7.41	1.81	0.29	0.9	Fine Silt	Poorly Sorted	Fine Skewed	Mesokurtic
162	1457B 29F1 009-011	Turbidites	181.3	7.23	1.81	0.26	0.98	V. Fine Silt	Poorly Sorted	Fine Skewed	Mesokurtic
163	1457B 29F1 120-122	Turbidites	182.32	7.21	1.86	0.3	0.92	V. Fine Silt	Poorly Sorted	Very Fine Skewed	Mesokurtic
164	1457B 31F1 045-047	Turbidites	191.07	7.76	1.84	0.1	0.82	V. Fine Silt	Poorly Sorted	Fine Skewed	Platykurtic

165	1457B 31F1 111-113	Turbidites	191.73	9.22	1.59	0.07	0.8	Medium Clay	Poorly Sorted	Symmetrical	Platykurtic
166	1457B 33F1 132-134	Turbidites	191.73	9.92	1.33	0.08	0.87	Medium Clay	Poorly Sorted	Symmetrical	Platykurtic
167	1457B 33F1 013-015	Turbidites	200.13	5.47	1.59	0.33	1.45	Medium Silt	Poorly Sorted	Very Fine Skewed	Leptokurtic
168	1457B 33F1 078-080	Turbidites	200.72	5.43	1.55	0.33	1.66	Medium Silt	Poorly Sorted	Very Fine Skewed	Very Leptokurtic
169	1457C 06R1 052-054	Turbidites	230.94	8.07	1.86	0.35	0.82	Coarse Clay	Poorly Sorted	Very Fine Skewed	Platykurtic
170	1457C 08R1 080-082	Turbidites	250.62	8.26	1.91	0.18	0.84	Coarse Clay	Poorly Sorted	Fine Skewed	Platykurtic
171	1457C 09R1 007-011	Turbidites	259.61	7.68	1.99	0.3	0.87	V. Fine Silt	Poorly Sorted	Very Fine Skewed	Platykurtic
172	1457C 10R1 092-094	Turbidites	270.14	10.03	1.35	0.01	0.88	Fine Clay	Poorly Sorted	Symmetrical	Platykurtic
173	1457C 18R2 006-010	Turbidites	348.37	7.13	1.78	0.27	1.03	V. Fine Silt	Poorly Sorted	Fine Skewed	Mesokurtic
174	1457C 24R2 014-016	Turbidites	406.69	8.04	1.8	-0.01	0.84	Coarse Clay	Poorly Sorted	Symmetrical	Platykurtic
175	1457C 24R2 107-109	Turbidites	407.47	7.69	1.95	0.07	0.83	V.Fine Silt	Poorly Sorted	Symmetrical	Platykurtic
176	1457C 29R1 099-103	Turbidites	454.53	7.24	2.14	0.32	1.04	V. Fine Silt	Very Poorly Sorted	Very Fine Skewed	Mesokurtic
177	1457C 38R1 043-045	Turbidites	541.25	8.27	1.83	0.22	0.87	Coarse Clay	Poorly Sorted	Fine Skewed	Platykurtic
178	1457C 38R2 124-126	Turbidites	543.56	8.33	1.77	0.05	0.99	Coarse Clay	Poorly Sorted	Symmetrical	Mesokurtic
179	1457C 38R2 126-128	Turbidites	543.56	8.22	1.84	0.18	0.89	Coarse Clay	Poorly Sorted	Fine Skewed	Platykurtic

180	1457C 40R2 5.5-7.5	Turbidites	561.57	8.45	1.76	0.06	1.01	Coarse Clay	Poorly Sorted	Symmetrical	Mesokurtic
181	1457C 40R2 042-044	Turbidites	561.95	7.18	1.87	0.22	0.86	V. Fine Silt	Poorly Sorted	Fine Skewed	Platykurtic
182	1457C 44R1 089-091	Turbidites	599.91	8.31	1.7	0.03	1.02	Coarse Clay	Poorly Sorted	Symmetrical	Mesokurtic
183	1457C 46R4 047-049	Turbidites	620.28	10.68	0.89	0.01	0.98	Fine Clay	Moderately Sorted	Symmetrical	Mesokurtic
184	1457C 46R4 064-066	Turbidites	620.45	8.69	1.74	0.06	1.04	Coarse Clay	Poorly Sorted	Symmetrical	Mesokurtic
185	1457C 49R6 030-034	Turbidites	625	8.6	1.93	0.11	0.81	Coarse Clay	Poorly Sorted	Fine Skewed	Platykurtic
186	1457C 58R2 006-008	Turbidites	736.07	8.13	3.61	-0.55	0.64	Coarse Clay	Very Poorly Sorted	Very Coarse Skewed	Very Platykurtic
187	1457C 58R2 016-018	Turbidites	736.17	6.53	2.08	0.28	0.87	Fine Silt	Very Poorly Sorted	Fine Skewed	Platykurtic
188	1457C 60R1 144-146	Turbidites	755.66	10.48	0.88	0.07	0.96	Fine Clay	Moderately Sorted	Symmetrical	Mesokurtic
189	1457C 60R2 30-32	Turbidites	756.02	5.8	2.36	0.34	1.07	Medium Silt	Very Poorly Sorted	Very Fine Skewed	Mesokurtic
190	1457C 61R3 011-015	Turbidites	758.29	9.17	1.6	0.13	0.84	Medium Clay	Poorly Sorted	Fine Skewed	Platykurtic
191	1457C 64R1 020-022	Turbidites	766.37	10.38	0.9	0.07	0.94	Fine Clay	Moderately Sorted	Symmetrical	Mesokurtic
192	1457C 65R1 069-071	Turbidites	803.41	6.37	2.2	0.33	0.81	Fine Silt	Very Poorly Sorted	Very Fine Skewed	Platykurtic

193	1457C 65R2 108-110	Turbidites	805.22	10.49	0.88	0.07	0.95	Fine Clay	Moderately Sorted	Symmetrical	Mesokurtic
194	1457C 67R3 004-008	Turbidites	824.83	7.66	1.94	0.17	0.78	V. Fine Silt	Poorly Sorted	Fine Skewed	Platykurtic
195	1457C 71R4 063-067	Turbidites	866.07	9.5	1.65	-0.03	0.88	Medium Clay	Poorly Sorted	Symmetrical	Platykurtic
196	1457C 83R6 005-009	Turbidites	984.77	7.98	2.02	-0.02	0.76	V. Fine Silt	Very Poorly Sorted	Symmetrical	Platykurtic

Note that rows containing turbidite samples are coloured in yellow, contourites in blue, hermiturbidites in brown and hemipelagites in white.

Appendix 3B

SEM micrographs of the different deep-water mudrock facies

Sample 1- Contourites (Depth 9m), subset A-D

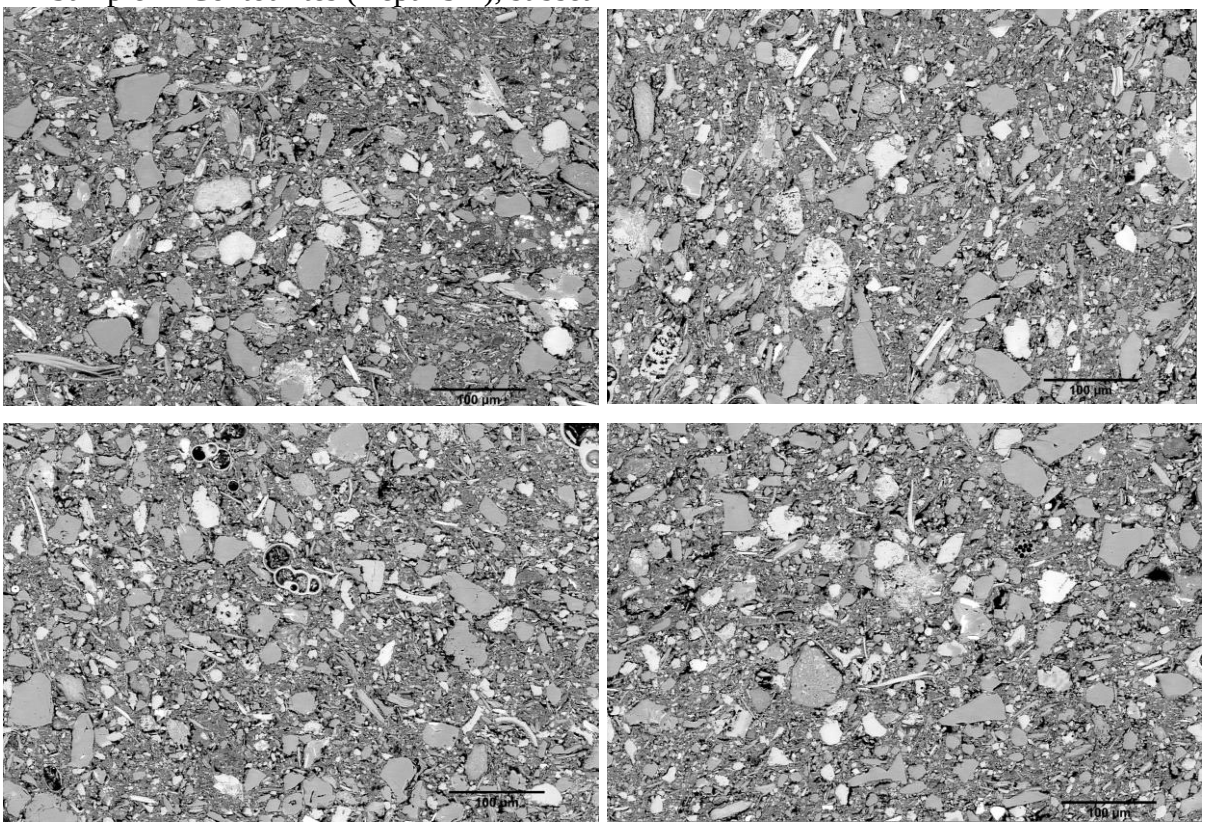

Sample 2- Contourites (Depth 10m), subset A-D

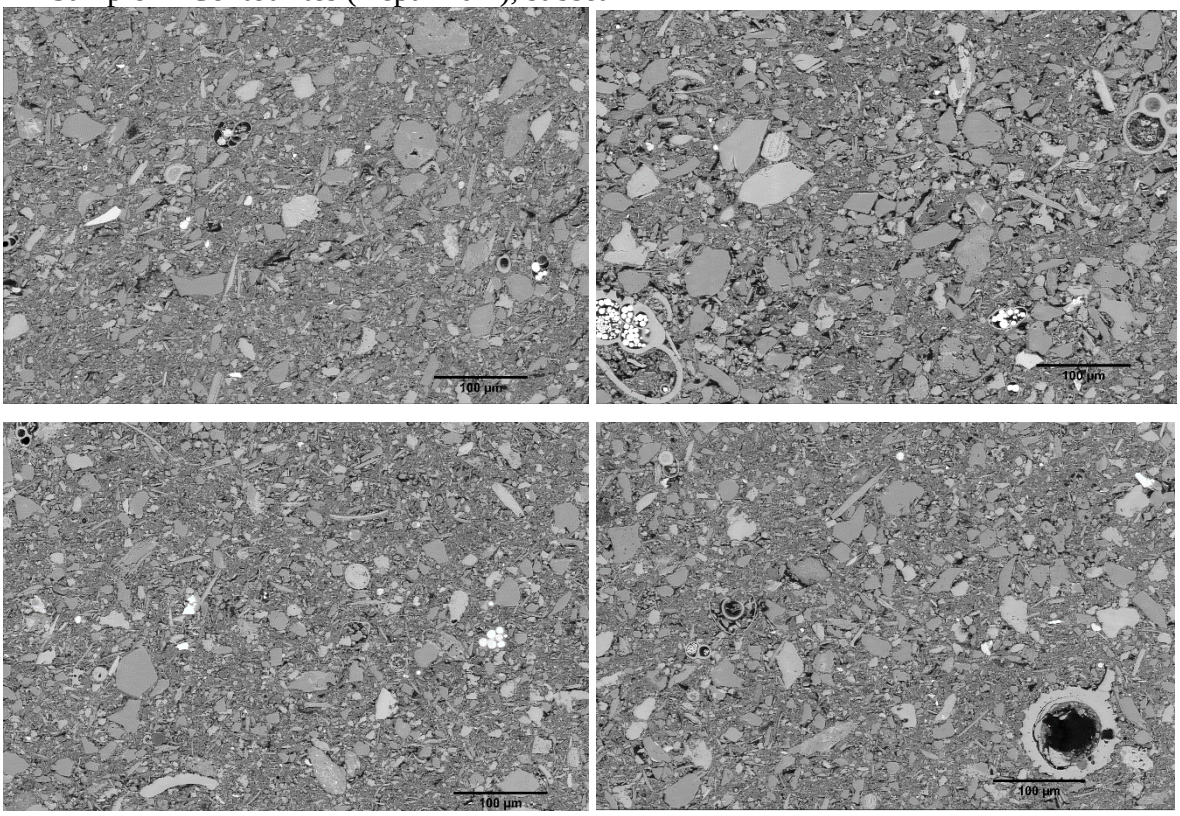

Sample 3- Contourites (Depth 14 m), subset A-D

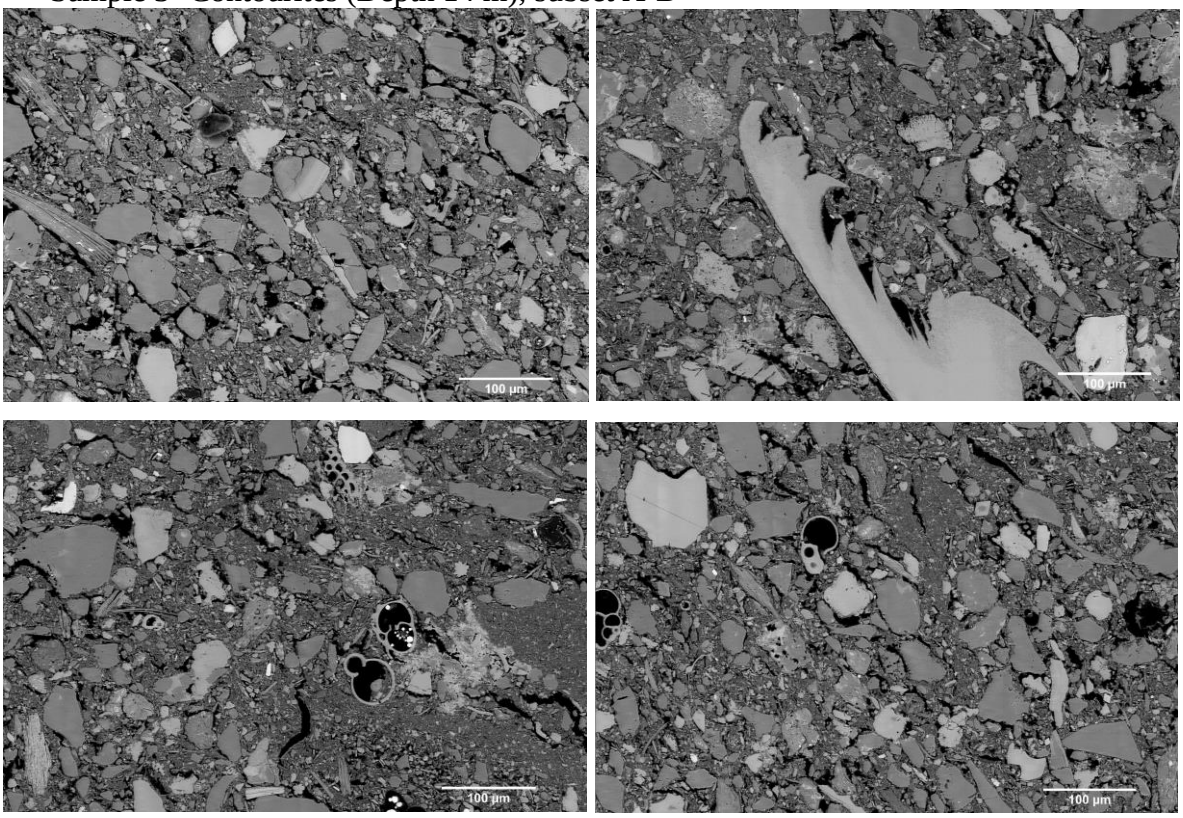

Sample 4- Contourites (Depth 15 m), subset A-D

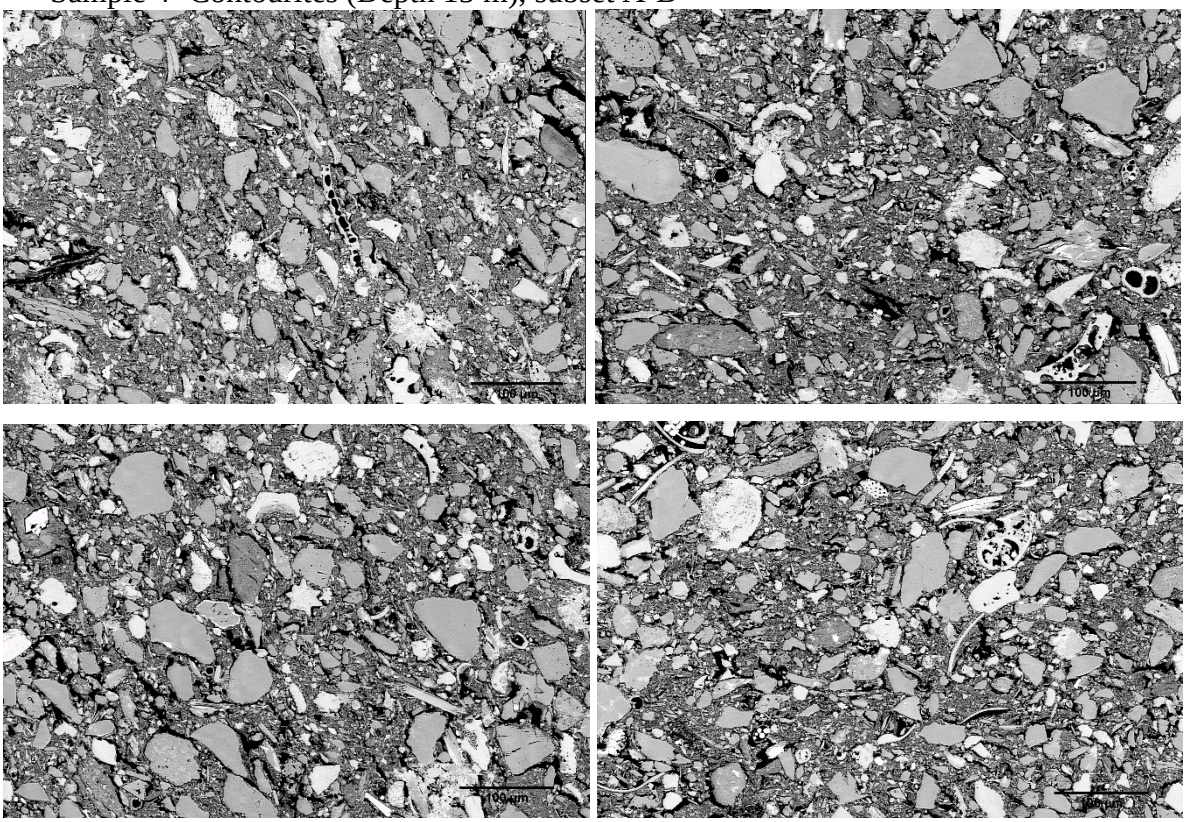

Sample 5- Contourites (Depth 16 m), subset A-D

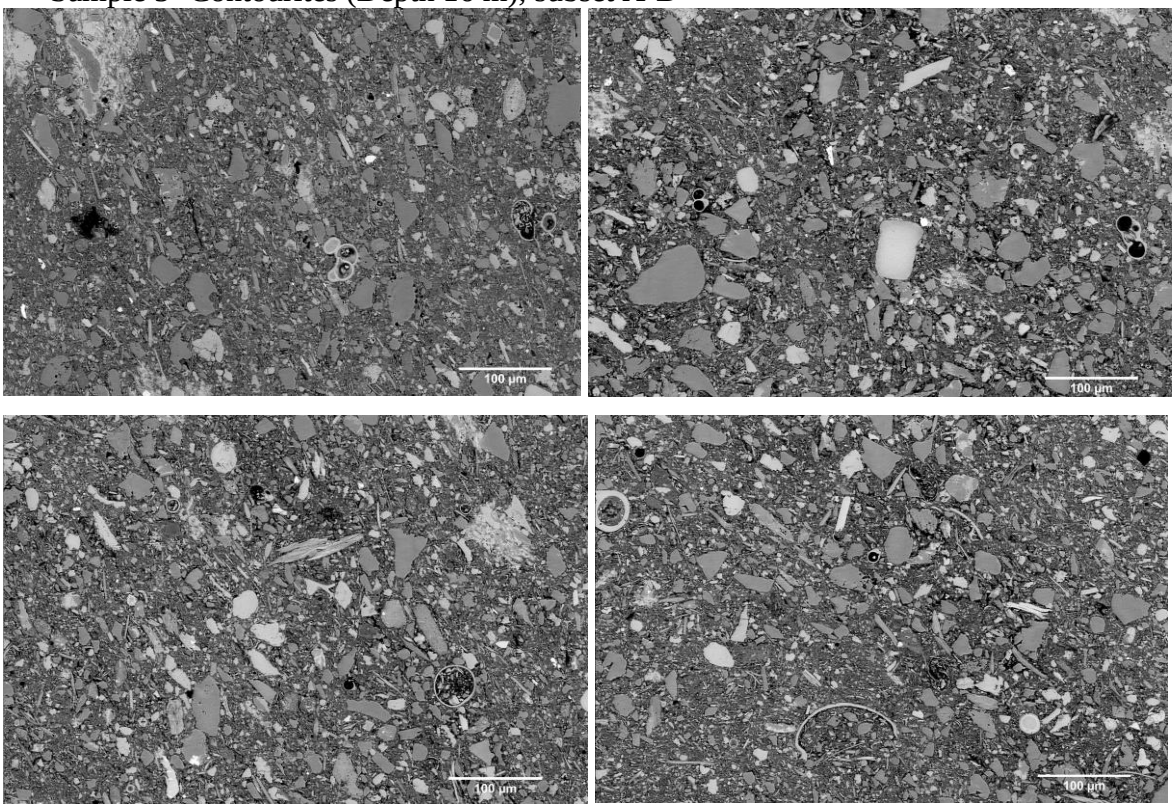

Sample 6- Contourites (Depth 42 m), subset A-F
Table 8.1

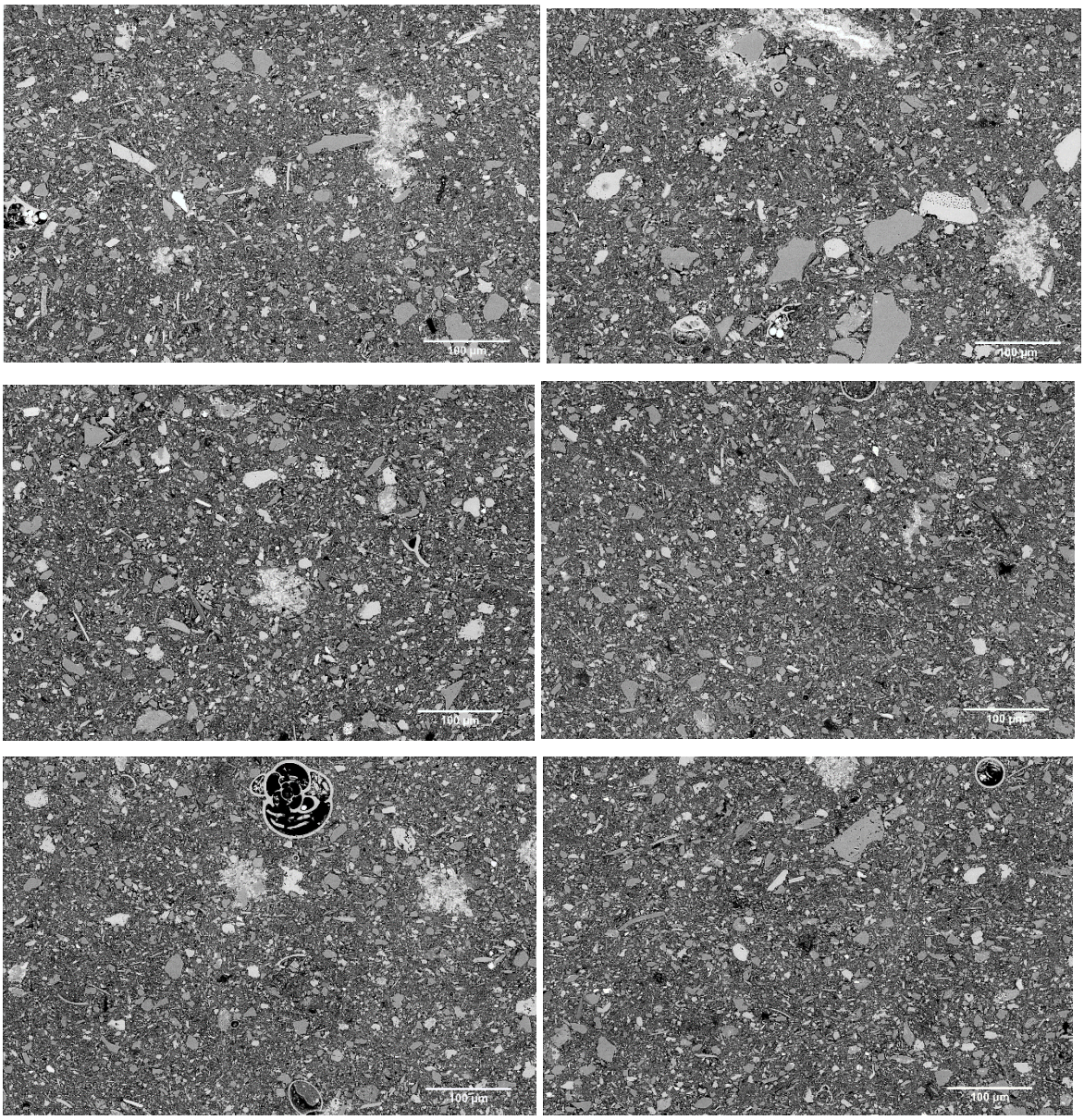

Sample 7- Contourites (Depth 151 m), subset A-F

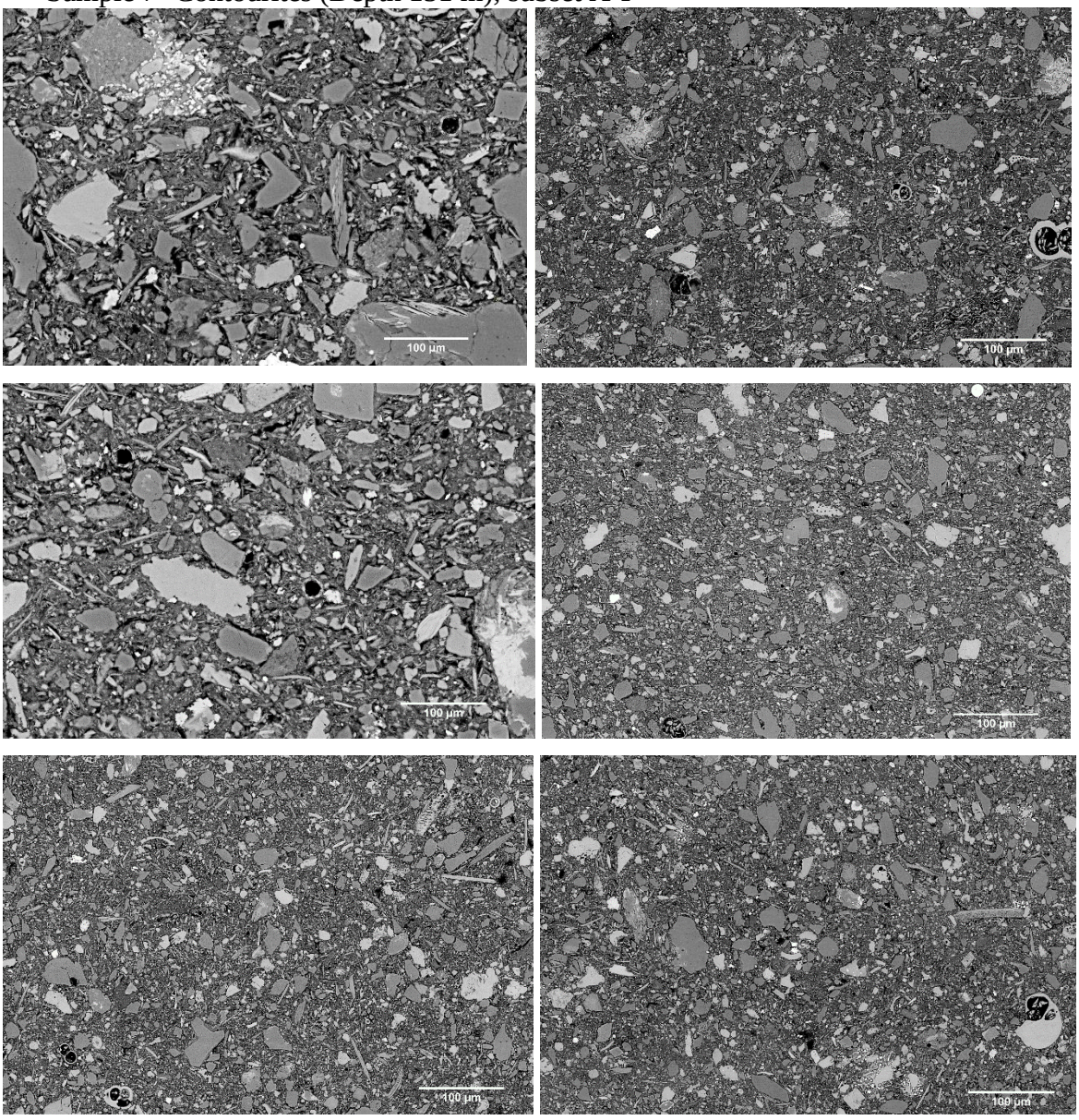

Sample 8- Contourites (Depth 253 m), subset A-D
Table 8.2

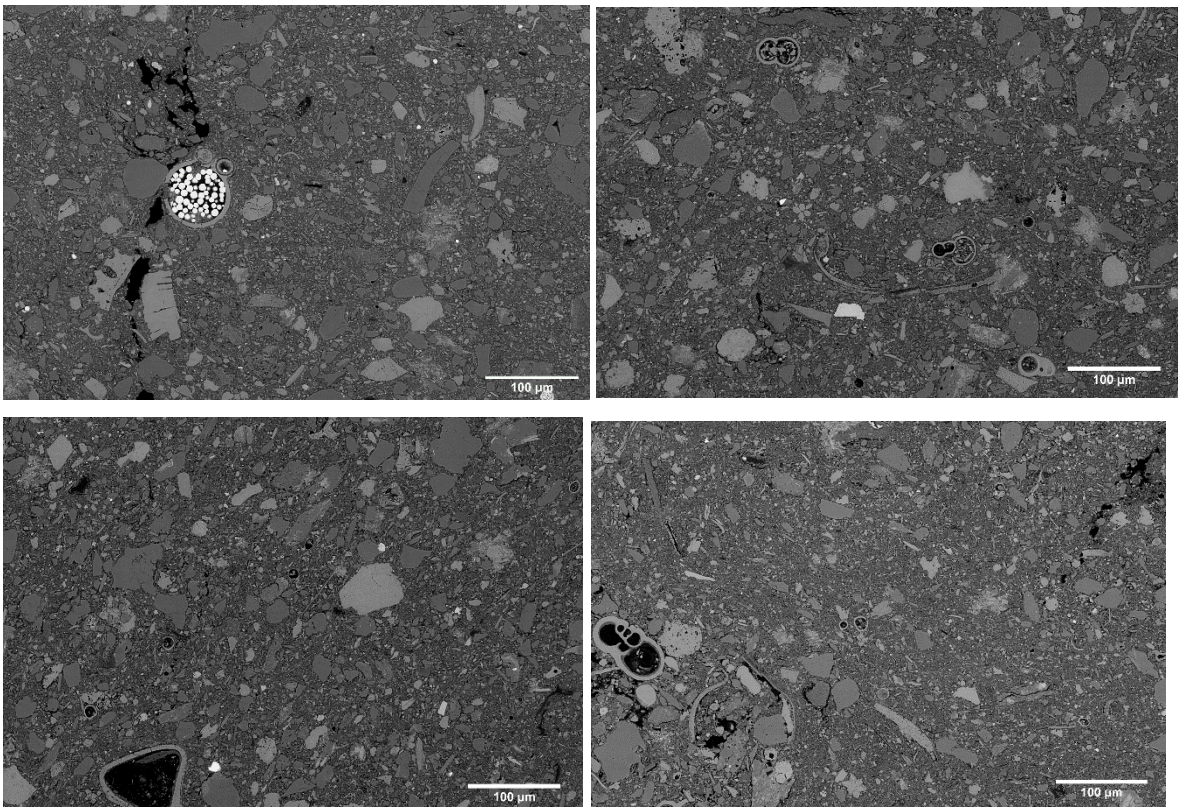

Sample 9- Contourites (Depth 343 m), subset A-D

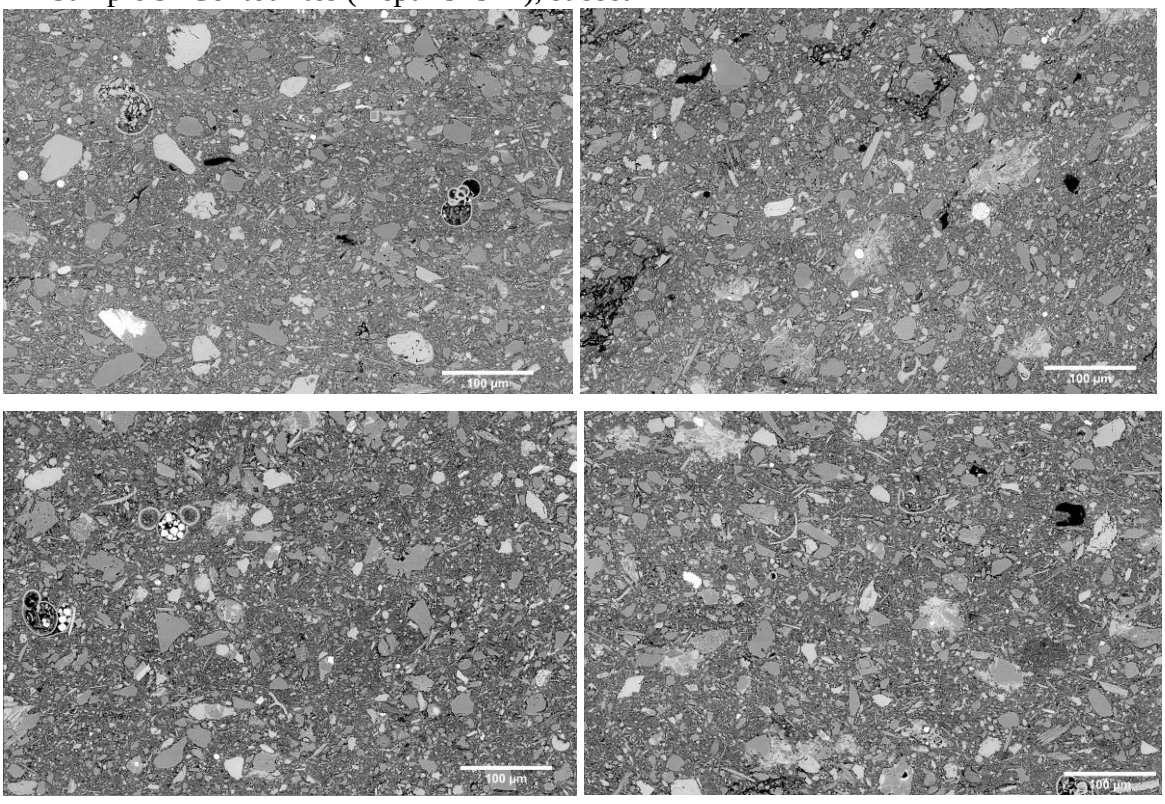

Sample 10- Contourites (Depth 510 m), subset A-D

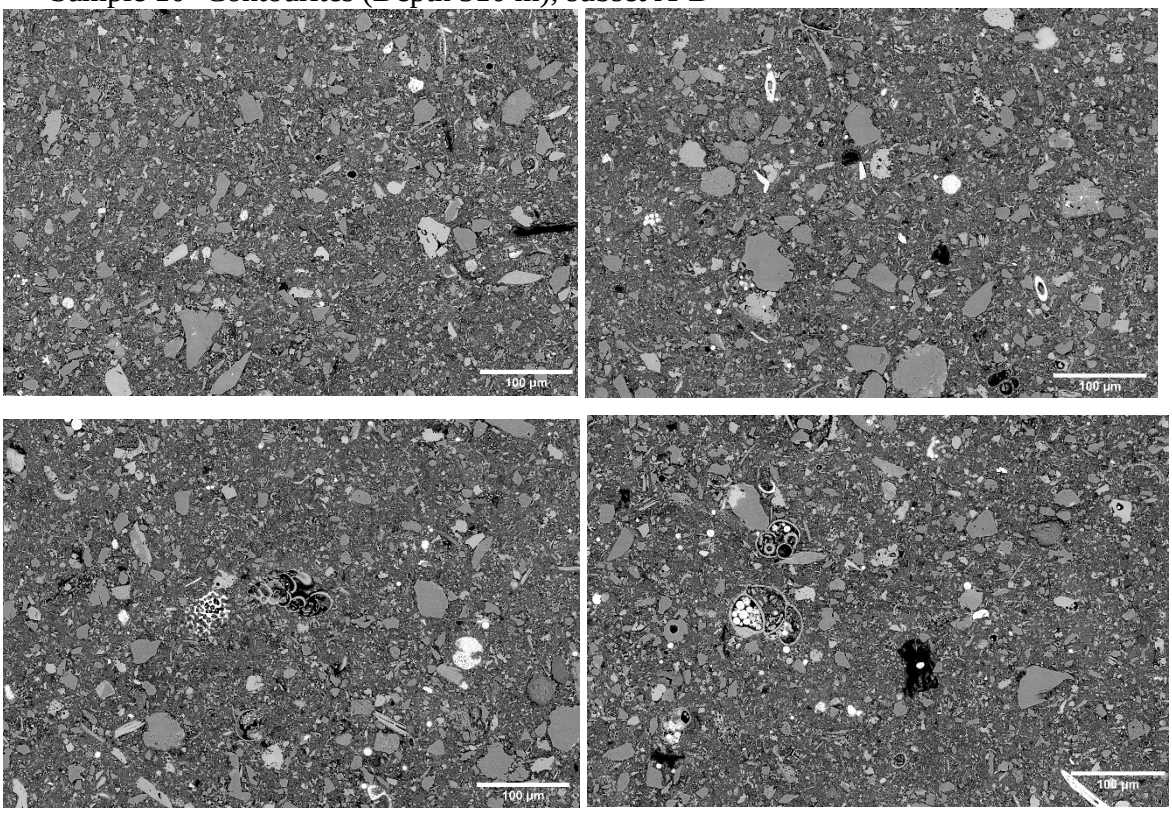

Sample 11- Contourites (Depth 563 m), subset A-D

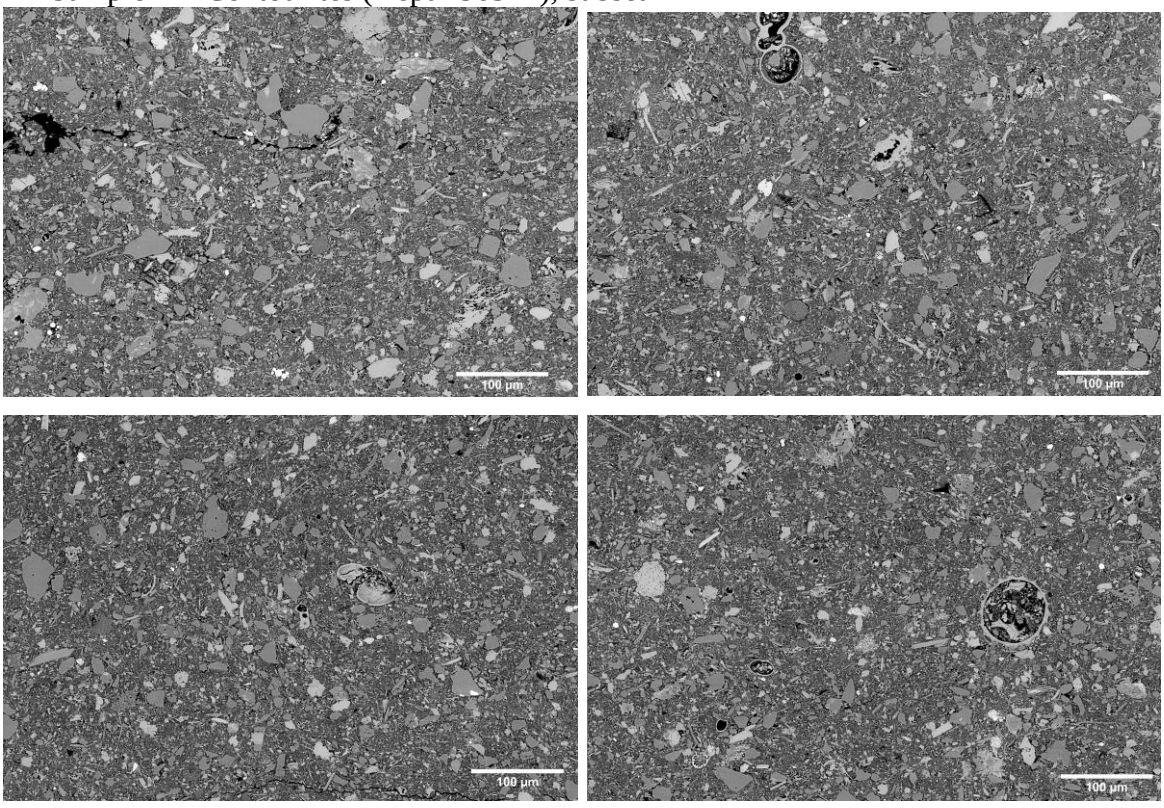

Sample 12- Contourites (Depth 653 m), subset A-D

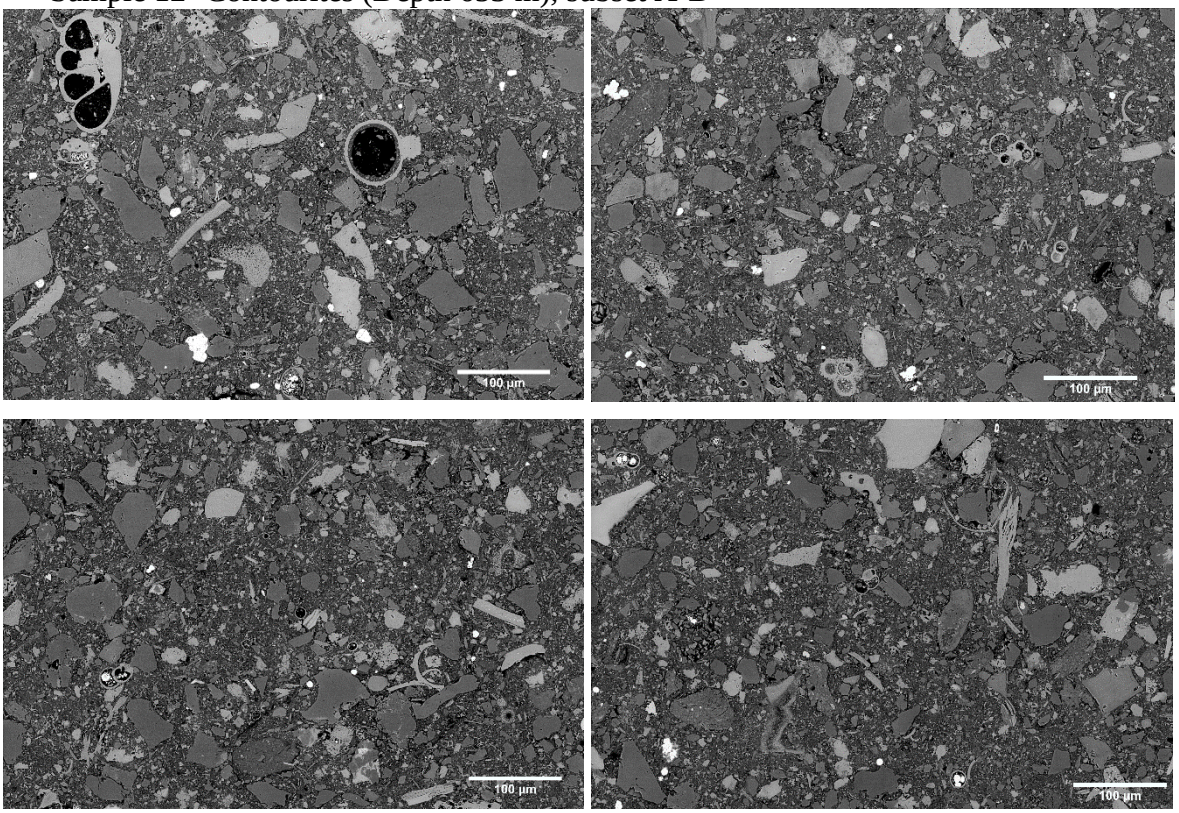

Sample 13- Contourites (Depth 734 m), subset A-E
Table 8.3

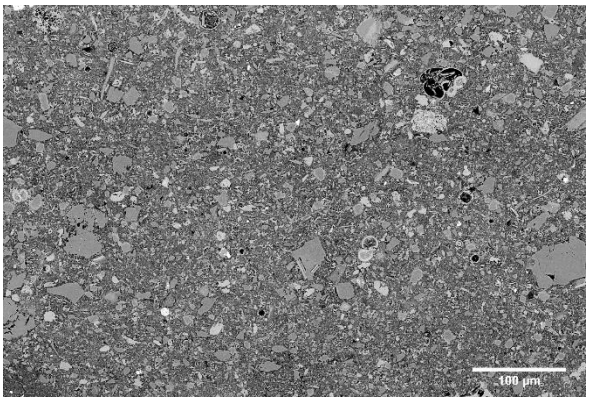

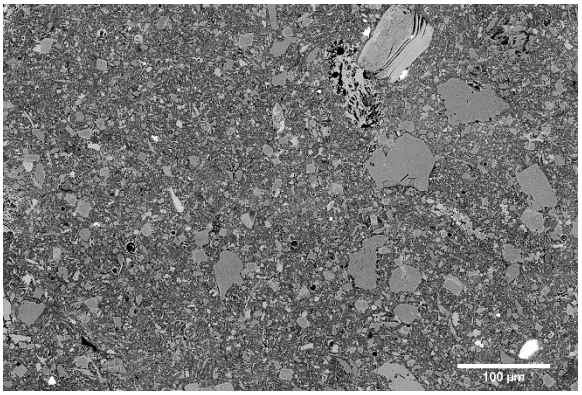

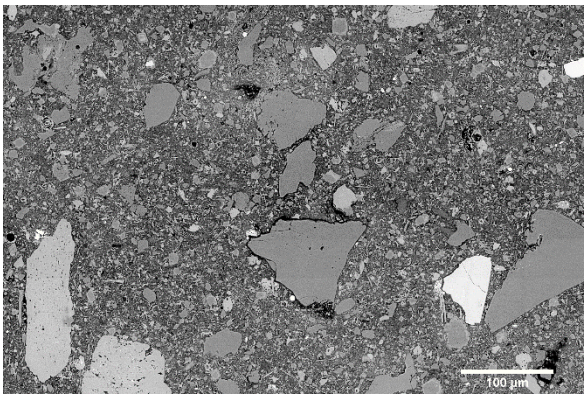

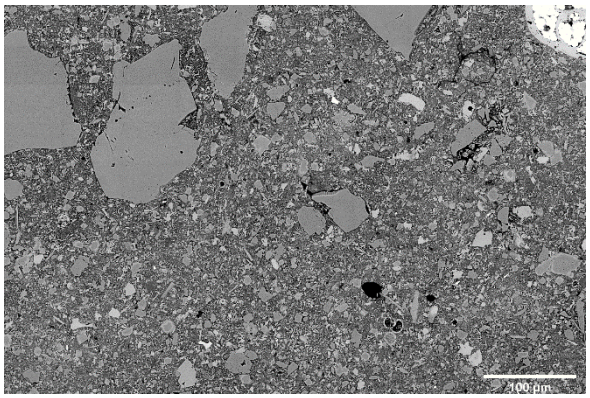

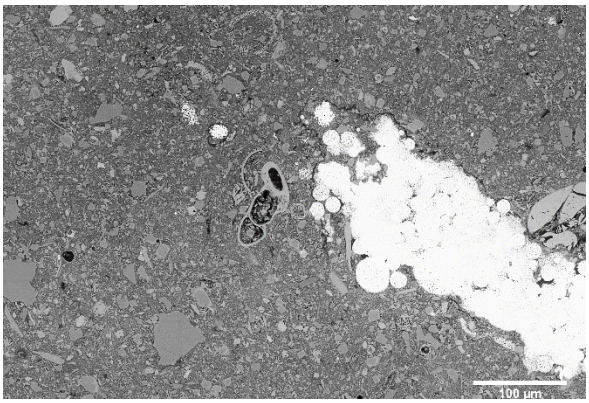

Sample 14- Contourites (Depth 763 m), subset A-E

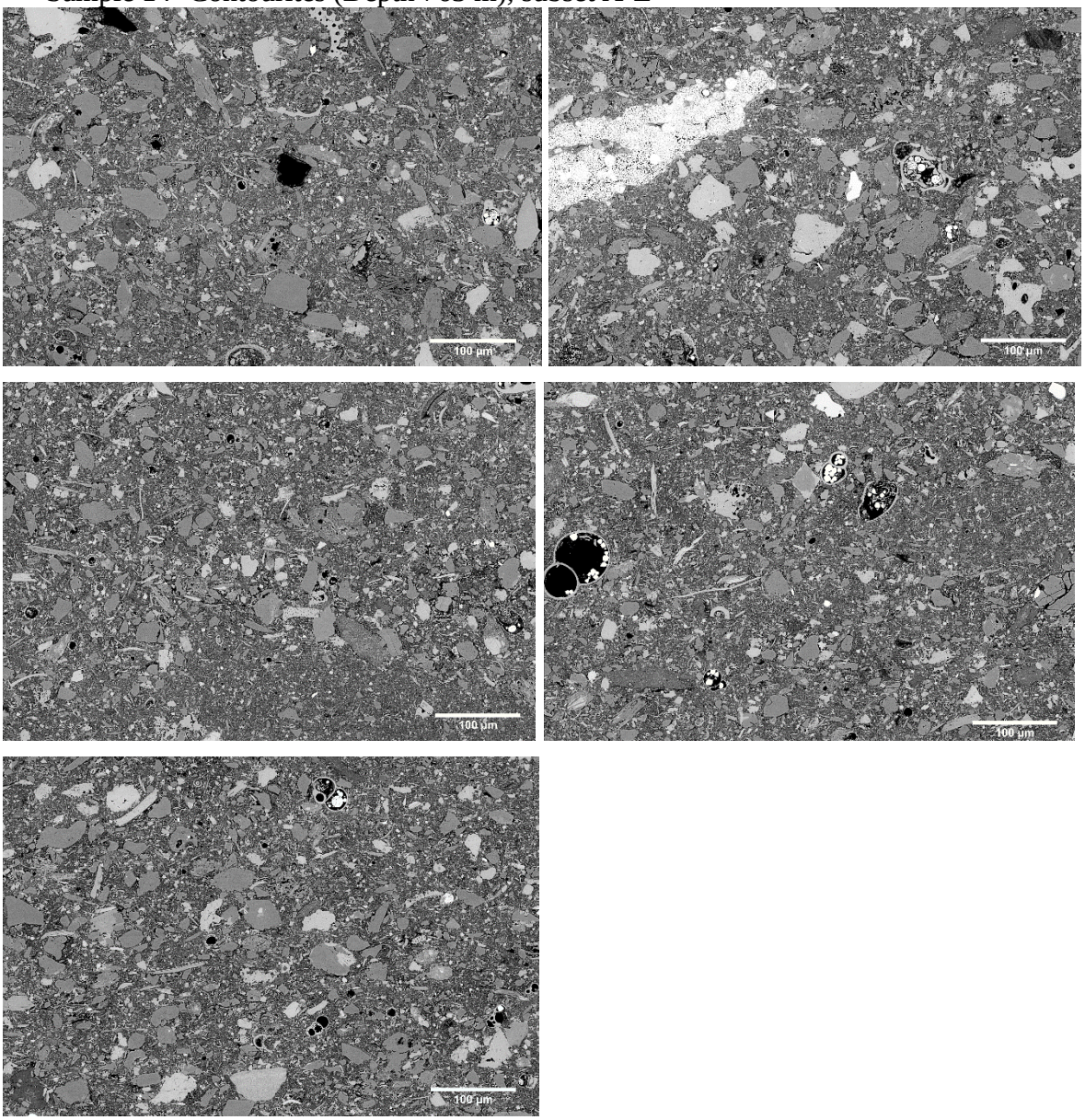

Sample 15- Contourites (Depth 808 m), subset A-F
Table 8.4

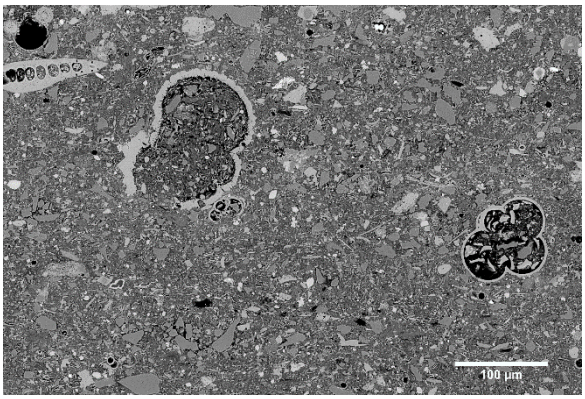

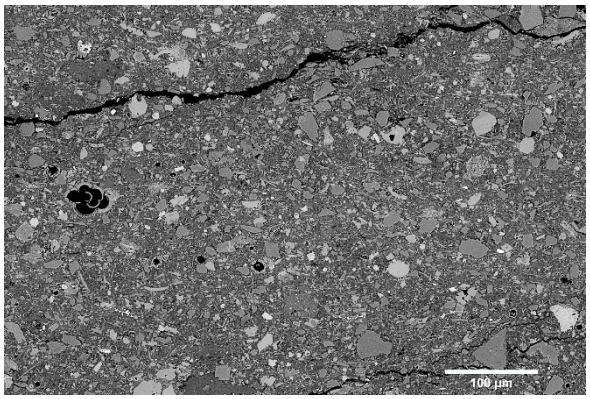

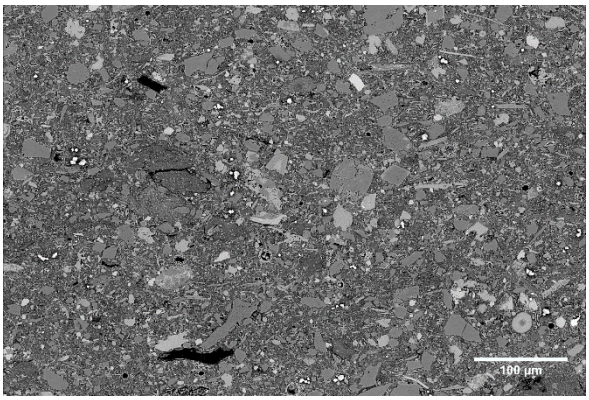

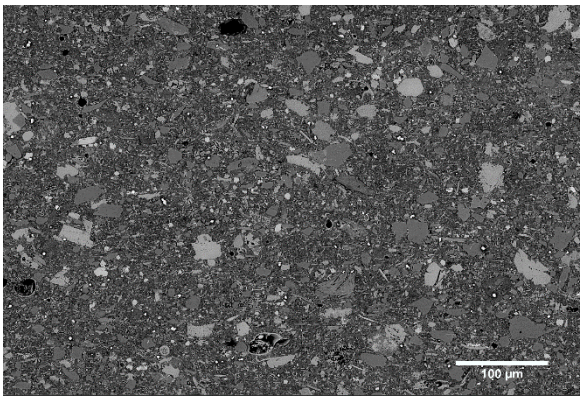

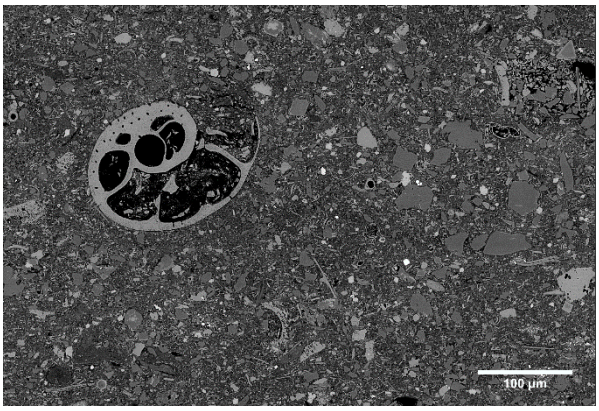

Sample 16- Contourites (Depth 860 m), subset A-E

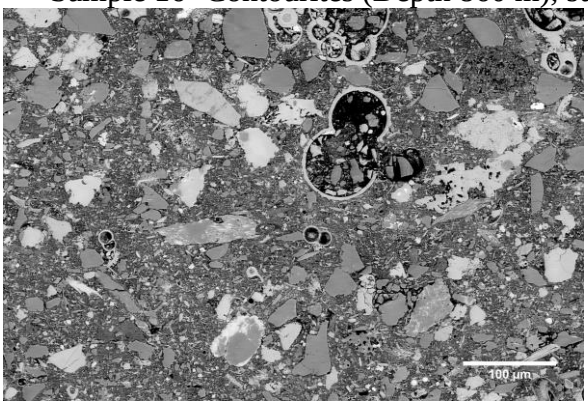

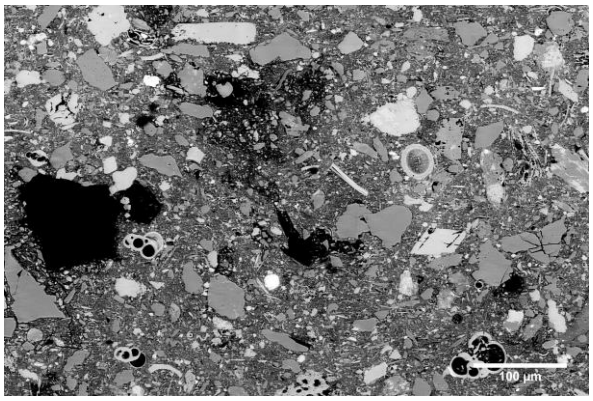

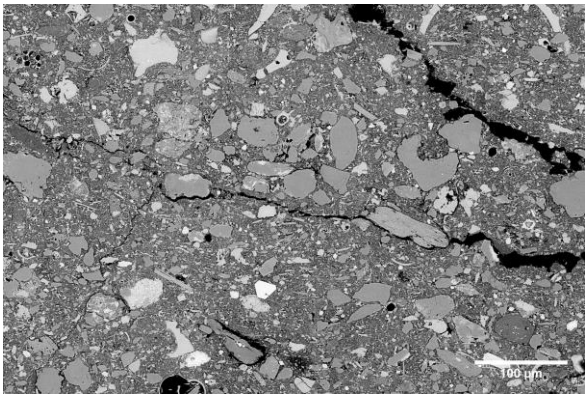

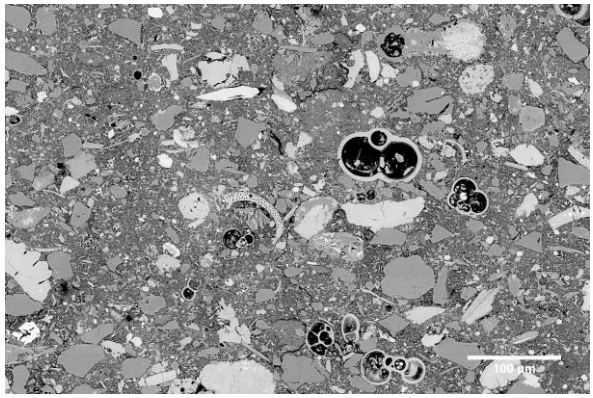

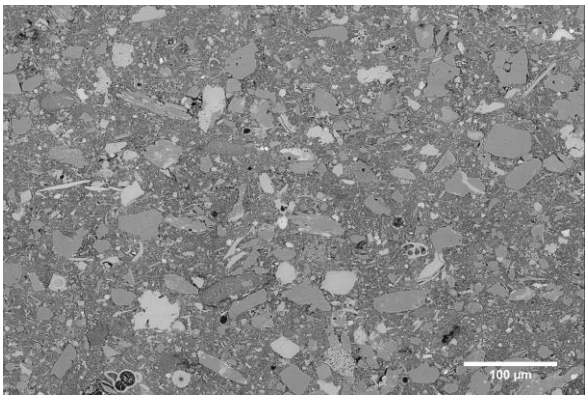

Sample 17- Contourites (Depth 943 m), subset A-E

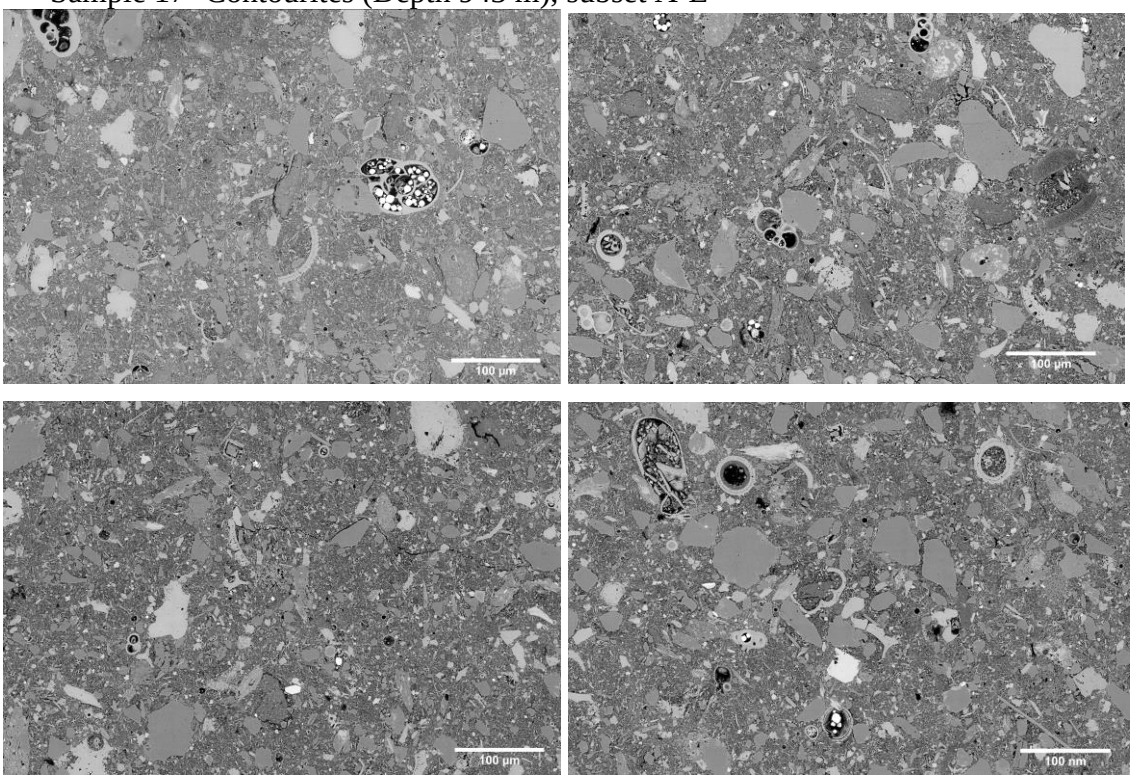

Sample 18- Hemipelagite (Depth 8 m), subset A-E

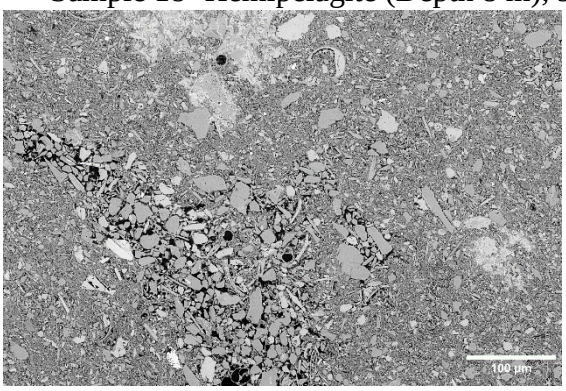

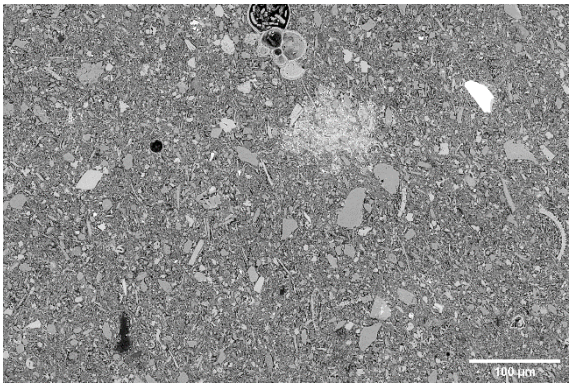

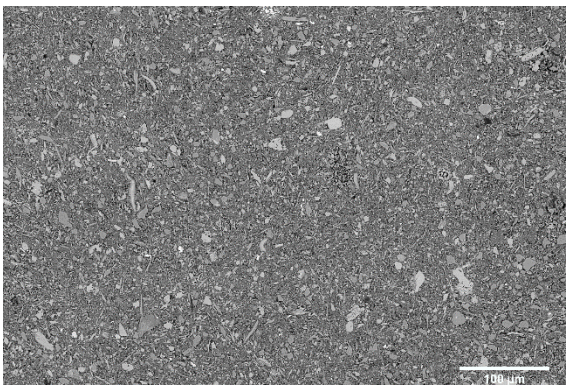

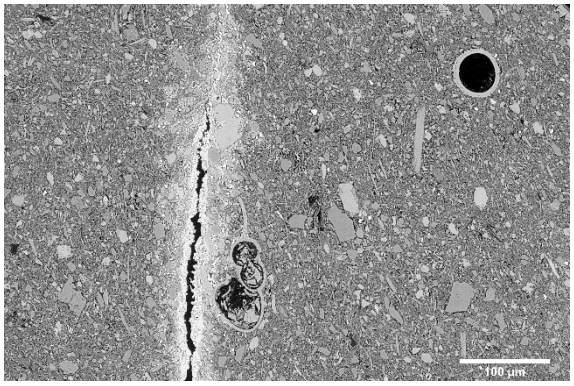

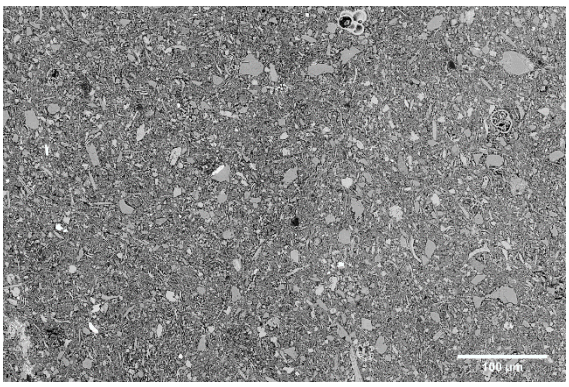

Sample 19- Hemipelagite (Depth 10 m), subset A-F

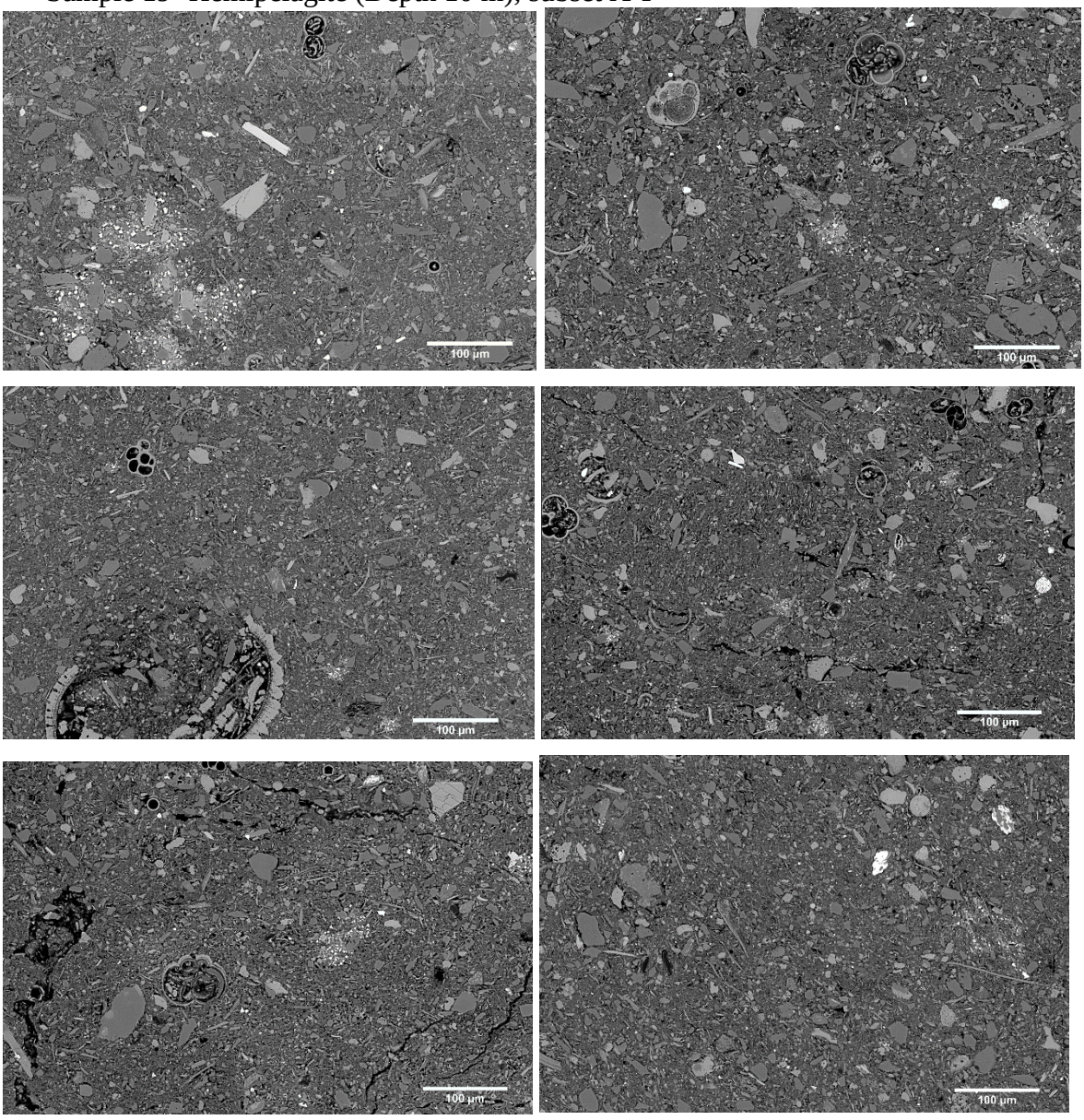

Sample 20- Hemipelagite (Depth 15 m), subset A-F

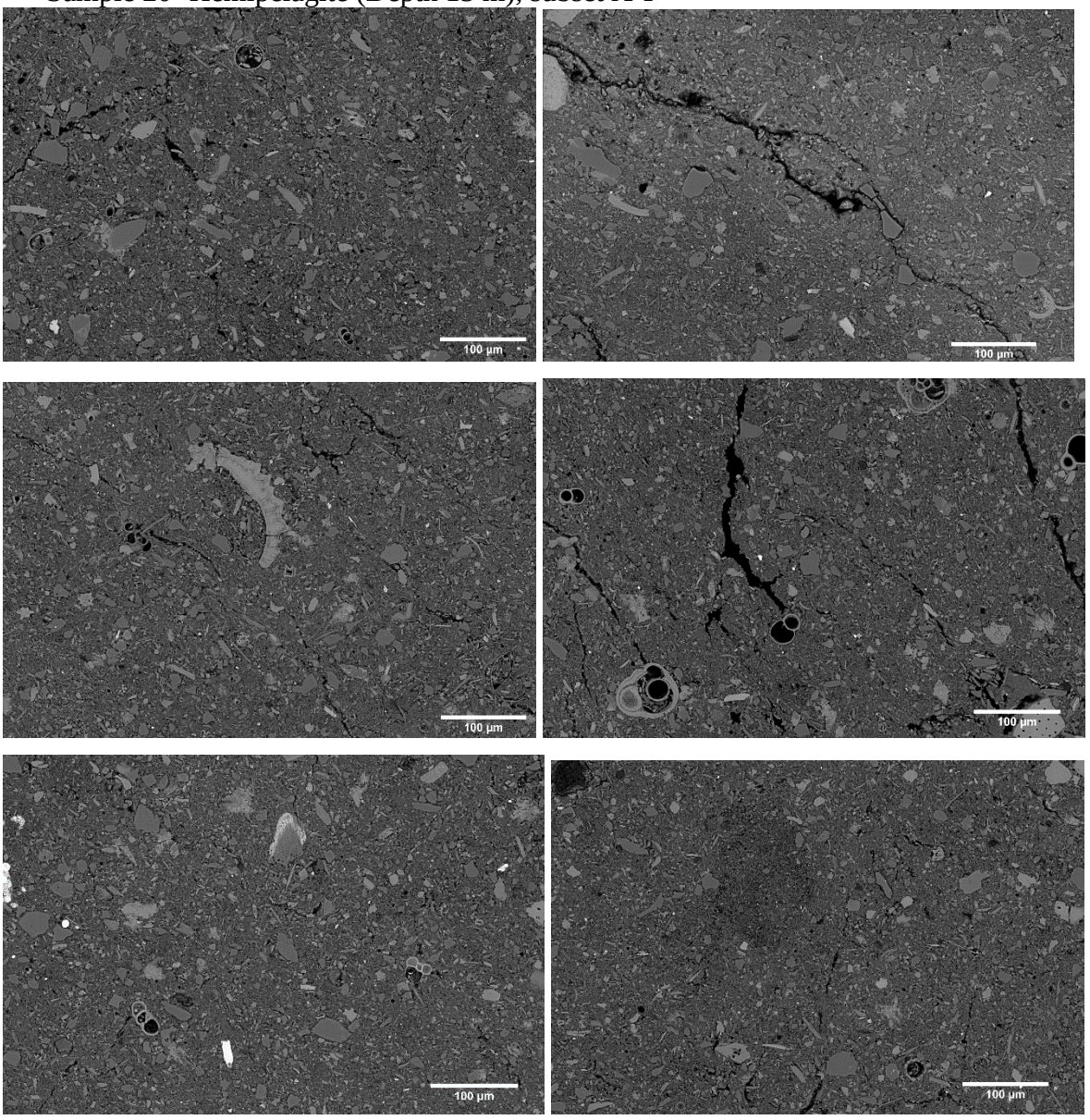

Sample 21- Hemipelagite (Depth 50 m), subset A-F

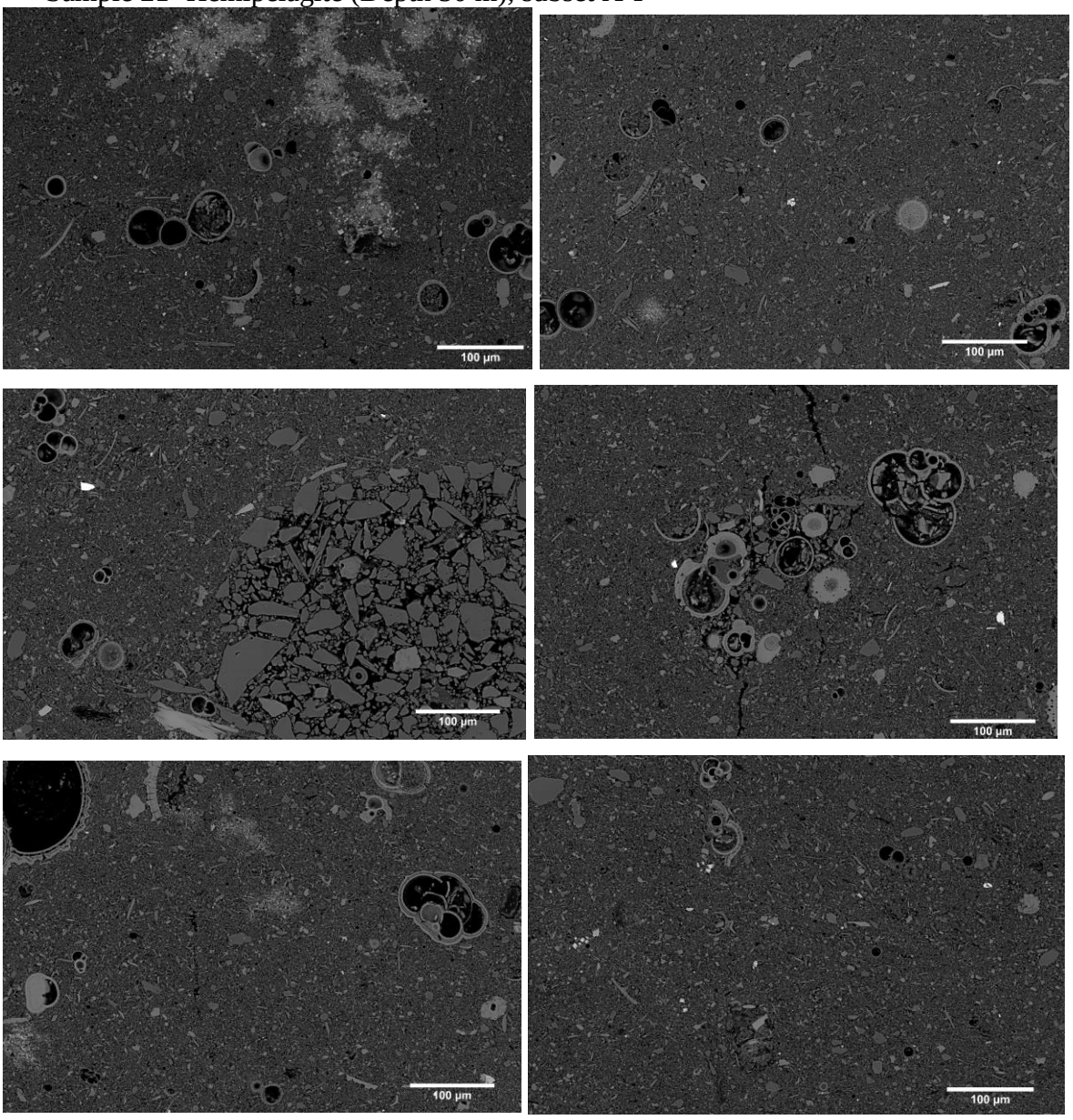

Sample 22- Hemipelagite (Depth 57 m), subset A-E

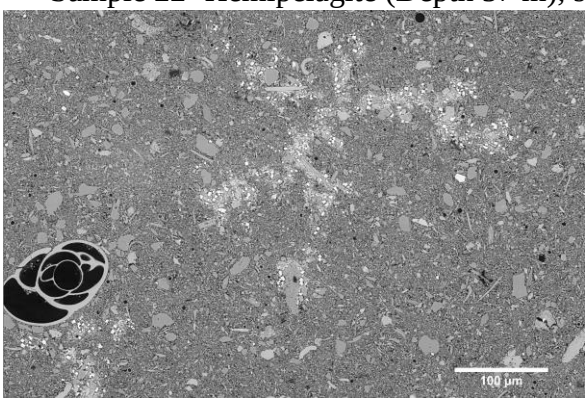

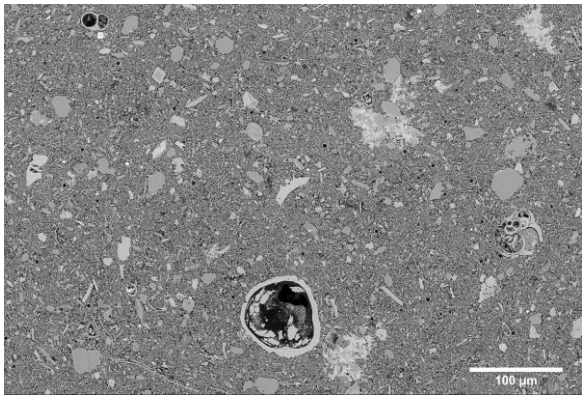

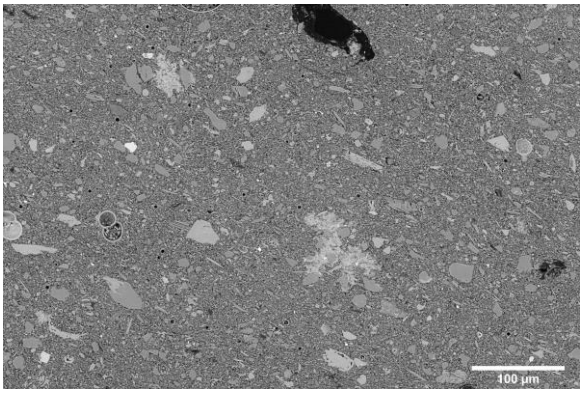

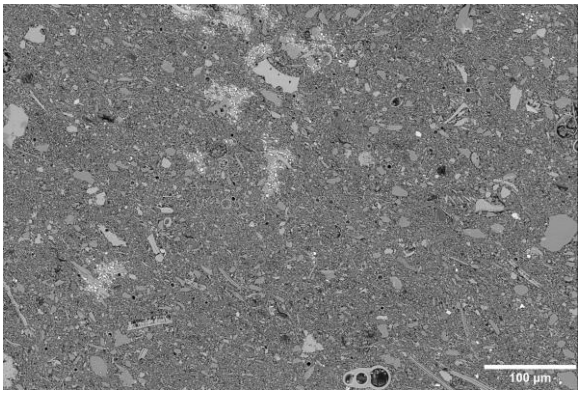

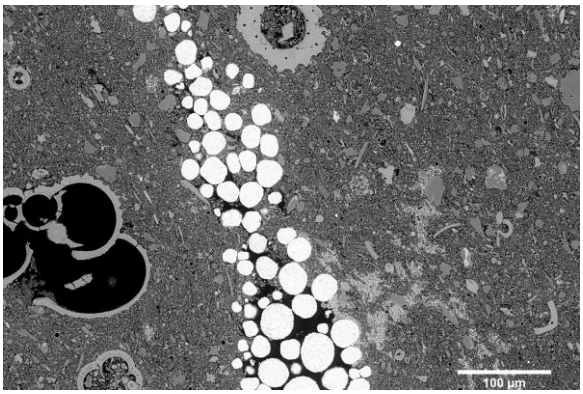

Sample 23- Hemipelagite (Depth 60 m), subset A-F

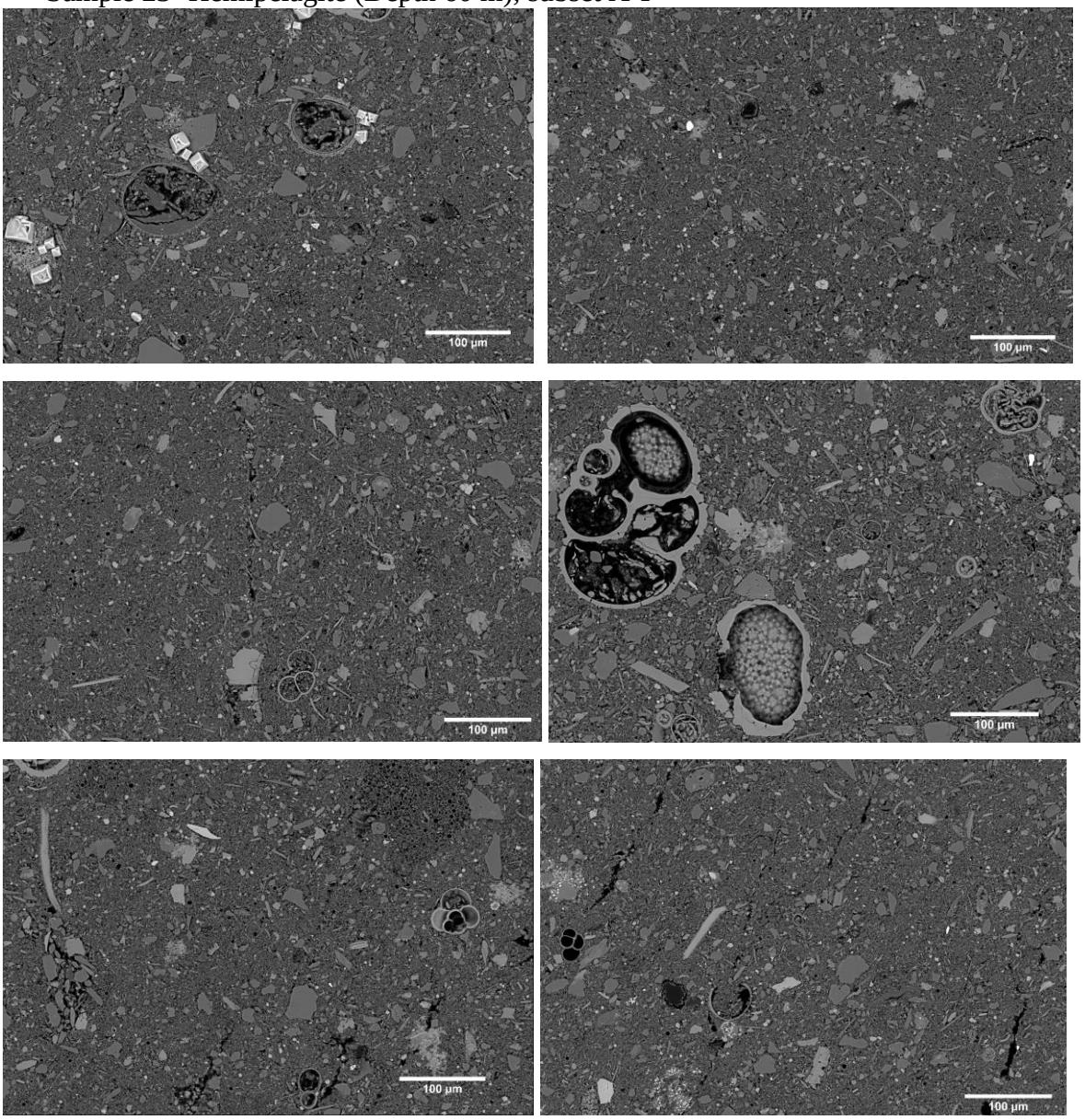

Sample 25- Hemipelagite (Depth 80 m), subset A-E

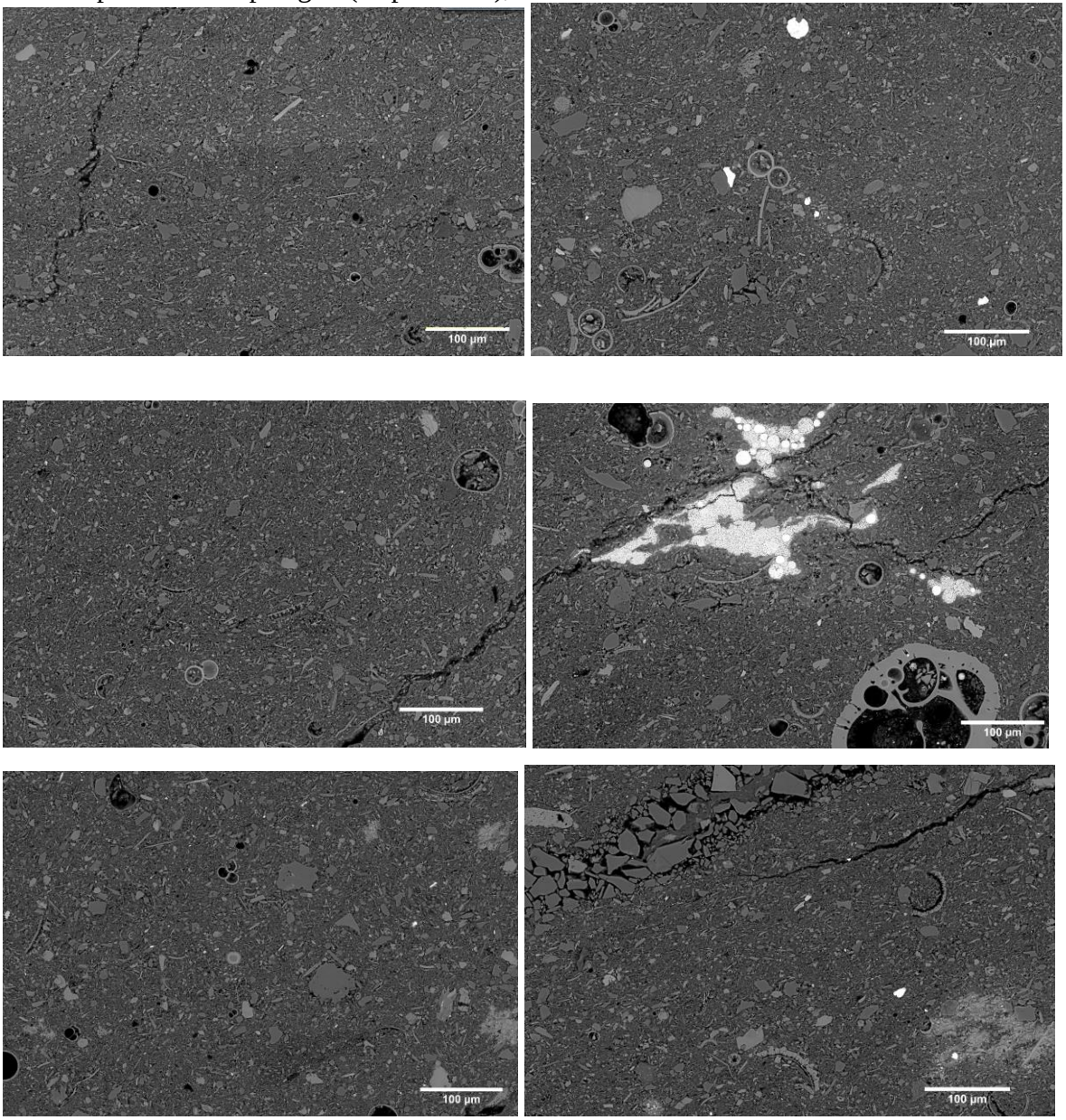

Sample 26- Hemipelagite (Depth 117 m), subset A-D

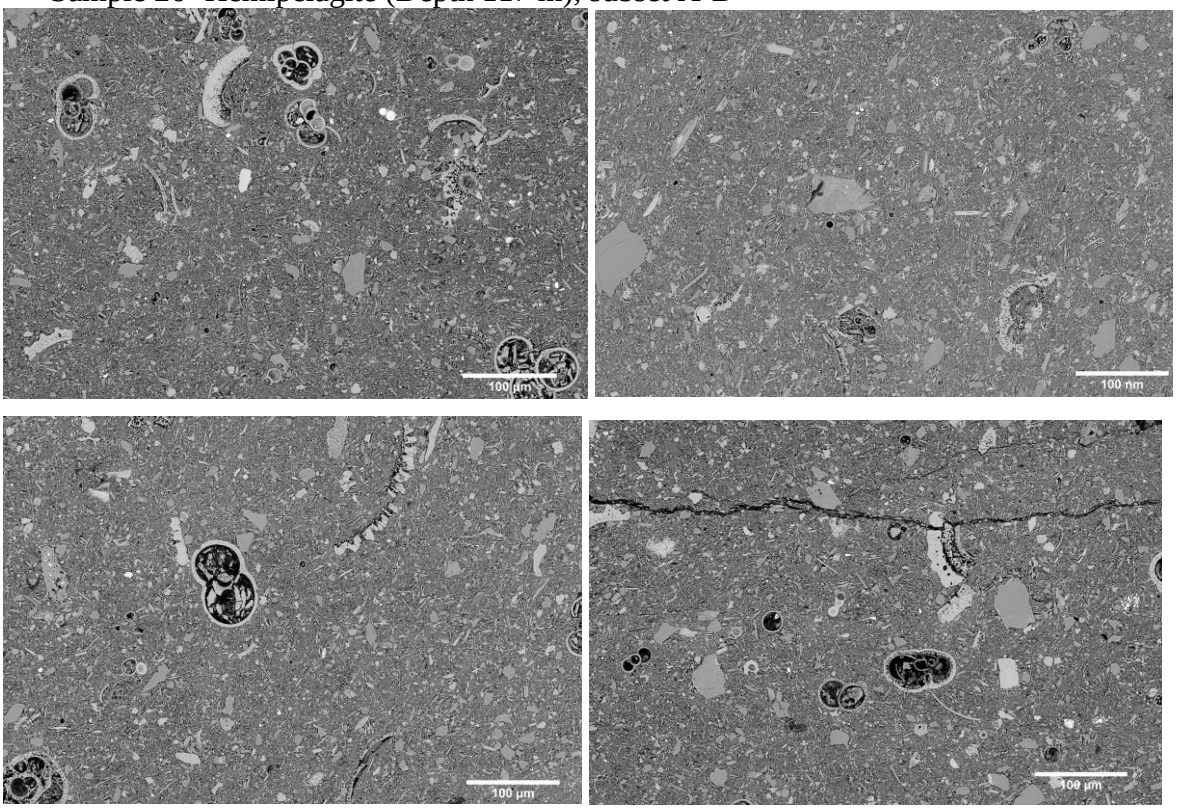

Sample 27- Turbidites (Depth 66 m), subset A-D

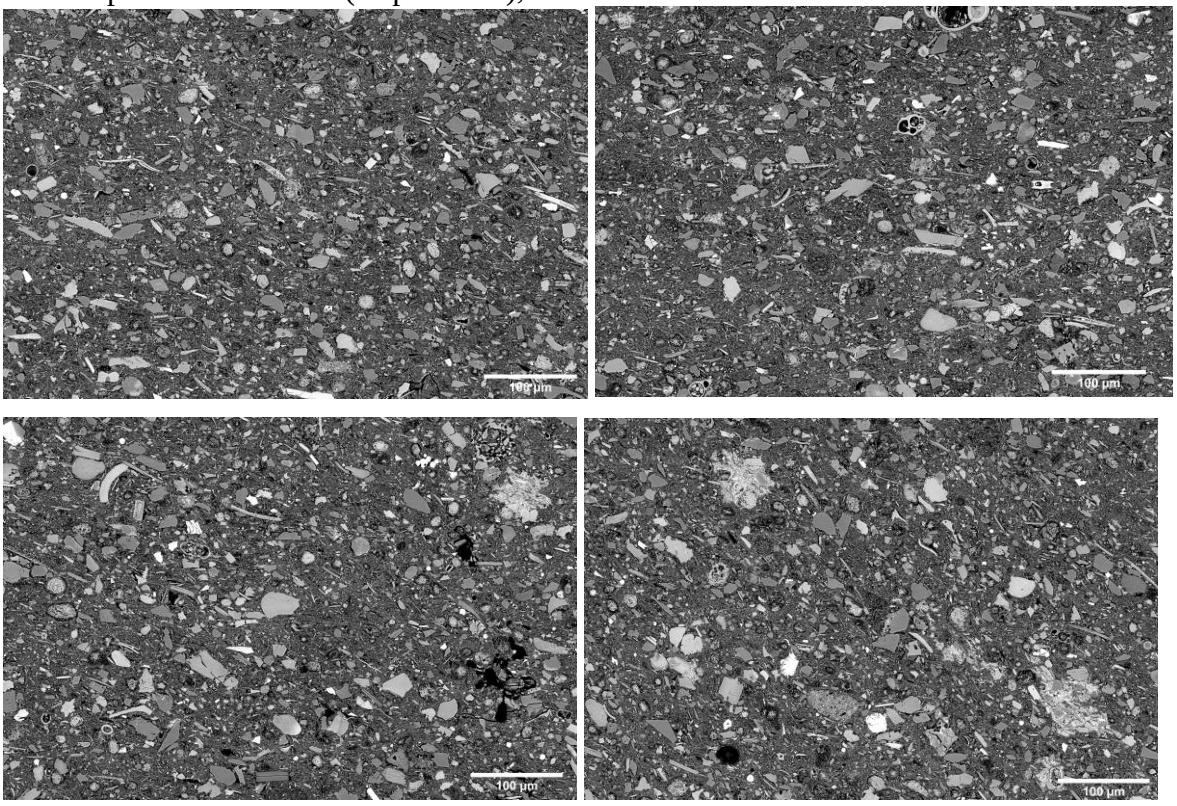

Sample 28- Turbidites (Depth 132 m), subset A-D

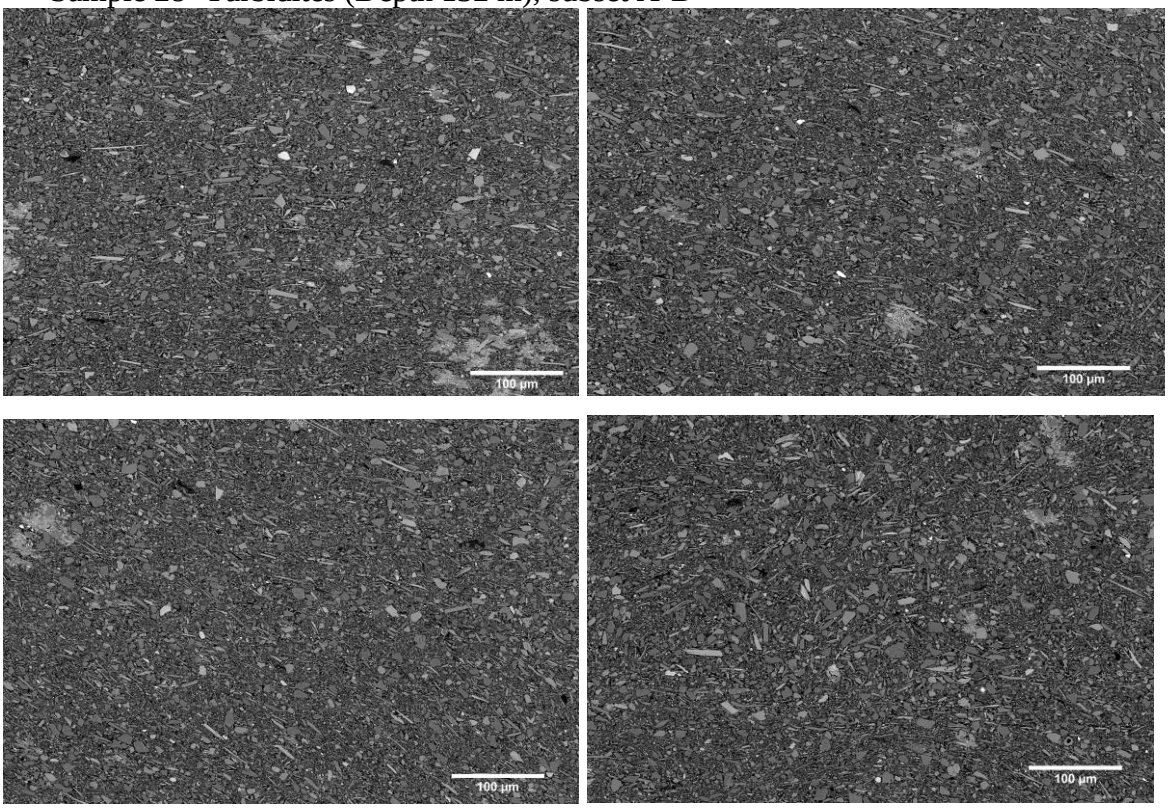

Sample 29- Turbidites (Depth 260 m), subset A-D

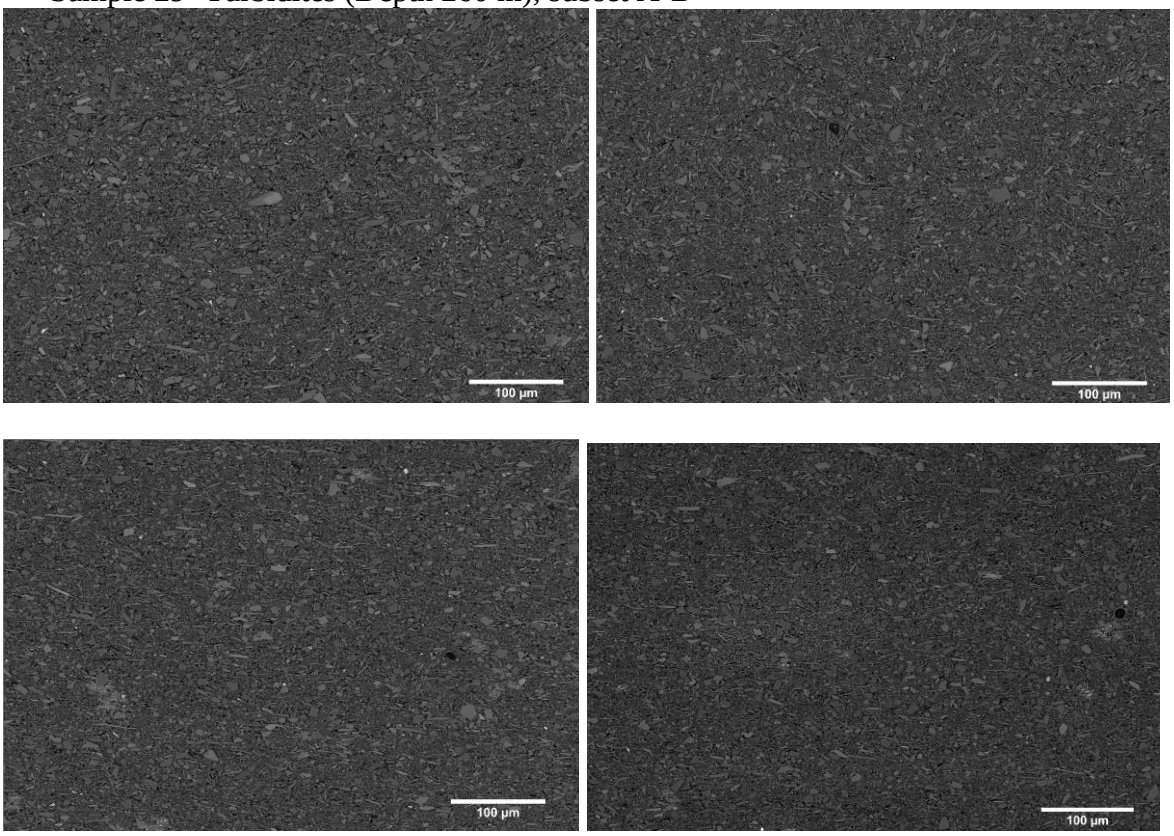

Sample 30- Turbidites (Depth 348 m), subset A-D

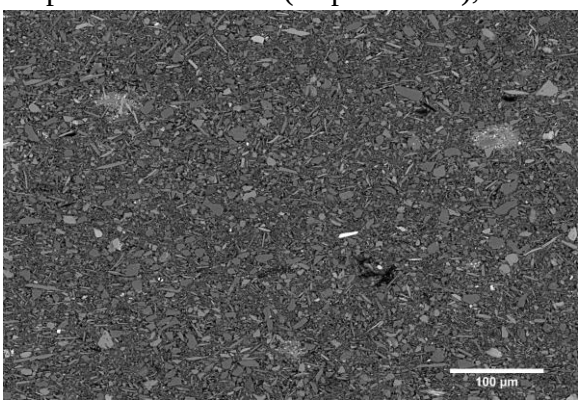

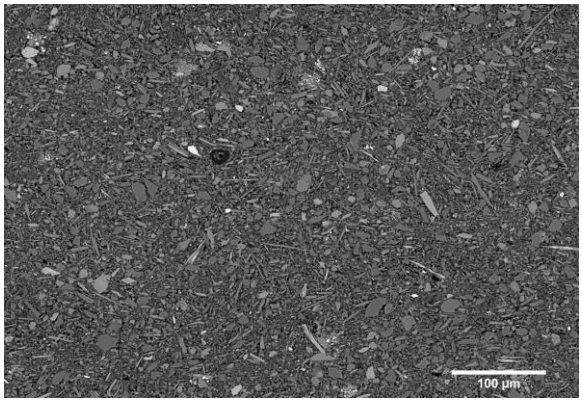

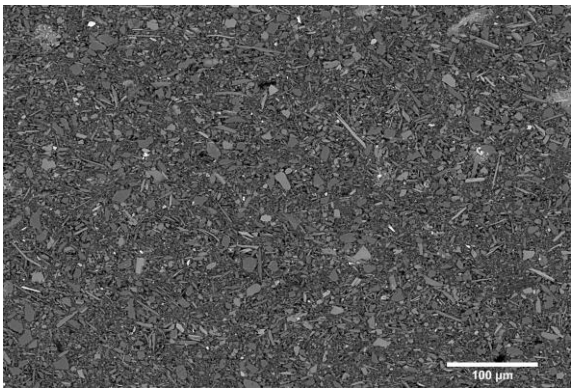

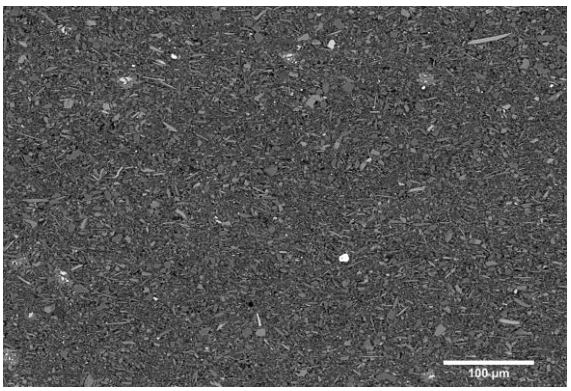

Sample 31- Turbidites (Depth 455 m), subset A-D

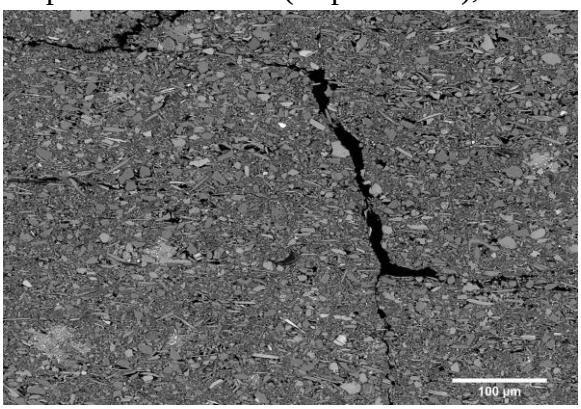

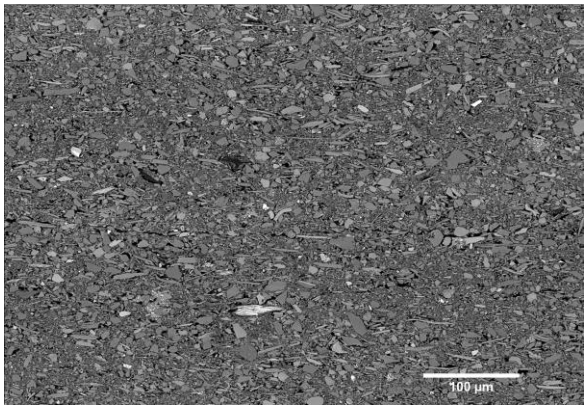

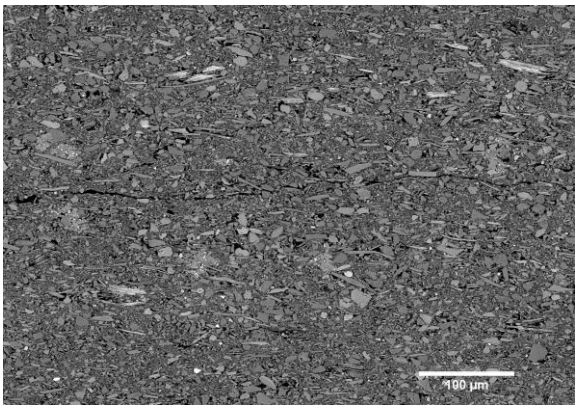

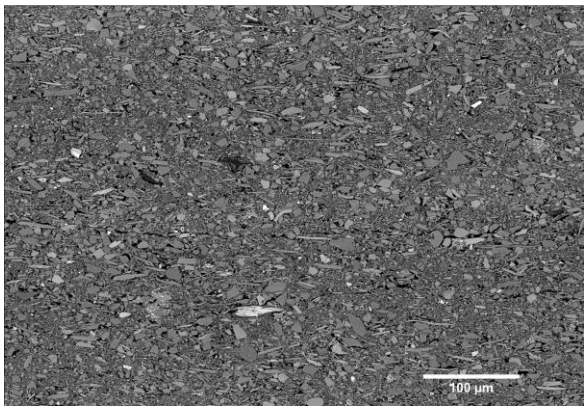

Sample 32- Turbidites (Depth 541 m), subset A-D

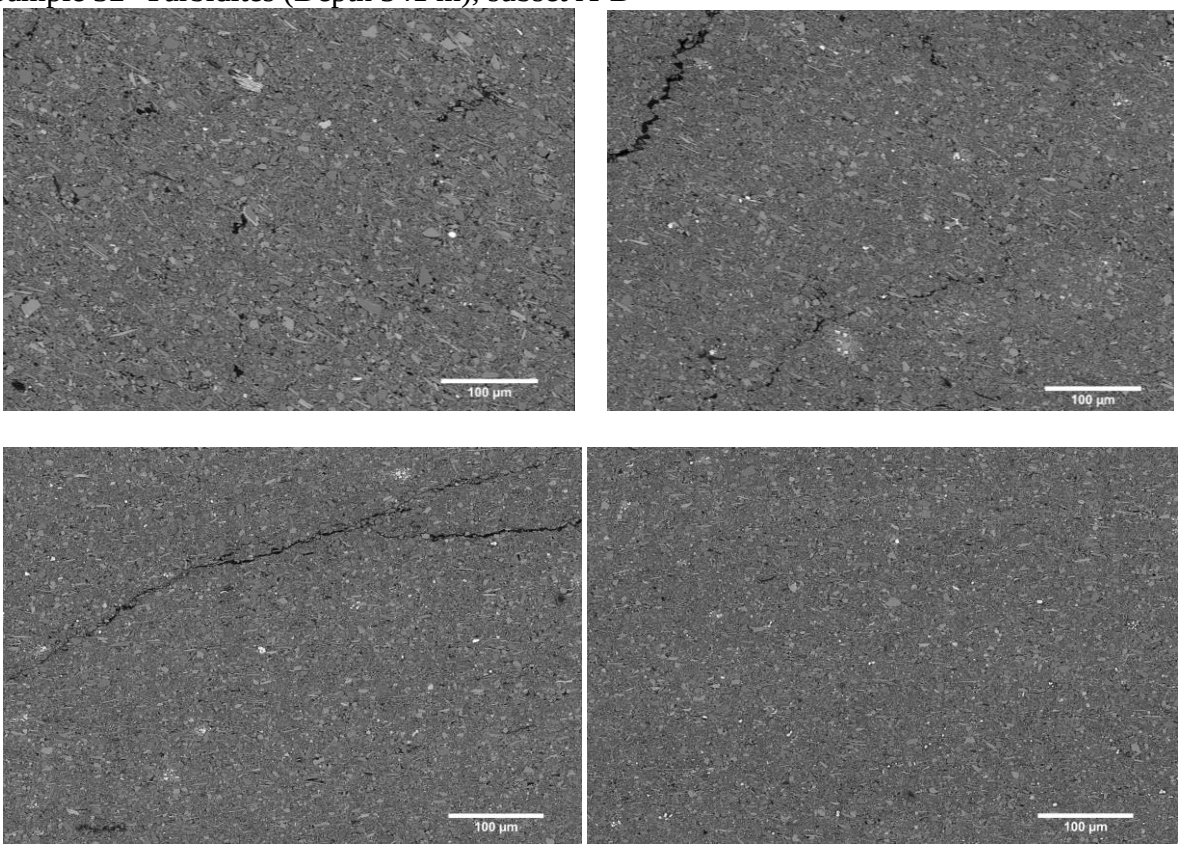

Sample 33- Turbidites (Depth 543 m), subset A-D

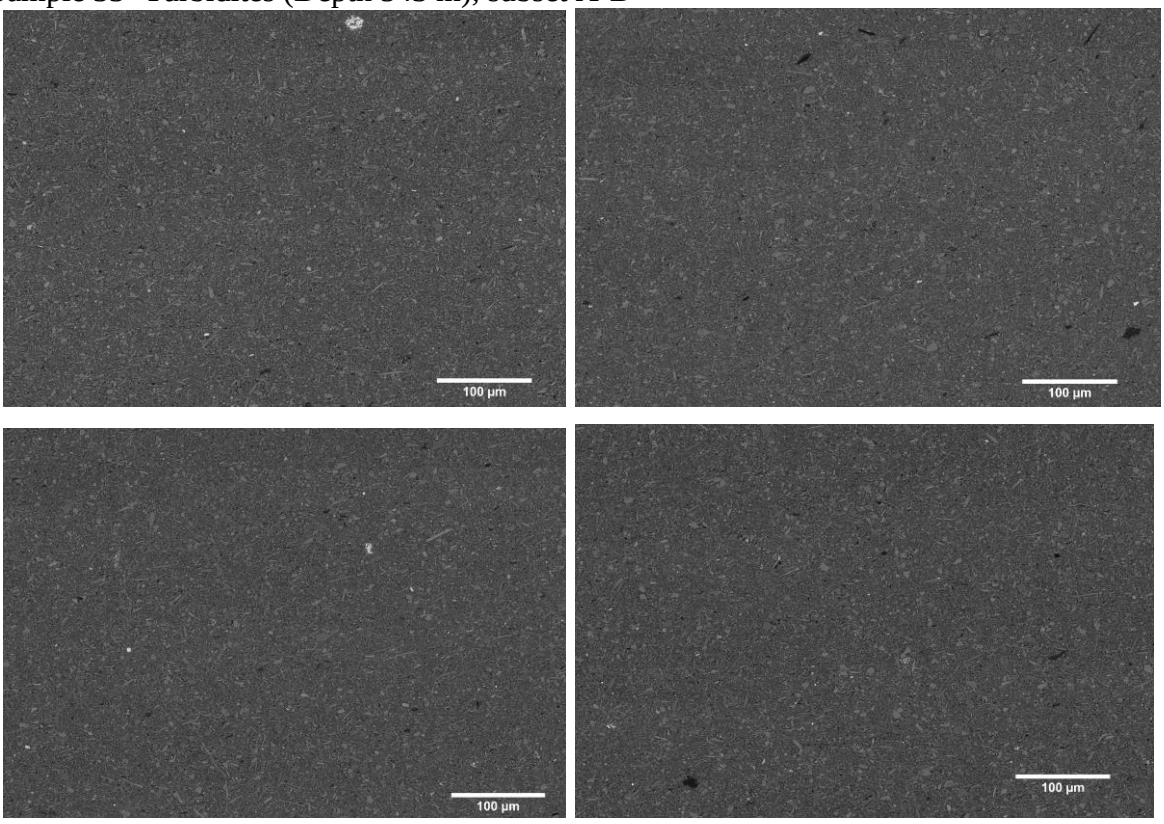

Sample 34- Turbidites (Depth 655 m), subset A-D

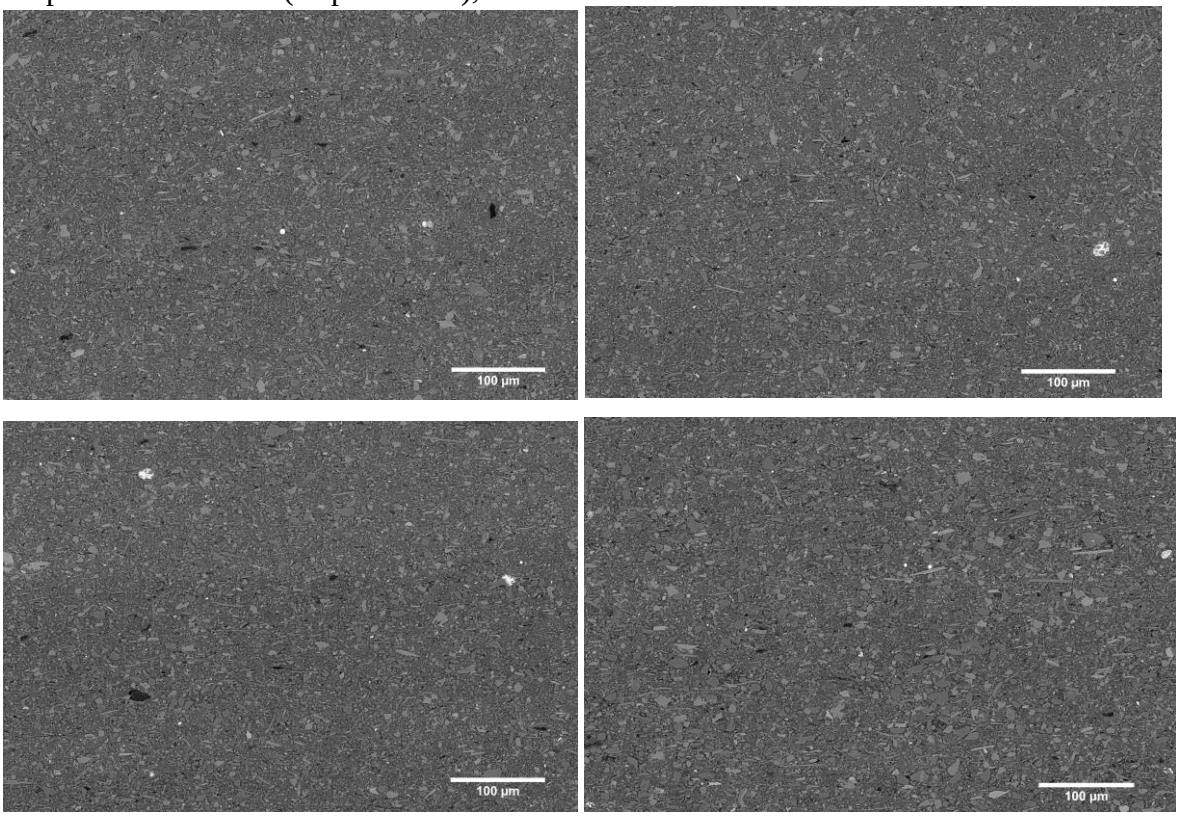

Sample 35- Turbidites (Depth 766 m), subset A-D

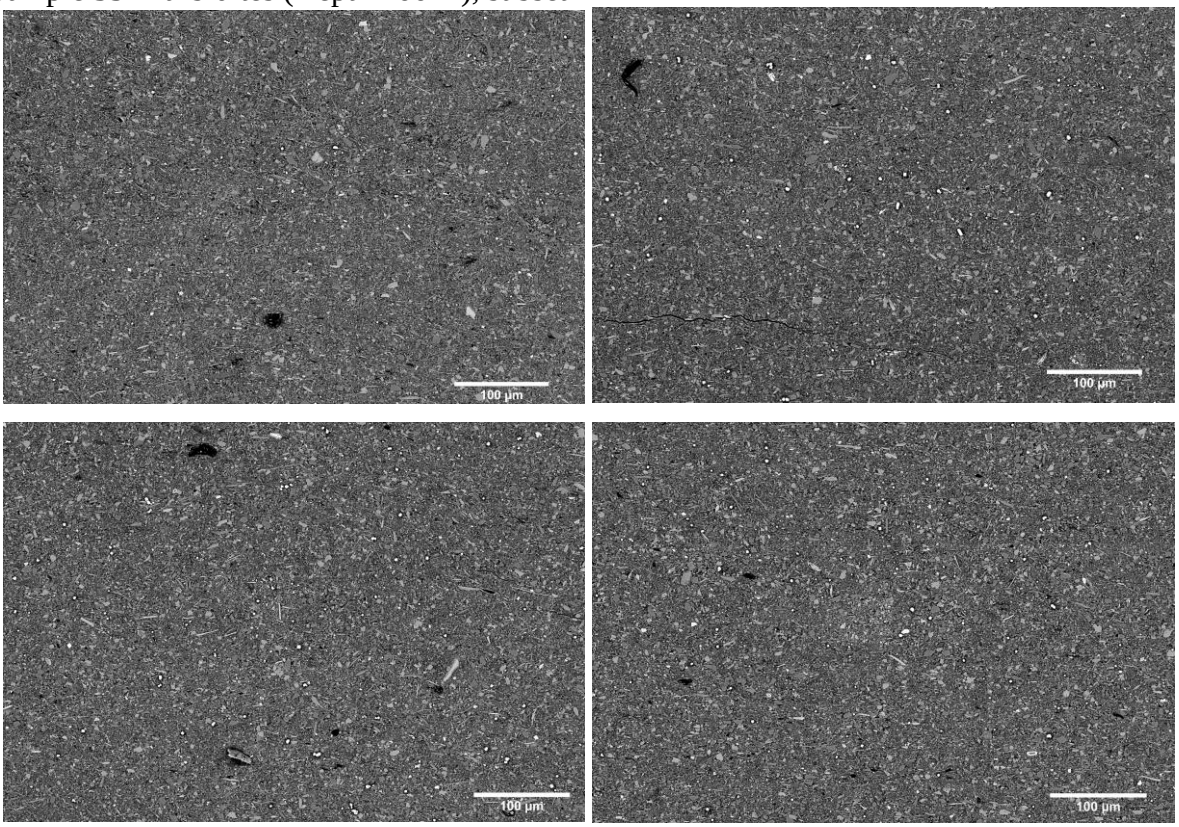

Sample 36- Turbidites (Depth 825 m), subset A-D

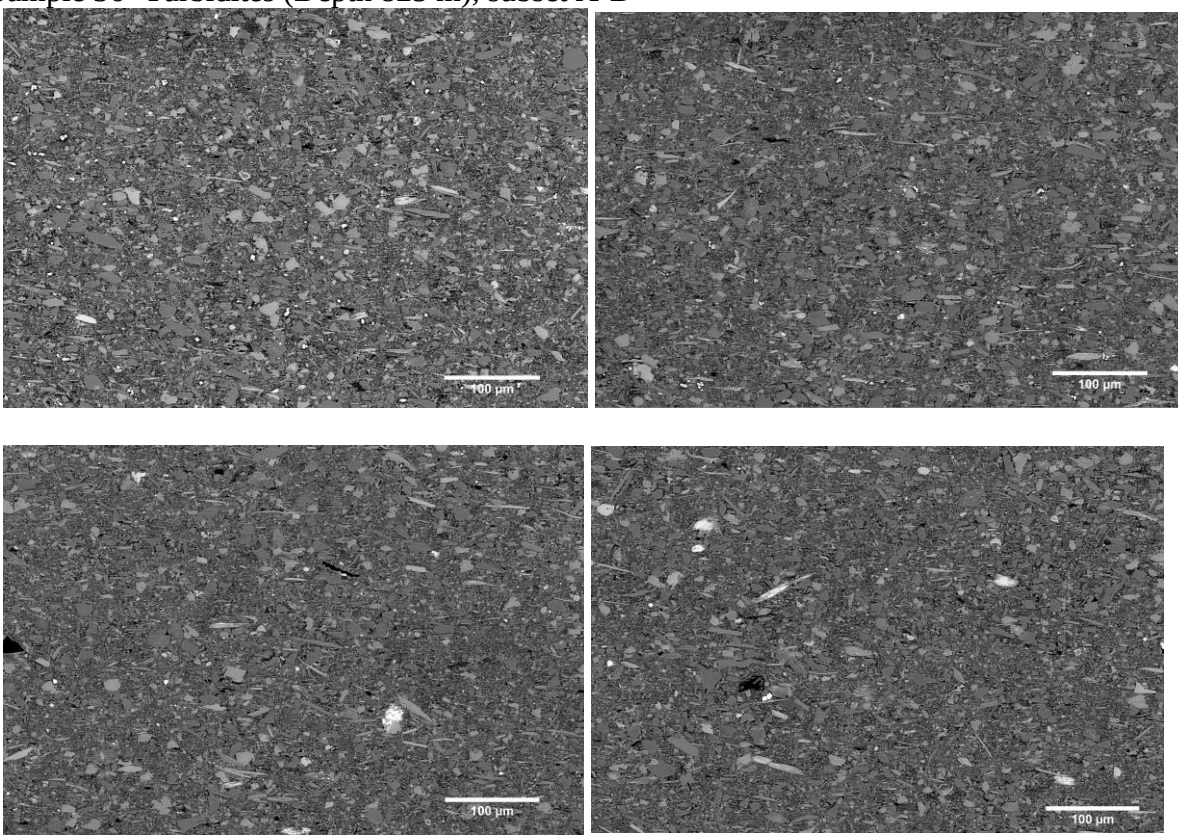

Sample 37- Turbidites (Depth 866 m), subset A-D

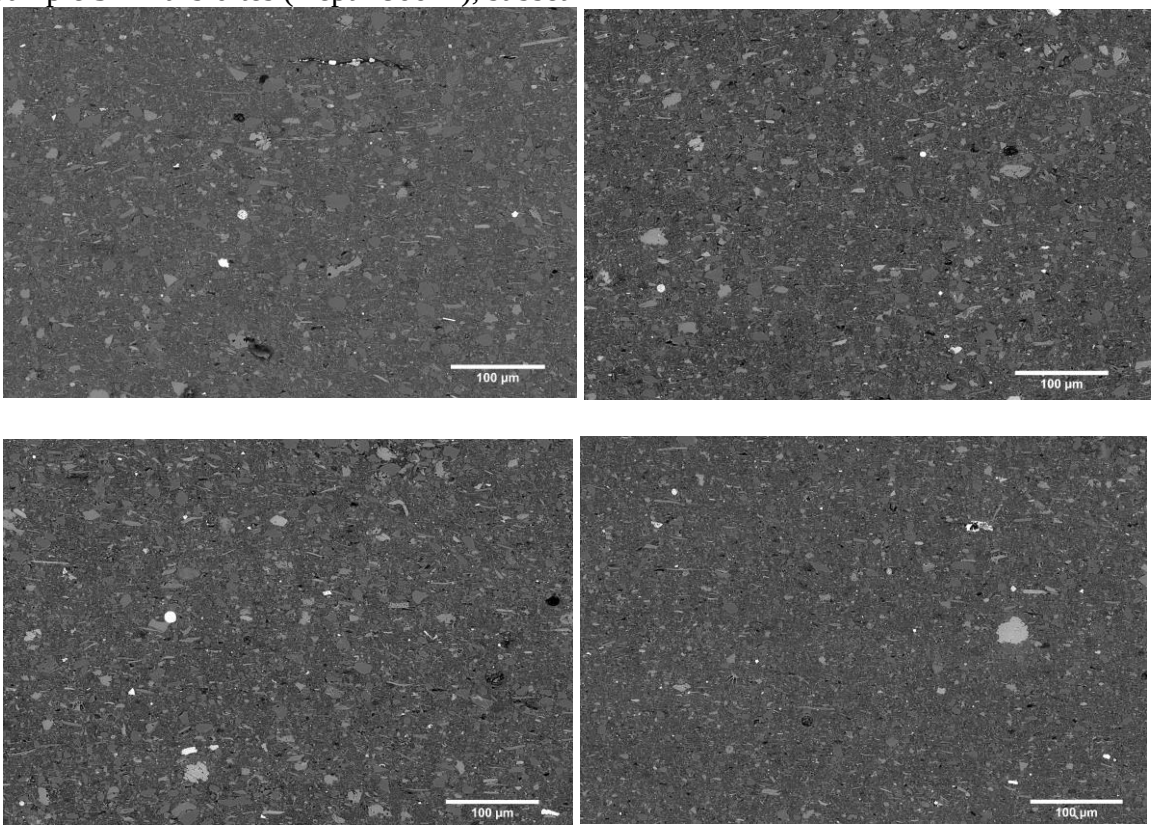

Sample 37- Turbidites (Depth 866 m), subset A-D

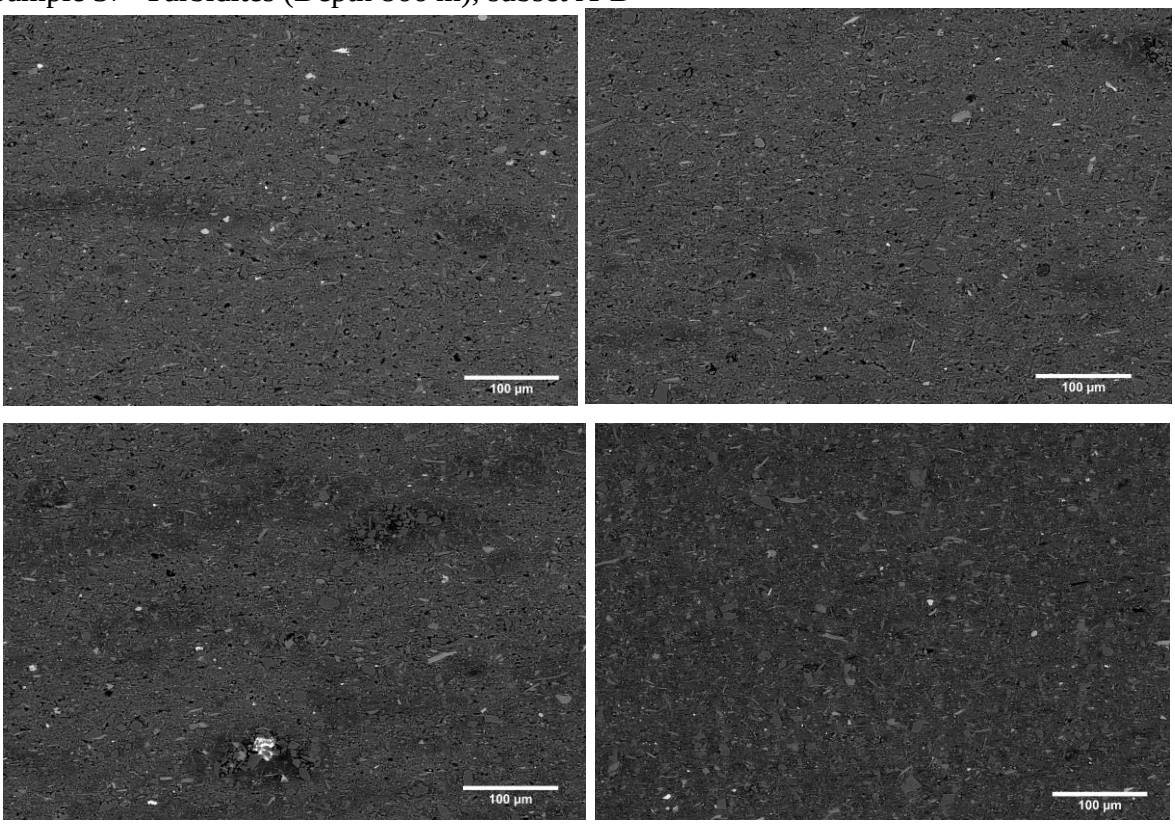

Appendix 3C

Circular statistical parameters

Sample 1. Contourite, depth: 9 m

ID	Cir. variance	STD	Dispersion	Std error	Cir kurtosis	Cir. skewness	Kappa	Entropy
1 (silt)	0.26	44.60°	4.93	0.05	-2.51	-0.10	0.62	2.79
1 (clay)	0.28	46.24°	6.16	0.02	0.57	0.01	2.37	2.81
2 (silt)	0.33	51.02°	11.46	0.08	-1.77	-0.19	0.42	2.85
2 (clay)	0.38	56.42°	22.90	0.05	-0.71	-0.15	0.29	2.86
3 (silt)	0.23	41.27°	3.52	0.04	-4.61	0.24	0.76	2.76
3 (clay)	0.28	46.93°	6.78	0.03	-2.32	0.03	0.54	2.82
4(silt)	0.22	40.47°	3.13	0.04	-4.63	-0.37	0.79	2.74
4 (clay)	0.28	46.37°	6.30	0.03	-2.42	-0.13	0.56	2.81

Sample 2. Contourite, depth: 10 m

ID	Cir. variance	STD	Dispersion	Std error	Cir kurtosis	Cir. skewness	Kappa	Entropy
1 (silt)	0.22	40.03°	3.17	0.03	-6.15	-0.45	0.81	2.74
1 (clay)	0.25	43.30°	4.48	0.02	-3.79	-0.17	0.67	2.78
2 (silt)	0.25	43.50°	4.54	0.05	-3.59	-0.22	0.67	2.78
2 (clay)	0.26	44.17°	4.78	0.02	-2.93	-0.09	0.64	2.79
3 (silt)	0.24	42.37°	3.98	0.04	-4.04	-0.16	0.71	2.77
3 (clay)	0.27	44.98°	5.30	0.02	-2.75	-0.07	0.61	2.80
4(silt)	0.25	43.77°	4.64	0.04	-3.32	-0.12	0.66	2.79
4 (clay)	0.27	45.60°	5.70	0.02	-2.55	-0.12	0.59	2.80

Sample 3. Contourite, depth: 14 m

ID	Cir. variance	STD	Dispersion	Std error	Cir kurtosis	Cir. skewness	Kappa	Entropy
1 (silt)	0.27	45.06°	5.66	0.06	-3.48	0.11	0.61	2.80
1 (clay)	0.34	52.34°	13.09	0.04	-1.28	0.29	0.38	2.85
2 (silt)	0.34	52.55°	13.54	0.12	-1.36	0.29	0.38	2.85
2 (clay)	0.33	51.75°	12.29	0.05	-1.29	0.15	0.40	2.85
3 (silt)	0.32	50.12°	9.55	0.09	-1.33	0.37	0.44	2.83
3 (clay)	0.31	49.62°	9.24	0.04	-1.59	0.24	0.46	2.83
4(silt)	0.32	50.25°	10.42	0.09	-1.79	-0.12	0.44	2.84
4 (clay)	0.38	56.36°	22.55	0.06	-0.96	0.25	0.29	2.86

Sample 4. Contourite, depth: 15 m

ID	Cir. variance	STD	Dispersion	Std error	Cir kurtosis	Cir. skewness	Kappa	Entropy
1 (silt)	0.28	46.48°	6.70	0.06	-3.22	0.22	0.56	2.81
1 (clay)	0.32	50.74°	11.23	0.03	-1.76	0.04	0.43	2.84
2 (silt)	0.27	44.99°	5.39	0.05	-3.10	0.33	0.61	2.83
2 (clay)	0.30	48.56°	8.55	0.03	-2.25	0.06	0.49	2.80
3 (silt)	0.27	45.70°	6.19	0.06	-3.55	0.16	0.58	2.83
3 (clay)	0.31	49.76°	9.53	0.03	0.30	0.30	0.45	2.83
4(silt)	0.22	40.54°	3.21	0.04	-4.78	0.08	0.79	2.81
4 (clay)	0.28	46.49°	6.44	0.03	-2.45	0.00	0.56	2.74

Sample 5. Contourite, depth: 16 m

ID	Cir. variance	STD	Dispersion	Std error	Cir kurtosis	Cir. skewness	Kappa	Entropy
1 (silt)	0.25	43.14°	4.63	0.04	-5.20	-0.34	0.68	2.78
1 (clay)	0.36	54.19°	17.14	0.03	-1.36	0.19	0.34	2.86
2 (silt)	0.28	46.61°	6.47	0.05	-2.58	0.37	0.55	2.81
2 (clay)	0.30	48.30°	7.81	0.02	-1.73	0.16	0.50	2.82
3 (silt)	0.26	44.92°	5.72	0.05	-4.40	0.11	0.61	2.80
3 (clay)	0.33	51.01°	11.02	0.02	-1.56	0.34	0.42	2.84
4(silt)	0.22	40.43°	3.14	0.03	-4.88	0.51	0.80	2.74
4 (clay)	0.27	45.71°	5.74	0.02	-2.46	0.19	0.58	2.80

Sample 6. Contourite, depth: 42 m

ID	Cir. variance	STD	Dispersion	Std error	Cir kurtosis	Cir. skewness	Kappa	Entropy
1 (silt)	0.39	56.93°	24.95	0.0947	-0.67	0.03	0.28	2.87
1 (clay)	0.48	65.17°	84.78	0.0622	-0.16	-0.02	0.15	2.88
2 (silt)	0.33	51.73°	12.9	0.0735	-1.83	0.03	0.4	2.85
2 (clay)	0.4	58.37°	30.6	0.0398	-0.55	-0.04	0.25	2.86
3 (silt)	0.36	54.03°	17.38	0.0845	-1.36	-0.03	0.34	2.86
3 (clay)	0.43	60.83°	43.6	0.0481	-0.35	0.03	0.21	2.87
4(silt)	0.36	53.93°	16.54	0.0802	-1	-0.06	0.34	2.87
4(clay)	0.48	65.43°	89.7	0.0663	-0.25	0.06	0.15	2.88
5(silt)	0.34	51.85°	12.38	0.0705	-1.16	0.04	0.4	2.85
5 (clay)	0.44	61.54°	48.67	0.0495	0.03	-0.33	0.2	2.86
6(silt)	0.26	44.24°	5.1	0.0452	-3.65	-0.03	0.64	2.794941
6 (clay)	0.36	53.99°	16.59	0.0293	-0.94	0	0.34	2.86

Sample 7. Contourite, depth: 151 m

ID	Cir. variance	STD	Dispersion	Std error	Cir kurtosis	Cir. skewness	Kappa	Entropy
1 (silt)	0.36	53.92°	16.10	0.14	-0.96	0.24	0.35	2.85
1 (clay)	0.39	56.66°	24.53	0.12	-0.07	-0.07	0.29	2.87
2 (silt)	0.32	50.70°	10.86	0.09	-1.50	-0.05	0.43	2.84
2 (clay)	0.41	58.46°	30.18	0.07	-1.00	0.18	0.25	2.87
3 (silt)	0.29	46.99°	7.28	0.09	-3.21	-0.08	0.54	2.83
3 (clay)	0.40	58.00°	27.71	0.10	-1.17	0.22	0.26	2.87
4(silt)	0.24	42.49°	4.15	0.05	-4.47	0.24	0.71	2.77
4 (clay)	0.35	52.99°	14.89	0.03	-1.65	-0.09	0.37	2.87
5(silt)	0.57	74.09°	396.71	0.47	-0.13	-0.02	0.07	2.88
5 (clay)	0.59	76.36°	584.85	0.23	-0.18	0.05	0.06	2.89

Sample 8. Contourite, depth: 253 m

ID	Cir. variance	STD	Dispersion	Std error	Cir kurtosis	Cir. skewness	Kappa	Entropy
1 (silt)	0.3	48.56°	8.56	0.0553	-2.25	0.02	0.49	2.83
1 (clay)	0.38	55.91°	22.22	0.026	-0.93	0	0.3	2.87
2 (silt)	0.35	53.53°	16.18	0.082	-1.32	0.05	0.35	2.87
2 (clay)	0.41	58.83°	33.63	0.0328	-0.71	-0.03	0.24	2.87
3 (silt)	0.28	45.99°	6.21	0.05	-2.89	-0.01	0.57	2.81
3 (clay)	0.44	62.00°	52.85	0.0376	-0.37	0.01	0.19	2.88
4(silt)	0.42	59.71°	37.57	0.1149	-0.51	0.01	0.23	2.87
4 (clay)	0.45	62.54°	56.91	0.0486	-0.55	-0.08	0.19	2.88

Sample 9. Contourite, depth: 343 m

ID	Cir. variance	STD	Dispersion	Std error	Cir kurtosis	Cir. skewness	Kappa	Entropy
1 (silt)	0.25	43.30°	4.57	0.0378	-4.08	0.05	0.67	2.78
1 (clay)	0.31	49.54°	9.71	0.025	-2.05	0.01	0.46	2.84
2 (silt)	0.29	47.46°	7.37	0.0483	-2.44	0.15	0.52	2.82
2 (clay)	0.36	53.72°	16.33	0.0318	1.16	0.07	0.35	2.85
3 (silt)	0.31	49.10°	8.99	0.0521	-1.95	0.01	0.47	2.85
3 (clay)	0.35	52.93°	14.63	0.0256	-1.22	0.07	0.37	2.84
4(silt)	0.32	49.88°	9.92	0.0598	-1.81	-0.1	0.45	2.84
4 (clay)	0.38	56.07°	22.7	0.0389	-0.92	-0.01	0.3	2.87

Sample 10. Contourite, depth: 510 m

ID	Cir. variance	STD	Dispersion	Std error	Cir kurtosis	Cir. skewness	Kappa	Entropy
1 (silt)	0.59	76.66°	635.94	0.5278	-0.05	-0.02	0.06	2.88
1 (clay)	0.61	78.84°	968.64	0.2116	-0.07	-0.01	0.05	2.88
2 (silt)	0.48	65.50°	91.86	0.2027	-0.28	0.03	0.15	2.88
2 (clay)	0.6	77.08°	685.21	0.1791	-0.12	-0.02	0.05	2.88
3 (silt)	0.54	71.43°	245.22	0.3304	-0.08	-0.02	0.09	2.88
3 (clay)	0.68	86.21°	4267.36	0.4631	-0.02	0	0.02	2.88
4(silt)	0.59	76.66°	635.94	0.5278	-0.05	-0.02	0.06	2.88
4 (clay)	0.61	78.84°	968.64	0.2116	-0.07	-0.01	0.05	2.88

Sample 11. Contourite, depth: 563 m

ID	Cir. variance	STD	Dispersion	Std error	Cir kurtosis	Cir. skewness	Kappa	Entropy
1 (silt)	0.24	42.34°	4.05	0.05	-4.39	-0.19	0.71	2.82
1 (clay)	0.33	51.68°	12.65	0.04	-1.55	0.02	0.40	2.85
2 (silt)	0.32	50.36°	10.13	0.09	-1.32	0.01	0.44	2.84
2 (clay)	0.37	54.87°	19.02	0.05	-0.98	-0.06	0.32	2.86
3 (silt)	0.37	54.88°	19.30	0.12	-1.17	0.07	0.32	2.86
3 (clay)	0.37	54.91°	19.34	0.05	-1.04	0.00	0.32	2.86
4(silt)	0.30	48.46°	8.24	0.08	-2.01	-0.06	0.49	2.83
4 (clay)	0.33	50.84°	11.24	0.04	-1.62	0.04	0.42	2.85

Sample 12. Contourite, depth: 653 m

ID	Cir. variance	STD	Dispersion	Std error	Cir kurtosis	Cir. skewness	Kappa	Entropy
1 (silt)	0.68	86.85°	4646.17	2.17	0.08	-0.04	0.02	2.88
1 (clay)	0.57	74.87°	452.64	0.26	-0.16	-0.02	0.07	2.89
2 (silt)	0.55	72.42°	284.42	0.49	-0.27	-0.05	0.08	2.88
2 (clay)	0.54	71.47°	243.37	0.21	-0.24	-0.06	0.09	2.89
3 (silt)	0.45	62.35°	56.31	0.22	-0.53	-0.01	0.19	2.88
3 (clay)	0.48	65.34°	90.24	0.13	-0.31	-0.02	0.15	2.88
4(silt)	0.50	67.25°	120.38	0.32	-0.30	0.07	0.13	2.87
4 (clay)	0.52	69.38°	175.82	0.17	-0.20	0.01	0.11	2.89

Sample 13. Contourite, depth: 734 m

ID	Cir. variance	STD	Dispersion	Std error	Cir kurtosis	Cir. skewness	Kappa	Entropy
1 (silt)	0.39	57.29°	26.27	0.0961	-0.69	-0.1	0.27	2.87
1 (clay)	0.49	66.31°	105.11	0.0505	-0.25	-0.01	0.14	2.88
2 (silt)	0.53	70.52°	206.87	0.2748	-0.07	-0.05	0.1	2.88
2 (clay)	0.57	74.82°	443.32	0.1427	0	-0.01	0.07	2.89
3 (silt)	0.54	71.20°	226.73	0.3389	-0.35	-0.04	0.09	2.88
3 (clay)	0.6	77.22°	701.36	0.2804	-0.04	0.03	0.05	2.89
4(silt)	0.45	62.84°	60.01	0.1664	-0.56	0.01	0.18	2.89
4 (clay)	0.58	75.48°	509.25	0.2318	-0.07	0.03	0.06	2.89
5(silt)	0.61	78.49°	880.5	0.6753	-0.15	0.02	0.05	2.89
5 (clay)	0.64	81.54°	1634.18	0.2538	-0.04	0.02	0.03	2.89

Sample 14. Contourite, depth: 763 m

ID	Cir. variance	STD	Dispersion	Std error	Cir kurtosis	Cir. skewness	Kappa	Entropy
1 (silt)	0.26	44.69°	5.36	0.06	-3.43	0.00	0.62	2.79
1 (clay)	0.32	50.73°	11.00	0.04	-1.57	0.03	0.43	2.85
2 (silt)	0.38	55.95°	21.53	0.14	-0.81	-0.17	0.30	2.87
2 (clay)	0.40	58.11°	30.17	0.08	-0.70	-0.01	0.26	2.86
3 (silt)	0.29	47.52°	7.28	0.07	-2.15	0.03	0.52	2.82
3 (clay)	0.31	49.62°	9.53	0.04	-1.75	-0.01	0.46	2.84
4(silt)	0.23	41.91°	3.83	0.05	-4.43	-0.03	0.73	2.77
4 (clay)	0.29	47.20°	7.09	0.03	-2.40	-0.11	0.53	2.83
5(silt)	0.22	40.24°	3.27	0.05	-5.89	-0.08	0.80	2.74
5 (clay)	0.31	49.33°	9.27	0.04	-1.92	0.02	0.47	2.84

Sample 15. Contourite, depth: 808 m

ID	Cir. variance	STD	Dispersion	Std error	Cir kurtosis	Cir. skewness	Kappa	Entropy
1 (silt)	0.31	49.46°	9.2	0.0605	-1.7	-0.15	0.46	2.83
1 (clay)	0.37	54.71°	18.86	0.033	-1.09	-0.04	0.33	2.86
2 (silt)	0.23	41.02°	3.49	0.0348	-5.11	-0.3	0.77	2.75
2 (clay)	0.3	48.70°	8.21	0.0218	-1.63	-0.01	0.49	2.83
3 (silt)	0.26	44.23°	5.07	0.0441	-3.66	-0.15	0.64	2.79
3 (clay)	0.34	52.14°	13.36	0.0275	-1.43	0.03	0.39	2.85
4(silt)	0.21	39.18°	2.85	0.0288	-6.26	-0.15	0.85	2.72
4 (clay)	0.32	50.04°	9.86	0.013	-1.49	-0.03	0.45	2.83
5(silt)	0.24	42.93°	4.32	0.0371	-4.06	0.14	0.69	2.77
5 (clay)	0.33	51.30°	11.58	0.0145	-1.27	-0.03	0.41	2.84

Sample 16. Contourite, depth: 860 m

ID	Cir. variance	STD	Dispersion	Std error	Cir kurtosis	Cir. skewness	Kappa	Entropy

1 (silt)	0.28	46.16°	6.18	0.0635	-2.57	-0.12	0.57	2.81
1 (clay)	0.32	50.41°	10.47	0.0313	-1.56	0.04	0.44	2.82
2 (silt)	0.26	44.37°	4.85	0.0469	-2.82	0.29	0.63	2.83
2 (clay)	0.25	43.33°	4.15	0.0129	-2.62	0.04	0.67	2.75
3 (silt)	0.24	42.22°	3.95	0.0373	-4.21	-0.02	0.72	2.76
3 (clay)	0.37	54.78°	19.05	0.0219	-1.14	-0.06	0.33	2.86
4(silt)	0.28	46.08°	6.32	0.0482	-2.96	0.06	0.57	2.81
4 (clay)	0.39	56.61°	24.71	0.0245	-0.95	-0.02	0.29	2.87

Sample 17. Contourite, depth: 943 m

ID	Cir. variance	STD	Dispersion	Std error	Cir kurtosis	Cir. skewness	Kappa	Entropy
1 (silt)	0.33	50.83°	11.05	0.0708	-1.48	-0.03	0.42	2.85
1 (clay)	0.46	63.69°	68.84	0.0519	-0.32	-0.02	0.17	2.88
2 (silt)	0.44	61.31°	47.86	0.1527	0.47	0.05	0.2	2.88
2 (clay)	0.53	70.01°	195.47	0.0987	-0.19	-0.01	0.1	2.89
3 (silt)	0.38	56.32°	22.98	0.1	-0.74	-0.02	0.29	2.87
3 (clay)	0.44	61.35°	48.55	0.0442	-0.51	0.04	0.2	2.89
4(silt)	0.5	67.58°	127.77	0.243	-0.32	0.03	0.12	2.88
4 (clay)	0.61	78.71°	940.93	0.1793	-0.07	0.02	0.05	2.89

Sample 18. Hemipelagite, depth: 8 m

ID	Cir. variance	STD	Dispersion	Std error	Cir kurtosis	Cir. skewness	Kappa	Entropy
1 (silt)	0.34	52.44°	13.46	0.0723	-1.12	0	0.38	2.850301
1 (clay)	0.43	61.16°	47.55	0.0442	-0.53	0.01	0.21	2.878526
2 (silt)	0.29	47.14°	7.22	0.0617	-2.69	-0.02	0.53	2.82
2 (clay)	0.43	60.37°	42.35	0.0407	-0.59	0	0.22	2.88
3 (silt)	0.48	65.86°	96.97	0.3094	-0.24	0.02	0.14	2.88
3 (clay)	0.6	77.42°	737.08	0.1831	-0.08	0.01	0.05	2.89
4(silt)	0.2	38.33°	2.63	0.0362	-7.17	-0.04	0.89	2.71
4 (clay)	0.32	50.62°	10.86	0.0222	-1.6	-0.03	0.43	2.85
5(silt)	0.32	50.18°	10.55	0.067	-2.01	0.08	0.44	2.84
5 (clay)	0.46	63.58°	68.5	0.0476	-0.38	0	0.17	2.88

Sample 19. Hemipelagite, depth: 10 m

ID	Cir. variance	STD	Dispersion	Std error	Cir kurtosis		Cir. skewness	Kappa	Entropy
1 (silt)	0.42	59.42°	35.76	0.1625	0.12		-0.64	0.23	2.67808802
1 (clay)	0.43	60.35°	42.08	0.1056	0.02		-0.6	0.22	2.677717601
2 (silt)	0.36	53.86°	16.42	0.1089	-0.1		-1.06	0.35	2.640115193
2 (clay)	0.39	57.29°	26.74	0.0769	0.04		-0.76	0.27	2.686395433
3 (silt)	0.35	53.51°	16.13	0.1058	-0.07		-1.4	0.36	2.64905582
3 (clay)	0.42	59.68°	37.46	0.0901	0.02		-0.52	0.23	2.68302784
4(silt)	0.38	56.31°	21.97	0.1162	-0.32		-0.86	0.29	2.67677533
4 (clay)	0.45	62.87°	59.22	0.1048	-0.1		-0.3	0.18	2.688119258
5(silt)	0.28	46.64°	6.77	0.0642	-0.05		-2.8	0.55	2.602869236
5 (clay)	0.35	53.28°	15.01	0.0591	-0.02		-0.99	0.36	2.651830491
6(silt)	0.26	44.87°	5.6	0.0633	-0.16		-3.79	0.61	2.653100133
6(clay)	0.37	54.91°	19.51	0.0669	0.04		-1.15	0.32	2.710439151

Sample 20. Hemipelagite, depth: 15 m

ID	Cir. variance	STD	Dispersion	Std error	Cir kurtosis	Cir. skewness	Kappa	Entropy
1 (silt)	0.32	50.45°	10.45	0.0857	-0.17	-1.57	0.43	2.68
1 (clay)	0.43	61.21°	47.87	0.0941	0.01	-0.54	0.21	2.70
2 (silt)	0.29	47.73°	7.8	0.0798	-0.02	-2.59	0.52	2.63
2 (clay)	0.36	54.14°	17.4	0.0691	0.1	-1.3	0.34	2.69
3 (silt)	0.36	53.76°	16.55	0.11	-0.09	-1.44	0.35	2.68
3 (clay)	0.41	58.41°	31.23	0.0771	0.08	-0.71	0.25	2.69
4(silt)	0.26	44.55°	5.12	0.0575	-0.1	-3.11	0.63	2.65
4 (clay)	0.33	50.97°	11.62	0.0482	-0.01	-2.1	0.42	2.68
5(silt)	0.44	61.55°	48.98	0.1855	0.08	-0.42	0.2	2.70
5 (clay)	0.47	64.68°	80.87	0.1261	0.01	-0.3	0.16	2.71
6(silt)	0.49	66.46°	107.42	0.2652	0.03	-0.31	0.14	2.71
6(clay)	0.53	70.16°	196.45	0.1872	0.06	-0.21	0.1	2.72

Sample 21. Hemipelagite, depth: 50 m

ID	Cir. variance	STD	Dispersion	Std error	Cir kurtosis	Cir. skewness	Kappa	Entropy
1 (silt)	0.29	46.96°	7.11	0.0765	-0.19	-3.05	0.54	2.81
1 (clay)	0.34	52.47°	13.84	0.0425	-0.05	-1.32	0.38	2.86
2 (silt)	0.36	53.87°	16.09	0.0892	0.07	-0.86	0.35	2.85
2 (clay)	0.35	53.51°	15.99	0.0461	-0.02	-1.21	0.35	2.86
3 (silt)	0.41	58.78°	31.99	0.1662	-0.07	-0.46	0.25	2.87
3 (clay)	0.39	56.73°	24.35	0.0735	-0.03	-0.71	0.28	2.87
4(silt)	0.44	61.53°	49.54	0.179	-0.06	-0.51	0.2	2.88
4 (clay)	0.42	60.20°	40.77	0.0753	0.04	-0.57	0.22	2.88
5(silt)	0.4	57.68°	27.47	0.1292	0.07	-0.57	0.27	2.87
5 (clay)	0.41	58.59°	31.49	0.068	0	-0.51	0.25	2.87
6(silt)	0.27	45.60°	6	0.0581	0.17	-3.27	0.59	2.81
6(clay)	0.3	48.02°	7.86	0.0307	0.1	-2.23	0.51	2.82

Sample 22. Hemipelagite, depth: 57 m

ID	Cir. variance	STD	Dispersion	Std error	Cir kurtosis	Cir. skewness	Kappa	Entropy
1 (silt)	0.41	59.09°	34.57	0.1192	-0.59	-0.02	0.24	2.87
1 (clay)	0.46	63.18°	62.65	0.0355	-0.54	0.07	0.18	2.87
2 (silt)	0.54	71.88°	267.98	0.3378	-0.14	-0.03	0.09	2.89
2 (clay)	0.59	76.22°	587.19	0.1004	-0.09	-0.02	0.06	2.89
3 (silt)	0.2	38.68°	2.69	0.038	-6.65	-0.39	0.88	2.73
3 (clay)	0.37	54.95°	19.33	0.0186	-0.99	0.01	0.32	2.86
4(silt)	0.23	41.39°	3.6	0.0452	-4.65	0.02	0.75	2.75
4 (clay)	0.39	57.11°	26.46	0.0241	-0.87	0.02	0.28	2.87
5(silt)	0.21	39.60°	2.98	0.0545	-5.93	-0.17	0.83	2.73
5 (clay)	0.35	53.44°	15.75	0.0238	-1.2	-0.07	0.36	2.85

Sample 223 Hemipelagite, depth: 60 m

ID	Cir. variance	STD	Dispersion	Std error	Cir kurtosis	Cir. skewness	Kappa	Entropy
1 (silt)	0.45	63.02°	61.4	0.2129	0.07	-0.52	0.18	2.71
1 (clay)	0.46	63.58°	68.22	0.106	0.01	-0.36	0.17	2.69
2 (silt)	0.46	64.03°	72.11	0.2134	-0.07	-0.42	0.17	2.71
2 (clay)	0.45	62.84°	59.31	0.1014	0.11	-0.37	0.18	2.69
3 (silt)	0.57	74.51°	427.21	0.5055	-0.02	-0.07	0.07	2.73
3 (clay)	0.55	72.65°	302.43	0.2401	-0.01	-0.21	0.08	2.71
4(silt)	0.49	66.53°	104.88	0.3057	-0.03	-0.47	0.14	2.72
4 (clay)	0.48	65.73°	93.09	0.1759	-0.04	-0.17	0.14	2.70
5(silt)	0.4	58.24°	30.78	0.144	-0.05	-0.78	0.26	2.69
5 (clay)	0.44	61.78°	51.99	0.0928	0.02	-0.49	0.2	2.69
6(silt)	0.28	46.61°	6.97	0.0662	-0.04	-3.22	0.55	2.62
6(clay)	0.34	52.05°	13.53	0.0475	-0.01	-1.66	0.39	2.67

Sample 24 Hemipelagite, depth: 80 m

ID	Cir. variance	STD	Dispersion	Std error	Cir kurtosis	Cir. skewness	Kappa	Entropy
1 (silt)	0.23	41.08°	3.57	0.0433	0.04	-5.27	0.77	2.54
1 (clay)	0.27	45.51°	5.9	0.0359	-0.08	-3.13	0.59	2.59
2 (silt)	0.25	43.89°	4.96	0.0528	-0.02	-4	0.65	2.57
2 (clay)	0.33	51.69°	12.51	0.0505	-0.13	-1.53	0.4	2.63
3 (silt)	0.32	50.56°	11.02	0.0734	0.02	-1.82	0.43	2.67
3 (clay)	0.35	52.82°	14.73	0.0516	-0.07	-1.59	0.37	2.67
4(silt)	0.24	42.37°	4.13	0.0639	0.48	-5.04	0.71	2.56
4 (clay)	0.3	48.00°	7.9	0.0498	-0.08	-2.3	0.51	2.61
5(silt)	0.33	51.35°	12.07	0.0819	0.06	-1.59	0.41	2.61
5 (clay)	0.37	54.61°	18.19	0.0579	0	-0.93	0.33	2.67
6(silt)	0.18	36.42°	2.11	0.0367	0.04	-8.52	0.99	2.45
6(clay)	0.22	40.15°	3.23	0.027	-0.05	-5.9	0.81	2.51

Sample 25 Hemipelagite, depth: 117 m

ID	Cir. variance	STD	Dispersion	Std error	Cir kurtosis	Cir. skewness	Kappa	Entropy
1 (silt)	0.37	54.68°	18.37	0.0699	-0.98	-0.1	0.33	2.86
1 (clay)	0.42	60.09°	39.57	0.0287	-0.49	-0.05	0.22	2.87
2 (silt)	0.26	44.83°	5.41	0.0396	-3.33	0.12	0.62	2.80
2 (clay)	0.38	55.73°	21.5	0.0226	-0.95	0.07	0.3	2.86
3 (silt)	0.3	48.81°	8.86	0.0517	-2.29	0.11	0.48	2.83
3 (clay)	0.42	59.59°	37.62	0.0285	-0.65	0.02	0.23	2.87
4(silt)	0.32	49.93°	9.82	0.0562	-1.61	0.05	0.45	2.84
4 (clay)	0.39	56.64°	24.28	0.0223	-0.78	-0.02	0.29	2.86

Sample 26 Turbidite, depth: 66 m

ID	Cir. variance	STD	Dispersion	Std error	Cir kurtosis	Cir. skewness	Kappa	
1 (silt)	0.16	34.21°	1.73	0.04	-12.12	0.34	1.12	2.63
1 (clay)	0.29	47.29°	7.10	0.03	-2.46	-0.31	0.53	2.82
2 (silt)	0.19	36.74°	2.32	0.05	-9.68	-0.04	0.98	2.68
2 (clay)	0.30	48.07°	8.14	0.03	-2.64	-0.14	0.50	2.83
3 (silt)	0.17	34.48°	1.77	0.04	-11.75	-0.70	1.11	2.63
3 (clay)	0.28	46.73°	6.76	0.03	-2.74	-0.21	0.55	2.82
4(silt)	0.17	35.27°	1.97	0.04	-11.13	0.02	1.06	2.65
4 (clay)	0.30	48.02°	7.63	0.03	-1.88	0.04	0.51	2.82

Sample 27 Turbidite, depth: 68 m

ID	Cir. variance	STD	Dispersion	Std error	Cir kurtosis	Cir. skewness	Kappa	Entropy
1 (silt)	0.15	32.12°	1.37	0.03	-14.79	0.25	1.26	2.58
1 (clay)	0.22	40.15°	3.12	0.01	-5.28	-0.08	0.81	2.74
2 (silt)	0.12	28.80°	0.98	0.02	-22.29	0.31	1.52	2.47
2 (clay)	0.19	37.69°	2.40	0.02	-7.16	-0.11	0.93	2.70
3 (silt)	0.18	36.28°	2.14	0.04	9.41	-0.16	1.00	2.68
3 (clay)	0.24	1.96°	3.80	0.02	-4.19	-0.12	0.73	2.77
4(silt)	0.15	32.66°	1.51	0.03	-15.41	-0.38	1.22	2.60
4 (clay)	0.23	41.33°	3.59	0.02	-4.75	0.02	0.75	2.76
5(silt)	0.16	34.00°	1.66	0.04	-11.82	0.17	1.13	2.62
5 (clay)	0.22	40.33°	3.27	0.04	-5.68	-0.14	0.80	2.75

Sample 28 Turbidite, depth: 132 m

ID	Cir. variance	STD	Dispersion	Std error	Cir kurtosis	Cir. skewness	Kappa	Entropy

1 (silt)	0.11	27.37°	0.86	0.02	-28.18	-0.35	1.65	2.43
1 (clay)	0.17	35.52°	1.94	0.02	-9.72	0.01	1.05	2.66
2 (silt)	0.12	28.73°	1.01	0.02	-24.41	0.46	1.53	2.48
2 (clay)	0.19	36.75°	2.22	0.02	-8.57	0.07	0.98	2.69
3 (silt)	0.10	26.79°	0.85	0.02	-33.44	-0.05	1.71	2.42
3 (clay)	0.17	34.96°	1.85	0.02	-10.72	0.30	1.08	2.65
4(silt)	0.22	40.08°	3.18	0.04	-5.79	0.06	0.81	2.74
4 (clay)	0.29	47.12°	7.17	0.04	-2.63	-0.02	0.54	2.82

Sample 29 Turbidite, depth: 260 m

ID	Cir. variance	STD	Dispersion	Std error	Cir kurtosis	Cir. skewness	Kappa	Entropy
1 (silt)	0.28	46.34°	6.54	0.0397	-2.92	-0.08	0.56	2.81
1 (clay)	0.42	59.54°	36.11	0.0436	-0.46	-0.06	0.23	2.82
2 (silt)	0.27	45.29°	5.68	0.0362	3.05	0	0.6	2.80
2 (clay)	0.36	54.51°	17.63	0.0303	-0.81	0.01	0.33	2.85
3 (silt)	0.15	32.13°	1.37	0.0183	-14.72	0.05	1.26	2.57
3 (clay)	0.28	46.64°	6.47	0.0193	-2.25	0.01	0.55	2.81
4(silt)	0.18	36.02°	1.99	0.0219	-8.44	-0.05	1.02	2.66
4 (clay)	0.3	48.31°	7.96	0.0215	-1.87	-0.02	0.5	2.82

Sample 30 Turbidite, depth: 348 m

ID	Cir. variance	STD	Dispersion	Std error	Cir kurtosis	Cir. skewness	Kappa	Entropy
1 (silt)	0.27	45.44°	5.86	0.0401	-3.18	0	0.59	2.80
1 (clay)	0.34	52.48°	13.52	0.0334	-1.1	-0.01	0.38	2.85
2 (silt)	0.3	48.02°	7.98	0.0487	-2.37	-0.07	0.51	2.82
2 (clay)	0.37	55.47°	20.32	0.0425	-0.81	0.07	0.31	2.86
3 (silt)	0.28	46.63°	6.74	0.0444	-2.76	-0.03	0.55	2.81
3 (clay)	0.36	53.75°	16.19	0.0388	-1.03	0.01	0.35	2.82
4(silt)	0.28	46.44°	6.61	0.044	-2.86	-0.05	0.56	2.81
4 (clay)	0.36	54.05°	16.8	0.0399	-0.97	0	0.34	2.85

Sample 31 Turbidite, depth: 455 m

ID	Cir. variance	STD	Dispersion	Std error	Cir kurtosis	Cir. skewness	Kappa	Entropy
1 (silt)	0.17	34.90°	1.78	0.0225	-9.98	-0.23	1.08	2.6
1 (clay)	0.29	47.77°	7.5	0.0236	-2.08	-0.03	0.51	2.82
2 (silt)	0.17	34.47°	1.69	0.0221	-10.14	-0.11	1.11	2.63
2 (clay)	0.29	47.13°	6.87	0.0227	-2.17	0.13	0.54	2.81
3 (silt)	0.17	34.81°	1.74	0.0226	-9.67	-0.01	1.09	2.64
3 (clay)	0.28	46.87°	6.63	0.0226	-2.15	0	0.54	2.81
4(silt)	0.17	35.28°	1.82	0.0234	-8.95	-0.14	1.06	2.64
4 (clay)	0.3	48.45°	8.16	0.0266	-1.91	0.01	0.50	2.83

Sample 32 Turbidite, depth: 541 m

ID	Cir. variance	STD	Dispersion	Std error	Cir kurtosis	Cir. skewness	Kappa	Entropy
1 (silt)	0.18	35.89°	1.99	0.0228	-9.02	-0.01	1.02	2.66
1 (clay)	0.29	47.16°	6.88	0.0197	-2.17	-0.19	0.53	2.82
2 (silt)	0.17	35.38°	1.86	0.0219	-9.26	0.31	1.05	1.05
2 (clay)	0.28	46.79°	6.62	0.0189	-2.34	-0.22	0.55	2.81
3 (silt)	0.19	37.58°	2.35	0.0244	-7.08	-0.1	0.93	2.69
3 (clay)	0.29	47.29°	7.14	0.0188	-2.31	0.01	0.53	2.82
4(silt)	0.19	37.02°	2.13	0.0228	-6.63	-0.11	0.96	2.68
4 (clay)	0.29	47.64°	7.46	0.0192	-2.23	-0.05	0.52	2.82

Sample 33 Turbidite, depth: 543 m

ID	Cir. variance	STD	Dispersion	Std error	Cir kurtosis	Cir. skewness	Kappa	Entropy
1 (silt)	0.26	44.01°	4.94	0.0354	-3.67	-0.04	0.65	2.79
1 (clay)	0.34	52.49°	13.77	0.0245	-1.25	0.02	0.38	2.85
2 (silt)	0.26	44.11°	4.87	0.0359	-3.28	0.02	0.64	2.79
2 (clay)	0.35	53.52°	15.67	0.0268	-1.04	0	0.35	2.85
3 (silt)	0.27	45.74°	5.83	0.0375	-2.57	-0.06	0.58	2.81
3 (clay)	0.34	52.39°	13.71	0.0243	-1.34	-0.02	0.38	2.82
4(silt)	0.27	45.70°	5.86	0.0373	-2.71	-0.09	0.58	2.80
4 (clay)	0.34	52.41°	13.56	0.0223	-1.22	-0.01	0.38	2.85

Sample 34 Turbidite, depth: 655 m

ID	Cir. variance	STD	Dispersion	Std error	Cir kurtosis	Cir. skewness	Kappa	Entropy
1 (silt)	0.26	44.29°	4.92	0.0356	-3.09	-0.1	0.64	2.79
1 (clay)	0.35	53.25°	14.48	0.0275	-0.76	-0.08	0.36	2.84
2 (silt)	0.27	45.16°	5.48	0.0375	-2.82	-0.03	0.6	2.80
2 (clay)	0.37	55.07°	19.05	0.03	-0.77	-0.01	0.32	2.86
3 (silt)	0.23	41.59°	3.59	0.031	-4.14	0.1	0.74	2.76
3 (clay)	0.35	53.17°	14.6	0.0288	-0.9	0	0.36	2.85
4(silt)	0.2	38.34°	2.53	0.0265	-6.28	-0.19	0.89	2.70
4 (clay)	0.32	50.09°	9.89	0.0252	-1.47	-0.06	0.44	2.81

Sample 35 Turbidite, depth: 766 m

ID	Cir. variance	STD	Dispersion	Std error	Cir kurtosis	Cir. skewness	Kappa	Entropy
1 (silt)	0.32	50.15°	9.86	0.0493	-1.34	0.01	0.44	2.83
1 (clay)	0.37	54.92°	19.06	0.0278	-0.93	-0.03	0.32	2.86
2 (silt)	0.34	52.05°	12.83	0.0577	-1.23	0.11	0.39	2.82
2 (clay)	0.39	56.56°	24.01	0.0314	-0.8	0.04	0.29	2.86
3 (silt)	0.36	54.13°	17.05	0.0661	-0.99	-0.04	0.34	2.85
3 (clay)	0.39	56.57°	24.13	0.032	-0.81	0	0.29	2.86
4(silt)	0.28	46.39°	6.34	0.0405	-2.44	0.06	0.56	2.81
4 (clay)	0.35	53.27°	15.33	0.0246	-1.16	-0.01	0.36	2.82

Sample 36 Turbidite, depth: 825 m

ID	Cir. variance	STD	Dispersion	Std error	Cir kurtosis	Cir. skewness	Kappa	Entropy
1 (silt)	0.12	28.86°	0.98	0.02	-22.09	-0.23	1.52	2.47
1 (clay)	0.17	35.47°	1.90	0.02	-9.40	0.01	1.05	2.66
2 (silt)	0.12	29.52°	1.06	0.03	-20.83	-0.10	1.46	2.50
2 (clay)	0.19	36.81°	2.33	0.02	-9.53	-0.11	0.97	2.69
3 (silt)	0.12	29.26°	1.01	0.02	-20.45	0.29	1.48	2.49
3 (clay)	0.16	34.20°	1.66	0.02	-10.82	0.10	1.12	2.63
4(silt)	0.11	28.20°	0.94	0.02	-25.03	0.12	1.58	2.46
4 (clay)	0.15	33.12°	1.51	0.02	-12.89	0.10	1.19	2.60

Sample 37 Turbidite, depth: 866 m

ID	Cir. variance	STD	Dispersion	Std error	Cir kurtosis	Cir. skewness	Kappa	Entropy
1 (silt)	0.12	29.18°	1.02	0.02	-21.54	0.41	1.49	2.49
1 (clay)	0.16	34.09°	1.62	0.01	-10.68	0.05	1.13	2.63
2 (silt)	0.09	5.12°	0.65	0.02	-33.78	0.01	1.89	2.33
2 (clay)	0.15	33.00°	1.46	0.01	-12.48	-0.11	1.20	2.60
3 (silt)	0.12	28.38°	0.98	0.02	-25.93	0.54	1.56	2.47
3 (clay)	0.17	34.60°	1.71	0.01	-10.02	0.14	1.10	2.64
4(silt)	0.06	20.85°	0.41	0.02	-60.64	-1.16	2.51	2.11
4 (clay)	0.11	27.56°	0.84	0.01	-24.65	0.23	1.64	2.43

Sample 38 Turbidite, depth: 985 m

ID	Cir. variance	STD	Dispersion	Std error	Cir kurtosis	Cir. skewness	Kappa	Entropy
1 (silt)	0.09	24.31°	0.59	0.03	-37.30	0.17	1.99	2.30
1 (clay)	0.11	27.59°	0.80	0.01	-22.06	0.02	1.63	2.42
2 (silt)	0.09	25.40°	0.63	0.02	-28.95	-1.41	1.86	2.33
2 (clay)	0.11	27.94°	0.85	0.01	-22.47	-0.92	1.60	2.43
3 (silt)	0.07	22.43°	0.49	0.03	-48.70	-0.86	2.25	2.18
3 (clay)	0.10	26.27°	0.71	0.01	-27.39	-0.17	1.77	2.37
4(silt)	0.09	24.94°	0.65	0.02	-36.38	-0.57	1.91	2.32
4 (clay)	0.10	26.28°	0.73	0.01	-28.85	0.01	1.76	2.38

List of Publications

Peer Reviewed Journals

1. Buckman, J., Bankole, S., Zihms, S., Lewis, H., Couples, G. and Corbett, P. (2017) 'Quantifying Porosity through Automated Image Collection and Batch Image Processing: Case Study of Three Carbonates and an Aragonite Cemented Sandstone', *Geosciences*, 7(3), pp. 1-19.
2. Bankole, S.A., Buckman, J., Stow, D. and Lever, H. (2018) 'Grain-size Analysis of mudrocks: A New Semi-Automated Method from SEM Images', *Journal of Petroleum Science and Engineering.* (in press).
3. Bankole, S.A., Buckman, J., Stow, D., Lever, H. (2018) 'Automated Image Analysis of Mud and Mudrock Microstructure and Characteristics of Hemipelagic Sediments: IODP Expedition 339', *Journal of Earth Science. (*in press).
4. Buckman, J., Mahoney, C., Bankole, S., Couples, G., Lewis, H., Wagner, T., März, C., Blanco, V., Stow, D. and Ruffell, A. (2018) 'Workflow model for the digitization of mudrocks', *Geological society London, Special Publications*. *(*in press).

Conference Proceeding Papers

Bankole, S., Stow, D., Lever, H. and Buckman, J. (2016) 'Microstructure of Mudrock and the Choice of Representative Sample' *Fifth EAGE Shale Workshop*. Catania, Italy. EAGE. (Poster Presentation).

Buckman, J.; Mahoney, C.; Bankole, S.; Nazari-Moghaddam, R.; Couples, G.; Lewis, H.; Wagner, T.; Marz, C.; Blanco, V.; Stow, D.; Jamiolahmady, M.; Ruffel, A. (2017) 'Workflow Model for the Digitization of Shale Rocks' Application of Analytical Techniques to Petroleum System Problems. In Proceedings of the Application of Analytical Techniques to Petroleum Systems Problems, London, UK (Oral Presentation).

Bankole, S.A., Buckman, J., Stow, D. (2018). Maximizing Information on Mudrock Microstructure through High-resolution Scanning electron Microscopy' Digital Imaging of Multi-scale Porous Materials, and Image-Based Simulation and Upscaling of Flow Properties. 10th International Conference on Porous Media and Annual meeting, New Orleans, USA (Oral Presentation).

References

Abouelresh, M. O. and Slatt, R. M. (2011) 'Shale depositional processes: Example from the Paleozoic Barnett Shale, Fort Worth Basin, Texas, USA', *Central European Journal of Geosciences*, 3(4), pp. 398-409.

Alonso, B., Ercilla, G., Casas, D., Stow, D. A. V., Rodríguez-Tovar, F. J., Dorador, J. and Hernández-Molina, F.-J. (2016) 'Contourite vs gravity-flow deposits of the Pleistocene Faro Drift (Gulf of Cadiz): Sedimentological and mineralogical approaches', *Marine Geology*, 377, pp. 77-94.

Altschaeffl, A. G. and Thevanayagam, S. (1991) 'Characterization of Clay Fabric', in Bennett, R., Bryant, W., Hulbert, M., Chiou, W. A., Faas, R. W., Kasprowicz, J., Li, H., Lomenick, T., O'brien, N. R., Pamukcu, S., Smart, P., Weaver, C. E. and Yamamoto, T. (eds.) *Microstructure of Fine-Grained Sediments*. Springer New York, pp. 291-295. 31.

Ambrose, R. J. (2011) *Micro-structure of gas shales and its effects on gas storage and production performance*. Ph.D thesis. University of Oklahoma.

Andrä, H., Combaret, N., Dvorkin, J., Glatt, E., Han, J., Kabel, M., Keehm, Y., Krzikalla, F., Lee, M., Madonna, C., Marsh, M., Mukerji, T., Saenger, E. H., Sain, R., Saxena, N., Ricker, S., Wiegmann, A. and Zhan, X. (2013a) 'Digital rock physics benchmarks—Part I: Imaging and segmentation', *Computers & Geosciences*, 50(Supplement C), pp. 25-32.

Andrä, H., Combaret, N., Dvorkin, J., Glatt, E., Han, J., Kabel, M., Keehm, Y., Krzikalla, F., Lee, M., Madonna, C., Marsh, M., Mukerji, T., Saenger, E. H., Sain, R., Saxena, N., Ricker, S., Wiegmann, A. and Zhan, X. (2013b) 'Digital rock physics benchmarks—part II: Computing effective properties', *Computers & Geosciences*, 50(Supplement C), pp. 33-43.

Anovitz, L. M. and Cole, D. R. (2015) 'Characterization and Analysis of Porosity and Pore Structures', in Steefel, C. I., Emmanuel, S. and Anovitz, L. M. (eds.) *Pore-Scale Geochemical Processes*. pp. 61-164.

Aplin, A. C., Fleet, A. J. and Macquaker, J. H. (1999) 'Muds and mudstones: Physical and fluid-flow properties', *Geological Society, London, Special Publications*, 158(1), pp. 1-8.

Aplin, A. C. and Macquaker, J. H. (2011) 'Mudstone diversity: Origin and implications for source, seal, and reservoir properties in petroleum systems', *American Association of Petroleum Geologists Bulletin*, 95(12), pp. 2031-2059.

Aplin, A. C., Matenaar, I. F., McCarty, D. K. and van der Pluijm, B. A. (2006) 'Influence of mechanical compaction and clay mineral diagenesis on the microfabric and pore-scale

properties of deep-water Gulf of Mexico mudstones', *Clays and Clay Minerals*, 54(4), pp. 500-514.

Aplin, A. C., Matenaar, I. F. and van der Pluijm, B. (2003) 'Influence of mechanical compaction and chemical diagenesis on the microfabric and fluid flow properties of Gulf of Mexico mudstones', *Journal of Geochemical Exploration*, 78–79, pp. 449-451.

Argus, D. F., Gordon, R. G., Demets, C. and Stein, S. (1989) 'Closure of the Africa Eurasia North America Plate motion circuit and tectonics of the Gloria Fault', *Journal of Geophysical Research-Solid Earth and Planets*, 94(B5), pp. 5585-5602.

Bahr, A., Jimenez-Espejo, F. J., Kolasinac, N., Grunert, P., Hernandez-Molina, F. J., Rohl, U., Voelker, A. H. L., Escutia, C., Stow, D. A. V., Hodell, D. and Alvarez-Zarikian, C. A. (2014) 'Deciphering bottom current velocity and paleoclimate signals from contourite deposits in the Gulf of Cadiz during the last 140 kyr: An inorganic geochemical approach', *Geochemistry Geophysics Geosystems*, 15(8), pp. 3145-3160.

Bąk, K., Bąk, M., Górny, Z. and Wolska, A. (2014) 'Environmental Conditions in a Carpathian Deep Sea Basin During the Period Preceding Oceanic Anoxic Event 2-A Case Study from the Skole Nappe', *Geologica Carpathica*, 65(6), pp. 433-450.

Bankole, S., Stow, D., Lever, H. and Buckman, J. (2016) 'Microstructure of Mudrock and the Choice of Representative Sample', in *Fifth EAGE Shale Workshop*. Catania, Italy: EAGE, pp. 99-103.

Bankole, S. A., Buckman, J., Stow, D. V. and Lever, H. (2018a) 'Automated Image Analysis of Mud and Mudrock Microstructure and Characteristics of Hemipelagic Sediments: IODP Expedition 339', *Journal of Earth Science*, p. (in press).

Bankole, S. A., Buckman, J., Stow, D. V. and Lever, H. (2018b) 'Grain-size Analysis of mudrocks: A New Semi-Automated Method from SEM Images', *Journal of Petroleum Science and Engineering*, p. (in press).

Baringer, M. O. and Price, J. F. (1999) 'A review of the physical oceanography of the Mediterranean outflow', *Marine Geology*, 155(1-2), pp. 63-82.

Barrett, E. P., Joyner, L. G. and Halenda, P. P. (1951) 'The determination of pore volume and area distributions in porous substances. I. Computations from nitrogen isotherms', *Journal of the American Chemical Society*, 73(1), pp. 373-380.

Bennett, R. H., Bryant, W. R. and Keller, G. H. (1981) 'Clay fabric of selected submarine sediments: fundamental properties and models', *Journal of Sedimentary Petrology*, 51(1), pp. 217-232.

Bennett, R. H., O'Brien, N. R. and Hulbert, M. H. (1991) 'Determinants of clay and shale microfabric signatures: processes and mechanisms. In Microstructure of Fine-Grained Sediments: From Mud to Shale', in Bennett, R. H., Bryant, W. R., Hulbert, M. H. and Bouma, A. H. (eds.) *Marine Geology*. New York: Springer-Verlag,, pp. 5–32.

Berens, P. (2009) 'CircStat: A MATLAB Toolbox for Circular Statistics', *Journal of Statistical Software*, 31(10), pp. 1-21.

Berge, P. A., Berryman, J. G. and Bonner, B. P. (1993) 'Influence of microstructure on rock elastic properties', *Geophysical Research Letters*, 20(23), pp. 2619-2622.

Berger, G., Velde, B. and Aigouy, T. (1999) 'Potassium sources and illitization in Texas Gulf Coast shale diagenesis', *Journal of Sedimentary Research*, 69(1), pp. 151-157.

Bernard, S., Horsfield, B., Schulz, H.-M., Schreiber, A., Wirth, R., Anh Vu, T. T., Perssen, F., Könitzer, S., Volk, H., Sherwood, N. and Fuentes, D. (2010) 'Multi-scale detection of organic and inorganic signatures provides insights into gas shale properties and evolution', *Chemie der Erde - Geochemistry*, 70, Supplement 3, pp. 119-133.

Bernard, S., Wirth, R., Schreiber, A., Schulz, H.-M. and Horsfield, B. (2012) 'Formation of nanoporous pyrobitumen residues during maturation of the Barnett Shale (Fort Worth Basin)', *International Journal of Coal Geology*, 103, pp. 3-11.

Bertier, P., Schweinar, K., Stanjek, H., Ghanizadeh, A., Clarkson, C. R., Busch, A., Kampman, N., Prinz, D., Amann-Hildenbrand, A. and Krooss, B. M. (eds.) (2016) *On the use and abuse of N2 physisorption for the characterization of the pore structure of shales*. Chantilly, VA: The Clay Minerals Society.

Beuselinck, L., Govers, G., Poesen, J., Degraer, G. and Froyen, L. (1998) 'Grain-size analysis by laser diffractometry: comparison with the sieve-pipette method', *CATENA*, 32(3–4), pp. 193-208.

Bhattacharya, G. C., Chaubey, A. K., Murty, G. P. S., Srinivas, K., Sarma, K. V. L. N. S., Subrahmanyam, V. and Krishna, K. S. (1994) 'Evidence for seafloor spreading in the Laxmi Basin, northeastern Arabian Sea', *Earth and Planetary Science Letters*, 125(1), pp. 211-220.

Blatt, H., Middleton, G. and Murray, R. (1980) *Origin of sedimentary rocks*. 2d ed edn. Englewood Cliff, New Jersey,: Prentice-Hall.

Bloch, S. (ed.) (1994) *Petrographic analysis of porosity and permeability*. Tulsa.: SEPM (Society for Sedimentary Geology).

Blott, S. J., Croft, D. J., Pye, K., Saye, S. E. and Wilson, H. E. (2004) 'Particle size analysis by laser diffraction', *Geological Society, London, Special Publications*, 232(1), pp. 63-73.

Blott, S. J. and Pye, K. (2001) 'GRADISTAT: a grain size distribution and statistics package for the analysis of unconsolidated sediments', *Earth Surface Processes and Landforms*, 26(11), pp. 1237-1248.

Blum, P. (1997) *Physical Properties Handbook: A Guide to the Shipboard Measurement of Physical Properties of Deep-Sea Cores: Ocean Drilling Program*. [Online]. Available at: http://www-odp.tamu.edu/publications/tnotes/tn26/TOC.HTM (Accessed: 11/08/2016).

Blume, H.-P., Brümmer, G. W., Fleige, H., Horn, R., Kandeler, E., Kögel-Knabner, I., Kretzschmar, R., Stahr, K. and Wilke, B.-M. (2016) 'Physical Properties and Processes', in *Scheffer/SchachtschabelSoil Science*. Berlin, Heidelberg: Springer Berlin Heidelberg, pp. 175-283.

Bons, P. and Jessell, M. W. (1996) 'Image analysis of microstructures in natural and experimental samples', in Declan, G. D. P. (ed.) *Computer Methods in the Geosciences*. Pergamon, pp. 135-166.

Boruah, A. and Ganapathi, S. (2015) 'Microstructure and pore system analysis of Barren Measures shale of Raniganj field, India', *Journal of Natural Gas Science and Engineering*, 26, pp. 427-437.

Bosl, W. J., Dvorkin, J. and Nur, A. (1998) 'A study of porosity and permeability using a lattice Boltzmann simulation', *Geophysical Research Letters*, 25(9), pp. 1475-1478.

Bouma, A. H. (2000a) 'Coarse-grained and fine-grained turbidite systems as end member models: applicability and dangers', *Marine and Petroleum Geology*, 17(2), pp. 137-143.

Bouma, A. H. (2000b) 'Fine-grained, mud-rich turbidite systems: Model and comparison with coarse-grained, sand-rich systems', *American Association of Petroleum Geologists Memoir*, 72(68), pp. 9-20.

Bowker, K. A. (2007) 'Barnett Shale gas production, Fort Worth Basin: issues and discussion', *American Association of Petroleum Geologists Bulletin*, 91(4), pp. 523-533.

Brackenridge, R., Stow, D. V., Hernández-Molina, F., Jones, C., Mena, A., Alejo, I., Ducassou, E., Llave, E., Ercilla, G. and A Nombela, M. (2018) 'Textural characteristics and facies of sand-rich contourite depositional systems', *Sedimentology*, pp. 1-30.

Brackenridge, R. E., Hernández-Molina, F. J., Stow, D. A. V. and Llave, E. (2013) 'A Pliocene mixed contourite-turbidite system offshore the Algarve Margin, Gulf of Cadiz: Seismic response, margin evolution and reservoir implications', *Marine and Petroleum Geology*, 46, pp. 36-50.

Browne, G. H. and Field, B. D. (1988) 'A review of Cretaceous-Cenozoic sedimentation and tectonics, east coast, South Island, New Zealand', *Sequences, Stratigraphy, Sedimentology: Surface and Subsurface*, 15, pp. 37-48.

Brunauer, S., Emmett, P. H. and Teller, E. (1938) 'Adsorption of gases in multimolecular layers', *Journal of the American chemical society*, 60(2), pp. 309-319.

Bryden, H. L. and Stommel, H. M. (1984) 'Limiting processes that determine basic features of the circulation in the Mediterranean Sea', *Oceanol. Acta*, 7(3), pp. 289-296.

Buckman, J. (2014) 'Use of automated image acquisition and stitching in scanning electron microscopy: Imaging of large scale areas of materials at high resolution', *Microscopy and Analysis*, 28(1), pp. 13-15.

Buckman, J., Bankole, S., Zihms, S., Lewis, H., Couples, G. and Corbett, P. (2017) 'Quantifying Porosity through Automated Image Collection and Batch Image Processing: Case Study of Three Carbonates and an Aragonite Cemented Sandstone', *Geosciences*, 7(3), pp. 1-19.

Buckman, J., Mahoney, C., Bankole, S., Couples, G., Lewis, H., Wagner, T., März, C., Blanco, V., Stow, D. and Ruffell, A. (2018) 'Workflow model for the digitization of mudrocks', *Geological society London, Special Publications*, p. (in press).

Busch, A., Alles, S., Gensterblum, Y., Prinz, D., Dewhurst, D. N., Raven, M. D., Stanjek, H. and Krooss, B. M. (2008) 'Carbon dioxide storage potential of shales', *International Journal of Greenhouse Gas Control*, 2(3), pp. 297-308.

Busch, A., Schweinar, K., Kampman, N., Coorn, A., Pipich, V., Feoktystov, A., Leu, L., Amann-Hildenbrand, A. and Bertier, P. (2017) 'Determining the porosity of mudrocks using

methodological pluralism', *Geological Society, London, Special Publications*, 454(1), pp. 15-38.

Buscombe, D., Rubin, D. M. and Warrick, J. A. (2010) 'A universal approximation of grain size from images of noncohesive sediment', *Journal of Geophysical Research: Earth Surface*, 115(F2), pp. 1-17.

Bustin, A. M. M. and Bustin, R. M. (2012) 'Importance of rock properties on the producibility of gas shales', *International Journal of Coal Geology*, 103, pp. 132-147.

Bustin, R. M., Bustin, A. M. M., Cui, A., Ross, D. and Pathi, V. M. (2008) 'Impact of Shale Properties on Pore Structure and Storage Characteristics', *Shale Gas Production Conference*. Fort Worth, Texas, U.S.A, 2008/1/1/. SPE: Society of Petroleum Engineers. doi: 10.2118/119892-MS Available at: https://www.onepetro.org:443/download/conference-paper/SPE-119892-MS?id=conference-paper%2FSPE-119892-MS.

Camp, W. K., Diaz, E. and Wawak, B. E. (2013) *Electron microscopy of shale hydrocarbon reservoirs*.

Camp, W. K., Egenhoff, S., Schieber, J. and Slatt, R. M. (2016) 'A compositional classification for grain assemblages in fine-grained sediments and sedimentary rocks-discussion', *Journal of Sedimentary Research*, 86(1), pp. 1-5.

Camp, W. K. and Wawak, B. (2013) 'Enhancing SEM grayscale images through pseudocolor conversion: Examples from eagle ford, Haynesville, and Marcellus Shales', *American Association of Petroleum Geologists Memoir*, (102), pp. 15-26.

Cao, T., Song, Z., Wang, S. and Xia, J. (2015) 'A comparative study of the specific surface area and pore structure of different shales and their kerogens', *Science China Earth Sciences*, 58(4), pp. 510-522.

Casagrande, A. (1932) 'The Structure of Clay and Its Importance in Foundation Engineering', 15, pp. 72-125.

Casey, B., Germaine, J. T., Flemings, P. B., Reece, J. S., Gao, B. and Betts, W. (2013) 'Liquid limit as a predictor of mudrock permeability', *Marine and Petroleum Geology*, 44, pp. 256-263.

Chalmers, G. R., Bustin, R. M. and Power, I. M. (2012) 'Characterization of gas shale pore systems by porosimetry, pycnometry, surface area, and field emission scanning electron

microscopy/transmission electron microscopy image analyses: Examples from the Barnett, Woodford, Haynesville, Marcellus, and Doig units', *AAPG bulletin*, 96(6), pp. 1099-1119.

Chalmers, G. R. L., Ross, D. J. K. and Bustin, R. M. (2012) 'Geological controls on matrix permeability of Devonian Gas Shales in the Horn River and Liard Basins, northeastern British Columbia, Canada', *International Journal of Coal Geology*, 103, pp. 120-131.

Chambers, J. M. (1983) *Graphical methods for data analysis*. Edited by Peter, J. B., William, S. C. and Richard, M. D. Boston, Massachusetts USA: Duxbury Press.

Charpentier, D., Worden, R. H., Dillon, C. G. and Aplin, A. C. (2003) 'Fabric development and the smectite to illite transition in Gulf ofMexico mudstones: an image analysis approach', *Journal of Geochemical Exploration*, 78–79(0), pp. 459-463.

Chaubey, A. K., Dyment, J., Bhattacharya, G. C., Royer, J. Y., Srinivas, K. and Yatheesh, V. 195 (2002a) 'Paleogene magnetic isochrons and palaeo-propagators in the Arabian and Eastern Somali basins, NW Indian Ocean' *Geological Society Special Publication* [Article]. pp. 71-85.

Chaubey, A. K., Gopala Rao, D., Srinivas, K., Ramprasad, T., Ramana, M. V. and Subrahmanyam, V. (2002b) 'Analyses of multichannel seismic reflection, gravity and magnetic data along a regional profile across the central-western continental margin of India', *Marine Geology*, 182(3–4), pp. 303-323.

Clarkson, C. R., Freeman, M., He, L., Agamalian, M., Melnichenko, Y. B., Mastalerz, M., Bustin, R. M., Radliński, A. P. and Blach, T. P. (2012) 'Characterization of tight gas reservoir pore structure using USANS/SANS and gas adsorption analysis', *Fuel*, 95, pp. 371-385.

Clarkson, C. R., Jensen, J. L. and Chipperfield, S. (2012) 'Unconventional gas reservoir evaluation: What do we have to consider?', *Journal of Natural Gas Science and Engineering*, 8, pp. 9-33.

Clarkson, C. R., Solano, N., Bustin, R. M., Bustin, A. M. M., Chalmers, G. R. L., He, L., Melnichenko, Y. B., Radliński, A. P. and Blach, T. P. (2013) 'Pore structure characterization of North American shale gas reservoirs using USANS/SANS, gas adsorption, and mercury intrusion', *Fuel*, 103, pp. 606-616.

Clift, P., Gaedicke, C., Edwards, R., Il Lee, J., Hildebrand, P., Amjad, S., White, R. S. and Schlüter, H.-U. (2002) 'The stratigraphic evolution of the Indus Fan and the history of sedimentation in the Arabian Sea', *Marine Geophysical Researches*, 23(3), pp. 223-245.

Clift, P. D. 195 (2002) 'A brief history of the Indus River' *Geological Society Special Publication* [Article]. pp. 237-258.

Clift, P. D., Shimizu, N., Layne, G. D., Blusztajn, J. S., Gaedicke, C., Schlüter, H. U., Clark, M. K. and Amjad, S. (2001) 'Development of the Indus Fan and its significance for the erosional history of the Western Himalaya and Karakoram', *Bulletin of the Geological Society of America*, 113(8), pp. 1039-1051.

Cohen, A. L. (1979) 'Critical point drying principles and procedures', *Scanning Electron Microscopy*, (2), pp. 303-324.

Corfield, R. I., Carmichael, S., Bennett, J., Akhter, S., Fatimi, M. and Craig, T. (2010) 'Variability in the crustal structure of the West Indian Continental Margin in the Northern Arabian Sea', *Petroleum Geoscience*, 16(3), pp. 257-265.

Corkum, A. G. and Martin, C. D. (2007) 'The mechanical behaviour of weak mudstone (Opalinus Clay) at low stresses', *International Journal of Rock Mechanics and Mining Sciences*, 44(2), pp. 196-209.

Crosby, K., Eberle, A. L. and Zeidler, D. (2016) 'Multi-beam SEM Technology for High Throughput Imaging', *MRS Advances*, 1(26), pp. 1915-1920.

Curry, K. J., Bennett, R. H., Mayer, L. M., Curry, A., Abril, M., Biesiot, P. M. and Hulbert, M. H. (2007) 'Direct visualization of clay microfabric signatures driving organic matter preservation in fine-grained sediment', *Geochimica et Cosmochimica Acta*, 71(7), pp. 1709-1720.

Curtis, M. E., Ambrose, R. J., Sondergeld, C. H. and Rai, C. S. (2010) *Canadian Unconventional Resources and International Petroleum Conference* Canada: Society of Petroleum Engineers.

Curtis, M. E., Cardott, B. J., Sondergeld, C. H. and Rai, C. S. (2012a) 'Development of organic porosity in the Woodford Shale with increasing thermal maturity', *International Journal of Coal Geology*, 103, pp. 26-31.

Curtis, M. E., Sondergeld, C. H., Ambrose, R. J. and Rai, C. S. (2012b) 'Microstructural investigation of gas shales in two and three dimensions using nanometer-scale resolution imaging', *American Association of Petroleum Geologists Bulletin*, 96(4), pp. 665-677.

Cuven, S., Francus, P. and Lamoureux, S. F. (2010) 'Estimation of grain size variability with micro X-ray fluorescence in laminated lacustrine sediments, Cape Bounty, Canadian High Arctic', *Journal of Paleolimnology*, 44(3), pp. 803-817.

Dall'Olio, E., Felletti, F. and Muttoni, G. (2013) 'Magnetic-fabric analysis as a tool to constrain mechanisms of deep-water mudstone deposition in the Marnoso Arenacea Formation (Miocene, Italy)', *Journal of Sedimentary Research*, 83(2), pp. 170-182.

Davies, D., Bryant, W., Vessell, R. and Burkett, P. (1991) 'Porosities, permeabilities, and microfabrics of Devonian Shales', in Bennett, R., Bryant, W., Hulbert, M., Chiou, W. A., Faas, R. W., Kasprowicz, J., Li, H., Lomenick, T., O'brien, N. R., Pamukcu, S., Smart, P., Weaver, C. E. and Yamamoto, T. (eds.) *Microstructure of Fine-Grained Sediments*. Springer New York, pp. 109-119. 10.

Davis, J. C. (1986) *Statistics and Data Analysis in Geology*. India: John Wiley and Sons.

Day-Stirrat, R. (2014) 'Clay Mineral Preferred Orientation-How to Predict It and What It Might Control', in *Fourth EAGE Shale Workshop*. Porto, Portugal: EAGE.

Day-Stirrat, R. J., Dutton, S. P., Milliken, K. L., Loucks, R. G., Aplin, A. C., Hillier, S. and van der Pluijm, B. A. (2010) 'Fabric anisotropy induced by primary depositional variations in the silt: Clay ratio in two fine-grained slope fan complexes: Texas Gulf Coast and northern North Sea', *Sedimentary Geology*, 226(1-4), pp. 42-53.

Dean, W. E., Leinen, M. and Stow, D. A. (1985) 'Classification of deep-sea, fine-grained sediments', *Journal of Sedimentary Research*, 55(2), pp. 250-256.

Delage, P. and Lefebvre, G. (1984) 'Study of the structure of a sensitive champlain clay and of its evolution during consolidation', *Canadian Geotechnical Journal*, 21(1), pp. 21-35.

Desbois, G., Urai, J. L. and Kukla, P. A. (2009) 'Morphology of the pore space in claystones - Evidence from BIB/FIB ion beam sectioning and cryo-SEM observations', *eEarth*, 4(1), pp. 15-22.

Desbois, G., Urai, J. L., Kukla, P. A., Konstanty, J. and Baerle, C. (2011) 'High-resolution 3D fabric and porosity model in a tight gas sandstone reservoir:A new approach to investigate microstructures from mm- to nm-scale combining argon beam cross-sectioning and SEM imaging', *Journal of Petroleum Science and Engineering*, 78(2), pp. 243-257.

Dewhurst, D. N., Aplin, A. C. and Sarda, J. P. (1999) 'Influence of clay fraction on pore-scale properties and hydraulic conductivity of experimentally compacted mudstones', *Journal of Geophysical Research B: Solid Earth*, 104(B12), pp. 29261-29274.

Dewhurst, D. N., Jones, R. M. and Raven, M. D. (2002) 'Microstructural and petrophysical characterization of Muderong Shale: Application to top seal risking', *Petroleum Geoscience*, 8(4), pp. 371-383.

Dewhurst, D. N., Yang, Y. and Aplin, A. C. (1999) 'Permeability and fluid flow in natural mudstones', *Geological Society Special Publication*, 158, pp. 23-43.

Diaz, E. and Walls, J. (2012) 'Shale reservoir properties from digital rock physics', in *3rd EAGE Shale Workshop: Shale Physics and Shale Chemistry*. Barcelona, Spain: EAGE.

Douglas, R. E., Gerhard, H. W. and Alyssa, W. K. (2016) 'Paragenesis of mineralized fractures And diagenesis of prominent North American Shales', *The Sedimentary Record*, 14(4), pp. 1-16.

Duarte, C. S. L. and Viana, A. R. 276 (2007) 'Santos Drift System: Stratigraphic organization and implications for late Cenozoic palaeocirculation in the Santos Basin, SW Atlantic Ocean' *Geological Society Special Publication* [Article]. pp. 171-198.

Dvorkin, J. and Nur, A. (1996) 'Elasticity of high-porosity sandstones: Theory for two North Sea data sets', *Geophysics*, 61(5), pp. 1363-1370.

Eberle, A. L., Schalek, R., Lichtman, J. W., Malloy, M., Thiel, B. and Zeidler, D. (2015) 'Multiple-Beam Scanning Electron Microscopy', *Microscopy Today*, 23(2), pp. 12-19.

Echlin, P. (2009) 'Sample Dehydration', in *Handbook of Sample Preparation for Scanning Electron Microscopy and X-Ray Microanalysis*. Springer US, pp. 97-136. 7.

Egenhoff, S. O. and Fishman, N. S. (2013) 'Traces in the dark-sedimentary processes and facies gradients in the upper shale member of the Upper Devonian-Lower Mississippian Bakken Formation, Williston Basin, North Dakota, U.S.A', *Journal of Sedimentary Research*, 83(9), pp. 803-824.

Elliott, R. and Strauss, P. (1967) 'A classification of Coal Measures rocks based on quartz content', *Compte Rendu de Congres Int. Strat. Geol. Carbonif. Sheffield*, 2, pp. 715-724.

Ellis, E. (2006) 'Solutions to the problem of substitution of ERL 4221 for vinyl cyclohexene dioxide in Spurr low viscosity embedding formulations', *Microscopy Today*, 14(4), pp. 32-33.

Erdman, N., Campbell, R. and Asahina, S. (2006) 'Precise SEM cross section polishing via argon beam milling', *Microscopy today*, 14(3), pp. 22-25.

Erdman, N. and Drenzek, N. (2013) 'Integrated preparation and imaging techniques for the microstructural and geochemical characterization of shale by scanning electron microscopy', *American Association of Petroleum Geologists Memoir*, (102), pp. 7-14.

Eshel, G., Levy, G. J., Mingelgrin, U. and Singer, M. J. (2004) 'Critical Evaluation of the Use of Laser Diffraction for Particle-Size Distribution Analysis', *Soil Science Society of America Journal*, 68(3), pp. 736-743.

Ewy, R. T. (2015) 'Shale/claystone response to air and liquid exposure, and implications for handling, sampling and testing', *International Journal of Rock Mechanics and Mining Sciences*, 80, pp. 388-401.

Expedition 317 Scientists (2010) 'Canterbury Basin Sea Level: Global and local controls on continental margin stratigraphy', *IODP Preliminary Report*, *317*, pp. 1-133.

Expedition 317 Scientists (2011) 'Expedition 317 summary', in Fulthorpe, C. S., Hoyanagi, K. B. P. and The Expedition 317 Scientists (eds.) *Proc. IODP*. Tokyo: Integrated Ocean Drilling Program Management International, Inc., pp. 1-86.

Expedition 339 Scientists (2012) 'Mediterranean outflow: environmental significance of the Mediterranean Outflow Water and its global implications', *IODP Preliminary Report339*

Expedition 339 Scientists (2013) 'Expedition 339 summary', in Stow, D. a. V., Hernández-Molina, F. J., Alvarez Zarikian, C. A. and The Expedition 339 Scientists (eds.) *Proc. IODP*, *339*. Tokyo: Integrated Ocean Drilling Program Management International, Inc.

Fernlund, J. M. R. (2005) 'Image analysis method for determining 3-D size distribution of coarse aggregates', *Bulletin of Engineering Geology and the Environment*, 64(2), pp. 159-166.

Fernlund, J. M. R., Zimmerman, R. W. and Kragic, D. (2007) 'Influence of volume/mass on grain-size curves and conversion of image-analysis size to sieve size', *Engineering Geology*, 90(3–4), pp. 124-137.

Fisher, N. I. (1993) *Statistical Analysis of Circular Data*. Cambridge Cambridge University Press.

Flawn, P. T. (1953) 'Petrographic Classification of Argillaceous Sedimentary and Low-Grade Metamorphic Rocks in Subsurface: Geological Notes', *American Association of Petroleum Geologists Bulletin*, 37(3), pp. 560-565.

Folk, R. L. (1980) *Petrology of sedimentary rocks*. Hemphill Publishing Company.

Folk, R. L. and Ward, W. C. (1957) 'Brazos River bar: A study in the significance of grain size parameters', *Journal of Sedimentary Research*, 27(1), pp. 3-26.

Fourier, D. (2017) 'Introduction to Digital Rock Physics and Predictive Rock Properties of Reservoir Sandstone', in *IOP Conference Series: Earth and Environmental Science*. IOP Publishing, p. pp. 012022.

Francus, P. (1998) 'An image-analysis technique to measure grain-size variation in thin sections of soft clastic sediments', *Sedimentary Geology*, 121(3–4), pp. 289-298.

Francus, P. and Pirard, E. (2004) 'Testing for sources of errors in quantitative image analysis', *Image analysis, sediments and paleoenvironments*, pp. 87-102.

Friedman, G. M. (1961) 'Distinction between dune, beach, and river sands from their textural characteristics', *Journal of Sedimentary Research*, 31(4), pp. 514-529.

Fulthorpe, C. S., Carter, R. M., Miller, K. G. and Wilson, J. (1996) 'Marshall Paraconformity: a mid-Oligocene record of inception of the Antarctic circumpolar current and coeval glacio-eustatic lowstand?', *Marine and Petroleum Geology*, 13(1), pp. 61-77.

Fulthorpe, C. S., Hoyanagi, K. and Blum, P. (2011) 'IODP expedition 317: Exploring the record of sea-level change off New Zealand', *Scientific Drilling*, (12), pp. 4-14.

Fulthorpe, C. S., Hoyanagi, K., Blum, P. and Geldmacher, J. (2009) 'Global and local controls on continental margin stratigraphy: Canterbury Basin, eastern South Island, New Zealand.', *IODP Scientific Prospectus, 317*.

Fulthorpe, C. S., Hoyanagi, K., Blum, P., Guèrin, G., Slagle, A. L., Blair, S. A., Browne, G. H., Carter, R. M., Ciobanu, M. C., Claypool, G. E., Crundwell, M. P., Dinarès-Turell, J., Ding, X., George, S. C., Hepp, D. A., Jaeger, J., Kawagata, S., Kemp, D. B., Kim, Y. G., Kominz, M. A., Lever, H., Lipp, J. S., Marsaglia, K. M., McHugh, C. M., Murakoshi, N., Ohi, T., Pea, L., Richaud, M., Suto, I., Tanabe, S., Tinto, K. J., Uramoto, G. and Yoshimura, T. (2010) 'Integrated ocean drilling program expedition 317 preliminary report canterbury basin sea level global and local controls on continental margin stratigraphy', *Integrated Ocean Drilling Program: Preliminary Reports*, (317), pp. 1-133.

Gamero Diaz, H., Lewis, R. and Miller, C. K. (2013) 'sCore: A Mineralogy Based Classification Scheme for Organic Mudstones', in *SPE Annual Technical Conference and Exhibition*. New Orleans, Louisiana, USA: Society of Petroleum Engineers.

García, M., Ercilla, G., Alonso, B., Estrada, F., Jané, G., Mena, A., Alvés, T. and Juan, C. (2015) 'Deep-water turbidite systems: A review of their elements, sedimentary processes and depositional models. Their characteristics on the iberian margins', *Boletin Geologico y Minero*, 126(2-3), pp. 189-218.

Goldstein, J., Newbury, D., Echlin, P., Joy, D., Lyman, C., Lifshin, E., Sawyer, L. and Michael, J. (2003) 'The SEM and Its Modes of Operation', in *Scanning Electron Microscopy and X-ray Microanalysis*. Springer US, pp. 21-60. 2.

Gonthier, E. G., Faugères, J. C. and Stow, D. A. V. 15 (1984) 'Contourite facies of the Faro Drift, Gulf of Cadiz' *Geological Society Special Publication*. pp. 275-292.

Graham, J. D., Rupp, J. A. and Schenk, O. (2015) 'Unconventional Gas Development in the USA: Exploring the Risk Perception Issues', *Risk Analysis*, 35(10), pp. 1770-1788.

Grainger, P. (1984) 'The classification of mudrocks for engineering purposes', *Quarterly Journal of Engineering Geology and Hydrogeology*, 17(4), pp. 381-387.

Grimm, K. (1992) 'Preparation of weakly consolidated, laminated hemipelagic sediment for high-resolution visual microanalysis: an analytical method', *Proceedings of the Ocean Drilling Program, Scientific Results*, 127/128(1), pp. 57-59.

Grove, C. and Jerram, D. A. (2011) 'jPOR: An ImageJ macro to quantify total optical porosity from blue-stained thin sections', *Computers & Geosciences*, 37(11), pp. 1850-1859.

Gu, X., Cole, D. R., Rother, G., Mildner, D. F. R. and Brantley, S. L. (2015) 'Pores in Marcellus Shale: A Neutron Scattering and FIB-SEM Study', *Energy & Fuels*, 29(3), pp. 1295-1308.

Gu, X., Mildner, D. F. R., Cole, D. R., Rother, G., Slingerland, R. and Brantley, S. L. (2016) 'Quantification of Organic Porosity and Water Accessibility in Marcellus Shale Using Neutron Scattering', *Energy & Fuels*, 30(6), pp. 4438-4449.

Hayton, S., Nelson, C. S., Ricketts, B. D., Cooke, S. and Wedd, M. W. (2001) 'Effect of mica on particle-size analyses using the laser diffraction technique', *Journal of Sedimentary Research*, 71(3), pp. 507-509.

Heilbronner, R. and Barrett, S. (2014) *Image analysis in earth sciences: Microstructures and textures of earth materials*. Berlin Heidelberg: Springer.

Hemes, S., Desbois, G., Urai, J. L., De Craen, M. and Honty, M. (2013) 'Variations in the morphology of porosity in the Boom Clay Formation: insights from 2D high resolution BIB-SEM imaging and Mercury injection Porosimetry', *Netherlands Journal of Geosciences-Geologie En Mijnbouw*, 92(4), pp. 275-300.

Hemes, S., Desbois, G., Urai, J. L., Schröppel, B. and Schwarz, J.-O. (2015) 'Multi-scale characterization of porosity in Boom Clay (HADES-level, Mol, Belgium) using a combination of X-ray μ-CT, 2D BIB-SEM and FIB-SEM tomography', *Microporous and Mesoporous Materials*, 208, pp. 1-20.

Hernández-Molina, F. J., Llave, E., Stow, D. A. V., García, M., Somoza, L., Vázquez, J. T., Lobo, F. J., Maestro, A., Díaz del Río, V., León, R., Medialdea, T. and Gardner, J. (2006) 'The contourite depositional system of the Gulf of Cádiz: A sedimentary model related to the bottom current activity of the Mediterranean outflow water and its interaction with the continental margin', *Deep Sea Research Part II: Topical Studies in Oceanography*, 53(11–13), pp. 1420-1463.

Hernández-Molina, F. J., Serra, N., Stow, D. A. V., Llave, E., Ercilla, G. and van Rooij, D. (2011) 'Along-slope oceanographic processes and sedimentary products around the Iberian margin', *Geo-Marine Letters*, 31(5-6), pp. 315-341.

Hernández-Molina, F. J., Sierro, F. J., Llave, E., Roque, C., Stow, D. A. V., Williams, T., Lofi, J., Van der Schee, M., Arnáiz, A., Ledesma, S., Rosales, C., Rodríguez-Tovar, F. J., Pardo-Igúzquiza, E. and Brackenridge, R. E. (2016) 'Evolution of the gulf of Cadiz margin and southwest Portugal contourite depositional system: Tectonic, sedimentary and paleoceanographic implications from IODP expedition 339', *Marine Geology*, 377, pp. 7-39.

Hernández-Molina, F. J., Stow, D., Alvarez-Zarikian, C., Acton, G., Bahr, A., Balestra, B., Ducassou, E., Flood, R., Flores, J. A., Furota, S., Grunert, P., Hodell, D., Jimenez-Espejo, F., Kim, J. K., Krissek, L., Kuroda, J., Li, B., Llave, E., Lofi, J., Lourens, L., Miller, M., Nanayama, F., Nishida, N., Richter, C., Roque, C., Pereira, H., Goñi Fernanda Sanchez, M., Sierro, F. J., Singh, A. D., Sloss, C., Takashimizu, Y., Tzanova, A., Voelker, A., Williams, T. and Xuan, C. (2013) 'IODP Expedition 339 in the Gulf of Cadiz and off West Iberia: Decoding the environmental significance of the Mediterranean outflow water and its global influence', *Scientific Drilling*, (16), pp. 1-11.

Hesse, R. (1975) 'Turbiditic and non-turbiditic mudstone of Cretaceous flysch sections of the East Alps and other basins', *Sedimentology*, 22(3), pp. 387-416.

Hildenbrand, A. and Urai, J. L. (2003) 'Investigation of the morphology of pore space in mudstones—first results', *Marine and Petroleum Geology*, 20(10), pp. 1185-1200.

Hints, R., Hade, S., Soesoo, A. and Voolma, M. (2014) 'Depositional framework of the East Baltic Tremadocian black shale revisited', *GFF*, 136, pp. 464-482.

Ho, N. C., Peacor, D. R. and van Der Pluijm, B. A. (1999) 'Preferred orientation of phyllosilicates in Gulf Coast mudstones and relation to the smectite-illite transition', *Clays and Clay Minerals*, 47(4), pp. 495-504.

Hodell, D., Lourens, L., Crowhurst, S., Konijnendijk, T., Tjallingii, R., Jiménez-Espejo, F., Skinner, L. and Tzedakis, P. C. (2015) 'A reference time scale for Site U1385 (Shackleton Site) on the SW Iberian Margin', *Global and Planetary Change*, 133, pp. 49-64.

Hodell, D. A., Lourens, L., Stow, D. A. V., Hernández-Molina, J., Alvarez Zarikian, C. A., Abrantes, F., Acton, G. D., Bahr, A., Balestra, B., Llave Barranco, E., Carrara, G., Crowhurst, S., Ducassou, E., Flood, R. D., Flores, J. A., Furota, S., Grimalt, J., Grunert, P., Jimenez-Espejo, F. J., Kyoung Kim, J., Konijnendijk, T., Krissek, L. A., Kuroda, J., Li, B., Lofi, J., Margari, V., Martrat, B., Miller, M. D., Nanayama, F., Nishida, N., Richter, C., Rodrigues, T., Rodríguez-Tovar, F. J., Freixo Roque, A. C., Sanchez Goni, M. F., Sierro Sánchez, F. J., Singh, A. D., Skinner, L., Sloss, C. R., Takashimizu, Y., Tjallingii, R., Tzanova, A., Tzedakis, C., Voelker, A., Xuan, C. and Williams, T. (2013) 'The "Shackleton Site" (IODP Site U1385) on the Iberian Margin', *Scientific Drilling*, (16), pp. 13-19.

Holcombe, R. (2011) 'GEOrient, ver 9.5.0. Software for graphical analyses of structural orientations', *Georient, Ver 9.5.0*.

Hoogakker, B. A. A., Rothwell, R. G., Rohling, E. J., Paterne, M., Stow, D. A. V., Herrle, J. O. and Clayton, T. (2004) 'Variations in terrigenous dilution in western Mediterranean Sea pelagic sediments in response to climate change during the last glacial cycle', *Marine Geology*, 211(1), pp. 21-43.

Horowitz, A. J. and Elrick, K. A. (1987) 'The relation of stream sediment surface area, grain size and composition to trace element chemistry', *Applied Geochemistry*, 2(4), pp. 437-451.

Houben, M., Barnhoorn, A., Drury, M., Peach, C. and Spiers, C. (2014) 'Microstructural Investigation of the Whitby Mudstone (UK) As an Analog for Posidonia Shale (NL)', in *76th EAGE Conference and Exhibition 2014*. Armsterdam, Netherlands.

Houben, M. E. (2013) *In situ characteriation of the microstructure and porosity of Opalinus Clay (Mont Terri Rock Laboratory, Switzerland)*. PhD thesis. Georessourcen und Materialtechnik, RWTH Aachen, Aachen.

Houben, M. E., Barnhoorn, A., Lie-A-Fat, J., Ravestein, T., Peach, C. J. and Drury, M. R. (2016) 'Microstructural characteristics of the Whitby Mudstone Formation (UK)', *Marine and Petroleum Geology*, 70, pp. 185-200.

Houben, M. E., Desbois, G. and Urai, J. L. (2013) 'Pore morphology and distribution in the Shaly facies of Opalinus Clay (Mont Terri, Switzerland): Insights from representative 2D BIB–SEM investigations on mm to nm scale', *Applied Clay Science*, 71, pp. 82-97.

Hoyanagi, K., Kawagata, S., Koto, S., Kamihashi, T., Ikehara, M. and (2014) 'Data report: Pleistocene benthic foraminiferal oxygen and stable carbon isotopes and their application for age models, Hole U1352, offshore New Zealand', in Fulthorpe, C. S., Hoyanagi, K., Blum, P. and The Expedition 317 Scientists (eds.) *Proc. IODP, 317*. Tokyo: Integrated Ocean Drilling Program Management International, Inc.

Huang, J., Cavanaugh, T. and Nur, B. (2013) 'An introduction to SEM operational principles and geologic applications for shale hydrocarbon reservoirs', *American Association of Petroleum Geologists Memoir*, (102), pp. 1-6.

Hurley, N. F., Zhang, T., Zhao, W. and Ibrahim, M. A. (2014) 'Methods to build 3D digital models of porous media using a combination of high- and low-resolution data and multi-point statistics'. Google Patents. Available at: https://www.google.com/patents/US8908925.

Hurst, C. W. (1987) *Post-depositional structural changes in clay sediments*. PhD thesis. Sheffield City Polytechnic.

Igathinathane, C., Pordesimo, L. O., Columbus, E. P., Batchelor, W. D. and Methuku, S. R. (2008) 'Shape identification and particles size distribution from basic shape parameters using ImageJ', *Computers and Electronics in Agriculture*, 63(2), pp. 168-182.

Ingram, R. L. (1953) 'Fissility of mudrocks', *Geological Society of America Bulletin*, 64(8), pp. 869-878.

Jacob, G., Kisch, H. J. and van der Pluijm, B. A. (2000) 'The relationship of phyllosilicate orientation, X-ray diffraction intensity ratios, and c/b fissility ratios in metasedimentary rocks of the Helvetic zone of the Swiss Alps and the Caledonides of Jämtland, central western Sweden', *Journal of Structural Geology*, 22(2), pp. 245-258.

Janssen, C., Kanitpanyacharoen, W., Wenk, H. R., Wirth, R., Morales, L., Rybacki, E., Kienast, M. and Dresen, G. (2012) 'Clay fabrics in SAFOD core samples', *Journal of Structural Geology*, 43, pp. 118-127.

Javadpour, F. (2009) 'Nanopores and Apparent Permeability of Gas Flow in Mudrocks (Shales and Siltstone)', *Journal of Canadian Petroleum Technology*, 48(8), pp. 16-21.

Jiang, Z. and Liu, L. a. (2011) 'A pretreatment method for grain size analysis of red mudstones', *Sedimentary Geology*, 241(1–4), pp. 13-21.

Jiang, Z., van Dijke, M. I. J., Sorbie, K. S. and Couples, G. D. (2013) 'Representation of multiscale heterogeneity via multiscale pore networks', *Water Resources Research*, 49(9), pp. 5437-5449.

Jim, C. Y. (1985) 'Impregnation of moist and dry unconsolidated clay samples using spurr resin for microstructural studies', *Journal of Sedimentary Petrology*, 55(4), pp. 597-599.

Jones, K. P. N., McCave, I. N. and Weaver, P. P. E. (1992) 'Textural and dispersal patterns of thick mud turbidites from the Madeira Abyssal plain', *Marine Geology*, 107(3), pp. 149-173.

Josh, M., Esteban, L., Delle Piane, C., Sarout, J., Dewhurst, D. N. and Clennell, M. B. (2012) 'Laboratory characterisation of shale properties', *Journal of Petroleum Science and Engineering*, 88–89, pp. 107-124.

Kameda, A., Dvorkin, J., Keehm, Y., Nur, A. and Bosl, W. (2006) 'Permeability-porosity transforms from small sandstone fragments', *Geophysics*, 71(1), pp. 11-19.

Kang, S. M., Fathi, E., Ambrose, R. J., Akkutlu, I. Y. and Sigal, R. F. (2011) 'Carbon dioxide storage capacity of organic-rich shales', *SPE Journal*, 16(4), pp. 842-855.

Kanitpanyacharoen, W., Kets, F. B., Wenk, H.-R. and Wirth, R. (2012) 'Mineral preferred orientation and microstructure in the Posidonia shale in relation to different degrees of thermal maturity', *Clays and Clay Minerals*, 60(3), pp. 315-329.

Kanitpanyacharoen, W., Vasin, R., Wenk, H. R. and Dewhurst, D. N. (2014) 'Linking preferred orientations to elastic anisotropy in muderong shale, Australia', *Geophysics*, 80(1), pp. C9-C19.

Kase, Y., Sato, M., Nishida, N., Ito, M., Mukti, M. M. r., Ikehara, K. and Takizawa, S. (2016) 'The use of microstructures for discriminating turbiditic and hemipelagic muds and mudstones', *Sedimentology*, 63(7), pp. 2066-2086.

Kasprzhitskii, A., Lazorenko, G., Yavna, V. and Daniel, P. (2016) 'DFT theoretical and FT-IR spectroscopic investigations of the plasticity of clay minerals dispersions', *Journal of Molecular Structure*, 1109, pp. 97-105.

Kaufhold, S., Dohrmann, R., Klinkenberg, M., Siegesmund, S. and Ufer, K. (2010) 'N2-BET specific surface area of bentonites', *Journal of Colloid and Interface Science*, 349(1), pp. 275-282.

Kawamura, K. and Ogawa, Y. (2004) 'Progressive change of pelagic clay microstructure during burial process: examples from piston cores and ODP cores', *Marine Geology*, 207(1–4), pp. 131-144.

Keller, L. M., Schuetz, P., Erni, R., Rossell, M. D., Lucas, F., Gasser, P. and Holzer, L. (2013) 'Characterization of multi-scale microstructural features in Opalinus Clay', *Microporous and Mesoporous Materials*, 170, pp. 83-94.

Keulen, N., Heilbronner, R., Stünitz, H., Boullier, A.-M. and Ito, H. (2007) 'Grain size distributions of fault rocks: A comparison between experimentally and naturally deformed granitoids', *Journal of Structural Geology*, 29(8), pp. 1282-1300.

Klaver, J., Desbois, G., Urai, J. L. and Littke, R. (2012) 'BIB-SEM study of the pore space morphology in early mature Posidonia Shale from the Hils area, Germany', *International Journal of Coal Geology*, 103, pp. 12-25.

Kolla, V. and Coumes, F. (1987) 'Morphology,internal structure, seismic stratigraphy, and sedimentation of Indus Fan', *American Association of Petroleum Geologists Bulletin*, 71(6), pp. 650-677.

Kominz, M. A., Miller, K. G., Browning, J. V., Katz, M. E. and Mountain, G. S. (2016) 'Miocene relative sea level on the New Jersey shallow continental shelf and coastal plain derived from one-dimensional backstripping: A case for both eustasy and epeirogeny', *Geosphere*, 12(5), pp. 1437-1456.

Kominz, M. A., Patterson, K. and Odette, D. (2011) 'Lithology dependence of porosity in slope and deep marine sediments', *Journal of Sedimentary Research*, 81(10), pp. 730-742.

Kong, M., Bhattacharya, R. N., James, C. and Basu, A. (2005) 'A statistical approach to estimate the 3D size distribution of spheres from 2D size distributions', *Geological Society of America Bulletin*, 117(1-2), pp. 244-249.

Krishna, K. S., Rao, D. G. and Sar, D. (2006) 'Nature of the crust in the Laxmi Basin (14 degrees-20 degrees N), western continental margin of India', *Tectonics*, 25(1), pp. 1-18.

Krynine, P. D. (1948) 'The megascopic study and field classification of sedimentary rocks', *Journal of Geology*, 56(2), pp. 130-165.

Kuila, U., McCarty, D. K., Derkowski, A., Fischer, T. B. and Prasad, M. (2014) 'Total porosity measurement in gas shales by the water immersion porosimetry (WIP) method', *Fuel*, 117, Part B, pp. 1115-1129.

Kuila, U. and Prasad, M. (2013) 'Specific surface area and pore-size distribution in clays and shales', *Geophysical Prospecting*, 61(2), pp. 341-362.

Kuila, U., Prasad, M., Derkowski, A. and McCarty, D. (2012) 'Compositional controls on mudrock pore-size distribution: an example from niobrara formation', *Society of Petroleum Engineers*.

Kwan, A. K. H., Mora, C. F. and Chan, H. C. (1999) 'Particle shape analysis of coarse aggregate using digital image processing', *Cement and Concrete Research*, 29(9), pp. 1403-1410.

Lambe, T. W. (1958) 'The structure of compacted clay', *Jnl. of the Soil Mech. and Foundn. Div ASCE*, 84, pp. 10-34.

Lash, G. G. and Blood, D. R. (2004) 'Origin of shale fabric by mechanical compaction of flocculated clay: Evidence from the Upper Devonian Rhinestreet shale, western New York, USA', *Journal of Sedimentary Research*, 74(1), pp. 110-116.

Lazar, O. R., Bohacs, K. M., Macquaker, J. H. S., Schieber, J. and Demko, T. M. (2015) 'Capturing key attributes of fine-grained sedimentary rocks in outcrops, cores, and thin sections: Nomenclature and description guidelines', *Journal of Sedimentary Research*, 85(3), pp. 230-246.

Lee, J. R. J., Smith, M. L. and Smith, L. N. (2007) 'A new approach to the three-dimensional quantification of angularity using image analysis of the size and form of coarse aggregates', *Engineering Geology*, 91(2–4), pp. 254-264.

Lemmens, H. and Richards, D. (2013) 'Multiscale imaging of shale samples in the scanning electron microscope', *American Association of Petroleum Geologists Memoir*, (102), pp. 27-35.

Lewis, D. W. and McConchie, D. M. (1994) *Analytical Sedimentology*. Great Britain: Chapman & Hall.

Lin, B. and Cerato, A. B. (2014) 'Applications of SEM and ESEM in Microstructural Investigation of Shale-Weathered Expansive Soils along Swelling-Shrinkage Cycles', *Engineering Geology*, 177, pp. 66-74.

Lin, B., Chen, M., Jin, Y. and Pang, H. (2015) 'Modeling pore size distribution of southern Sichuan shale gas reservoirs', *Journal of Natural Gas Science and Engineering*, 26, pp. 883-894.

Llave, E., Hernández-Molina, F. J., Stow, D. A. V., Fernández-Puga, M. C., García, M., Vázquez, J. T., Maestro, A., Somoza, L. and Díaz del Río, V. (2007) 'Reconstructions of the Mediterranean Outflow Water during the quaternary based on the study of changes in buried mounded drift stacking pattern in the Gulf of Cadiz', *Marine Geophysical Researches*, 28(4), pp. 379-394.

Llave, E., Matias, H., Hernández-Molina, F. J., Ercilla, G., Stow, D. A. V. and Medialdea, T. (2011) 'Pliocene–Quaternary contourites along the northern Gulf of Cadiz margin: sedimentary stacking pattern and regional distribution', *Geo-Marine Letters*, 31(5), pp. 377-390.

Loizeau, J. L., Arbouille, D., Santiago, S. and Vernet, J. P. (1994) 'Evaluation of a wide range laser diffraction grain size analyser for use with sediments', *Sedimentology*, 41(2), pp. 353-361.

Lonardelli, I., Wenk, H. R. and Ren, Y. (2007) 'Preferred orientation and elastic anisotropy in shales', *Geophysics*, 72(2), pp. D33-D40.

Loucks, R. G., Reed, R. M., Ruppel, S. C. and Hammes, U. (2010) 'Preliminary classification of matrix pores in mudrocks', *Gulf Coast Association of Geological Societies Transactions*, 60, pp. 435-441.

Loucks, R. G., Reed, R. M., Ruppel, S. C. and Hammes, U. (2012) 'Spectrum of pore types and networks in mudrocks and a descriptive classification for matrix-related mudrock pores', *American Association of Petroleum Geologists Bulletin*, 96(6), pp. 1071-1098.

Loucks, R. G., Reed, R. M., Ruppel, S. C. and Jarvie, D. M. (2009) 'Morphology, genesis, and distribution of nanometer-scale pores in siliceous mudstones of the mississippian barnett shale', *Journal of Sedimentary Research*, 79(12), pp. 848-861.

Lovie, S. (2005) 'Empirical Quantile–Quantile Plots', in *Encyclopedia of Statistics in Behavioral Science*. John Wiley & Sons, Ltd.

Lowell, S., Shields, J. E., Thomas, M. A. and Thommes, M. (2012) *Characterization of porous solids and powders: surface area, pore size and density*. Springer Science & Business Media.

Lu, H., Fulthorpe, C. S. and Mann, P. (2003) 'Three-dimensional architecture of shelf-building sediment drifts in the offshore Canterbury Basin, New Zealand', *Marine Geology*, 193(1–2), pp. 19-47.

Lundegard, P. D. and Samuels, N. D. (1980) 'Field classification of fine-grained sedimentary rocks', *Journal of Sedimentary Research*, 50(3), pp. 781-786.

Macquaker, J. and Howell, J. (1999) 'Small-scale (< 5.0 m) vertical heterogeneity in mudstones: implications for high-resolution stratigraphy in siliciclastic mudstone successions', *Journal of the Geological Society*, 156(1), pp. 105-112.

Macquaker, J. H. and Adams, A. (2003) 'Maximizing information from fine-grained sedimentary rocks: an inclusive nomenclature for mudstones', *Journal of Sedimentary Research*, 73(5), pp. 735-744.

Macquaker, J. H. and Jones, C. R. (2002) 'A sequence-stratigraphic study of mudstone heterogeneity: a combined petrographic/wireline log investigation of Upper Jurassic Mudstones from the North Sea (UK)', *Geological Applications of Well Logs. AAPG Methods in Exploration Series*, 13, pp. 123-141.

Maldonado, A., Somoza, L. and Pallares, L. (1999) 'The Betic orogen and the Iberian-African boundary in the Gulf of Cadiz: geological evolution (central North Atlantic)', *Marine Geology*, 155(1-2), pp. 9-43.

Malod, J. A., Droz, L., Kemal, B. M. and Patriat, P. (1997) 'Early spreading and continental to oceanic basement transition beneath the Indus deep-sea fan: Northeastern Arabian Sea', *Marine Geology*, 141(1-4), pp. 221-235.

Malverns Instruments Limited (2012) 'A basic guide to particle characterization'. March 23, 2016. p. 26. Available at: http://www.cif.iastate.edu/sites/default/files/uploads/Other_Inst/Particle%20Size/Particle%20Characterization%20Guide.pdf.

Mardia, K. V. and Jupp, P. E. (2000) *Directional Statistics, Directional Statistics.* Chichester: John Wiley and Sons.

Martínez-Nistal, A., Veniale, F., Setti, M. and Cotecchia, F. (1999) 'A scanning electron microscopy image processing method for quantifying fabric orientation of clay geomaterials', *Applied Clay Science*, 14(4), pp. 235-243.

Matenaar, I. F. (2002) *Compaction and microfabric rearrangement of fine-grained siliciclastic sediments*. PhD thesis. University of Newcastle -Upon-Tyne.

Mehana, M. and El-monier, I. (2016) 'Shale characteristics impact on Nuclear Magnetic Resonance (NMR) fluid typing methods and correlations', *Petroleum*, 2(2), pp. 138-147.

Miall, A. D. (2015) *Stratigraphy: A modern synthesis*. Switzerland: Springer International Publishing.

Miles, P. R., Munschy, M. and Ségoufin, J. (1998) 'Structure and early evolution of the Arabian Sea and east Somali Basin', *Geophysical Journal International*, 134(3), pp. 876-888.

Milliken, K. (2014) 'A Compositional Classification for Grain Assemblages in Fine-Grained Sediments and Sedimentary Rocks', *Journal of Sedimentary Research*, 84(12), pp. 1185-1199.

Milliken, K., Choh, S.-J., Papazis, P. and Schieber, J. (2007) '"Cherty" stringers in the Barnett Shale are agglutinated foraminifera', *Sedimentary Geology*, 198(3–4), pp. 221-232.

Milliken, K. L. (2016) 'A compositional classification for grain assemblages in fine-grained sediments and sedimentary rocks-reply', *Journal of Sedimentary Research*, 86(1), pp. 6-10.

Milliken, K. L., Rudnicki, M., Awwiller, D. N. and Zhang, T. (2013) 'Organic matter-hosted pore system, Marcellus Formation (Devonian), Pennsylvania', *American Association of Petroleum Geologists Bulletin*, 97(2), pp. 177-200.

Milner, M., McLin, R. and Petriello, J. (2010) *Society of Petroleum Engineers - Canadian Unconventional Resources and International Petroleum Conference 2010*.

Minshull, T. A., Lane, C. I., Collier, J. S. and Whitmarsh, R. B. (2008) 'The relationship between rifting and magmatism in the northeastern Arabian Sea', *Nature Geosci*, 1(7), pp. 463-467.

Moiola, R. and Weiser, D. (1968) 'Textural parameters: an evaluation', *Journal of Sedimentary Research*, 38(1), pp. 45-53.

Mondol, N. H., Bjørlykke, K., Jahren, J. and Høeg, K. (2007) 'Experimental mechanical compaction of clay mineral aggregates—Changes in physical properties of mudstones during burial', *Marine and Petroleum Geology*, 24(5), pp. 289-311.

Moon, C. and Hurst, C. (1984) 'Fabric of muds and shales: an overview', *Geological Society, London, Special Publications*, 15(1), pp. 579-593.

Moon, C. F. (1972) 'The microstructure of clay sediments', *Earth-Science Reviews*, 8(3), pp. 303-321.

Mulder, T., Faugères, J. C. and Gonthier, E. (2008) 'Chapter 21 Mixed Turbidite–Contourite Systems', in Rebesco, M. and Camerlenghi, A. (eds.) *Developments in Sedimentology*. Elsevier, pp. 435-456.

Mulder, T., Hüneke, H. and Van Loon, A. J. (2011) 'Chapter 1 - Progress in Deep-Sea Sedimentology', in Heiko, H. and Thierry, M. (eds.) *Developments in Sedimentology*. Elsevier, pp. 1-24.

Mulder, T., Razin, P. and Faugeres, J. C. (2009) 'Hummocky cross-stratification-like structures in deep-sea turbidites: Upper Cretaceous Basque basins (Western Pyrenees, France)', *Sedimentology*, 56(4), pp. 997-1015.

Mulder, T., Syvitski, J. P. M., Migeon, S., Faugères, J. C. and Savoye, B. (2003) 'Marine hyperpycnal flows: Initiation, behaviorand related deposits. A review', *Marine and Petroleum Geology*, 20(6-8), pp. 861-882.

Munson, E. O., Chalmers, G. R. L., Bustin, R. M. and Li, K. (2016) 'Utilizing smear mounts for X-ray diffraction as a fully quantitative approach in rapidly characterizing the mineralogy of shale gas reservoirs', *Journal of Unconventional Oil and Gas Resources*, 14, pp. 22-31.

Mutti, E., Bernoulli, D., Lucchi, F. R. and Tinterri, R. (2009) 'Turbidites and turbidity currents from Alpine 'flysch' to the exploration of continental margins', *Sedimentology*, 56(1), pp. 267-318.

Mutti, E. and Normark, W. R. (1987) 'Comparing Examples of Modern and Ancient Turbidite Systems: Problems and Concepts', in Leggett, J. K. and Zuffa, G. G. (eds.) *Marine Clastic Sedimentology: Concepts and Case Studies*. Dordrecht: Springer Netherlands, pp. 1-38.

Mutti, E., Tinterri, R., Remacha, E., Mavilla, N., Angella, S. and Fava, L. 39 (1999) 'An introduction to the analysis of ancient turbidite basins from an outcrop perspective' *American Association of Petroleum Geologists Continuing Education Course Note Series*. pp. 1-97.

Naini, B. R. and Talwani, M. (1982) 'Structural framework and the evolutionary history of the continental margin of western India', *Studies in Continental Margin Geology*, 34, pp. 167-191.

Nishida, N. (2016) 'Microstructure of muddy contourites from the Gulf of Cádiz', *Marine Geology*, 377, pp. 110-117.

Noiriel, C., Gouze, P. and Bernard, D. (2004) 'Investigation of porosity and permeability effects from microstructure changes during limestone dissolution', *Geophysical research letters*, 31(24).

Normark, W. R. and Piper, D. J. W. (1991) 'Initiation processes and flow evolution of turbidity currents: implications for the depositional record', *From shoreline to abyss: contributions in marine geology in honor of Francis Parker Shepard*, 46, pp. 207-230.

Nygard, R., Gutierrez, M., Hoeg, K. and Bjorlykke, K. (2004) 'Influence of burial history on microstructure and compaction behaviour of Kimmeridge clay', *Petroleum Geoscience*, 10(3), pp. 259-270.

O'Brien, N. and Slatt, R. M. (1990) *Argillaceous rock atlas*. New York: Springer-Verlag.

O'Brien, N. R. (1970) 'The fabric of shale-an electron microscope study', *Sedimentology*, 15(3-4), pp. 229-246.

O'Brien, N. R. (1987) 'The effects of bioturbation on the fabric of shale', *Journal of Sedimentary Petrology*, 57(3), pp. 449-455.

O'Brien, N. R., Brett, C. E. and Taylor, W. L. (1994) 'Microfabric and taphonomic analysis in determining sedimentary processes in marine mudstones - example from Silurian of New-York', *Journal of Sedimentary Research Section a-Sedimentary Petrology and Processes*, 64(4), pp. 847-852.

O'Brien, N. R., Nakazawa, K. and Tokuhashi, S. (1980) 'Use of clay fabric to distinguish turbiditic and hemipelagic siltstones and silts', *Sedimentology*, 27(1), pp. 47-61.

O'Brien, N. R. and Pietraszek-Mattner, S. (1998) 'Origin of the fabric of laminated fine-grained glaciolacustrine deposits', *Journal of Sedimentary Research*, 68(5), pp. 832-840.

O'Brien, N. R., Slatt, R. M. and Senftle, J. (1994) 'The significance of oil shale fabric in primary hydrocarbon migration', *Fuel*, 73(9), pp. 1518-1522.

Ochoa, J., Wolak, J. and Gardner, M. H. (2013) 'Recognition criteria for distinguishing between hemipelagic and pelagic mudrocks in the characterization of deep-water reservoir heterogeneity', *American Association of Petroleum Geologists Bulletin*, 97(10), pp. 1785-1803.

Odom, I. E. (1967) 'Clay fabric and its relation to structural properties in Mid-Continent Pennsylvanian sediments', *Journal of Sedimentary Petrology*, 37(2), pp. 610-623.

Otiede, D. O., Wu, K. and Olafuyi, O. A. (2012) '3D Pore Space Characterization for Classification of Flow Properties of Reservoir Rocks', 2012/1/1/. SPE: Society of Petroleum Engineers. doi: 10.2118/162977-MS Available at: https://www.onepetro.org:443/download/conference-paper/SPE-162977-MS?id=conference-paper%2FSPE-162977-MS.

Pak, T., Butler, I. B., Geiger, S., van Dijke, M. I. J., Jiang, Z. and Surmas, R. (2016) 'Multiscale pore-network representation of heterogeneous carbonate rocks', *Water Resources Research*, 52(7), pp. 5433-5441.

Pal, N. R. and Pal, S. K. (1993) 'A review on image segmentation techniques', *Pattern Recognition*, 26(9), pp. 1277-1294.

Pandey, D. K., Clift, P. D., Kulhanek, D. K., Andò, S., Bendle, J. A. P., Bratenkov, S., Griffith, E. M., Gurumurthy, G. P., Hahn, A., Iwai, M., Khim, B.-K., Kumar, A., Kumar, A. G., Liddy, H. M., Lu., H., Lyle, M. W., Mishra, R., Radhakrishna, T., Routledge, C. M., Saraswat, R., Saxena, R., Scardia, G., Sharma, G. K., Singh, A. D., Steinke, S., Suzuki, K., Tauxe, L., Tiwari, M., Xu, Z. and Yu, Z. (2015) 'Deep sea drilling in the Arabian Sea: constraining tectonic-monsoon interactions in South Asia', *IODP Preliminary Report355*, pp. 1-46.

Passey, Q. R., Bohacs, K., Esch, W. L., Klimentidis, R. and Sinha, S. (2010) 'From oil-prone source rock to gas-producing shale reservoir–geologic and petrophysical characterization of unconventional shale-gas reservoirs', in Beijing, China: SPE.

Picard, M. D. (1971) 'Classification of fine-grained sedimentary rocks', *Journal of Sedimentary Research*, 41(1), pp. 179-195.

Pickering, K. T. and Hiscott, R. N. (2015) *Deep marine systems: processes, deposits, environments, tectonics and sedimentation*. American Geophysical Union.

Pinheiro, L. M., Wilson, R. C. L., Pena dos Reis, R., Whitmarsh, R. B. and Ribeiro, A. (1996) 'The western Iberia margin: A geophysical and geological overview', *Proceedings of the Ocean Drilling Program, Scientific Results*, 149, pp. 3-23.

Piper, D. J. W. (1977) *Manual of Sedimentological techniques*. Dalhousie University: Department of Geology and Oceanography.

Piper, D. J. W. and Deptuck, M. (1997) 'Fine-grained turbidites of the Amazon Fan: Facies characterization and interpretation', *Proceedings of the Ocean Drilling Program, Scientific Results,* 155, pp. 79-108.

Piper, D. J. W. and Normark, W. R. (2009) 'Processes that initiate turbidity currents and their influence on turbidites: A marine geology perspective', *Journal of Sedimentary Research*, 79(6), pp. 347-362.

Plink-Björklund, P. and Steel, R. J. (2004) 'Initiation of turbidity currents: outcrop evidence for Eocene hyperpycnal flow turbidites', *Sedimentary Geology*, 165(1–2), pp. 29-52.

Plint, A. G. (2014) 'Mud dispersal across a Cretaceous prodelta: Storm-generated, wave-enhanced sediment gravity flows inferred from mudstone microtexture and microfacies', *Sedimentology*, 61(3), pp. 609-647.

Potter, P. E., Maynard, J. B. and Depetris, P. J. (2005) *Mud and mudstones: Introduction and overview*. Berlin Heidelberg: Springer Berlin

Potter, P. E., Maynard, J. B. and Pryor, W. A. (1980) *Sedimentology of shale*. Springer-Verlag New York.

Prins, M. A., Postma, G., Cleveringa, J., Cramp, A. and Kenyon, N. H. (2000) 'Controls on terrigenous sediment supply to the Arabian Sea during the late Quaternary: the Indus Fan', *Marine Geology*, 169(3–4), pp. 327-349.

Rebesco, M. (2014) 'Contourites☆', in *Reference Module in Earth Systems and Environmental Sciences*. Elsevier, pp. 1-16.

Rebesco, M., Hernández-Molina, F. J., Van Rooij, D. and Wåhlin, A. (2014) 'Contourites and associated sediments controlled by deep-water circulation processes: State-of-the-art and future considerations', *Marine Geology*, 352, pp. 111-154.

Reed, R. M., Loucks, R. G. and Ruppel, S. C. (2014) 'Comment on "Formation of nanoporous pyrobitumen residues during maturation of the Barnett Shale (Fort Worth Basin)" by Bernard et al. (2012)', *International Journal of Coal Geology*, 127, pp. 111-113.

Reichelt, R. (2007) 'Scanning Electron Microscopy', in Hawkes, P. and Spence, J. H. (eds.) *Science of Microscopy*. Springer New York, pp. 133-272. 3.

Reynolds, S. and Gorsline, D. S. (1991) 'Silt Microfabric of Detrital, Deep Sea Mud(stone)s (California Continental Borderland) as Shown by Backscattered Electron Microscopy', in Bennett, R. H., Bryant, W. R., Hulbert, M. H., Chiou, W. A., Faas, R. W., Kasprowicz, J., Li, H., Lomenick, T., O'brien, N. R., Pamukcu, S., Smart, P., Weaver, C. E. and Yamamoto, T. (eds.) *Microstructure of Fine-Grained Sediments: From Mud to Shale*. New York, NY: Springer New York, pp. 203-211.

Reynolds, S. and Gorsline, D. S. (1992) 'Clay microfabric of deep-sea, detrital mud(stone)s, California continental borderland', *Journal of Sedimentary Petrology*, 62(1), pp. 41-53.

Rhodes, M. E., Bijeljic, B. and Blunt, M. J. (2008) 'Pore-to-field simulation of single-phase transport using continuous time random walks', *Advances in Water Resources*, 31(12), pp. 1527-1539.

Rodríguez-Tovar, F. J. and Dorador, J. (2014) 'Ichnological analysis of Pleistocene sediments from the IODP Site U1385 "Shackleton Site" on the Iberian margin: Approaching paleoenvironmental conditions', *Palaeogeography, Palaeoclimatology, Palaeoecology*, 409, pp. 24-32.

Rodríguez-Tovar, F. J., Dorador, J., Grunert, P. and Hodell, D. (2015) 'Deep-sea trace fossil and benthic foraminiferal assemblages across glacial Terminations 1, 2 and 4 at the "Shackleton Site" (IODP Expedition 339, Site U1385)', *Global and Planetary Change*, 133, pp. 359-370.

Røgen, B., Gommesen, L. and Fabricius, I. L. (2001) 'Grain size distributions of chalk from image analysis of electron micrographs', *Computers & Geosciences*, 27(9), pp. 1071-1080.

Rouquerol, F., Rouquerol, J., Sing, K. S. W., Maurin, G. and Llewellyn, P. (eds.) (2014) *Adsorption by Powders and Porous Solids: Principles, Methodology and Applications*. Oxford: Academic Press.

Rouquerol, J., Avnir, D., Fairbridge, C. W., Everett, D. H., Haynes, J. M., Pernicone, N., Ramsay, J. D. F., Sing, K. S. W. and Unger, K. K. 66 (1994) 'Recommendations for the characterization of porous solids (Technical Report)' *Pure and Applied Chemistry*. pp. 1739-1758 8. (Accessed: 2016-02-23t20:02:10.537+01:00).

Rubin, D. M. (2004) 'A simple autocorrelation algorithm for determining grain size from digital images of sediment', *Journal of Sedimentary Research*, 74(1), pp. 160-165.

Sahagian, D. L. and Proussevitch, A. A. (1998) '3D particle size distributions from 2D observations: Stereology for natural applications', *Journal of Volcanology and Geothermal Research*, 84(3-4), pp. 173-196.

Saidian, M., Kuila, U., Rivera, S., Godinez, L. J. and Prasad, M. (2014) 'Porosity and pore size distribution in mudrocks: A comparative study for haynesville, niobrara, monterey and eastern european silurian formations', *Society of Petroleum Engineers - SPE/AAPG/SEG Unconventional Resources Technology Conference*. Denver, Colorado, USA, 2014/8/25/. Unconventional Resources Technology Conference. doi: 10.15530/urtec-2014-1922745.

Sanei, H., Ardakani, O. H., Ghanizadeh, A., Clarkson, C. R. and Wood, J. M. (2016) 'Simple petrographic grain size analysis of siltstone reservoir rocks: An example from the Montney tight gas reservoir (Western Canada)', *Fuel*, 166, pp. 253-257.

Saner, S., Cagatay, M. N. and Al Sanounah, A. M. (1996) 'Relationships between shale content and grain-size parameters in the Safaniya Sandstone reservoir, NE Saudi Arabia', *Journal of Petroleum Geology*, 19(3), pp. 305-320.

Saraji, S. and Piri, M. (2015) 'The representative sample size in shale oil rocks and nano-scale characterization of transport properties', *International Journal of Coal Geology*, 146, pp. 42-54.

Schieber, J. (1999) 'Distribution and deposition of mudstone facies in the Upper Devonian Sonyea Group of New York', *Journal of Sedimentary Research*, 69(4).

Schieber, J. (2003) 'Simple gifts and buried treasures—implications of finding bioturbation and erosion surfaces in black shales', *The Sedimentary Record*, 1(2), pp. 4-8.

Schieber, J. (2010) 'Common themes in the formation and preservation of intrinsic porosity in shales and mudstones - Illustrated with examples across the phanerozoic', in *SPE Unconventional Gas Conference*. Pittsburgh, Pennsylvania, USA: SPE, pp. 428-437.

Schieber, J. (2011) 'Shifting Paradigms in Shale Sedimentology-The Implications of Recent Flume Studies for Interpreting Shale Fabrics and Depositional Environments', in *Recovery–CSPG CSEG CWLS Convention*. Calgary, Canada: Canadian society of exploration Geophysicists, pp. 1-4.

Schieber, J. (2014) 'Traces in the dark-sedimentary processes and facies gradients in the Upper Devonian-Lower Mississippian upper shale member of the Bakken Formation, Williston Basin, North Dakota, U.S.A. - Discussion', *Journal of Sedimentary Research*, 84(10), pp. 837-838.

Schieber, J. (2015) 'Discussion: "Mud dispersal across a Cretaceous prodelta: Storm-generated, wave-enhanced sediment gravity flows inferred from mudstone microtexture and microfacies"', *Sedimentology*, 62(1), pp. 389-393.

Schieber, J., Southard, J. and Thaisen, K. (2007) 'Accretion of mudstone beds from migrating floccule ripples', *Science*, 318(5857), pp. 1760-1763.

Schieber, J. and Zimmerle, W. (1998) 'Introduction and overview: the history and promise of shale research', in Schieber J, Zimmerle W and P., S. (eds.) *Shales and Mudstones*. Schweizerbart'sche Verlagsbuchhandlung (Nagele u. Obermiller): Stuttgart, E, pp. 1-10.

Schindelin, J., Arganda-Carreras, I., Frise, E., Kaynig, V., Longair, M., Pietzsch, T., Preibisch, S., Rueden, C., Saalfeld, S., Schmid, B., Tinevez, J. Y., White, D. J., Hartenstein, V., Eliceiri, K., Tomancak, P. and Cardona, A. (2012) 'Fiji: an open-source platform for biological-image analysis', *Nature Methods*, 9(7), pp. 676-682.

Schneider, C. A., Rasband, W. S. and Eliceiri, K. W. (2012) 'NIH Image to ImageJ: 25 years of image analysis', *Nature Methods*, 9(7), pp. 671-675.

Schnurrenberger, D., Russell, J. and Kelts, K. (2003) 'Classification of lacustrine sediments based on sedimentary components', *Journal of Paleolimnology*, 29(2), pp. 141-154.

Seemann, T., Bertier, P., Krooss, B. M. and Stanjek, H. (2017) 'Water vapour sorption on mudrocks', *Geological Society, London, Special Publications*, 454, pp. 201-233.

Sergeyev, Y. M., Grabowska-Olszewska, B., Osipov, V. I., Sokolov, V. N. and Kolomenski, Y. N. (1980) 'The classification of microstructures of clay soils', *Journal of Microscopy*, 120(3), pp. 237-260.

Shanmugam, G. (2000) '50 years of the turbidite paradigm (1950s—1990s): deep-water processes and facies models—a critical perspective', *Marine and Petroleum Geology*, 17(2), pp. 285-342.

Shanmugam, G. (2006) 'Chapter 1 Introduction and process sedimentology', in Shanmugam, G. (ed.) *Handbook of Petroleum Exploration and Production*. Elsevier, pp. 1-17.

Shanmugam, G. (2012a) 'Chapter 1 - Introduction', in Shanmugam, G. (ed.) *Handbook of Petroleum Exploration and Production*. Elsevier, pp. 1-40.

Shanmugam, G. (2012b) 'Chapter 4 - Bottom-Current Reworked Sands', in Shanmugam, G. (ed.) *Handbook of Petroleum Exploration and Production*. Elsevier, pp. 129-219.

Shanmugam, G. (2017) 'The contourite problem', in *Sediment provenance–influence on composition from source to sink*. Elsevier, pp. 183-254.

Shepard, F. P. (1954) 'Nomenclature based on sand-silt-clay ratios', *Journal of Sedimentary Research*, 24(3).

Shephard, L. E. and Rutledge, A. K. (1991) 'Clay Fabric of Fine-Grained Turbidite Sequences from the Southern Nares Abyssal Plain', in Bennett, R., Bryant, W., Hulbert, M., Chiou, W. A., Faas, R. W., Kasprowicz, J., Li, H., Lomenick, T., O'brien, N. R., Pamukcu, S., Smart, P., Weaver, C. E. and Yamamoto, T. (eds.) *Microstructure of Fine-Grained Sediments*. Springer New York, pp. 61-72. 6.

Shi, B., Wu, Z., Inyang, H., Chen, J. and Wang, B. (1999) 'Preparation of soil specimens for SEM analysis using freeze-cut-drying', *Bulletin of Engineering Geology and the Environment*, 58(1), pp. 1-7.

Silin, D. and Kneafsey, T. (2012) 'Shale Gas: Nanometer-Scale Observations and Well Modelling', *Journal of Canadian Petroleum Technology*, 51(6), pp. 464-475.

Sing, K. (2001) 'The use of nitrogen adsorption for the characterisation of porous materials', *Colloids and Surfaces A: Physicochemical and Engineering Aspects*, 187-188, pp. 3-9.

Sing, K. S. W. (1982) 'Reporting physisorption data for gas solid systems with special reference to the determination of surface are and porosity', *Pure and Applied Chemistry*, 54(11), pp. 2201-2218.

Sintubin, M. (1994) 'Clay fabrics in relation to the burial history of shales', *Sedimentology*, 41(6), pp. 1161-1169.

Slatt, R. M. (2011) 'Important Geological Properties of Unconventional Resource Shales', *Central European Journal of Geosciences*, 3(4), pp. 435-448.

Slatt, R. M. and O'Brien, N. R. (2011) 'Pore types in the Barnett and Woodford gas shales: Contribution to understanding gas storage and migration pathways in fine-grained rocks', *American Association of Petroleum Geologists Bulletin*, 95(12), pp. 2017-2030.

Smart, P. and Tovey, N. K. (1982) *Electron microscopy of solis and sediments: techniques*. Oxford: Clarendon Press

Soe, A. K. K., Osada, M., Takahashi, M. and Sasaki, T. (2009) 'Characterization of drying-induced deformation behaviour of Opalinus Clay and tuff in no-stress regime', *Environmental Geology*, 58(6), pp. 1215-1225.

Sokolov, V. N. and O'Brien, N. R. (1990) 'A fabric classification of argillaceous rocks, sediments, soils', *Applied Clay Science*, 5(4), pp. 353-360.

Solum, J. G. and van der Pluijm, B. A. (2009) 'Quantification of fabrics in clay gouge from the Carboneras fault, Spain and implications for fault behavior', *Tectonophysics*, 475(3), pp. 554-562.

Sondergeld, C. H., Ambrose, R. J., Rai, C. S. and Moncrieff, J. (2010) *SPE Unconventional Gas Conference 2010*.

Sondergeld, C. H., Curtis, M. E. and Rai, C. S. (2012) 'Application of FIB/SEM and Argon Ion Milling to the Study of Foliated Fine Grained Organic Rich Rocks', *Microscopy and Microanalysis*, 18(S2), pp. 622-623.

Spears, D. (1980) 'Towards a classification of shales', *Journal of the Geological Society*, 137(2), pp. 125-129.

Sperazza, M., Moore, J. N. and Hendrix, M. S. (2004) 'High-resolution particle size analysis of naturally occurring very fine-grained sediment through laser diffractometry', *Journal of Sedimentary Research*, 74(5), pp. 736-743.

Srivastava, S. P., Schouten, H., Roest, W. R., Klitgord, K. D., Kovacs, L. C., Verhoef, J. and Macnab, R. (1990) 'Iberian plate kinematics - a jumping plate boundary between Eurasia and Africa', *Nature*, 344(6268), pp. 756-759.

Stelting, C. E., Bouma, A. H. and Stone, C. G. (2000) 'Fine-Grained Turbidite Systems: Overview', *American Association of Petroleum Geologists Memoir*, 72(68), pp. 1-8.

Storti, F. and Balsamo, F. (2010) 'Particle size distributions by laser diffraction: Sensitivity of granular matter strength to analytical operating procedures', *Solid Earth*, 1(1), pp. 25-48.

Stow, D. (1985a) 'Deep-sea clastics: where are we and where are we going?', *Geological Society, London, Special Publications*, 18(1), pp. 67-93.

Stow, D., Brackenridge, R., Patel, U. and Toulmin, S. (2012) 'Geohazards and Ocean Hazards in Deepwater: Overview and Methods of Assessment', 2012/4/30/. OTC: Offshore Technology Conference. doi: 10.4043/23697-MS Available at: https://www.onepetro.org:443/download/conference-paper/OTC-23697-MS?id=conference-paper%2FOTC-23697-MS.

Stow, D. and Piper, D. (1984a) 'Deep-water fine-grained sediments: facies models', *Geological Society, London, Special Publications*, 15(1), pp. 611-646.

Stow, D. and Piper, D. 15 (1984b) 'Deep-water fine-grained sediments; history, methodology and terminology' *Geological Society Special Publication* [Article]. pp. 3-14.

Stow, D. A. (1979) 'Distinguishing between fine-grained turbidites and contourites on the Nova Scotian deep water margin', *Sedimentology*, 26(3), pp. 371-387.

Stow, D. A. (1981) 'Fine-grained sediments: terminology', *Quarterly Journal of Engineering Geology and Hydrogeology*, 14(4), pp. 243-244.

Stow, D. A. (1985b) 'Fine-grained sediments in deep water: An overview of processes and facies models', *Geo-Marine Letters*, 5(1), pp. 17-23.

Stow, D. A. and Omoniyi, B. A. (2018) 'Thin-Bedded Turbidites: Overview and Petroleum Perspective', *American Association of Petroleum Geologists Memoir*, 115, p. (in press).

Stow, D. A. V. (2005) *Sedimentary rocks in the Field: a color guide*. Taylor and Francis Group.

Stow, D. A. V. and Bowen, A. J. (1978) 'Origin of lamination in deep sea, fine-grained sediments', *Nature*, 274, pp. 324–328.

Stow, D. A. V. and Bowen, A. J. (1980) 'A physical model for the transport and sorting of fine-grained sediment by turbidity currents', *Sedimentology*, 27(1), pp. 31-46.

Stow, D. A. V., Faugères, J., Gonthier, E., Cremer, M., Llave, E., Hernández-Molina, F. J., Somoza, L. and Díaz-Del-Río, V. 22 (2002a) 'Faro-Albufeira drift complex, northern Gulf of Cadiz' *Geological Society Memoir* [Article]. pp. 137-154.

Stow, D. A. V. and Faugères, J. C. (2008) 'Chapter 13 Contourite Facies and the Facies Model', in Rebesco, M. and Camerlenghi, A. (eds.) *Developments in Sedimentology*. Elsevier, pp. 223-256.

Stow, D. A. V., Hernández-Molina, F. J., Llave, E., Bruno, M., García, M., Díaz del Rio, V., Somoza, L. and Brackenridge, R. E. (2013) 'The Cadiz Contourite Channel: Sandy contourites, bedforms and dynamic current interaction', *Marine Geology*, 343, pp. 99-114.

Stow, D. A. V., Huc, A. Y. and Bertrand, P. (2001) 'Depositional processes of black shales in deep water', *Marine and Petroleum Geology*, 18(4), pp. 491-498.

Stow, D. A. V., Hunter, S., Wilkinson, D. and Hernández-Molina, F. J. (2008) 'Chapter 9 The Nature of Contourite Deposition', in Rebesco, M. and Camerlenghi, A. (eds.) *Developments in Sedimentology*. Elsevier, pp. 143-156.

Stow, D. A. V. and Johansson, M. (2000) 'Deep-water massive sands: nature, origin and hydrocarbon implications', *Marine and Petroleum Geology*, 17(2), pp. 145-174.

Stow, D. A. V., Ogawa, Y., Lee, I. T. and Mitsuzawa, K. 22 (2002b) 'Neogene contourites, Miura-Boso forearc basin, SE Japan' *Geological Society Memoir*. pp. 409-419.

Stow, D. A. V. and Shanmugam, G. (1980) 'Sequence of structures in fine-grained turbidites: Comparison of recent deep-sea and ancient flysch sediments', *Sedimentary Geology*, 25(1-2), pp. 23-42.

Stow, D. A. V. and Tabrez, A. R. 129 (1998) 'Hemipelagites: processes, facies and model' *Geological Society Special Publication*. pp. 317-337.

Stow, D. V., Faugères, J. C., Viana, A. and Gonthier, E. (1998) 'Fossil contourites: A critical review', *Sedimentary Geology*, 115(1-4), pp. 3-31.

Strachan, L. J., Bostock, H. C., Barnes, P. M., Neil, H. L. and Gosling, M. (2016) 'Non-cohesive silt turbidity current flow processes; insights from proximal sandy-silt and silty-sand turbidites, Fiordland, New Zealand', *Sedimentary Geology*, 342, pp. 118-132.

Subrahmanyam, C. and Chand, S. (2006) 'Evolution of the passive continental margins of India—a geophysical appraisal', *Gondwana Research*, 10(1–2), pp. 167-178.

Suleimenova, A., Bake, K. D., Ozkan, A., Valenza, J. J., Kleinberg, R. L., Burnham, A. K., Ferralis, N. and Pomerantz, A. E. (2014) 'Acid demineralization with critical point drying: A method for kerogen isolation that preserves microstructure', *Fuel*, 135, pp. 492-497.

Suttle, M. D., Genge, M. J. and Russell, S. S. (2017) 'Shock fabrics in fine-grained micrometeorites', *Meteoritics & Planetary Science*, 52(10), pp. 2258-2274.

Swapp, S. M. (2016) 'Scanning Electron Microscopy (SEM)'. 01/11/2016. Available at: http://serc.carleton.edu/research_education/geochemsheets/browse.html.

Swartz, J. F. and Lindsley-Griffin, N. (1990) 'An improved impregnation technique for studying structure of unlithified cohesive sediments', *Proceedings of the Ocean Drilling Program, Scientific Results,* , 112, pp. 87-91.

Syvitski, J. P., Leblanc, K. W. G. and Asprey, K. W. (1991) 'Interlaboratory, interinstrument calibration experiment', in Syvitski, J. P. M. (ed.) *Principles, Methods and Application of Particle Size Analysis*. Cambridge, UK: Cambridge University Press, pp. 174–193.

Talwani, M. and Reif, C. (1998) 'Laxmi Ridge - A continental sliver in the Arabian Sea', *Marine Geophysical Researches*, 20(4), pp. 259-271.

Terry, R. D. and Chilingar, G. V. (1955) 'Summary of "Concerning some additional aids in studying sedimentary formations," by M. S. Shvetsov', *Journal of Sedimentary Research*, 25, pp. 229-234.

Terzaghi, K. (1925) *Erdbaumechanik auf bodenphysikalischer Grundlage*. Liepzig, Vienna.

Thommes, M. and Cychosz, K. A. (2014) 'Physical adsorption characterization of nanoporous materials: progress and challenges', *Adsorption-Journal of the International Adsorption Society*, 20(2-3), pp. 233-250.

Tovey, N. K., Smart, P., Hounslow, M. W. and Leng, X. L. (1992) 'Automatic orientation mapping of some types of soil fabric', *Geoderma*, 53(3), pp. 179-200.

Uchman, A. and Wetzel, A. (2011) 'Chapter 8 - Deep-Sea Ichnology: The Relationships Between Depositional Environment and Endobenthic Organisms', in Hüneke, H. and Mulder, T. (eds.) *Developments in Sedimentology*. Elsevier, pp. 517-556.

Udden, J. A. (1914) 'Mechanical composition of clastic sediments', *Geological Society of America Bulletin*, 25(1), pp. 655-744.

Uruski, C. I. (2012) '14 - Deepwater frontier basins: New Zealand A2 - Roberts, D.G', in Bally, A. W. (ed.) *Regional Geology and Tectonics: Phanerozoic Passive Margins, Cratonic Basins and Global Tectonic Maps*. Boston: Elsevier, pp. 486-532.

Van Olphen, H. (1963) *An Introduction to Clay Colloid Chemistry*. Interscience, New York.

Vandeginste, V. and John, C. M. (2013) 'Diagenetic implications of stylolitization in pelagic carbonates, Canterbury Basin, offshore New Zealand', *Journal of Sedimentary Research*, 83(3), pp. 226-240.

Viana, A. R., Almeida, W., Nunes, M. C. V. and Bulhões, E. M. 276 (2007) 'The economic importance of contourites' [Article]. London: Geological Society Special Publication, pp. 1-23.

Wang, F. P., Reed, R. M., John, A. and Katherine, G. (2009) 'Pore networks and fluid flow in gas shales', in *SPE Annual Technical Conference and Exhibition*. ociety of Petroleum Engineers, pp. 1550-1557.

Wang, Y., Zhu, Y., Chen, S. and Li, W. (2014) 'Characteristics of the Nanoscale Pore Structure in Northwestern Hunan Shale Gas Reservoirs Using Field Emission Scanning Electron Microscopy, High-Pressure Mercury Intrusion, and Gas Adsorption', *Energy & Fuels*, 28(2), pp. 945-955.

Wang, Z. and Krupnick, A. (2013) 'A Retrospective Review of Shale Gas Development in the United States: What Led to the Boom?', *Resources for the Future DP*, pp. 1-39.

Weaver, C. E. (1980) 'Fine-grained rocks: Shales or physilites', *Sedimentary Geology*, 27(4), pp. 301-313.

Wenk, Voltolini, Mazurek, Loon, V. L. R. and Vinsot (2008a) 'Preferred Orientations and Anisotropy in Shales: Callovo-Oxfordian Shale (France) and Opalinus Clay (Switzerland)', *Clays and Clay Minerals*, 56(3), pp. 285-306.

Wenk, H.-R., Voltolini, M., Kern, H., Popp, T. and Mazurek, M. (2008b) 'Anisotropy in shale from Mont Terri', *The Leading Edge*, 27(6), pp. 742-748.

Wenk, H. R., Lutterotti, L., Kaercher, P., Kanitpanyacharoen, W., Miyagi, L. and Vasin, R. (2014) 'Rietveld texture analysis from synchrotron diffraction images. II. Complex multiphase materials and diamond anvil cell experiments', *Powder Diffraction*, 29(3), pp. 220-232.

Wentworth, C. K. (1922) 'A scale of grade and class terms for clastic sediments', *The Journal of Geology*, 30, pp. 377-392.

Wetzel, A. and Uchman, A. (2012) 'Chapter 22 - Hemipelagic and Pelagic Basin Plains', in Knaust, D. and Bromley, R. G. (eds.) *Developments in Sedimentology*. Elsevier, pp. 673-701.

Wetzel, A., Werner, F. and Stow, D. A. V. (2008) 'Chapter 11 Bioturbation and Biogenic Sedimentary Structures in Contourites', in Rebesco, M. and Camerlenghi, A. (eds.) *Developments in Sedimentology*. Elsevier, pp. 183-202.

Wierzchos, J., Ascaso, C., Garciagonzalez, M. T. and Kozak, E. (1992) 'A new method of dehydration for pure clay materials using Peldri II', *Clays and Clay Minerals*, 40(2), pp. 230-236.

Wilkinson, S. and Fenton, C. (2015) 'The Influence of Geological History on Preferred Particle Orientation and the Observed Anisotropy of Over Consolidated UK Mudrocks', in Lollino, G., Giordan, D., Thuro, K., Carranza-Torres, C., Wu, F., Marinos, P. and Delgado, C. (eds.) *Engineering Geology for Society and Territory - Volume 6*. Springer International Publishing, pp. 805-808. 144.

Wirth, R. (2009) 'Focused Ion Beam (FIB) combined with SEM and TEM: Advanced analytical tools for studies of chemical composition, microstructure and crystal structure in geomaterials on a nanometre scale', *Chemical Geology*, 261(3–4), pp. 217-229.

Wu, K., Jiang, Z., Couples, G., Van Dijke, M. and Sorbie, K. (2007) 'Reconstruction of multi-scale heterogeneous porous media and their flow prediction', in *International Symposium of the Society of Core Analysts, Calgary, Canada*.

Wu, K., Van Dijke, M. I. J., Couples, G. D., Jiang, Z., Ma, J., Sorbie, K. S., Crawford, J., Young, I. and Zhang, X. (2006) '3D Stochastic Modelling of Heterogeneous Porous Media – Applications to Reservoir Rocks', *Transport in Porous Media*, 65(3), pp. 443-467.

Yang, F., Ning, Z. F. and Liu, H. Q. (2014) 'Fractal characteristics of shales from a shale gas reservoir in the Sichuan Basin, China', *Fuel*, 115, pp. 378-384.

Yang, Y. and Aplin, A. C. (2007) 'Permeability and petrophysical properties of 30 natural mudstones', *Journal of Geophysical Research: Solid Earth*, 112(3).

Yang, Y. and Aplin, A. C. (2010) 'A permeability–porosity relationship for mudstones', *Marine and Petroleum Geology*, 27(8), pp. 1692-1697.

Yu, C. Y., Chow, J. K. and Wang, Y.-H. (2016) 'Pore-size changes and responses of kaolinite with different structures subject to consolidation and shearing', *Engineering Geology*, 202, pp. 122-131.

Zaitoun, N. M. and Aqel, M. J. (2015) 'Survey on Image Segmentation Techniques', *Procedia Computer Science*, 65(Supplement C), pp. 797-806.

Zhang, P., Hu, L., Meegoda, J. N. and Gao, S. (2015) 'Micro/Nano-pore Network Analysis of Gas Flow in Shale Matrix', *Scientific Reports*, 5, pp. 1-11.

Zhao, X. B. (1998) 'Measurement and calculation of three-dimensional grain sizes and size distribution functions', *Microscopy and Microanalysis*, 4(04), pp. 420-427.

Zitellini, N., Gràcia, E., Matias, L., Terrinha, P., Abreu, M. A., DeAlteriis, G., Henriet, J. P., Dañobeitia, J. J., Masson, D. G., Mulder, T., Ramella, R., Somoza, L. and Diez, S. (2009) 'The quest for the Africa–Eurasia plate boundary west of the Strait of Gibraltar', *Earth and Planetary Science Letters*, 280(1–4), pp. 13-50.